Mathematical Modelling of the Drilling Process for Real-time Applications in Drilling Simulation, Interpretation and Assistance

by

Eric Cayeux

Thesis submitted in fulfilment of
the requirements for the degree of
DOCTOR PHILOSOPHIAE
(Dr. Philos.)

University of
Stavanger

Faculty of Science and Technology
Department of Petroleum Engineering
2019

University of Stavanger
N-4036 Stavanger
Norway
www.uis.no

ISBN: 978-82-7644-913-6
ISSN:1890-1387
PhD: Thesis UiS No. 506

Preface

This thesis is submitted for the degree of Doctor Philosophiae (Dr. Philos.) within Petroleum Technology at the Department of Petroleum Engineering, University of Stavanger, Norway.

The background work that has been conducted for the preparation of this thesis, has been motivated by the desire to contribute with new directions and solutions to the problem of automatic drilling interpretation and assistance. This research question is very complex, and it is believed that it requires the involvement of many disciplines including, albeit not exhaustively, drilling engineering, physics, applied mathematics, cybernetics, software engineering and social sciences. Each of these fields of study have their own methodologies and utilize terminology and concepts, where the same words or expressions have precise, but sometime different definitions. It is therefore a perilous task to synthetize such a work without causing misinterpretations by readers having different perspectives on the topic. Therefore, it has been deliberately chosen to write this document with a standpoint that focuses solely on the use of physics and mathematical modelling methods applied to the drilling engineering domain (see Fig. 1).

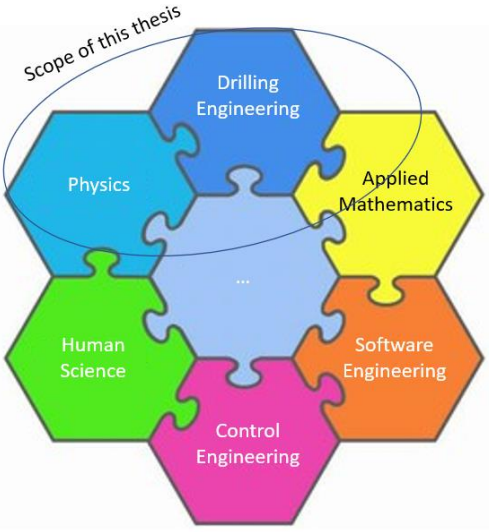

Fig. 1: Drilling automation involves multiple disciplines, yet the scope of this thesis is limited to the mathematical modelling of the drilling process for real-time applications in drilling simulation, interpretation and assistance.

This thesis consists of two parts. The first one presents a synthesis of the work performed to address the mathematical modelling of the drilling process for applications in the domain of real-time drilling simulation, interpretation and assistance. Part I has five chapters:

1. The introduction describes the general setting of the drilling process and standard drilling operations as well as classical drilling events. The organization of the drilling team is also succinctly described.
2. The state-of-the-art section presents known results on which the presented work is built upon.
3. Chapter 3 first explains the mathematical models that have been derived to support several real-time drilling applications. These models concern the drilling hydraulic and drill-string mechanic domains. Three types of real-time drilling applications are described: drilling simulator environment, drilling symptom detection and assistance to drilling control.
4. This chapter gives an overview of the associated published work.
5. Finally, a summary of the presented work is given, and future work directions are described.

As the number of attached papers in the second part of this thesis is limited to six, the first part of the thesis contains direct citations from other of my publications that are relevant for this thesis. Note that the citations of chapter 2 "State of the Art" do not claim that the exposed facts are my contributions: they are just citations from other own publications that were exposing relevant state of the art descriptions.

The second part consists of the following six papers:

Paper I Cayeux, E., Daireaux, B., Dvergsnes, E.W., Leulseged, A., Bruun, B. T., Herbert, M.: *Advanced Drilling Simulation Environment for Testing New Drilling Automation Techniques and Practices.* SPE-150941-PA, published in SPE Drilling & Completion Journal, Volume 27, Number 4, December 2012, pp. 559-573.

Paper II Cayeux, E., Mesagan, T., Tanripada, S., Zidan, M., Fjelde, K.K.: *Real-Time Evaluation of Hole Cleaning Conditions Using a Transient Cuttings Transport Model*. SPE-163492-PA. Published in SPE Drilling and Completion, Volume 29, Number 1, 2014, pp. 5-21.

Paper III Cayeux, E., Daireaux, B., Dvergsnes, E. W., Sælevik, G.: *Early Symptom Detection Based on Real-Time Evaluation of Downhole Conditions: Principles and Results from several North Sea Drilling Operations*. SPE-150422-PA, published in SPE Drilling & Completion Journal, Volume 27, Number 4, December 2012, pp. 546-558.

Paper IV Cayeux, E., Kucs, R., Gibson, N.: *Mathematical Modeling of Drilling Operations by Use of Nitrogen-Enriched Mud: A Case Study by Use of a Recorded Drilling Data-Set*. SPE 167884-PA. Published in SPE Drilling & Completion, Volume 29, Number 4, 2014, pp. 438-453.

Paper V Cayeux, E., Daireaux, B. and Dvergsnes, E. W.: *Automation of Mud-Pump Management Application to Drilling Operations in the North-Sea*. SPE-128285-PA, published in SPE Drilling & Completion Journal, Volume 26, Number 1, March 2011, pp. 41-51.

Paper VI Cayeux, E., Daireaux, B. and Dvergsnes, E. W.: *Automation of Draw-works and Top-drive Management to Minimize Swab/Surge and Poor-Downhole-Condition Effects*. SPE-128286-PA, published in SPE Drilling & Completion Journal, Volume 26, Number 4, December 2011, pp. 557-568.

Summary

For the last thirty years, mathematical modelling has been used to develop software solutions that support drilling engineering activities at the planning stage of drilling operations. But it is only for the last decade that mathematical models have been used for the real-time support of drilling operations.

Moving from a pure engineering perspective to having models that can respect real-time requirements, necessitates many improvements of the subjacent mathematical modelling of the drilling process. First, it is not anymore possible to ignore transient behaviors that were somewhat irrelevant at the planning stage. Second, there is a need for solutions that should be fast enough to cope with the real-time constraints of the drilling process.

With the perspective of creating applications that can support the drilling process in real-time, the following mathematical models have been developed:

- Drilling fluid behavior. The properties of drilling fluids depend on their composition and pressure-temperature conditions. For instance, the pressure-temperature dependence of the mass density of drilling fluids, depends on the individual PVT-properties (Pressure-Volume-Temperature) of each of the components and their relative volume fractions. Therefore, the addition of drill-cuttings in the drilling fluid also changes the drilling fluid PVT-behavior. Furthermore, the rheological behavior of drilling fluids depends also on its composition. We have found that the rheological behavior of a KCl/polymer water-based mud is simultaneously modified by the relative proportion of barite and sand. Furthermore, it is known that drilling fluids are thixotropic. Yet, we found that the thixotropic behavior of drilling fluids is different from the one of other thixotropic fluids and we have determined that one of the causes for the discrepancy is related to the presence of solids in the fluid mix. We have developed a method to estimate the rheological behavior and its associated uncertainty, as a function of the modification of the solid proportions.
- Drill-string mechanical sub-models coupled with hydraulic effects. Hydraulic pressure has also an impact on drill-string mechanical forces not only because the fluid mass density modifies buoyancy but more generally because viscous pressure gradients generate net forces along the drill-string. These hydraulic related forces are superposed to those engendered by mechanical friction and elastic deformation.
- Steady state and transient drill-string mechanical models. Steady state torque and drag models utilizing the above-mentioned drill-string mechanical sub-models can be used to assess some characteristics of the drilling process when constant velocities are prevalent. But, during a drilling operation, there are many moments during which the drill-

string displacement is in transient mode. Therefore, it is also important to have access to transient torque and drag models with a fast response time.

- Transient cuttings transport model. The transport of cuttings is obviously influenced by hydraulic circulation but also drill-string rotational speed, at least in the deviated parts of a well. On the other hand, the presence of drill-cuttings in suspension or settling on the low-side of the borehole, influences pressure losses and mechanical forces along the drill-string. Therefore, the estimation of the transient displacement of drill-cuttings plays an important role in the overall estimation of the actual drilling conditions during a drilling operation. However, a transient cuttings transport model shall also be sufficiently fast, especially when it is used in real-time applications.

Equipped with such models of the drilling process that are compatible with real-time constraints, then it is possible to solve problems that are relevant for the assistance of drilling operations.

A first domain of application is related to the estimation, in real-time, of surface and downhole sensor values as a function of external commands like the block position and speed, the top-drive rotational velocity and the pump rates. We will refer to this domain of application as “drilling simulation”. However, comparison of measured values with simulated ones, require the proper modelling of the sensors and the impact of their actual position on the readings. For instance, drilling fluid is retained in the flowline and mud treatment equipment. Therefore, to simulate pit volumes, it is important to model the retention mechanism.

Transient hydraulic, mechanical and heat transfer models, associated with precise modelling of sensor measurements, can then be used to interpret the current actual drilling conditions, because if their estimated parameters differ from the measurements, then a possible reason is that something unexpected is happening downhole. However, such drilling symptom detection method necessitates two additional conditions to be fulfilled:

- The models shall be calibrated. Regardless of the quality of the drilling models, the inputs to these models are always known with a limited degree of accuracy and therefore their outputs may differ from measurements for that simple reason. However, it is important to distinguish between uncertainties that are related to properties that do not change substantially during a given drilling operation, from those that can change at any time. To avoid influencing the calibration of time invariant properties with possible side effects of the deterioration of the drilling condition, it is important to utilize drilling conditions by

which undesirable side effects have no or little influence on the measurements that are used to calibrate the property.

- Uncertainty of the modelled outputs shall be estimated. Calibration may reduce the uncertainty on the model outputs, but it does not eliminate it completely. It is therefore important to estimate the uncertainty of the predicted values. To achieve this, it is necessary to capture the precision by which the inputs of the process are known and to propagate that uncertainty throughout the modelling of the outputs.

With continuously calibrated models and an estimation of the current downhole conditions, then it is possible to address some preliminary drilling process assistance functions:

- Safety triggers. During the execution of automation functions, the situation awareness of the driller is reduced as he does not drive the drilling machines himself. Therefore, it shall not be attempted to automate any functions before a minimum set of protection functions are in place. Such safety triggers shall detect and react to incidents related to the axial and rotational movement of the drill-string and, of course, associated with pressure. Example of such safety triggers are:
    - Reactions to overpulls and set-down weights.
    - Reactions to abnormal torques.
    - Reactions to abnormal pressures.
- Safeguards. Any drill-string or drilling fluid movements shall not generate a drilling incident. Therefore, commands to the drilling machines shall be kept within safe operational envelopes. For instance, upward movement of the drill-string shall not decrease the downhole pressure below the pore pressure or the collapse pressure of the open hole formations. Similarly, the applied flowrate combined with a possible downward movement and rotation of the drill-string shall not overpass the fracturing pressure of open hole formation rocks.
- Automated procedures. Protected by safety triggers and operating within acceptable safeguards, then it is possible to automate some standard procedures. However, such automatic procedures must continuously be adapted to the current drilling conditions. For instance, the length of a friction must be modified to account for the current drill-string length and mechanical friction, or the flowrate applied during the ream-down sequence of a reciprocation procedure shall be reduced as a function of the current potential surging risk.

Acknowledgements

The presented work has been developed through several research projects.

The first one is DrillTronics, funded by Equinor, ENI and BP. I would like to thank Fionn Iversen, the project leader of that project, for steering the project through its various phases of development. Many people from Equinor, ENI and BP have had a great influence on the DrillTronics project, but I would like to address a particular thank to Arne Torsvoll from Equinor who has played a key role in constantly supporting the project, even when its outcome was still unclear.

During the offshore test of DrillTronics, I have met extremely interesting and professional people from both Equinor and SeaWell. Their open-minded attitude and positive feedback have been very important for the success of the project. I am particularly grateful to Hans Freddy Larsen and Roald Kluge, both from Equinor, for their support during the testing of DrillTronics on Statfjord C.

The automatic detection of drilling symptoms, DrillScene, and the virtual rig has been developed during the eLAD project (e-Laboratory for Automated Drilling). I would like to thank Mohsen Balov from Equinor for the essential role that he played when following up the eLAD project. Mona Wahlen was the project leader of eLAD. She opened my mind on the importance of people and organization when introducing new technologies, and for that reason I am very thankful.

Lately, most of my publications have been conducted through the project "P1.3 Drilling Process Optimization" financed by the DrillWell center headed by Sigmund Stokka. During many years, Sigmund has been a sparring partner for many of my new ideas and thoughts. It is always reassuring to know that Sigmund will ask the right questions and help formulating the best solutions. Thank you very much for all the assistance that you have provided me during these brain storming sessions.

Through many meetings, I have had the pleasure to get guidance by Bjørn Rudshaug and Halvor Kjørholt from Equinor on the most relevant research directions applicable to the automation of the drilling process.

Thanks to all my colleagues at NORCE, and especially the Drilling and Well Modelling group. Thank you for sharing your knowledge and for all the fruitful discussions we have had.

A particular thank to Jan Einar Gravdal who suggested to summarize in a thesis the research that I had done on drilling automation.

I would also like to thank the NORCE management team for supporting me through this adventure and especially Helga Gjeraldstveit, the research director of the Drilling and Well Modelling group, who has provided invaluable help in managing the research group activities and support to all my initiatives.

Fifteen years ago, Anna Aabø offered me a position as a research scientist at IRIS (now NORCE). That has been the start of this journey of the automation of the drilling process. Since then, I have had the chance to dig deeper and deeper in the arcane of drilling. Now, I realize that I understand less than I thought when I started as it revealed to be ever more complex by every problem that I tried to solve. But I enjoyed every single step of that adventure. Thank you, Anna, for giving me this opportunity.

My closest colleagues during most of my research career are of course Benoît Daireaux and Erik Dvergsnes, but also Amare Leulseged and Hans Joakim Skadsem, and not surprisingly they are co-authors on many of my publications. Together we make a very effective team. We are complementary but at the same time we share a common way of thinking and a joint interest in solving problems and better understand the nature of physical phenomenon. They have been instrumental partners of the research presented in this thesis.

Last but not least, I would like to thank my wife Jane Kirsten and children, Sandra, David and Alexanna. I am forever thankful for your patience and encouragement while I was working on those projects and preparing this thesis.

Stavanger, 2019 Eric Cayeux

Contents

1 INTRODUCTION 1

2 STATE OF THE ART 11

2.1 REAL-TIME ESTIMATION OF THE INTERNAL STATE 12

2.1.1 Drilling Hydraulic 12

2.1.1.1 Motivation for Transient Hydraulic Modelling: Combined Effects of Fluid Compressibility and Viscous Behavior 12

2.1.1.2 Motivation for Transient Hydraulic Modelling: Barite Sag 13

2.1.1.3 Drilling Hydraulic Network 14

2.1.1.4 Pressure and Temperature Dependence of Drilling Fluid Densities 17

2.1.1.5 Pressure Losses in Concentric Annuli 21

2.1.1.6 Pressure Losses in Eccentric Annuli 25

2.1.1.7 Pressure Losses in Annuli with Rotation of the Inner Pipe 27

2.1.1.8 Pressure Losses in Annuli with Axial Movement of the Inner Pipe 29

2.1.1.9 Pressure Losses in Annuli Across Tool-joint 30

2.1.1.10 Pressure Losses in Tubulars 31

2.1.1.11 Pressure Losses through Measurement While Drilling Tools and Bits 32

2.1.1.12 Pressure and Temperature Dependence of Rheological Behavior 33

2.1.1.13 Gel Strength 34

2.1.1.14 Thixotropy in Viscous Flow 34

2.1.1.15 Effect of Thixotropy on Rheological Behavior after a Gelled Period 39

2.1.1.16 Condition to Suspend Cuttings in Gelled Condition 41

2.1.1.17 Cuttings Slip Velocity in near Vertical Annuli 41

2.1.1.18 Apparent Fluid Viscosity in the Presence of Solid Particles 43

2.1.1.19 Cuttings Bed and Critical Transport Velocity 46

2.1.1.20 Cuttings Carrying Index 46

2.1.1.21 Cuttings Particle Size Distribution 47

2.1.1.22 Transient Hydraulic Pressure Loss Calculation for a Multi-components and Multi-phases Flow 49

2.1.1.23 Hydraulic Network 51

2.1.2 Drill-string Mechanics 52

2.1.2.1 Motivation for Coupling Mechanical Evaluations with Hydraulic Calculations 53

2.1.2.2 Motivation for Utilizing Transient Mechanical Estimations 54

2.1.2.3 Mechanical Friction 58

2.1.2.4 Friction Force between a Tube in Continuous Contact with the Borehole 62

2.1.2.5 Influence of Temperature and Pressure on Pipe Length 63

2.1.2.6 Modelling of Torsional Motion 64
2.1.2.7 Modelling of Axial Motion 68
2.1.2.8 Modelling of Coupled Rotational and Axial Motion 72
2.1.3 Heat Transfer 75
2.1.4 Wellbore Position, Uncertainty and Tortuosity 79
2.2 DRILLING SIMULATORS 83
2.3 SYMPTOM DETECTION 84
2.3.1 Quick Event Detection 84
2.3.1.1 Gain/loss Detection 84
2.3.1.2 Abnormal Pump Pressure 89
2.3.1.3 Overpull/Set-down Weight Detection 91
2.3.1.4 Abnormal Torque Detection 93
2.3.2 Pre-event Detection 94
2.3.2.1 Torque and Drag Charts 94
2.3.2.2 Methods Based on the Analysis of a Combination of Signals 95
2.4 ASSISTANCE TO THE CONTROL OF DRILLING MACHINES 98

3 MATHEMATICAL MODELLING AND REALTIME DRILLING APPLICATIONS 101

3.1 DRILLING HYDRAULIC 101
3.1.1 Mass Density of a Fluid Mix 102
3.1.1.1 Mass Density Based on Fluid Mixing Sequence 103
3.1.1.2 Determination of HGS Concentration Based on Composition and Density Measurement 105
3.1.1.3 Resulting Mass Density when Mixing Two Fluids 107
3.1.1.4 Summary 108
3.1.2 Impact of Time on Rheometer Measurements 108
3.1.2.1 Summary 120
3.1.3 Impact of Solid Particles in Suspension on Drilling Fluid Rheology 120
3.1.3.1 Influence of Sand Particles on the Apparent Rheological Behavior of an Unweighted KCl/Polymer WBM 120
3.1.3.2 Influence of Barite Concentration on the Apparent Rheological Behavior of an KCl/Polymer WBM 127
3.1.3.3 Max Packing Concentration of a Mix of Sorted Sand and Barite 131
3.1.3.4 Apparent Rheological Behavior for a KCl/Polymer WBM in the Presence of Barite and Monodispersed Sand Particles 133
3.1.3.5 Summary 137
3.1.4 Transient Cuttings Transport 138
3.1.4.1 Cuttings Slips Velocity in Inclined Annuli 138

3.1.4.2 Particle Settling and Change of Particle Size Distribution 146
3.1.4.3 Transformation of the Cuttings PSD by Grinding 154
3.1.4.4 Summary 155
3.2 DRILL-STRING MECHANICS 156
3.2.1 Decomposition of the Drill-string 156
3.2.2 Transient Solver 158
3.2.3 Mechanical Friction 161
3.2.4 Forces Related to Viscous Flow 169
3.2.5 Boundary Condition at the Bit 177
3.2.6 Effect of Solid Particle Grinding on Torque 181
3.2.7 Summary 186
3.3 DRILLING SIMULATION 186
3.3.1 Retention Inside Return Flowline 187
3.3.2 Flow in the Solid Control Equipment 192
3.3.3 Calculation of the Volume in the Pit 196
3.3.4 Summary 198
3.4 DRILLING INTERPRETATION 199
3.4.1 Estimation of Uncertainty of Drilling Fluid PVT Behavior 199
3.4.1.1 Summary 201
3.4.2 Estimation of Uncertainty of Drilling Fluid Rheological Behavior .. 202
3.4.2.1 Summary 207
3.4.3 Impact of Wellbore Position Uncertainty on Geo-pressure Margins 208
3.4.3.1 Estimation of Vertical Depth Uncertainty Caused by Wellbore Position Uncertainty 208
3.4.3.2 Geo-Pressure Margin Uncertainties 211
3.4.3.3 Summary 214
3.4.4 State Estimation of the non-Holonomic Drilling Process 215
3.4.4.1 Summary 219
3.4.5 Global Calibration of Ill-defined Configuration Information 220
3.4.5.1 Summary 223
3.4.6 Calibration of non-Constant Drilling Process Parameters 223
3.4.6.1 Estimation of Static and Kinetic Frictions 224
3.4.6.2 Estimation of Annulus Hydraulic Friction Correction Factor 227
3.4.6.3 Estimation of the Bit Aggressivity and Formation Strength 229
3.4.6.4 Summary 231
3.4.7 Accuracy of Pressure, Tension and Torque Estimations 231
3.4.7.1 Summary 233
3.4.8 Integration of Distributed Measurements to Improve Estimation Accuracy 233

3.4.8.1 Summary 236
3.4.9 Closest Approach for Downhole Pressure Proximity to Geo-pressure Margins 236
3.4.9.1 Summary 239
3.4.10 Early Detection of the Deterioration of the Drilling Conditions . 239
3.4.10.1 Summary 243
3.5 DRILLING ASSISTANCE 243
3.5.1 Fault Detection Isolation and Recovery 246
3.5.1.1 Overpull and Set-down Weight Detection and Reaction 247
3.5.1.2 Top-drive Over-torque Detection and Reaction 249
3.5.1.3 Pump Overpressure Detection and Reaction 252
3.5.1.4 Summary 260
3.5.2 Safe Operation Envelope 261
3.5.2.1 Maximum flowrate in steady state circulation 262
3.5.2.2 Minimum Duration for Breaking Circulation 264
3.5.2.3 Maximum Mud Pump Acceleration 267
3.5.2.4 Swab & Surge Safe Operation Envelope 271
3.5.2.5 Summary 275
3.5.3 Automation of Drilling Procedures 276
3.5.3.1 Pump Startup 276
3.5.3.2 Friction Test 281
3.5.3.3 Reciprocation 284
3.5.3.4 Summary 288
4 OVERVIEW OF PUBLISHED WORK 289
4.1 PUBLICATIONS RELATED TO DRILLING SIMULATION 291
4.1.1 Paper I: Advanced Drilling Simulation Environment for Testing New Drilling Automation Techniques and Practices 291
4.1.2 Paper II: Real-Time Evaluation of Hole Cleaning Conditions Using a Transient Cuttings Transport Model 292
4.2 PUBLICATION RELATED TO DRILLING INTERPRETATION 292
4.2.1 Paper III: Early Symptom Detection Based on Real-Time Evaluation of Downhole Conditions: Principles and Results from several North Sea Drilling Operations 292
4.2.2 Paper IV: Mathematical Modeling of Drilling Operations by Use of Nitrogen-Enriched Mud: A Case Study by Use of a Recorded Drilling Data-Set 293
4.3 PUBLICATION RELATED TO DRILLING ASSISTANCE 293

4.3.1 Paper V: Automation of Mud-Pump Management Application to Drilling Operations in the North-Sea *293*
4.3.2 Paper VI: Automation of Draw-works and Top-drive Management to Minimize Swab/Surge and Poor-Downhole-Condition Effects *294*

5 CONCLUSION **295**

5.1 FUTURE WORK 298

6 BIBLIOGRAPHY **303**

A ABSOLUTE VOLUME FRACTION OF A COMPONENT IN A FLUID MIX 323

B EFFECT OF SAND PARTICLES CONCENTRATION AND SIZE ON THE RHEOLOGICAL BEHAVIOR OF AN UNWEIGHTED WBM **324**

C EFFECT OF BARITE CONCENTRATION ON THE RHEOLOGICAL BEHAVIOR OF A WBM **336**

D EFFECT OF SAND PARTICLE CONCENTRATION ON THE RHEOLOGICAL BEHAVIOR OF A WEIGHTED WBM **338**

PAPER I **347**

PAPER II **365**

PAPER III **385**

PAPER IV **399**

PAPER V **417**

PAPER VI **429**

Nomenclature

List of Abbreviations

AC	Alternate Current
API	American Petroleum Institute
BHA	Bottom Hole Assembly
BOP	Blow-Out Preventer
CCI	Cuttings Carrying Index
CCS	Confined Compressive Strength
CFD	Computational Fluid Dynamic
CFL	Courant–Friedrichs–Lewy
CPG	Collapse Pressure Gradient
CRT	Casing Running Tool
CSFV	Critical Settling Fluid Velocity
CTFV	Critical Transport Fluid Velocity
DC	Drill-Collar
DCS	Drilling Control System
DGD	Dual Gradient Drilling
DOC	Drill Out Cement
DOF	Degree Of Freedom
ECD	Equivalent Circulating Density
EMW	Equivalent Mud Weight
ERD	Extended Reach Drilling
ESD	Equivalent Static Density
FBCT	Flow-Back Circulating Tool
FDIR	Fault Detection Isolation and Recovery

FIT	Formation Integrity Test
FPG	Fracturing Pressure Gradient
FRT	Free Rotating Torque
FRW	Free Rotating Weight
HFTO	High Frequency Torsional Oscillations
HGS	High Gravity Solid
HPHT	High-Pressure High-Temperature
HWDP	Heavy Weight Drill-Pipe
iBOP	Internal Blow Out Preventer
ID	Internal Diameter
IWCF	International Well Control Forum
KOP	Kick-Off Point
LCM	Loss Circulation Material
LGS	Low Gravity Solid
LOT	Leak-Off Test
LWD	Logging While Drilling
MP	Mud Pump
MPD	Managed Pressure Drilling
MRU	Motion Reference Unit
MSE	Mechanical Specific Energy
MW	Mud Weight
MWD	Measurement While Drilling
NPT	Non-Productive Time
OBG	Over Burden pressure Gradient
OBM	Oil Based Mud

PDM	Positive Displacement Motor
PID	Proportional-Integral-Derivative
POOH	Pull Out Of Hole
PSD	Particle Size Distribution
PUW	Pick-Up Weight
PVT	Pressure Volume Temperature
PWD	Pressure While Drilling
PPG	Pore Pressure Gradient
RCD	Rotating Control Device
RIH	Run In Hole
RMS	Root Mean Square
ROC	Rate Of Change
ROP	Rate Of Penetration
RSS	Rotary Steerable System
SCR	Silicon Control Rectifier
SOE	Safe Operating Envelope
SOW	Slack-Off Weight
SWOB	Surface Weight On Bit
TD	Top-Drive
TD	Total Depth
TTRD	Through Tubing Rotary Drilling
TVD	True Vertical Depth
TVT	True Vertical Thickness
VFD	Variable Frequency Drive
WBM	Water Based Mud

WOB	Weight On Bit
XLOT	eXtended Leak-Off Test

List of symbols

$1_{\delta_p, d_s}$ indicator function that a particle of equivalent diameter d_s has travelled the distance δ_p in a finite time [dimensionless]

A parameter of the Robertson-Stiff model [$ML^{-1}T^{B-2}$](Pa.s^B)

$A_\perp$ cross-sectional area [L^2](m^2)

A_0 cross-section area calculated with the outer diameter of a pipe [L^2](m^2)

A_{bit} bit area [L^2](m^2)

A_c cuttings bed area [L^2](m^2)

A_{fl_i} cross sectional area of the fluid in section i [L^2](m^2)

$A_{fluidized}$ cross-sectional area of the fluidized layer of a cuttings bed [L^2](m^2)

A_i cross-sectional area calculated with the inner diameter of a pipe [L^2](m^2)

$A_{i,s}$ cross-sectional area at position i [L^2](m^2)

A_o parameter of the base-oil PVT model [ML^{-3}](kg/m^3)

$A_{orifice}$ total flow area [L^2](m^2)

A_p area of the horizontal projection of a particle [L^2](m^2)

$A_{pi,i}$ area of the inside of the pipe body of element i [L^2](m^2)

$A_{po,i}$ area of the outside of the pipe body of element i [L^2](m^2)

A_{screen} area of the shale shaker screen [L^2](m^2)

$A_{tji,i}$ area of the inside of a tool-joint of element i [L^2](m^2)

$A_{tjo,i}$ area of the outside of a tool-joint of element i [L^2](m^2)

$A_{\dot{\gamma}}$ fitting coefficient for pressure and temperature dependence of shear stress [$ML^{-1}T^{-2}$](Pa)

$A_{\Phi_{sb}}$ parameter of the empirical model describing the maximum packing concentration of a mix of barite and sand [dimensionless]

a exponent in the Mewis and Wagner formulation of the flocculation function [dimensionless]

$\vec{a}$ acceleration [LT^{-2}](m/s^2)

a_b max braking acceleration [LT^{-2}](m/s^2)

a_{max} maximum acceleration while moving axially a stand [LT^{-2}](m/s^2)

a_u semi-axis of the wellbore position uncertainty in the X-direction of coordinate system passing through the axes of the ellipsoid [L](m)

B parameter of the Robertson-Stiff model (dimensionless)

B_o parameter of the base-oil PVT model [$ML^{-3}\vartheta^{-1}$]($kg/(m^3K)$)

B_w parameter of the brine density model [$ML^{-3}\vartheta^{-1}$]($kg/(m^3K)$)

$B_{\dot{\gamma}}$ fitting coefficient for pressure and temperature dependence of shear stress [ϑ^{-1}](K^{-1})

$B_{\Phi_{sb}}$ parameter of the empirical model describing the maximum packing concentration of a mix of barite and sand [dimensionless]

b exponent in the Mewis and Wagner formulation of the flocculation function [dimensionless]

$\hat{b}$ unit binormal vector in the Frenet-Serret coordinate system [dimensionless]

b_b component of the binormal vector of the Frenet-Serret coordinate system attached to the fluid flow in the $\hat{b}_s$ direction [dimensionless]

$\hat{b}_f$ normal unit vector of the Frenet-Serret coordinate system attached to the fluid flow [dimensionless]

b_n component of the binormal vector of the Frenet-Serret coordinate system attached to the fluid flow in the $\hat{n}_s$ direction [dimensionless]

$\hat{b}_p$ binormal unit vector in a coordinate system attached to a particle [dimensionless]

$\hat{b}_s$ normal unit vector of the spherical coordinate system attached to a borehole cross-section [dimensionless]

b_t component of the binormal vector of the Frenet-Serret coordinate system attached to the fluid flow in the $\hat{t}_s$ direction [dimensionless]

C parameter of the Robertson-Stiff model [T^{-1}](s^{-1})

$\vec{C}$ torque [ML^2T^{-2}](m.N)

C_B Bond grinding coefficient [$L^{5/2}T^{-2}$]($Jm^{½}/kg$)

C_{bob} torque on the bob of a Couette rheometer [ML^2T^{-2}](m.N)

C_{crit} impact of critical fluid velocity on CCI [dimensionless]

C_D drag coefficient [dimensionless]

C_{ecc} correction factor from concentric to eccentric configuration [dimensionless]

$C_{G",i}$ torque originating from the loss component of the complex shear modulus at element i [ML^2T^{-2}](Nm)

$\vec{C}_{i,j}$ jth torque source at element i [ML^2T^{-2}](Nm)

C_{incl} impact of hole inclination on CCI [dimensionless]

$\vec{C}_{i,\mu_k}$ kinetic friction torque at contact point i [ML^2T^{-2}](Nm)

$\vec{C}_{i,\mu_s}$ static friction torque at contact point i [ML^2T^{-2}](Nm)

C_K Kick grinding coefficient [L^2T^{-2}](J/kg)

C_L lift drag coefficient [dimensionless]

C_M pitch moment coefficient [dimensionless]

C_{nozzle} pressure loss constant for the flow through nozzles [L^4](m^4)

C_o parameter of the base-oil PVT model [$L^{-2}T^{-2}$]($kg/(m^3Pa)$)

$C_{p_{clean,j}}$ specific heact capacity of the cleaned fluid arriving at the pit at time step j [$L^2T^{-2}\,\vartheta^{-1}$](J/(kg.K))

C_{p_f} fluid specific heat capacity [$L^2T^{-2}\,\vartheta^{-1}$](J/(kg.K))

C_{p_i} specific heat capacity of component i in a fluid mix [$L^2T^{-2}\,\vartheta^{-1}$](J/(kg.K))

$C_{p_{tank,j}}$ specific heat capacity of the fluid contained in the tank at time step j [$L^2T^{-2}\,\vartheta^{-1}$](J/(kg.K))

C_R von Rittinger grinding coefficient [L^3T^{-2}](J.m/kg)

C_{rot} correction factor to account for pipe rotation [dimensionless]

C_{rpm} impact of eccentricity and rotational speed on CCI [dimensionless]

C_s Stokes drag coefficient [dimensionless]

C_{screen} conductance of the screen of a shale shaker [L](m)

C_{size} impact of particle size on CCI [dimensionless]

C_t torque [ML^2T^{-2}](Nm)

C_{tort} impact of borehole tortuosity on CCI [dimensionless]

C_{turb} impact of turbulent flow, on CCI [dimensionless]

C_{visc} impact of drilling fluid viscosity on CCI [dimensionless]

C_w parameter of the brine density model [$L^{-2}T^{-2}$](kg/(m^3Pa))

C_{xwd} pressure loss constant [L^4](m^4)

$C_{\dot{\gamma}}$ fitting coefficient for pressure and temperature dependence of shear stress [$M^{½}L^{-½}T^{-1}$]($Pa^{½}$)

C_{μ_k,μ_s} cost function of the calibration of the static and kinetic friction [dimensionless]

CCI cuttings carrying index [dimensionless]

CCS confined compressive strength [$ML^{-1}T^{-2}$](Pa)

c exponent in the Mewis and Wagner formulation of the flocculation function [dimensionless]

$\vec{c}$ external moment gradient (per unit length) [MLT^{-2}](N)

c_{ecc} critical transport fluid velocity's correction factor for eccentricity [dimensionless]

$c_{geo(D)}$ critical transport fluid velocity's correction factor for hole diameter [dimensionless]

$c_{geo(inc)}$ critical transport fluid velocity's second correction factor for hole inclination [dimensionless]

$c_{geo(PV)}$ critical transport fluid velocity's correction factor for drilling fluid's plastic viscosity [dimensionless]

$\vec{\bar{c}}_i$ averaged values of all inputs to the system over the time window $\left[t_{s_i}, t_{f_i}\right]$

c_{inc} critical transport fluid velocity's first correction factor for inclination [dimensionless]

c_{mwt} critical transport fluid velocity's correction factor for mud weight [dimensionless]

c_{nozzle} nozzle discharge coefficient [dimensionless]

c_{rpm} critical transport fluid velocity's correction factor for drill-string rotational speed [dimensionless]

c_{size} critical transport fluid velocity's correction factor for particle size [dimensionless]

D_{h_i} hydraulic diameter at section i [L](m)

$\overline{D}_{h_i}$ average hydraulic diameter between sections i and $i+1$ [L](m)

D_o parameter of the base-oil PVT model [$L^{-2}T^{-2}\vartheta^{-1}$](kg/($m^3$PaK))

D_u inverse covariance matrix of the wellbore position uncertainty in the local coordinate of the ellipsoid oriented by its axes [L^{-2}](m^{-2})

D_w parameter of the brine density model [$L^{-2}T^{-2}\vartheta^{-1}$](kg/($m^3$PaK))

$D_{\dot{\gamma}}$ fitting coefficient for pressure and temperature dependence of shear stress [$M^{½}L^{-½}T^{-1}$]($Pa^{½}$)

DLS_i curvature at position i [L^{-1}](rd/m)

d exponent in the Mewis and Wagner formulation of the flocculation function [dimensionless]

d_{bit} bit diameter [L](m)

d_{bl} lower bound of the particle diameter to apply the Bond grinding formula [L](m)

d_{bu} upper bound of the particle diameter to apply the Bond grinding formula [L](m)

d_{fl_i} depth of liquid in a flowline at section i [L](m)

d_{hyd} hydraulic diameter [L](m)

d_i internal diameter [L](m)

d_o outer pipe diameter [L](m)

d_p pipe diameter [L](m)

d_{pe} weighted average pipe diameter including the tool-joint [L](m)

d_s diameter of a solid particle [L](m)

$\bar{d}_s$ averaged solid particle diameter [L](m)

$\bar{d}_s^*$ normalized average sand particle diameter [dimensionless]

$\bar{d}_{s_m}$ maximum sand particle diameter [L](m)

d_{screen} mesh size for shale shaker screen [L](m)

d_{s_i} 80th percentile of the particle size on the input side of the grinding machine [L](m)

d_{s_o} 80th percentile of the particle size on the output side of the grinding machine [L](m)

d_{TJ} tool-joint diameter [L](m)

d_w wellbore diameter [L](m)

dp_{TJ} pressure loss across tool-joint [$ML^{-1}T^{-2}$](Pa)

$\left(\frac{dp}{ds}\right)_{axial\ velocity}$ pressure loss gradient in concentric configuration with account for the pipe axial velocity [$ML^{-2}T^{-2}$](Pa/m)

$\left(\frac{dp}{ds}\right)_{conc}$ pressure loss gradient in concentric configuration [$ML^{-2}T^{-2}$](Pa/m)

$\left(\frac{dp}{ds}\right)_{ecc}$ pressure loss gradient in eccentric configuration [$ML^{-2}T^{-2}$](Pa/m)

$\left(\frac{dp}{ds}\right)_{ecc+rot}$ pressure loss gradient in an eccentric configuration with drill-pipe rotation [$ML^{-2}T^{-2}$](Pa/m)

$\left(\frac{dp}{ds}\right)_{ecc+rot+ax}$ pressure loss gradient in an eccentric configuration with drill-pipe rotation and axial displacement [$ML^{-2}T^{-2}$](Pa/m)

E Young modulus [$ML^{-1}T^{-2}$](Pa)

E_{MS} mechanical specific energy per drilled volume [$ML^{-1}T^{-2}$](J/m^3)

E_o parameter of the base-oil PVT model [$L^{-1}M^{-1}T^{-4}$](kg/(m^3Pa^2))

E_w parameter of the brine density model [$L^{-1}M^{-1}T^{-4}$](kg/(m^3Pa^2))

$E_{\dot{\gamma}}$ fitting coefficient for pressure and temperature dependence of shear stress [$\vartheta ML^{-1}T^{-2}$](K.Pa)

e eccentricity [dimensionless](proportion)

F total mass flux [MT^{-1}](kg/s)

$\hat{F}$ mixed vector of forces and moments

F_a axial load [MLT^{-2}](N)

$F_b, \vec{F}_b$ buoyancy force [MLT^{-2}](N)

F_{bit} force on bit [MLT^{-2}](N)

$\widetilde{F}_{bit}$ averaged measured force on bit over a time window Δt_{ROP} [MLT^{-2}](N)

$\bar{F}_{bit}$ averaged estimated force on bit over a time window Δt_{ROP} [MLT^{-2}](N)

$\vec{F}_{\mathrm{Cyl}}$ force acting on a cylinder element [MLT^{-2}](N)

$F_D, \vec{F}_D$ drag force [MLT^{-2}](N)

$F_{E",i}$ axial force originating from the material loss component of the complex modulus on an element i [MLT^{-2}](N)

$\hat{F}_{FRW}$ estimated free rotating top of string force [MLT^{-2}](N)

$\vec{F}_{f,p}$ force exerted on fluid by pressure between two cross-sections [MLT^{-2}](N)

$F_g, \vec{F}_g$ gravitational force [MLT^{-2}](N)

$\vec{F}_{i,g}$ gravitational force at position i [MLT^{-2}](N)

$\vec{F}_{i,j}$ the jth net force applied to element i [MLT^{-2}](N)

$\vec{F}_{i,n}$ normal force at position i [MLT^{-2}](N)

$F_{i,\mu}$ Stribeck friction force at a contact point i [MLT^{-2}](N)

$\vec{F}_{i,\mu_k}$ kinetic friction force at a contact point i [MLT^{-2}](N)

$\vec{F}_{i,\mu_s}$ static friction force at a contact point i [MLT^{-2}](N)

$\vec{F}_L$ lift force [MLT^{-2}](N)

F_o parameter of the base-oil PVT model [$L^{-1}M^{-1}T^{-4}\vartheta^{-1}$](kg/($m^3Pa^2K$))

F_{tos} force at the top of the string [MLT^{-2}](N)

$F_{tos,i}$ measured top of string force at time step i [MLT^{-2}](N)

$\hat{F}_{tos,i}$ estimated top of string force at time step i [MLT^{-2}](N)

$\vec{F}_{v,i}$ force originating from shear stress at the wall exerted by the fluid on the element i [MLT^{-2}](N)

$F_{vp,i}$ viscous pressure loss axial force at position i [MLT^{-2}](N)

F_w parameter of the brine density model [$L^{-1}M^{-1}T^{-4}\vartheta^{-1}$](kg/($m^3Pa^2K$))

$\vec{F}_W$ gravitational force [MLT^{-2}](N)

$\bar{F}_{WOB}$ average WOB force [MLT^{-2}](N)

F_{wob} contact force between the bit and the formation [MLT^{-2}](N)

$\vec{F}_{\mu_k}$ friction force [MLT^{-2}](N)

f Fanning friction [dimensionless]

f factor used to account for the effect of particles on viscosity [dimensionless]

$\vec{f}$ external force gradient (per unit length) [MT^{-2}](N/m)

f_{bed} particle size distribution density of solids contained in a cuttings bed [dimensionless]

$\vec{f}_c$ normal force per unit length [MT^{-2}](N/m)

$f'_{c\,0}$ relative volume fraction of a compressible and thermally-dilatable component at reference conditions of pressure and temperature [dimensionless]

$\tilde{f}_{c_{hgs}}$ absolute volume fraction of high gravity solid in the mud report formulation [dimensionless]

f_{c_i} absolute volume fraction of the i-component in a fluid mix [dimensionless]

$\tilde{f}_{c_i}$ absolute volume fraction of the i-component in a fluid mix as defined in the mud report [dimensionless]

f'_{c_i} relative volume fraction of the i-component in a fluid mix [dimensionless]

f_{c_n} component in the normal direction of the normal force per unit length [MT^{-2}](N/m)

f_{cutt} volume fraction of cuttings separated by the shale shaker [dimensionless]

f_{d_i} Darcy friction factor between sections i and $i+1$ [dimensionless]

$f_{ext,i}$ external force [MLT^{-2}](N)

f_{fs} volume fraction of formation solid contained in the drilling fluid [dimensionless]

f_i volume fraction of the i-component of a fluid mix [dimensionless]

f_l Fanning friction at the limit of laminar flow [dimensionless]

$f_{S^*_{KCl}}$ probability density function of the normalized KCl salinity [dimensionless]

$f_{S^*_{XG}}$ probability density function of the normalized polymer volumetric concentration [dimensionless]

f'_s relative volume fraction of solid in a fluid mix [dimensionless]

$f'_{s\,0}$ relative volume fraction of solid in a fluid mix at reference conditions of pressure and temperature [dimensionless]

f_t Fanning friction at the limit of turbulent flow [dimensionless]

f_{tr} transitional Fanning friction [dimensionless]

$f_{\phi^*_b}$ probability density function of the normalized barite volume fraction [dimensionless]

f_v annulus hydraulic friction correction factor [dimensionless]

G material shear modulus [$ML^{-1}T^{-2}$](Pa)

G' elastic shear modulus [$ML^{-1}T^{-2}$](Pa)

$G^{"}$ loss shear modulus [$ML^{-1}T^{-2}$](Pa) g gravitation acceleration [LT^{-2}](m/s^2)

H_{ij} element of the inverse covariance describing the wellbore position uncertainty at a given depth [L^{-2}](m^{-2})

h lubricant film thickness [L](m)

h_c cuttings bed height [L](m)

h_h heave semi-amplitude [L](m)

h_{L_i} head loss in a flowline between sections i and $i+1$ [L](m)

h_t heat transfer coefficient [$MT^{-2}\,\vartheta^{-1}$](J/(m^2.K))

I moment of inertia [ML^2](kg.m^2)

I_i polar mass moment of inertia [ML^2](kg.m^2)

$\hat{\imath}$ unit vector in a cartesian orthonormal base [dimensionless]

$\hat{\imath}_x$ unit vector pointing in the north direction [dimensionless]

i_y dimensionless coordinate in a linear interpolation [dimensionless]

$\hat{\imath}_y$ unit vector pointing in the east direction [dimensionless]

i_z dimensionless coordinate in a linear interpolation [dimensionless]

$\hat{\imath}_z$ unit vector pointing downward [dimensionless]

$\hat{\jmath}$ unit vector in a cartesian orthonormal base [dimensionless]

J_b moment of inertia of a particle around the rotation axis $\hat{b}_p$ [ML^2](kg.m^2)

J_i polar moment of inertia [L^4](m^4)

J_{gb} moment of inertia of the gear-box [ML^2](kg.m^2)

J_n moment of inertia of a particle around the rotation axis $\hat{n}_p$ [ML^2](kg.m^2)

J_r moment of inertia of a motor rotor [ML^2](kg.m^2)

J_{TD} apparent moment of inertia of the top-drive

J_t moment of inertia of a particle around the rotation axis $\hat{t}_p$ [ML^2](kg.m^2)

K consistency index [$ML^{-1}T^{n-2}$](Pa.s^n)

K' equivalent power law consistency index [$ML^{-1}T^{n-2}$](Pa.s^n)

K^* dimensionless consistency index [dimensionless]

$K_{0\%}$ consistency index at 0% solid concentration [$ML^{-1}T^{n-2}$](Pa.s^n)

K_b consistency index of a fluid containing solely barite particles [$ML^{-1}T^{n-2}$](Pa.s^n)

$K^*{}_b$ normalized consistency index for the sole effect of barite [dimensionless]

$\widetilde{K}_b$ approximation function of the consistency index of a weighted KCl/polymer WBM [$ML^{-1}T^{n-2}$](Pa.s^n)

$\widetilde{K}_b^*$ approximation function of the normalized consistency index of a weighted KCl/polymer WBM [dimensionless]

K_s scaling factor in particle size reduction through grinding [dimensionless]

$\widetilde{K}_s^*$ approximation function of the contribution from sand particles to the normalized consistency index of a weighted KCl/polymer WBM [dimensionless]

K_t clinging factor [dimensionless]

$\hat{k}$ unit vector in a cartesian orthonormal base [dimensionless]

k_a axial spring constant [MT^{-2}](N/m)

$k_{a,i}$ axial spring constant at element i [MT^{-2}](N/m)

$k_{E",i}$ loss modulus axial damping coefficient [MT^{-1}](N.s/m)

$k_{G",i}$ loss modulus torsional damping coefficient [ML^2T^{-1}](N.m.s/rd)

k_{screen} permeability of screen used in shale shakers [L^2](m^2)

k_T thermal conductivity [$MLT^{-3}\,\vartheta^{-1}$](W/(m.K))

k_t torsional spring constant [ML^2T^{-2}](N.m/rd)

$k_{t,i}$ torsional spring constant at element i [ML^2T^{-2}](N.m/rd)

L distance or length [L](m)

L'_A length of drill-line on the right side of a pulley after applying a tension T_A [L](m)

L_{A_0} length at rest of drill-line on the right side of a pulley at initial conditions [L](m)

l_0 original length under atmospheric pressure conditions [L](m)

l length [L](m)

l_a length of the particle's axis of rotational symmetry [L](m)

l_b maximum diameter perpendicular to the axis of rotation [L](m)

l_{bob} length of the bob in a Couette rheometer [L](m)

l_c chord of the particle involved in the pitch moment calculation [L](m)

l_p length of a prolate particle [L](m)

l_p length of the pipe body [L](m)

l_T length of a pipe adjusted for thermal expansion [L](m)

l_{TJ} tool-joint length [L](m)

M molar mass [MN^{-1}](kg/mol)

$\vec{M}$ bending moment vector [ML^2T^{-2}](Nm)

M_1 a weighting factor [dimensionless]

$\vec{M}_f$ friction generated moment [ML^2T^{-2}](Nm)

$\dot{m}$ mass flowrate [MT^{-1}](kg/s)

m_{c_i} mass of i-component [M](kg)

$m_{clean,j}$ mass of cleaned fluid entering the pit at time step j [M](kg)

m_{cs} number of discretized angular positions in a cross-section

m_f mass of fluid [M](kg)

m'_f mass of fluid arriving from a first branch [M](kg)

m''_f mass of fluid arriving from a second branch [M](kg)

m_i mass of a discretized portion of the drill-string [M](kg)

$\dot{m}_i$ mass-rate at position i [MT-1](kg/s)

m_{KCl} mass of KCl [M](kg)

m_l mass of brine [M](kg)

$m_{MP,j}$ mass of fluid exiting the tank to the mud pumps at time step j [M](kg)

m_s mass of a solid particle [M](kg)

$m_{tank,j}$ mass of fluid contained in the tank at time step j [M](kg)

m_{XG} mass of polymer [M](kg)

N number of components in the fluid mix

N_b number of experiments performed to analyze the sensitivity of the rheological behavior with barite

N_u Nusselt number [dimensionless]

n flow index [dimensionless]

n' equivalent power law flow index [dimensionless]

$\hat{n}$ unit normal vector in a Frenet-Serret coordinate system [dimensionless]

n^* dimensionless flow index [dimensionless]

$n_{0\%}$ flow index at 0% solid concentration [dimensionless]

n_b flow index of a fluid containing solely barite particles [dimensionless]

n_b component of the normal vector of the Frenet-Serret coordinate system attached to the fluid flow in the $\hat{b}_s$ direction [dimensionless]

$\tilde{n}_b$ approximation function of the flow index of a weighted KCl/polymer WBM [dimensionless]

$n^*{}_b$ normalized flow index for the sole effect of barite [dimensionless]

$\tilde{n}_b^*$ approximation function of the normalized flow index of a weighted KCl/polymer WBM [dimensionless]

n_{cs} number of discretized radial positions in a cross-section

$\hat{n}_f$ normal unit vector of the Frenet-Serret coordinate system attached to the fluid flow [dimensionless]

n_g grinding index [dimensionless]

$\vec{n}_i$ normal unit vector at a point i [dimensionless]

n_m number of motors

n_n component of the normal vector of the Frenet-Serret coordinate system attached to the fluid flow in the $\hat{n}_s$ direction [dimensionless]

$\hat{n}_p$ unit vector along perpendicular direction to the long axis of a particle [dimensionless]

$\hat{n}_s$ normal unit vector of the spherical coordinate system attached to a borehole cross-section [dimensionless]

$\tilde{n}_s^*$ approximation function of the contribution from sand particles to the normalized flow index of a weighted KCl/polymer WBM [dimensionless]

n_t component of the normal vector of the Frenet-Serret coordinate system attached to the fluid flow in the $\hat{t}_s$ direction [dimensionless]

P load per unit projected area [$ML^{-1}T^{-2}$] (Pa))

P_{cs} a point in a cross-section

$P_{p_{f\to s}}$ transformation matrix from the Frenet-Serret coordinate system attached to the fluid flow to the spherical coordinate system associated with the cross-section [dimensionless]

$P_{p_{g\to s}}$ transformation matrix from a geographical coordinate system to the spherical coordinate system associated with a cross-section [dimensionless]

P_u transfer matrix to transform a wellbore position uncertainty ellipsoid from global coordinates to a local coordinate system oriented by the ellipsoid axes [dimensionless]

P_{w_i} wetted perimeter at section i [L](m)

P_τ heat generated per unit time by mechanical friction [ML^2T^{-3}](J/s)

p absolute pressure [$ML^{-1}T^{-2}$](Pa)

p_0 absolute pressure at the top of the mud column [$ML^{-1}T^{-2}$](Pa)

p_0 reference pressure [$ML^{-1}T^{-2}$](Pa)

p_a borehole pressure [$ML^{-1}T^{-2}$](Pa)

$\partial_s p_a$ pressure loss gradient in an annulus [$ML^{-2}T^{-2}$](Pa/m)

$\partial_s p_a^*$ dimensionless pressure loss gradient in an annulus [dimensionless]

$\partial_s p_{a_0}$ pressure loss gradient in an annulus at 0% concentration of particles [$ML^{-2}T^{-2}$](Pa/m)

$p_{a_{15}}$ P15 percentile of the estimated borehole pressure [$ML^{-1}T^{-2}$](Pa)

$p_{a_{50}}$ P50 percentile of the estimated borehole pressure [$ML^{-1}T^{-2}$](Pa)

$p_{a_{50-15}}$ difference between the P50 and P15 percentiles of the estimated borehole pressure [$ML^{-1}T^{-2}$](Pa)

$p_{a_{85}}$ P85 percentile of the estimated borehole pressure [$ML^{-1}T^{-2}$](Pa)

$p_{a_{85-50}}$ difference between the P85 and P50 percentiles of the estimated borehole pressure [$ML^{-1}T^{-2}$](Pa)

p_{bh} borehole pressure [$ML^{-1}T^{-2}$](Pa)

p_c critical pressure [$ML^{-1}T^{-2}$](Pa)

p_{cp} collapse pressure [$ML^{-1}T^{-2}$](Pa)

p_{fp} fracturing pressure [$ML^{-1}T^{-2}$](Pa)

p_g gauge pressure [$ML^{-1}T^{-2}$](Pa)

$\vec{p}_g$ vector of the parameters that are globally calibrated

$\hat{\vec{p}}_g$ best estimation of the parameters that are globally calibrated

p_i internal pressure [$ML^{-1}T^{-2}$](Pa)

p_l overburden pressure [$ML^{-1}T^{-2}$](Pa)

p_{MP} mud pump pressure [$ML^{-1}T^{-2}$](Pa)

$\hat{p}_{MP}$ estimated mud pump pressure [$ML^{-1}T^{-2}$](Pa)

p_o external pressure [$ML^{-1}T^{-2}$](Pa)

p_{pore} pore pressure [$ML^{-1}T^{-2}$](Pa)

p_r reduced pressure [dimensionless]

Q volumetric flowrate [L^3T^{-1}](m^3/s)

Q_{clean} volumetric flowrate of the cleaned mud flowing out of the shale shaker [L^3T^{-1}](m^3/s)

Q_{cut} volumetric flowrate of the separated cuttings from the shale shaker [L^3T^{-1}](m^3/s)

Q_f fluid thermal energy [ML^2T^{-2}](J)

Q_{fl} volumetric flowrate in a flowline [L^3T^{-1}](m^3/s)

Q_{MP} volumetric flowrate of drilling fluid being pumped by the mud pumps [L^3T^{-1}](m^3/s)

$Q_{MP_{max}}$ maximum mud pump flowrate that does not generate an annulus pressure that is larger than the fracturing pressure along the open hole section [L^3T^{-1}](m^3/s)

$\dot{Q}_{MP_{max}}$ maximum mud pump acceleration for changing the flowrate to another one [L^3T^{-2}](m^3/s^2)

Q_{MP_S} starting mud pump flowrate [L^3T^{-1}](m^3/s)

$Q_{MP_{safe}}$ maximum mud pump flowrate that does not generate an annulus pressure that is larger than the fracturing pressure along the open hole section, with a given obstruction size in the annulus [L^3T^{-1}](m^3/s)

$\dot{Q}_{MP_{stop}}$ minimum mud pump flowrate deceleration [L^3T^{-2}](m^3/s^2)

Q_{fl_0} volumetric flowrate of drilling fluid arriving at the shale shaker from the flowline outlet [L^3T^{-1}](m^3/s)

Q_{out} measured flowrate out of the well [L^3T^{-1}](m^3/s)

$\hat{Q}_{out}$ estimated flowrate out of the well [L^3T^{-1}](m^3/s)

$\mathcal{R}$ universal gas constant [$ML^2T^{-2}\vartheta^{-1}N^{-1}$] J/(mol.K)

$\vec{R}$ reaction force [MLT^{-2}](N)

Re' generalized Herschel-Bulkley Reynolds number [dimensionless]

$\bar{R}_{e_i}$ average Reynolds number between sections i and $i+1$ [dimensionless]

Re_l' limit for laminar flow of the generalized Reynolds number [dimensionless]

Re_p particle Reynolds number [dimensionless]

Re_t' limit for turbulent flow of the generalized Reynolds number [dimensionless]

R_{fl} radius of a flowline [L](m)

$\vec{R}_i$ reaction force at a contact point i [MLT^{-2}](N)

RMS root mean square of the accelerations during a time window Δt_γ [LT^{-2}](m/s^2)

r radial displacement of the pipe axis compared to the wellbore axis [L](m)

$\vec{r}$ radial position vector [L](m)

$\hat{r}$ unit vector in the radial direction [dimensionless]

$\dot{\vec{r}}$ radial velocity vector [LT^{-1}](m/s)

r' radial distance of the pipe axis of rotation compared to the wellbore axis [L](m)

$\vec{r}_0$ mean position of the well [L](m)

r_{bob} radius of the bob in a Couette rheometer [L](m)

r_{cup} radius of the cup of a Couette rheometer [L](m)

$\vec{r}_h$ highest point of the wellbore position ellipsoid of uncertainty at a given depth [L](m)

r_i radius of rotation at contact point i [L](m)

$\vec{r}_i$ radius vector from the point of application of the tension $\vec{T}_i$ to Ω [L](m)

$\vec{r}_{i,j}$ jth radial vector for element i [L](m)

r_l radius of the drill-line on the drum [L](m)

$\vec{r}_l$ lowest point of the wellbore position ellipsoid of uncertainty at a given depth [L](m)

r_o outer radius [L](m)

r_p aspect ratio of axisymmetric particles [dimensionless]

$\vec{r}_{p_0}$ initial direction of the axis of rotation of a particle in a starting cross-section [dimensionless]

r_w wellbore radius [L](m)

S action [ML^2T^{-1}](J.s)

S_i state of the drilling system corresponding to time interval $\left[t_{s_i}, t_{f_i}\right]$

S_0 parameter of the brine density model [ML^{-3}](kg/m^3)

S_1 parameter of the brine density model [ML^{-3}](kg/m^3)

S_2 parameter of the brine density model [ML^{-3}](kg/m^3)

S_3 parameter of the brine density model [ML^{-3}](kg/m^3)

S_{KCl} mass fraction of KCl in the liquid phase [dimensionless]

S_{KCl_m} maximum mass fraction of KCl in the liquid phase [dimensionless]

S_{XG} mass concentration of polymer in the liquid phase [dimensionless]

S^*_{KCl} normalized salinity [dimensionless]

S_{XG_m} reference mass concentration of polymer in the liquid phase [dimensionless]

S^*_{XG} normalized mass concentration of polymer [dimensionless]

s curvilinear abscissa [L](m)

s_{bh} curvilinear abscissa of the bottom hole [L](m)

$s_{ca_{max}}$ curvilinear abscissa of the closest approach to the maximum geo-pressure boundary while accounting for the uncertainty of the borehole pressure [L](m)

$s_{ca_{min}}$ curvilinear abscissa of the closest approach to the minimum geo-pressure boundary while accounting for the uncertainty of the borehole pressure [L](m)

s_{cs} curvilinear abscisssa of the deepest casing shoe [L](m)

s_{fl} flowline slope [dimensionless](m/m)

s_i curvilinear abscissa [L](m)

T temperature [ϑ](K)

$\vec{T}$ tension [MLT^{-2}](N)

T_0 reference temperature [ϑ](K)

Ta Taylor number [dimensionless]

T_c critical temperature [ϑ](K)

$T_{clean,j}$ temperature of the cleaned fluid arriving at the pit at time step j [ϑ](K)

T_f fluid temperature [ϑ](K)

T_i temperature at the interface or temperature of the i^{th} being mixed [ϑ](K)

$\vec{T}_i$ tension at position i [MLT^{-2}](N)

T_r reduced temperature [dimensionless]

T_s tension at curvilinear abscissa s [MLT^{-2}](N)

T_t tangential component of the tension [MLT^{-2}](N)

$T_{tank,j}$ temperature of the fluid contained in the tank at time step j [ϑ](K)

TVD true vertical depth [L](m)

TVD_0 true vertical depth at the top of the mud column [L](m)

TVD_{th} true vertical depth referred to the top hole elevation [L](m)

t time [T](s)

t torque state variable [MT^{-2}](N.m/m^2)

$\hat{t}$ unit tangent vector [dimensionless]

t_0 initial time [T](s)

t_1 time of first gel strength measurement [T](s)

t_2 time of second gel strength measurement [T](s)

t_b component of the tangent vector of the Frenet-Serret coordinate system attached to the fluid flow in the $\hat{b}_s$ direction [dimensionless]

t_f end of a time interval [T](s)

$\hat{t}_f$ unit tangent vector of the Frenet-Serret coordinate system attached to the fluid flow [dimensionless]

t_{gel} time with a reference to the last moment when the shear rate turns to zero [T](s)

t_h heave period [T](s)

$\vec{t}_i$ tangential unit vector at contact point i [dimensionless]

$\hat{t}_i$ unit tangent vector at position i [dimensionless]

t_n component of the tangent vector of the Frenet-Serret coordinate system attached to the fluid flow in the $\hat{n}_s$ direction [dimensionless]

$\hat{t}_p$ unit vector along the long axis of a particle [dimensionless]

t_s start of a time interval [T](s)

$\hat{t}_s$ unit tangent vector of the spherical coordinate system attached to a borehole cross-section [dimensionless]

t_{step} time with a reference to the last step change in shear rate [T](s)

t_t component of the tangent vector of the Frenet-Serret coordinate system attached to the fluid flow in the $\hat{t}_s$ direction [dimensionless]

t_{term} time by which a particle has reached terminal velocity [T](s)

t_{so} time during a slack-off [T](s)

t_{ss} time to reach hydraulic steady state conditions [T](s)

t_{step} time with a reference to the last step change in shear rate [T](s)

t_t time by which terminal velocity is reached [T](s)

$\widehat{U}$ mixed displacement vector

UCS uniaxial compressive strength [$ML^{-1}T^{-2}$](Pa)

UCS_{max} maximum value of the UCS in an investigation interval [$ML^{-1}T^{-2}$](Pa)

UCS_{min} minimum value of the UCS in an investigation interval [$ML^{-1}T^{-2}$](Pa)

u axial displacement [L](m)

$\vec{u}$ displacement vector [L](m)

$\vec{u}_{p_0}$ initial position of a particle in a starting cross-section [L](m)

$\hat{u}_t$ transformed unit vector $\hat{t}_p$ in the coordinate system associated with the fluid [dimensionless]

u_x displacement in the x direction [L](m)

u_y displacement in the y direction [L](m)

u_z displacement in the z direction [L](m)

V_c volume of a compressible and thermally-dilatable component [L^3](m^3)

V_{c_i} volume of the i-component of a fluid mix [L^3](m^3)

V_f volume of fluid [L^3](m^3)

V_j volume at time step j [L^3](m^3)

V_s volume of a particle [L^3](m^3)

V_{screen} volume of drilling fluid passing through the screen of a shale shaker [L^3](m^3)

V_{tank} volume of mud contained in the tank [L^3](m^3)

v velocity [LT^{-1}](m/s)

$\bar{v}$ average velocity [LT^{-1}](m/s)

$\vec{v}_a$ axial slip velocity [LT^{-1}](m/s)

$\bar{v}_{bit}$ rate of penetration [LT^{-1}](m/s)

$\bar{v}_c$ average cuttings transport velocity [LT^{-1}](m/s)

v_{cs} critical Stribeck velocity [LT^{-1}](m/s)

$\bar{v}_{com}$ center of mass velocity [LT^{-1}](m/s)

$\bar{v}_{csfv}$ critical settling fluid velocity [LT^{-1}](m/s)

$\bar{v}_{csfv_{d_s}}$ critical settling fluid velocity for a particle size d_s [LT^{-1}](m/s)

v_{ctfv} critical transport fluid velocity [LT^{-1}](m/s)

$\bar{v}_{ctfv_{d_s}}$ critical transport fluid velocity for a particle size d_s [LT^{-1}](m/s)

v_{ds} axial velocity of the drill-string at a specific abscissa and time [LT^{-1}](m/s)

$\bar{v}_f$ bulk fluid velocity [LT^{-1}](m/s)

$\vec{v}_f$ fluid velocity vector [LT^{-1}](m/s)

$\bar{v}_{fl_i}$ bulk fluid velocity in a flowline at section i [LT^{-1}](m/s)

$\bar{v}_{fluidized}$ bulk velocity of the fluidized layer of a cuttings bed [LT^{-1}](m/s)

v_i velocity of an element i [LT^{-1}](m/s)

$\vec{v}_i$ velocity vector at a position i [LT^{-1}](m/s)

$\bar{v}_{i_{com}}$ Centre of mass velocity of component i [LT^{-1}](m/s)

v_{f_b} fluid bulk velocity [LT^{-1}](m/s)

$\bar{v}_k$ Cross-sectional average velocity of a phase k [LT^{-1}](m/s)

$\bar{v}_{\dot{m}}$ Velocity of the mass flux through the walls [LT^{-1}](m/s)

$\bar{v}_{mix}$ average velocity of a mix of cuttings and fluid in a cross-section [LT^{-1}](m/s)

$\vec{v}_p$ particle velocity vector [LT^{-1}](m/s)

$\vec{v}_{p_0}$ initial velocity of a particle in a starting cross-section [LT^{-1}](m/s)

v_{p_a} pipe axial velocity [LT^{-1}](m/s)

$\bar{v}_{p_i}$ vertical velocity of a pulley i [LT^{-1}](m/s)

$\vec{v}_r$ rotational slipping velocity [LT^{-1}](m/s)

v_s slip velocity magnitude [LT^{-1}](m/s)

$\vec{v}_s$ slip velocity vector [LT^{-1}](m/s)

$\bar{v}_s$ average slip velocity in a cross-section [LT^{-1}](m/s)

v_{screen} fluid velocity through the screen of a shale shaker [LT^{-1}](m/s)

$\bar{v}_{s_{ctfv}}$ bulk slip velocity at the CTFV conditions for a given PSD [LT^{-1}](m/s)

v_{s_x} slip velocity of a particle of size x [LT^{-1}](m/s)

$v_{x_{i,j}}$ x-component of the velocity at a 2-dimensional discretized position i, j [LT^{-1}](m/s)

v_{x_P} x-component of the velocity at position P [LT^{-1}](m/s)

$v_{y_{i,j}}$ y-component of the velocity at a 2-dimensional discretized position i, j [LT^{-1}](m/s)

v_{y_P} y-component of the velocity at position P [LT^{-1}](m/s)

$v_{z_{i,j}}$ z-component of the velocity at a 2-dimensional discretized position i, j [LT^{-1}](m/s)

v_{z_P} z-component of the velocity at position P [LT^{-1}](m/s)

v_{μ_k} corrected sliding velocity to account for the effect of rotational friction [LT^{-1}](m/s)

W power [ML^2T^{-3}](W)

W_{fl} width of a flowline [L](m)

W_{TJ_g} power at the tool-joint spend on grinding particles [ML^2T^{-3}](W)

WOB weight on bit [M](kg)

w lateral displacement [L](m)

ϖ weight on bit related state variable [ML^{-1}](kg/m)

w_{c_i} mass fraction of the i-component of a fluid mix [dimensionless]

w'_{c_i} mass fraction of the i-component of a fluid arriving from a first branch [dimensionless]

w''_{c_i} mass fraction of the i-component of a fluid arriving from a second branch [dimensionless]

w_i mass fraction of a component i in a fluid mix [dimensionless]

$\vec{w}_{i,j}$ the jth linear force applied to element i [MT^{-2}](N/m)

w_p width of a prolate particle [L](m)

w_t weight fraction of a salt [dimensionless]

x coordinate in the $\hat{\imath}$ direction of the inertial frame [L](m)

$\hat{x}$ unit vector in a global coordinate system pointing in the north direction [dimensionless]

x_0 particle position at time t_0 [L](m)

$\vec{x}_b$ a triplet of Φ_{b}^*, S_{KCl}^* and S_{XG}^* [dimensionless]

x_h x-component of the high-side top of the wellbore position ellipsoid of uncertainty at a given depth [L](m)

$\vec{x}_i$ position vector of element i [L](m)

$\vec{x}_{i_b}$ a triplet of $\Phi_{\mathrm{b}i}^*$, $S_{KCl_i}^*$ and $S_{XG_i}^*$ corresponding to the measurement i [dimensionless]

x_k mass fraction of phase k (dimensionless)

x_l x-component of the low-side top of the wellbore position ellipsoid of uncertainty at a given depth [L](m)

x_p particle position [L](m)

x_{rms_i} RMS of shear stresses until measurement i [dimensionless]

$x_{\Omega'''}$ coordinate of the osculator center in the $\hat{\imath}$ direction of the inertial frame [L](m)

y coordinate in the $\hat{\jmath}$ direction of the inertial frame [L](m)

y_a distance from the wall to the plug region [L](m)

$\hat{y}$ unit vector in a global coordinate system pointing in the east direction [dimensionless]

y_h y-component of the high-side top of the wellbore position ellipsoid of uncertainty at a given depth [L](m)

$y_{i,j}$ coordinate at the 2-dimensional discretized position [L](m)

y_l y-component of the low-side top of the wellbore position ellipsoid of uncertainty at a given depth [L](m)

y_P y-component of the coordinates of a point P [L](m)

$y_{\Omega'''}$ coordinate of the osculator center in the $\hat{\jmath}$ direction of the inertial frame [L](m)

Z gas compressibility factor [dimensionless]

$z_{i,j}$ coordinate at a 2-dimensionsal discretized position [L](m)

z_P z-component of the coordinates of a point P [L](m)

z TVD [L](m)

$\hat{z}$ unit vector in a global coordinate system pointing in the downward vertical direction [dimensionless]

z' distance between Ω' and $\Omega_\perp$ [L](m)

z_0 initial TVD [L](m)

z_h z-component of the high-side top of the wellbore position ellipsoid of uncertainty at a given depth [L](m)

z_l z-component of the low-side top of the wellbore position ellipsoid of uncertainty at a given depth [L](m)

Greek letters:

α_0 amplification parameter of the structure parameter for the yield stress coefficient [dimensionless]

α_1 time damping coefficient [T^{-1}](s^{-1})

α_2 time damping coefficient [T^{-1}](s^{-1})

α_3 amplification parameter of the structure parameter for the consistency index coefficient [dimensionless]

α_4 amplification parameter of the structure parameter for the flow index coefficient [dimensionless]

α_a amplification parameter in thixotropic model [dimensionless]

α_{fl_i} kinetic energy correction factors at section i of a flowline [dimensionless]

α_i azimuth at position i [dimensionless](rd)

α_p incidence angle of a particle to the fluid flow direction [dimensionless](rd)

α_{ref} calibration factor for the estimation of the kinetic friction between bit and formation as a function of the CCS [$M^{-1}LT^2$](pa^{-1})

α_T linear thermal expansion coefficient [Θ^{-1}](1/K)

$\alpha_{TJ,rot}$ pressure loss ratio to account for the effect of rotation on pressure loss across tool-joint [dimensionless]

α_z z-component of the normal to the wellbore position uncertainty ellipsoid at a given depth [L^{-1}](m^{-1})

α^+ amplification function for λ^+ [dimensionless]

α_0^+ parameter of the bilinear form representing the amplification function α^+ [dimensionless]

α_1^+ parameter of the bilinear form representing the amplification function α^+ [dimensionless]

α_2^+ parameter of the bilinear form representing the amplification function α^+ [dimensionless]

α_3^+ parameter of the bilinear form representing the amplification function α^+ [dimensionless]

α^- amplification function for λ^- [dimensionless]

α_0^- parameter of the bilinear form representing the amplification function α^- [dimensionless]

α_1^- parameter of the bilinear form representing the amplification function α^- [dimensionless]

α_2^- parameter of the bilinear form representing the amplification function α^- [dimensionless]

α_3^- parameter of the bilinear form representing the amplification function α^- [dimensionless]

$\dot{\gamma}$ shear rate [T^{-1}](s^{-1})
$\vec{\gamma}_p$ particle acceleration [LT^{-2}](m/s^2)
$\dot{\gamma}_i$ shear rate after a step change [T^{-1}](s^{-1})
$\dot{\gamma}_s$ shear rate around a particle moving in a background fluid [T^{-1}](s^{-1})
$\dot{\gamma}_{w_i}$ shear rate at the wall between sections i and $i+1$ [T^{-1}](s^{-1})
ΔL length variation [L](m)

Δp_{screen} pressure loss through the screen of a shale shaker [$ML^{-1}T^{-2}$](Pa)
$\Delta p_{va,i}$ pressure difference between outside of the string at position i [$ML^{-1}T^{-2}$](Pa)
$\Delta p_{vs,i}$ pressure difference between inside of the string at position i [$ML^{-1}T^{-2}$](Pa)
Δp_{XWD} pressure loss through special elements of the BHA [$ML^{-1}T^{-2}$](Pa)
ΔT variation of temperature compared to a reference temperature [Θ](K)
Δt time step [T](s)
Δt_{ROP} time window for the evaluation of the average torque on bit and WOB while estimating the ROP [T](s)
Δt_{ss} minimum time window for considering that the flow is in steady state condition [T](s)
Δt_u duration of the uniform movement while tripping a stand [T](s)
$\Delta\theta$ twist angle [dimensionless](rd)
δ_p distance of investigation for particle transport [L](m)

δ_{rms} distance to be minimized [dimensionless]

δl_{fl} distance between two discretized sections of a flowline [L](m)

δl_i length of an element between position i and $i+1$ [L](m)

δp_{fl_i} pressure loss between sections i and $i+1$ in a flowline [$ML^{-1}T^{-2}$](Pa)

$\partial_s p$ viscous pressure loss gradient in a pipe [$ML^{-2}T^{-2}$](Pa/m)

ε elongation [dimensionless]

ϵ wall roughness [L](m)

ε_{FRT} threshold of the free rotating torque to perform mechanical friction calibration [ML^2T^{-2}](N.m)

ε_{gc} threshold for considering measurements to be used in global calibration [dimensionless]

$\varepsilon_{p_{MP_{ss}}}$ threshold of standard deviation for the mud pump pressure [$ML^{-1}T^{-2}$](Pa)

$\varepsilon_{Q_{MP_{ss}}}$ threshold of standard deviation for the mud pump flowrate [L^3T^{-1}](m^3/s)

$\varepsilon_{Q_{out}}$ acceptable tolerance for the flowrate out rate of change during a pump stop [L^3T^{-1}](m^3/s)

$\varepsilon_{Q_{out_{ss}}}$ threshold of standard deviation for the flowrate out of the well [L^3T^{-1}](m^3/s)

ε_{ss} threshold value to consider that the conditions are steady state [dimensionless]

ε_{ϕ_b} scaling factor used by a radial basis function [dimensionless]

η_{bit} efficiency factor of the bit [dimensionless]

ϑ average inclination [dimensionless](rd)

θ angle [dimensionless](rd)

$\vec{\theta}$ rotation vector [dimensionaless](rd)

$\dot{\vec{\theta}}$ angular velocity [T^{-1}](rd/s)

$\ddot{\vec{\theta}}$ angular acceleration [T^{-2}](rd/s^2)

θ_b rotation angle around the direction $\hat{b}_p$ [dimensionless](rd)

$\dot{\theta}_{ds}$ angular velocity of the drill-string at specific curvilinear abscissa and time [T^{-1}](rd/s)

ϑ_i inclination at position i [dimensionless](rd)

θ_i angular position [dimensionless](rd)

θ_i angle at position i of a portion of drill-pipes that follow a circular arc or twist angle of element i [dimensionless](rd)

θ_n rotation angle around the direction $\hat{n}_p$ [dimensionless](rd)

ϑ_s inclination at the curvilinear abscissa s along the trajectory [dimensionless](rd)

$\dot{\theta}_{bob}$ angular velocity of the bob in a Couette rheometer [T^{-1}](rd/s)

$\dot{\theta}_{TJ}$ angular velocity of the tool-joint [T^{-1}](rd/s)

θ_t rotation angle around the direction $\hat{t}_p$ [dimensionless](rd)

θ_u azimuth angle on the wellbore position uncertainty ellipsoid [dimensionless](rd)

K diameter ratio [dimensionless]

κ compressibility [$L^{-2}T^2$](kg/m^3/Pa)

κ''' curvature in the osculating circle [L^{-1}](m^{-1})

K_f curvature in the Frenet-Serret coordinate system attached to the fluid flow [L^{-1}](m^{-1})

Λ volume ratio of mud to cuttings [dimensionless]

Λ_{ci} mass per unit volume of the i-component in a fluid mix [ML^{-3}](kg/m^3)

Λ'_{ci} mass per resulting volume after the addition of the i-component in a fluid mix [ML^{-3}](kg/m^3)

λ structure parameter [dimensionless]

λ^+ structure parameter characterizing structuration [dimensionless]

$\lambda^+_{\dot{\gamma}_{i-1}}$ structure parameter just prior to the change of shear rate [dimensionless]

$\lambda^+_{\dot{\gamma}_i,\infty}$ structure parameter for shear rate $\dot{\gamma}_i$ at time $t \to \infty$ [dimensionless]

λ^- structure parameter characterizing de-structuration [dimensionless]

$\lambda^{-}_{\dot{\gamma}_{i-1}}$ de-structuration parameter just prior to the change of shear rate [dimensionless]

$\lambda^{-}_{\dot{\gamma}_i,\infty}$ de-structuration parameter for shear rate $\dot{\gamma}_i$ at time $t \to \infty$ [dimensionless]

$\lambda_{\dot{\gamma},\infty}$ structure parameter at shear rate $\dot{\gamma}$ at time infinity [dimensionless]

μ shear stress function [$ML^{-1}T^{-2}$](Pa)

μ_0 original viscosity of a Newtonian fluid [$ML^{-1}T^{-1}$](Pa.s)

μ_{eff} effective viscosity [$ML^{-1}T^{-1}$](Pa.s)

μ_{eff_i} effective viscosity of the fluid contained between sections i and $i+1$ [$ML^{-1}T^{-1}$](Pa.s)

μ_k kinetic friction coefficient [dimensionless]

$\mu_{k_{bit}}$ kinetic friction factor for the bit/rock interaction [dimensionless]

$\mu_{k,r}$ effective kinetic friction in pure rotation [dimensionless]

μ_p apparent viscosity of a fluid with solid particles in suspension [$ML^{-1}T^{-1}$](Pa.s)

μ_r dimensionless apparent viscosity of a fluid with solid particles in suspension [dimensionless]

μ_{ref} reference kinetic friction for bit/rock interaction [dimensionless]

μ_s coefficient of static friction [dimensionless]

ν Poisson's ratio [dimensionless]

ξ term used in the definition of the equivalent power law flow index [dimensionless]

Ξ set of component indices from the union of Ξ' and Ξ''

Ξ' set of component indices for a fluid arriving from a first branch

Ξ'' set of component indices for a fluid arriving from a second branch

ρ mass density [ML^{-3}](kg/m^3)

ρ_b bulk mass density [ML^{-3}](kg/m^3)

ρ_c mass density of a compressible and thermally-dilatable component [ML^{-3}](kg/m^3)

ρ_{c_0} mass density of a compressible and thermally-dilatable component at reference conditions of pressure and temperature [ML^{-3}](kg/m^3)

ρ_{c_i} mass density of the i-component in a fluid mix [ML^{-3}](kg/m^3)

ρ_{clean} mass density of the fluid after having passed the shale shaker [ML^{-3}](kg/m^3)

$\rho_{clean,j_{T_{tank,j}}}$ mass density of the fluid arriving at the pit after conversion to the tank temperature at time step j [ML^{-3}](kg/m^3)

ρ_{cutt} mass density of cuttings separated from the shale shaker [ML^{-3}](kg/m^3)

ρ_f fluid mass density [ML^{-3}](kg/m^3)

$\tilde{\rho}_f$ fluid mass density based on the mud report formulation [ML^{-3}](kg/m^3)

ρ_{f_0} fluid mass density at reference conditions of pressure and temperature [ML^{-3}](kg/m^3)

ρ_{f_i} mass density of a fluid mix after adding the i-component [ML^{-3}](kg/m^3)

$\bar{\rho}_{fl_i}$ average mass density of fluid contained in between sections i and $i+1$ in a flowline [ML^{-3}](kg/m^3)

ρ_{fl_o} mass density of the fluid flowing out of the flowline [ML^{-3}](kg/m^3)

ρ_{fs} mass density of formation solid [ML^{-3}](kg/m^3)

ρ_g mass density of a gas [ML^{-3}](kg/m^3)

ρ_{hgs} mass density of high gravity solid [ML^{-3}](kg/m^3)

ρ_i mass density of the i-component of a fluid mix [ML^{-3}](kg/m^3)

ρ_j mass density at time step j [ML^{-3}](kg/m^3)

ρ_l mass density of the liquid phase in a fluid mix [ML^{-3}](kg/m^3)

ρ_m mass density of a fluid mix [ML^{-3}](kg/m^3)

ρ_{mi} mass density of the mud on the inside of a pipe [ML^{-3}](kg/m^3)

ρ_{mix} mass density of the mix [ML^{-3}](kg/m^3)

ρ_{mo} mass density of the mud on the outside of a pipe [ML^{-3}](kg/m^3)

ρ_o mass density of a base-oil [ML^{-3}](kg/m^3)

ρ_p mass density of the pipe material [ML^{-3}](kg/m^3)

ρ_s solid mass density [ML^{-3}](kg/m^3)

ρ_{screen} mass density of the fluid retained on the screen of a shale shaker [ML^{-3}](kg/m^3)

ρ_{tank} mass density of the drilling fluid contained in the active pit [ML^{-3}](kg/m^3)

Σ Covariance matrix of the wellbore position uncertainty at a given depth [L^2](m^2)

σ composite standard deviation of the surface height [L](m)

σ_a axial stress [$ML^{-1}T^{-2}$](Pa)

τ shear stress [$ML^{-1}T^{-2}$](Pa)

τ_* experimentally fitted yield stress scaling factor [$ML^{-1}T^{-2}$](Pa)

τ_{bit} torque on bit [ML^2T^{-2}](N.m)

$\bar{\tau}_{bit}$ average torque on bit [ML^2T^{-2}](N.m)

$\bar{\tau}_{bit,\mu_{ref}}$ average torque on bit over a time window Δt_{ROP} [ML^2T^{-2}](N.m)

τ_{ds} torque on drill-string [ML^2T^{-2}](N.m)

$\tau_{ext,i}$ external torque [ML^2T^{-2}](N.m)

τ_{gel} gel strength [$ML^{-1}T^{-2}$](Pa)

τ_j measured shear stress corresponding to shear rate j [$ML^{-1}T^{-2}$](Pa)

$\tilde{\tau}_j$ estimated shear stress at measurement j [$ML^{-1}T^{-2}$](Pa)

τ_p pitch moment exerted by a fluid on a slipping particle [ML^2T^{-2}](N.m)

τ_s torque at curvilinear abscissa s [ML^2T^{-2}](N.m)

$\tau_{TD,i}$ measured top-drive torque at time step i [ML^2T^{-2}](N.m)

$\hat{\tau}_{TD,i}$ estimated top-drive torque at time step i [ML^2T^{-2}](N.m)

τ_{TJ} total torque on a tool-joint [ML^2T^{-2}](N.m)

τ_{TJ_g} torque on the tool-joint due to grinding of particles [ML^2T^{-2}](N.m)

τ_{TJ_μ} torque on the tool-joint originating from mechanical friction [ML^2T^{-2}](N.m)

τ_v viscous stress [$ML^{-1}T^{-2}$](Pa)

τ_w shear stress at the wall [$ML^{-1}T^{-2}$](Pa)

τ_{w_i} shear stress at the wall between sections i and $i+1$ [$ML^{-1}T^{-2}$](Pa)

τ_γ yield stress [$ML^{-1}T^{-2}$](Pa)

$\tau_{\gamma,t_{gel}}$ yield stress as a function of the elapsed time since last gelation period [$ML^{-1}T^{-2}$](Pa)

$\tau_{\dot{\gamma}}$ shear stress function of pressure and temperature at a given shear $\dot{\gamma}$ [$ML^{-1}T^{-2}$](Pa)

τ_γ^* dimensionless yield stress [dimensionless]

$\tau_{\gamma_{0\%}}$ yield stress at 0% concentration of solid particles [$ML^{-1}T^{-2}$](Pa)

τ_{γ_b} yield stress of a fluid containing solely barite solid particles [$ML^{-1}T^{-2}$](Pa)

$\tau_{\gamma_b}^*$ normalized yield stress for the sole effect of barite [dimensionless]

$\tilde{\tau}_{\gamma_b}$ approximation function for the yield stress of a weighted KCl/Polymer WBM [$ML^{-1}T^{-2}$](Pa)

$\tilde{\tau}_{\gamma_b}^*$ approximation function of the normalized yield stress of a weighted KCl/polymer WBM [dimensionless]

$\tilde{\tau}_{\gamma_s}^*$ approximation function of the contribution from sand particles to the normalized yield stress of a weighted KCl/polymer WBM [dimensionless]

Φ azimuth [dimensionless](rd)

Φ volume fraction of particles in the fluid [dimensionless]

Φ^* normalized volume fraction [dimensionless]

Φ_b volumetric concentration of barite [dimensionless]

ϕ_b real-valued radial basis function [dimensionless]

Φ_b^* normalized volume fraction of barite [dimensionless]

Φ_{bm} maximum packing concentration of barite [dimensionless]
Φ_{fs} volumetric concentration of formation solid [dimensionless]
Φ_{hgs} volumetric concentration of high gravity solid [dimensionless]
Φ'_{hgs} volumetric concentration of high gravity solid in a weighted drilling fluid without formation solids [dimensionless]
Φ_m maximum packing concentration of particles in a fluid [dimensionless]
Φ_s total volumetric concentration of all solids in a mix [dimensionless]
Φ_{sb} ratio of the volumetric amount of sand to the volumetric amount of barite [dimensionless]
Φ_{s_m} maximum packing concentration of sand [dimensionless]
Φ_s^* normalized volume fraction of all solids in a liquid mix [dimensionless]
ϕ_u polar angle on the wellbore position uncertainty ellipsoid [dimensionless](rd)
φ angle of internal friction [dimensionless](rd)
φ' azimuth of the pipe with regards to the global coordinate system [dimensionless](rd)
ϕ_s azimuth at the curvilinear abscissa s along the trajectory [dimensionless](rd)
Ψ set of phase state indices
ψ' inclination of the pipe with the global coordinate system [dimensionless](rd)
Ω center of rotation [L](m)
ω angular velocity [T^{-1}](rd/s)
$\vec{\omega}$ angular velocity vector [T^{-1}](rd/s)
$\dot{\vec{\omega}}$ angular acceleration vector [T^{-2}](rd/s^2)
Ω_0 wellbore axis center [L](m)
ω_{bit} angular velocity of the bit [T^{-1}](rd/s)
$\bar{\omega}_{bit}$ average angular velocity of the bit [T^{-1}](rd/s)
ω_{ds} angular velocity of the drill-string [T^{-1}](rd/s)
ω_{p_0} initial angular velocity around an axis of rotation of a particle in a starting cross-section [T^{-1}](rd/s)

Mathematical Notations

$\forall$	for all element in a set
$\exists$	it exists an element
$\in$	operator between an element and a set that indicates that the element belongs to the set
$\mid$	such that
$\Rightarrow$	imply
$\Leftrightarrow$	logically equivalent
$\subset$	operator between two sets that indicate that the set on the left side is included in the set on the right side
$\times$	cross product of two sets or the cross product of two vectors
$\rightarrow$	in a function definition, this operator indicates the source set on the left side and the destination set on the right side
$\mathbb{R}$	The set of real numbers
$\vec{u}$	An element of a vector space
$\|\|\vec{u}\|\|$	The Euclidian norm of a vector
$\hat{u}$	A unit vector, i.e.$\|\|\hat{u}\|\| = 1$

Number Notations

Note that in this document, the decimal point separator is sometime denoted "." and other time ",". This is because some of the software used to generate graphs and pictures are configured with the European decimal point notation while others utilize the American notation. However, as comma is never used as a thousand separator, there should not any ambiguity for the reader.

Block Diagram Notation

We will use block diagrams to represent the principal functions of the systems that are discussed in this document. A function is represented by a block with inputs, outputs and external contextual information (see Fig. 2).

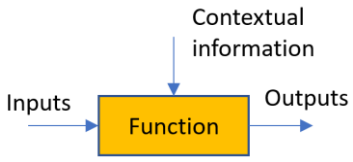

Fig. 2: Schematic representation of a function in a block diagram.

When the same input is connected to several function blocks, a take-off point is used (see Fig. 3):

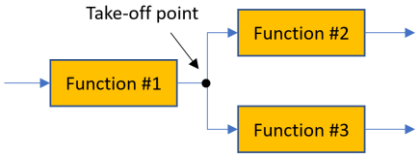

Fig. 3: Illustration of a take-off point where the same input is used for several functions.

Several inputs may have to be combined before being passed to a function. This can be a summation (see Fig. 4a), the minimum of all inputs (see Fig. 4b), the maximum of all inputs (see Fig. 4c) or the one or the other, i.e. a switch (see Fig. 4d). In the latter case, there is also a command input to change the position of the switch. For the first case, the summation accounts for possible negations of some of the input signals that is indicated by a "-" sign.

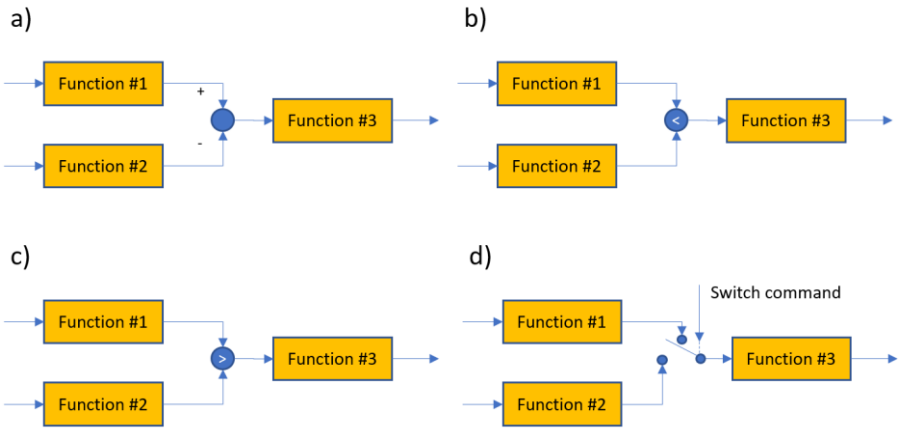

Fig. 4: Combination of input signals by a) summation, b) minimum, c) maximum, d) switching.

In a block diagram, not all the functions work necessarily at the same rhythm. In the block diagram notation, the functions that work at a similar tempo are encapsulated into a rounded box. This notation imposes that slower functions are always outside of faster ones and therefore the delineation of functions with similar time response always include those with a faster refresh rate. This defines a control hierarchy where the outer elements are the slowest and the deeper ones are the fastest (see Fig. 5).

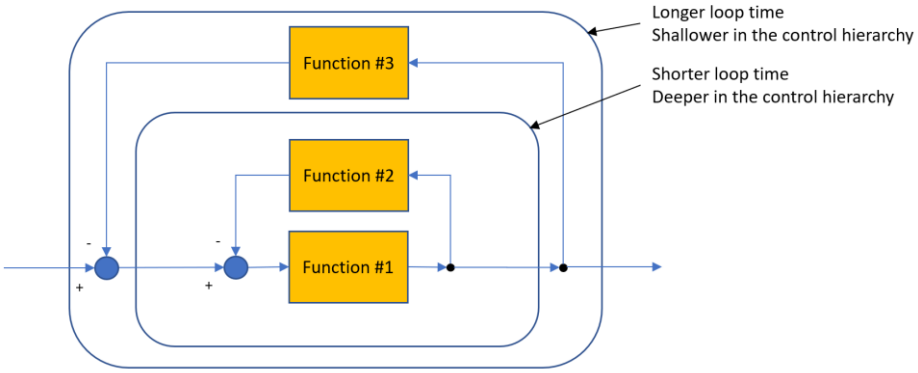

Fig. 5: Illustration of the encapsulation of levels in control hierarchy by rounded boxes.

State Diagram Notation

To describe the behavior of some systems, we will also use state diagrams. When a system has a finite number of well-defined states, these are represented in a directed graph where the arrows represent transitions from one state to another. A state is depicted by an elliptical box and a terminal state, i.e. a state from which it is not possible to transit to another state, is marked by a thicker border (see Fig. 6).

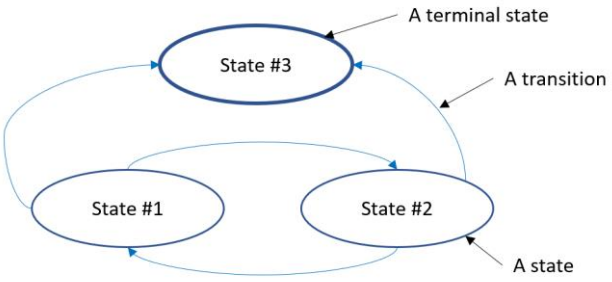

Fig. 6: Example of a state diagram where “State #3” is a terminal state as there are no transitions that exit from that state.

A diamond symbol indicates a dynamic condition for branching from one state to other states. It is also referred as a trigger (see Fig. 7).

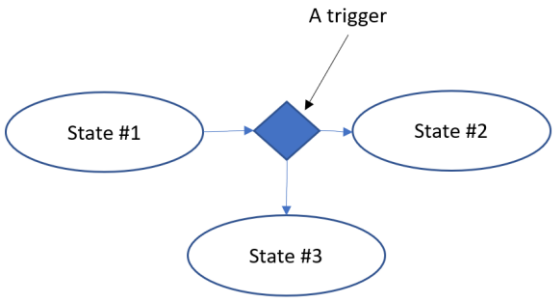

Fig. 7: A trigger represents the possible dynamic condition to transit one state to several other states.

Part I

Mathematical Modelling of the Drilling Process for Real-time Applications

1 Introduction

To access underground energy resources, whether in the form of hydrocarbons fluids or as a heat source for geothermal applications, it is necessary to drill a hole that connect a surface location to a specific place into the earth crust (see Fig. 8). In many cases, it is necessary to drill wells of several kilometers[1] to reach the target zone.

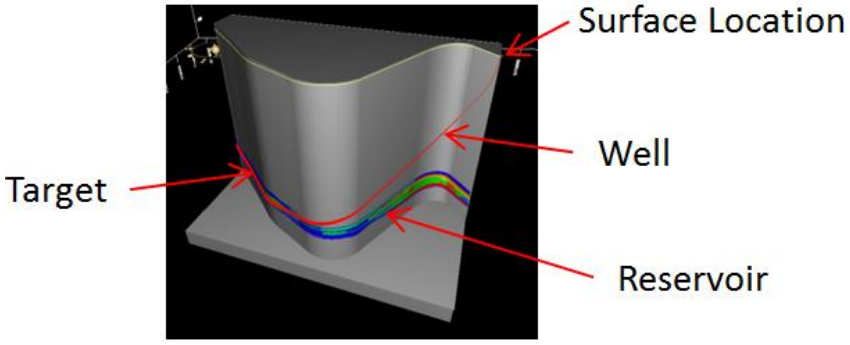

Fig. 8: A well starting from a surface location and reaching a hydrocarbon bearing reservoir.

"The drilling process consists in pressing and rotating a drill-bit against the formation rock to cut into the sediments and thereby create a borehole. To remove the produced cuttings from the hole, one uses a flow of drilling fluid (see Fig. 9) that transports the formation rocks up to the surface, where they are separated from the drilling fluid, using a system of screens with different meshes (so-called shale shakers). The clean drilling fluid flows back into the mud pits and therefore can be reused.

1 To date, the longest well ever drilled is 13500mMD long in the Chayvo field (drilled in 2015).

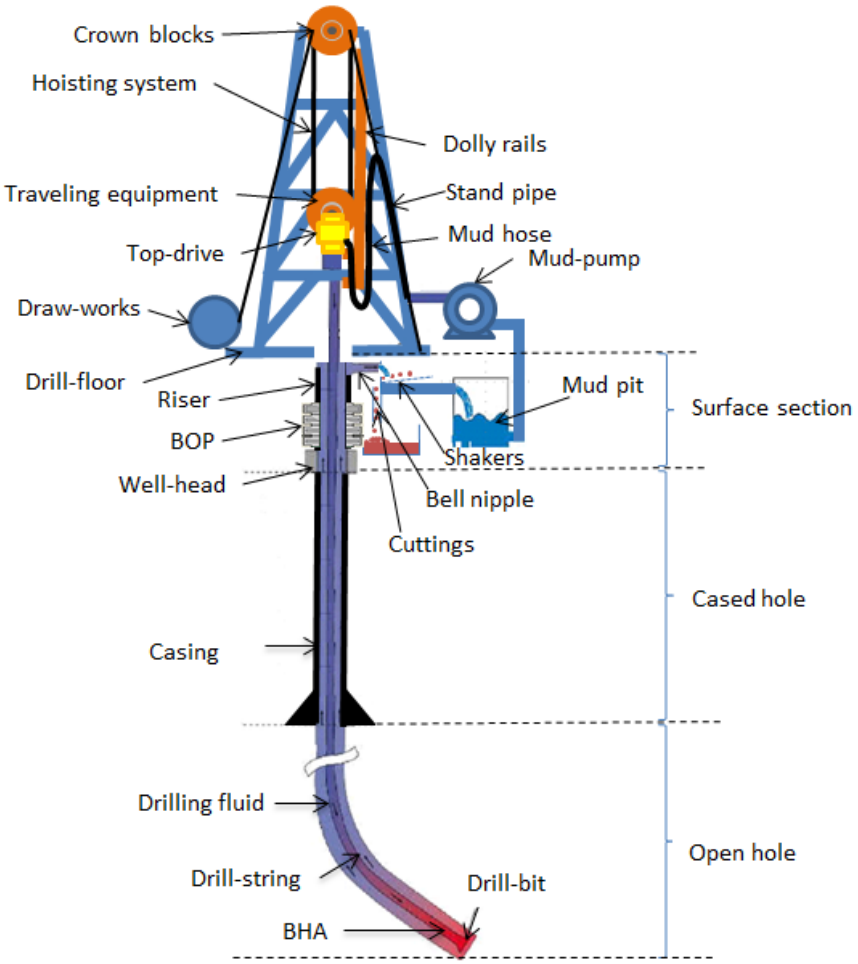

Fig. 9: Schematic view of the main component of a drilling rig and a well.

To allow for the flow of fluid down to the bit, a hollow drill-string is used. Mud pumps (MP) are used to circulate the fluid into the drill-string and after exiting at the bit, the mud continues its path to the surface within the annulus, i.e. the inter-space between the borehole and the drill-string. The same drill-string is used to exert a force from the bit upon the formation. The drill-string hangs in a hoisting system (typically a draw-works, a ram rig or a rack and pinion hoisting system) that controls the position and velocity of the drill-string inside the borehole. The bit can be rotated in two different ways: either using a downhole rotating machine, e.g. a positive displacement motor (PDM) or a

turbine, whose shaft is directly connected to the drill bit or by rotating the whole drill-string." [2]

The lower part of the drill-string is called the bottom hole assembly (BHA). It consists of elements that provide weight on bit (WOB), like drill-collars (DC), components that assist with the directional control, e.g. stabilizers, bent-subs or rotary steerable systems (RSS), and measurement tools such as measurement while drilling (MWD), pressure while drilling (PWD), logging while drilling (LWD) or mechanical subs.

"When rotating the whole drill-string, two methods can be used: either a rotary table which rotates a special hexagonal pipe connected to the top of the drill-string (a so-called kelly), or a top-drive (TD) which consists of a motor whose shaft is connected to the top of the drill-string by a saver-sub.

The role of the drilling fluid is not limited to the transport of the cuttings back to the surface. It also ensures that the pressure in the borehole is:

- Sufficient to stabilize the wellbore walls, i.e. larger than the collapse pressure of the formation rocks.
- Larger than the pressure of the fluid contained in the porous rock, also called the pore pressure, so that formation fluid does not flow uncontrolled into the well while drilling.
- Lower than the fracturing pressure limit of the open hole formations and thereby risking uncontrolled losses of drilling fluid to the formation." [1]

Therefore, at any depth of the open hole section, the borehole pressure shall be larger than the maximum of the collapse and pore pressures and smaller than the fracturing pressure of the formation. This defines a so-called geo-pressure window demarcated by lower and upper pressure bounds.
The hydrostatic pressure at any depth of the borehole can be estimated by integrating the effect of gravity on the mud column [2]:

$$p(TVD) = p_0 + \int_{TVD_0}^{TVD} g\rho_m(z)dz \tag{1}$$

2 This description of the drilling process follows the structure described in the paper by Cayeux and Lande (2013) [1]

where p is the absolute pressure, TVD is the true vertical depth, p_0 is the absolute pressure at the top of the mud column referred by the true vertical depth TVD_0, g is the gravitation acceleration and ρ_m is the drilling fluid density. In conventional drilling, p_0 is the atmospheric pressure while in back pressure managed pressured drilling (MPD), p_0 is the pressure below the rotating control device (RCD).

If the density of the drilling fluid is supposed to be constant, then eq. (1) simplifies to:

$$p(TVD) = p_0 + g\rho_m(TVD - TVD_0) \tag{2}$$

As pressure increases with depth, the graphical representation of the mud window as a function of depth is not always very convenient, because a narrow geo-pressure margin would appear very small due to the large span of pressure across the considered depth range. Therefore, it is usual to represent geo-pressure values in equivalent mud weight (EMW), by converting pressure at any given vertical depth into the fluid density that would have caused the same hydrostatic pressure at the same vertical depth:

$$EMW = \frac{p - p_0}{g(TVD - TVD_0)} \tag{3}$$

Note that if one uses gauge pressure (p_g) instead of absolute pressure and if the true vertical depth is referred to the elevation of the top of the mud column, then the expression simplifies into:

$$EMW = \frac{p_g}{gTVD_{th}} \tag{4}$$

where TVD_{th} is the TVD referred to the top of the borehole. Eq. (4) is the definition of equivalent mud weight that is used by many authors[3]

Then pore, collapse and fracturing pressures can be converted into equivalent mud weight. They are then referred to as pore pressure gradient (PPG), collapse pressure gradient (CPG) and fracturing pressure gradient (FPG).

The circulation of drilling fluid in the annulus causes pressure losses due to viscous friction. Therefore, the hydrostatic pressure gradient, also called in

3 Note that for the rest of this document, we will only use absolute pressure.

EMW the equivalent static density (ESD), gets modified by those pressure losses and result in an equivalent circulating density (ECD). The ECD increases with flowrate as shown in Fig. 10.

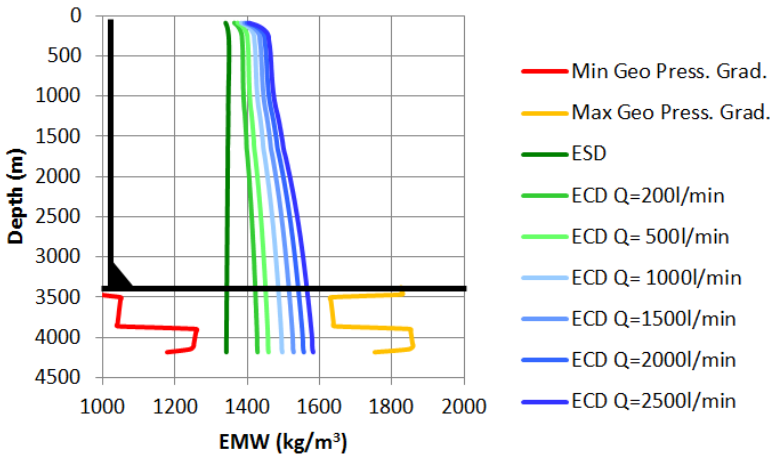

Fig. 10: This graph shows how the annulus ECD increases when the flowrate rises.

As the PPG and CPG tends to increase with vertical depth, there is a limit by which the ESD gets too close to the lower bound of the geo-pressure window while, at the same time, it is impossible to increase the mud weight any further as the ECD would be too close to the FPG, therefore limiting the possible flowrate to clean the hole. It is then necessary to set in place a tube which purpose is to isolate the interior of the borehole from the formation rocks. That tube is cemented in place at its bottom, to create a seal between its interior and the formations. When the tube is suspended in the well-head then it is called a casing. The portion of the borehole that is isolated from the formation is called the cased hole. After the hole has been cased, it is possible to resume drilling, with a new proper mud density. This operation can be repeated several times, resulting in drilling with smaller and smaller hole sizes. It is also possible that the tube isolating the interior of the borehole from external rocks, is suspended at the bottom of the previous casing string. In that case, it is called a liner. Sometime the last tube that is set in the borehole, is not plain as the others, but is made of screens that allow for the passage of hydrocarbon fluids while hindering sand production from the reservoir formation.

On top of the well-head, there is a surface section that ensures that drilling fluids can be collected just below the drill floor. The surface section includes a blow-out preventer (BOP) that can be activated to close the borehole in case of a formation fluid influx and one or two risers, depending on whether the drilling operation is onshore or offshore and in the latter case, whether the operation is conducted from a fixed platform or a floater.

Section drilling consists of a series of operations with the purpose of extending the depth of the well to a planned section total depth (TD) utilizing a certain hole size and to set in place a casing, a liner or sand-screens. The typical operations involved in section drilling are:

- Run in hole (RIH) to the current TD of the borehole with the new drill-string.
- Drill out cement (DOC) or mill a window in the current casing if the wellbore to be drilled is a sidetrack
- Drill a few meters of new formation and perform a formation integrity test (FIT), a leak-off test (LOT) or an extended leak-off test (XLOT) to check if the fracturing pressure limit at the tie in point is sufficient and to gather information about the local minimum horizontal stress (only possible with a LOT or a XLOT).
- Drill to section TD.
- Circulate the hole clean.
- Pull out of hole (POOH).
- Run in hole with the casing string, liner or sand-screens.
- Displace and set cement.
- Unlatch the running string for a liner or sand-screens.
- POOH the running string for a liner or sand-screens.

The management of a section drilling operation consists in reaching high performance levels while keeping the risk of drilling incidents at an acceptable level. Performance is essentially a question of speed and short delays: fast RIH, fast drilling, fast POOH, shortest possible circulation duration, etc. But, at the same time, a drilling operation may encounter many incidents such as:

- Kicks, i.e. unexpected influx of formation fluids in the borehole.
- Wellbore instabilities where the formation rocks break apart in so-called cavings that fall into the borehole.
- Lost circulations when drilling fluids leak inside the open hole section.
- Bridging or pack-offs caused by the partial or complete obstruction of the annulus therefore impeding the circulation of drilling fluids.
- Stuck pipes when the drill-string movement is hindered because of cuttings or cavings accumulations, differential sticking, excessive

friction between the borehole and the drill-string, key seats in the borehole, formation swelling or plastic-flowing.
- Detrimental drill-string vibrations that can reduce drilling performance, but also damage the bit, PDM, RSS, MWD, LWD, PWD or cause tool-joint wear and even failure, and wellbore instabilities by mechanical shocks against the formation rocks.
- Drill-string buckling that can limit achievable weight on bit, but that may also cause premature failure of the drill-string by excessive concentration of stresses on the drill-pipes.
- Pipe washouts where the drill-string starts leaking to the annulus at an unexpected position.
- Pipe failures due to excessive torque, tension or because of material fatigue.
- Formation washouts produced by the erosion of formation rocks when utilizing excessive drilling fluid flow at the bit without sufficient advancement.
- Directional control problems caused by either failure of the directional tools or difficulties to steer the well when crossing faults or when encountering formation layers with a high strength contrast, e.g. a hard stringer.
- Downhole telemetry failure when either the MWD stops working or when the high-speed network of the wired drill-pipe telecommunication system gets broken.

On the other hand, the possible actions that can be performed during a drilling operation, are limited. In conventional drilling, the driller can:

- Control the elevation and speed of the top of the drill-string using the hoisting system.
- Control the angle and rotational speed of the top of the drill-string by utilizing the top-drive (or the rotary table and the kelly).
- Control the flowrate into the drill-string by changing the mud pump speed.
- Set the drill-string in-slips and add or remove pipes to the drill-string.

Besides, the mud engineer can:

- Control the drilling fluid density.
- Modify the mud rheological behavior and its gelation characteristics.

The directional drilling engineer can:

- Decide on changing the settings of the RSS, when one is used, by downlinking new set-points for the tool-face and tool deflection proportion.

- Or choose on when to slide, at which tool-face and for how long when utilizing a PDM.

The operational geologist can:

- Decide when the section TD is reached.
- Choose to change the direction of the well when performing geo-steering to place the borehole as ideally as possible for future production.

In addition, the drilling team is assisted by:

- A data logger whose responsibilities are to gather real-time information about the return flow from the well. Such information includes the quantity of additional gases that have been transported together with the drilling fluid, the characteristics of cuttings and cavings, and abnormal pit volume variations (gain or loss).
- An MWD engineer who oversees the collection of downhole information and verifies that directional measurements are correct.
- An LWD engineer who is responsible for applying proper corrections, and checking the quality, of formation evaluation log measurements.

In the chain of command and control, the driller is responsible for the primary safety of the drilling operation. However, when small deviations from the plan are required, the decisions are taken by the drilling supervisor based on advices from the tool-pusher. More critical decisions are taken by the drilling superintendent or, for extreme cases, by the asset manager.

Recognizing that the number of control actions that the driller can perform are very limited (top of string elevation and orientation, axial and rotational speeds, and drilling fluid flowrate inside the drill-string), the first research question that we would like to address is whether it is possible to estimate the internal state of the system based on the commands provided to the drilling machines, how that can be verified and with which accuracy.

The second research question addressed by this thesis is whether such a continuous estimation of the internal state of the system, based on the commands to the drilling machines, can be utilized to assist drilling operations. We will focus on three domains of application:

- Simulation: the most straightforward domain of application of a trustworthy estimator of the internal state of the system is to create high fidelity real-time simulators. Such simulation environments can be used for training purposes, but also for the preparation of complex

drilling operations or the testing and validation of new drilling procedures and technical solutions.

- Detection of the deterioration of the drilling conditions: many drilling incidents are preceded by weak signals that reflect the deterioration of the downhole drilling conditions. The early detection of the worsening of the drilling situation can help taking proactive actions to avoid the occurrence of drilling incidents and therefore maintaining the progress of the drilling operation without any disruptions.
- Assistance to the driller in controlling the drilling machines:
    - Some of the drilling incidents necessitate a quick detection and reaction to avoid an escalation into a more serious situation. Either because the initial signals are weak or because of a lack of attention from the driller, it is common that his reaction time is too slow, and that the drilling operation endures serious delays because of late reactions.
    - The utilization of excessive accelerations or speeds may also be the source of drilling incidents. Therefore, the application of continuously updated operating envelopes can reduce the risk of occurrence of some drilling incidents.
    - The automatization of standard drilling procedures may increase consistency and improve the quality of collected information. However, such automatic drilling procedures shall operate within acceptable operating envelopes and be protected by automatic reactions to quick events.

Note that in the context of this research work, the control operated by the mud engineer on the mud properties, the steering of the well made by the directional drilling engineer and the geo-steering decisions taken by the operational geologist are all considered as external factors, outside the scope of this thesis.

Furthermore, pipe handling activities are not considered to have an influence on the drilling state except for the change of length of the drill-string and the duration that they take.

2 State of the Art

A schematic representation of the well construction life cycle is shown on Fig. 11. Each of these tasks necessitates some form of modelling of the drilling process.

Fig. 11: Schematic representation of the well construction life cycle. Each of these tasks have their own requirements for modelling of the drilling process. In the context of this thesis, we focus on the requirements for modelling during the construction part of the cycle, i.e. for real-time applications.

Yet, the modelling requirements may differ substantially from one task to the other. The work presented here, focuses on the modelling of the drilling process for real-time applications that are used during the actual construction of the well. In that context, it is important that the modelling of the drilling process

reproduces many of the transient effects that occur during a drilling operation, because that will be the only way to distinguish a normal drilling situation from an abnormal one. This section is written with this perspective in mind. This section describes the current state of the art for the following aspects: drilling hydraulic modelling, drill-string mechanical modelling, heat transfer modelling, wellbore position uncertainty, drilling simulator environments, drilling symptom detection and assistance to the control of drilling machines

2.1 Real-time estimation of the Internal State

2.1.1 Drilling Hydraulic

"Drilling hydraulic calculations are systematically performed during the engineering phase of the preparation of a well, for estimating maximum ECDs during drilling, optimizing bit hydraulics, assessing surge and swab pressures during RIH and POOH and evaluating cuttings transport capabilities. By nature, these estimations made at the planning stage, only require steady state hydraulic calculations except for swab and surge assessments. Therefore, the latter tend to be treated with specific solutions ([3], [4]) without accounting for neither the effects of circulation nor pipe rotation."[4]

2.1.1.1 Motivation for Transient Hydraulic Modelling: Combined Effects of Fluid Compressibility and Viscous Behavior

"Relying solely on steady state hydraulic evaluations to estimate the internal state of a real-time drilling operation, is insufficient, in many cases, as the periods where transient behavior dominate the downhole hydraulic conditions may last for many ten seconds and sometime even several minutes (see Fig. 12). Furthermore, there are many drilling conditions by which the dissociation between circulation and swab/surge induced by axial movement of the drill-string, do not hold, as the axial displacement of the drill-string while circulating has a direct impact on the downhole hydraulic conditions. This is the case for instance during reaming (see Fig. 12) or pulling out of hole with lubrication[5].

4 Excerpt from my contribution to the text of the paper by Pastusek et al. (2019) [200]

5 Pulling out of hole with lubrication consists in applying a relatively small flowrate while pulling the drill-string without rotation.

The modelling and verification of transient effects with a conjoint movement of the drilling fluid and drill-string has been initiated in the early 2000's [5]." [6]

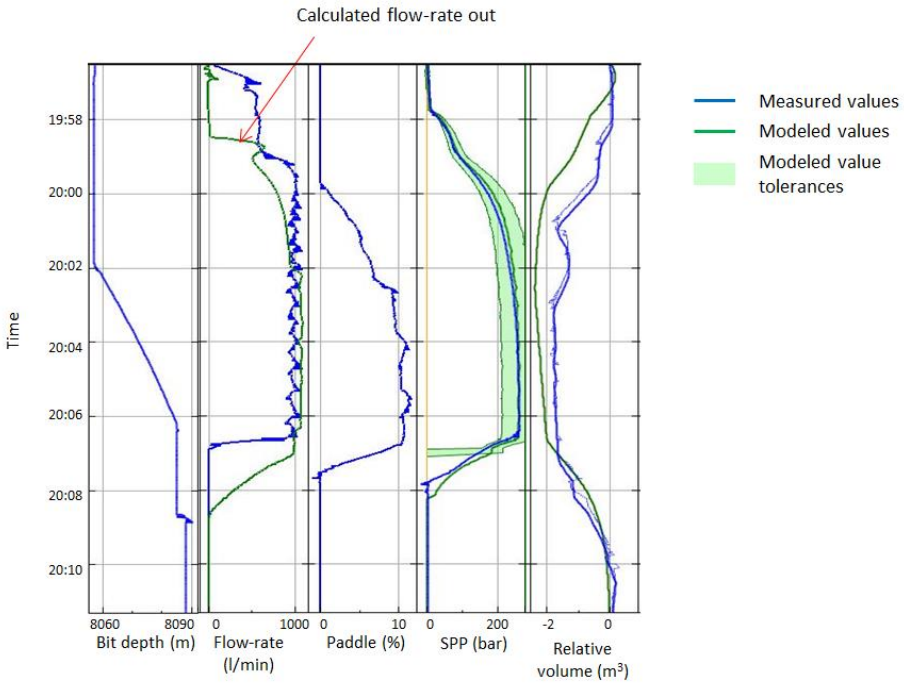

Fig. 12: Comparison between calculated and measured values when reaming down one stand in a long horizontal well (bit depth 8080mMD).

2.1.1.2 Motivation for Transient Hydraulic Modelling: Barite Sag

Another reason that motivates the use of transient hydraulic models for real-time drilling applications, is related to the actions of some components of the drill-string. One of them, is the float valve that is placed inside the BHA to avoid a backflow through the pipes in case of a kick. When there is a float-valve in the BHA, then the drill-string will not fill while running in hole. It is therefore necessary to pour drilling fluid into the drill-string at regular intervals to avoid that the difference of pressure between the interior and the exterior of the drill-pipe may collapse the pipes. A drilling hydraulic model that is used during run

6 Excerpt from my contribution to the text of the paper by Pastusek et al. (2019) [200]

in hole operations shall therefore maintain the level of liquid inside the drill-string to estimate properly at which time the mud column may start moving. This can be complexified when the density, or the temperature, of the fluid that is used to fill the drill-string, is different from the one contained in the annulus as it is described in Cayeux (2012) [6] (see Fig. 13), as the movement of the fluid column can take place even before the whole drill-string is filled, i.e. there is no increase of the pump pressure, because of a gravitational imbalance between the mud column contained in the drill-string and the one in the annulus.

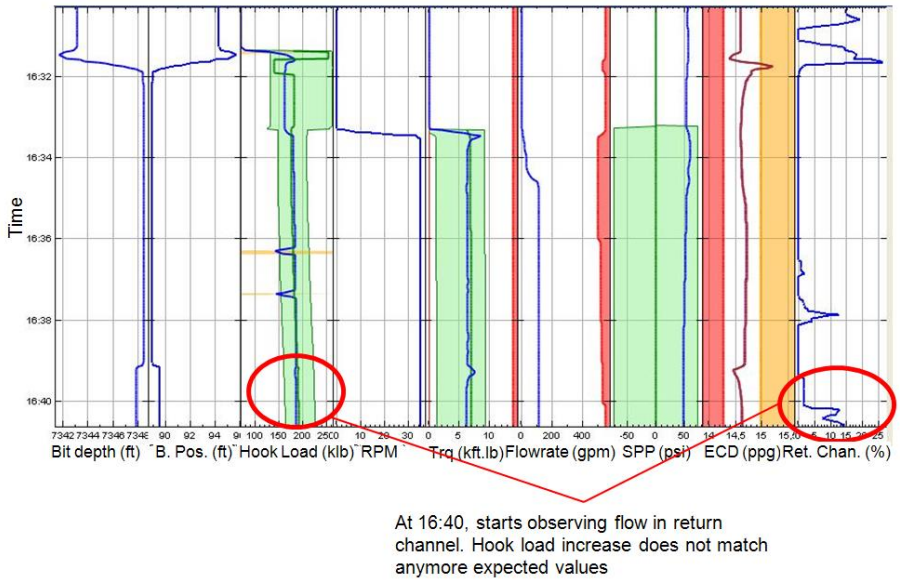

Fig. 13: After filling the pipes for 7 minutes, mud returns could be observed in the return channel even though there was no increase of the pump pressure.

2.1.1.3 Drilling Hydraulic Network

"In conventional drilling and with a simple drill-string and BHA, the drilling hydraulic system is composed of two branches connected at the level of the bit: the drill-string branch and the annulus branch (see Fig. 14). Note that if the bit is off bottom, the annulus branch is longer than the drill-string one. But several junction points may exist, if there are components like circulation-subs, hole openers, under-reamers, downhole motors in the drill-string, because such

elements provide access from the inside of the drill-string to the annulus at other places than the bit. The result is a network of inter-connected branches."[7]

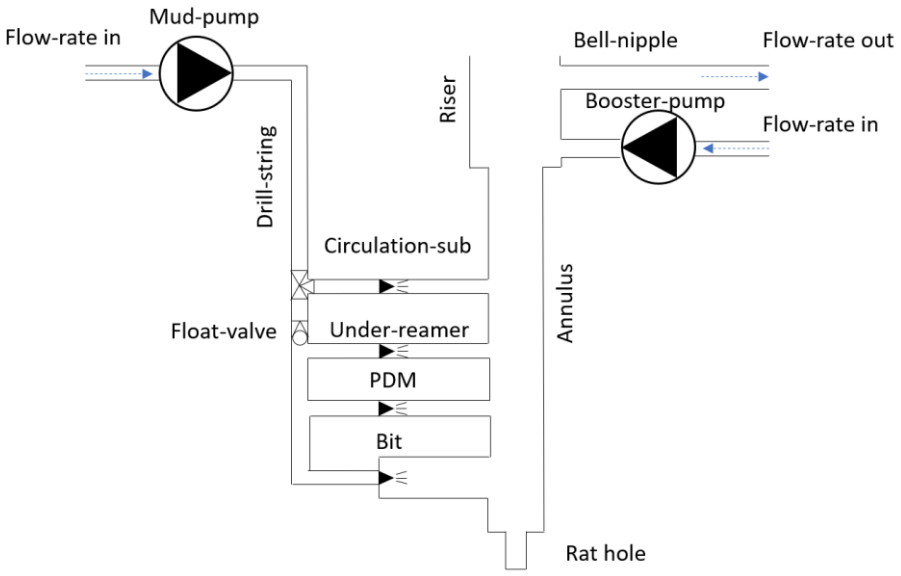

Fig. 14: The drilling hydraulic system is a network of interconnected branches.

When utilizing an under-reamer or a hole-opener, there is necessarily a rat hole. As a consequence, depending on whether the bit is on bottom, partly inside the rat hole or above the rat hole, the annulus around the BHA is constituted of one or two diameters with a variable position of the top of hole with regards to the bit.

Furthermore, when the borehole is not completely cased, there is always a float-valve in the drill-string to ensure that in case of a kick, formation fluids will not flow through the drill-string. Therefore, when running in hole, the drill-string will not fill by itself and the liquid level inside the drill-pipes depend on when the drill-string has been filled and how much the drill-string has been tripped in since the last activation of the mud pumps.

7 Excerpt from Cayeux (2012) [6]

In an offshore context, while drilling from a floater, it is also usual to utilize booster pumping, i.e. pumping from the bottom of the marine riser to increase drilling fluid velocity such that cuttings get better transported inside the large diameter riser.

Combined with the other permanent or manually activated leakage paths to the annulus, there are many possible flow paths in the hydraulic network as illustrated by Fig. 15.

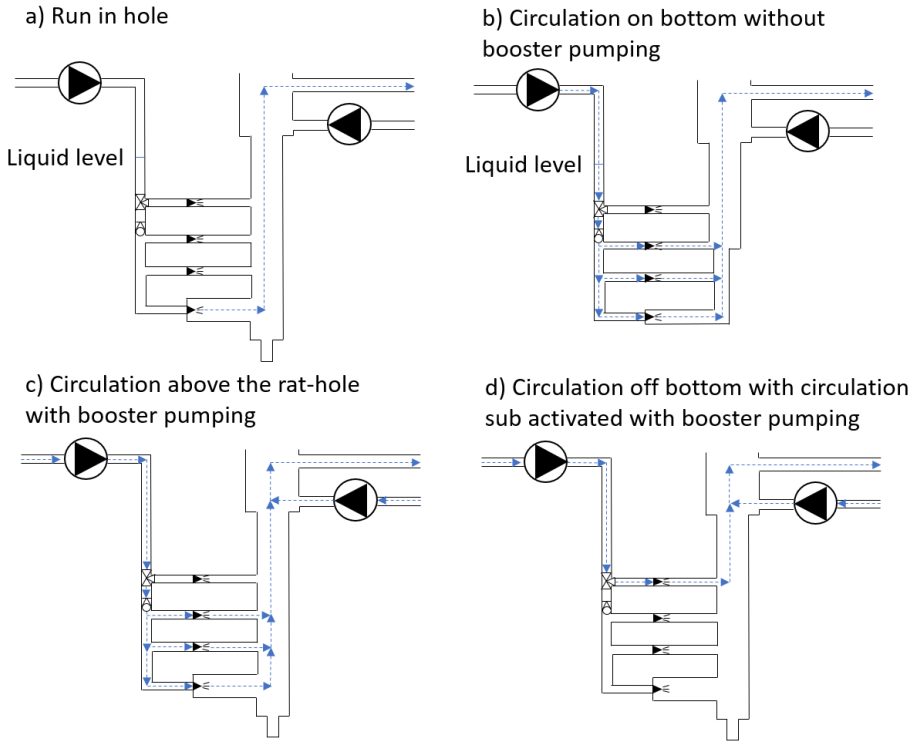

Fig. 15: Examples of flow paths: a) when running in hole, b) when circulating on bottom without booster pumping, c) when circulating above the rat hole with booster pumping, d) when circulating through the circulation sub and with booster pumping.

Cayeux et al. (2014) [7] gives a more complete description of a generalized hydraulic network that encompasses several drilling methods, including back-pressure MPD and dual gradient drilling (DGD).

However, despite the importance of the proper modeling of the hydraulic conditions resulting from the effect of float-valves, anti-spill valves in casing running tools (CRT), partial or complete passage between the interior of the drill-string and the annulus, or any additional pumps and branches that the hydraulic network may have, there has been, to date, almost no mentioning of these intricacies in the literature.

2.1.1.4 Pressure and Temperature Dependence of Drilling Fluid Densities

There are several types of drilling fluids ranging from mists and foams to water-based mud (WBM) and oil-based mud (OBM). Their composition is quite variable but include several components in each of the standard phases of matter excluding plasma, i.e. gas, liquid and solid. Some of the components are part of the original drilling fluid formulation while others are transported with the drilling fluid as part of the drilling process, like formation gas (e.g. hydrocarbon-based but also carbon dioxide, CO_2, and hydrogen sulfide, H_2S), formation liquids like brines or hydrocarbons, and solids such as cuttings and cavings.

Mists and foams normally utilize air or nitrogen (N_2) as the base gas component and a solution of potassium chloride (KCl) with polymers as the liquid phase, with the possible addition of bentonite clay as a viscosifier.

More generally, hydrophilic and oleophilic clays are commonly used as a viscosifier in many drilling fluid formulations. One usually refers to such clays as low gravity solid (LGS) in contrast to weighting material, such as barite, that will be referred to as high gravity solid (HGS).

Because the formation rocks may be naturally fractured, or fractures have been induced as a consequence of excessive annulus pressure, it may be necessary to add lost circulation materials (LCM) so that formation fractures can get sealed. LCM can be based on calcium carbonate ($CaCO_3$) particles of different sizes (fine, medium, coarse, extra-coarse) or various types of magma fibers.

Taking into consideration the composition of the drilling fluid, its apparent density is given by the combination of the densities of its components weighted by the volume fraction of each element:

$$\rho_m = \sum_{i \in \Omega} f_i \rho_i \text{ , with } \sum_{i \in \Omega} f_i = 1 \tag{5}$$

where ρ_m is the density of the drilling fluid, Ω is the set of indices for the different components, f_i is the volume fraction of the i-component and ρ_i is the corresponding mass density.

Because of the necessity to drill in high-pressure and high-temperature (HPHT) conditions, Isambourg et al. (1998) [8] investigated the effect of pressure and temperature on the drilling fluid density. They found that the compressibility and thermal expansion of drilling fluid, for the applicable ranges of pressure and temperature that are typical of drilling operations, are not constant but at least bilinear and therefore, mud densities are biquadratic functions of pressures and temperatures.

As a consequence, the API Recommended Practice 13D propose a model of the mass density of brines that has nine-parameters model [9]:

$$\rho_w = (S_0 + S_1 w_t + S_2 w_t^2 + S_3 w_t^3 + B_w T) + (C_w + D_w T)p + (E_w + F_w T)p^2 \tag{6}$$

where ρ_w is the mass density of the brine, w_t is the weight fraction of the salt at normal condition of temperature and pressure (atmospheric pressure and 297K). $S_0, S_1, S_2, S_3, B_w, C_w, D_w, E_w,$ and F_w are the coefficients of the model. The parameters can be estimated using the model described by Kemp et al. (1989) [10] that gives estimates of the mass density of brines based on the mix of multiple salts typically used in drilling operations, e.g. natrium chloride (NaCl), potassium chloride (KCl) and calcium chloride ($CaCl_2$) (see fig. 5 in Paper II).

The base oil mass density can be approximated by a six-parameters model as proposed by the API Recommended Practice 13D [9]:

$$\rho_o = (A_o + B_o T) + (C_o + D_o T)p + (E_o + F_o T)p^2 \tag{7}$$

where ρ_o is the base oil mass density and $A_o, B_o, C_o, D_o, E_o, F_o$ are the base oil mass density model parameters. Zamora et al. (2013) [11] published the pressure-volume-temperature (PVT) behavior of several base oils.

Fig. 6 in Paper II illustrates the pressure and temperature dependence of a typical base oil, while Fig. 16 shows the variability that exists in the pressure dependence of the mass density of several base-oil used in OBMs.

As a drilling fluid is a mixture of several components, both liquids and solids, Zamora et al. (2013) recommend using the method described by Hoberock et al. (1982) [12] and Peters et al. (1990) [13] to obtain the density of the fluid mix. However, this method only accounts for just a few components, namely a base oil, a brine, a single weighting material type and cuttings, while in practice modern drilling fluids may have many more components such as low gravity solids used for modifying the viscosity, loss circulation materials (LCM) of different sorts and even sometime gas as with foam or aerated drilling.

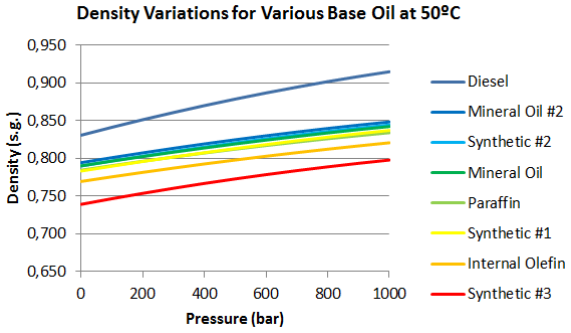

Fig. 16: Example of density dependence on pressure at 50°C for different base oils (ref. Cayeux and Lande, 2013 [1]).

The PVT behavior of gas can be described using a real gas law:

$$\rho_g = \frac{pM}{Z\mathcal{R}T} \tag{8}$$

where $\mathcal{R}$ is the universal gas constant (*i.e.* the product of the Boltzmann's constant and the Avogadro's number, $\mathcal{R}$ = 8.314462175 J/(mol.K)), M is the molar mass of the gas and Z is the gas compressibility factor. It is possible to obtain the gas compressibility factor by solving the generalized compressibility factor correlation (Rao 1997, [14]):

$$\left(Z + \frac{27p_r}{64ZT_r^2}\right)\left(1 - \frac{p_r}{8ZT_r}\right) = 1 \tag{9}$$

where p_r and T_r are the reduced pressured and temperature for the gas, given by:

$$p_r = \frac{p}{p_c} \; and \; T_r = \frac{T}{T_c} \tag{10}$$

and p_c and T_c are the critical pressure and temperature of the gas. Note that for nitrogen $M = 0.028$ kg/mol, T_c =126.3K and p_c= 3390000 pa, and for air M = 0.02897kg/mol, T_c = 132.6K and p_c = 3771000Pa. Eq. (9) can be re-written as a cubic equation:

$$Z^3 - \left(\frac{p_r}{8T_r} + 1\right) Z^2 + \frac{27p_r}{64T_r^2} Z - \frac{27{p_r}^2}{512{T_r}^3} = 0 \tag{11}$$

This equation can be solved numerically in order to obtain Z as a function p_r and T_r. Fig. 17 shows the gas compressibility factor for nitrogen over a typical range of pressure and temperature encountered in drilling operations. For low temperature (30°C) and pressures around 100bar, the correction factor approaches 0.96, while for high temperature (150°C) and high pressure (500bar), it is close to 1.29.

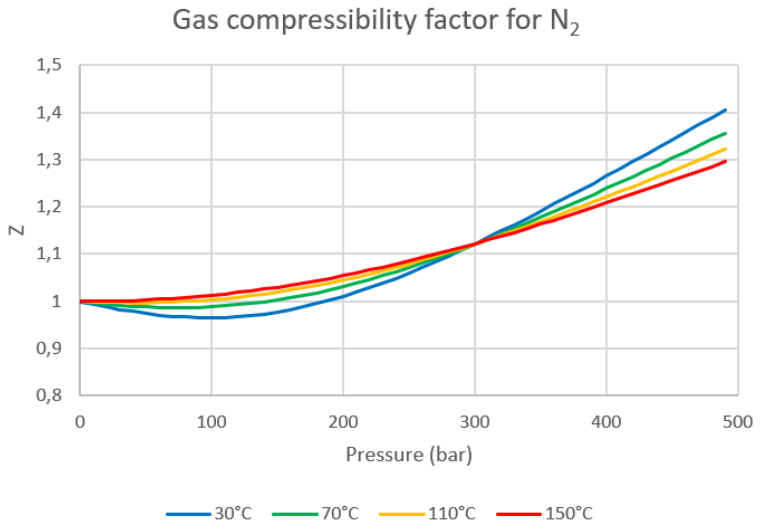

Fig. 17: Compressibility factor as a function of pressure and temperature calculated with the cubic eq. (11).

2.1.1.5 Pressure Losses in Concentric Annuli

"Besides, with the advent of real-time drilling operation centers, around 2005, started an interest in developing solutions that were targeting the real-time simulation of drilling hydraulics [15] with the use of more realistic rheological behaviors than the traditional Bingham plastic ($\tau = \tau_\gamma + K\dot{\gamma}$, where τ is the shear stress, τ_γ is the yield stress, K is the consistency index and $\dot{\gamma}$ is the shear rate) and Power Law models ($\tau = K\dot{\gamma}^n$ where n is the flow index). The two mostly used advanced constitutive laws in the drilling industry are the one from Herschel-Bulkley ($\tau = \tau_\gamma + K\dot{\gamma}^n$) [16] and the one from Robertson-Stiff ($\tau = A(\dot{\gamma} + C)^B$, where A, B and C are the parameters of the flow-curve) [17]. "[8]

Typically, the flow-curve is measured in a Couette rheometer where the torque on the bob (C_{bob}) is utilized to extract the shear stress at the wall as a function of the angular velocity (ref. [18]):

$$C_{bob} = 2\pi K l_{bob} \left(\frac{2\dot{\theta}_{bob}}{n} \frac{\left(r_{cup} r_{bob}\right)^{2/n}}{\left(r_{cup}\right)^{2/n} - \left(r_{bob}\right)^{2/n}} \right)^n \qquad (12)$$

where K and n are respectively the consistency and flow indices of the fluid, $\dot{\theta}_{bob}$ is the angular velocity of the bob, l_{bob} is the bob length, and r_{cup} and r_{bob} are respectively the cup and bob radii.

"In practice, there are typically at least six rheometer measurements (sometime eight) that associate shear stresses with shear rates. Robertson and Stiff described a procedure to best fit their model with the overdetermined set of measurements. On the other hand, the fitting of rheometer measurements with a Herschel-Bulkley model has always been the source of discrepancies between investigators, as small variations on the estimation of the yield stress could lead to large variations of the estimated consistency and flow indices. In 2008, Mullineux [19] published a method that makes the estimation of all three parameters much more stable. The comparison of actual rheometer measurements from eleven drilling fluid samples with their fitted models using the Herschel-Bulkley and Robertson-Stiff flow-curves, showed that the Robertson-Stiff model gives a good overall fitting to the measurements while

8 Excerpt from my contribution to the text of the paper by Cayeux et al. (2017) [186]

the Herschel-Bulkley rheological behavior has a better fitting at low shear-rates [20], which is similar to the results obtained by Beirute and Flumerfelt (1977) on cement slurry [21].”[9]

Roberston and Stiff published a procedure to estimate the pressure loss in a tube and in a concentric annulus using the thin slot approximation when utilizing their rheological model for laminar flow. Kelessidis et al. (2006) [22] did the same for a Herschel-Bulkley fluid. The method is based on calculating the fluid velocity profile in a cross section of a concentric annulus as a function of the pressure-drop gradient, then on integrating over the area the velocities, to determine the corresponding flowrate. As it is an inverse formulation, it is necessary to use an iterative algorithm to get the pressure drop gradient as a function of the flowrate. Fig. 18 illustrates the fluid velocities in such a cross-section. One can notice that there is a constant velocity region in between the outer and inner parts of the annulus. This is the plugged region.

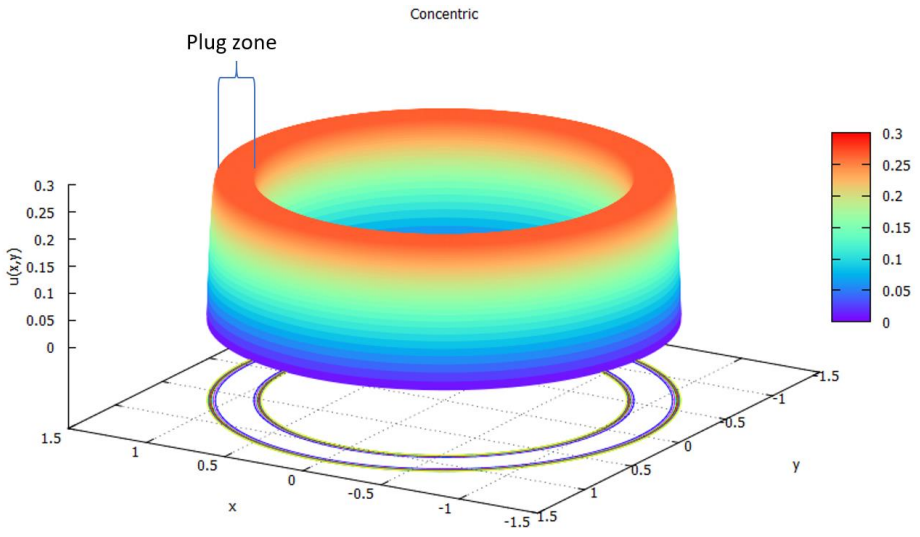

Fig. 18: 3D representation of the fluid velocity in a cross-section of a concentric annulus.

9 Excerpt from my contribution to the text of the paper by Cayeux et al. (2017) [186]

This approach has been extended to turbulent flow by Founargiotakis et al. (2008) [23] by converting the original Herschel-Bulkley rheological behavior to an equivalent power-law rheological model:

$$\begin{cases} K' = \dfrac{\tau_\gamma + K\left(\dfrac{2n'+1}{3n'}\dot{\gamma}_{N_w}\right)^{n'}}{\left(\dot{\gamma}_{N_w}\right)^{n'}} \\ n' = \dfrac{n(1-\xi)(n\xi+n+1)}{1+n+2n\xi+2n^2\xi^2} \end{cases} \tag{13}$$

where K' and n' are respectively the consistency and flow indices of the equivalent power-law rheological behavior, ξ is $\frac{2\tau_\gamma}{h\left(\frac{dp}{ds}\right)_{conc}}$ and $\left(\frac{dp}{ds}\right)_{conc}$ is the viscous pressure drop gradient. Then the generalized Herschel-Bulkley Reynolds number is defined by:

$$Re' = \frac{(2h)^{n'}\rho_f {\bar{v}_f}^{2-n'}}{K' 12^{n'-1}} \tag{14}$$

where $h = \frac{d_w - d_o}{2}$ is the annulus thickness following the thin plate approximation, d_w is the wellbore diameter and d_o is the pipe outer diameter, ρ_f is the fluid mass density, $\bar{v}_f$ is the bulk fluid velocity. Laminar and turbulent flows are defined respectively by $Re' < 3250 - 1150n' = Re'_l$ and $Re' > 4150 - 1150n' = Re'_t$.

In laminar flow, the viscous pressure loss gradient is obtained by solving numerically:

$$Q = \left(\frac{\left(\frac{dp}{ds}\right)_{conc}}{K}\right)^m \frac{2W\left(h/2\right)^{m+2}(1-\xi)^{m+1}}{(m+1)(m+2)}(\xi+m+1) \tag{15}$$

where Q is the flowrate, $m = \frac{1}{n}$ and $W = \frac{\pi\left(d_w^2 - d_o^2\right)}{4h}$.

In turbulent flow, the pressure loss is estimated through a Fanning friction factor f:

$$f = \frac{h}{4\rho_f {\bar{v}_f}^2}\left(\frac{dp}{ds}\right)_{conc} \tag{16}$$

Founargiotakis et al. (2008) [23] suggest defining the Fanning friction factor for Herschel-Bulkley fluid as:

$$\frac{1}{\sqrt{f}} = \frac{4}{n'^{0.75}} \log_{10}\left(Re' f^{1-\frac{n'}{2}}\right) - \frac{0.395}{n'^{1.2}} \tag{17}$$

For transitional flow, a linear interpolation between the laminar and turbulent values of the pressure drop is taken in between the two Reynolds numbers defining the end of the laminar flow regime and the start of the fully turbulent flow:

$$f_{tr} = f_l + \frac{(Re' - Re'_l)(f_t - f_l)}{Re'_t - Re'_l} \tag{18}$$

where $f_l = \frac{24}{Re'_l}$ and f_t is the result of eq. (17) with the Reynolds number Re'_t.

In transitional and turbulent flow, the shear stress at the wall, τ_w, can be estimated using:

$$Q = hW\sqrt{\frac{2\tau_w}{f\rho_f}} \tag{19}$$

while in laminar flow, the shear stress at the wall is:

$$\tau_w = \frac{h}{2}\left(\frac{dp}{ds}\right)_{conc} \tag{20}$$

However, comparison of results obtained between the thin slot approximation and computational fluid dynamic (CFD) simulations shows that the thin slot approximation is acceptable (within 3% difference) for diameter ratio $\frac{d_o}{d_w} \geq 0.5$ [24]. This is because, for lower values of the diameter ratio, the difference of curvature between the outer and inner cylinders plays an important role in the pressure losses as it causes a dissymmetry between the velocity profile at the outer region of the annular, compared to the inner region (see Fig. 19). For smaller values of diameter ratio, it is necessary to resort to CFD computations or finite difference schemes to solve a set of partial differential equations as explained in Erge et al. (2013) [25].

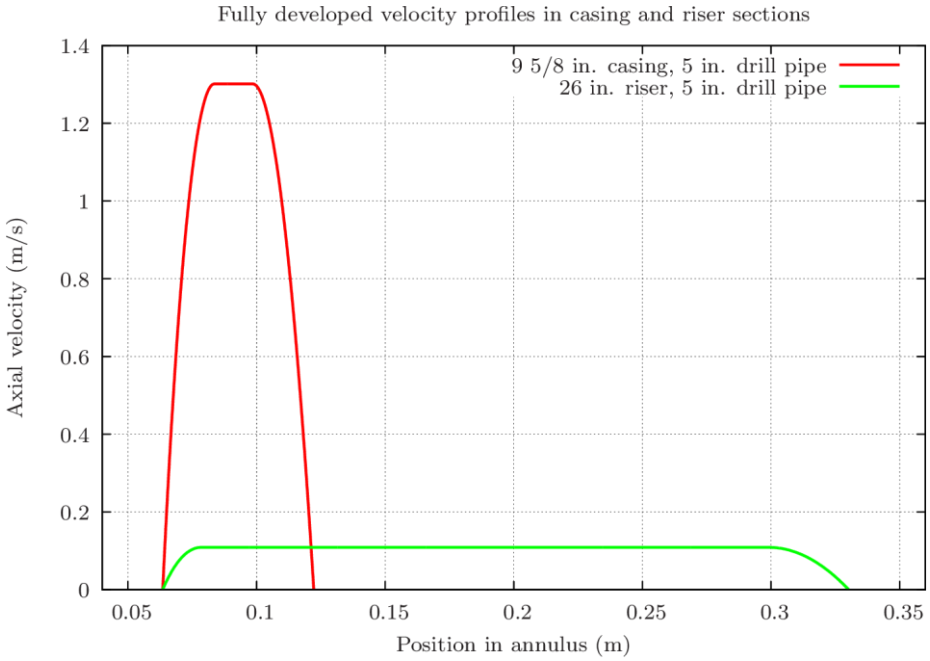

Fig. 19: This graph shows that the velocity profile gets more asymmetric when the diameter ratio gets smaller ($\frac{d_o}{d_w} = 0.51$ for the 5-in drill-pipe in a 9 5/8-in casing, $\frac{d_o}{d_w} = 0.19$ for the 5-in drill-pipe in a 26-in riser) (Courtesy H.J. Skadsem).

2.1.1.6 Pressure Losses in Eccentric Annuli

Furthermore, in deviated wells, the drill-string is decentered and therefore the concentric hypothesis does not hold. This is simply because the drill-pipes rest on the low side of the borehole supported by their tool-joints. The eccentricity of the pipe body is then defined as: $e = \frac{2r}{d_w - d_o}$ where r is the radial displacement of the pipe axis compared to the wellbore axis central line, d_w is the wellbore diameter and d_o is the pipe diameter. Investigators have looked at the inclusion of the effects of pipe eccentricity on the flow of Herschel-Bulkley fluids in annuli [26]. As illustrated with Fig. 20, with sufficiently large eccentricity, it is possible that the fluid stays static on the narrow side of the annulus.

The numerical stability of solutions to the flow in eccentric annulus is a problem, since solvers converge slowly due to numerical problems when approaching the plug zones, as erratic oscillations in the effective viscosity persist for long periods.

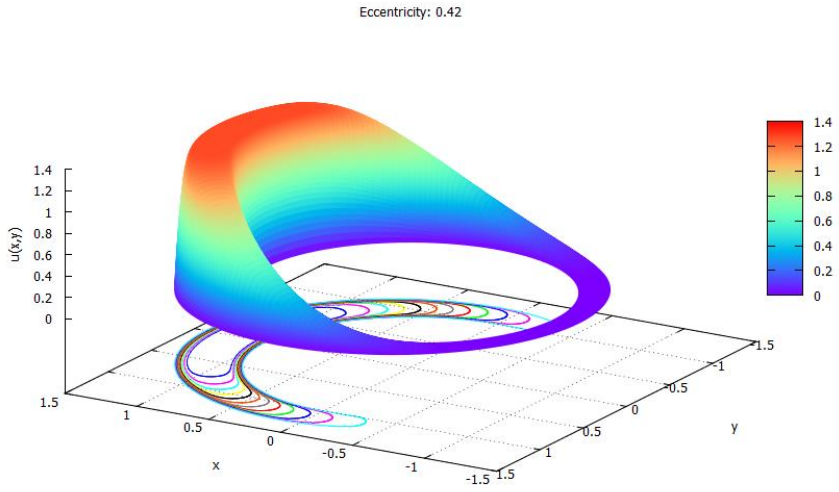

Fig. 20: With sufficiently large eccentricity, the fluid does not move on the narrow side of the annulus (Courtesy H.J. Skadsem).

This fact makes such solutions far too slow and computer intensive to be used in real-time applications. The alternative to numerical computations is to use correlations. Haciislamoglu and Langlinais (1990) [27] published a correlation that convert the pressure drop estimated for concentric flow in laminar conditions to the one that would be obtained for an eccentric configuration. A few years later, Haciislamoglu and Cartalos (1994) [28] published a similar correlation for turbulent flow. If one denote $\left(\frac{dp}{ds}\right)_{conc}$ the frictional pressure gradient calculated for a concentric annulus, then the frictional pressure gradient in the eccentric case $\left(\frac{dp}{ds}\right)_{ecc}$ is defined by:

$$\left(\frac{dp}{ds}\right)_{ecc} \approx C_{ecc}\left(\frac{dp}{ds}\right)_{conc} \tag{21}$$

where C_{ecc} is the correction correlation from concentric to eccentric conditions, and s is the curvilinear abscissa. In laminar flow, C_{ecc} can be expressed as:

$$C_{ecc} = 1 - 0.072\left(\frac{e}{n}\right)\left(\frac{d_o}{d_w}\right)^{0.8454} - \frac{3}{2}\left(e^2\sqrt{n}\right)\left(\frac{d_o}{d_w}\right)^{0.1852} + 0.96e^3\sqrt{n}\left(\frac{d_o}{d_w}\right)^{0.2527} \quad (22)$$

and in turbulent flow:

$$C_{ecc} = 1 - 0.048\left(\frac{e}{n}\right)\left(\frac{d_o}{d_w}\right)^{0.8454} - \frac{2}{3}\left(e^2\sqrt{n}\right)\left(\frac{d_o}{d_w}\right)^{0.1852} + 0.285e^3\sqrt{n}\left(\frac{d_o}{d_w}\right)^{0.2527} \quad (23)$$

For transitional flow, a linear interpolation based on the generalized Reynolds number is made between the calculated values for laminar and turbulent conditions.

Haciislamoglu and Cartalos do not give explicitly the domain of validity for these correlations, but the graphs used in the publication have a span of Reynolds number between 10 and 10000, which gives an indication of the range of Reynolds number that have been used to derive the correlations.

The accuracy of such a methodology has been estimated by comparison with CFD calculations [24] and using a laboratory scale flow loop equipped with a differential pressure sensor [29]. In both cases, it has been found to be very accurate for laminar flow when utilizing a generalized flow behavior index instead of the value from the Herschel-Bulkley rheological curve. This is simply because the original correlation had been developed for power law fluids [30]. On the other hand, the correlation is somewhat less precise for transitional and turbulent flows.

2.1.1.7 Pressure Losses in Annuli with Rotation of the Inner Pipe

The effect of pipe rotation has been a source of problems with respect to the estimation of pressure losses in annuli, as laboratory experiments have shown that under the correct conditions, the frictional pressure drop can decrease with rotation and in other conditions it can increase. On the other hand, measured pressure losses in full scale experiments [31] and in actual drilling operations

have always shown that frictional pressure losses always increase with increasing pipe rotational speed.

The reason for the possible decrease of pressure losses with pipe rotation is linked to the decrease of the apparent viscosity of yield stress power law fluid with increasing shear stress. Nevertheless, passed a certain level of rotational speed, inertial effects dominate, and the pressure losses increase again. These inertial effects are caused by the centrifugal force that applies to drilling fluid when it is displaced radially, and which therefore can initiate Taylor vortices.

Numerical simulations also reproduce this effect for concentric configurations (see Fig. 21), but with sufficient pipe eccentricity, numerical and experimental studies show that the frictional pressure drop always increases for all rotational speed.

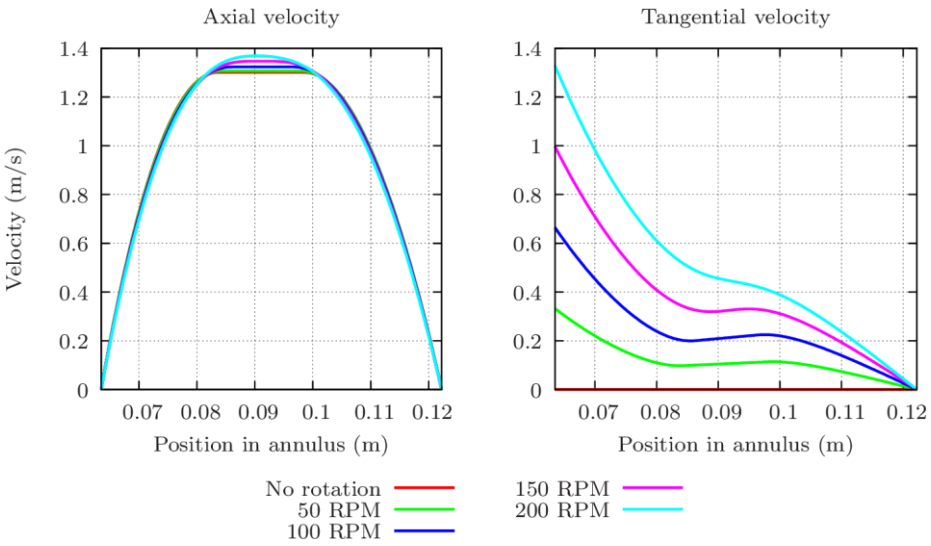

Fig. 21: This graph shows the effect of pipe rotation on the axial and tangential velocities in a concentric annulus with a 5-in inner pipe and 9 5/8-in borehole (Courtesy H.J. Skadsem).

One can therefore obtain an estimation of the pressure loss gradient in an eccentric configuration with drill-pipe rotation $\left(\frac{dp}{ds}\right)_{ecc+rot}$, by applying a rotation specific correlation correction:

$$\left(\frac{dp}{ds}\right)_{ecc+rot} \approx C_{rot} C_{ecc} \left(\frac{dp}{ds}\right)_{conc} \quad (24)$$

where C_{rot} is the rotation correction correlation. Based on measurements made at the full-scale test rig Ullrigg, an empirical definition of C_{rot} is given by:

$$C_{rot} = 1 + max\left(0, 1.639 - \frac{394.63}{Re'}\right)\frac{\sqrt{Ta}}{Re'} \quad (25)$$

where Ta is the Taylor number:

$$Ta = \frac{d_o(d_w - d_o)^3}{16}\left(\frac{\rho_f \dot{\theta}}{2\pi\mu_{eff}}\right)^2 \quad (26)$$

where $\dot{\theta}$ is the angular rotational speed and μ_{eff} is the effective viscosity, i.e. $\mu_{eff} = \frac{\tau}{\dot{\gamma}}$.

Eq. (25) has been derived from experimental data where the Taylor number varied between 0 and 420000, and the Reynolds number was comprised between 10 and 2000.

2.1.1.8 Pressure Losses in Annuli with Axial Movement of the Inner Pipe

The axial movement of drill-pipes disturbs the fluid velocity profile in a cross section of an annulus, since to respect the no-slip at the walls condition, the fluid velocity shall be zero at the wellbore wall and equals to the pipe axial velocity on the other side. When solving this problem for a Newtonian fluid in a concentric annulus [32], it is possible to reformulate the pressure drop estimation to the one of a static drill-pipe by multiplying the bulk fluid velocity by a correction factor called the clinging factor [33]:

$$\left(\frac{dp}{ds}\right)_{axial\ velocity}\left(v_{f_b}, v_{p_a}\right) = \left(\frac{dp}{ds}\right)_{conc}\left(K_t v_{f_b}\right) \quad (27)$$

with K_t being the clinging factor and $\left(\frac{dp}{ds}\right)_{axial\ velocity}$ being the pressure drop gradient accounting for the pipe axial velocity, v_{f_b} the fluid bulk velocity and v_{p_a} the pipe axial velocity. For the Newtonian concentric case in laminar conditions, K_t can be expressed as:

$$K_t = \frac{1}{2\ln\frac{d_o}{d_w}} + \frac{\left(\frac{d_o}{d_w}\right)^2}{1-\left(\frac{d_o}{d_w}\right)^2} \tag{28}$$

Solutions have been presented for more complex rheological behavior like power law [34] and Bingham plastic [35] [36]. Podryadinkin et al. (2014) [37] have demonstrated that numerical schemes can solve this problem for concentric annuli in the presence of fluid following a Herschel-Bulkley behavior, unfortunately at the expense of much computational resources. In 2015, Gjerstad and Time [38] have presented an explicit approximation to this problem for Herschel-Bulkley fluids for concentric annuli, which has a good accuracy compared to numerical solutions and that does not need iterations to get an estimation of the frictional pressure drop. As there are multiple cases, depending on the relative motion of the pipe and the position of the plug region in the annulus, we leave the reader to look at the full description in Gjerstad and Time (2015) [38].

One can therefore obtain an estimation of frictional pressure loss gradient that account for the pipe axial velocity, the eccentricity and the pipe rotational velocity:

$$\left(\frac{dp}{ds}\right)_{ecc+rot+ax} \approx C_{rot}C_{ecc}\left(\frac{dp}{ds}\right)_{conc}\left(K_t v_{f_b}\right) \tag{29}$$

2.1.1.9 Pressure Losses in Annuli Across Tool-joint

Pressure losses in annuli are also influenced by any places where the drilling fluid passes through positions where the annulus cross-section varies rapidly over a short distance. This is for instance the case when passing by the tool-joints of drill-pipes. Simoes et al. (2007) [39] addressed that problem, by running multiple CFD simulations for a wide range of geometrical and fluid rheological behavior combinations and thereafter by fitting a friction factor that captures the effect of tool-joints on the annulus pressure losses. In 2011, Enfis et al. [40] used a similar approach but this time using actual pressure drops measurements taken with a laboratory test setup. The pressure loss across a tool-joint of length l_{TJ} is given by:

$$dp_{TJ} = \alpha_{TJ,rot} 2 f_{TJ} \frac{\rho_f \overline{v}_f{}^2}{d_{hyd}} 5 l_{TJ} \tag{30}$$

where f_{TJ} is a friction factor for non-rotating pipe, $d_{hyd} = d_w - d_{TJ}$ is the hydraulic diameter for a tool-joint diameter d_{TJ} and $\alpha_{TJ,rot}$ is a pressure loss ratio reflecting the effect of pipe rotation:

$$\alpha_{TJ,rot} = 0.773 \left(0.64 + \frac{\tau_\gamma}{\rho_f \overline{v}_f{}^2} \right)^{1.83} e^{1.06} n^{0.183} Ta^{0.024} Re^{0.022} \left(\frac{d_w}{d_o} - 1 \right)^{-0.231} \tag{31}$$

Eq. (31) is valid for Taylor number between 40 and 478000 and Reynolds number between 30 and 8600. The Taylor number is calculated with a weighted average pipe diameter $d_{pe} = \frac{l_p d_o + l_{TJ} d_{TJ}}{l_p + l_{TJ}}$ (l_p is the length of the body part of the pipe, d_{TJ} is the tool-joint diameter).

The friction factor correlation for Herschel-Bulkley fluid is:

$$f_{TJ} = 2.87 \left(0.308 + \frac{\tau_\gamma}{\rho_f \overline{v}_f{}^2} \right)^{0.599} e^{-0.97} n^{0.186} Re^{-0.63} \left(\frac{d_w}{d_o} - 1 \right)^{-0.073} \tag{32}$$

Enfis et al. [40] do not indicate the domain of validity of the above equation except that it has been developed using the same experimental data as those used to derive the correlation (31). So, it is assumed that it is valid for Reynolds numbers between 30 and 8600.

2.1.1.10 Pressure Losses in Tubulars

Otherwise, the pressure loss inside the drill-string is associated with a simpler geometry than in the annulus as it is generated by the fluid flow in a cylindrical pipe where the effect of rotation does not need to be considered. In laminar flow, following the approach of Kelessidis et al. (2006) [22], the viscous pressure loss gradient is obtained by solving numerically:

$$\mathrm{Q} = \frac{\pi n \left(\frac{d_i \partial_s p}{4} - \tau_\gamma\right)^{1+\frac{1}{n}}}{K^{\frac{1}{n}} \left(\frac{\partial_s \mathrm{p_v}}{2}\right)^3} \left(\frac{\left(\frac{d_i \partial_s p}{4} - \tau_\gamma\right)^2}{1+3n} + \frac{2\tau_\gamma \left(\frac{d_i \partial_s p}{4} - \tau_\gamma\right)}{1+2n} + \frac{\tau_\gamma^2}{1+n} \right) \tag{33}$$

where $\partial_s p$ is the viscous pressure loss gradient in a pipe and d_i is the inner pipe diameter.

For turbulent flow in a pipe eq. (19) is replaced by:

$$f = \frac{d_i}{8\rho_f {\bar{v}_f}^2} \partial_s p \tag{34}$$

and the same principles as those explained in section 2.1.1.5 for the estimation of the viscous pressure losses in annuli in turbulent and transitional flow are used.

2.1.1.11 Pressure Losses through Measurement While Drilling Tools and Bits

Yet, there are a few components that should be handled in a specific manner. The pressure losses through special elements of the BHA like the MWD, PWD, LWD, RSS can be treated as a pressure loss through an orifice:

$$\Delta \mathrm{p}_{XWD} = \frac{\dot{m}^2}{C_{xwd} \rho_m} \tag{35}$$

where $\Delta \mathrm{p}_{XWD}$ is the pressure loss through the special element of the BHA, $\dot{m}$ is the mass flowrate, ρ_m is the density of the drilling mud and C_{xwd} is the pressure loss constant of the tool that must be provided by the tool manufacturer. For the pressure drop through nozzles, as the ones found on a bit, a hole opener or an under-reamer, the same formula can be used but in this case, the pressure loss constant (C_{nozzle}) can be expressed as [41]:

$$C_{nozzle} = 1.975 {c_{nozzle}}^2 {A_{orifice}}^2 \tag{36}$$

where c_{nozzle} is the nozzle discharge coefficient and $A_{orifice}$ is the total flow area. As pointed out by Wells and Pessier (2003), the nozzle discharge

coefficient depends on the geometry of the nozzle, e.g. round, star, slot, Y, cross, fluted, dual-jet, K-nozzle [41].

2.1.1.12 Pressure and Temperature Dependence of Rheological Behavior

As for any fluids, the rheological behavior of drilling muds depends on temperature [42]. Standard rheometer measurements are made at 50°C only, but sometime the mud engineer also reports model 35 rheometer measurements at two other temperatures, like for instance 20°C and 80°C. However, if these measurements are made with a standard model 35 apparatus, there is a poor control of the temperature during the measurement and even though the fluid sample has been cooled down or warmed up to a given temperature, it is not unusual that the temperature changes throughout the scan of different shear rates.

In addition, the rheological behavior of drilling fluids depends also on pressure and as they are exposed to a wide range of pressures, this fact impacts substantially the viscous flow behavior of the fluid, as it can be seen on fig. 9 and 10 of Paper II. The pressure dependence of the rheological behavior can only be measured with rheometers that allow for the pressurization of the sample.

Otherwise, it is necessary to rely on pressure and temperature extrapolation models for specific mud types. The pressure and temperature dependence of the shear stress of drilling fluids follows an Arrhenius law as pointed out by Houwen and Geehan (1986) [42]. So, for a mud type, it is possible to make several pressure and temperature measurements of different samples of that type of mud and thereafter perform a fitting of the coefficients of the pressure/temperature dependence function to the measurements. Then when shear stresses are measured at a given pressure and temperature for a new sample of that type of mud, it is possible to extrapolate the shear stresses at other pressures and temperatures by applying the calibrated Arrhenius models. Froitland et al. (2011) [43] define the fitting curve as:

$$\tau_{\dot{\gamma}} = \left(A_{\dot{\gamma}} + D_{\dot{\gamma}}\sqrt{p} + \frac{E_{\dot{\gamma}}}{T}\right) e^{\left(B_{\dot{\gamma}} \times T + \frac{C_{\dot{\gamma}}}{\sqrt{p}}\right)} \tag{37}$$

where $\tau_{\dot{\gamma}}$ is the shear stress at a given shear rate $\dot{\gamma}$, p is the pressure, T is the temperature and $A_{\dot{\gamma}}$, $B_{\dot{\gamma}}$, $C_{\dot{\gamma}}$, $D_{\dot{\gamma}}$, $E_{\dot{\gamma}}$ are the calibration parameters for that drilling fluid at the given shear rate $\dot{\gamma}$.

2.1.1.13 Gel Strength

"The American Petroleum Institute (API) recommended practice to estimate gelation properties is to measure gel strengths at 3 rpm with a model 35 rheometer after a resting duration of $t_1 = 10s$ and $t_2 = 600s$ [44] [45]. Bjørkevoll et al. (2003) [46] showed that the gel strength of drilling fluids increases logarithmically with time. However, as a logarithmic function tends to $-\infty$ when $t \to 0$, for small durations, the gel strength is considered to increase linearly with time from an initial value, the yield stress. Therefore, they propose to express the gel strength (τ_{gel}) as a function of time in the following way:

$$\begin{cases} \tau_{gel}(t) = \tau_\gamma + \dfrac{t}{t_1}\left(\tau_{gel}(t_1) - \tau_\gamma\right), \forall t \in [0, t_1] \\ \tau_{gel}(t) = \tau_{gel}(t_1) + \dfrac{\tau_{gel}(t_2) - \tau_{gel}(t_1)}{\log(t_2 - t_1)} \log(t - t_1), \forall t > t_1 \end{cases} \quad (38)$$

"[10]

2.1.1.14 Thixotropy in Viscous Flow

"Furthermore, the shear stresses used to represent the rheological behavior of drilling fluids are the ones corresponding to readings made with a rheometer after stabilization of the measurement. In practice, it takes a minimum time before steady state conditions are reached for every change of shear rate. This is because drilling fluids are thixotropic, i.e. their flow properties depend on the history of the applied shear stresses [47].

Fig. 22 shows how a WBM responds to a scan of shear rates from high to low and then from low to high. One should notice that after changing the shear rate, it takes several ten seconds to reach the steady state shear stress.

Cheng and Evans (1965) [48] proposed to express the rheological behavior of a thixotropic fluid as a function of the shear rate and a structure parameter λ.

10 Excerpt from my contribution to the text of the paper by Cayeux et al. (2018) [186]

The latter parameter describes how the micro-structures develops as a function of time and the shear rate. It is defined by the following differential equation:

$$\frac{d\lambda}{dt} = F(\lambda, \dot{\gamma}) \tag{39}$$

where F is a well-chosen phenomenological function that describes the equilibrium between the flocculation and the deflocculation processes.

Based on multiple publications that follows the structure parameter concept, Mewis and Wagner (2009) [49] propose a general formulation of F:

$$F(\lambda, \dot{\gamma}) = k_1 \dot{\gamma}^a (1-\lambda)^b - k_2 \dot{\gamma}^c \lambda^d \tag{40}$$

where k_1 and k_2 are respectively the coefficients that characterize the breakdown and the buildup of floccules, and a, b, c and d are either explicitly specified by the model or fitted to a series of observations.

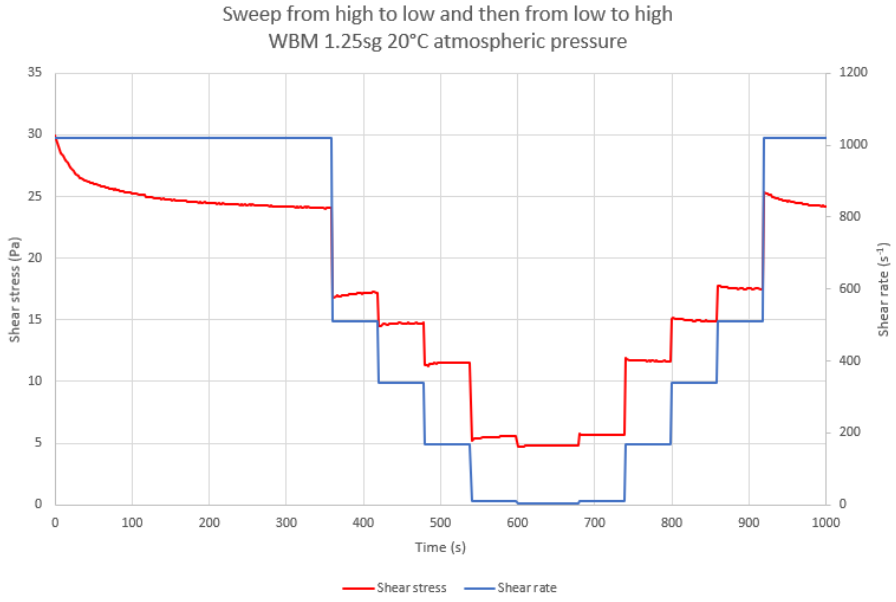

Fig. 22: Illustration of the time dependence, due to thixotropy, when changing the speed of a scientific rheometer with a water-based mud (WBM).

One of the simplest model that has sufficient characteristics to describe yield stress fluids with the effect of thixotropy is the model developed by Coussot et al. (2002) [50]. These authors have studied the thixotropic effects on clay

suspensions and the model has been applied to an oil-based mud [51]. Therefore, it can be of interest to investigate how their model fits with measurements made with various drilling fluids.

The model of Coussot et al. relies on the following definition of the structure parameter:

$$\frac{d\lambda}{dt} = k_1 - k_2\dot{\gamma}\lambda \tag{41}$$

and therefore, in terms of the general formulation of Mewis and Wagner corresponds to the following exponent coefficients: $a = 0, b = 0, c = 1$ and $d = 1$.

As discussed in Møller et al. (2006) [52], the structure parameter in the Coussot model can be interpreted as the degree of interconnection of the microstructure, for example with a bentonite colloidal gel that would be the number of connections per unit volume. It is therefore a positive value with no special maximum bound, i.e. $\lambda \in [0, \infty[$.

At equilibrium, the structure parameter reaches λ_{eq} such that:

$$\lambda_{eq} = \lim_{t_{step} \to \infty} \lambda = \frac{k_1}{k_2\dot{\gamma}} \tag{42}$$

The relationship between the shear stress and the shear rate is defined as a modification of an effective viscosity:

$$\tau = \mu_0(1 + \lambda^n)\dot{\gamma} \tag{43}$$

where μ_0 and n are additional parameters of the model. It should also be noted that when $\dot{\gamma} \to 0$, the shear stress tends to 0 when $n \leq 1$ and therefore can model a fluid with no yield stress. But when $n \geq 1$, then the model exhibits a yield stress as pointed out by Møller et al. (2006) [52].

The Coussot model can be fitted to a sequence of measurements made with a scientific rheometer when performing multiple variations of the shear rate. The fitting algorithm used in the next example is based on simulated annealing and utilizes an objective function (δ_{rms}) that is the cumulative sum of the RMS (root mean square):

$$\delta_{rms} = \sum_{i=1}^{k} x_{rms_i} = \sum_{i=1}^{k} \sqrt{\frac{\sum_{j=1}^{i} (\tau_j - \tilde{\tau}_j)^2}{i}} \tag{44}$$

where x_{rms_i} is the RMS at measurement i, τ_j and $\tilde{\tau}_j$ are respectively the measured and estimated shear stresses corresponding to the measurement j. The reason for using the cumulative sum of the RMS instead of the final RMS, is to ensure that the fit is acceptable everywhere during the sequence.

The optimization of the Coussot model parameters applied to a scan of different shear rates of a WBM with mass density 1.25sg gives the following value: $k_1 = 300, k_2 = 0.3, \mu_0 = 0.011$ and $n = 0.80$. As it can be seen on Fig. 23, the Coussot model estimates very large spikes of shear stress, each time the shear rate is changed.

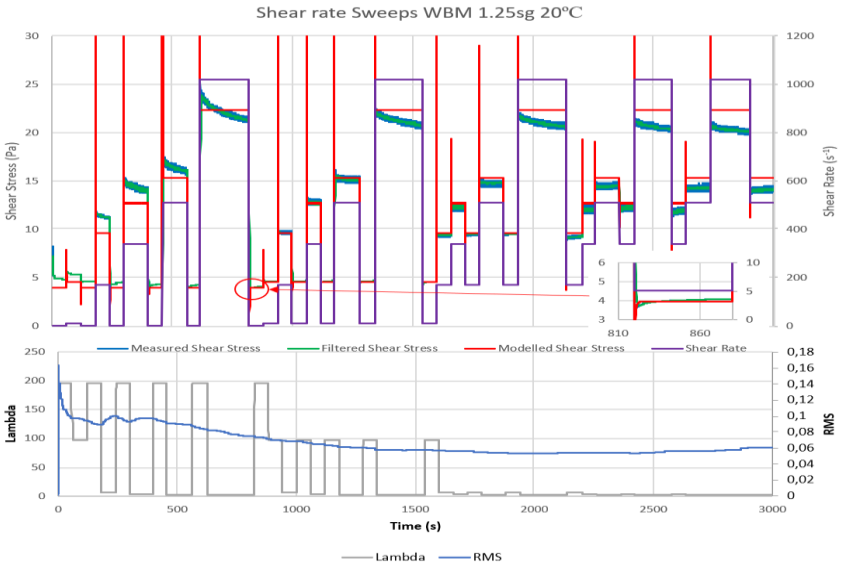

Fig. 23: The top graph shows a comparison between the measured shear stresses and estimated values utilizing the Coussot model when applying a sequence of different shear rates to a WBM of mass density 1.25sg. The bottom graph shows the corresponding structure parameter (λ) and the RMS."[11]

11 Excerpt from my contribution to the text of the paper by Cayeux et al. (2018) [186]

The RMS varies between 0.05 and 0.1. The model predicts a decay of the shear stress when switching to low shear rates that is similar to the one that is measured, but it does not manage to predict the evolution of the variations of shear stresses when switching to higher shear rates than at the starting point.

Skadsem et al. (2019) [53] wanted to check whether the non-conformant response of drilling fluids compared with published thixotropic behaviors, was caused by the presence of solids. They analyzed the thixotropic response of unweighted versions of the same WBM and OBM that were used for our study of the thixotropic behavior of drilling fluids. They found that one of the published thixotropic models (Dullaert and Mewis 2006) [54] could reproduce the general trend observed with measurements made with the OBM, when stepping down the shear rate (see Fig. 24).

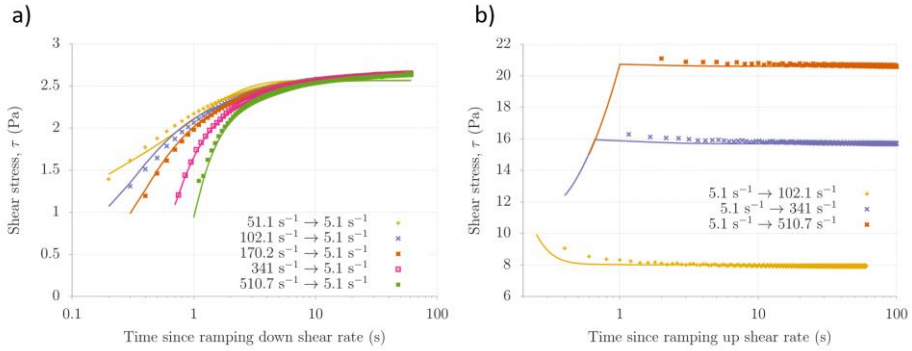

Fig. 24: Measurements and model predictions for shear stresses for an unweighted OBM: a) following shear rate steps down to 5.1 s^{-1}, b) following shear rate steps up from 5.1 s^{-1} (courtesy of Skadsem et al. 2019 [53]).

As it can be seen on Fig. 24b, and in contrast to Fig. 25 that shows step-ups from 10.2s^{-1} for the weighted version (1750kg/m^3) of the same OBM, the time to reach steady state conditions when stepping up is shorter for the unweighted version of the drilling fluid.

Despite the reasonable results for the modelling of the stepping up and down of an unweighted OBM, the model from Dullaert and Mewis (2006) is not so well suited to reproduce the thixotropic behavior of an unweighted WBM, as it can be seen on Fig. 26.

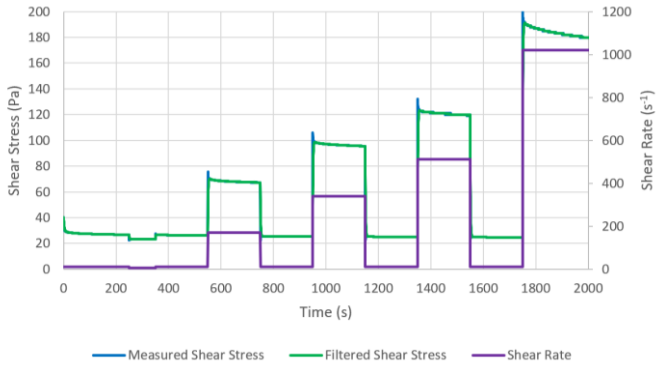

Fig. 25: Series of step ups and downs from a shear rate based of 10.2s^{-1} with a weighted version (1750kg/m^3) of the same OBM as used in Fig. 24.

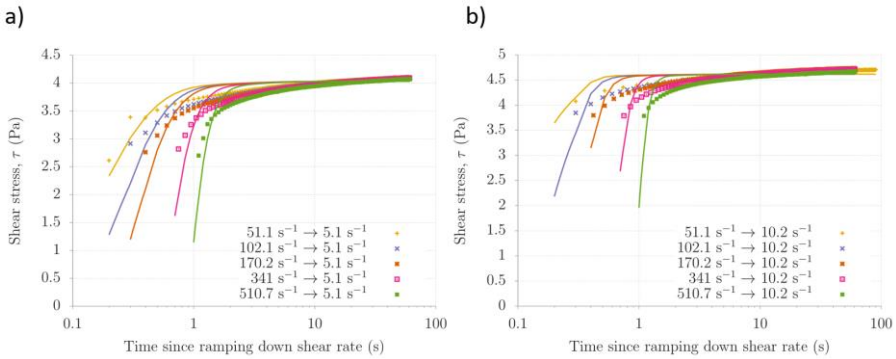

Fig. 26: Measurements and model predictions for shear stresses in a WBM following: a) shear rate steps down to 5.1 s^{-1}, b) shear rate steps down to 10.2 s^{-1} (courtesy of Skadsem et al. 2019 [53]).

2.1.1.15 Effect of Thixotropy on Rheological Behavior after a Gelled Period

"As a consequence of thixotropy, when viscous flow is established after a gelation period, the flow behavior of the fluid is altered for some time before reaching a steady state behavior. Fig. 27 illustrates this effect.

An OBM is placed into a scientific rheometer and is sheared at 1020s^{-1} for 10 min. Then the fluid is left resting without rotation for another 10 min.

Afterward, an increasing shear rate is applied to the fluid from low to high values, following by a ramping down, i.e. from high to low shear rates. There is a clear difference between the shear stresses and associated effective viscosity as a function of the direction by which they are reached.

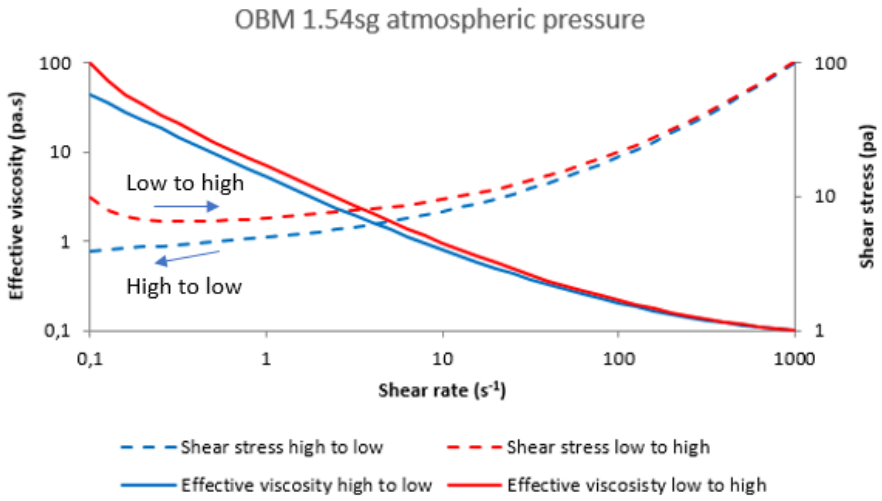

Fig. 27: After resting for 10 minutes, a sweep of shear rates for low to high values is performed before reducing the shear rates back to small values. Because of thixotropy, the shear stresses differ substantially depending on whether they were reached from a lower shear rate or a higher one.

In practical terms, this means that the rheological behavior of drilling muds is altered for some time after a gelation period. Based on the hypothesis that gelling and gel breaking affects essentially the yield stress in the Herschel-Bulkley formulation, Bjørkevoll and Gjeraldstveit (2003) [55] define a modified Herschel Bulkley model that accounts for the persistence of gelation after gel breaking:

$$\tau = \tau_\gamma + \left(\tau_{gel}(t_0) - \tau_\gamma\right)\left(M_1 e^{-\alpha_1(t-t_0)} + (1-M_1)e^{-\alpha_2(t-t_0)}\right) + K\dot{\gamma}^n \quad (45)$$

where t_0 is the time when flow is reinitiated, $\tau_{gel}(t_0)$ is the gel strength just before viscous flow is established, as calculated with eq. (38) as a function of the gel duration, M_1 is a weighting factor, α_1 and α_2 are time damping

coefficients. Based on downhole measurements taken during several drilling operations in the North Sea and Brazil [56], the authors of this report found a good match with $M_1 = 0.8$, $\alpha_1 = \frac{1}{10}s^{-1}$, $\alpha_2 = \frac{1}{500}s^{-1}$."[12] To simplify the notation, we will denote $\tau_{\gamma,t_{gel}}$ the group $\tau_\gamma + \left(\tau_{gel}(t_0) - \tau_\gamma\right)\left(M_1 e^{-\alpha_1(t-t_0)} + (1-M_1)e^{-\alpha_2(t-t_0)}\right)$.

2.1.1.16 Condition to Suspend Cuttings in Gelled Condition

The propensity of drilling fluids to gel whenever flow is stopped, is also important to maintain cuttings particle in suspension. The combined effect of gravitation and buoyancy forces on a cuttings particle result in pressures around the particle surface. If these pressures are lower than the gel strength of the fluid at a given time, then the particle will be kept in position inside the fluid. So far, this problem has been solved analytically for a spherical particle in a Bingham plastic fluid. In this case, the stability condition is [57]:

$$\tau_{gel} > \frac{g d_s}{6}\left(\rho_s - \rho_f\right) \tag{46}$$

where g is the gravitational acceleration, d_s is the diameter of the solid particle, ρ_s is the mass density of the solid particle and ρ_f is the mass density of the drilling fluid.

2.1.1.17 Cuttings Slip Velocity in near Vertical Annuli

However, when the solid particle moves within a drilling fluid in a vertical section of a well, it is subject to a drag force F_D:

$$F_D = \frac{1}{2}\rho_f {v_s}^2 C_D A_\perp \tag{47}$$

where v_s is the slip velocity, i.e. the relative velocity of the solid particle to the fluid, $A_\perp$ is the cross-sectional area of the solid particle in the direction of movement and C_D is the drag coefficient. Eq. (47) defines the Rayleigh drag force.

The drag coefficient (C_D) in this formula has a constant value only for objects that have a blunt form factor and when the particle Reynolds number (Re_p) is

12 Excerpt from my contribution to the text of the paper by Cayeux et al. (2018) [186]

large enough to produce turbulence behind the object ($Re_p > 1000$). For a spherical particle, Re_p is defined as:

$$Re_p = \frac{\rho_f v_s d_s}{\mu_{eff}} \tag{48}$$

The drag coefficient of a rough sphere at high particle number is about 0.40 to 0.45 [58].

For lower Reynolds number, the drag coefficient is expressed as a function of the particle Reynolds number (see Fig. 28).

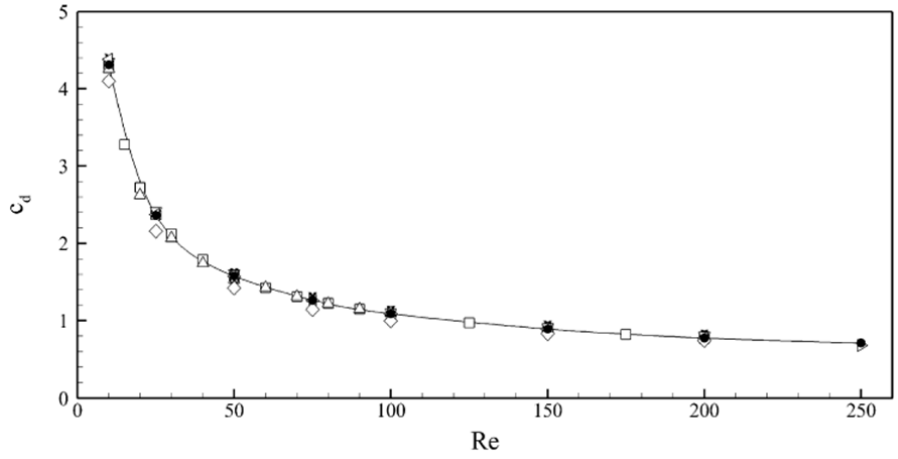

Fig. 28: Rayleigh's drag coefficient as a function of the particle Reynolds number for a sphere (courtesy Richter and Nikrityuk 2012 [59]).

There are many empirical correlations for the drag coefficient depending on which physical phenomena have been accounted for or not. These factors are the shape of the solid particle, e.g. spherical, cylindrical, ellipsoidal, irregular, the nature of the viscous properties of the fluid, e.g. Newtonian, pseudo-plastic, Bingham pseudo-plastic, viscoelastic, and the flow regime often expressed as a range of applicability in terms of a particle Reynolds number (Re_p).

For instance, Chien (1994) [60] defines a drag coefficient that applies to irregular particle shapes in non-Newtonian fluids for a range of particle Reynolds number between 0.001 and 10000. In comparison with other similar models like Gabitto & Tsouris (2008) [61], Ganser (1993) [62], Haider &

Levenspiel (1989) [63], Hölzer & Somme (2008) [64], Swamee & Ojha (1991) [65], the Chien model is both simple to use and gives consistent results with regard to alternate empirical solutions [66]. There are other relationships that are more precise, like the one from Morrison (2013) [67], but on the other hand they are more limited in their applicability, as for instance the Morrison empirical model only applies to spherical particles. With an estimation of the drag force, it is then possible to determine the terminal velocity of a particle moving vertically relatively to a fluid, by solving the following equation:

$$F_g + F_b + F_D = 0 \tag{49}$$

where F_g and F_b are respectively the gravitational and buoyancy forces. The sum of the gravitational and buoyancy forces being:

$$F_g + F_b = (\rho_s - \rho_f)V_s g \tag{50}$$

where V_s is the volume of the particle.

2.1.1.18 Apparent Fluid Viscosity in the Presence of Solid Particles

Furthermore, the presence of solid particles in a fluid impacts its apparent viscosity. Einstein (1906) [68] was the first to provide a formulation of the change of apparent viscosity by the presence of solid particles in a Newtonian fluid:

$$\mu_r = 1 + f\Phi \tag{51}$$

where f was determined to be $\frac{5}{2}$ using statistical physics, and $\mu_r = \frac{\mu_p}{\mu_0}$ is a dimensionless apparent viscosity, with μ_p being the apparent viscosity of the fluid with solid particles and μ_0 the viscosity of the fluid without solid particles. However, the value of $f = \frac{5}{2}$ is only true for very low concentrations and it has never been possible to reproduce the theoretical result through experiments. Several investigators have attempted to come with other relationship that would fit better with observations.

Hatschek (1911) [69] proposed a model of the dimensionless apparent viscosity of Newtonian fluids for a larger range of concentrations (see Fig. 29):

$$\begin{cases} \mu_r = 1 + 4.5\Phi, \forall \Phi < 0.74 \\ \mu_r = \dfrac{1}{1 - \Phi^{1/3}}, \forall\, \Phi \geq 0.74 \end{cases} \tag{52}$$

This model has been used in Paper IV to estimate the change of viscosity caused by cuttings on a foam while drilling an exploration well in Iraq. Note that the definition from Hatschek has a discontinuity at concentration $\Phi = 0.74$, since the two functions only intersect at $\Phi = 0$. In practice, a pack-off will be experienced much earlier than such solid concentrations are reached and for the particular context of Paper IV, this does not cause any problems.

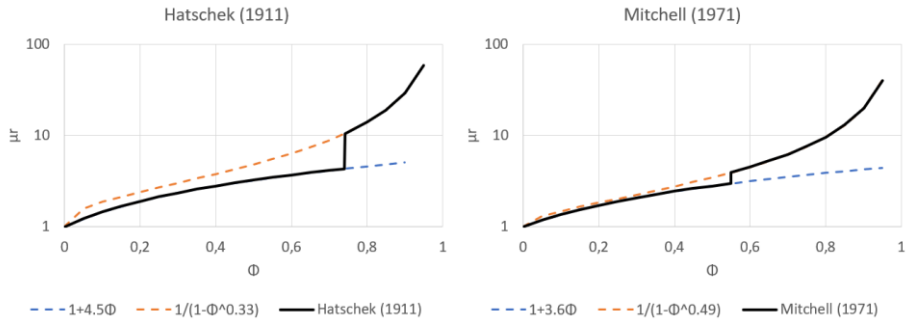

Fig. 29: Hatschek and Mitchell models for apparent normalized viscosity of particles dispersed in Newtonian fluids.

Mitchell (1971) [70] has investigated the change of apparent viscosity for aerated fluids and arrived at the following definition:

$$\begin{cases} \mu_r = 1 + 3.6\Phi, \forall \Phi < 0.54 \\ \mu_r = \dfrac{1}{1 - \Phi^{0.49}}, \forall\, \Phi \geq 0.54 \end{cases} \tag{53}$$

Here again, there is a discontinuity at $\Phi = 0.54$. Mitchell's apparent viscosity model has been used in Paper IV to estimate the foam viscosity. As the foam quality, i.e. the volume fraction of gas to liquid, is typically between 75 and 90%, the discontinuity does not cause numerical problems when used in the context of Paper IV.

One important fact that should be kept in mind when establishing relationships for the apparent dimensionless viscosity, is that it should tend to infinity when

the concentration gets close to the maximum packing concentration Φ_m. Maron & Pierce (1956) [71] proposed a relationship that verifies this condition:

$$\mu_r = \left(1 - \frac{\Phi}{\Phi_m}\right)^{-2} \tag{54}$$

Mueller et al. (2009) [72] have studied the effect of the non-sphericity of the solid particles on the apparent change of viscosity of the suspension. Considering only particles that have an axis of rotation like prolates, oblates, cylinders, rods, discs, etc., the non-sphericity can be characterized by a particle aspect ratio $r_p = \frac{l_a}{l_b}$ where l_a is the length of the particle's axis of rotational symmetry and l_b is its maximum diameter perpendicular to that axis.

Mueller et al. (2009) [72] found that the resulting rheological behavior modification can be expressed with the Herschel-Bulkley formulation. They have found a good match with their experimental data using eq. (54), to define the consistency index:

$$K = \mu_0 \left(1 - \frac{\Phi}{\Phi_m}\right)^{-2} \tag{55}$$

They have also found an empirical relationship for the flow index valid for $\frac{\Phi}{\Phi_m} \leq 0.8$:

$$n = 1 - 0.2 r_p \left(\frac{\Phi}{\Phi_m}\right)^4 \tag{56}$$

Based on their measurements, they found that an appreciable yield stress only developed for $\frac{\Phi}{\Phi_m} \geq 0.8$. Utilizing the Maron-Pierce model as a starting point, they define the following relationship for the yield stress:

$$\tau_\gamma = \tau_* \left(\left(1 - \frac{\Phi}{\Phi_m}\right)^{-2} - 1\right) \tag{57}$$

where τ_* shall be fitted to experimental data. With their data, they found: $\tau_* = 0.234Pa$ for $r_p = 0.13$, $\tau_* = 0.150Pa$ for $r_p = 1$, $\tau_* = 0.0585Pa$ for $r_p = 1.75$, $\tau_* = 0.106Pa$ for $r_p = 4.69$, $\tau_* = 0.087Pa$ for $r_p = 9.17$.

2.1.1.19 Cuttings Bed and Critical Transport Velocity

"In an inclined portion of a well, it is possible that cuttings particle will not be transported by the fluid. In that case, they will settle on the low side and accumulate in a cuttings bed [73]. Larsen (1990, 1997) [74] [75] conducted many experiments in a large flow loop at the University of Tulsa, to observe at which flowrate cuttings beds start to form for a wide variety of conditions. The corresponding bulk fluid velocity is often referred to as the critical transport fluid velocity (v_{ctfv}). Later, Jalukar (1993) [76] and Bassal (1995) [77] extended the number of experiments to cover the effects of hole size and pipe rotation. Larsen, Jalukar and Bassal proposed an empirical model to estimate v_{ctfv} based on their observations.

$$v_{ctfv} = (\bar{v}_c + \bar{v}_s . c_{inc} . c_{size} . c_{mwt} . c_{ecc}) . c_{geo(D)} . c_{geo(PV)} . c_{geo(inc)} . c_{rpm} \quad (58)$$

where $\bar{v}_c$ is the average cuttings transport velocity, $\bar{v}_s$ is the average slip velocity, and the remaining parameters are correction factors: for inclination (c_{inc} and $c_{geo(inc)}$), cuttings particle size (c_{size}), mud weight (c_{mwt}), drill-pipe eccentricity (c_{ecc}), drill-pipe rotation (c_{rpm}), hole diameter ($c_{geo(D)}$) and drilling fluid's plastic viscosity ($c_{geo(PV)}$)."[13]

It should also be noted that experimental studies indicate that the inclination limit for the formation of cuttings bed is around 35°. [78].

2.1.1.20 Cuttings Carrying Index

"A drill-cuttings carrying index (CCI) is a value, usually defined between 0 and 1, that describes whether the local conditions at a given depth along the annulus are favorable for transporting cuttings or not. Typically, 0 is associated with very poor conditions for hole cleaning while 1 corresponds to perfect conditions for transport of cuttings. Following the base lines of the Larsen, Jalukar and Bassal empirical model for estimating the v_{ctfv}, Froitland [79], defined a CCI by combining the effectivity of the various effects on hole cleaning. These effects are:

13 Excerpt from Cayeux 2019 [198]

- Hole inclination (C_{incl})
- Critical fluid velocity (C_{crit})
- Eccentricity and drill-string rotational speed (C_{rpm})
- Cuttings particle size (C_{size})
- Drilling fluid viscosity (C_{visc})
- Borehole tortuosity (C_{tort})
- Influence of turbulence (C_{turb})

Therefore, the cuttings carrying index is defined as:

$$CCI = 1 - \min(1, \max(0, C_{incl}.C_{crit}.C_{rpm}.C_{size}.C_{visc}.C_{tort}.C_{turb})) \quad (59)$$

where $C_{incl}, C_{crit}, C_{rpm}, C_{size}, C_{visc}, C_{tort}$ and C_{turb} are curved fitted functions on the measurements made by Larsen, Bassal and Jalukar."[14]

2.1.1.21 Cuttings Particle Size Distribution

"The experiments of Larsen, Bassal and Jalukar have shown that the cuttings particle size influences greatly the capacity of drilling fluid to transport cuttings.

On the other hand, in deviated wells, cuttings are grinded by the rotation of the drill-string while being transported. Accurate measurements of particle size distribution of cuttings materials, when they arrive at surface, show a wide range of dimensions starting from a few microns and ending at several centimeters [80](see Fig. 30).

In particle size distribution (PSD) analysis, it is usual to model the probability density using the Rosin-Rammler [81] distribution, i.e. a sub-category of the Weibull [82] distribution:

$$f(d_s; P_{80}, m) = \begin{cases} 1 - \ln(0.2)\left(\frac{d_s}{P_{80}}\right)^m, \forall d_s \geq 0 \\ 0, \forall d_s < 0 \end{cases} \quad (60)$$

14 Excerpt from Cayeux 2019 [198]

where f is the probability density function, d_s is the particle size, P_{80} is the 80th percentile of the particle distribution and m describes the spread in the distribution.

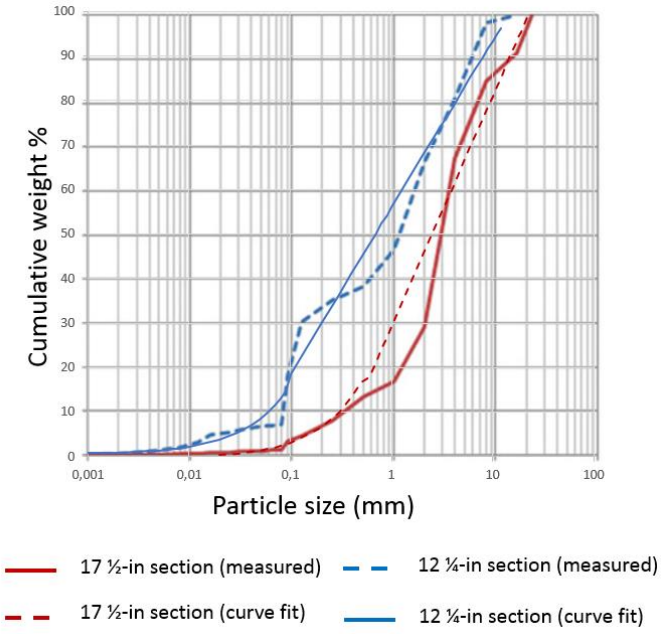

Fig. 30: Particle size distribution of the cuttings produced in the 17 ½-in and 12 ¼-in sections at Trolla (courtesy of Saasen et al. 2013).

However, there are strong indications that the cuttings size distribution produced by the bit is of a much narrower nature than what is observed when the cuttings arrived at the shakers. For instance, when drilling with a dual concentric drill-string drilling method [83], cuttings are transported in the inner drill-pipe and therefore not subject to any grinding by the drill-sting, and therefore arrives intact to the surface. Belarde and Vestavik (2011) [83] reported that when alternating from conventional drilling to the dual-concentric drilling method within the same drilling operation, significant variations in size and shape of the cuttings could be observed (see fig. 13 in Paper II).

As of today, there is no theoretical description of the grinding mechanism of particles. However, the milling industry utilizes empirical formulas, that link the grinding power per mass rate to the change of particle size:

$$\begin{cases} d_{s_i} \geq d_{bu}, \frac{W}{\dot{m}} = C_K\left(\ln d_{s_i} - \ln d_{s_o}\right) \\ d_{bu} > d_{s_i} > d_{bl}, \frac{W}{\dot{m}} = C_B\left(\frac{1}{\sqrt{d_{s_o}}} - \frac{1}{\sqrt{d_{s_i}}}\right) \\ d_{s_i} \leq d_{bl}, \frac{W}{\dot{m}} = C_R\left(\frac{1}{d_{s_o}} - \frac{1}{d_{s_i}}\right) \end{cases} \quad (61)$$

where $d_{bu} = 50mm$ and $d_{bl} = 0.050mm$ are respectively the upper and lower bounds of the particle size for which the second formula can be applied, $d_{bl} = 0.050mm$ is the lower bound W is the power used for grinding, $\dot{m}$ is the feed mass rate, d_{s_i} and d_{s_o} are respectively the P_{80} of the particle size at the input and output, C_K, C_B and C_R are respectively the Kick, Bond and von Rittinger grinding coefficients. In order to ensure a continuity between these formulas, the grinding coefficients shall respect $C_K = 1.151 C_B {d_{bu}}^{-0.5}$ and $C_R = 0.5 C_B {d_{bl}}^{-0.5}$. Of course, cuttings particles do not get as large as $50mm$, but cavings can be larger than that. "[15] From various publications such as Hukki (1961) [84] or van Schoor and Sandenbergh (2012) [85], it can be found that C_B is in the order of magnitude of 200 to 400 $Jm^{0.5}/kg$.

2.1.1.22 Transient Hydraulic Pressure Loss Calculation for a Multi-components and Multi-phases Flow

"As we have seen in the previous sections, drilling fluids are often a mix of different components. Some of those components are part of the fluid formulation, while others result from the drilling process itself like cuttings and formation fluids. The components of the fluid can be found in different phase states, including liquid phases like brine and oil, solid phases as for example bentonite, barite, LCM or cuttings, and gaseous phases as for instance formation gas. Therefore, multi-phase and multi-component flow shall be used. It should be noted that in normal drilling conditions, the dimensions of the solid particles, liquid droplets and gas bubbles remain very small compared to the dimensions of a cross-section of the conduits where the fluid flows. Therefore, it is acceptable to use a drift-flux formulation where the different phases are mixed together but each component has a slip velocity relatively to a reference one. The drift-flux approximation allows to transform the original 3-

15 Excerpt from Cayeux 2019 [198].

dimensional problem into a 1-dimension one, thus simplifying greatly the calculations."[16]

Equipped with the above considerations for pressure losses and the mechanisms for estimating the relative slip of components between each other's and the possible deposition or return to suspension of solid particles, it remains to integrate the dynamic behavior of drilling fluid along a branch of a hydraulic network as a function of boundary conditions.

For this, we need to write two balance equations that describe the interface exchange of mass and momentum (Navier-Stokes).

"With the drift-flux approximation, the mass balance for each component can be written [86]:

$$A_{\perp}\kappa\,\frac{\partial p}{\partial t}+\rho_{mix}\frac{\partial A_{\perp}}{\partial t}+\frac{\partial F}{\partial s}=\sum_{i\in\Omega}\partial_s\dot{m}_i \tag{62}$$

where i is an index representing a component of the fluid, Ω is a set of components, t is time, s is the curvilinear abscissa, p is the pressure, $A_{\perp}$ is the cross-sectional area of a fluid element, $\kappa=\frac{\partial\rho_{mix}}{\partial p}$ is the mixture compressibility factor, ρ_{mix} is the mass density of the mix, F is the total mass flux, $\partial_s\dot{m}_i$ is the mass flux per unit length through the walls of component i."[17]

The mass fluxes through the walls describe external contributions to the mass balance. That can be formation fluid entering the borehole, or losses of drilling fluid to the formation, but also cuttings produced by the bit, being deposited in a bed, returning to suspension from a bed, or formation rocks entering the borehole because of wellbore instabilities or washouts.

It should also be noted that the cross-sectional area may change through time because of the work of the bit or reamers, but also because of cuttings accumulation on the low side, as the consequence of wellbore instabilities or wellbore washouts.

16 Excerpt from my contribution to the text of the paper by Cayeux et al. (2014) [187]

17 Excerpt from my contribution to the text of the paper by Cayeux et al. (2014) [187]

"Similarly, the momentum balance can be written as follow [86]:

$$\frac{\partial F}{\partial t} + \frac{\partial}{\partial s}(\bar{v}_{com}F) + \mu F = -\frac{\partial}{\partial s}(A_{\perp}\rho_{mix}H) - A_{\perp}\frac{\partial p}{\partial s} - A_{\perp}\rho_{mix}g\cos\vartheta + \partial_s \dot{m}\bar{v}_{\dot{m}} \quad (63)$$

where $\bar{v}_{com}$ is the centre of mass velocity, μ is the shear stress function, $H = \sum_{k\in\Psi}\sum_{l>k}(\bar{v}_k - \bar{v}_l)^2 x_k x_l$ with $\bar{v}_k$ being the cross-sectional average velocity of a phase k and x_k being its mass fraction, ϑ is the average inclination of the fluid element and $\bar{v}_{\dot{m}}$ is the velocity of the mass flux through the walls.

Note that the solution to the system of partial differential equations defined by eq. (62) and (63) depends on boundary conditions which may change through time. It is therefore natural to integrate the system of partial differential equations using a stepwise integration in time. The stability of the integration of such hyperbolic partial differential equations is conditioned by the Courant–Friedrichs–Lewy (CFL) criteria [87] and because of the very high velocity of pressure waves in drilling fluids, any explicit method may require very small time-steps to be stable. By considering the pressure wave propagation implicitly, the focus is then shifted to the evolving process of mass redistribution which is much slower than the one of acoustic wave propagations. Therefore, reasonable time steps can be used to respect the CFL condition. After discretization of those equations in space, a semi-implicit finite difference method is used to solve the mass transport and pressure distribution [88] [89] in a continuous conduit, possibly of variable size. "[18]

2.1.1.23 Hydraulic Network

"Discontinuities, like concentrated sources (*e.g.* pumps), abrupt change of cross-sectional area (*e.g.* bit, valves) or junctions where three pipes meet, delimit the start and end of hydraulic branches. The connection between the different branches defines a hydraulic network. The simplest hydraulic network can be found with conventional drilling. It has two branches with the drill-pipe on one side connected through the bit to the annulus on the other side. In addition, downhole equipment may create discontinuities like with valves or connect the interior of the drill-string with the annulus at other places than the

18 Excerpt from my contribution to the text of the paper by Cayeux et al. (2014) [187]

bit. There are also possible connections between the drill-string interior and the annulus at the level of a circulation sub, an under-reamer or a downhole motor, therefore creating even more branches in the hydraulic circuit.

For area discontinuities, there is a pressure jump between the end of the one branch and the start of the other branch. A pump is described by a source term in the form of a mass flux. Junctions are characterized by equal pressure at the connection between the three branches and an equilibrium of the mass fluxes (the sum of the mass fluxes of at the junction is 0). Therefore, a junction is characterized by four unknowns: three mass fluxes and one pressure. A junction system of dimension $4m \times 4m$, where m is the number of junctions, can be assembled and solved, therefore providing the missing boundary conditions for all the branches of the hydraulic network."[19]

2.1.2 Drill-string Mechanics

At the time where rotary BHAs were the most widely used way of controlling the directional behavior of a drill-string, mathematical models have been developed to estimate the side forces on stabilizers and the tilt angle at the bit. The purpose of those calculations was to predict which build-up or drop-off rates could be expected during a drilling operation. Some of the initial solutions were based on the Rayleigh-Ritz method as described by Walker (1973) [90] and later Toutain (1981) [91] [92] [93], while other developed solutions utilized the finite element method as presented by Birades et al. (1988, 1989) [94] [95] [96]. However, these solutions were only concentrating on the lower part of the drill-string, i.e. the BHA, and were solely utilized for directional behavior prediction. The advent of orientable PDMs and RSSs made less important the accurate prediction of the directional behavior of rotary BHAs.

During that same decade, Johanscik et al. (1984) [97] started to investigate how mechanical friction influences the build-up of torque and drag forces along the whole drill-string with the purpose of estimating the maximum pick-up weight and torque that could be expected when drilling a section.

19 Excerpt from my contribution to the text of the paper by Cayeux et al. (2014) [187]

Since then, torque and drag mechanical calculations are an integral part of any drilling engineering evaluations performed at the planning stage of drilling operations.

However, the utilization of drill-string mechanical calculations in real-time applications necessitates to account for additional physical phenomena that are not necessarily important during the well planning phase.

2.1.2.1 Motivation for Coupling Mechanical Evaluations with Hydraulic Calculations

For instance, during drilling operations, it is typical to observe a substantial reduction of the free-rotating weight while the flowrate is changed, as illustrated by Fig. 31.

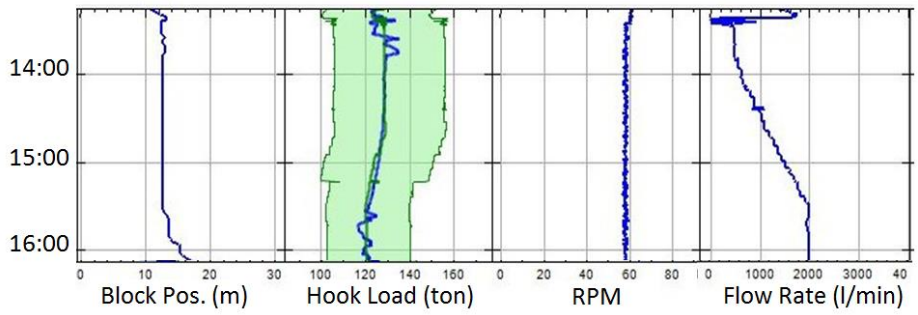

Fig. 31: Effect of change of flowrate on hook load while rotating the drill-string

Similarly, the hook-load may reduce significantly while running in hole with a casing or a liner string because of the forces induced by surging pressures (see Fig. 32). Since the surging pressures depend on the running speed, the slack-off weight is also influenced by the tripping speed.

In both cases, the origin of the variation of hook-load is related to hydraulic effects that are seldom accounted for in torque and drag models utilized for well engineering. Therefore, any attempt at utilizing, in real-time applications, drill-string mechanical models that do not account for hydraulic effects will result in significant discrepancies between model predictions and observations.

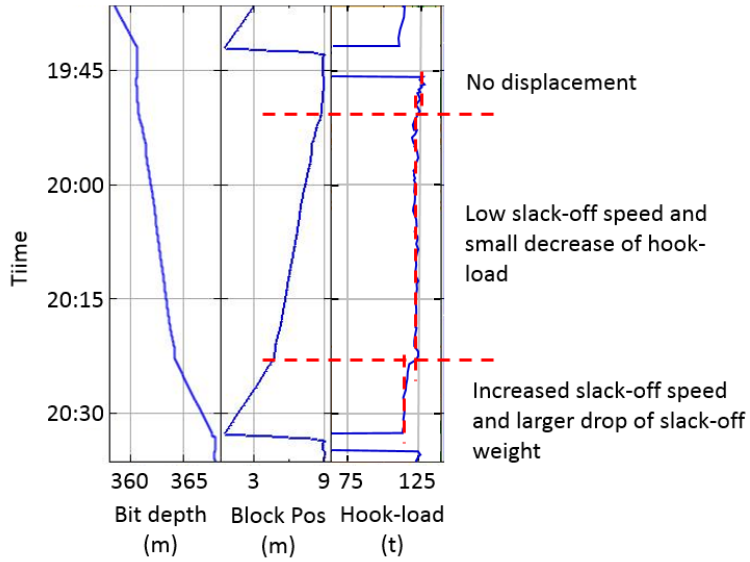

Fig. 32: While running in hole with a 13 3/8-in casing string, the slack-off weight decreases when the running speed increases.

2.1.2.2 Motivation for Utilizing Transient Mechanical Estimations

It is not only true that drilling hydraulic influences drill-string mechanics, as the reverse also applies, since drill-string vibrations can affect annulus downhole pressures. Fig. 33 illustrates a situation where large stick-slips are experienced during the whole drilling of the 8 ½-in section of a well in the North Sea. As one can see from the measurements, the peak to peak downhole rotational velocity lays far above 180 rpm during the first half the operation and stays between 20 and 90 rpm during the second half. The measured downhole pressure variations induced by the heavy stick-slips are in the range of 0.02sg in EMW and 0.004sg later. Note that in this case, there are other sources of deviation for the downhole pressure as there are strong indications that a large cuttings bed has formed during the drilling operation (see Cayeux et al. 2016 for more details about that drilling operation [98]).

This example shows that the estimation of drill-string vibrations is important during drilling operations to better estimate downhole pressures. However, most drill-string vibration solutions available for well engineering focus solely on computing the natural frequencies of the drill-string and are therefore not

well adapted to the problem at hand. Real-time drilling applications that want to estimate the impact of drill-string vibration on pressure losses would benefit of having access to dynamic drill-string mechanical models operating in the time domain and utilizing real-time boundary conditions.

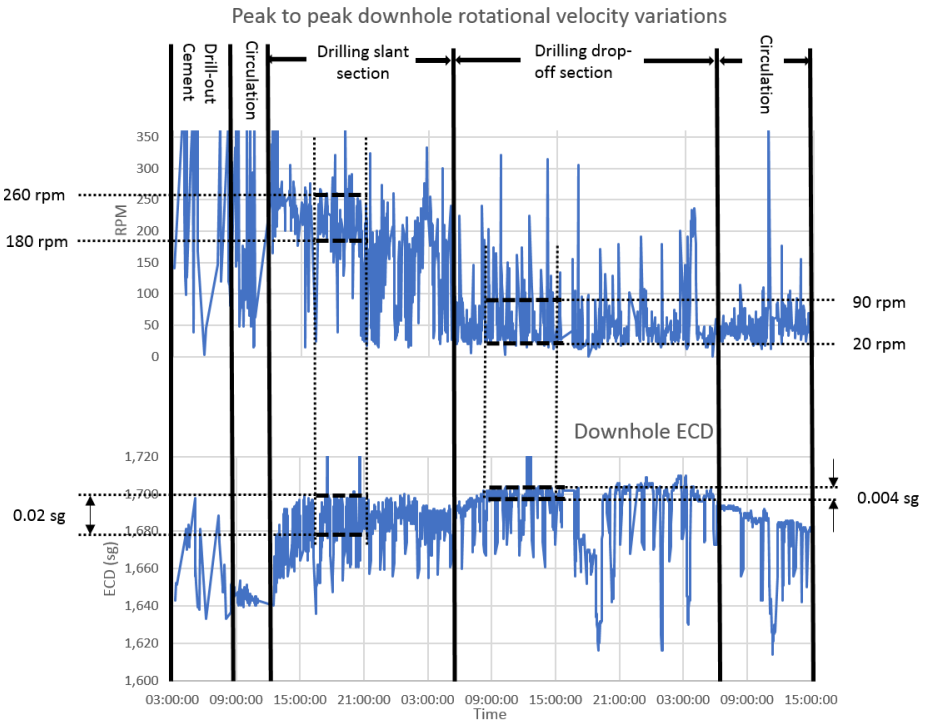

Fig. 33: Downhole measurements of stick-slips and ECD during the drilling of the 8 ½-in section.

Furthermore, steady state torque and drag models are not well adapted to the interpretation of periods where there is a transition between conditions which are dominated by the rotational movement of the drill-string to a situation where the axial movement is prevalent. As illustrated by Fig. 34, a decaying top-drive torque is measured during the whole pick-up and slack-off of the drill-string while conducting a friction test prior to making a connection, even though the top-drive speed is measured to be zero. In parallel, one can notice that the pick-up and slack-off weights change continuously during the friction test while a steady state torque/drag model would predict that the pick-up and slack-off

weights should be constant during the displacement as they should depend only on the direction of movement but neither the axial speed nor the block position.

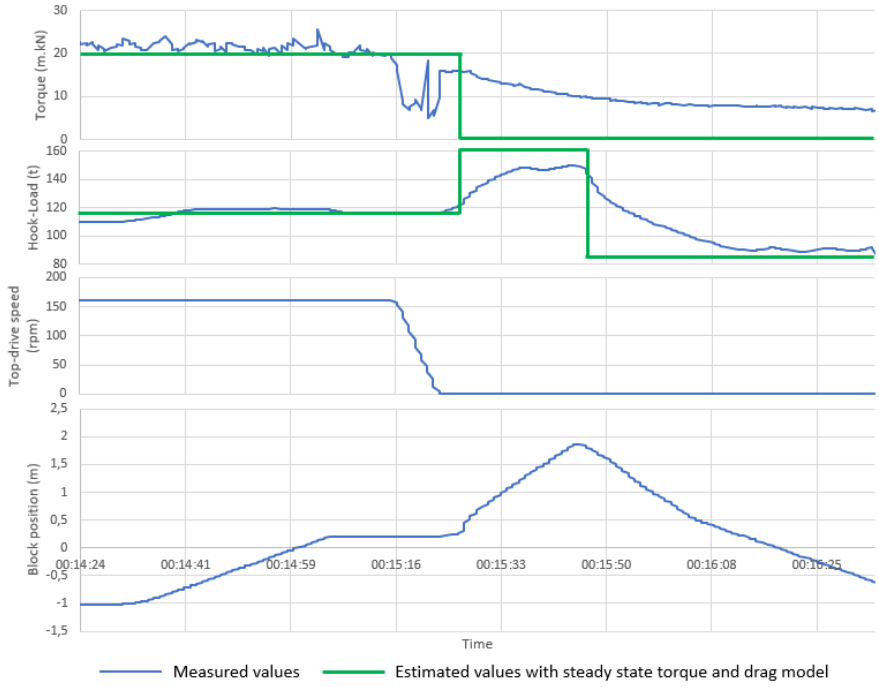

Fig. 34: Time-based log of a friction test where it can be observed that the top-drive torque decays while picking-up and slacking-off while the top-drive is not rotating.

This problem is even more exacerbated when considering drilling operations conducted from a floater. Fig. 35 shows that the hook-load varies by up to 20t when pulling a drill-string off bottom on a semi-sub where the heave compensator has been deactivated. It should be noticed that the hook-load variations do not follow a stepwise function as a steady state torque and drag model would predict but correspond to a function with a continuous first derivative.

Furthermore, the evaluation of the bit depth on a floater requires more complex solutions than just adding the total drill-string length to the top-of-string position referred to a fixed elevation, as residual movement of the top-of-string

position induced by imperfect heave compensation may lead to the situation depicted on Fig. 36.

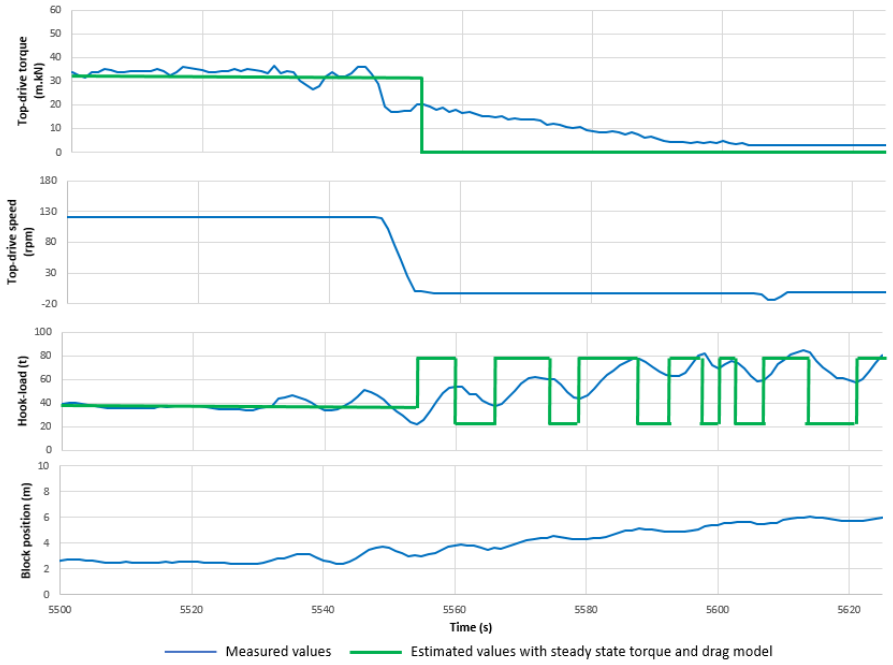

Fig. 35: Effect of heave movement on hook-load when the bit is off bottom.

In this drilling example, i.e. where a weight on bit is applied, the resulting oscillations of the top-of-string position are directly transferred to the bit depth by the drilling control system and consequently the bottom hole depth is deepened, intermittently, at the few occasions where the bit depth gets larger than the last estimated maximum bit depth. This leads to spurious evaluation of the ROP that can be detrimental for any model that would estimate how cuttings are transported during the drilling operation. Obviously, the elasticity of the drill-string plays a major role on how the bit really moves compared to the top-of-string, but also the bit/rock interaction is important to determine the advancement of the bit when the bit is in contact with the formation rock. Drill-string mechanical models used for drilling engineering tend to consider the drill-string elasticity for buckling estimation in steady state conditions, but not in a dynamic way. This is yet another reason why a real-time drilling application needs to utilize transient torque and drag models that implement

many more physical conditions than those traditionally used for drilling engineering evaluations.

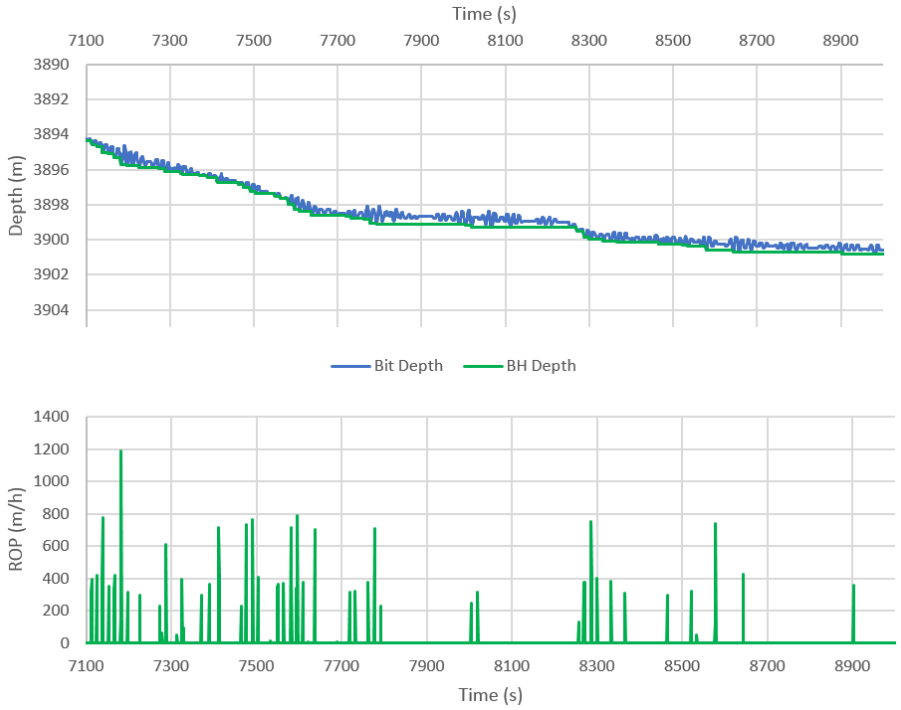

Fig. 36: Spurious estimation of bottom hole depths and ROPs when drilling from a floater.

We will now review the known foundations necessary for developing a transient torque and drag model that is adapted to real-time drilling applications.

2.1.2.3 Mechanical Friction

"The friction force is the tangential force that opposes the relative motion of solid bodies in contact with each other's, and it is equal to the force required to maintain the bodies in a static equilibrium (static friction force) or that opposes the relative motion (kinetic friction force) of the solid bodies. Empirical results originating from the early work of Leonardo da Vinci, Guillaume Amontons and Charles-Augustin Coulomb, indicate that a simple approximation of the

kinetic friction is a force in the opposite direction of movement that is proportional to the normal force in between the contact surfaces:

$$\vec{F}_{\mu_k} = -\mu_k \vec{R}.\hat{n}\frac{\vec{v}}{v_{\mu_k}} \tag{64}$$

where $\vec{F}_{\mu_k}$ is the kinetic friction, μ_k is the kinetic friction coefficient, $\vec{R}$ is the contact force at the position of the sliding surfaces, $\hat{n}$ is the normal unit vector at contact, $\vec{v}$ is the velocity of the moving surface relative to the other solid (see Fig. 37a) and v_{μ_k} is a normalization velocity magnitude that will be discussed later.

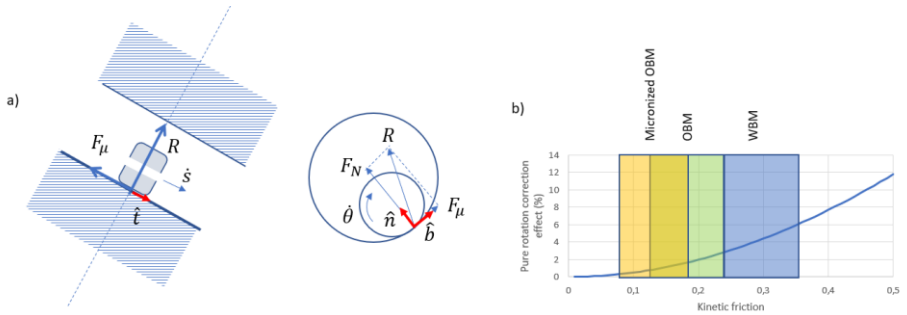

Fig. 37: a) schematic representation of the generation of torques and drag forces at the contact points by reaction forces, b) relative importance of the pure rotation kinetic friction factor reduction for typical drilling fluid systems.

The kinetic friction force component in the binormal direction ($\hat{b}$) generates a friction torque at the contact point:

$$C_{\mu_k} = r_o \vec{F}_{\mu_k} \cdot \hat{b} \tag{65}$$

where C_{μ_k} is the kinetic friction torque at the contact point, and r_o is the radius of rotation at the contact point. In practice, r_o is the tool-joint radius of the drill-pipes and heavy weight drill-pipes (HWDP). "[20]

20 Excerpt from my contribution to the text of the paper by Cayeux et al. 2017 [188]

Note that in pure rotation, the normal force $F_N = \vec{R}.\hat{n}$ is smaller in magnitude than R, because it must be combined vectorially with the tangentially oriented kinetic friction force to obtain the contact force. Therefore, the effective rotational kinetic friction, $\mu_{k,r}$, is smaller than the kinetic friction [99]:

$$\mu_{k,r} = \frac{\mu_k}{\sqrt{1+\mu_k^2}} \tag{66}$$

Typical water-based muds have a kinetic friction factor between 0.25 and 0.35. With such drilling fluids, the effective rotational kinetic friction is reduced by about 6% at most. Normal oil-based muds and micronized OBM usually induce lower kinetic friction coefficient, and the correction of effective pure rotation kinetic friction is only by a few percents (see Fig. 37b).

The axial velocity component for the drag force is ([99]):

$$\frac{\vec{v}.\hat{t}}{v_{\mu_k}} = \frac{\dot{s}}{\sqrt{\dot{s}^2 + (1+\mu_k^2)\left(r\dot{\theta}\right)^2}} \tag{67}$$

where $\hat{t}$ is a unit vector in the axial direction, s is the curvilinear abscissa of the contact point, $\dot{\theta}$ is the angular velocity of the point at the contact point, and $v_{\mu_k} = \sqrt{\dot{s}^2 + (1+\mu_k^2)\left(r\dot{\theta}\right)^2}$ is the corrected velocity magnitude to account for the effect rotational friction.

The tangential velocity component to be used in torque calculations is ([99]):

$$\frac{\vec{v}.\hat{b}}{v_{\mu_k}} = \frac{r\dot{\theta}}{\sqrt{\dot{s}^2 + (1+\mu_k^2)\left(r\dot{\theta}\right)^2}} \tag{68}$$

"The static friction force ($\vec{F}_{\mu_s}$) has a magnitude and direction such that the solid bodies do not slide on each other's and is bounded by:

$$\left\|\vec{F}_{\mu_s}\right\| < \mu_s \vec{R}.\hat{n} \tag{69}$$

where μ_s is the static coefficient of friction, and usually, $\mu_s > \mu_k$.

Similarly, the static friction torque (C_{μ_s}) has a magnitude such that the solid bodies do not slide on each other's and is bounded by:

$$C_{\mu_s} < r_o \mu_s \vec{R}.\hat{n} \tag{70}$$

When a wetting liquid is present and near the interface of a surface contact, liquid bridges, or menisci, are formed between the surfaces. The negative pressure difference across the meniscus surface generates an attractive force that, in addition to a rate-dependent viscous force, determines the adhesive force of a wetted interface. Fluid film lubrication can be separated into the five regimes: i) surface contact dominated, ii) boundary lubrication, iii) mixed lubrication, iv) elastohydrodynamic lubrication and v) hydrodynamic lubrication. In the drilling context, we are essentially working in the first two regions, i.e. surface contact dominated and boundary lubrication.

These regimes are often characterized by the lubricant film parameter, *i.e.* the ratio between mean fluid film thickness, h, and the composite standard deviation of surface height, σ. When the friction force is plotted as a function of velocity, viscosity or the product of the two, a nonlinear relationship qualitatively represented by the curve in the right part of Fig. 38 can be seen. Here, friction force is plotted as a function of $\mu_e v/P$ where μ_e is the fluid film viscosity, v is the velocity and P is load per unit projected area.

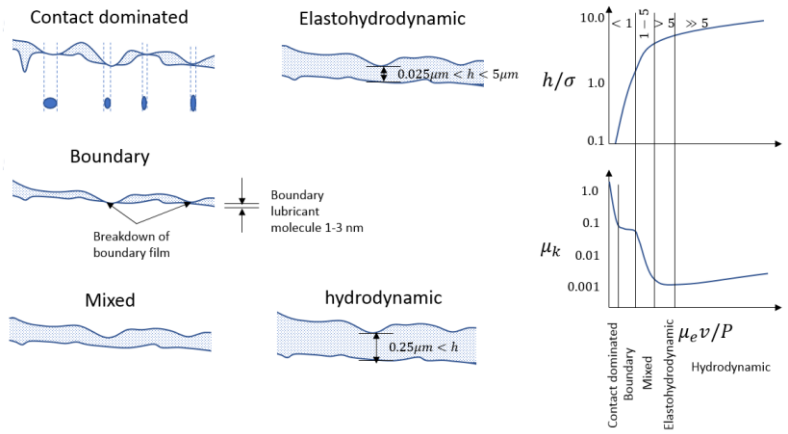

Fig. 38: Lubricant film parameter (h/σ) and coefficient of friction plotted as functions of $\mu_e v/P$, from (Bhushan 1999) [100].

Because of the complex interaction between the surfaces in contact and the presence of fluid, the transition from static to kinetic friction is not totally independent from the sliding velocity. The evolution of the friction force as a function of velocity, for a constant velocity motion, is called the Stribeck curve after the work of Stribeck (1902) [101]. Tustin (1947) [102] proposes a simple model for the transition between static and kinetic friction:

$$F_{i,\mu} = F_{i,\mu_k} + \left(F_{i,\mu_s} - F_{i,\mu_k}\right)e^{-\frac{|v|}{v_{cs}}} \tag{71}$$

where v is the relative velocity between the sliding bodies, and v_{cs} is the critical Stribeck velocity. "[21]

2.1.2.4 Friction Force between a Tube in Continuous Contact with the Borehole

Johancsik et al. (1984) [97] solve the torque and drag problem by recursive integration of tensions and torques along the drill-string, assuming that the pipes are in continuous contact with the borehole. The recursion starts at the bottom of the drill-string where the tension is zero when the bit is off-bottom or equals to the opposite of the force applied to the bit if the bit is in contact with the formation, following the convention that a compression force is negative, and a tension is positive. Then the tension at the top of a short element of length δl_i is increased by (see Fig. 39):

$$\Delta T_i = F_{i,g}\cos\vartheta \pm \mu_k F_{i,n} \tag{72}$$

with $F_{i,g} = \rho_s\left(1 - \frac{\rho_m}{\rho_s}\right)A_{i,s}\delta l_i\, g$, where ρ_s is the mass density of the tube, ρ_m is the mass density of the drilling fluid, $A_{i,s}$ is the cross-sectional area of the tube, g is the gravitational acceleration, ϑ is the inclination, $F_{i,n}$ is the normal force between the tube element and the borehole and one uses $+$ for the second term when pulling and $-$ when slacking off.

Considering that the change of inclination is $\Delta\vartheta$ and the change of azimuth is $\Delta\Phi$ between the bottom and the top of the element, then the normal force at the contact is:

21 Excerpt from my contribution to the text of the paper by Cayeux et al. 2017 [188]

$$F_{i,n} = \sqrt{(T_i \Delta\Phi \sin\vartheta)^2 + \left(T_i \Delta\vartheta + F_{i,g} \sin\vartheta\right)^2} \tag{73}$$

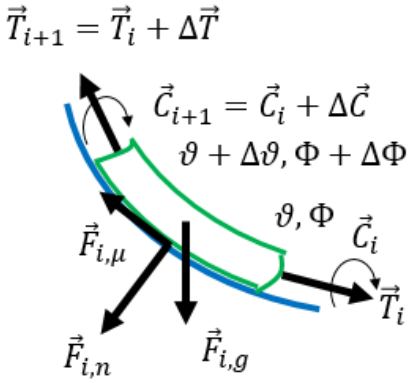

Fig. 39: Pipe element in continuous contact with the borehole

The Johanscik model assumes that the drill-string follows exactly the trajectory, i.e. that the bending stiffness of any element is negligible. This hypothesis is acceptable for standard drill-pipes and HWDP (up to an OD of 6 5/8-in), as long as the curvature remains limited (typically below 5°/30m) and when the part of the drill-string that is compressed, for example when applying a WOB, is short compared to the part of the drill-string that is in tension.

The buoyancy factor $1 - \frac{\rho_m}{\rho_s}$ does not account for a different mud density in the outside and inside of the pipe element. Therefore, it has been extended to $\frac{A_0(1-\rho_{mo}/\rho_s)-A_i(1-\rho_{mi}/\rho_s)}{A_0-A_i}$ [103] where ρ_{mo} and ρ_{mi} are respectively the mud density outside and inside the element, and A_0 is the cross-sectional area calculated with the outer diameter of the pipe and A_i is the cross-sectional area calculated with the inner diameter of the element.

2.1.2.5 Influence of Temperature and Pressure on Pipe Length

Thermal expansion influences the length of a pipe:

$$l_T = \alpha_T l_0 \Delta T \tag{74}$$

where α_T is the linear thermal expansion coefficient, l_0 is the original length under atmospheric pressure conditions and at a reference temperature, and ΔT is the temperature variation compared to the reference temperature.

Lubinski and Althouse (1962) [104] showed that the length of a pipe is also influenced by the current interior and exterior pressures:

$$l = \alpha_T l_0 \Delta T \left(1 + \frac{2\nu}{E(A_0 - A_i)}(A_0 p_o - A_i p_i)\right) \tag{75}$$

where l is the pipe length under pressure conditions, ν is the Poisson's ratio, E is the Young modulus, A_0 is the external cross-sectional area, A_i is the interior cross-sectional area, p_o is the outside pressure and p_i is the inside pressure.

This effect is often referred as pipe ballooning. So, the length of the drill-string varies as a function of the pressure conditions.

2.1.2.6 Modelling of Torsional Motion

For a long time, modelling of drill-string vibrations has mostly focused on the torsional movement. For instance, Navarro-López and Cortés (2007) [105] describes a finite difference discretization of the drill-string to model torsional movements. The idea is to replace a portion of the drill-string by an equivalent massless spring that has an equivalent torsional constant and that is connected to a zero-thickness disk with an equal moment of inertia than the one of the original portions of the drill-string. The lumped disk is in contact with the borehole and kinetic friction applies wherever the disk slips on the borehole (see Fig. 40).

Therefore, we obtain a system of partial differential equations, with the generic form of each equation being:

$$I_i l_i \frac{\partial^2 \theta_i}{\partial t^2} = k_{t,i}(\theta_i - \theta_{i-1}) - k_{t,i+1}(\theta_i - \theta_{i+1}) + \tau_{ext,i} \tag{76}$$

where I_i is the polar mass moment of inertia, l_i is the length of the discretized element, $k_{t,i} = \frac{G J_i}{l_i}$ is an equivalent torsional spring constant, G is the shear modulus of the material, J_i is the polar moment of inertia, θ_i is an angle referred to an initial angular position and $\tau_{ext,i}$ is the external torque applied on the disk.

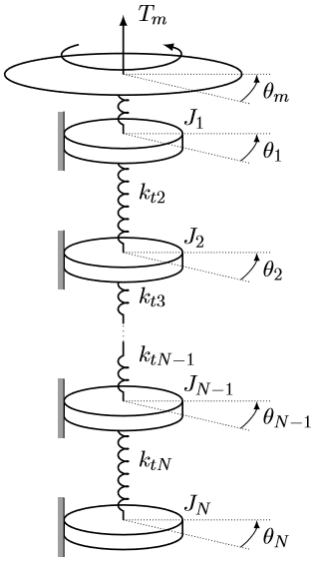

Fig. 40: Finite difference discretization of the torsional deformation of the drill-string by a series of coupled torsion springs (courtesy Navarro-López and Cortés (2007) [105]).

This system of partial differential equations can be solved for small time steps and an estimation of the torsional movement of the drill-string can be estimated as a function of time-dependent boundary conditions.

Some authors [106] lump the whole drill-string into as few elements as possible; just the number that is sufficient to represent the sections of drill-string with the largest torsional stiffness contrasts, like for example the BHA, the HWDPs and the drill-pipes. This approach reduces the resolution complexity while maintaining a trustworthy time-response of the modelled system. This type a simplification is acceptable when trying to solve problems related to torsional oscillation mitigation, because these problems are essentially dominated by time delays, however it is not well-suited for the precise estimation of torques along the drill-string as it is difficult to express precisely the distributed external torques that apply along the drill-string. For instance, kinetic frictional torques depend on the normal forces exerted at the contacts between the drill-string and the borehole, and since side forces are highly dependent on the inclination and the curvature of the borehole, which in turn varies substantially all along a deviated well, lumping the total effect of

the external torques for a long section of pipes, introduces a large degree of imprecision.

At the bit, there are two possible boundary conditions as either it is free to rotate, and its angular velocity can be determined by estimating the action of external torques, or the bit angular position is imposed, for example when in a sticking state while the bit is on bottom and stick-slips are experienced, therefore contributing to the generation of the local torque conditions. "The torque on bit (τ_{bit}) can be estimated from the WOB using the relationship from Pessier and Fear (1992) [107]:

$$\tau_{bit} = -sign(\omega_{bit})\mu_{k_{bit}} d_{bit} |F_{wob}| \tag{77}$$

where $\mu_{k_{bit}}$ is equivalent to a kinetic friction factor, d_{bit} is the bit diameter, F_{wob} is the contact force between the bit and the formation and ω_{bit} is the bit angular velocity.

Caicedo and Calhoun (2005) [108] give an empirical estimation of the coefficient of friction as a function of the confined compressive strength (CCS) of the rock to be drilled: $\mu_{k_{bit}} = 0.09402 e^{-1.16\times10^{-9}\, CCS}$. To keep a sense of generality, we can use:

$$\mu_{k_{bit}} = \mu_{ref} e^{-\alpha_{ref}\, CCS} \tag{78}$$

where $\mu_{ref} = 0.09402$ and $\alpha_{ref} = -1.16 \times 10^{-9}$ by default."[22] The CCS is a function of the uniaxial compressive strength (UCS) of the formation, the rock material internal angle of friction (φ) and a pressure difference. For permeable rocks, a typical relation is [109]:

$$CCS = UCS + \left(p_{bh} - p_{pore}\right)\left(1 + \frac{2\sin\varphi}{1-\sin\varphi}\right) \tag{79}$$

while for impermeable formations, the CCS can be expressed as [109]:

$$CCS = UCS + \left(p_{bh} - p_{pore} + \frac{p_l - p_{bh}}{3}\right)\left(1 + \frac{2\sin\varphi}{1-\sin\varphi}\right) \tag{80}$$

22 Excerpt from Cayeux (2018) [185]

where p_{bh} is the borehole pressure, p_{pore} is the pore pressure and p_l is the overburden pressure. The overburden pressure, or lithostatic pressure, is defined as [2]:

$$p_l(Z) = p_0 + \int_{Z_0}^{Z} g\rho_b(z)dz \tag{81}$$

where Z is a TVD, ρ_b is the bulk mass density of the material at a particular depth and p_0 is the pressure at Z_0.

The top boundary condition is imposed by the top-drive, or the rotary table. Most authors integrate the rotary system into their model by considering the additional moment of inertia corresponding to the motor rotor and its associated gear-box. Kyllingstad (2017) [110] defines the apparent moment of inertia of the top-drive (J_{TD}) as:

$$J_{TD} = n_m {n_{gr}}^2 J_r + J_{gb} \tag{82}$$

where J_r and J_{gb} are respectively the moment of inertia of the motor rotor and gear box, n_m is the number of motors, and n_{gr} is the gear ratio.

To control the top-drive speed, the variable frequency drive (VFD) that drives the electrical motor, has a proportional-integral-derivative (PID) controller that utilizes the measured angular position of the rotor taken by an encoder placed on the rotor shaft. A schematic representation of the top-drive motor and its VFD with the PID controller is shown on Fig. 41, where $\dot{\alpha}_{set}$ and $\dot{\alpha}_{meas}$ are respectively the requested and measured rotor rotational speed, and τ_{TD} is the top of string torque. Kyllingstad (2017) [110] explains that the feedback block *R* represents the mechanical friction in the motor and gear box. $H_{\dot{\alpha}}$ and H_τ are respectively the rotational velocity and torque transfer functions that can typically capture possible time delays introduced by the controller."[23]

This control structure of the top-drive can be modified in different ways to perform an active stick-slip mitigation. Over the last two decades, several control structures have been proposed and utilized. Amongst them, there are

23 Excerpt from Cayeux (2018) [185]

the torque feedback [111], soft torque [112], soft speed [113] and Z-torque [114] methods.

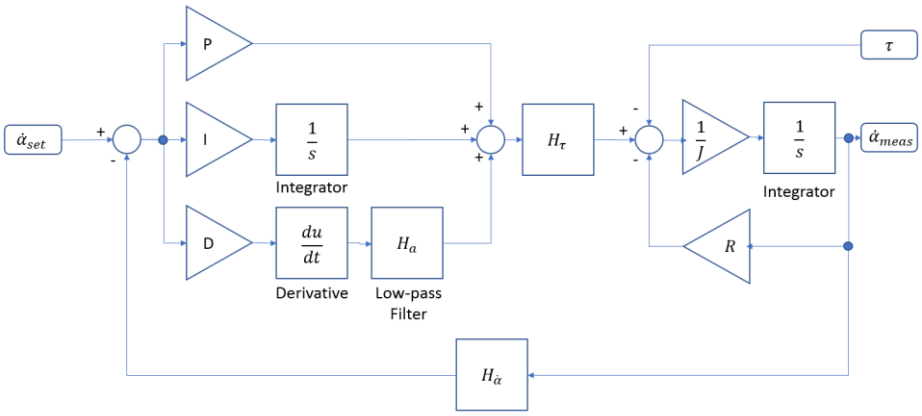

Fig. 41: Model of a top-drive and its VFD with a PID controller (inspired from Kyllingstad 2017 [110]).

2.1.2.7 Modelling of Axial Motion

The idea of discretizing the drill-string into short elements that are lumped into equivalent mechanical spring/mass systems can be used to model the axial displacement of a drill-string [115]. This time, zero-thickness disks of equivalent masses to the original drill-string portions are connected to each other's by massless axial springs having a similar axial spring constant as the modelled length of the drill-string (see Fig. 42). External forces, including gravitation and kinetic friction, apply on each of the disks. The discretization results in a system of partial differential equations following the generic form:

$$m_i \frac{\partial^2 s_i}{\partial t^2} = -k_{a,i}(s_i - s_{i-1} - l_i) + k_{a,i+1}(s_{i+1} - s_i - l_{i+1}) + f_{ext,i} \quad (83)$$

where m_i is the equivalent mass, $k_{a,i} = \frac{EA_i}{l_i}$ is the equivalent axial spring constant, E is the Young modulus of the material, A_i is the cross-sectional area, l_i is the length at rest of the discretized portion of the drill-string, s_i is the curvilinear abscissa of the disk position and $f_{ext,i}$ represents the external forces that applies on the discretized portion of the drill-string. These external forces

include the effect of gravitation, pressure-induced forces, viscous and mechanical frictions.

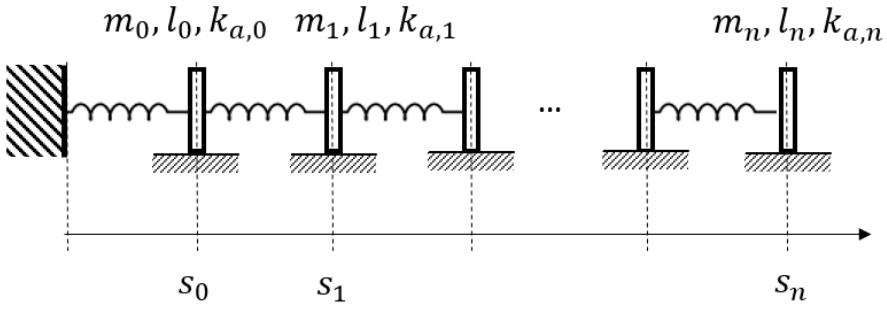

Fig. 42: Finite difference discretization of the axial deformation of the drill-string by a series of coupled axial springs.

The bottom boundary condition at the bit is either a free axial displacement that is only constrained by the action of external forces, or there is an imposed axial velocity, i.e. a rate of penetration ($\bar{v}_{bit}$), when the bit is in contact with the formation. It should be noted that the ROP is a function of the WOB ($F_{wob} = \text{WOB. g}$), the bit rotational speed (ω_{bit}) and the in-situ strength of the formation. Therefore, we need to establish a relationship between the ROP and the WOB.

From drill-off tests made at different rotational speed, we can notice that the ROP increases proportionally with the WOB until a transition value, called the founder point, where the ROP can actually decrease when applying larger WOB (see Fig. 43). Dupriest and Koederitz (2005) [116] have found that during the linear increasing phase of the ROP/WOB response curve, there was a significative relationship with the mechanical specific energy (MSE). The MSE, denoted here E_{MS}, has been introduced by Teale (1965) [117]:

$$E_{MS} = \frac{|\bar{\tau}_{bit}|\bar{\omega}_{bit}}{\bar{v}_{bit}\, A_{bit}} + \frac{|\bar{F}_{WOB}|}{A_{bit}} \tag{84}$$

where $\bar{\tau}_{bit}$ is the average bit torque, $\bar{\omega}_{bit}$ is the average angular velocity of the bit and A_{bit} is the bit area.

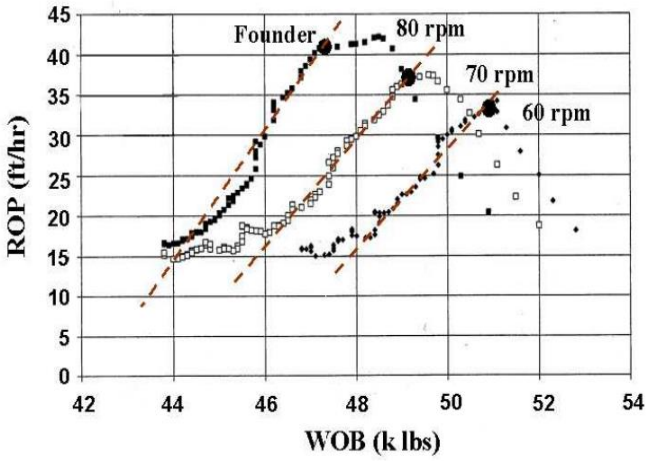

Fig. 43: Drill-off tests performed at three different rotational velocities (courtesy of Dupriest and Koederitz (2005) [116].

The same authors found that the MSE can be related to the formation strength and they indicated that the bit efficiency factor (η_{bit}) is between 0.3 and 0.4 for PDC bits:

$$CCS = \eta_{bit} E_{MS} \tag{85}$$

The top boundary condition is imposed by the hoisting system. "Most modern rotary drilling rigs are equipped with hoisting systems based on either conventional draw-works or modern ram-rig or rack and pinion hoisting arrangements.

The conventional hoisting system installed on most rotary drilling rigs today is based on a block-and-tackle hoisting principle and is composed of a draw-works, a crown block and a traveling block, a drilling line, a number of sheaves connected to the crown block and to the traveling block. The draw-works consists of a drum wound with drill line, as well as motors, brakes and a transmission line. The drill line is often divided into a dead line, support lines and a fast line: The dead line is the length of drill line from the dead line anchor, fixed to the drill floor across from the draw-works, and up to the first sheave (as seen from the dead line anchor) in the crown block. The drill line connects the crown block and the traveling block by an even number of supporting lines that run over sheaves at either block. Finally, the fast line is the length of drill

line from the last sheave (as seen from the dead line anchor) in the crown block and down to the draw-works drum. Consequently, the traveling block is raised (lowered) by spooling drill line onto (out of) the draw-works drum." [24]

With a draw-works hoisting system, heave compensation can be achieved either with a crown-mounted compensator or by utilizing actively the draw-works itself (see Fig. 44).

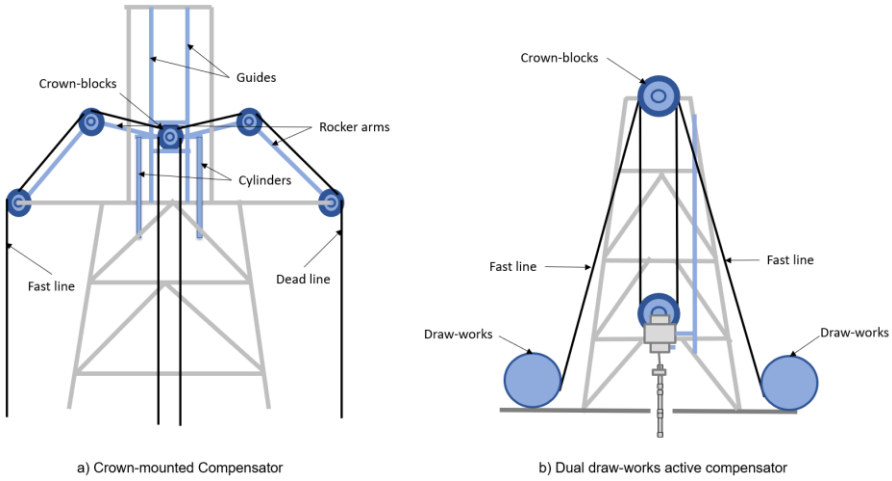

Fig. 44: Heave compensation with draw-works hoisting systems can be done with a) a crown-mounted compensator or b) utilizing active draw-works compensation like for example with a dual draw-works system.

With a crown-mounted heave compensator, the crown-block is mounted on an assembly that can move up and down within vertical guides. It is supported by cylinders that work either passively as a damping system or actively by displacing the crown-block position such that the motion of the drill-string is solely relative to a fixed elevation on the earth and therefore independent of the rig's own motion. The drill-line passes through rocker arms that ensure that the length of wire between the drum of the draw-works and the crown-block, and the length of cable between the crown-block and the dead-line anchor are very

24 Excerpt from my contribution to the text of the paper by Cayeux et al. 2015 [189]

close to be constant. Fig. 45 shows a mechanical equivalent of a draw-work system with a crown-mounted compensator.

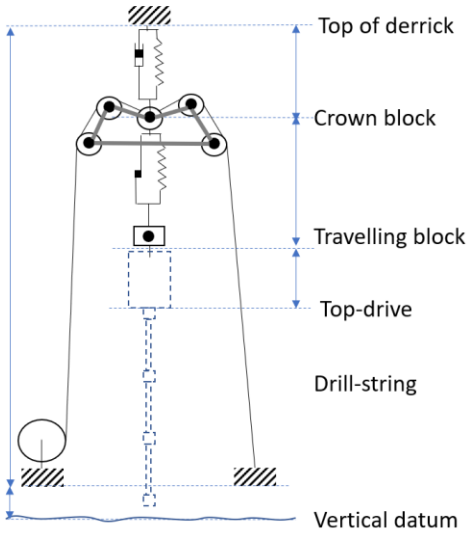

Fig. 45: Mechanical equivalent of draw-work hoisting system with a crown-mounted heave compensation.

With the active draw-works heave compensation system, the drill-line is spooled in and out of the drum such that the traveling block moves only relatively to a fixed elevation on the earth. To avoid a premature wear of the drill-line because of the repetitive spooling around the crown and traveling sheaves around the same position [118], especially when drilling with a low ROP, modern active draw-work heave compensation system utilizes two draw-works, one on each side the drill-line. It is then possible to vary the position of the drill-line that passes around the sheaves even when the drill-string stays at the same elevation [119]. Here the mechanical stiffness of the hoisting system is like the one of draw-works on a fixed platform, i.e. without the influence the heave compensation system.

2.1.2.8 Modelling of Coupled Rotational and Axial Motion

Bakhtiari-Nejad and Hosseinzadeh (2017) [120] emphasize on the importance of considering the axial elastic movement also when modeling stick-slip vibrations as the axial movement influence the bit rock interaction especially

with non-constant top of string velocity. However, their modelling only concerns vertical wells and does not consider the effect of mechanical friction along the drill-string nor the effect of pressure along the drill-string. The authors introduce viscous damping both for the torsional and axial movements but do not give any indications about its physical origin.

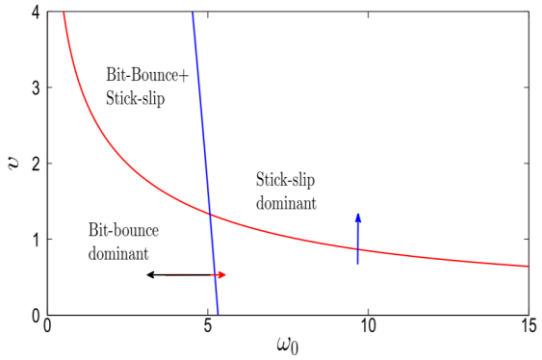

Fig. 46: Stability map for coupled axial and torsional bit motion (courtesy Gupta and Wahi, 2016 [121]). Here, ω_0 and v are dimensionless quantities representing respectively the rotational speed and axial feed at the top of drill-string.

A more detailed analysis of the bit/rock interaction while considering a coupled axial and torsional motion of the bit is presented by Gupta and Wahi (2016) [121]. The proposed model allows to estimate stability maps showing when bit-bounce, stick-slip or simultaneous bit-bounce and stick-slip can dominate as a function of WOB and bit rotational speed (see Fig. 46). Yet the utilized model is based on several restrictive assumptions: the well is vertical, the whole drill-string is lumped into one single element, the traveling-equipment velocity and top-drive rotational speed are constant, the formation strength is homogenous, there is no explicit consideration of hydraulically induced forces, even though viscous damping is incorporated in the axial and torsional displacements but without being explicitly linked to hydraulic effects.

Yet in the limited context of vertical drilling, Aarsnes and van de Wouw (2017) [122] avoid utilizing the globally lumped approach that has been used by many authors, by considering the drill-string as a transmission line that is characterized by two independent wave equations, an axial and a rotational one.

Coupling between torsion and axial motion happens at the level of the bit when it is in contact with the formation. They consider two configurations: one with a single type of drill-pipes and one with two sections with drill-pipes of different dimensions. In this paper, they only consider torsional instabilities, i.e. stick-slip.

The focus of the authors is to estimate stability maps. They find that stability is much more complex than what has been previously estimated using low-order lumped models and that the complexity increases when considering two different drill-pipe sizes instead of only one. They also find that the stability is largely affected by the pseudo reflection coefficient given by the amount of damping of the torsional dynamics, i.e. in practice the top-drive apparent stiffness since the context is vertical drilling (see Fig. 47 where $\overline{\Omega}$ is a dimensionless number representing the top-drive rotational speed, $\overline{V}$ a dimensionless number representing the top of string velocity and η_t a pseudo reflection coefficient given by the amount of damping of the torsional dynamics).

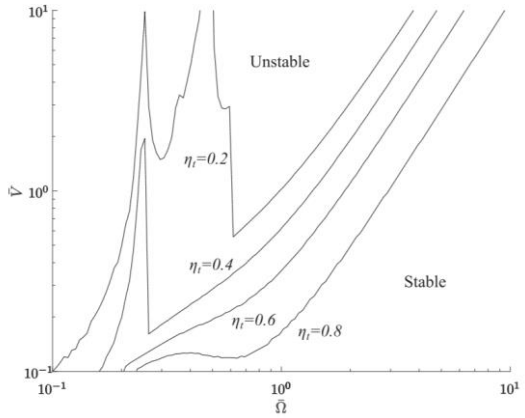

Fig. 47: Stability map for a drill-string composed of a single type of drill-pipe (courtesy of Aarsnes and van de Wouw, 2017 [122]).

As pointed out by Pastusek et al. (2016) [123], drilling from a floater under the effects of heave movement, which is far from being a constant vertical feed at the top of drill-string, has also a strong impact on the bit/rock interaction stability and remains to be modelled properly.

2.1.3 Heat Transfer

“As we have seen in section 2.1.1, many drilling fluid properties, e.g. density and rheological behavior, depend on temperature. Therefore, in situ temperature conditions impact the estimation of downhole pressure both in hydrostatic and hydrodynamic conditions.

To a lesser extent, temperature influences the material properties of drill-string components, e.g. Young’s modulus, Poisson’s ratio, ultimate strength, (see Fig. 48). For drilling operations related to the production of hydrocarbons, the downhole temperature seldom exceeds 200ºC [124], but in geothermal applications, the formation temperature can exceed 300ºC [125]. For instance, in such high temperature applications, the elasticity of steel material may decrease by 2 to 6% compared to normal atmospheric conditions of temperature.

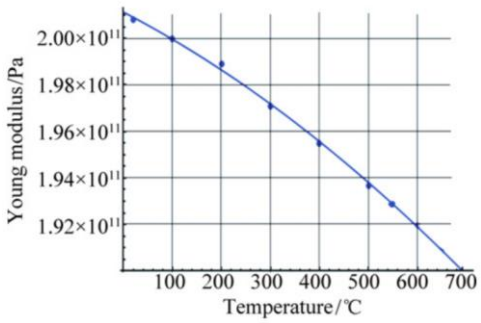

Fig. 48: Dynamic Young modulus for a steel sample as a function of temperature as measured by Wagner et al. (2012) [126]

On the other hand, pressure losses caused by drilling fluid circulation, mechanical friction between the drill-string and the borehole and the work of the bit while drilling formation rock, result in heat generation that influences the actual heat transfer between the drilling fluid and the surrounding environment. Consequently, we can expect that hydraulic, mechanical and heat transfer conditions are tightly linked together. Therefore, it is important to be able to model the heat transfer during drilling operations in order to capture the whole physical behavior of the drilling system composed of the drill-string, drilling fluid, casing strings and the surrounding environment.

In a heat transfer perspective, the description of the surrounding environment should inform about which portion of riser, casing or drill-string is directly exposed to atmospheric conditions, which portion of marine riser, casing or drill-string is in contact with water in an offshore context, and which portion of casing, liner or open-hole section exchanges heat with underground formations (see Fig. 49).

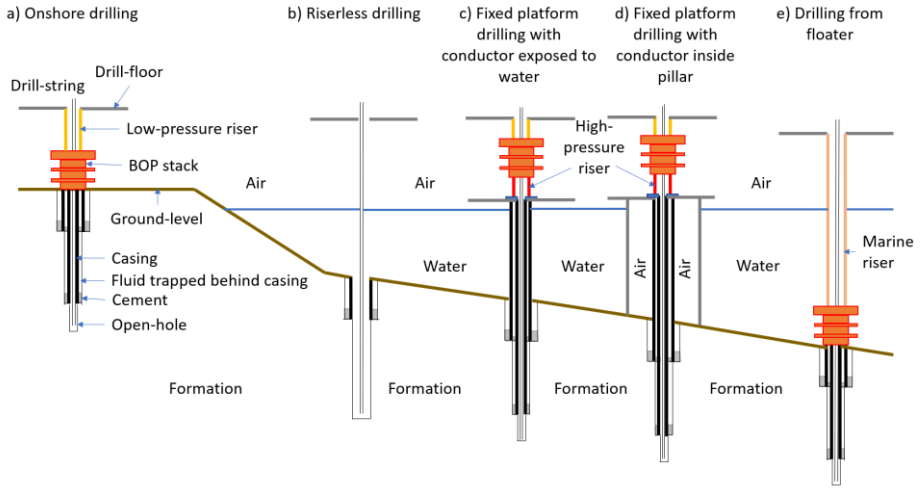

Fig. 49: Illustration of different environment for heat transfer: a) onshore drilling, b) riser-less drilling, c) drilling from a fixed platform with conductor exposed to water, d) drilling from a fixed platform with conductor enclosed in platform pillars, e) drilling from a floater.

In practice, heat is exchanged by advection, conduction and convection. In view of the small temperature gradients, heat transfer by radiation can be neglected. The drilling fluid contained in the drill-string exchanges heat with the drill-string tubular by convection and advection when there is circulation. The annulus drilling fluid transfers heat also by convection and advection in case of fluid movement, to the drill-pipe on the one side and with the formation (when in open hole) or the casing string on the other side. Heat can be exchanged from the casing string either by conduction through cement or by convection through the trapped fluid behind the casing to the next layer, which can either be another casing string or the formation (see fig. Fig. 50). Heat transfer on the one side of

solid elements, e.g. drill-pipe, casing-string, cement, formation, to the other side of the same element is the result of conduction.

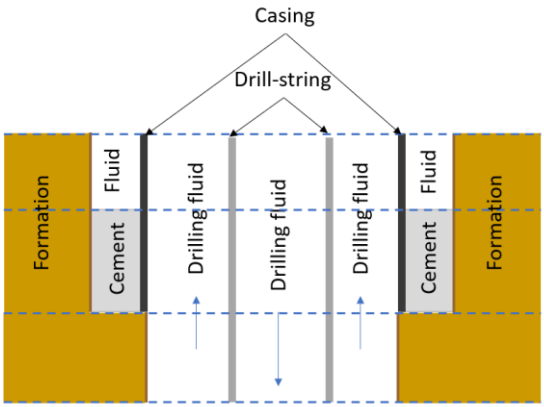

Fig. 50: Schematic representation of the different materials involved in the heat exchange.

In addition, advection heat transfer can relate to:

- the loss of drilling fluid to the formation, for example because of natural or induced fractures,
- the gain of formation fluid in the annulus because of underbalanced conditions,
- the passage of drilling fluid from the drill-string to the annulus, e.g. at the bit, under-reamer, hole opener, circulation-sub, bearings of downhole motor, drill-pipe washout,
- additional flow like when utilizing booster pumping in a marine riser or a dual-gradient drilling method.

The heat exchange, due to convection, between a fluid and a solid interface is described by Newton's law of cooling:

$$\frac{dQ_f}{dt} = h_t A\left(T_i - T_f\right) \tag{86}$$

where Q_f is the thermal energy, h_t is the heat transfer coefficient, A is the area where heat transfer takes place, T_i is the temperature at the interface, T_f is the average temperature of the fluid.

It is then usual to introduce the Nusselt number (N_u):

$$N_u = \frac{h_t L}{k_T} \tag{87}$$

where L is a characteristic length, for instance here a diameter and k_T is the thermal conductivity of the fluid. The Nusselt number is then estimated utilizing empirical models as a function of the flow regime, i.e. laminar, transitional or turbulent and the rheological behavior of the fluid. Ferreira et al. (2017) [127] list a few correlations for the Nusselt number.

The heat generation from pressure losses can be expressed as:

$$\frac{dT}{ds} = \frac{1}{\rho_f C_{p_f}} \frac{dp}{ds} \tag{88}$$

where s is the curvilinear abscissa, ρ_f is the fluid mass density, C_{p_f} is the fluid specific heat capacity.

Note that the specific heat capacity of a mix of components is the weighted average of the specific heat capacities of each of the components, with weights corresponding to their mass fractions:

$$C_{p_f} = \sum_{i \in \Omega} w_i C_{p_i}, \text{with} \sum_{i \in \Omega} w_i = 1 \tag{89}$$

where C_{p_f} is the specific heat capacity of the fluid mix, Ω is the set of indices for the different components, w_i is the mass fraction of the i-component and C_{p_i} is the corresponding specific heat capacity.

Note also that the temperature of a mix of n different fluids is:

$$T_f = \sum_{i \in [1,n]} w_i C_{p_i} T_i, \text{with} \sum_{i \in [1,n]} w_i = 1 \tag{90}$$

where T_f is the resulting temperature of the mix, T_i and C_{p_i} are respectively the original temperature and the specific heat capacity of the i^{th} fluid being mixed.

The heat generation from drill-string friction against the borehole is:

$$\frac{dP_\tau}{ds} = \omega_{ds} \frac{d\tau_{ds}}{ds} \tag{91}$$

where P_τ is the heat generated per unit time, ω_{ds} is the angular drill-string velocity, τ_{ds} is the torque along the drill-string.

Marshall and Bentsen (1982) [128] formulated the Fourier equation for the drilling heat transfer problem in the context of vertical wells and described a transient solver based on the finite difference method. For this thesis, we have used the framework defined by Corre et al. (1984) [129], who have extended the initial publication by Marshall and Bentsen to deviated wells.

More recently Kumar and Samuel (2013) [130] have described an analytical solution dedicated to the analysis of heat transfer in steady state conditions. Their study highlights the importance of the thermo-physical properties of the drilling fluid like the specific heat capacity and thermal conductivity. However, it should be noted that the proposed model assumes that the temperature at the external interface to the annulus is constant, i.e. the effect of multiple casing strings and the thermo-physical properties of the formation rocks are not accounted for. Finally, it is important to be aware that the thermo-physical properties of both drilling fluids and formation rocks are a function of temperature [129]. Unfortunately, very little focus has been put on the measurement or the estimation of the specific heat capacity and thermal conductivity of drilling fluids and their temperature dependence."[25]

2.1.4 Wellbore Position, Uncertainty and Tortuosity

"The position of a well cannot be measured directly because it is difficult to make direct spatial measurements through the earth crust (both electro-magnetic and pressure waves are quickly attenuated and dispersed when traveling through rock materials). The current practice is to derive the position by integrating tangential measurements made along the borehole. Indeed, at a given location, it is relatively simple to measure the inclination ϑ of the wellbore axis compared to the gravitational field and to measure the direction, i.e. the azimuth: Φ, of the well axis relative to the geomagnetic field or by recording direction changes using a gyroscope. Furthermore, the length of the borehole is approximated by the length of the drill-string, thereby providing a curvilinear abscissa s for the measurement.

The measurement of the inclination, azimuth and measured depth may be slightly biased for each survey station. If that bias is systematic, then the errors

25 Extended excerpt from my contribution to the text of the paper by Pastusek et al. (2019) [200]

accumulate and, after integration, result in a potentially large discrepancy between the estimated borehole position and the true position of the well. The importance of systematic errors in the calculation of wellbore trajectories has been reported and analyzed by Wolff and de Wardt (1981) [131]. These authors recognized six sources causing systematic errors on the measurement of inclination, azimuth and measured depth. The authors also developed a method for calculating the region of space that, with a given probability, will contain a survey station. This region of space is defined by a 3x3 covariance matrix and corresponds to an ellipsoid (see Fig. 51):

$$\Sigma = \begin{bmatrix} var(x,x) & cov(x,y) & cov(x,z) \\ cov(x,y) & var(y,y) & cov(y,z) \\ cov(x,z) & cov(y,z) & var(z,z) \end{bmatrix} \tag{92}$$

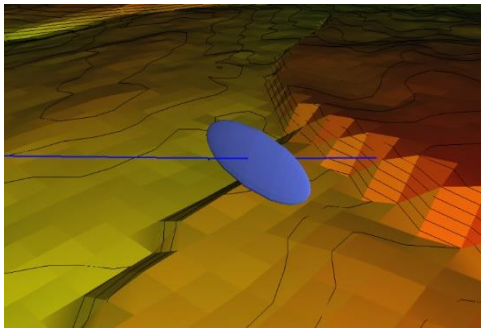

Fig. 51: Ellipsoid of uncertainty at certain depth of a deviated well.

Further analysis of the problem of wellbore position uncertainty estimations has led to more advanced models. One dedicated to magnetic measurements is described by Williamson (2000) [132], which is now considered as today's industry standard. An extension to this model to encompass gyroscopic measurements has been described by Torkildsen et al. (2008) [133]. Note that the new formalism still uses a covariance matrix to describe the wellbore position uncertainty at a given survey station.

The prediction interval for the multivariate normal distribution yields a region defined by:

$$\Delta\vec{r}^{T} \cdot \Sigma^{-1} \cdot \Delta\vec{r} \leq \chi_3^2(p), \tag{93}$$

where Σ^{-1} represents the inverse covariance matrix, $\chi_3^2(p)$ is the quantile function for probability p of the chi-squared distribution with 3 degrees of freedom (see Fig. 52), $\Delta\vec{r} = \vec{r} - \vec{r}_0$ with $\vec{r}_0$ being the mean position of the well, and $\vec{r}$ the borehole position when accounting for the uncertainty. This is the definition of an ellipsoid in a 3-dimensional space.

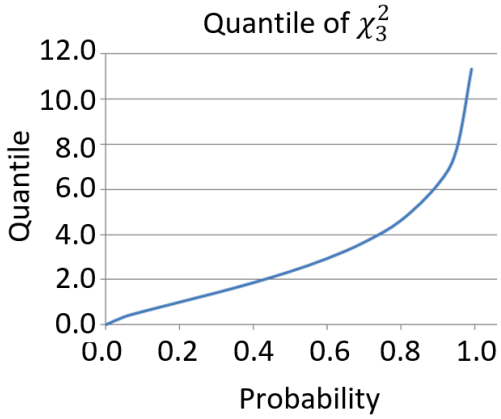

Fig. 52: Quantile function for probability p of the chi-squared function with 3 degrees of freedom.

So, if we choose $\chi_3^2(p) = 1$ then we obtain an ellipsoid that represents the region with about a 20% chance of containing the actual trajectory. We need to take $\chi_3^2(p) = 7.8147$ to calculate the ellipsoid that has a 95% chance of containing the real position of the well. Similarly, to obtain a 99% confidence of containing the trajectory, we need to calculate the ellipsoid based on $\chi_3^2(p) = 11.3449$. In that manner, for any given confidence factor, it is possible to calculate the ellipsoid of uncertainties at each survey station of the trajectory. "[26]

Systematic errors in wellbore positioning tools are visible when two or more instruments are run in the same borehole. In the following example (see Fig.

26 Excerpt from my contribution to the text of the paper by Cayeux et al. (2014) [187]

53), we compare the MWD inclinations and azimuths taken every stand with the continuous inclinations and azimuths measured every 0.3m by the RSS. There is an average positive inclination bias between the two measurements of about 0.3°. The combined effect of the inclination and azimuth differences results in a distance between the two trajectories reaching 2.5m at several depths along the borehole.

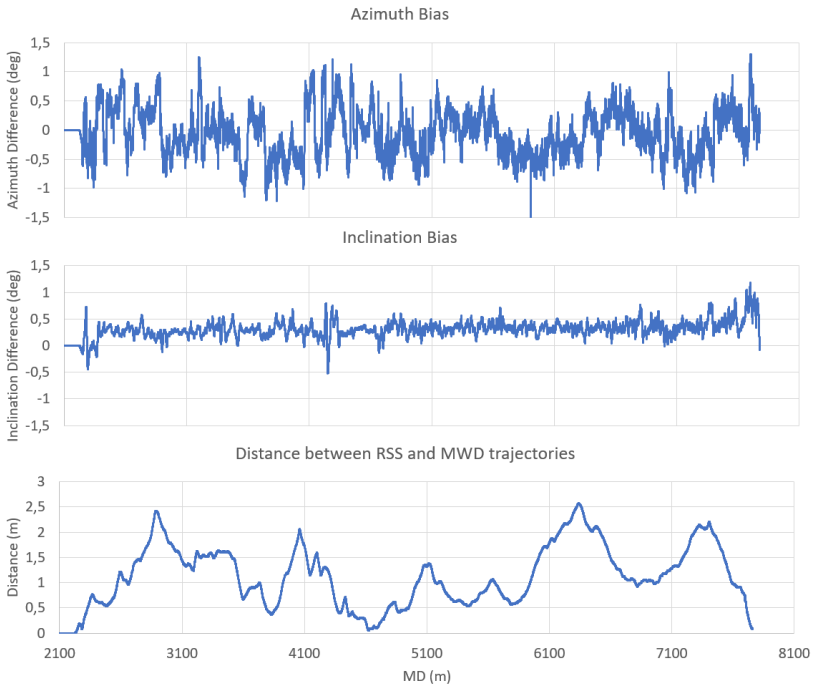

Fig. 53: Inclination and azimuth biases between continuous measurements taken by the RSS compared with survey stations at each stand. The distance between the two trajectories is shown on the bottom graph.

More particularly, a systematic bias on the vertical depth estimation may lead to errors in the calculation of the hydrostatic pressure (ref eq. (1)) along the hydraulic circuit, which may, in turn, impact the assessment of the proximity of the wellbore pressure to the geo-pressure margins.

Furthermore, an actual trajectory is usually more tortuous than the planned one, simply because of the directional work performed during the drilling operation. This has a direct impact on the side forces along the drill-string and BHA (ref.

eq. (73), and consequently on mechanical friction engendered torques and forces. For real-time applications, it is therefore important to utilize the actual trajectory instead of the planned one, as otherwise torque and drag estimations could be under-evaluated. But as the survey stations are usually taken at connection time, i.e. once per stand, there is a possibility that the trajectory is even more tortuous than reported by the MWD. This is true when drilling with PDMs because a downhole motor introduces a very large DLS each time it is used in sliding mode for orientation work. This is typically done half-way through the drilling of stand, and the survey stations tend to smooth out these very high curvatures. So for torque and drag calculation purposes, additional tortuosity may be added to the actual trajectory when drilling with PDMs to better capture the actual tortuosity of the trajectory.

On the contrary, with an RSS, the steering continues with the same parameters until the next command is downlinked to the tool, which is typically done once per stand. Therefore, the small-scale tortuosity of wells drilled with RSS is not much different from the one measured with the MWD. In addition, an RSS send continuous inclination and azimuth measurements through mud pulse or high-speed telemetry, and therefore micro-tortuosity is directly accessible through those measurements. However, the continuous inclination and azimuth measurements shall not be used for trajectory calculations as their precision is usually lower than the one made with the MWD.

2.2 Drilling Simulators

With the advent of the mechanization of the drill-floor and remote control by drilling control chairs [134], started the need for training drilling crews to use drilling workstations and computerized drilling control systems (DCS). The major drilling equipment manufacturers have built large and advanced training facilities with the focus of realistic top-side simulation, i.e. the drilling machines and their associated pipe handling equipment. These training facilities are centered around very realistic 3D rendering of the drill-floor in dome-based projection room while utilizing physics-based simulation of single pipe, stand and machine movements [135]. However, these training simulators usually do not address any modelling of sub-surface processes.

The idea of including drilling process simulation in a full fledge top-side simulator has been first motivated by the need to improve the preparation of the

drilling crews ahead of unusual drilling operations like through tubing rotary drilling (TTRD) or ERD operations [136]. Later, such combination of downhole simulation environment with virtual drilling equipment management has been used for rehearsing kick procedures prior to drilling a well under HPHT conditions with back-pressure MPD [137]. With such environments, it is possible to achieve more realistic well control training situations than those obtained when utilizing the very simplified simulators used during International Well Control Forum (IWCF) certification courses, for instance because of the possibility to simulate gas absorption in oil based muds [138].

These combined downhole and top-side simulators can also be used to improve the drilling operation plan by allowing to run virtual testing of the coming operation as part of the concept: life cycle drilling simulation [139].

Yet apart from well control simulation, there has been little focus on simulating other types of drilling incidents in these advanced simulation environments, such as pack-offs, stuck pipes, mud losses, pipe washouts, etc. at the exception of one publication about tight hole simulation [140], which is in fact based on the work published in this thesis in section 3.3.

2.3 Symptom Detection

Symptom detection is the first step of a diagnosis procedure. The consecutive action consists in determining the most likely causes to the observed deviations from normality. The third and last step of the process entails defining a plan of actions to either cure the problem or to acquire additional information that will help sorting out any doubts that may remain. Even though the two last activities of the diagnosis process are of great interest, in the context of this thesis we will only focus on symptom detection.

Symptoms can be decomposed in two categories: quick drilling events and prior indications before a larger drilling incident.

2.3.1 Quick Event Detection

2.3.1.1 Gain/loss Detection

In the drilling context, the concept of quick event detection has been coined by Aldred et al. (2008) [141]. The objective of the authors is gain/loss detection, i.e. the symptom, with an associated classifier, i.e. the plausible cause, that can

either be a kick, a loss circulation incident or a pipe washout. The gain/loss symptom is extracted from either a comparison of the flowrate out with the flowrate in, also called a delta-flow method, abnormal variations of the active volume and the standpipe pressure. The flowrate out is based on measurements made with a flow paddle, while the flowrate in relies on pump rates from a stroke counter. During steady state conditions, gain or loss can reliably be detected as shown in the loss circulation incident illustrated by Fig. 54.

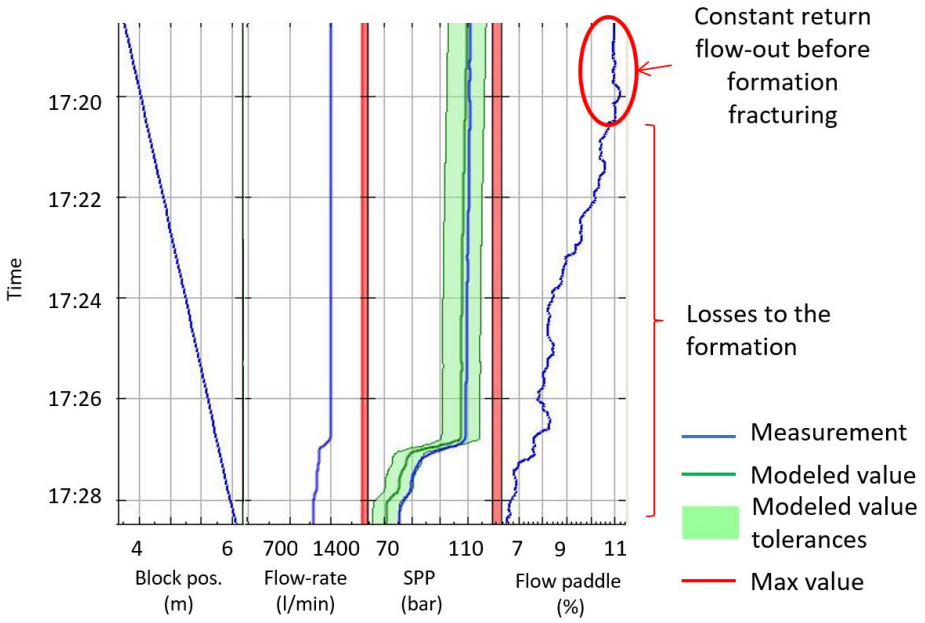

Fig. 54: Example of a loss circulation incident while pumping at a constant flowrate and lifting the drill-string at constant axial velocity.

However, the method does not seem to account for neither the effect of mud compressibility nor the retention of drilling fluid in the return flowline and associated mud treatment equipment. This can easily lead to many false alarms, especially during connection-time when the mud pumps are stopped and a few minutes later restarted. Indeed, the change of downhole pressure when the pumps are cycled, results in mud expansion and thereafter compression, that impacts the quantity of drilling fluid that is contained in the borehole, while at the same time, drilling fluid, retained in the flowline, first returns to the pit and afterward accumulates in the mud treatment equipment as a consequence of the

sequence of pump stop and start. Fig. 55 shows the active volume variations during pipe connections for the four sections, 17 ½-in, 12 ¼-in, 8 ½-in and 6-in, of a typical well drilled in the North Sea.

It is unfortunate that a gain/loss detection method is not reliable while making a connection, as a large proportion of kicks starts when returning to hydrostatic conditions [142]. Fig. 56 shows a situation where a kick starts when the mud pump rate is reduced to a low value because of a pack-off situation.

At start, one can see the flow-back to the pit originating from the accumulation of drilling fluid in the return flowline and mud treatment equipment, but contrary to what one would expect, the pit volume continues to increase. Because the drilling team is focused on managing the pack-off situation, it takes a long time before the influx situation is detected.

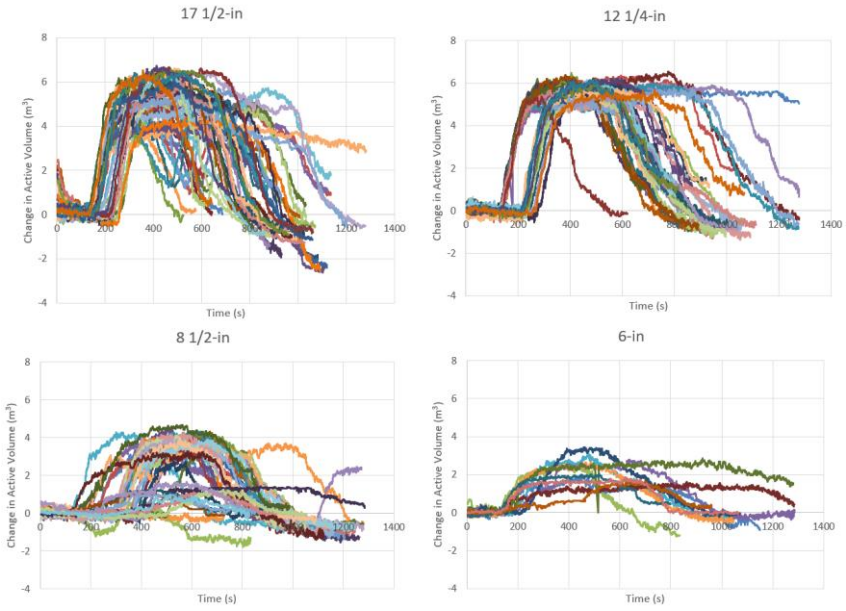

Fig. 55: Active volume variations during pump cycling for the four drilled sections of a typical well in the North Sea.

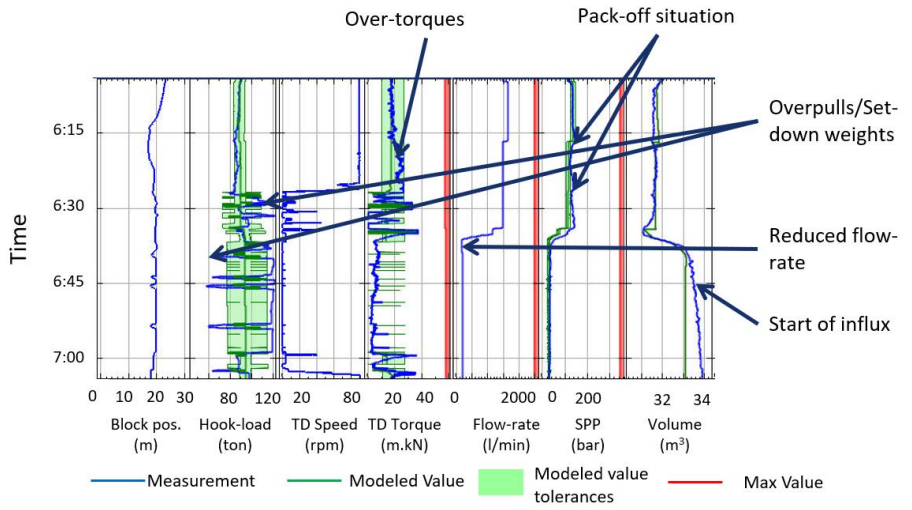

Fig. 56: Because of a pack-off situation, the flowrate is reduced to a low value. At the same as the downhole pressure reduces, a kick starts and is not detected immediately, because the drilling team is focused on the pack-off incident.

Tarr et al. (2016) [143] address the problem of detecting influx during pump stop by applying pattern matching techniques to check whether the current active volume variations match one of the last observed flow-backs that have been recorded during the few latest connections. This method may reduce the number of false alarms during connection, if the stopping and starting of the pumps are not too dissimilar. However, it will not be able to cope with unobserved situations as the one shown on fig. 21 of Paper III where the flowrate is first reduced and then increased, yet not returning to its initial set-point.

Instead of using a pattern matching method to verify that the current situation is normal, it is possible to utilize a model of the physical effects that contribute to the observations. Such a model will be described in section 3.3. Godhavn and Hauge (2018) [144] utilize a similar approach, yet after applying model reduction so that configuration can be kept to a strict minimum.

With methods based on simplified models or pattern matching, it is also necessary to utilize the pump pressure as a filtering mechanism, as when there is a float-valve in the BHA, it may be necessary to pump a relatively large

volume of drilling fluid to fill the air gap at the top of the drill-string when initiating the circulation, otherwise, unnecessary mud loss alarms would be generated. Fig. 13 shows a situation where the drill-string is filled at a flowrate of 100gpm (380l/min), the SPP is about 50psi (3.4barg), i.e. corresponding to the hydrostatic pressure of the mud column in the stand pipe, and the flow paddle proportion is zero most of the time. Without considering the fact that the pump pressure is as low as it can be, such a situation would look like a total mud loss case while actually a more than 500m air gap is being filled after tripping in hole with a float sub in the BHA.

Another difficulty of automatic gain/loss detection is connected to pit transfer and direct mixing in the active pit. Fig. 57 shows a situation where an abnormal active pit volume is observed while the mud pumps are stopped. At the same time, the flow paddle opening does not return to zero and in fact stays as high as 25%. Those two facts would tend to indicate that there is a kick, but in fact, it is a transfer of mud from the trip tank to the active pit.

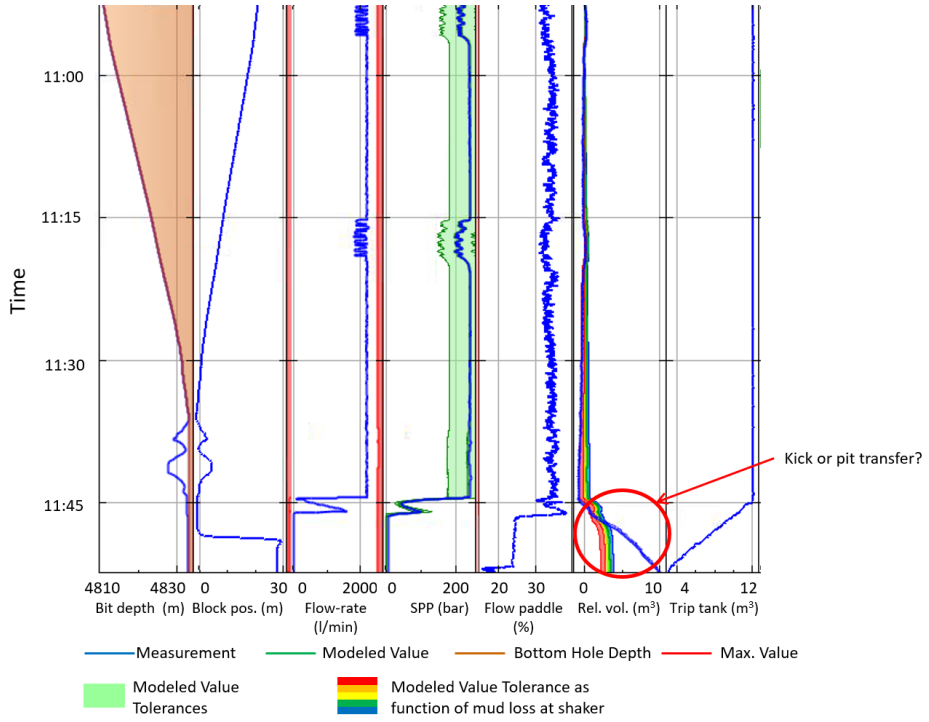

Fig. 57: In this time-based log, during the connection there is an abnormal increase of pit volume while at the same time the flow-paddle opening stays at

25% when the mud pumps are still stopped. This looks very much like a kick except that it is a mud transfer from the trip tank to the active pit.

Yet another problem that complexifies automatic kick detection, arises from ill-defined pumping conditions. When drilling from a floater with a marine riser, it is common to use booster pumping to help transporting the cuttings above the subsea BOP. This is yet another example of the importance of treating the hydraulic system as a network as pointed out in section 2.1.1.3.

2.3.1.2 Abnormal Pump Pressure

A sudden change of pump pressure is another type of quick event. The SPP can either increase or decrease abnormally.

Fig. 58 illustrates an over-pressure situation while reaming-up. For this situation, the hook-load decreases at the same moment as the SPP increases while the drill-string rotates at 80rpm. The combination of these two symptoms is a strong evidence of an obstruction in the annulus that causes pressure build-up below the restriction, since the mud pumps run, and lifting of the drill-string by a piston effect. On a terminology perspective, note that a partial obstruction of the annulus corresponds to a bridging incident while the term pack-off is reserved for a total obstruction of the annulus.

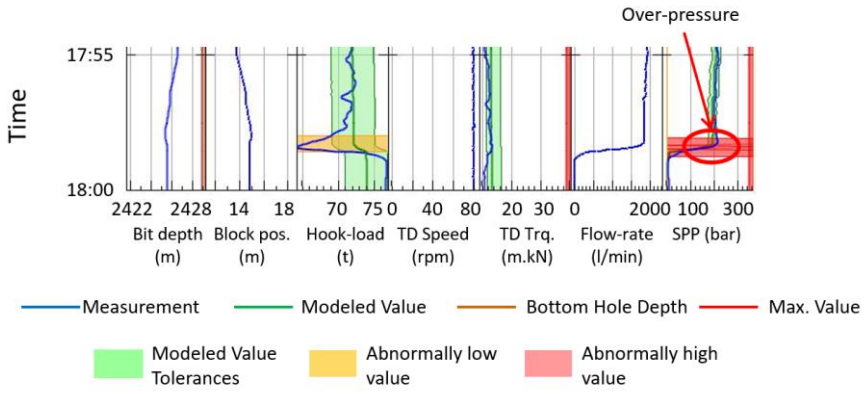

Fig. 58: While reaming-up, and over-pressure is detected, and the mud pumps are stopped. One can notice that because of the over-pressure, the hook-load drops because the build-up of pressure below the obstruction pushes the drill-string.

An increase of pump pressure is not necessarily linked to an annulus obstruction as it can also be caused by an obstruction in the drill-string itself. Fig. 59 illustrates such a situation. In this case, the drill-string has just been run in a cased hole just above the cement and circulation is established for the first time and therefore it is unlikely that any obstruction may exist in the annulus. After starting the pumps at about 2000l/min, the SPP increases suddenly by approximatively 50bar. As the problem does not disappear, the pumps are stopped and then restarted. This time the pump pressure takes normal values. It is likely that some hindrance inside the BHA caused the observed over-pressure.

The pump pressure can also unexpectedly decrease, for example because of a pipe washout. This can be seen on Fig. 60 where the SPP drops by about 6bar in a period of 2 hours while the flowrate remains unchanged.

Daison and Mukund (2008) [145] point out that one can rely on multiple information sources to diagnose a pipe washout. They emphasize on the fact that the MWD turbine rotational speed is also affected by the decrease of flow through the BHA when the washout is located above the MWD and therefore monitoring the MWD turbine speed sent by mud pulse telemetry can be an efficient way to detect prematurely close to the BHA pipe washouts.

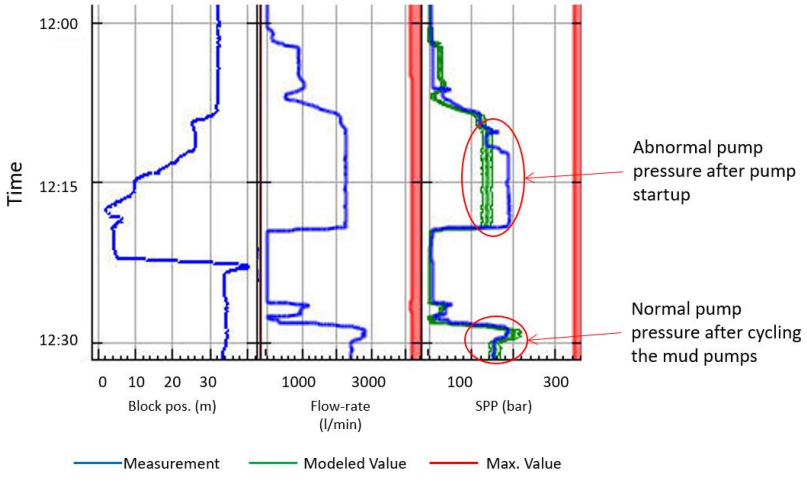

Fig. 59: Abnormal pump pressure due to an obstruction in the drill-string.

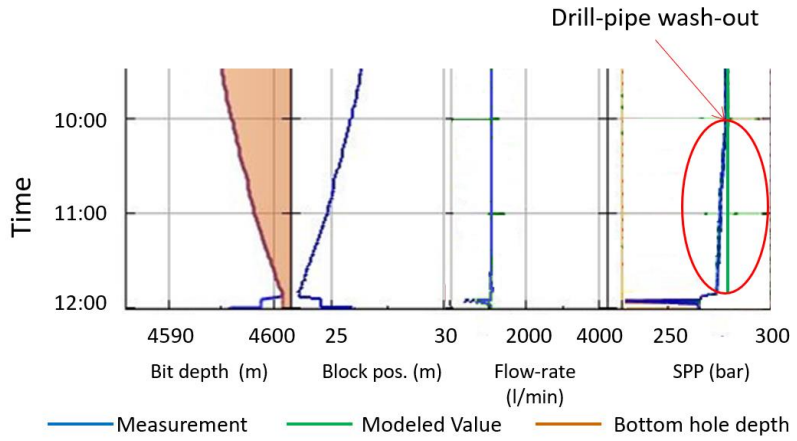

Fig. 60: Example of a drill-pipe wash-out while drilling.

But a decrease of SPP or of the MWD turbine rotational speed can also be caused by a problem at the mud pumps. Spoeker and Litzlbauer (2002) [146] utilize high sampling rate pressure measurements at the mud pumps to detect problems in triplex pumps, like leak at the suction or discharge valves with two drilling fluids: a bentonite spud mud and a K_2CO_3 WBM.

Kyllingstad and Nessjøen (2011) [147] argue that with long wells and more compressible drilling fluids, the signature of high frequency pressure measurements may be insufficient to detect precisely problems with the pump valves and especially which one is faulty. They propose to use accelerometer measurements placed on each valve block to detect precisely any deteriorations of the pump valves. But both previous methods require the installation of additional instrumentation to detect a possible defect at the mud pump. More recently, Ambrus et al. (2018) [148] developed a methodology based on a Bayesian network to determine the most probable cause to abnormal pump pressure decrease, therefore sorting out automatically the most likely reason between a pipe washout and a mud pump failure.

2.3.1.3 Overpull/Set-down Weight Detection

When the drill-string moves axially, its displacement can be hindered. This results in an increase of hook-load when moving upward or a decrease of hook-load when moving downward. In such a situation, it is important to stop the

movement as quickly as possible, as otherwise the drill-string may get stuck after applying excessive forces where the drill-string movement was impeded. Modern drilling control systems have a function to stop the upward hoisting motion when the hook-load exceed a certain limit, but that threshold is usually set to the maximum tensile yield of the weakest pipe element in the drill-string. Relying on this limit to stop the movement would result in a severe stuck-pipe situation. Therefore, overpulls and set-down weights limits are slight deviations from expectable hook-loads, depending on whether there is rotation or not and the direction of movement. Fig. 61 illustrates an example of overpulls and set-down weight experienced while pulling out of hole. The threshold margin is 4t above the expected pick-up weight and 4t below the anticipated slack-off weight.

The threshold values shall not be too restrictive as variations of hook-load can be expected during an axial movement of the drill-string. When there is a ledge somewhere along the borehole, it is common to observe spikes of hook-loads each time the shoulder of an element passes over a diameter disparity (see Fig. 62), and as long as there is no definitive stopping of the drill-string movement, this is not causing any harms.

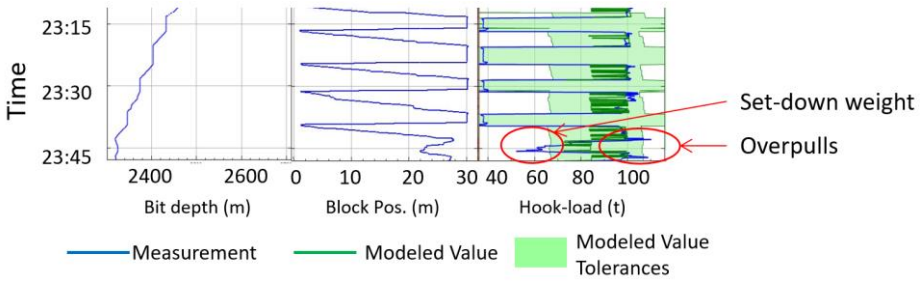

Fig. 61: Example of two overpulls and one set-down weight while pulling out of hole.

In case of differential sticking, for instance when there are large diameter elements in contact with the borehole in a depth range with a high permeability and a low pore pressure, it is important to be able to apply a sufficient force to overpass the differential sticking force. Fig. 63 (courtesy of Mason et al. (2013) [149]) shows a typical hook-load signature when running in hole with a casing string subject to differential sticking. There is a clear low hook-load value,

marked in red, before the casing string starts moving. In such a situation, this low hook-load should not be considered as a set-down weight.

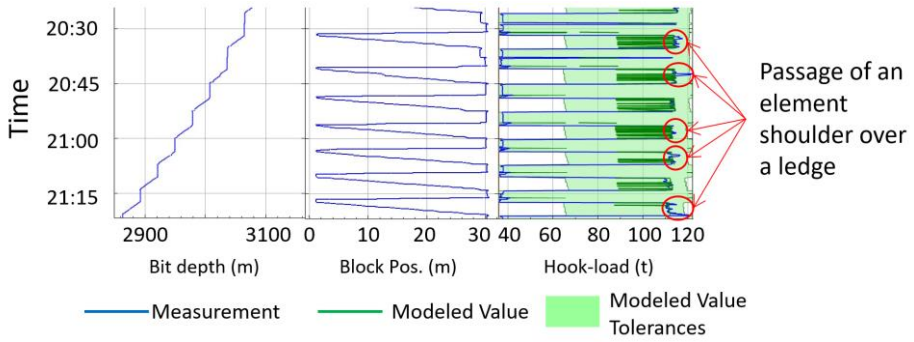

Fig. 62: This time-based log illustrates the hook-load signature when a large element passes over a ledge.

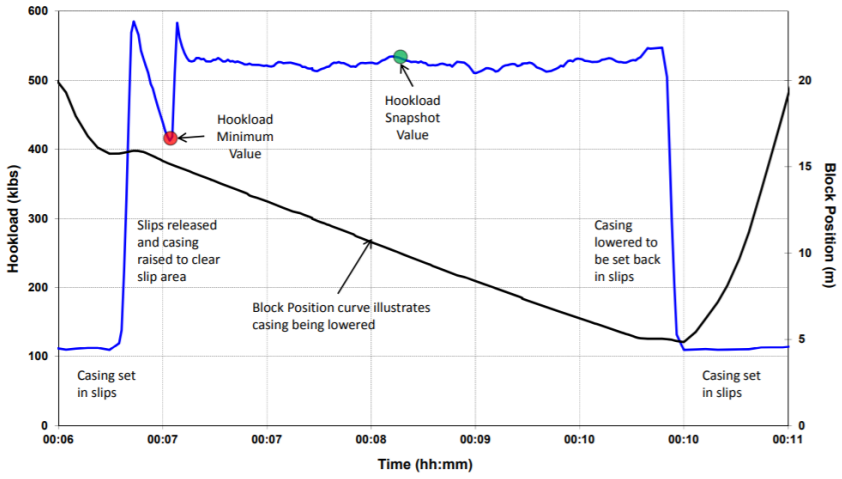

Fig. 63: Hook-load signature when running in hole with a casing string that is subject to differential sticking (courtesy of Mason et al. 2013 [149]).

2.3.1.4 Abnormal Torque Detection

Another situation where quick events can occur is when there are abnormally high torques building up along the drill-string. Even though the driller can

configure a maximum torque that shall not be exceeded by the top-drive, this value is usually the make-up torque or a torsional yield limit for the weakest pipe in the drill-string. If the drill-string gets stuck, allowing the torque to reach such a high value could jeopardize consequent efforts to free the drill-string. It is therefore desirable to stop the rotation when an abnormally high torque is detected (see Fig. 64). However, it is very common that the top-drive torque is erratic, like for instance when there are stick-slips. In such a case, torque spikes can be quite large and yet one shall not stop the top-drive rotation.

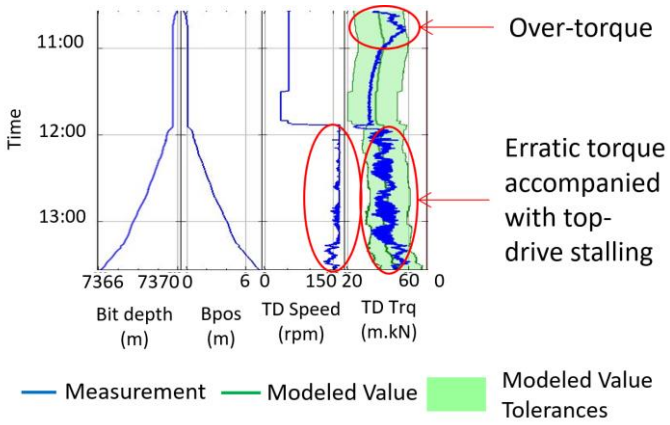

Fig. 64: Back-reaming in a tight hole with first an over-torque situation while the top-drive speed was kept at 50rpm and then stick-slips and intermittent stalling of the top-drive when the rotational speed has been increased to 150rpm.

2.3.2 Pre-event Detection

A complementary class of symptoms compared to quick events are pre-event ones. Pre-event symptoms are indications of the deteriorations of downhole conditions before any drilling incidents have yet been observed.

2.3.2.1 Torque and Drag Charts

The comparison of measured pick-up weight (PUW), slack-off weight (SOW), free-rotating weight (FRW) and free-rotating torque (FRT) with pre-computed charts where these values have estimated for different friction factor is one of

the oldest prior symptom analysis tool that has been used during drilling operations [150] (see Fig. 65). Any deviations from the curve corresponding to the best friction factor is an indication that some unplanned effects impact drag forces or torques.

Originally, these charts were filled manually during a drilling operation after a friction test was executed before making a connection. Cayeux and Daireaux (2009) [151] reported one of the first attempts to automate the construction of these drag and torque charts. They also applied the technique to tripping and accounted for fill-pipe operations while running in hole. They also accounted for the effect of circulation on measured hook-loads.

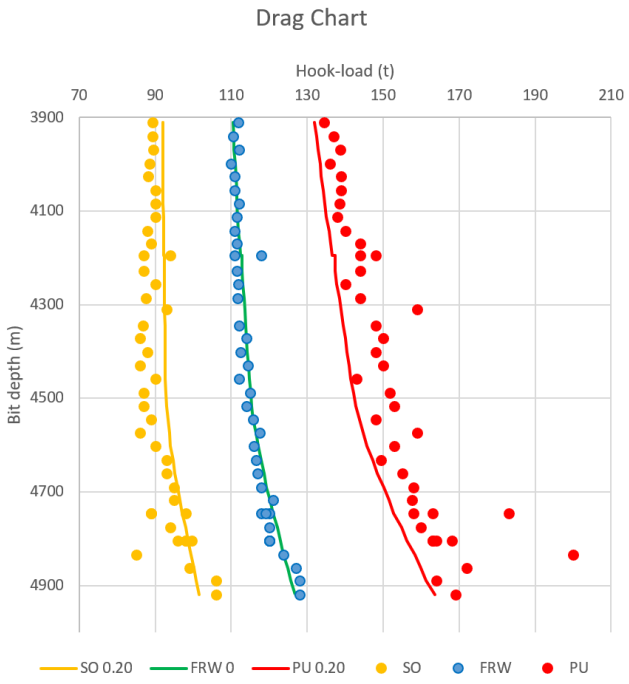

Fig. 65: Example of a PUW, SOW and FRW chart based on the 8 ½-in section of S-shape well drilled in the North Sea.

2.3.2.2 Methods Based on the Analysis of a Combination of Signals

Gulsrud et al. (2009) [152] propose to detect the deterioration of hole cleaning conditions by analyzing a correlation of the downhole annulus pressure with top-drive torque. If the downhole pressure is not available, they use the SPP

instead, yet noticing that the pump pressure contains information about the circulation inside the drill-string that may decrease the ability to detect problems with hole cleaning. Their method consists in calculating the product of the pressure skewness with a normalized standard deviation of the top-drive torque and to count the number of instances over a time window when this product is positive.

Wong et al. (2013) [153] report that the initial method described by Aldred et al. (2008) [141] was not reliable when utilized with PDM. The method has been extended to utilize simultaneously the SPP and the MWD turbine RPM to detect pipe washouts. Nevertheless, they indicate that changes of mud density can cause the generation of false alarms during the time it takes to displace the well with the new drilling fluid.

Machine learning techniques have been tested to perform automatic warning of the risk of imminent incidents based on real-time drilling signals. One of them is case-based reasoning [154]. The main idea is to describe fault states and their relation to symptoms as an ontology and then to associate observed cases, i.e. drilling incidents, with factual symptoms. Thereafter, the method can highlight probable drilling incidents that may occur in view of the current real-time drilling symptoms and how they can be associated with already observed cases. A radar plot [155] provides an easily understandable view of the current situation where the most probable incidents move toward the center of the graph when their probability increase (see Fig. 66).

This methodology depends on the ability to reliably detect symptoms and on capturing many example cases to provide a sufficient basis for the probabilistic associative reasoning mechanism. In the described solution [154], symptom detection is based on very simple analysis of the real-time drilling signals. But, contractual data confidentiality agreements have, in practice, posed a problem, as they have limited the possibility to build a large library of cases that is necessary for this machine learning method [156].

Advanced models of the drilling process are used for real-time supervision of the drilling process and are associated to 3D visualization (see Fig. 67). The published examples [157] [158] [159] concern mostly ECD management, but the system utilizes also torque and drag and ROP management [160]. For the ECD management cases, the method consists in comparing modelled downhole pressure for the whole open hole section with the geo-pressure margins such

that risk of formation fluid influx, hole collapse and formation fracturing can be detected. It is not clear whether uncertainty of the modelled downhole pressure is accounted for in the risk estimation.

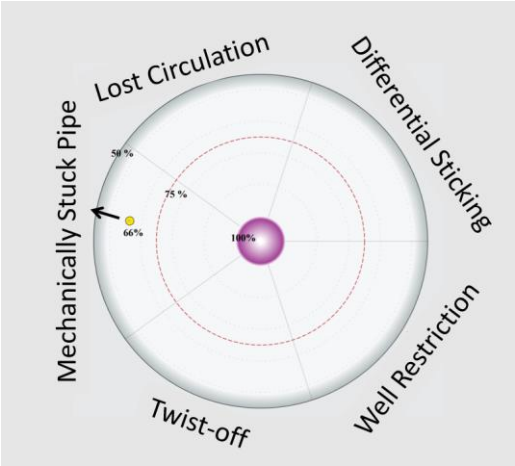

Fig. 66: Radar plot of probable drilling incident (courtesy of Le, 2012 [155]).

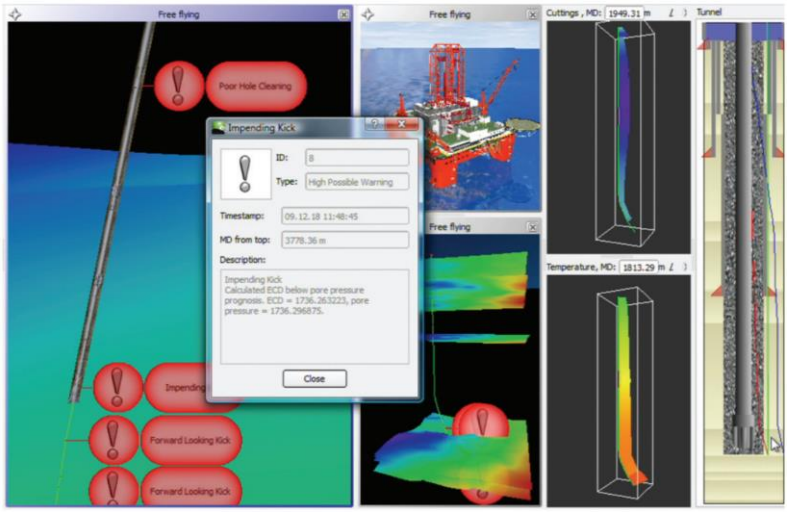

Fig. 67: Warning about an impending kick as the downhole pressure is lower than the pore pressure in the open hole section (courtesy of Rommetveit et al., 2011, [159]).

2.4 Assistance to the Control of Drilling Machines

With more and more interest in drilling automation solutions, the drilling control system providers have started to propose solutions that allow external vendors to interact with the DCS [161]. The DCS becomes a repository of automatic sequences that can be activated on demand by the driller, like for instance "tag bottom" or "drill a stand". The automation of a sequence of actions can be described as a finite state machine[27]. It can either be a deterministic automaton when there is exactly one transition for each input, or a non-deterministic state machine if that condition is not respected. Mathematically, a deterministic finite state machine is a quintuple $(\Sigma, S, s_0, \delta, F)$ where [162]:

- Σ is the input alphabet (a finite, non-empty set of symbols),
- S is a finite, non-empty set of states,
- s_0 is an initial state, $s_0 \in S$,
- δ is the state-transition function: $\delta: S \times \Sigma \rightarrow S$,
- F is the set of final states (possibly empty), $F \subset S$.

By ensuring that standard actions are always executed the same way, it is possible to achieve a greater consistency and a performance improvement (see Fig. 68).

However, a certain adaptability of the procedure is necessary as downhole conditions change continuously. For instance, the elasticity of the drill-string can be very different at the end of the section compared to the starting conditions and therefore the necessary stick-up height to lift the bit off bottom may have to be adapted during the operation. Furthermore, drilling incidents may occur at any time during the execution of a standard procedure. It is therefore important that safety trigger functions protect an automatic procedure while it runs. Finally, the actual downhole conditions, like poor hole cleaning, can dictate modifications of velocities and accelerations utilized when the

27 A finite state machine is an abstract machine that can be in one of a finite number of states.

automatic function performs. Adaptability and safeguarding have not been addressed, so far, in the proposed drilling control vendor solutions, therefore leaving that responsibility to the driller.

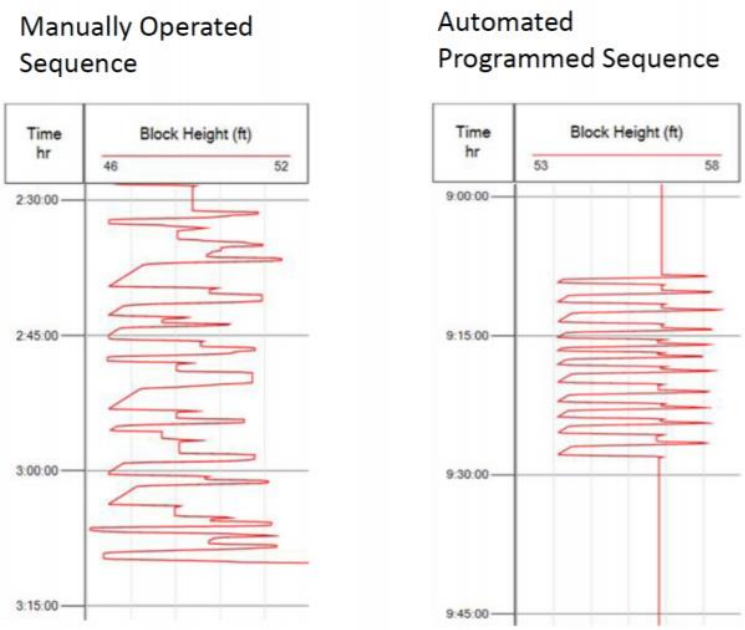

Fig. 68: Comparison between multiple bottom tagging executed manually (left-hand side) and automatically (right-hand side) (courtesy Iversen et al. 2016 [163]).

3 Mathematical Modelling and Realtime Drilling Applications

The work presented in this section describes extensions in the domain of drilling hydraulic and drill-string mechanics that have been made to some of the basic models outlined in section “2 State of the Art”. The objective of these extensions is to provide a sufficient level of flexibility and accuracy to solve example applications such as:

- Drilling simulator environment
- Detection of the deterioration of the drilling conditions prior to the occurrence of drilling events
- Active assistance to operate the drilling machines during drilling operations

3.1 Drilling Hydraulic

Many real-time drilling process applications make use of drilling hydraulic modelling, as it provides information about downhole pressures, the ability to transport cuttings, pressure loss-related heat generation, advection and convection-related heat transfers, and pressure-related forces on the drill-string.

An efficient multi-phase and multi-component transient hydraulic model, utilizing the drift-flux approach as the one described in section 2.1.1.22, is the basis of this work. The existing model can solve arbitrary hydraulic networks (ref. section 2.1.1.23). It accounts for the pressure and temperature dependence of the mass density and rheological behavior of drilling fluids as defined in sections 2.1.1.4 and 2.1.1.12. Pressure loss calculations in the annulus includes the effects of eccentricity, pipe rotational and axial movements, as outlined in sections 2.1.1.5, 2.1.1.6, 2.1.1.7 and 2.1.1.8, as well as pressure losses through downhole tools and bit (ref. 2.1.1.10). Gelling effects, utilizing eq. (38) (section 2.1.1.13) and eq. (45) (section 2.1.1.15), are integrated in the model. Transported cuttings are assumed to be always in suspension, with a cutting slip-velocity that is not dependent on the local borehole inclination, therefore following the principles exposed in section 2.1.1.17.

Real-time drilling applications necessitate some extensions to this original drilling hydraulic modelling framework.

For instance, the number of components constituting the drilling fluid is limited to two liquid-components (a brine and a base-oil), two solid-components (a weighting material and one type of cuttings particle) and one gas-phase. In a real-time drilling operation context, this is quickly insufficient, especially for the solid-phase point of view. Indeed, a typical OBM utilizes oleophilic clays as part of its composition, which has a mass density that cannot be assimilated to standard weighting material like barite. More generally, LCM particles of different sizes and made of various materials, can be added to the drilling fluid, as pointed out in section 2.1.1.21. Furthermore, cuttings particles have a large variety of dimensions and may originate from formation rocks of variable bulk densities. Unfortunately, the standard drilling fluid density models, as those referred to in section 2.1.1.4, do not account for so many components in the calculation of the bulk density of a drilling fluid and therefore, there is a need to generalize the calculations of the bulk fluid density of drilling fluids, as a function of pressure and temperature, for a large number of components.

A connected problem that arises from the multiple solids composing the drilling fluid mix, is a change of the apparent rheological behavior of the drilling fluid. We have seen in section 2.1.1.18 that some work has been published about the change of the apparent rheological behavior of Newtonian fluids by the presence of solid particles, but little has been published about the impact on the apparent rheological behavior of solid particles on Herschel-Bulkley fluids.

Finally, as pointed out in sections 2.1.1.19 and 2.1.1.20, cuttings are not always transported in suspension. It is therefore important to extend the capability of the hydraulic model to account for the effects of cuttings sedimentation and cuttings bed erosion. Cuttings particles passing between a tool-joint and the borehole are grinded as explained in section 2.1.1.21, and it is necessary to estimate the evolution of the particle size distribution as a function of the drilling operational conditions.

3.1.1 Mass Density of a Fluid Mix

Because the gas and liquid phases are compressible and dilatable, the volume fractions of the different components change with pressure and temperature, but not necessarily at the same rate. With changes of pressure and temperature, the volume occupied by the dispersion medium reduces or expands. As a

consequence, the distances between the dispersed particles change and therefore the volume fraction occupied by the dispersed component evolves not only because of its own compressibility and thermal expansion but also because of the compression and dilatation of the dispersion medium (see fig. 7 in Paper II).

Let us consider first, uncompressible and non-thermally-dilatable solid particles in suspension in a compressible and thermally-dilatable fluid. At a different pressure and temperature, the relative volume fraction of solid (f_s') in the liquid mix is:

$$f_s' = \frac{f_{s\,0}'\rho_f}{(1 - f_{s\,0}')\rho_{f_0} + f_{s\,0}'\rho_f} \tag{94}$$

where $f_{s\,0}'$ and ρ_{f_0} are respectively the solid volume fraction and the fluid mass density under the reference temperature and pressure condition, ρ_f is the mass density of the fluid at the new conditions of pressure and temperature. A demonstration of eq. (94) has been published in Paper II and Paper IV.

In the general case, both the dispersed component and the background fluid are compressible and thermally-dilatable. Let us consider that the initial relative volume fraction of the compressible and thermally-dilatable component is $f_{c\,0}'$ at initial conditions of temperature (T_0) and pressure (p_0). The relative volume fraction of that component (f_c') in the fluid mix at a different condition of pressure and temperature can then be expressed as:

$$f_c' = \frac{f_{c\,0}'\rho_{c_0}\rho_f}{(1 - f_{c\,0}')\rho_{f_0}\rho_c + f_{c\,1}'\rho_{c_0}\rho_f} \tag{95}$$

where ρ_{c_0} is the component density at initial conditions, ρ_{f_0} is the background fluid density at initial conditions, ρ_c is the component density at current conditions and ρ_f is the background fluid density at current conditions. The derivation can be found in Paper IV.

3.1.1.1 Mass Density Based on Fluid Mixing Sequence

Let us consider the incremental mixing of a multi-component fluid. Each component is added, one at a time in the fluid mix. A usual way to describe the additional quantity of a component that is mixed with the previous version of the fluid mix at step i of the mixing sequence, is in mass per unit volume, here

denoted Λ_{c_i}. The relative volume fraction ($f'_{c\,i}$) of the component in the new fluid mix is:

$$f'_{c\,i} = \frac{\Lambda_{c_i}}{\rho_{c_i} + \Lambda_{c_i}} \tag{96}$$

where ρ_{c_i} is the mass density of the component at the reference conditions of pressure and temperature (see derivation in Cayeux et al. 2013 [164]). Utilizing eq. (5), the new mass density of the fluid mix at that i -iteration is:

$$\rho_{f_i} = f'_{c\,i}\rho_{c_i} + (1 - f'_{c\,i})\rho_{f_{i-1}} \tag{97}$$

Therefore, we can calculate the absolute volume fraction (f_{c_i}) of each component in the fluid mix as a function of the mixing sequence (see demonstration in Appendix A):

$$\begin{cases} f_{c_N} = f'_{c\,N} \\ f_{c_n} = f'_{c\,n} \prod_{i=n+1}^{N} \left(1 - f'_{c\,i}\right), \forall n \in [1, N-1] \end{cases} \tag{98}$$

where N is the total number of components and n is the component number in the mixing sequence. The principles of this calculation have been exposed in Paper II and Paper IV.

Fig. 69 illustrates the combined effects of pressure, temperature and composition, here through cuttings in suspension, on the mass density of a KCl/polymer drilling fluid of nominal mass density 1277kg/m^3 at 15°C with a KCl volumetric concentration of 11.8 vol% and 2 vol% of xanthan gum.

This example starts from geothermal conditions, for which case the mass density of the drilling fluid inside the drill-string and in the annulus are identical at any depths, yet this density decreases with depth as the temperature increases and thermal expansion has a larger effect than compressibility. Then the flowrate is increased and because of the larger pressure in the drill-string than in the annulus, the mass density of the drilling fluid contained in the drill-string is larger than the one in the annulus. After five minutes of circulation, heat transfer effects start to be visible and the temperature of the fluid inside the drill-string deviates from the one filling the annulus with the consequence of an even larger difference between the mass densities of the fluid inside the drill-

string and the annulus. As a final step in this sequence, drilling is initiated first at 30m/h and then increased to 60m/h. As it can be seen on the figure, the cuttings in suspension modify greatly the mass density of the drilling fluid in the annulus.

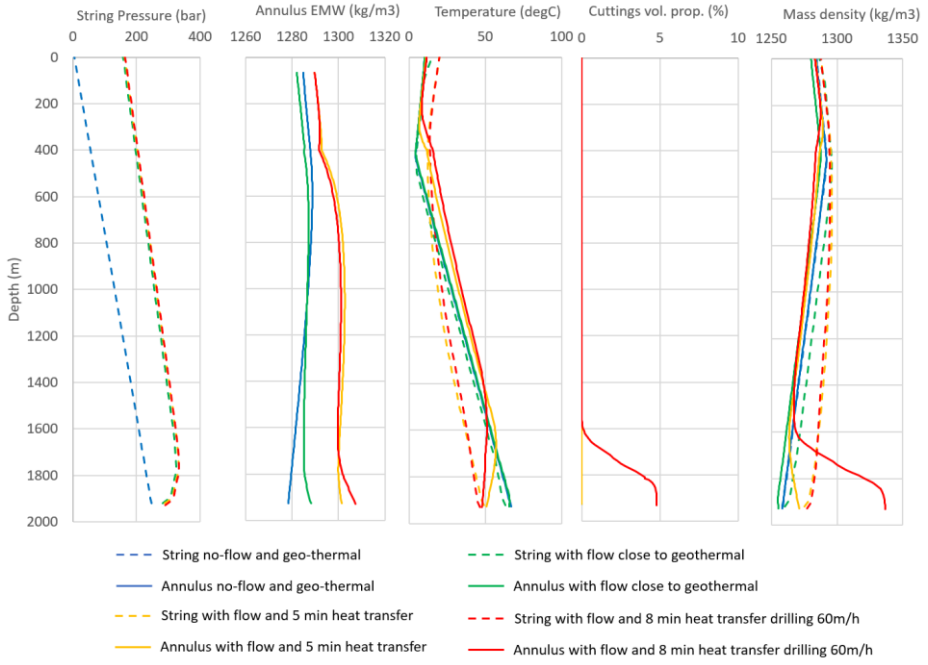

Fig. 69: Effect of pressure, temperature and cuttings proportion on drilling fluid mass density.

3.1.1.2 Determination of HGS Concentration Based on Composition and Density Measurement

It is common that the composition of the drilling fluid contained in the pit is defined in mud reports. Furthermore, the actual mass density of the drilling fluid may be measured in situ and in real-time, under other conditions of pressure and temperature than those used in the mud report. As it is likely that a conversion of the mass density performed from the drilling fluid composition to the real-time measurement conditions of pressure and temperature will differ, it is necessary to perform a correction of the drilling fluid composition.

The volume fraction of one of the components is modified to reconciliate the drilling fluid composition with the measured mass density. But as the change of the volume fraction of one component impacts the volume fractions of the other components, it is more convenient to change the volume fraction of the component that has the largest mass density, i.e. the high gravity solid, as the resulting effect on the other components is less significant.

Let us suppose that the volume fractions of the original drilling fluid composition have been converted to the conditions of pressure and temperature of the real-time mass density measurement. Then we have:

$$\tilde{\rho}_f = \tilde{f}_{c_{hgs}} \rho_{c_{hgs}} + \sum_{\substack{i=1 \\ i \neq hgs}}^{N} \tilde{f}_{c_i} \rho_{c_i} \tag{99}$$

where $\tilde{\rho}_f$ is the expected mass density based on the fluid composition defined in the mud report, hgs is the index of the high gravity solid component and $\tilde{f}_{c_i}$ is the volume fraction of the i-component based on the original fluid composition. The latter equation can be re-written as:

$$\tilde{\rho}_f = \tilde{f}_{c_{hgs}} \rho_{c_{hgs}} + \left(1 - \tilde{f}_{c_{hgs}}\right) \left(\sum_{\substack{i=1 \\ i \neq hgs}}^{N} \frac{\tilde{f}_{c_i}}{1 - \tilde{f}_{c_{hgs}}} \rho_{c_i} \right) \tag{100}$$

where $\sum_{\substack{i=1 \\ i \neq hgs}}^{N} \frac{\tilde{f}_{c_i}}{1 - \tilde{f}_{c_{hgs}}} \rho_{c_i}$ is the density of the fluid after removing the hgs-component.

If we measure a fluid density ρ_f instead of $\tilde{\rho}_f$ and if we assume that the formulation of the fluid excluding the hgs-component has not changed, then the volume fraction of the hgs-component shall respect:

$$\rho_f = f_{c_{hgs}} \rho_{c_{hgs}} + \left(1 - f_{c_{hgs}}\right) \left(\sum_{\substack{i=1 \\ i \neq hgs}}^{N} \frac{\tilde{f}_{c_i}}{1 - \tilde{f}_{c_{hgs}}} \rho_{c_i} \right) \tag{101}$$

$$\Leftrightarrow f_{c_{hgs}} = \frac{\rho_f - \sum_{\substack{i=1 \\ i\neq hgs}}^{N} \frac{\tilde{f}_{c_i}}{1-\tilde{f}_{c_{hgs}}}\rho_{c_i}}{\rho_{c_{hgs}} - \sum_{\substack{i=1 \\ i\neq hgs}}^{N} \frac{\tilde{f}_{c_i}}{1-\tilde{f}_{c_{hgs}}}\rho_{c_i}}$$

Note that if $\rho_{c_{hgs}} = \sum_{\substack{i=1 \\ i\neq hgs}}^{N} \frac{\tilde{f}_{c_i}}{1-\tilde{f}_{c_{hgs}}}\rho_{c_i}$, then $\rho_f = f_{c_{hgs}}\rho_{c_{hgs}} + \left(1 - f_{c_{hgs}}\right)\left(\sum_{\substack{i=1 \\ i\neq hgs}}^{N} \frac{\tilde{f}_{c_i}}{1-\tilde{f}_{c_{hgs}}}\rho_{c_i}\right) \Leftrightarrow \rho_f = f_{c_{hgs}}\rho_{c_{hgs}} + \left(1 - f_{c_{hgs}}\right)\rho_{c_{hgs}} \Leftrightarrow \rho_f = \rho_{c_{hgs}}$, therefore the denominator of the above equation is unlikely to be equal to zero.

3.1.1.3 Resulting Mass Density when Mixing Two Fluids

We have seen in section 2.1.1.3 that the drilling hydraulic circuit is, in general, a network. For that reason, at the junction between two branches, two fluids, with possible different formulations, mix together and we need to evaluate the composition and mass density of the resulting fluid mix. The pressure at the junction point is identical for all three branches, but the temperature in each branch is likely to be different.

For the moment, we assume that the absolute volume fractions of the components from the two fluids arriving from each branch have been converted to the condition of pressure and temperature associated with the resulting temperature of the fluid mix. Then we can convert the absolute volume fractions in mass fractions:

$$f_{c_i} = \frac{V_{c_i}}{V_f} = \frac{m_{c_i}\rho_f}{\rho_{c_i} m_f} = w_{c_i}\frac{\rho_f}{\rho_{c_i}} \Leftrightarrow w_{c_i} = f_{c_i}\frac{\rho_{c_i}}{\rho_f} \tag{102}$$

where $w_{c_i} = \frac{m_{c_i}}{m_f}$ is the mass fraction of the i-component.

Let us denote Ξ' the set of components of the first fluid and Ξ'' the set of components of the second fluid, then we can define mass fractions for the original composition of each of the fluids in the set of components $\Xi = \Xi' \cup \Xi''$. Note that the weight fractions of the components that are not present in the original composition are set to zero, i.e. $\forall i \in \Xi - \Xi', w_{c_i} = 0$.

The composition of the first fluid, expressed over the set of components Ξ, is $\{w'_{c_i}, i \in \Xi\}$ and the composition of the second fluid, expressed other the same

set of components, is $\{w_{c_i}^{"}, i \in \Xi\}$. When a mass m_f' of the first fluid mixes with a mass $m_f^{"}$ of the second fluid, the new composition is $\{w_{c_i}, i \in \Xi\}$ where $w_{c_i} = \frac{m_f' w_{c_i}' + m_f^{"} w_{c_i}^{"}}{m_f' + m_f^{"}}$. We can calculate the density of the resulting fluid mix by dividing the total mass of the mix by the occupied volume:

$$\rho_f = \frac{\sum_{i\in\Xi}\left(m_f' w_{c_i}' + m_f^{"} w_{c_i}^{"}\right)}{\sum_{i\in\Xi}\left(m_f' w_{c_i}' + m_f^{"} w_{c_i}^{"}\right)/\rho_{c_i}} \tag{103}$$

3.1.1.4 Summary

Relations to transform the volume fraction of a mix of two components from one condition of pressure and temperature to another condition of pressure and temperature are given.
The absolute volume fraction of a component is provided as a function of the relative volume fractions corresponding to the mixing sequence.
The volume fraction of one component of the mix is estimated based on the mass density and the volume fractions of the other components.
The fluid density of the mix of two multi components fluids is provided as a function of their original respective volume fractions and the masses of fluids that are mixed together.

3.1.2 Impact of Time on Rheometer Measurements

We have seen in sections 2.1.1.13, 2.1.1.14 and 2.1.1.15 that drilling fluids have a time-dependent response that can be measured with scientific rheometers. We have also seen that standard thixotropic models do not manage to reproduce accurately the time response of the shear stress to step-changes in shear rates for WBM and OBM. In this section, we will attempt to define an alternative thixotropic model that has a better ability to reproduce the time-dependent response of non-thixotropic fluid.

We will use the measurements of Fig. 70 to illustrate how we derived the new model. “Fig. 70 shows measurements made with a scientific rheometer on an unweighted KCl/polymer fluid. The rheometer speed has been changed up and

down between 200, 100, 50, 20, 10 and $5s^{-1}$ to exhibit the effect of thixotropy when changing from a high to low shear rates and from low to high shear rates.

First, we would like to know which exponents of eq. (40) fit best the measurements made with drilling fluids. To obtain that information, we proceed by investigating any sequence where the shear stress has stabilized before the step change in shear rate is applied and which ends up with a stable shear stress after the step change. In that way, we know that the structure parameter (λ) has reached an asymptotic value before the step change and will reach another asymptotic value after the step change. We denote $\lambda_{\dot{\gamma},\infty}$ the asymptotic value of the structure parameter for a given shear rate $\dot{\gamma}$ at time $t \to \infty$. For such situations, we can expect that the shear stresses at the previous and new shear rates correspond to steady state values and we expect that in steady state conditions, the fluid follows a unique Herschel-Bulkley rheological behavior. We also disregard the first minutes of measurement that are under the influence of the remnant effects of gelling as explained in section 2.1.1.15.

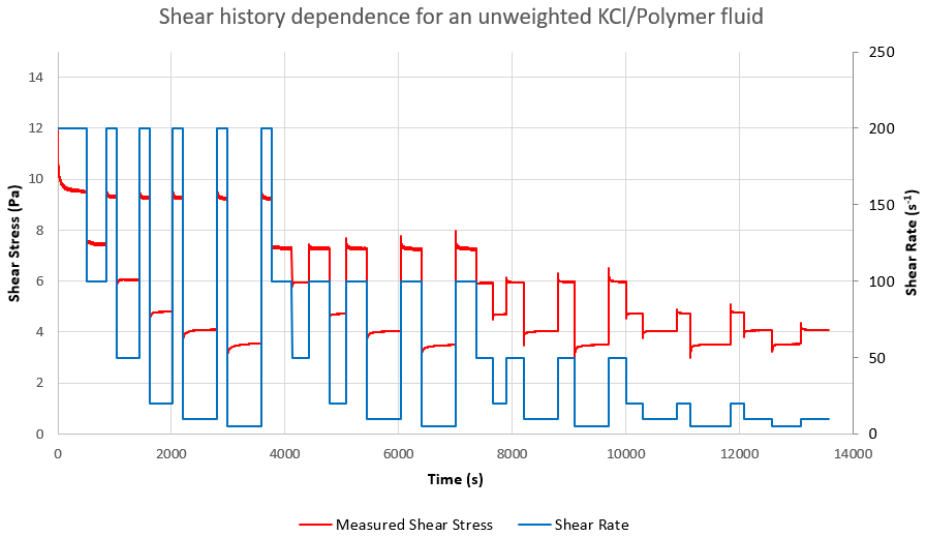

Fig. 70: Measured shear stress of an unweighted KCl/polymer fluid during the application of various changes of shear rates. All measurements have been made with a scientific rheometer.

We assume that the impact of thixotropy on the shear stress can be modelled as an amplification factor of the Herschel-Bulkley rheological behavior:

$$\tau_{\dot{\gamma},\lambda} = \left(1 + \alpha_a \frac{\lambda - \lambda_{\dot{\gamma}_{i,\infty}}}{\lambda_{\dot{\gamma}_{i-1}} - \lambda_{\dot{\gamma}_{i,\infty}}}\right)\left(\tau_{\gamma,t_{gel}} + K\dot{\gamma}^n\right) \tag{104}$$

where α_a is an amplification function that depends on $\dot{\gamma}_{i-1}$ and $\dot{\gamma}_i$, $\dot{\gamma}_i$ being the current shear rate and $\dot{\gamma}_{i-1}$ being the previous shear rate, and $\lambda_{\dot{\gamma}_{i-1}}$ is the structure parameter just before the change of shear rate. Note that this function tends to the steady state Herschel-Bulkley rheological behavior when $t \to \infty$.

Fig. 71 shows the best fitted results when utilizing $a = 0$, $b = 1$, $c = 1$ and $d = 4$ (ref. eq. (40)) when the shear rate is increased, while Fig. 72 shows the best fitted results when the shear rate is decreased, here with $a = 0$, $b = 5$, $c = 1$ and $d = 1$.

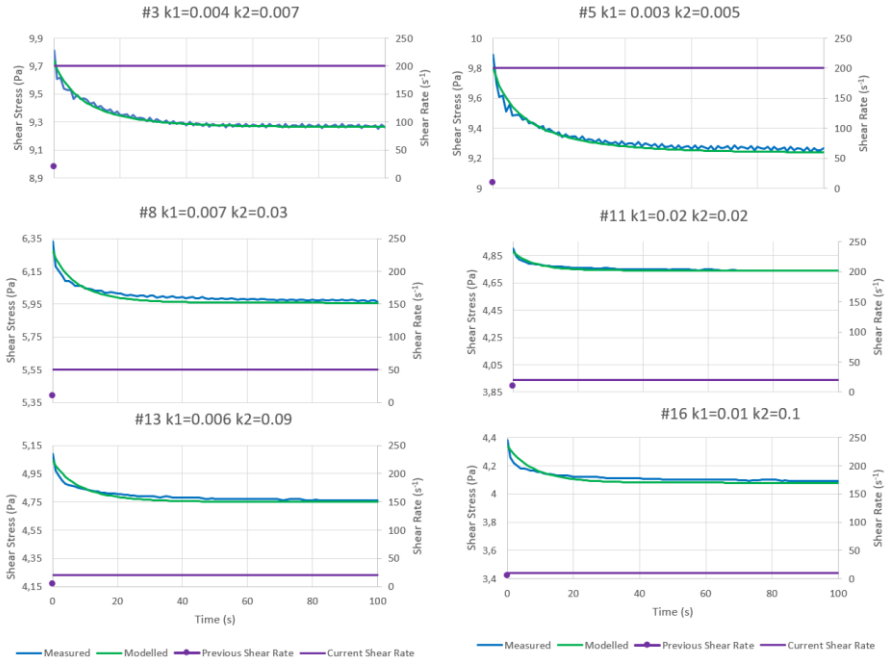

Fig. 71: Sequences for which the shear stress is asymptotic before and after stepping up the shear rate. Here, the structure parameter follows the differential equation $\frac{d\lambda}{dt} = k_1(1-\lambda) - k_2\,\dot{\gamma}\lambda^4$.

We can notice that the coefficients k_1 and k_2 are of the same order of magnitude for the cases where the shear rate is stepped up. Similarly, k_1 and k_2 are of the same order of magnitude for the cases where the shear rate is stepped down.

Yet they are totally different from each other's depending on whether the shear rate is increased or decreased.

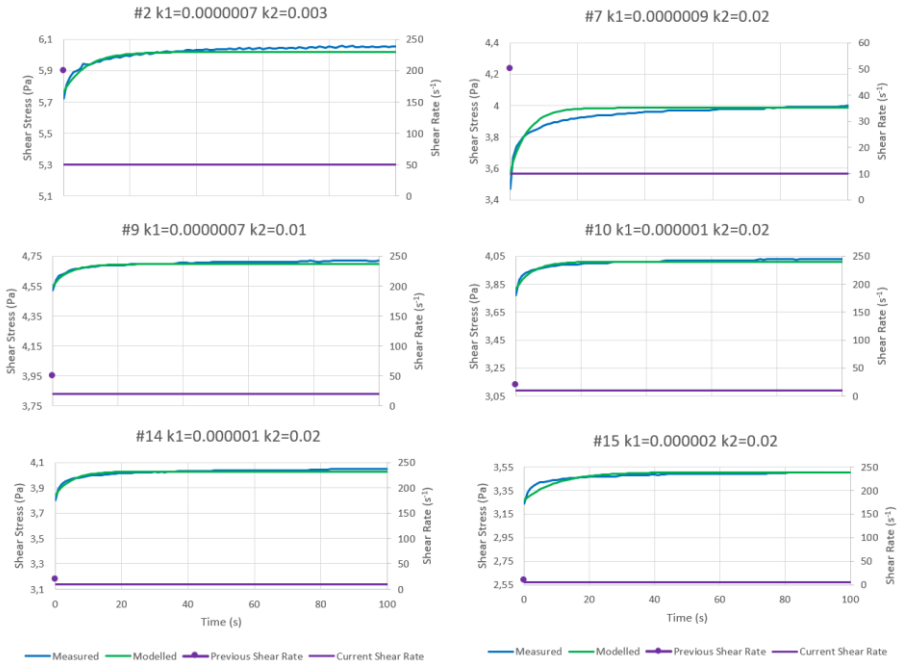

Fig. 72: Sequences for which the shear stress is asymptotic before and after stepping down the shear rate. Here, the structure parameter follows the differential equation $\frac{d\lambda}{dt} = k_1(1-\lambda)^5 - k_2\,\dot{\gamma}\lambda$

Also, when a pair k_1 and k_2, gives good match for the stepping down case, they also give a very poor match for the stepping up cases, and vice versa. This is illustrated by Fig. 73. The same equation of the structure parameter is used as for Fig. 71, which was based on step changes from low to high shear rates. This time, step changes from high to low shear rates are used. When utilizing similar k_1 and k_2 to the closest step-up samples (here #6 uses k_1 and k_2 from #5, and #7 uses k_1 and k_2 from #8), the modelled response does not match well with the measurements.

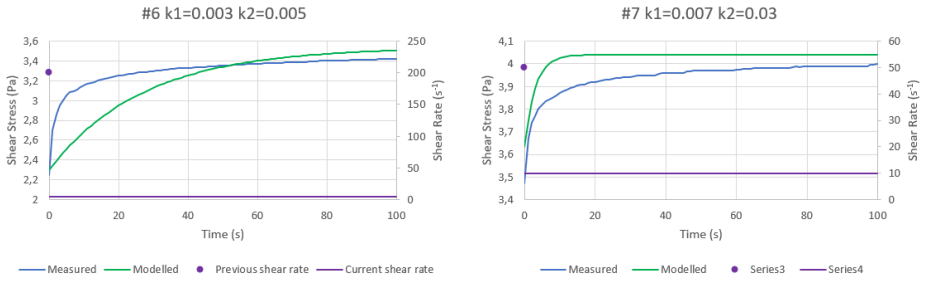

Fig. 73: Compared to the results of Fig. 71, which corresponds to step changes from low to high shear rates, the equation $\frac{d\lambda}{dt} = k_1(1-\lambda) - k_2\,\dot{\gamma}\lambda^4$ does not give a very good fit for step changes from high to low shear rates when utilizing similar k_1 and k_2 to the closest step-up samples (here #6 uses k_1 and k_2 from #5, and #7 uses k_1 and k_2 from #8).

Now, considering that we need to distinguish whether the shear rate is increased or decreased separately, we can try to find the power parameters b and d that allows for the best match with the measurements. Fig. 74 shows the root means square values for both cases. The optimum parameters are $b = 1$ and $d = 4$ for increasing shear rates and $b = 5$ and $d = 1$ for decreasing shear rates.

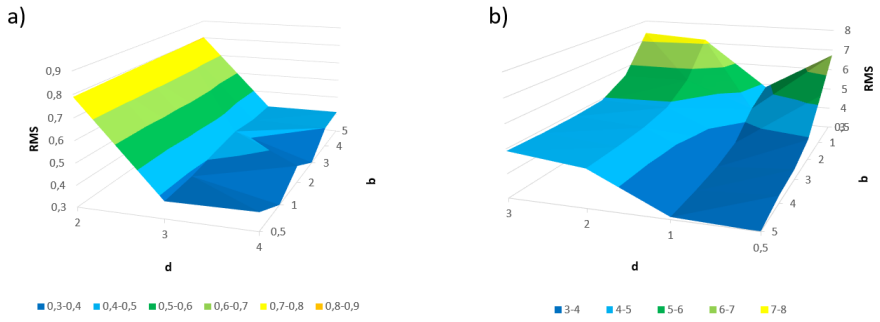

Fig. 74: a) from low to high shear rate (minimum for b=1 and d=4) b) from high to low shear rate (minimum for b=5 and d=1)

To reconciliate successions of stepping up and down and vice versa, we consider that there are two structure parameters: one that characterizes

structuration (λ^+), i.e. that reflects what happens when the shear rate is stepped down, and one that characterizes de-structuration (λ^-), i.e. corresponding to stepping up the shear rate. The thixotropy model is then:

$$\begin{cases} \tau_{\dot{\gamma},\lambda^+,\lambda^-} = \left(1 + \alpha^+ \dfrac{\lambda^+ - \lambda^+_{\dot{\gamma}_i,\infty}}{\lambda^+_{\dot{\gamma}_{i-1}} - \lambda^+_{\dot{\gamma}_i,\infty}} + \alpha^- \dfrac{\lambda^- - \lambda^-_{\dot{\gamma}_i,\infty}}{\lambda^-_{\dot{\gamma}_{i-1}} - \lambda^-_{\dot{\gamma}_i,\infty}}\right)\left(\tau_{\gamma,t_{gel}} + K\dot{\gamma}^n\right) \\ \dfrac{d\lambda^+}{dt} = k_1^+(1-\lambda^+)^5 - k_2^+\,\dot{\gamma}\lambda^+ \\ \dfrac{d\lambda^-}{dt} = k_1^-(1-\lambda^-) - k_2^-\,\dot{\gamma}(\lambda^-)^4 \end{cases} \quad (105)$$

where α^+ is the amplification function for λ^+, α^- is the amplification function for λ^-, k_1^+ and k_2^+ are the respective parameters of the behavior of λ^+, k_1^- and k_2^- are the respective parameters of the behavior of λ^-, $\lambda^+_{\dot{\gamma}_i,\infty}$ and $\lambda^-_{\dot{\gamma}_i,\infty}$ are respectively the structuration and de-structuration parameters for $\dot{\gamma}_i$ when $t \to \infty$, and $\lambda^+_{\dot{\gamma}_{i-1}}$ and $\lambda^-_{\dot{\gamma}_{i-1}}$ are respectively the structuration and de-structuration parameters just before the change of shear rate.

The amplification factors for the example of the unweighted KCl/polymer fluid are shown on Fig. 75. In a first approximation, the amplification function can be described as a bilinear form of the logarithmic of the shear rates:

$$\begin{cases} \alpha^+(\dot{\gamma}_{i-1},\dot{\gamma}_i) = \alpha_0^+ + \alpha_1^+ \log\dot{\gamma}_{i-1} + \alpha_2^+ \log\dot{\gamma}_i + \alpha_3^+ \log\dot{\gamma}_{i-1}\log\dot{\gamma}_i\,,\dot{\gamma}_{i-1} > \dot{\gamma}_i \\ \alpha^+(\dot{\gamma}_{i-1},\dot{\gamma}_i) = 0,\dot{\gamma}_{i-1} \le \dot{\gamma}_i \\ \alpha^-(\dot{\gamma}_{i-1},\dot{\gamma}_i) = \alpha_0^- + \alpha_1^- \log\dot{\gamma}_{i-1} + \alpha_2^- \log\dot{\gamma}_i + \alpha_3^- \log\dot{\gamma}_{i-1}\log\dot{\gamma}_i\,,\dot{\gamma}_{i-1} < \dot{\gamma}_i \\ \alpha^-(\dot{\gamma}_{i-1},\dot{\gamma}_i) = 0,\dot{\gamma}_{i-1} \ge \dot{\gamma}_i \end{cases} \quad (106)$$

with α_0^+, α_1^+, α_2^+, α_3^+, α_0^-, α_1^-, α_2^- and α_3^- parameters that shall be calibrated. The complete time-dependent rheological behavior model has 18 parameters: $\tau_{gel}(t_1)$, $\tau_{gel}(t_2)$, M_1, τ_γ, K, n, k_1^+, k_2^+, k_1^-, k_2^-, α_0^+, α_1^+, α_2^+, α_3^+, α_0^-, α_1^-, α_2^-, α_3^-.

Fig. 76 shows a comparison between calibrated model values and measurements made with a scientific rheometer when the shear rate is alternated between 5, 10, 20, 50, 100 and 200s^{-1} for an unweighted KCl/polymer fluid. The model matches the measurements from the start, i.e. when there are remnant effects of gelling, to the end, where those effects are fully dissipated. There is an acceptable match both for changes corresponding to step-up and to step-down of the shear rate.

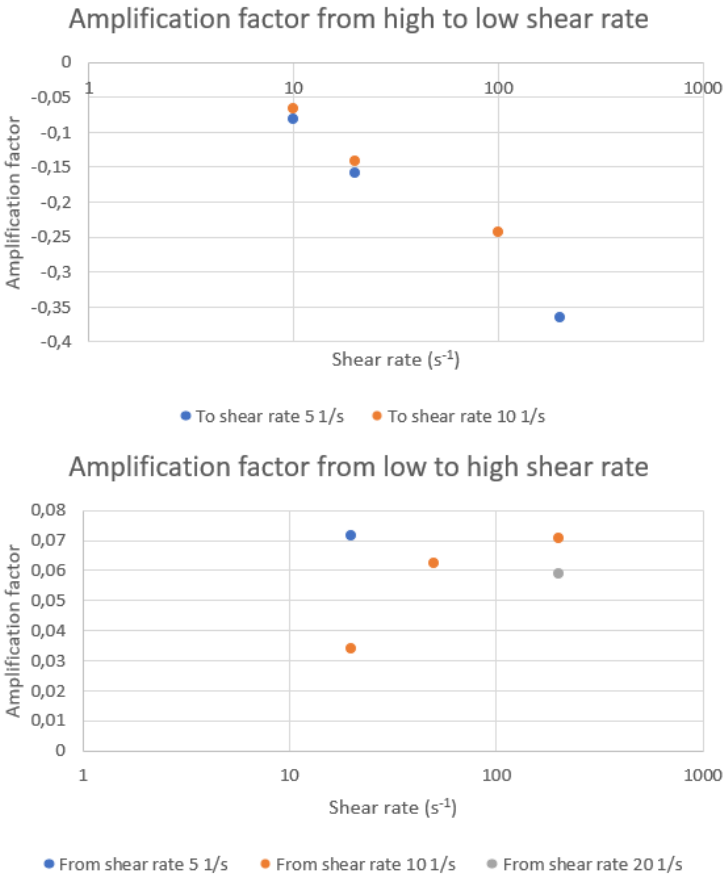

Fig. 75: Amplification factors from high to low shear rates (top), and from low to high shear rate (bottom).

To verify whether thixotropic effects have a significance on pressure losses, experiments have been made with a flow-loop designed to highlight the importance of thixotropy on frictional pressure gradients.

Fluid is pumped into a cavity of large diameter (internal diameter 0.14m, length 0.34m) such that during its traversal, the bulk fluid velocity gets very low, then it continues its journey through a glass tube of small diameter (internal diameter 15mm) before being pumped back into the loop from a tank of small capacity (to minimize the transfer time). A differential pressure sensor is positioned 3.6m after the transition from low to high shear rate and it measures the pressure

drop over a distance of 1.48m (see Fig. 77). The distance to the start of the small tube is sufficiently large for entrance effects to be negligible. With this configuration, after circulation is established, the fluid is constantly under displacement and therefore gelling does not occur anywhere along the hydraulic circuit.

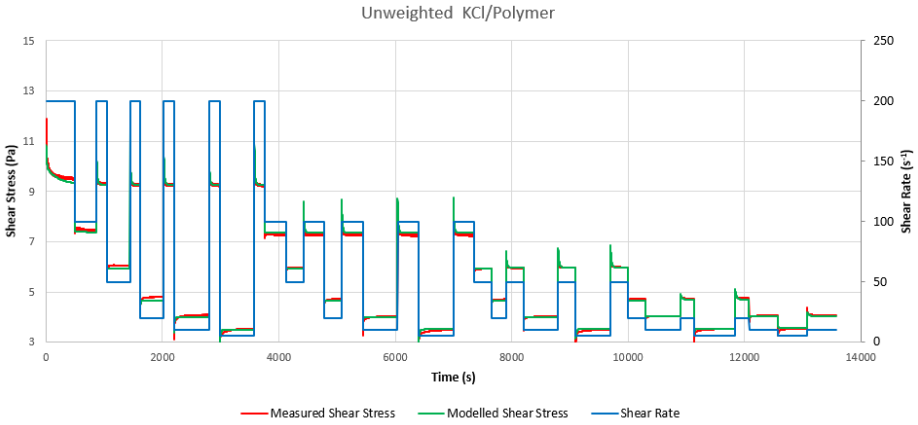

Fig. 76: Comparison of the measured and modelled shear rates for a sequence where the shear rate is modified between 5, 10, 20, 50, 100 and 200s^{-1}. The measurements are made with an unweighted KCl/polymer fluid."[28]

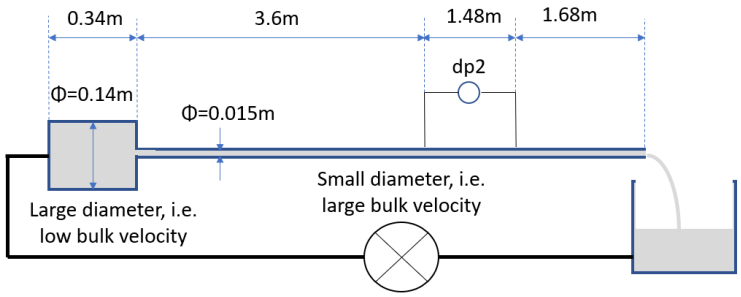

Fig. 77: Flow-loop with a differential pressure positioned several meters behind a configuration that causes a large change of shear rate in circulated fluid.

28 Excerpt from Cayeux (2020) [191]

The precision of the differential pressure measurements has been verified by circulating a viscous Newtonian fluid (glycerin at 20%vol) and by comparing measurements at different flowrates with estimated pressure drops corresponding to the rheological flow-curve of the fluid obtained with a scientific rheometer. The flow-curve of the glycerin solution has been measured with a scientific rheometer and confirms the expected Newtonian rheological behavior (see Fig. 78).

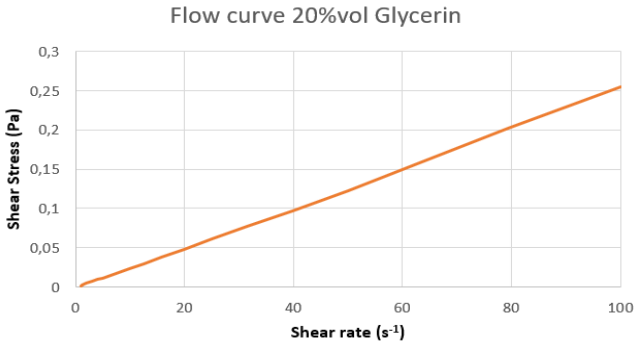

Fig. 78: Flow-curve obtained with a scientific rheometer of an aqueous solution of glycerin at 20%vol concentration.

Fig. 79 shows a comparison between the measured pressure loss gradients during laminar flow and the theoretical pressure loss gradient estimated using the Newtonian fluid viscosity measured with the scientific rheometer. The percentage error increases at very low flowrate because of the very low pressure-gradient, reaching 8% for a pressure gradient of 20Pa/m, but for gradients above 50Pa/m, the error is lower than ±2%.

Fig. 80 shows the measured pressure loss gradient during a sequence where the pump rate is stepped up from approx. 1l/min to 8l/min. The fluid is a KCl/polymer with a mass density of 1250kg/m^3. As with the rheometer measurements, the pressure loss gradients evolve with time for each pump rate step change.

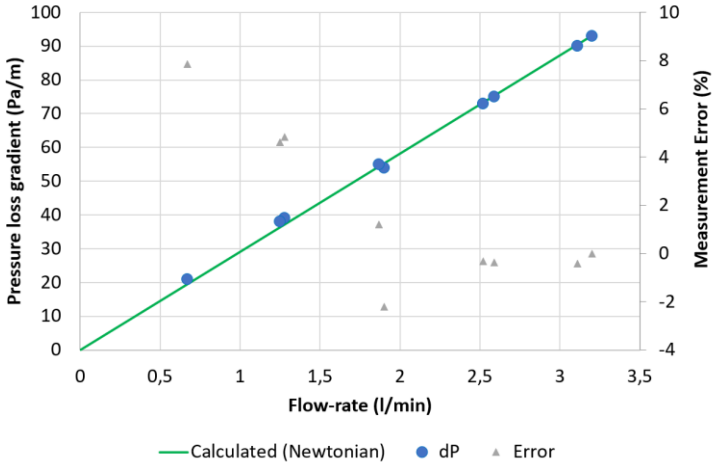

Fig. 79: Comparison between calculated and measured pressure loss gradients and associated error for fluid based on an aqueous solution of glycerin at 20%vol.

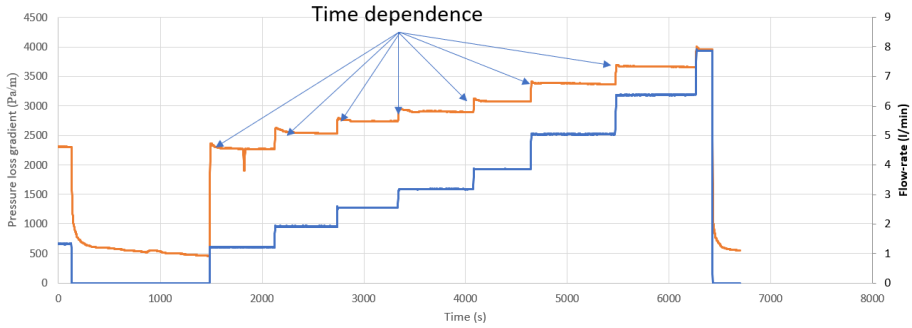

Fig. 80: Measured time dependence of the pressure drop in the flow-loop for changes in the shear history of a KCl/polymer of mass density 1250kg/m^3.

The minimum delay to reach 90% of the pressure loss gradient measured 500s after a pump rate step change, ranges from 130s, corresponding to a flowrate of 2.5l/min, to approx. 300s for a flowrates around 6.5l/min. Fig. 81 shows the delays corresponding to the first and last occurrences of the pressure drop gradient equivalent to 90% of the one measured 500s after a step change.

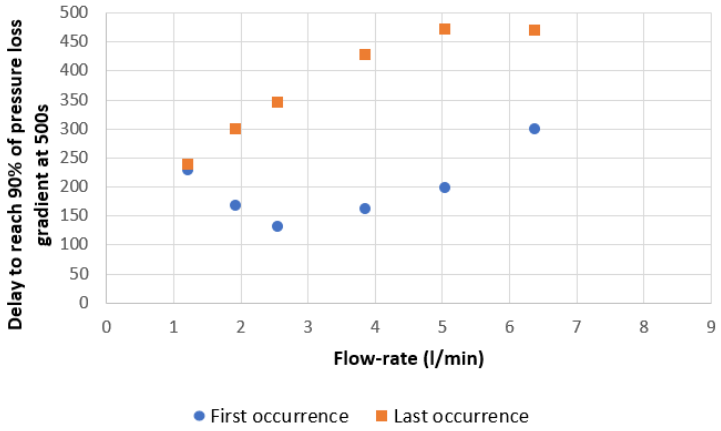

Fig. 81: Delay to reach 90% of the pressure loss gradient measured 500s after the flowrate step change.

A sample of the fluid has been measured with a scientific rheometer (21 measurements with shear rates logarithmically spaced between 1 and 100s^{-1}) with a procedure designed to avoid barite sagging and side effects of thixotropy (see description in section 3.1.3.1). The fitted Herschel Bulkley parameters are $\tau_y = 1.65Pa,\ K = 1.25Pa.s^n, n = 0.364$. The relative differences between the measurements and the Herschel-Bulkley model are within -0.83% and 1.92% (see Fig. 82). It is then possible to calculate the steady state pressure drop gradient based on the Herschel-Bulkley rheological behavior of the fluid in identical conditions of temperature.

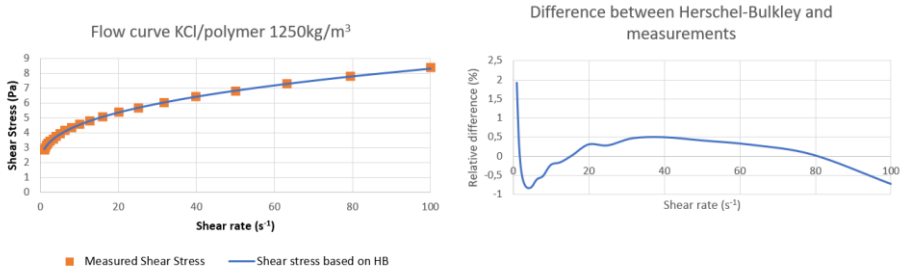

Fig. 82: Flow curve at 23°C for the KCl/polymer 1250kg/m3 used in the flow-loop.

If we compare the measured pressure drop gradient taken 10s after the pump rate step change, with the one estimated with the Herschel Bulkley rheological behavior in steady state conditions, we can see a difference ranging from 4 to 11% (see Fig. 83). The calculation method for pressure losses of Herschel Bulkley fluids is the one by Kelessidis et al. (2006) [22].

Note that the measured pressure gradients after 500s still differ from the theoretical steady state ones, calculated with the Herschel-Bulkley rheological model. This is because the differential pressure sensor is positioned only 3.6m behind the change of diameter in the circuit. With such a proximity, the fluid is still under the influence of the shear history. Considering that thixotropic effects are insignificant passed at least 300s for flowrate around 6.5l/min, then the differential pressure sensor should have been placed at least 180m behind the change of pipe diameter[29]. This indicates that the shear history applied to thixotropic drilling fluids, have consequences over long distances.

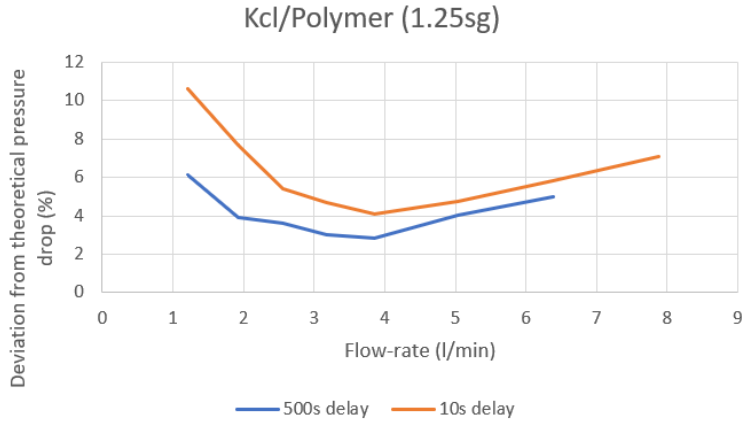

Fig. 83: Deviation between measured pressure losses and the one calculated from steady state conditions while circulating a KCl/Polymer WBM 1250kg/m^3, 10s and 500s after a step change of corresponding to Fig. 80.

29 Calculations made for a pipe internal diameter of 15mm.

3.1.2.1 Summary

A time-dependent rheological model is proposed that accounts for the impact of remnant effects after gelling and shear history.
The model is equivalent to a Herschel-Bulkley rheological behavior in steady state conditions.
The thixotropic effects are not only visible in a rheometer but also directly on pressure loss gradients measured in a flow-loop.
Thixotropic effects results in 4 to 10% increase of pressure losses compared to steady state calculations, at short distances (a few meters) after a change of shear conditions when the flowrate is stepped up.

3.1.3 Impact of Solid Particles in Suspension on Drilling Fluid Rheology

As described in section 2.1.1.18, the presence of solid particles in a Newtonian fluid changes its apparent viscosity. Current publications (see section 2.1.1.18) report that the apparent rheological behavior of Newtonian fluids that contain neutrally buoyant solid particles in suspension, turn to the one of a Herschel-Bulkley fluid. Unfortunately, there has been little work published so far on how suspensions of non-neutrally buoyant solid particles modify the apparent viscous properties of shear thinning with yield stress fluids. It is therefore interesting to investigate how the apparent rheological behavior of a drilling fluid is influenced by the presence of solid particles like cuttings or LCM.

3.1.3.1 Influence of Sand Particles on the Apparent Rheological Behavior of an Unweighted KCl/Polymer WBM

"A series of measurements have been made with a Physica MCR 301 scientific rheometer manufactured by Anton Paar™, by introducing different proportions of sorted[30] sand particles in an unweighted KCl/polymer WBM (here the polymer is xanthan gum).

30 There are five series of sorted sand particles: from 0 to 45µm, from 45 to 63 µm, from 63 to 90µm, from 90 to 125µm and from 125 to 150µm.

The difference of mass density between the based fluid (1074kg/m^3) and the sand (2650kg/m^3), combined with the fact that the base fluid is shear thinning with a yield stress, result in a tendency for the solid particles to sag at high shear rates, therefore causing an irreversible modification of the fluid-mix during an experiment. To avoid that problem, all the measurements have utilized shear rates lower or equal to 100s^{-1}.

A pre-shear at 100s^{-1} is applied for 300s prior to taking a measurement series. It can be seen on Fig. 84 that the shear stress variation during the last minute of the pre-shear period is within 1.5% compared to the final measurement taken at the end of the pre-shear sequence, therefore indicating that thixotropic effects are minimal and there is not substantial sedimentation of solid particles even at the highest volumetric concentrations. The measurements of Fig. 84 are based on an unweighted KCl/Polymer drilling fluid loaded with sand particles between 64 and 90μm.

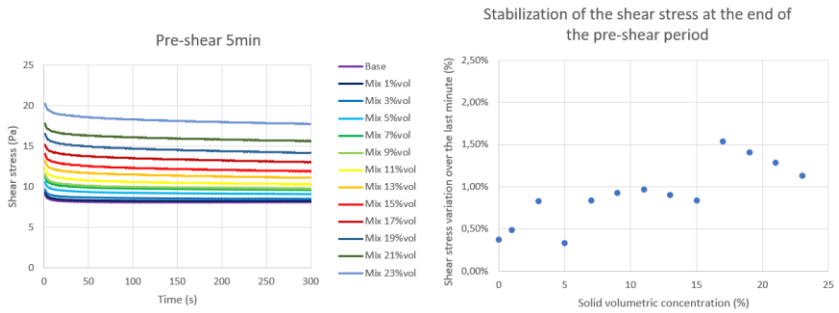

Fig. 84: The variation of shear stress during the last minute of the pre-shear period of 5 min at 100s^{-1} is lower than 1.5% of the final shear stress value. Values obtained for an unweighted KCl/Polymer drilling fluid loaded with various volumetric concentrations of sorted sand particles between 64 and 90μm.

To check that the fluid has not been subject to an irreversible modification during the measurement procedure, all series of measurements have been taken from high to low shear-rates followed by a low to high shear-rate sweep. Then, the shear stresses from the two sweeps have been compared for signs of fluid deterioration during the experiment. Furthermore, as pointed out in section 3.1.2, the thixotropic nature of drilling fluids may require a substantial amount

of time before the shear stress stabilizes after a change of shear rate. For that reason, shear rates have been kept constant for 10s before proceeding to the next step change. Fig. 85a shows a time series of measurements taken with an unweighted KCl/polymer WBM. The shear stresses measured during the high to low shear rate sweep and those taken during the low to high shear rate series are almost identical. As it can be seen on the right-hand side graph (b), the difference between the measurement sweeps does not exceed 3.5% for all sand particle concentrations (results based on a sorted sand with dimensions between 63 and 90µm).

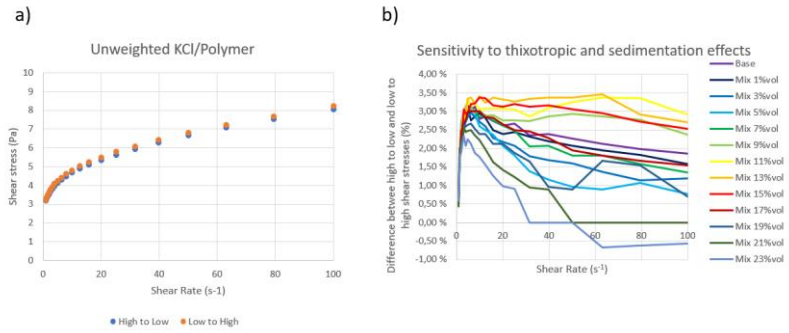

Fig. 85: a) Rheometer measurements obtained with an unweighted KCl/polymer WBM with a sweep of shear rates from high to low followed by a series of measurements taken from low to high shear rates. b) Differences between the shear stresses measured during the high to low and low to high sweeps for different concentrations of sorted sand particles between 63 and 90µm.

The fit of a Herschel-Bulkley rheological behavior to rheometer measurements is of good quality. For instance, Fig. 86 shows that the difference between the measurements taken with an unweighted KCl/polymer without any solid particles and the fitted rheological behavior $\tau = 2.23 + 1.009\dot{\gamma}^{0.379}$ is lesser than 1.5% for all measured shear stresses.

Similar results are obtained for drilling fluid loaded with various concentrations of sorted sand particles. As it can be seen on Fig. 87, the maximum difference between the fitted Herschel-Bulkley rheological behaviors and the measurements is lower than 2.5%, regardless of the concentration of sorted sand particles, here with a size between 63 and 90µm. In fact, 2.5% is only

reached for very small values of the shear rates that have corresponding low values for the shear stresses and therefore where the measurement error itself starts to be significant. If we disregard the values taken at the lowest shear rates, the error is within ±1%.

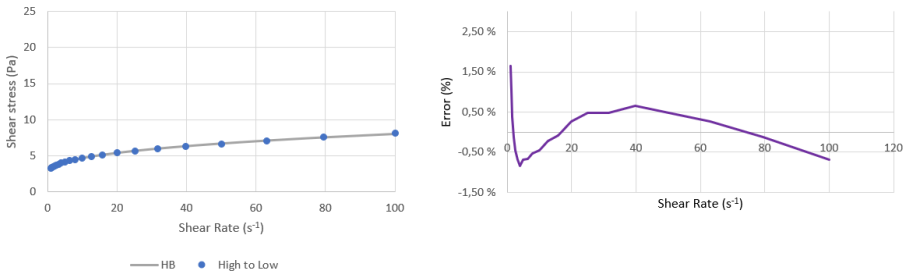

Fig. 86: a) Fitting of a Herschel-Bulkley rheology with the rheometer measurements taken with an unweighted KCl/Polymer drilling fluid without any solid particles, b) difference between measurements and fitted Herschel-Bulkley rheological behavior corresponding to the values shown on the left graph.

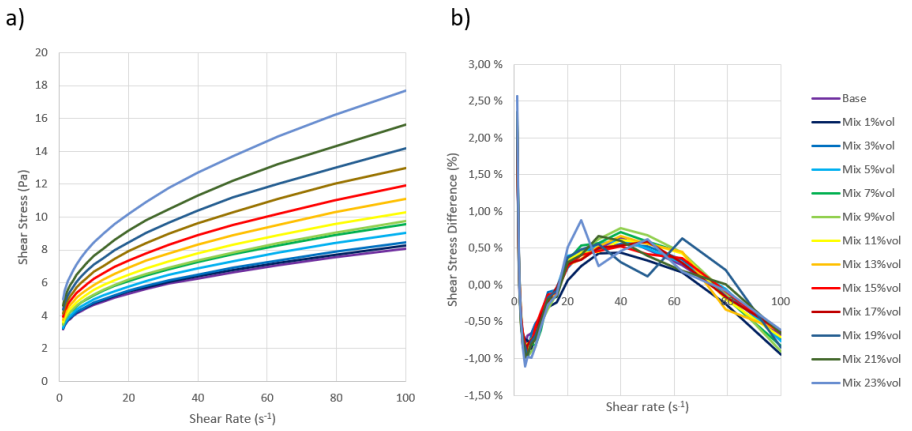

Fig. 87: a) Fitted Herschel-Bulkley rheological behavior corresponding to measurements made with difference concentrations of sorted sand particles (63 to 90µm), b) difference between fitted Herschel-Bulkley rheology and measurements for the values shown on the left graph.

It is legitimate to question whether the measurements are reproducible and especially if aging of the drilling fluid can influence the results. Fig. 88 shows two series of measurements made on the same drilling fluid sample with a time interval of 24 hours. The fluid sample is based on an unweighted KCl/polymer WBM loaded with 11%vol of sorted sand particles, which sizes are comprised between 45 and 63µm. As it can be seen, the differences between the two measurements series do not exceed 1.5%.

Let us consider the normalized volume fraction of particles in the fluid $\Phi^* = \frac{\Phi}{\Phi_m}$ where Φ_m is the maximum packing concentration.

A direct measurement of the maximum packing concentration has been performed by filling a 100ml flask with sand particles and by measuring the quantity of water that can fill the voids. From these direct measurements, the maximum packing concentration of fine sand, i.e. passing through the 45µm mesh, is $\Phi_{s45_m} = 68.4\%$. For other mesh size, the values are: $\Phi_{s45-63_m} = 58.9\%$, $\Phi_{s63-90_m} = 58.7\%$, and $\Phi_{s90-125_m} = 58.7\%$.

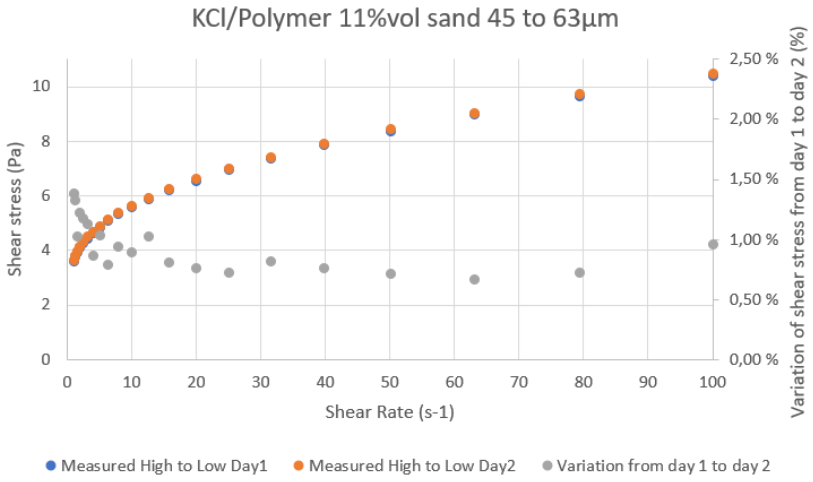

Fig. 88: Evaluation of the repeatability of the rheological measurements from one day to the other.

Let us also define dimensionless Herschel-Bulkley parameters as $\tau_Y^* = \frac{\tau_Y}{\tau_{Y_{0\%}}}$, $K^* = \frac{K}{K_{0\%}}$ and $n^* = \frac{n}{n_{0\%}}$, where $\tau_{Y_{0\%}}, K_{0\%}$ and $n_{0\%}$ are respectively the yield

stress, consistency index and flow index of the base- fluid without solid particles.

We can now analyze the change of the dimensionless yield stress, consistency index and flow index as a function of the normalized solid concentration. Fig. 89 shows the results from measurements[31] made when introducing sorted sand particles in an unweighted KCl/polymer WBM.

From Fig. 89, one can notice that very fine particles (<45µm) have a stronger effect on the increase of the apparent viscosity than larger particles.

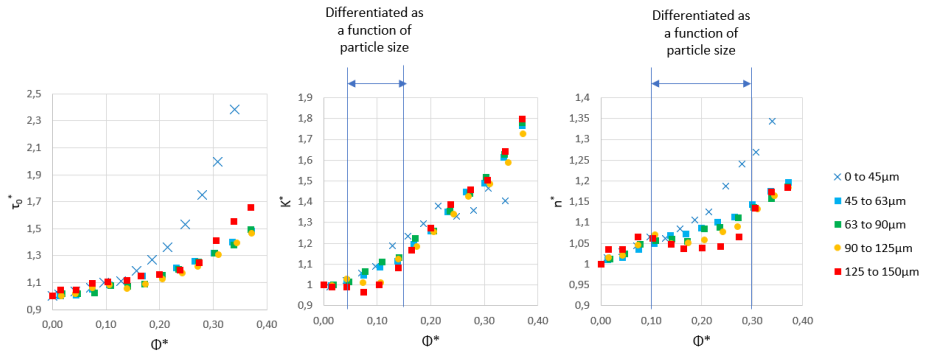

Fig. 89: Dimensionless Herschel-Bulkley parameters for an unweighted KCl/polymer WBM as a function of the normalized volume fraction for different sorted sand particles.

For particles larger than 45µm, τ_y^* is not well differentiated for different particle sizes, K^* is mostly differentiated as a function of the particle sizes only between 5 and 15% normalized volumetric solid concentration, while n^* is more differentiated between 10 and 30%. In practice, that means that sizes of particle larger than 45µm, do not influence much the apparent fluid viscosity for normalized concentrations below 5%. Above 5%, there is an influence of the particle size on the apparent viscosity, however it mostly influences the consistency index between 5 and 15% normalized volume concentration, and mostly the flow index above 10%.

31 Appendix B provides the details of the measurements.

To illustrate the effect of the change of apparent viscosity as a function of the particle size and concentration, we will compare pressure drop gradients in an annulus, denoted here $\partial_s p_a$. The following results are based on the calculation method described by Kelessidis et al. (2006) [22] (ref. section 2.1.1.5). The left-side graph of Fig. 90 shows the pressure drop gradient as a function of the different normalized solid concentrations and the results obtained from the measurements made with an unweighted KCl/polymer fluid loaded with sorted sand particles in the range 0 to 45µm. The right-hand side graph shows the same results but in terms of the dimensionless pressure drop gradient, i.e. $\partial_s p_a^* = \frac{\partial_s p_a}{\partial_s p_{a_0}}$ where $\partial_s p_{a_0}$ is the pressure loss gradient without any sand particles. The calculations are made for an 8 ½-in hole size with concentric and non-rotating 5-in drill-pipe, with flowrates between 500 and 3000l/min.

From 0 to 15% normalized concentration, the pressure loss gradient increases by approximatively 30%. Passed this value, the pressure loss gradient increases exponentially and has doubled for all analyzed flowrates by 28% normalized volumetric concentration.

As it can be seen on Fig. 91, the pressure loss gradient is the largest with the smallest particle size and decreases monotonically with increasing particle dimension. However, the rate of decrease drops fast with the particle diameter.

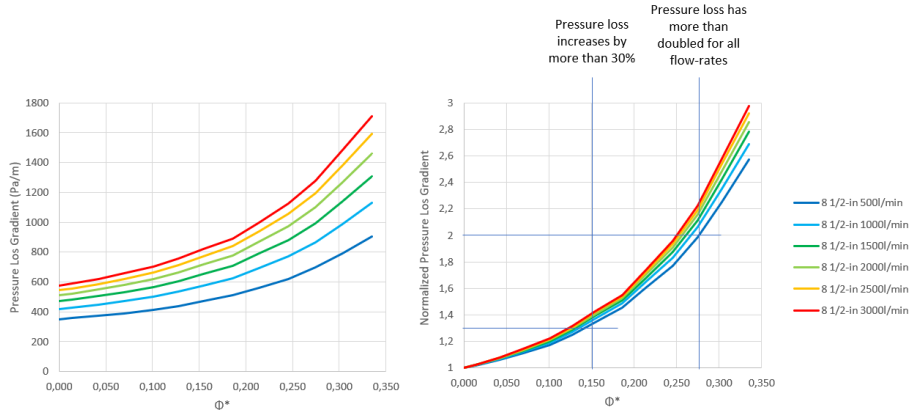

Fig. 90: Effect of the sand concentration, for particles smaller than 45µm, on the pressure loss gradient while circulating between 500 and 3000l/min in a concentric annulus with an external diameter of 8 ½-in and an internal diameter of 5-in.

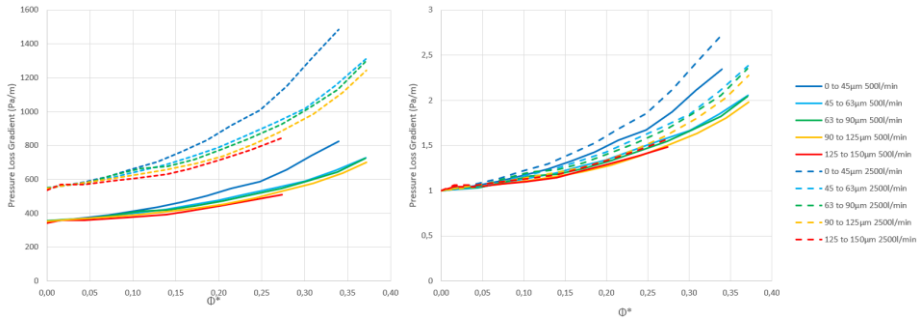

Fig. 91: Comparison of the pressure loss gradients (absolute on the left and dimensionless on the right) for two different flowrates (solid line = 500l/min, dashed line = 2500l/min) with five particle sizes when circulating an unweighted KCl/Polymer fluid in a 8 ½-in borehole with a concentric 5-in DP.

3.1.3.2 Influence of Barite Concentration on the Apparent Rheological Behavior of an KCl/Polymer WBM

The most common way to increase mud weight is to add high mass density solid particles, like barite, in suspension in the drilling fluid. Barite has a mass density of 4100 to 4200 kg/m^3, which is much larger than the one of formation rocks, as cuttings mass density is usually comprised between 2000 and 2800kg/m^3. Typical barite powder is poly-dispersed with dimensions ranging from 1 to 100µm (see Fig. 92). A direct quantification has been made by measuring the amount of water that can be contained in a flask of 100ml filled with barite. The obtained maximum packing concentration of barite is 63.4%.

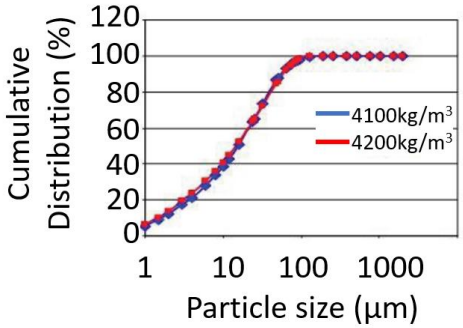

Fig. 92: Typical size distribution for standard barite powder used in the preparation of drilling fluids (courtesy of Schlumberger [165]).

Similar measurements as those described in section 3.1.3.1 have been made to study the impact of barite concentration on the change of the apparent rheological behavior of a KCl/Polymer WBM (see Appendix C). Fig. 93 shows the results in terms of normalized yield stress ($\tau^*_{\gamma_b} = \frac{\tau_{\gamma_b}}{\tau_{\gamma_{0\%}}}$), normalized consistency index ($K^*{}_b = \frac{K_b}{K_{0\%}}$) and normalized flow index ($n^*{}_b = \frac{n_b}{n_{0\%}}$) where $\tau_{\gamma_{0\%}}$, $K_{0\%}$ and $n_{0\%}$ being the respective yield stress, consistency index and flow index of the base fluid, i.e. without barite, and τ_{γ_b}, K_b and n_b being the respective yield stress, consistency and flow index for the current mix of base fluid with barite.

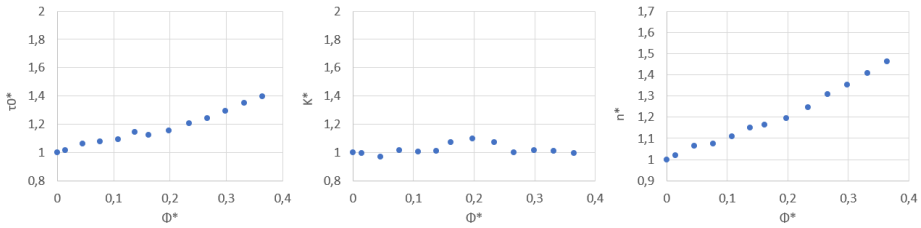

Fig. 93: Normalized yield stress ($\tau^*_{\gamma_b}$), consistency index ($K^*{}_b$) and flow index ($n^*{}_b$) for the sole effect of normalized volumetric barite concentration (Φ^*_b).

In addition to the barite concentration, the salinity and the polymer concentration also influences the apparent rheological behavior of the KCl/polymer WBM as shown on Fig. 94. So, there are altogether three parameters that influence the rheological behavior of this type of fluid:

- the normalized barite concentration ($\Phi^*_b = \frac{\Phi_b}{\Phi_{b_m}}$, where Φ_b is the volumetric concentration of barite and Φ_{b_m} is the maximum volumetric concentration of barite),
- the normalized salinity ($S^*_{KCl} = \frac{S_{KCl}}{S_{KCl_m}}$, where $S_{KCl} = \frac{m_{KCl}}{m_l}$ is the mass concentration of KCl in the brine, i.e. m_{KCl} is the mass of KCl and m_l the brine mass, S_{KCl_m} is the maximum mass concentration of an aqueous solution of KCL at 100°C, i.e. 36.05%)
- the normalized polymer concentration ($S^*_{XG} = \frac{S_{XG}}{S_{XG_m}}$, where $S_{XG} = \frac{m_{XG}}{m_l}$ is the mass concentration of polymer in the brine, i.e. m_{XG} is the mass of polymer and m_l is the brine mass, S_{XG_m} is a normalization polymer mass fraction that is chosen to be 1%, since larger concentration leads

to gel-like viscosity levels).

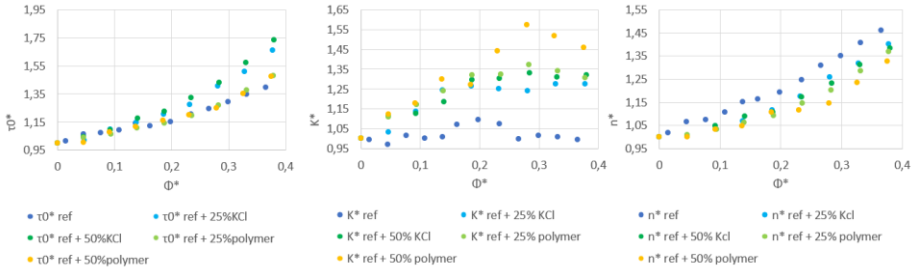

Fig. 94: Normalized yield stress, consistency index and flow index for various salinity and polymer concentrations.

The Herschel-Bulkley parameters have been estimated for several combinations of Φ_{b}^*, S_{KCl}^* and S_{XG}^*. We recourse to a linear combination of radial basis functions to approximate these results:

$$\sum_{i=1}^{N_b} w_i \, \phi_b\left(\left\|\vec{x}_b - \vec{x}_{i_b}\right\|, \varepsilon_{\phi_b}\right) \tag{107}$$

where w_i are weights that shall be estimated as a function of series of calculated Herschel-Bulkley parameters from the series of measurements, ϕ_b is a well-chosen radial basis function, ε_{ϕ_b} is a well-chosen scaling factor used by the radial basis function, $\vec{x}_{i_b}$ is a triplet of $\Phi_{\mathrm{b}i}^*$, $S_{KCl_i}^*$ and $S_{XG_i}^*$ corresponding to the measurement i, N_b is the total number of experiments and $\vec{x}_b$ is a triplet of Φ_{b}^*, S_{KCl}^* and S_{XG}^* for which the value shall be estimated.

Typical radial basis functions are [166]:

- Cubic: $\phi_b\left(r, \varepsilon_{\phi_b}\right) = \left(r + \varepsilon_{\phi_b}\right)^3$
- Thin plate spline: $\phi_b\left(r, \varepsilon_{\phi_b}\right) = r^2 \ln\left(\varepsilon_{\phi_b} r\right)$
- Gaussian: $\phi_b\left(r, \varepsilon_{\phi_b}\right) = e^{-\varepsilon_{\phi_b} r^2}$
- Inverse Multi-quadratic: $\phi_b\left(r, \varepsilon_{\phi_b}\right) = \frac{1}{\sqrt{r^2 + \varepsilon_{\phi_b}{}^2}}$

- Multi-quadratic: $\phi_b(r, \varepsilon_{\phi_b}) = \sqrt{r^2 + {\varepsilon_{\phi_b}}^2}$

One third of the measurements have been used to estimate the weighting factors and the remaining values have been kept in a set of test samples. Utilizing the test set, we have been able to find which of the five radial basis function together with which scaling factor ε_{ϕ_b} minimize the sum of differences between the prediction and the measurements. This process has been applied to the absolute Herschel-Bulkley parameters and to the normalized Herschel-Bulkley ones. We have therefore obtained three approximation functions for the absolute Herschel-Bulkley parameters of a weighted KCl/polymer WBM as a function of the normalized barite concentration, normalized salinity and normalized polymer mass fraction:

$$\begin{cases} \tilde{\tau}_{\gamma_b}(\Phi_b^*, S_{KCl}^*, S_{XG}^*) \\ \tilde{K}_b(\Phi_b^*, S_{KCl}^*, S_{XG}^*) \\ \tilde{n}_b(\Phi_b^*, S_{KCl}^*, S_{XG}^*) \end{cases} \tag{108}$$

where $\tilde{\tau}_{\gamma_b}$, $\tilde{K}_b$ and $\tilde{n}_b$ are respectively the approximation functions for the yield stress, consistency index and flow index of a weighted KCl/polymer WBM (see Fig. 95).

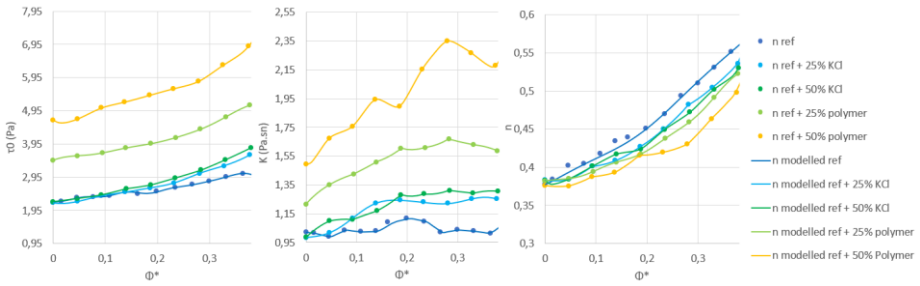

Fig. 95: Herschel-Bulkley parameters and modelled values utilizing the corresponding radial basis functions.

In addition, we have three other approximation functions for the normalized Herschel-Bulkley parameters of a weighted KCl/polymer WBM as a function of the normalized barite concentration, normalized salinity and normalized polymer mass fraction:

$$\begin{cases} \tilde{\tau}^*_{\gamma_b}(\Phi^*_b, S^*_{KCl}, S^*_{XG}) \\ \widetilde{K}^*_b(\Phi^*_b, S^*_{KCl}, S^*_{XG}) \\ \widetilde{K}^*_b(\Phi^*_b, S^*_{KCl}, S^*_{XG}) \end{cases} \quad (109)$$

where $\tilde{\tau}^*_{\gamma_b}, \widetilde{K}^*_b$ and $\widetilde{K}^*_b$ are respectively the approximation functions for the normalized yield stress, consistency index and flow index of a weighted KCl/polymer WBM (see Fig. 96).

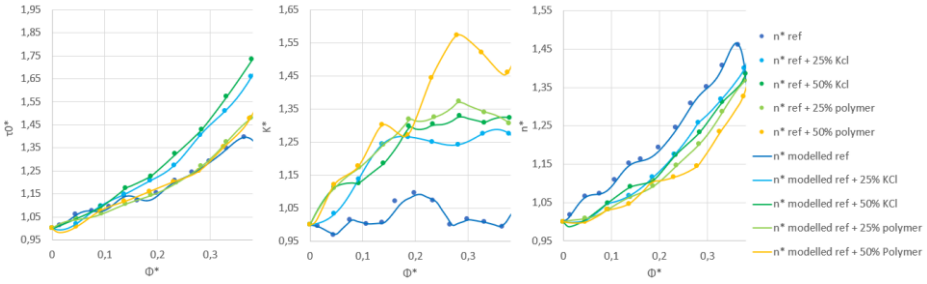

Fig. 96: Measured normalized Herschel-Bulkley parameters and modelled values utilizing the corresponding radial basis functions.

3.1.3.3 Max Packing Concentration of a Mix of Sorted Sand and Barite

Before investigating the impact of sand concentration on the apparent rheological behavior of weighted KCl/Polymer drilling fluids, we need to study the max packing concentration of a mix of barite with sorted sands.

We have measured the maximum packing concentration (Φ_m) of three different mix of sorted sand (<45µm, between 63 and 90 µm, and between 90 and 125 µm) with barite, by measuring the volume of water that can be contained in a 100ml flask filled with a given proportion of sand to barite (Φ_{sb},where $\Phi_{sb} = 0$ when there is only barite, $\Phi_{sb} = \infty$ when there is only sand). The results are shown on Fig. 97.

One can notice that the maximum packing concentration is not a monotonic function of the proportion of sand to barite. A tentative curve fitting consists in superposing a sigmoid curve ($\frac{1}{1+e^{-x}}$) and a function that looks like an impulse. A possible choice for the impulse-like function is $\frac{\epsilon}{x^2+\epsilon^2}$ as it is known that it converges to a Dirac delta function, i.e. $\delta(x) = \frac{1}{\pi}\lim_{\epsilon\to 0}\frac{\epsilon}{x^2+\epsilon^2}$. The sigmoid

function shall be modified to ensure that it tends to the maximum packing concentration of pure barite (Φ_{b_m}) when the proportion tends to 0 and to the maximum packing concentration of only sand (Φ_{s_m}) when the proportion tends to infinity.

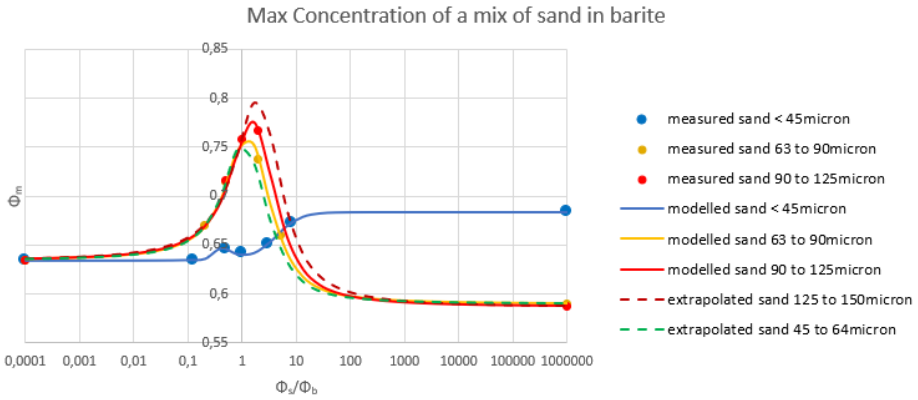

Fig. 97: Maximum packing concentration of a mix of barite and fine sorted sand (<45µm).

Curve fitting has been made with the following function:

$$\Phi_m = \Phi_{b_m} + \frac{(\Phi_{s_m} - \Phi_{b_m})}{1+e^{A_{\Phi_{sb}}\left(log_{10}\Phi_{sb}+B_{\Phi_{sb}}\right)}} + \frac{C_{\Phi_{sb}}}{D_{\Phi_{sb}}\left(C^2_{\Phi_{sb}}+\left(log_{10}\Phi_{sb}+E_{\Phi_{sb}}\right)^2\right)} \qquad (110)$$

where $A_{\Phi_{sb}}$, $B_{\Phi_{sb}}$, $C_{\Phi_{sb}}$, $D_{\Phi_{sb}}$ and $E_{\Phi_{sb}}$ are the model parameters. The fitted parameters are given in Table 1.

Table 1: Fitted parameters for eq. (110) based on measurements displayed on Fig. 97 utilizing a mix of barite and sorted sand.

	Φ_{b_m}	Φ_{s_m}	$A_{\Phi_{sb}}$	$B_{\Phi_{sb}}$	$C_{\Phi_{sb}}$	$D_{\Phi_{sb}}$	$E_{\Phi_{sb}}$	r^2
<45µm	0,634	0,684	4,500	-0,625	0,125	438,5	0,3	1,000
63 to 90µm		0,589			0,475	16,0	-0,1	0,997
90 to µm		0,587			0,500	13,5	-0,2	0,996

The reference sand used for all the measurements had only a little proportion of particles between 45 and 63µm and between 125 and 150µm, so it has been difficult to gather a sufficient quantity of sand for these two specific particle sizes to perform a full analysis of the max packing concentration as a function of the proportion of sand to barite. Instead, we have extrapolated the max packing concentration curves utilizing the fitted empirical models for 63 to 90 µm and for 90 to 125 µm. The reason for choosing these two reference curves is simply that the max packing concentration for all four sorted sand is almost identical when there is only sand and no barite (see Fig. 97).

3.1.3.4 Apparent Rheological Behavior for a KCl/Polymer WBM in the Presence of Barite and Monodispersed Sand Particles

We will now investigate the effect of monodispersed sand particles in a weighted KCl/Polymer WBM.

We would like to calculate the total solid concentration (Φ_s) in a fluid that contains both sand and barite as a function of the initial barite concentration prior to adding the sand particles (Φ'_{hgs}) and the resulting density of the mix after blending sand (ρ_m). In addition, we know the density of barite (ρ_{hgs}), the density of sand (ρ_{fs}) and the density of the base fluid (ρ_l). First, we can extract the concentration of sand in the mix from the density of the final blend:

$$\begin{aligned}\rho_m &= \Phi_{fs}\rho_{fs} + \left(1-\Phi_{fs}\right)\left(\Phi'_{hgs}\rho_{hgs} + \left(1-\Phi'_{hgs}\right)\rho_l\right) \\ &\Leftrightarrow \Phi_{fs} = \frac{\rho_m - \Phi'_{hgs}\rho_{hgs} - \left(1-\Phi'_{hgs}\right)\rho_l}{\rho_{fs} - \Phi'_{hgs}\rho_{hgs} - \left(1-\Phi'_{hgs}\right)\rho_l}\end{aligned} \tag{111}$$

Second, we can note that the actual concentration of barite (Φ_{hgs}) in the final mix is:

$$\Phi_{hgs} = \left(1-\Phi_{fs}\right)\Phi'_{hgs} \tag{112}$$

Finally, the solid concentration in the final mix is the sum of both the contribution from barite and sand:

$$\begin{aligned}\Phi_s &= \Phi_{fs} + \Phi_{hgs} \\ &= \frac{\rho_m - \Phi'_{hgs}\rho_{hgs} - \left(1-\Phi'_{hgs}\right)\rho_l}{\rho_{fs} - \Phi'_{hgs}\rho_{hgs} - \left(1-\Phi'_{hgs}\right)\rho_l}\left(1 - \Phi'_{hgs}\right) + \Phi'_{hgs}\end{aligned} \tag{113}$$

Let us define Φ_s^* the quotient of the total solid concentration (Φ_s) to the maximum packing concentration (Φ_m). Utilizing rheometer measurements of a mix with fine sorted sand particles (<45µm), the normalized yield stresses, consistency indices and flow indices for an unweighted, a 1250kg/m^3, a 1500kg/m^3 and a 1750kg/m^3 KCl/Polymer fluid as a function of the total solid concentration are displayed on Fig. 98. Fig. 99, Fig. 100 and Fig. 101. These figures show similar results obtained with respectively particles between 45 and 63µm, 63 and 90µm, 90 and 125µm.

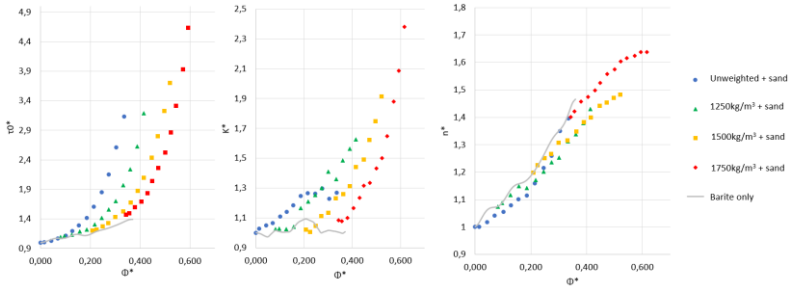

Fig. 98: Normalized yields stresses, consistency indices and flow indices as a function of the normalized total solid concentration for an unweighted, 1250kg/m^3, 1500kg/m^3 and 1750kg/m^3 KCl/Polymer drilling fluids mixed with fine sand particles (<45µm).

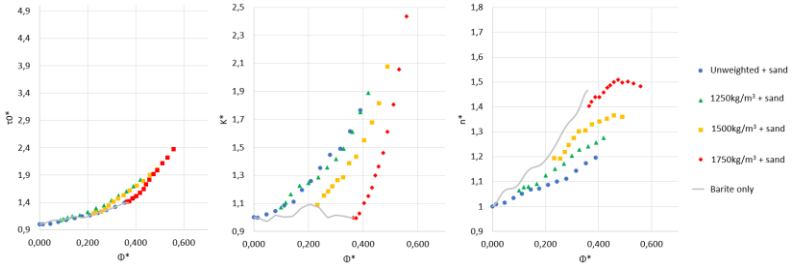

Fig. 99: Normalized yields stresses, consistency indices and flow indices as a function of the normalized total solid concentration for an unweighted, 1250kg/m^3, 1500kg/m^3 and 1750kg/m^3 KCl/Polymer drilling fluids mixed with sand particles (45 to 63µm).

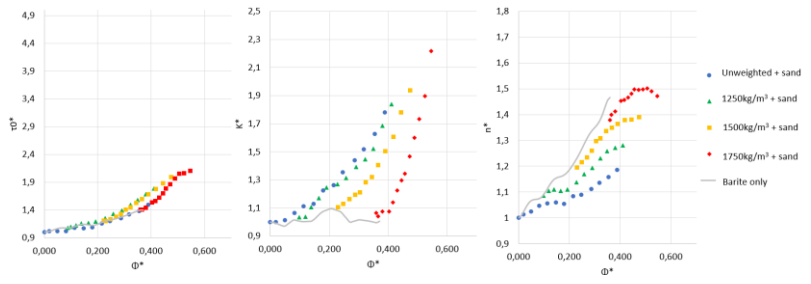

Fig. 100: Normalized yields stresses, consistency indices and flow indices as a function of the normalized total solid concentration for an unweighted, 1250kg/m^3, 1500kg/m^3 and 1750kg/m^3 KCl/Polymer drilling fluids mixed with sand particles (64 to 90µm).

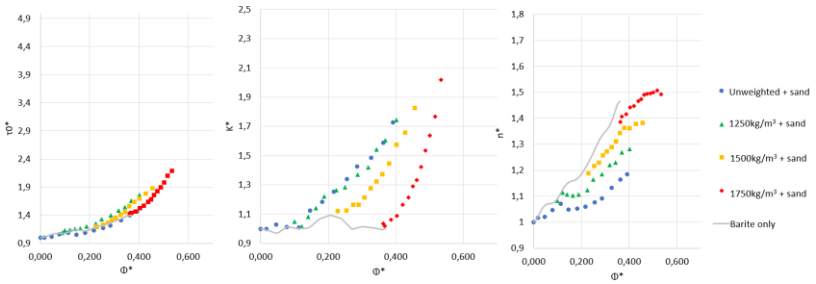

Fig. 101: Normalized yields stresses, consistency indices and flow indices as a function of the normalized total solid concentration for an unweighted, 1250kg/m^3, 1500kg/m^3 and 1750kg/m^3 KCl/Polymer drilling fluids mixed with sand particles (90 to 125µm).

As it can be expected, the Herschel-Bulkley parameters are close to those obtained for the same mud formulation when the sand proportion is equal to zero. Therefore, we model the Herschel-Bulkley parameters of a mix of a KCl brine with polymer, barite and sand as the superposition of functions that describe the effect of barite, KCl salinity and polymer concentration together with functions that account for the effect of the sand proportion and the sand particle size:

$$\begin{cases} \tau_Y^*(\Phi_b^*, S_{KCl}^*, S_{XG}^*, \Phi_s^*) = \tilde{\tau}_{Y_b}^*(\Phi_b^*, S_{KCl}^*, S_{XG}^*) + \tilde{\tau}_{Y_s}^*(\Phi_b^*, \Phi_s^* - \Phi_b^*, \bar{d}_s^*) \\ K^*(\Phi_b^*, S_{KCl}^*, S_{XG}^*, \Phi_s^*) = \tilde{K}_b^*(\Phi_b^*, S_{KCl}^*, S_{XG}^*) + \tilde{K}_s^*(\Phi_b^*, \Phi_s^* - \Phi_b^*, \bar{d}_s^*) \\ n^*(\Phi_b^*, S_{KCl}^*, S_{XG}^*, \Phi_s^*) = \tilde{n}_b^*(\Phi_b^*, S_{KCl}^*, S_{XG}^*) + \tilde{n}_s^*(\Phi_b^*, \Phi_s^* - \Phi_b^*, \bar{d}_s^*) \end{cases} \quad (114)$$

where $\bar{d}_s^*$ is the normalized average equivalent particle diameter, i.e. $\bar{d}_s^* = \frac{\bar{d}_s}{\bar{d}_{s_m}}$ ($\bar{d}_s$ is the average particle size and $\bar{d}_{s_m} = 125\mu m$ is the maximum average particle diameter considered in the experiment), $\tilde{\tau}_{\dot{\gamma}_s}^*$, $\widetilde{K}_s^*$ and $\tilde{n}_s^*$ are the respective functions that models the impact of the sand concentration and the sand particle size for the yield stress, consistency index and flow index. Note that the average particle diameter for the finest sand particles (<45µm) is calculated based on the fact that 70% of the particles are smaller than 20µm).

The functions $\tilde{\tau}_{\dot{\gamma}_s}^*$, $\widetilde{K}_s^*$ and $\tilde{n}_s^*$ are described by radial basis interpolators as described by eq. (107). The optimum radial basis functions and their associated scaling factors (ε_{ϕ_s}) have been optimized to minimize the least square distance to test samples. The set of test samples represent 2/3 of the total number of derived Herschel-Bulkley parameters from the rheological measurements made with the scientific rheometer."[32]

At this point, it is possible to utilize the above-described model to estimate how cuttings in suspension alter the rheological behavior of drilling fluids at in situ conditions. Fig. 102 shows results corresponding to the final stage of the case described at the end of section 3.1.1.1 and illustrated by Fig. 69.

The same KCl/polymer fluid (mass density 1277kg/m^3 at 15°C with a KCl volumetric concentration of 11.8 vol% and 2 vol% of xanthan gum) has a rheological behavior described by the measurements made with a Model 35 at 20°C (black curve on the graph). The conversions of the rheological behavior from one condition of pressure and temperature to another condition of pressure and temperature, utilize eq. (37) with coefficients, i.e. $A_{\dot{\gamma}}$, $B_{\dot{\gamma}}$, $C_{\dot{\gamma}}$, $D_{\dot{\gamma}}$, $E_{\dot{\gamma}}$, that have been calibrated for a KCl/polymer fluid. Note that the temperature of the fluid at the level of the flowline is 11°C, i.e. cooler than the temperature made with the rheometer, while the temperature of the fluid at the pump is 20°C. The evaluation of the rheological behavior in the annulus at the level of the bit, i.e. where there is 5vol% of sand particles with a size between 90 and 125µm) is done by combining eq. (114) and eq. (37). It is then noticeable that the rheological behavior of the drilling fluid in the presence of cuttings in suspension is more viscous than the one estimated at 1600m, even though the

32 Excerpt from my contribution to the text of the paper by Cayeux and Leulseged (2019) [190]

temperature of the fluid in the annulus is almost constant (50°C) between the bit and 1600m and without the presence of cuttings we should have almost identical rheological behaviors.

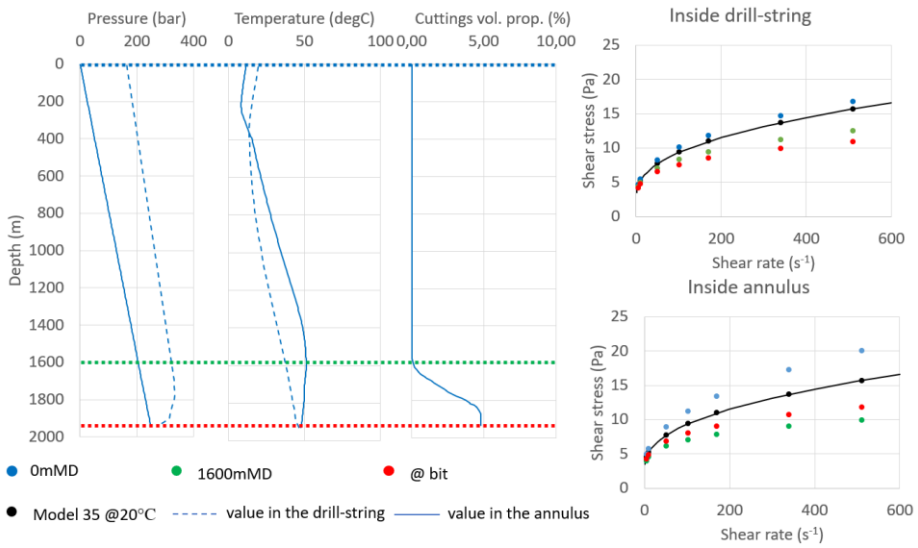

Fig. 102: Comparison of the estimated rheological behavior of a KCl/polymer drilling fluid under different conditions of pressures and temperatures, and with 5%vol of cuttings 90 to 125µm in suspension (in the annulus between 1600 and 1930m)

3.1.3.5 Summary

A procedure to measure with a scientific rheometer the steady state rheological behavior of thixotropic shear thinning with yield stress fluids loaded with non-buoyant solid particles has been defined and its precision and repeatability has been verified.
The influence of barite concentrations on the change of apparent rheological behavior of KCl/polymer drilling fluids has been measured and an empirical model has been defined.

The impact of sand particles on the apparent rheological behavior of KCl/polymer drilling fluids have been experimentally studied and an empirical model has been derived using radial basis function interpolation.
An empirical max packing concentration law is provided for various proportions of barite and sand, and with various sand sizes.
The impact of sand concentrations on pressure loss gradients is influenced by the barite concentration.

3.1.4 Transient Cuttings Transport

3.1.4.1 Cuttings Slips Velocity in Inclined Annuli

We have seen in section 2.1.1.17 how the cuttings slip velocity is calculated in near vertical borehole by solving eq. (49) at the terminal velocity of the particle. However, it is important to generalize the estimation of the slip velocity of particles at borehole inclinations that are larger than a few degrees.

"For the non-vertical case, the viscous force applied to the particle can be decomposed in a drag force $\vec{F}_D$ oriented with the fluid flow and a lift force $\vec{F}_L$ that is perpendicular to the fluid flow. In addition, the particle is subject to gravity ($\vec{F}_g$) and buoyancy ($\vec{F}_b$). The force equilibrium is therefore:

$$\vec{F}_g + \vec{F}_b + \vec{F}_D + \vec{F}_L = \mathrm{m}_s \vec{\gamma}_p \qquad (115)$$

where m_s is the mass of the solid particle and $\vec{\gamma}_p$ is the particle acceleration. If the particle reaches a terminal velocity after a finite time t_{term}, then $\forall t > t_{term}, \vec{\gamma}_p = 0$.

Let us consider a borehole cross-section at a curvilinear abscissa s along the trajectory. The local inclination is ϑ_s and the azimuth is ϕ_s with regards to a geographical coordinate system where $\hat{x}$ is a unit vector in the north direction, $\hat{y}$ is a unit vector in the east direction and $\hat{z}$ is a unit vector in the TVD direction. It is then possible to define a borehole coordinate system ($\hat{t}_s, \hat{n}_s, \hat{b}_s$) oriented by these two angles such that $\hat{t}_s$ is perpendicular to the borehole cross-section, $\hat{n}_s$ is contained in a vertical plane, i.e. $\hat{n}_s = \frac{\hat{z} - (\hat{z}\cdot\,\hat{t}_s)\,\hat{t}_s}{|\hat{z} - (\hat{z}\cdot\,\hat{t}_s)\,\hat{t}_s|}$, $|\hat{z} - (\hat{z}\cdot\,\hat{t}_s)\,\hat{t}_s| \neq 0$ and $\hat{b}_s = \hat{t}_s \times \hat{n}_s$ (see Fig. 103a). If $|\hat{z} - (\hat{z}\cdot\,\hat{t}_s)\,\hat{t}_s| = 0$, i.e. the tangent is vertical, then $\hat{n}_s$ is chosen to be equal to $\hat{x}$. The transformation matrix $P_{s_{g\to s}}$ from the geographical coordinate system to the borehole coordinate system is:

$$P_{s\,g\to s} = \begin{pmatrix} \sin\vartheta_s \cos\phi_s & \sin\vartheta_s \sin\phi_s & \cos\vartheta_s \\ -\cos\vartheta_s \cos\phi_s & -\cos\vartheta_s \sin\phi_s & \sin\vartheta_s \\ \sin\phi_s & -\cos\phi_s & 0 \end{pmatrix} \tag{116}$$

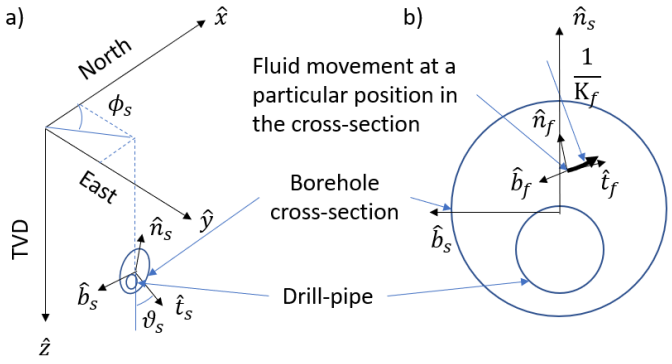

Fig. 103: a) Representation of the borehole coordinate system attached to a cross-section of the borehole at a curvilinear abscissa s along the trajectory: $\hat{t}_s$ is the tangent, $\hat{n}_s$ is the normal, $\hat{b}_s$ is the binormal, $\hat{x}, \hat{y}, \hat{z}$ are unit vectors of a geographical coordinate system and ϑ_s and ϕ_s are respectively the inclination and azimuth at the curvilinear abscissa s. b) at a position in a cross-section, a Frenet-Serret coordinate system $(\hat{t}_f, \hat{n}_f, \hat{b}_f)$ is attached to the fluid stream that follows a local curvature K_f.

The combined effect of gravity and buoyancy (see eq. (50)) can then be expressed in the borehole coordinate system associated with a cross-section as:

$$\vec{F}_g + \vec{F}_b = (\rho_s - \rho_f) V_s g (\cos\vartheta_s\, \hat{t}_s + \sin\vartheta_s\, \hat{n}_s) \tag{117}$$

The lift force is defined in a similar way to the drag force (ref. eq. (47)):

$$F_L = \frac{1}{2}\rho_f \|\vec{v}_s\|^2 C_L A_\perp \tag{118}$$

where C_L is a lift drag coefficient. The drag force is oriented by the direction of the fluid flow while the lift force is in a normal direction to the fluid flow as defined by a Frenet-Serret coordinate system associated with the flow (see Fig. 103b). In such a Frenet-Serret coordinate system, the tangent unit vector is $\hat{t}_f = \frac{\vec{v}_f}{\|\vec{v}_f\|} = t_t \hat{t}_s + t_n \hat{n}_s + t_b \hat{b}_s$ with $\vec{v}_f$ the velocity of the fluid in the spherical

inertial frame of reference $(\hat{t}_s, \hat{n}_s, \hat{b}_s)$, the normal vector is $\hat{n}_f = \frac{1}{\mathrm{K}_f}\frac{d\hat{t}_f}{ds} = n_t\hat{t}_s + n_n\hat{n}_s + n_b\hat{b}_s$ where K_f is the curvature and the binormal is $\hat{b}_f = \hat{t}_f \times \hat{n}_f = b_t\hat{t}_s + b_n\hat{n}_s + b_n\hat{b}_s$. Then it is possible to define a transformation matrix, $P_{p_{f\to s}}$, from the Frenet-Serret coordinate system attached to the fluid flow to the borehole coordinate system associated with the cross-section:

$$P_{p_{f\to s}} = \begin{pmatrix} t_t & n_t & b_t \\ t_n & n_n & b_n \\ t_b & n_b & b_b \end{pmatrix} \tag{119}$$

The coordinates of the drag and lift forces in the borehole coordinate system associated with the cross-section are:

$$\begin{cases} \vec{F}_D = -\frac{1}{2}\rho_f {v_s}^2 C_D A_\perp \left(t_t\hat{t}_s + t_n\hat{n}_s + t_b\hat{b}_s\right) \\ \vec{F}_L = \frac{1}{2}\rho_f {v_s}^2 C_L A_\perp \left(n_t\hat{t}_s + n_n\hat{n}_s + n_b\hat{b}_s\right) \end{cases} \tag{120}$$

The velocity of a particle, $\vec{v}_p$, in the borehole coordinate system associated with the cross-section is:

$$\vec{v}_p = \vec{v}_f - \vec{v}_s \tag{121}$$

where $\vec{v}_f$ is the fluid velocity and $\vec{v}_s$ is the slip velocity. Therefore, the position of the particle, x_p, at an instant t, can be calculated by integrating the velocity over time, from an initial condition, x_0, at instant t_0:

$$x_p = \int_{t_0}^{t} \vec{v}_f - \vec{v}_s dt + x_0 \tag{122}$$

On the other hand, the particle acceleration is limited to the time derivative of the slip velocity, as a consequence of the steady state flow hypothesis in a cross-section, for which the time derivative is zero:

$$\vec{v}_p = -\vec{v}_s \tag{123}$$

Then, Eq. (115) can be written explicitly in the borehole coordinate system associated with the cross-section as:

$$\begin{cases} (\rho_s - \rho_f)V_s g\cos\vartheta_s - \frac{1}{2}\rho_f {v_s}^2 C_D A_\perp t_t + \frac{1}{2}\rho_f {v_s}^2 C_L A_\perp n_t = -\rho_s V_s \dot{\vec{v}}_s . \hat{t}_s \\ -(\rho_s - \rho_f)V_s g\sin\vartheta_s - \frac{1}{2}\rho_f {v_s}^2 C_D A_\perp t_n + \frac{1}{2}\rho_f {v_s}^2 C_L A_\perp n_n = -\rho_s V_s \dot{\vec{v}}_s . \hat{n}_s \\ -\frac{1}{2}\rho_f {v_s}^2 C_D A_\perp t_b + \frac{1}{2}\rho_f {v_s}^2 C_L A_\perp n_b = -\rho_s V_s \dot{\vec{v}}_s . \hat{b}_s \end{cases} \quad (124)$$

We have seen in section 2.1.1.17 that C_D is a function of the slip velocity through the particle number Re_p. It is the same for the lift drag coefficient C_L. The equations (124) define a system of three non-linear ordinary differential equations in $\vec{v}_s$, that can be integrated numerically based on proper estimations of C_D and C_L.

The origin of a lift force on a particle can be linked to its rotation around its center of gravity [167], also referred as the Magnus effect, or a gradient of fluid velocity across the cross-sectional area exposed to the fluid flow [168]. It can also result from the shape of the particle. Unfortunately, until recently there has been little focus on estimating the lift drag coefficient for blunt objects. Zastawny et al. 2012 [169] have published a lift drag coefficient correlation for ellipsoids at low and medium Reynolds number for two aspect ratios. Ouchene et al. 2015 [170] have verified the correlation using direct numerical simulation, yet with discrepancies reaching 20%. The same authors published in 2016 [171] new correlations of the drag and lift coefficients for ellipsoid shapes with and aspect ratio between 1 and 32 and for Reynolds number between 1.21 and 240. With these new correlations, the mean error compared to direct numerical simulation does not exceed 8% for the lift coefficient and 6% for the drag coefficient.

It should also be noted that a pitch moment applies on the particle when there is incidence angle (α_p) and there is an asymmetry in the exposed surface to fluid flow. The pitch moment is oriented by the normal vector to the fluid flow, i.e. $\hat{n}_f$, and its magnitude is $\tau_p = \frac{1}{2}\rho_f {v_s}^2 C_M A_\perp l_c$, where C_M is the pitch moment coefficient and l_c is the chord of the particle in the direction of the flow. Note that $A_\perp$ and l_c are characteristics dimensions of the particle that should be independent on the incidence angle. To follow the convention utilized by Ouchene et al. (2016), $A_\perp$ is posed to be $\pi\frac{d_s^2}{4}$ and $l_c = \frac{d_s}{2}$, where d_s is the equivalent diameter of the particle that would give the same volume as the particle, i.e. $d_s = \sqrt[3]{\frac{6V_s}{\pi}}$.

Even though these new correlations fill a void in the estimation of lift, drag and torque coefficients on particles, it is likely that their precision is not as good as the one published by their authors, when applied to drilling fluids and drill-cuttings. First because, drill-cuttings have an irregular shape and the assumption of a prolate geometry is probably not well respected. Second, because drilling fluids are more complex than those used in the direct numerical simulations of Ouchene et al. (2016). For instance, the presence of barite particles, which are also solid particles, causes a mutual interaction between particles that is not accounted by these correlations (see section 3.1.3 for illustrations of the change of apparent rheological behavior of a drilling fluid as a function of the mixture of barite and sand particles). Also, the thixotropic behavior of drilling fluids has a probable direct influence on the rearrangement of solid particles in between each other's as described in section 3.1.2. Nevertheless, lacking any better correlations more adapted to drilling fluids, the empirical relations of Ouchene et al. for C_D, C_L and C_M are used as a starting point for the estimation of the 3-dimensional movement of a solid particle in an annulus.

Utilizing Euler's rotation equations of a solid body in a coordinate system attached to the particle ($\hat{t}_p, \hat{n}_p, \hat{b}_p$), we have three additional equations:

$$\begin{cases} \tau_p \hat{n}_f . \hat{t}_p = J_t \ddot{\theta}_t + (J_b - J_n)\dot{\theta}_n \dot{\theta}_b \\ \tau_p \hat{n}_f . \hat{n}_p = J_n \ddot{\theta}_n + (J_t - J_b)\dot{\theta}_t \dot{\theta}_b \\ \tau_p \hat{n}_f . \hat{b}_p = J_b \ddot{\theta}_b + (J_n - J_t)\dot{\theta}_t \dot{\theta}_n \end{cases} \quad (125)$$

where J_t, J_n and J_b are respectively the moment of inertia of the particle relatively to the axes of rotation $\hat{t}_p$, $\hat{n}_p$ and $\hat{b}_p$, and θ_t, θ_n and θ_b are respectively the rotation angles around the directions $\hat{t}_p$, $\hat{n}_p$ and $\hat{b}_p$.

The transformation matrix from the local particle coordinate system to the annulus cross-section coordinate system is the product of the individual rotations along the three directions associated with the particles:

$$\begin{pmatrix} \cos\theta_b & -\sin\theta_b & 0 \\ \sin\theta_b & \cos\theta_b & 0 \\ 0 & 0 & 1 \end{pmatrix} \begin{pmatrix} \cos\theta_n & 0 & \sin\theta_n \\ 0 & 1 & 0 \\ -\sin\theta_n & 0 & \cos\theta_n \end{pmatrix} \begin{pmatrix} 1 & 0 & 0 \\ 0 & \cos\theta_t & -\sin\theta_t \\ 0 & \sin\theta_t & \cos\theta_t \end{pmatrix} \quad (126)$$

To calculate the left terms of eq. (125), first the pitch moment vector shall be transformed to the cross-section coordinate system by utilizing the transformation matrix (119), then the result shall be transformed to the local

coordinate system associated with the particle by utilizing the inverse of the transformation matrix (126).

If we assimilate the particle to a prolate characterized by a length l_p and a width w_p, then the volume of the particle is $V_s = \frac{\pi}{6} w_p^2 l_p$, and the moments of inertia are $J_t = \rho_p V_s \frac{2{w_p}^2}{5}$ and $J_n = J_b = \rho_p V_s \frac{{w_p}^2 + {l_p}^2}{5}$.

The incidence angle α_p is the angle of the vector along the length of the prolate, i.e. $\hat{t}_p$, with regards to the local fluid flow direction ($\hat{t}_f$). We first convert $\hat{t}_p$ into the coordinate system associated with the cross-section by applying the transformation matrix (126) and then we convert the result to the coordinate system attached with the fluid flow by applying the inverse of the transformation matrix (119), and finally we can calculate the incidence angle by utilizing the classical definition of a solid angle:

$$\alpha_p = \cos^{-1} \hat{u}_t \,.\, \hat{t}_f \tag{127}$$

where $\hat{u}_t$ is the transformed unit vector $\hat{t}_p$ in the fluid coordinate system.

Note that in the determination of the Reynolds particle number, we should estimate the effective viscosity of the fluid around the particle. If the fluid is characterized by a Herschel-Bulkley rheological behavior, then the effective viscosity is:

$$\mu_{eff} = \frac{\tau_{\dot{\gamma}}}{\dot{\gamma}_s} + K {\dot{\gamma}_s}^{n-1} \tag{128}$$

The shear rate around the particle ($\dot{\gamma}_s$) is contributed by the local shear in the fluid ($\dot{\gamma}$) and the slip velocity of the particle compared to the background fluid:

$$\dot{\gamma}_s = \dot{\gamma} + \frac{v_s}{d_s} \tag{129}$$

The local shear rate of the fluid in the cross-section is defined by the local gradient of the fluid velocity:

$$\dot{\gamma} = \frac{\partial v_f}{\partial \mathrm{y}} + \frac{\partial v_f}{\partial \mathrm{z}} \tag{130}$$

where y and z are the respective components in the directions $\hat{n}_s$ and $\hat{b}_s$. Note that here $\frac{\partial v_f}{\partial \mathrm{x}} = 0$, i.e. the derivative of the fluid velocity in the perpendicular direction to the cross-section, since we have supposed a steady state flow.

The cross-section is discretized in n_{cs} radial and m_{cs} angular positions, denoted respectively i, j (see Fig. 104).

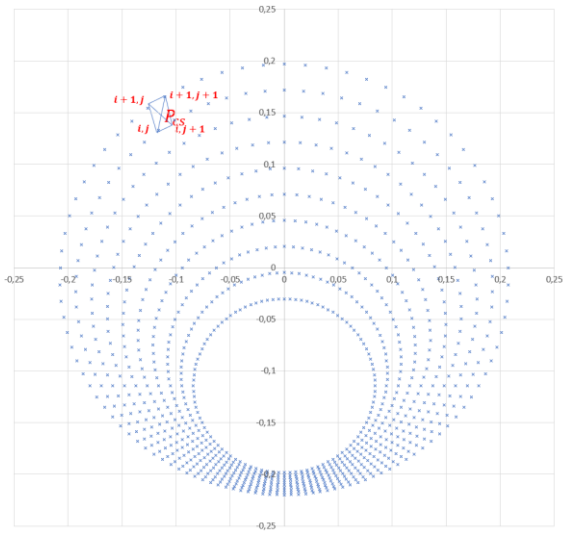

Fig. 104: Discretization of a cross-section, here based on a 17 ½-in borehole with a 6 5/8-in drill-pipe with an eccentricity caused by a 8 ½-in tool-joint.

For each combination of i and j, there is a cartesian position $y_{i,j}\hat{n}_s + z_{i,j}\hat{b}_s$. Note that these vertices are not organized in a regular grid and therefore the closest neighbors to a discretized position i, j define a quadrilateral and not a rectangle. To determine if a point P_{cs} is contained in such a quadrilateral, then it is sufficient to sum the four angles of each sectors starting from P_{cs} to the two consecutive vertices of the quadrilateral and check that it is equal to 2π. For such a point P_{cs}, it is then possible to determine the corresponding dimensionless coordinates, i_y and $i_z \in [0,1]$ in its enclosing quadrilateral such that the coordinates of the point can be reconstructed from a bilinear interpolation within the quadrilateral vertices:

$$\begin{cases} y_P = y_{i,j}(1-i_y)(1-i_z) + y_{i+1,j}i_y(1-i_z) + y_{i,j+1}(1-i_y)i_z + y_{i+1,j+1}i_y i_z \\ z_P = z_{i,j}(1-i_y)(1-i_z) + z_{i+1,j}i_y(1-i_z) + z_{i,j+1}(1-i_y)i_z + z_{i+1,j+1}i_y i_z \end{cases} \quad (131)$$

where y_P and z_P are the respective coordinates in the $\hat{n}_s$ and $\hat{b}_s$ directions of the point P_{cs}, $y_{i,j}$ and $z_{i,j}$ are the respective coordinates of the discretized position at indices i, j in the directions $\hat{n}_s$ and $\hat{b}_s$ of the enclosing quadrilateral. There are usually two solutions to this system of equations and we just chose the one where both i_y and i_z belong to the interval $[0,1]$.

When the dimensionless bilinear coordinates are determined, it is then possible to obtain a bilinear interpolation of the fluid velocity vector at that position:

$$\begin{cases} v_{x_P} = v_{x_{i,j}}(1-i_y)(1-i_z) + v_{x_{i+1,j}} i_y(1-i_z) + v_{x_{i,j+1}}(1-i_y) i_z + v_{x_{i+1,j+1}} i_y i_z \\ v_{y_P} = v_{y_{i,j}}(1-i_y)(1-i_z) + v_{y_{i+1,j}} i_y(1-i_z) + v_{y_{i,j+1}}(1-i_y) i_z + v_{y_{i+1,j+1}} i_y i_z \\ v_{z_P} = v_{z_{i,j}}(1-i_y)(1-i_z) + v_{z_{i+1,j}} i_y(1-i_z) + v_{z_{i,j+1}}(1-i_y) i_z + v_{z_{i+1,j+1}} i_y i_z \end{cases} \quad (132)$$

where v_{x_P}, v_{y_P} and v_{z_P} are the respective coordinates of the velocity vector at the point P_{cs} in the $\hat{t}_s$, $\hat{n}_s$ and $\hat{b}_s$ directions, and $v_{x_{i,j}}, v_{y_{i,j}}$ and $v_{z_{i,j}}$ are the respective coordinates of the fluid velocity vector at the discretized position i, j in the directions $\hat{t}_s$, $\hat{n}_s$ and $\hat{b}_s$.

Based on the discretization and the bilinear interpolation described above, it is then possible to estimate the fluid shear rate at any position in the cross-section utilizing a small increment approximation of eq. (130):

$$\dot{\gamma}(y,z) = \frac{v_f(y,z) - v_f(y+\Delta y, z)}{\Delta y} + \frac{v_f(y,z) - v_f(y, z+\Delta z)}{\Delta z} \quad (133)$$

where Δy and Δz are small increments in the respective directions $\hat{n}_s$ and $\hat{b}_s$.

The fluid velocity in a cross-section of an annulus depends not only on the rheological behavior of the fluid and the flowrate but also on the pipe rotation as it is illustrated by the 3D-graphs a and b of Fig. 105. Note that in virtue of the no slip at the wall assumption, the fluid velocity is always zero at the borehole wall. The 3D-graphs c and d of Fig. 105 show the shear rates in the same configuration. It should be noted that the shear rate is the largest at the borehole and pipe walls and smallest in between.

We can now solve the system of ordinary differential equations defined by eq. (124) and (125) for the movement of a prolate in the fluid flow as a boundary problem where the particle starting conditions are its initial position ($\vec{u}_{p_0}$) and velocity ($\vec{v}_{p_0}$) in a cross-section of origin and associated with an initial value of its spin velocity (ω_{p_0}) around a rotation axis ($\vec{r}_{p_0}$). Typically, we calculate

the displacement of such a particle for approximatively 9m, i.e. the distance between two tool-joints, as the fluid velocity field cannot be considered in steady state conditions when the fluid passes the drill-pipe connections.

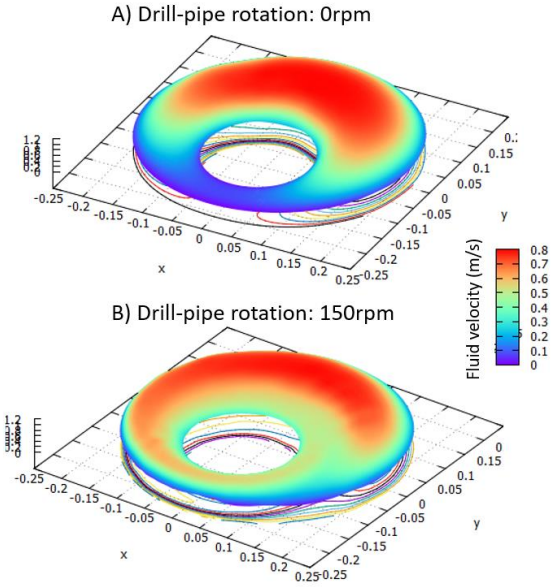

Fig. 105: Illustration of the effect of pipe rotation and eccentricity on the fluid velocity (A and B) distributions in a 17 ½-in borehole with 5-in drilling pipe supported by 6 5/8-in tool joints without rotation (A) and rotating at 60 rpm (B).

3.1.4.2 Particle Settling and Change of Particle Size Distribution

Depending on the flow and pipe movement and the initial conditions at the starting position of the particle, it may travel the distance of investigation in a finite time or never reach the target cross-section, either because it has arrived at a position where it does not move or because it drops in the opposite direction to the fluid flow.

Let us define the indicator function $1_{\delta_p,d_s}$ that equals to one if a particle of equivalent diameter d_s reaches a certain distance δ_p from given initial starting conditions $(\vec{u}_{p_0}, \vec{v}_{p_0}, \omega_{p_0}, \vec{r}_{p_0})$ and zero on the contrary. If the indicator function is equal to one for any initial conditions, then the bulk fluid velocity $\bar{v}_f$ is larger than the CTFV for that size of particles ($\overline{v}_{ctfv_{d_s}}$):

$$\forall \vec{u}_{p_0}, \vec{v}_{p_0}, \omega_{p_0}, \vec{r}_{p_0}, 1_{\delta_{p,d_s}} = 1 \Leftrightarrow \bar{v}_f \geq \bar{v}_{ctfv_{d_s}} \quad (134)$$

This definition can replace the one from Larsen et al. (1997) [75] (see section 2.1.1.19), that was based on visual observations of whether particles sedimented or not during large scale flow-loop experiments.

Similarly, we can also define a critical settling fluid velocity (CSFV) for that particle size ($\bar{v}_{csfv_{d_s}}$) such that the indicator function is equal to 0 regardless of the starting conditions:

$$\forall \vec{u}_{p_0}, \vec{v}_{p_0}, \omega_{p_0}, \vec{r}_{p_0}, 1_{\delta_{p,d_s}} = 0 \Leftrightarrow \bar{v}_f \leq \bar{v}_{csfv_{d_s}} \quad (135)$$

In practice, the feed source of particles at the starting cross-section is not composed of a single particle size, but instead by a whole variety of particle dimensions that are described by a PSD ($f(d_s; P_{80}, m)$).

We can now generalize the CTFV and the CSTV to a feed described by a PSD. The CTFV ($\bar{v}_{ctfv}$) is the limit of the fluid bulk velocity by which all the indicator functions remain equal to 1 for all particle dimensions that are sufficiently represented in the PSD, and for all possible initial conditions:

$$\forall \vec{u}_{p_0}, \vec{v}_{p_0}, \omega_{p_0}, \vec{r}_{p_0}, \forall d_s | f(d_s; P_{80}, m) > \varepsilon, 1_{\delta_{p,d_s}} = 1 \Leftrightarrow \bar{v}_f \geq \bar{v}_{ctfv} \quad (136)$$

where ε is the condition for a particle size to be sufficiently represented in the PSD.

Similarly, the CSFV ($\bar{v}_{csfv}$) is the limit of the fluid bulk velocity by which all the indicator function remains equal to 0 for all particle dimensions that are sufficiently represented in the PSD and for all possible initial conditions:

$$\forall \vec{u}_{p_0}, \vec{v}_{p_0}, \omega_{p_0}, \vec{r}_{p_0}, \forall d_s | f(d_s; P_{80}, m) > \varepsilon, 1_{\delta_{p,d_s}} = 0 \Leftrightarrow \bar{v}_f \leq \bar{v}_{csfv} \quad (137)$$

In fact, it can be noted that the CTFV for a PSD is the minimum of all the relevant $\bar{v}_{ctfv_{d_s}}$:

$$\bar{v}_{ctfv} = \min_{d_s | f(d_s; P_{80}, m) > \varepsilon} \bar{v}_{ctfv_{d_s}} \quad (138)$$

Similarly, the CSFV for a PSD is the maximum of all the relevant $\bar{v}_{csfv_{d_s}}$:

$$\bar{v}_{csfv} = \max_{d_s | f(d_s; P_{80}, m) > \varepsilon} \bar{v}_{csfv_{d_s}} \tag{139}$$

At the CTFV, it is possible to estimate a bulk slip velocity for a given PSD ($\bar{v}_{s_{ctfv}}$):

$$\bar{v}_{s_{ctfv}} = \int_0^{\infty} f(x; P_{80}, m)\, v_{s_x} dx \tag{140}$$

where v_{s_x} denotes the slip velocity of a particle of size x.

Next, we can define a cuttings carrying index (see section 2.1.1.20) for a specific particle size as the probability that the indicator function equals one for any starting conditions for the particle, i.e. $P\left(1_{\delta_p, d_s} = 1; d_s | \forall \vec{u}_{p_0}, \vec{v}_{p_0}, \omega_{p_0}, \vec{r}_{p_0}\right)$. This CCI is such that it is equal to zero when the bulk fluid velocity is lower than $\bar{v}_{csfv_{d_s}}$ and equals to one when it is greater than $\bar{v}_{ctfv_{d_s}}$. For any bulk fluid velocity in between the $\bar{v}_{csfv_{d_s}}$ and the $\bar{v}_{ctfv_{d_s}}$, the value of the function represents the probability that a particle will be transported directly.

When $P\left(1_{\delta_p, d_s} = 1; d_s | \forall \vec{u}_{p_0}, \vec{v}_{p_0}, \omega_{p_0}, \vec{r}_{p_0}\right) \in [0,1[$, some particles are transported passed the distance δ_p and others not. We can now generalize the CCI for a specific PSD, as the probability of any particle that are sufficiently represented in the PSD, to be transported over the distance δ_p, for any possible initial conditions:

$$P\left(1_{\delta_p, d_s} = 1 | \forall d_s \; such \; that \; f(d_s; P_{80}, m) > \varepsilon, \forall \vec{u}_{p_0}, \vec{v}_{p_0}, \omega_{p_0}, \vec{r}_{p_0}\right) \tag{141}$$

The number of particles that settle at a given cross-section, depends also on the PSD of the feed-source. Consequently, the PSD of the settling particles is not necessarily identical to the one of the feed-source and it needs to be evaluated as a function of the current conditions, e.g. bulk fluid velocity and pipe rotational speed. Also, the overall PSD of the settled particles evolves with time since the settling PSD is not constant. It is therefore necessary to evaluate the current PSD of the settled particles at any time step of the simulation. Finally,

the PSD of particles that pass the studied position without settling is different from the feed-source and shall be estimated.

The settling particle concentration (Φ) cannot exceed the maximum packing concentration (Φ^*), which depends on the particle size of the settling particles and the barite concentration in the fluid as we have seen in section 3.1.3.3.

There are two cases: either the lateral position of settling particles in a cross-section is loosely constrained like for example when particles are not directly transported in a near vertical section, or they sediment on the low side of the borehole, typically when the local wellbore inclination is greater than 35°."[33]

If the particles remain free to move laterally, they contribute to a change of the apparent rheological behavior of the drilling fluid as described in section 3.1.1.4 and may cause pack-off situations as the pressure losses in the region of high particle concentration increases dramatically, as we have seen in the above referred section.

In the case where particles sediment on the low side of the annulus, the volume occupied by the settled particles increases as long as particles continue to sediment and as a consequence the cross-sectional area left for the fluid flow decreases. The reduction of the fluid flow area leads to an increase of the bulk fluid velocity. The change of the bulk fluid velocity modifies the PSD of the settling particles and at a certain point, the CCI may become equal to one, meaning that no more particles settle anymore at that position. This corresponds to the maximum cuttings bed size that can be obtain for a given PSD of the feed-source and the current flow and pipe movement conditions.

The cuttings bed height is a function of the number of particles that have sedimented, their maximum packing concentration and the geometrical configuration of the annulus, including the borehole and pipe diameters but also the pipe axis eccentricity.

As it can be seen on fig. 12 of Paper II, there are three possible configurations:

1. The cuttings bed is lower than the bottom side of the eccentric pipe.
2. The cuttings bed covers partially the pipe.

33 Excerpt from Cayeux (2019) [198]

3. The pipe is completely covered by the cuttings bed.

The height of the cuttings bed (h_c) is then obtained by solving the following equation eq. (27) of Paper II. However, note that there is an error for the last condition in eq. (27) of Paper II. It should be:

$$\begin{aligned} if\ h_c > r_w - e + r_p, A_c \\ &= \pi r_w^2 - \text{acos}\left(\frac{h_c - r_w}{r_w}\right) r_w^2 \\ &+ (2r_w - h_c)\sqrt{r_w^2 - (2r_w - h_c)^2} - \pi r_p^2 \end{aligned} \tag{142}$$

utilizing the same nomenclature as in Paper II.

The top of the cuttings bed is exposed to the fluid flow and its packing density is lower than at deeper depths. It is therefore possible for those top particles to be displaced by erosion. However, existing mechanistic models describing this phenomenon do not account for the pipe movement and therefore they have little practical use in a drilling operation context. Solving the mechanical erosion of the top of the cuttings bed when considering the effect of the pipe movements is a very difficult problem that is not yet solved to the best of our knowledge. Instead, we have adopted an empirical solution that consists in considering that the cross-sectional and velocity of the fluidized layer of particles that is susceptible to be displaced by erosion, is proportional to the CCI. Indeed, since the CCI accounts for the bulk fluid velocity, the pipe movement and the PSD, it can be considered as a plausible indicator of the erosion rate.

$$\begin{aligned} A_{fluidized} = P\Big(1_{\delta_{p,d_s}} = 1 | \forall d_s\ such\ that\ f_{bed}(d_s; P_{80}, m) \\ > \varepsilon, \forall \vec{u}_{p_0}, \vec{v}_{p_0}, \omega_{p_0}, \vec{r}_{p_0}\Big) A_c \end{aligned} \tag{143}$$

where $A_{fluidized}$ is the cross-sectional area of fluidized particles at the top of the cuttings bed, f_{bed} is the particle density distribution of the particles belonging to the bed.

$$\begin{aligned} \bar{v}_{fluidized} = P\Big(1_{\delta_{p,d_s}} = 1 | \forall d_s\ such\ that\ f_{bed}(d_s; P_{80}, m) \\ > \varepsilon, \forall \vec{u}_{p_0}, \vec{v}_{p_0}, \omega_{p_0}, \vec{r}_{p_0}\Big)\left(\bar{v}_f - \bar{v}_{s_{ctfv}}\right) \end{aligned} \tag{144}$$

where $\bar{v}_{fluidized}$ is the bulk velocity of the fluidized layer and $\bar{v}_{s_{ctfv}}$ is the bulk slip velocity at CTFV conditions.

At this point, it is possible to evaluate how cuttings get transported or deposited in complex wellbore architecture and well trajectories, under variable circulation and rotation conditions. The next examples are estimated utilizing the well trajectory and wellbore architecture depicted on Fig. 106. Note that this case has been described in more details in Cayeux et al. (2016) [98].

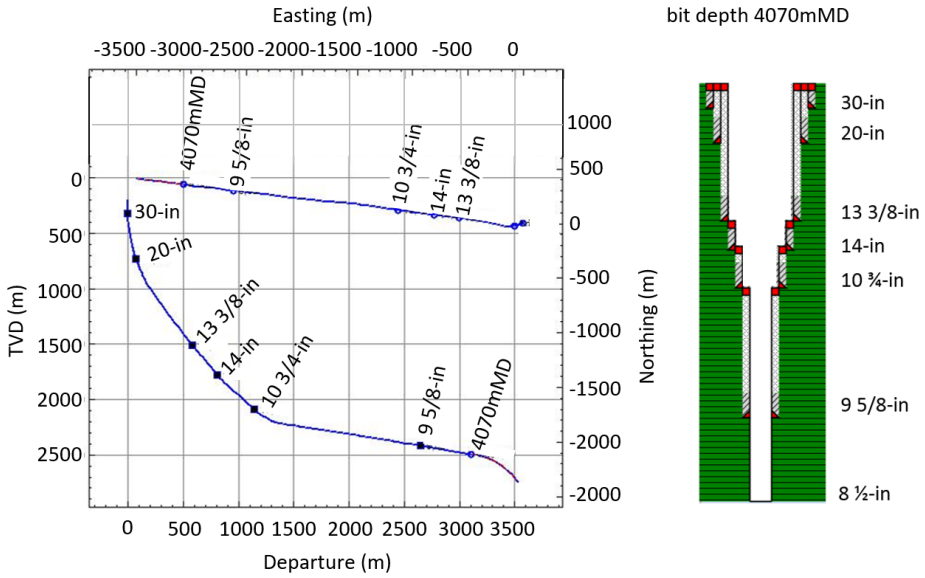

Fig. 106: Trajectory and wellbore architecture.

This well has a tapered casing architecture and therefore is challenging for cuttings transport as, while drilling the 8 ½-in section, the flowrate has to be restricted because of the proximity of the downhole pressure to the formation fracturing pressures, in the open hole section, and yet the borehole diameters, at shallower depths, are as large as a 14-in and 13 3/8-in. As it can be seen on Fig. 107 (step 1), the transient cuttings transport model estimates that there is a cuttings bed between 1100 and 2100mMD. However, a stable bed thickness has been reached, and the cuttings are transported passed that bed, up to surface when utilizing the current flowrate of 2180l/min and a top-drive speed of 145rpm. However, in step 2, when the top-drive is stopped while performing a pick-up and slack-off procedure to measure downhole mechanical friction, the model estimates that some of the cuttings that were transported in suspension below 2100mMD, settle on the low-side and others stays in suspension.

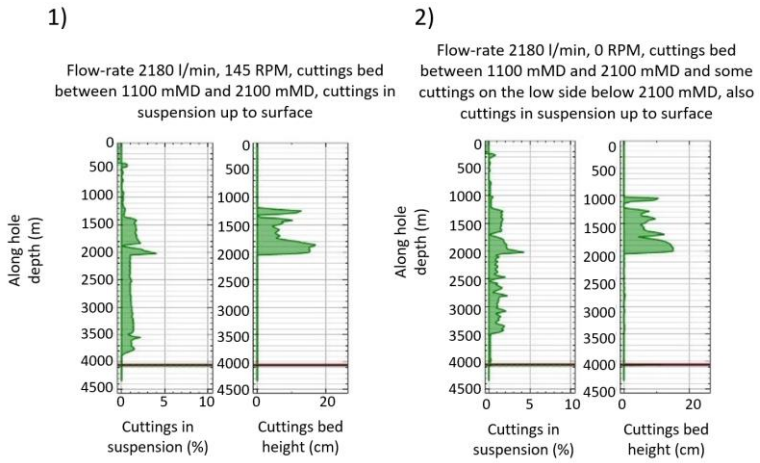

Fig. 107: Step 1) Just finished to drill a stand with flowrate 2180l/min and top-drive speed 145rpm. Step 2) Prepare to perform a friction test, the top-drive speed is reduced to 0rpm.

However, when the mud pumps are stopped, just prior to making a connection, the model estimates that most cuttings below 2100mMD deposit on the low side. This is because of the high inclination below this depth and the short travel for cuttings to reach the low side (see step 3 in Fig. 108). Just after the connection, in step 4, the mud pumps are restarted but because a survey is taken, there is no top-drive rotation. The model estimates that with the slightly lower flowrate (1920l/min) and no drill-string rotation, the cuttings cannot return in suspension.

It is only from step 5 (see Fig. 109) that the temporary cuttings bed, below 2100mMD, disappears. This is the consequence of the drill-string rotation that is resumed to 146rpm and the flowrate that is increase to 2150l/min. Indeed, the combined effect of drill-pipe rotation with a larger axial flow velocity is favorable to lift the solid particles that were on the low side and displace them in the region of high axial fluid velocity on the high-side of the annulus.

This example illustrates that the above-described model is capable to estimate the displacement of solid particles with a complex wellbore architecture and

that the results depend on the sequence of operations that are executed, i.e. that transport of cuttings in a borehole is a nonholonomic system.[34]

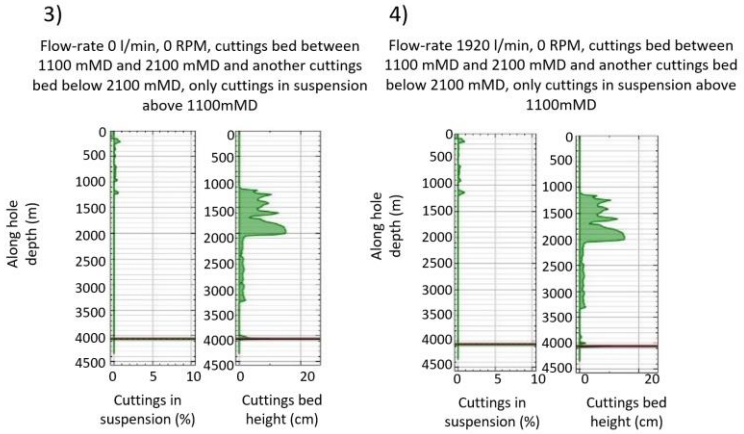

Fig. 108: Step 3) Prepare for connection, the mud pumps are stopped. Step 4) After adding a new stand, restart the mud pumps without rotation in order to take a survey.

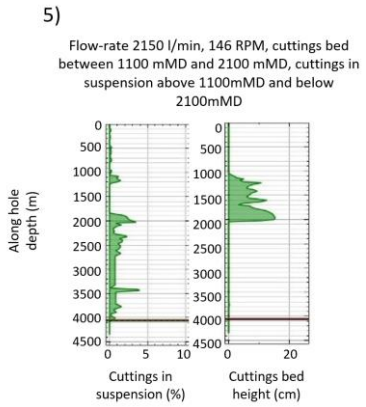

Fig. 109: Step 5) Resume drilling, the mud pumps are back to full-speed as well as the top-drive.

34 The state of a nonholonomic system depends on the path taken to reach it.

3.1.4.3 Transformation of the Cuttings PSD by Grinding

"Whenever a particle may pass between the tool-joint and the borehole, it can be grinded. This can happen simply because of the distribution of particles in a cross-section but also when particles are settling on the low side in a cuttings bed.

In order to utilize the grinding empirical relationship described in eq. (61), we need to estimate the energy absorbed by the grinding process at each tool joint.

For a rotating tool-joint in contact with the borehole, the grinding power can be related to the excess torque (τ_{TJ_g}) at the tool-joint compared to the torque generated by mechanical friction (τ_{TJ_μ}):

$$\tau_{TJ_g} = \tau_{TJ} - \tau_{TJ_\mu} \tag{145}$$

where τ_{TJ} is the actual torque at the tool joint. The grinding power at the tool-joint (W_{TJ_g}) is then:

$$W_{TJ_g} = \tau_{TJ_g}\dot{\theta}_{TJ} \tag{146}$$

where $\dot{\theta}_{TJ}$ is the angular velocity of the tool joint.

The free rotating torque, measured when there are no cuttings inside the borehole, gives a reference for the torque that is solely related to mechanical friction. At a later stage, if the free rotating torque is larger than the one that would have been induced by only mechanical friction, then we can suppose that it is related to the grinding of cuttings passing by the tool-joints. By taking the difference between the two, we can estimate the grinding power that is provided to the milling process. Based on estimations of the position of cuttings under transport, we can distribute that grinding power at different positions along the drill-string and therefore we can estimate how much impact it has on the size reduction of particles during their transport.

For instance, if we assume that the cuttings generated by a PDC bit are well-sorted and around 15mm in equivalent diameter and that we drill at 60m/h and rotate the drill-string at 160rpm with a drill-string where the tool-joints have a diameter of 7-in, then we can estimate the evolution of the particle size distribution along the drill-string, starting from the bit, as a proportion of the particles get grinded while passing the rotating tool-joints.

Fig. 110 shows the results for a 1000m long 17 ½-in hole section (a) and for a 1800m long 12 ¼-in section (b). We can see that when cuttings arrive at the surface, the model predicts that the PSD will range from 1 to 15 mm for the 17 ½-in section and between 100µm and 15mm for the 12 ¼-in hole size.

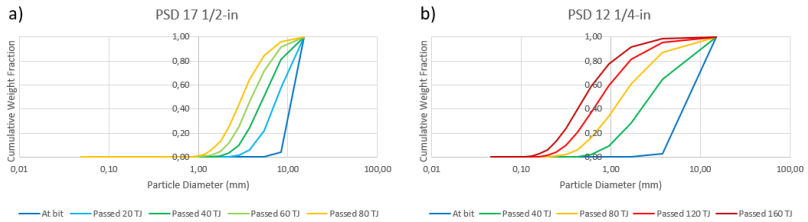

Fig. 110: Evolution of the PSD of cuttings when drilling at 60m/h with a drill-string rotation of 160rpm while passing through 7-in tool-joints in 1000m long 17 ½-in hole section (a) and a 1800m long 12 ¼-in section (b).”[35]

3.1.4.4 Summary

A method to calculate the 3D trajectory of a prolate particle in a 3D velocity field of a shear thinning yield stress fluid flowing in an eccentric annular with rotation of the inner string, has been described.
Statistical methods have been developed to estimate the critical transport fluid velocity and the critical settling fluid velocity.
The probability of presence of a prolate particle can then be estimated from its initial conditions in between two tool-joints.
In case a particle is trapped under a tool-joint, its size reduction is estimated as a function of an estimated grinding torque.
When particles sediment on the low side of the borehole, the erosion rate of the cuttings bed is estimated as a function of changes in cross-sectional area and estimated CCI.

35 Excerpt from Cayeux (2019) [198]

3.2 Drill-string Mechanics

We have seen in the previous section that the drill-string movement influences hydraulic calculations, as for example the capability to transport cuttings in suspension or the grinding of cuttings particles as they pass under rotating tool-joints. Conversely, hydraulic pressure and grinding of cuttings influence the mechanical behavior of the drill-string. So, even though the topic of this section is drill-string mechanics, hydraulic effects that impact the dynamic behavior of the drill-string are accounted for and is illustrated through actual examples.

3.2.1 Decomposition of the Drill-string

"Except for a limited portion of drill-collars staying on the low-side of the wellbore where the contact with the borehole wall can be considered as continuous, the rest of the drill-string is in contact only at specific positions, either because of the presence of stabilizers in the BHA or simply because of the drill-pipe tool-joints. We will call an element of the drill-string, or in short, an element, the portion of a drill-string in between two contact points (see Fig. 111). An element i along the drill-string is subject to external and internal forces and torques. Some of those forces and torques are distributed and others can be assimilated to concentrated ones because their region of application is small compared to the dimension of the element. For instance, forces and torques applied to the tool-joints or the stabilizer blades may be aggregated to point forces and torques because the length of the tool-joint or the stabilizer blade is much shorter than the distance between two adjacent contacts (typically there is a factor ten in between those lengths).

We will denote $\vec{w}_{i,j}$ a distributed force j, i.e. a force per unit length, applied to element i. The net force resulting from this distributed force on the element i is:

$$\vec{F}_{i,j} = \int_{s_i}^{s_{i+1}} \vec{w}_{i,j}\, ds \tag{147}$$

where s is the curvilinear abscissa, and the length of the element is $l_i = s_{i+1} - s_i$. From position i to position $i+1$, the inclination changes from ϑ_i to ϑ_{i+1} and the azimuth from α_i to α_{i+1} following a curvature DLS_i.

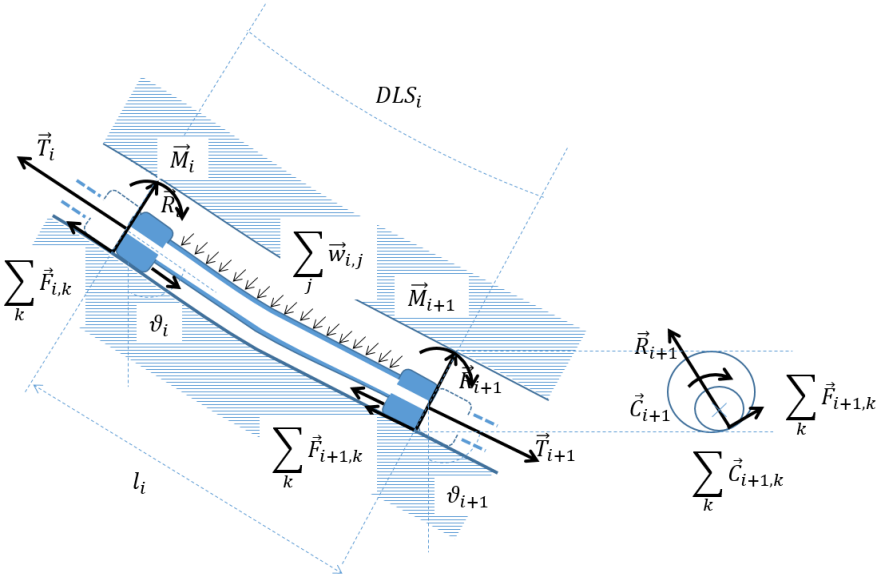

Fig. 111: Schematic representation of forces and torques applied to an element in between two contact points.

A torque induced by a force j on element i is denoted by $\vec{C}_{i,j}$ and is the cross-product of the radius of rotation by the force:

$$\vec{C}_{i,j} = \vec{r}_{i,j} \times \vec{F}_{i,j} \tag{148}$$

Therefore, a force generates a torque when it is not collinear with the direction of the radius of rotation.

The external forces applied to an element are:

- Gravitation and buoyancy forces
- Pressure related forces caused by the relative movement of fluid
- Forces produced by viscous friction
- Mechanical friction in between the element and the borehole
- Reaction forces in between the element and the borehole

The internal forces applied to an element are:

- Tensions at both ends of the element ($\vec{T}$)
- Torques applied at the ends of the element ($\vec{C}$)
- Bending moments along the element ($\vec{M}$)

"If we consider that the material used in the drill-string is elastic and that it follows Hooke's law, then we have:

$$\begin{cases} \sigma_a = E\dfrac{\partial u(s,t)}{\partial s} \\ \tau = rG\dfrac{\partial \theta(s,t)}{\partial s} \\ M = EI\dfrac{\partial^2 w(s,t)}{\partial s^2} \end{cases} \tag{149}$$

where σ_a is the axial stress, τ is the shear stress, E is the Young's modulus, G is the shear modulus, M is the bending moment about the neutral axis, I is the second moment of area about the neutral axis, u is the displacement in the axial direction, θ is the twist angle and w is the deflection."[36]

The lateral deflection of the pipe results in four degrees of freedom: two lateral displacements and two rotations. So altogether, there are six degrees of freedom when we add the axial displacement and the torsional twist. Addressing the problem of the lateral displacement for the whole drill-string is very computer intensive as it requires to solve a minimization problem, in order to respect the principle of least action. As we wish to create a model that is compatible with real-time constraints, we assume that as long as there is no buckling and the string is not too stiff, the bending efforts can be neglected. We are left with two variables: the axial and the torsional displacements, which are related to the tension T_s and torque τ_s by (obtained after integration of eq. (149) over a cross-section):

$$\begin{cases} T_s = EA\dfrac{\partial u(s,t)}{\partial s} \\ \tau_s = GJ\dfrac{\partial \theta(s,t)}{\partial s} \end{cases} \tag{150}$$

where A is the cross-sectional area and J the polar moment of inertia.

3.2.2 Transient Solver

"Eq. (150) shows that the elastic deformation of an element introduces a dependence on time that we would like to model. As a first approximation,

36 Excerpt from my contribution to the text of the paper by Cayeux et al. 2017 [188]

because we do not calculate the lateral displacement of the pipes in the borehole, we assume that the contact points are defined by the position of the tool-joints in the drill-string and the stabilizers in the BHA.

The second approximation concerns the assimilation of each element to a disc that is connected to the previous element by a massless spring which works both in the axial and torsional directions (see Fig. 112).

Hooke's law for a linear spring is usually expressed as:

$$F_a = k_a \Delta L \tag{151}$$

where F_a is the axial force, k_a is the spring constant and ΔL the displacement from the equilibrium position. Therefore, the element i is characterized by an equivalent linear spring constant:

$$k_{a,i} = \frac{E A_i}{l_i} \tag{152}$$

where $k_{a,i}$ is the equivalent spring constant, A_i is the cross-sectional area of the element i and l_i is the length of the element at rest. If the element has varying dimensions along its length, one shall integrate over the length to obtain the equivalent spring constant.

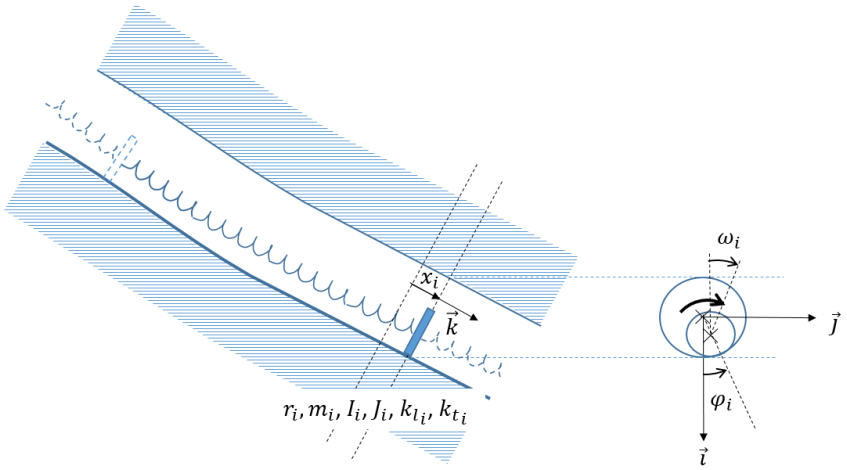

Fig. 112: Schematic representation of the assimilation of an element as solid disc connected to the previous element by a linear and torsional spring.

Similarly, the Hooke's law for a torsional spring is:

$$C_t = k_t \Delta\theta \tag{153}$$

where C_t is the torque, k_t is the torsional spring constant and $\Delta\theta$ the twist angle. Thus, an equivalent torsional spring constant can be defined as:

$$k_{t,i} = \frac{GJ_i}{l_i} \tag{154}$$

where $k_{t,i}$ is the equivalent spring constant and J_i is the polar moment of inertia. For elements with varying dimensions, it is necessary to integrate over the length, to obtain the equivalent spring constant.

The disc can move axially by a displacement x_i from its resting position and it can rotate by an angle θ_i.

The force balance on the disc at position i depends on the actions from the element at positions $i-1$ and $i+1$:

$$m_i \ddot{x}_i = -k_{a,i}(x_i - x_{i-1} - l_i) + k_{a,i+1}(x_{i+1} - x_i - l_{i+1}) + \sum_j \vec{F}_{i,j} \,.\, \hat{t} \tag{155}$$

where x_i is the curvilinear abscissa of the disc, l_i is the length at rest of the element, m_i is the lumped mass of the disk and $\vec{F}_{i,j}$ are the external forces and $\hat{t}$ is the tangent unit vector. If the element has varying dimensions along its length, one shall integrate over the length to obtain the total mass.

In addition, we have the torque balance equation:

$$I_i \ddot{\theta}_i = -k_{t,i}(\theta_i - \theta_{i-1}) + k_{t,i+1}(\theta_{i+1} - \theta_i) + \sum_j C_{i,j} \tag{156}$$

where I_i is the lumped polar moment of inertia of the element i."[37] If the element has varying dimensions along its length, one shall integrate over the length to obtain the equivalent polar moment of inertia.

37 Excerpt from my contribution to the text of the paper by Cayeux et al. (2017) [188]

In dynamic conditions, the uniaxial and shear moduli shall be considered as complex numbers, where the real part represents the elastic behavior of the material, i.e. the storage moduli which we have referred to as E and G, respectively, for the uniaxial and shear moduli, while the imaginary part characterizes a viscous effect in the material. The imaginary part is also referred as the loss coefficient and is denoted $E^{"}$ for the uniaxial modulus and $G^{"}$ for the shear modulus. The ratio of the loss and storage moduli is the loss factor. For steel the loss factor is about 0.5×10^{-3} to 0.7×10^{-3}, i.e. the loss modulus is in the range of one to two thousand times smaller than the storage modulus. The loss modulus is the source of a viscous-like force ($F_{E^{"},i}$) and torque ($C_{G^{"},i}$) that are proportional to the velocity:

$$\begin{cases} F_{E^{"},i} = -k_{E^{"},i}\dot{x}_i \\ C_{G^{"},i} = -k_{G^{"},i}\dot{\theta}_i \end{cases} \tag{157}$$

where $k_{E^{"},i}$ and $k_{G^{"},i}$ are respectively the loss modulus axial damping coefficient and the loss modulus torsional damping coefficient.

Eq. (155) can be updated with the loss force in the material:

$$\begin{aligned} m_i\ddot{x}_i = &-k_{a,i}(x_i - x_{i-1} - l_i) + k_{a,i+1}(x_{i+1} - x_i - l_{i+1}) \\ &+ F_{E^{"},i} + \sum_j \vec{F}_{i,j} \,.\, \hat{t} \end{aligned} \tag{158}$$

Similarly, eq. (156) can now be updated to include the material loss torque:

$$I_i\ddot{\theta}_i = -k_{t,i}(\theta_i - \theta_{i-1}) + k_{t,i+1}(\theta_{i+1} - \theta_i) + C_{G^{"},i} + \sum_j C_{i,j} \tag{159}$$

The material loss force and torque are sources of positive damping as they act in the opposite direction to movement and are proportional to the velocity. The natural damping of axial and torsional oscillations is observed through measurements made at the BHA and along the drill-string, and therefore even though $F_{E^{"},i}$ and $C_{G^{"},i}$ are small, they cannot be neglected.

3.2.3 Mechanical Friction

When the surface of the drill-string at a point of contact i, slips on the borehole surface, due to the combined action of an axial and rotational

movement, there is a friction force ($\vec{F}_{\mu_k,i}$) that acts in the opposite direction to the slipping movement, characterized by a velocity vector $\vec{v}_{s_i}$. The direction of the velocity vector is directly related to the axial velocity $\dot{x}_i$ and the rotational velocity at the contact between the surfaces $\dot{\theta}_i \frac{d_{p,i}}{2} \hat{b}$, where $\dot{\theta}_i$ is the angular velocity, $d_{p,i}$ is the pipe diameter at the position of contact and $\hat{b}$ is the unit vector in the tangential plane to the contact between the surfaces that is perpendicular to the tangent unit vector $\hat{t}$ and the normal vector $\hat{n}$ (see Fig. 113). Note that for drill-pipes and HWDP, the relevant diameter at the position of contact is the one of the tool-joint.

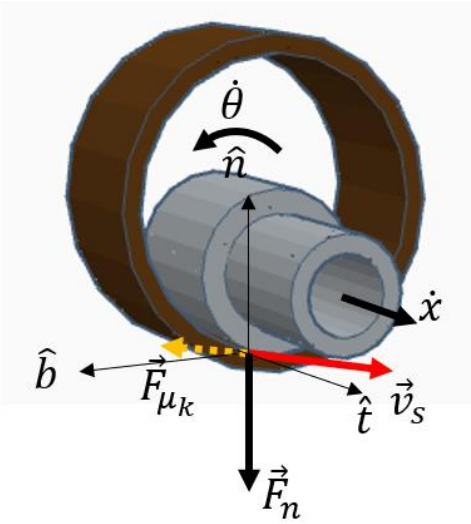

Fig. 113: Schematic representation of contact between a tool-joint and the borehole.

We can write the slip velocity at a contact point as:

$$\vec{v}_{s_i} = \dot{x}_i \hat{t} + \dot{\theta}_i \frac{d_{p,i}}{2} \hat{b} \tag{160}$$

However, if static friction applies, i.e. $v_s = 0$, then the static friction force, $\vec{F}_{\mu_s,i}$, balances exactly the sum of all external forces in the plane directed $\hat{t}$ and $\hat{b}$:

$$\vec{F}_{\mu_s,i} + \left(\sum \vec{F}_{ext,i} \,.\, \hat{t}\,\right)\hat{t} + \left(\sum \vec{F}_{ext,i} \,.\, \hat{b}\right)\,\hat{b} = 0 \tag{161}$$

The static friction force does not exceed the static friction force magnitude limit as we have seen with eq. (69). When sliding starts, the kinetic friction force can be expressed using a Stribeck formulation described by eq. (71).

We can now expand eq. (155) and (156) to include the effect of mechanical friction:

$$\begin{aligned} m_i\ddot{x}_i = {} & -k_{a,i}(x_i - x_{i-1} - l_i) + k_{a,i+1}(x_{i+1} - x_i - l_{i+1}) \\ & + F_{E",i} + \vec{F}_{g,i}.\hat{t} + \vec{F}_{b,i}.\hat{t} + \vec{F}_{\mu,i}.\hat{t} + \sum_j \vec{F}_{i,j} \end{aligned} \tag{162}$$

and

$$\begin{aligned} I_i\ddot{\theta}_i = {} & -k_{t,i}(\theta_i - \theta_{i-1}) + k_{t,i+1}(\theta_{i+1} - \theta_i) + C_{G",i} + \tau_{\mu,i} \\ & + \sum_j C_{i,j} \end{aligned} \tag{163}$$

where $\vec{F}_{g,i}$ and $\vec{F}_{b,i}$ are respectively the gravitational and buoyancy forces, $\vec{F}_{\mu,i}$ and $\tau_{\mu,i}$ are respectively the mechanical friction force and torque, either kinetic or static. Note that the static and kinetic friction factors must be calibrated: this is addressed in section 3.4.6.1.

When static friction applies, torsion and stretch may remain at the level of the contact. This explains the observation of the top-drive torque remaining high after the top-drive rotation has been stopped in deviated wells (see Fig. 34). To help untwisting the drill-string, the top-drive controller is used in torque-control mode by setting a zero-torque set-point. Consequently, the top-drive rotates in the opposite direction until the top-drive torque reaches zero. This action does remove the torque on the top-drive, but it is possible that the drill-string is still twisted and with some torque deeper into the well. Fig. 114 illustrates this situation through a simulation made with the described transient torque and drag model on an 8200m long drill-string after stopping the top-drive rotation and zero-torqueing the top of the drill-string. First, one can notice that when the top-drive speed has reached zero, the estimated top-drive torque is still large as a result of static friction keeping the drill-string twisted. Second, at the end of the simulation of the zero-torque procedure, there is still a torque along the drill-string even though the estimated top-drive torque is zero.

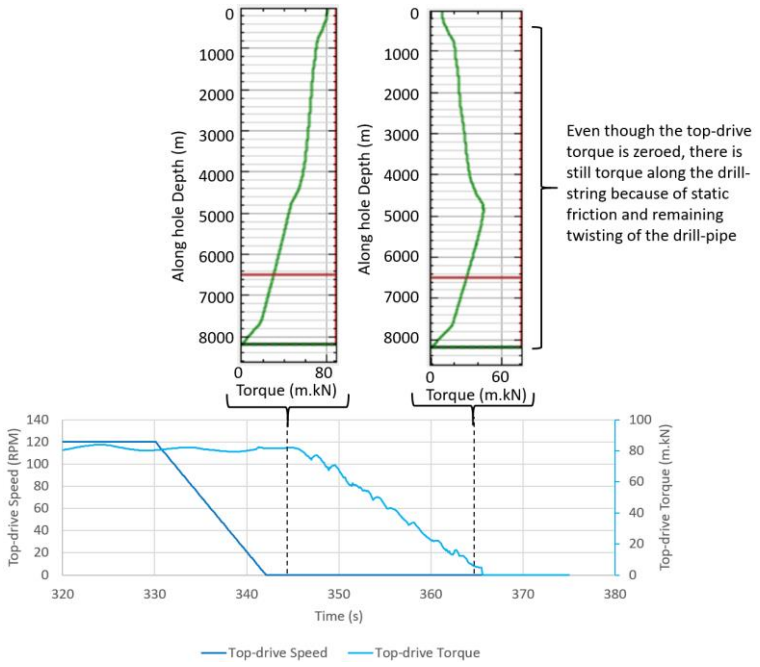

Fig. 114: After stopping the top-drive, the remaining top-drive torque is removed, yet the drill-string is still twisted at deeper depths and substantial amount of torque remains at the contact between the tool-joints and the borehole (results from simulations made with the described transient torque and drag model).

According to the Stribeck eq. (71), "$F_{\mu,i}$ increases when v_{s_i} tends to zero, therefore the mechanical friction force has a negative damping effect when the velocity gets close to zero. This can cause stick-slip situations even when the bit is off bottom and especially if the top-drive speed is somewhat moderate. In a deviated well, when the top-drive speed is ramped up from zero to a certain target value, the bottom of the drill-string does not rotate immediately, as it is necessary to counteract static friction at the contact points between the drill-string and the borehole in the deviated parts of the well. This results in a progressive increase of the top-drive torque as well as the creation of torsional waves that are reflected deeper and deeper when more and more of the drill-string gets in motion. Fig. 115 illustrates that effect with a simulation performed using the described transient torque and drag model on an ERD well at bit depth 8100mMD in a 6-in hole section. The top-drive is ramped up from 0 to 50rpm.

It takes 53s before the bit starts to rotate and when it does rotate, its estimated initial peak rotational speed reaches 110rpm. The peak amplitude for the bit rotational speed depends predominantly on kinetic and static frictions along the borehole, the shape of the trajectory, the torsional elasticity and moment of inertia of the drill-string. In practice, the longer is the drill-string and the more friction torque there is along the drill-string, the more delayed the bit will start to rotate after the top-drive has started.

After the initial peak rotational amplitude of the BHA, the bit rotational velocity decreases and may return to being stationary, therefore having parts of the drill-string being subject to static friction forces. It is therefore necessary to build up more torque along the drill-string to overcome the static friction forces and the accumulated torque can result in a new peak of rotational speed at the bit, therefore causing stick-slips even when the bit is off bottom. This effect is illustrated by Fig. 116 where off bottom stick-slip gets established with a period of 12.3s for this 8100m long drill-string while the top-drive speed is maintained constant at 50rpm.

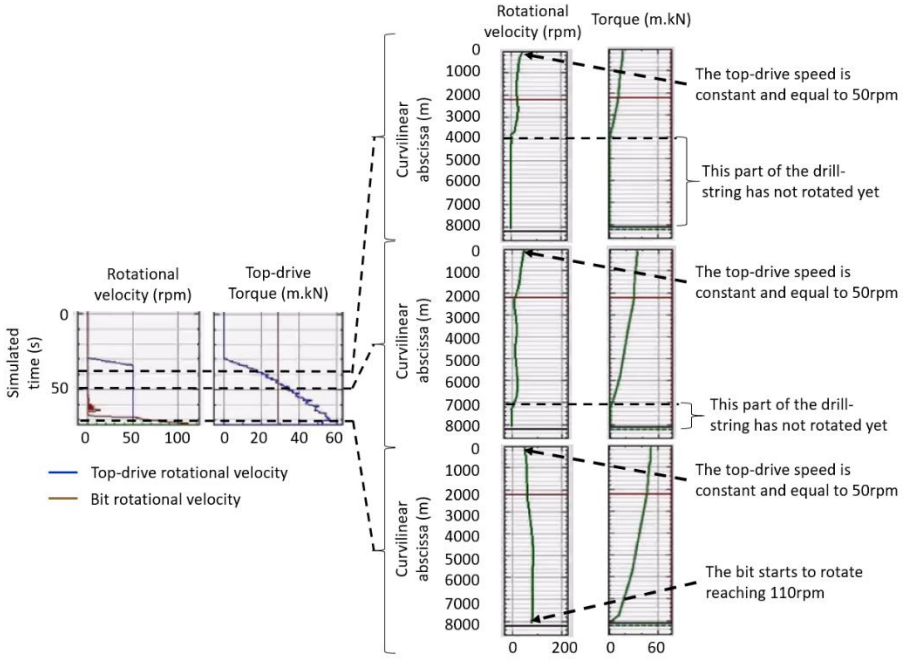

Fig. 115: When starting the top-drive in a deviated well, the bit does not rotate immediately as torque needs to be built up along the drill-string to overpass the effect of mechanical friction.

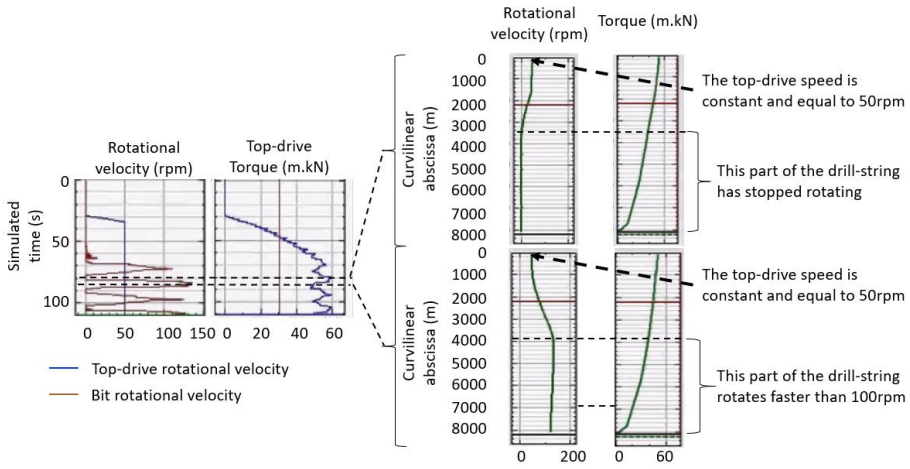

Fig. 116: After a large peak bit rotational velocity, the drill-string can enter a stick-slip mode even when the bit is off bottom because some parts of the drill-string get stationary and static friction forces necessitate an increase of torque to regain torsional motion.

This model prediction needs to be verified by actual measurements. For this, we will use measurements made with a high frequency magnetometer (more than 200Hz) while drilling several wells in the North Sea.

The recommended procedure for top-drive startup is often to ramp up the rotational speed in stages until the nominal rotational speed is reached. The motivation for this practice is to be gentle with the casing and open hole formations during the drill-string rotational acceleration. Yet, if we look at the measured rotational speed of the BHA, measured with the high frequency magnetometer (see Fig. 117 and Fig. 118), for these particular examples, for top-drive rotational speeds below 140rpm, there are systematic stick-slip situations.

Typically, the peak rotational speed of the BHA is larger than twice of the top-drive speed. For instance, we can see on Fig. 118 that for a top-drive speed of 30rpm, the peak BHA rotational speed reaches 200rpm. On the other hand, for this particular case, when the top-drive speed is larger than 140rpm, torsional oscillations at the BHA are damped out quickly.

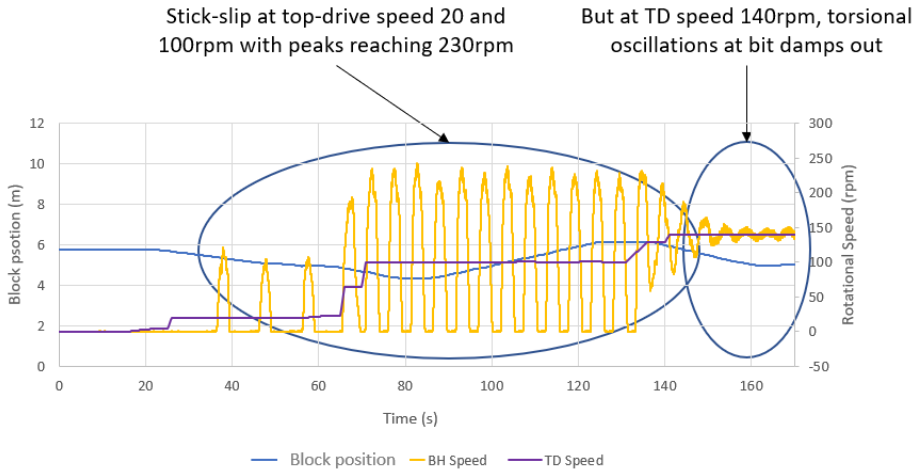

Fig. 117: Top-drive startup for the 3rd drilled stand (bit depth 3376mMD) during the drilling of an 8 ½ x 9 ½ -in section (the bottom hole speed is measured with a high frequency magnetometer).

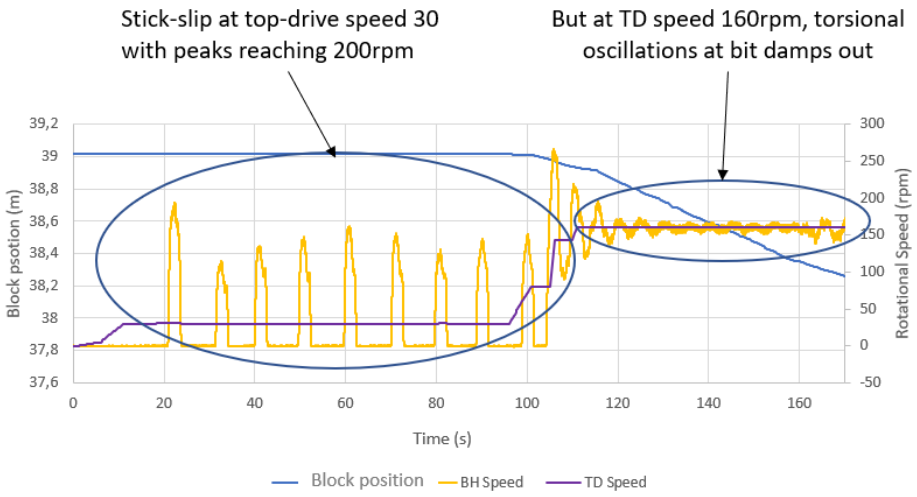

Fig. 118: Top-drive startup for the 5th drilled stand (bit depth 3422mMD) during the drilling of an 8 ½ x 9 ½ -in section (the bottom hole speed is measured with a high frequency magnetometer).

Also, one can notice that the downhole rotation is delayed by about 10s compared to the start of the top-drive, for a drill-string length of approximatively 3400m."[38]

Another effect of mechanical friction is that when kinetic friction applies, eq. (160) introduces a dependence between eq. (162) and (163) at every contact point. Let us return to the friction test example of Fig. 34. We have seen that there is still a torque on the drill-string when the top-drive has stopped. In the example of Fig. 34, the driller has not applied the zero torque function of the top-drive controller and the drill-string is still twisted when the pick-up phase of the friction test is started. As the drill-string is picked up, it both moves axially and at the same time untwists, as a consequence of the dependence between eq. (162) and (163) through eq. (160). The trapped torque along the string dissipates while the drag forces increase, resulting in a progressive increase of the hook-load. Fig. 119 compares the measured top-drive torque and hook-load with the estimated values obtained from the transient torque and drag model. One can see a close similarity between the measured and modelled values.

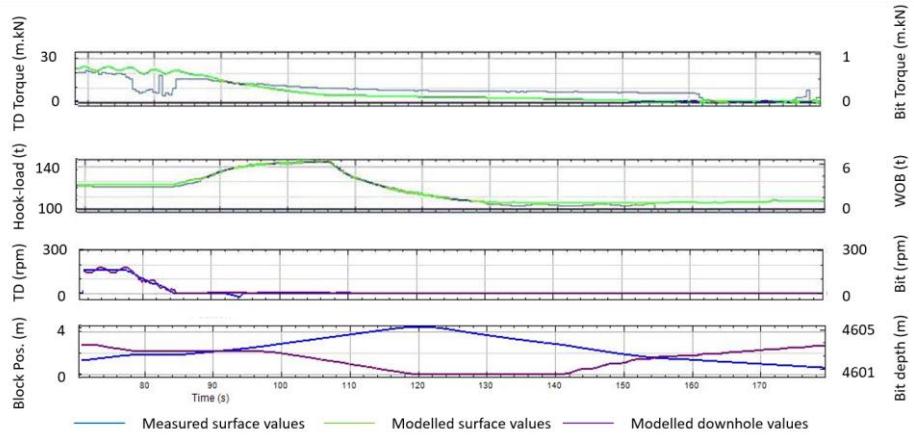

Fig. 119: Comparison of modelled and measured values during the execution of a friction test (corresponding to Fig. 34).

38 Excerpt from my contribution to the text of the paper by Cayeux et al. 2020 [173]

Fig. 120 illustrates the level of dynamic that can be reproduced with the described transient mechanical model. In this example, after drilling a stand in a horizontal well, the drill-string is picked up off bottom and the top-drive is stopped. The rig is subject to heave and the heave compensator is turned off. The blue curves are for measured values and the green and brown curves are for respectively estimated values at the top-side and downhole. It is interesting to notice that the model can reproduce the slow decrease of top-drive torque that takes place after the top-drive speed has reached zero.

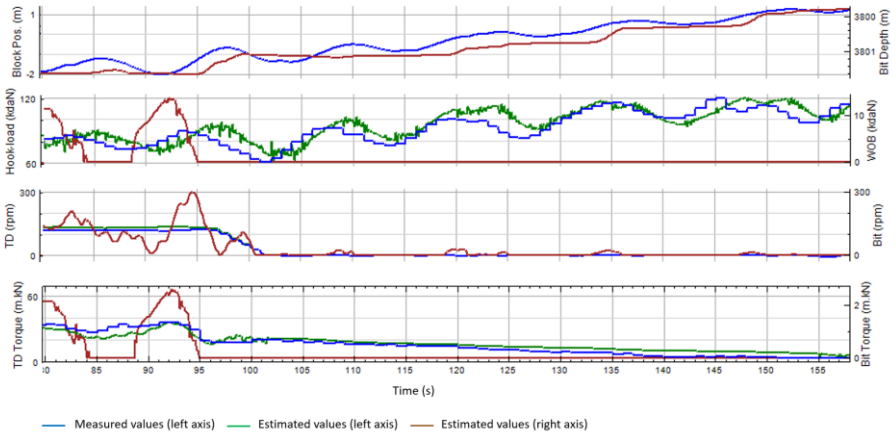

Fig. 120: Estimation of bit depth, hook-load, WOB, top-drive torque, and bit rotational velocity utilizing the described transient mechanical model while picking up the drill-string off bottom, stopping the top-drive after the heave compensator has been turned off, on a rig subject to heave.

3.2.4 Forces Related to Viscous Flow

When the drill-string and the drilling fluid contained in the annulus are in relative motion, there is a viscous force ($F_{v,i}$) acting on an element of surface S:

$$\vec{F}_{vp,i} = -\iint_S \tau_{w,i} \frac{\vec{v}_i}{\|\vec{v}_i\|} ds \tag{164}$$

where $\tau_{w,i}$ denotes the wall shear stress and $\vec{v}_i$ is the relative velocity of the pipe compared to the fluid. The shear stress at the wall is determined using eq. (19) for turbulent and transitional flow and (20) for laminar flow.

In a similar way as the shear stress at the wall in a Couette rheometer generates a torque when there is rotation, the viscous fluid stress at the wall engenders a torque on the pipe body when the pipe rotates. This torque ($C_{v,i}$) can be approximated using standard Couette rheometer formulations like the one given by eq. (12) where the cup and bob radii are respectively replaced by the wellbore ($\frac{d_{0,i}}{2}$) and pipe ($\frac{d_{p,i}}{2}$) radii, and the length is the element length.

Note that $F_{v,i}$ and $C_{v,i}$ are in most cases small compared to other forces and torques. For instance, in an 8 ½-in hole size, with 5 ½-in drill-pipes and with a relatively viscous fluid described by a Herschel-Bulkley behavior like $\tau = 7 + 2.2\dot{\gamma}^{0.48}$, at a flowrate of 2700l/min, the shear rate at the wall is approx. 500s^{-1} and therefore the shear stress at the drill-pipe wall is about 50Pa. The surface area of 1m of 5 ½-in drill-pipe is approx. 0.015m^2 and therefore the axial viscous force is not larger than 0.77N/m. Similarly, for the same example, with a rotational speed of 160rpm, the viscous torque per unit length is approx. 0.57 N.m/m. These terms are small, but yet of comparable magnitude as the forces and torques originating from the loss component of the material complex moduli. They are also a source of positive damping as they always act in the opposite direction to the relative movement of the string compared to the fluid and increase in magnitude with the relative velocity.
Eq. (162) can now be updated to account for the viscous damping force:

$$\begin{aligned} m_i\ddot{x}_i = &-k_{a,i}(x_i - x_{i-1} - l_i) + k_{a,i+1}(x_{i+1} - x_i - l_{i+1}) \\ &+ F_{E",i} + \vec{F}_{g,i}.\hat{t} + \vec{F}_{b,i}.\hat{t} + \vec{F}_{\mu,i}.\hat{t} + \vec{F}_{v,i}.\hat{t} \\ &+ \sum_j \vec{F}_{i,j} \end{aligned} \tag{165}$$

And similarly, the viscous damping torque can be included in eq. (163):

$$\begin{aligned} I_i\ddot{\theta}_i = &-k_{t,i}(\theta_i - \theta_{i-1}) + k_{t,i+1}(\theta_{i+1} - \theta_i) + C_{G",i} + \tau_{\mu,i} \\ &+ C_{v,i} + \sum_j C_{i,j} \end{aligned} \tag{166}$$

"Another external force that is applied on the drill-string is related to hydraulic pressure. In hydrostatic conditions and without drill-string movement, the effect of pressure translates into the buoyancy force that applies on the tubulars. But when the fluid moves, either because of pumping or because of the drill-string own motion, there are frictional pressure losses. The resulting pressure gradient is oriented in the axial direction. The integration of the axially directed pressure gradient on an axisymmetric tube does not result in an external force.

However, for each change of pipe diameter, the axially directed pressure gradient engenders a net force that is axially oriented (see Fig. 121). This concerns for instance the flanks of tool-joints, the change of pipe diameters and the bit.

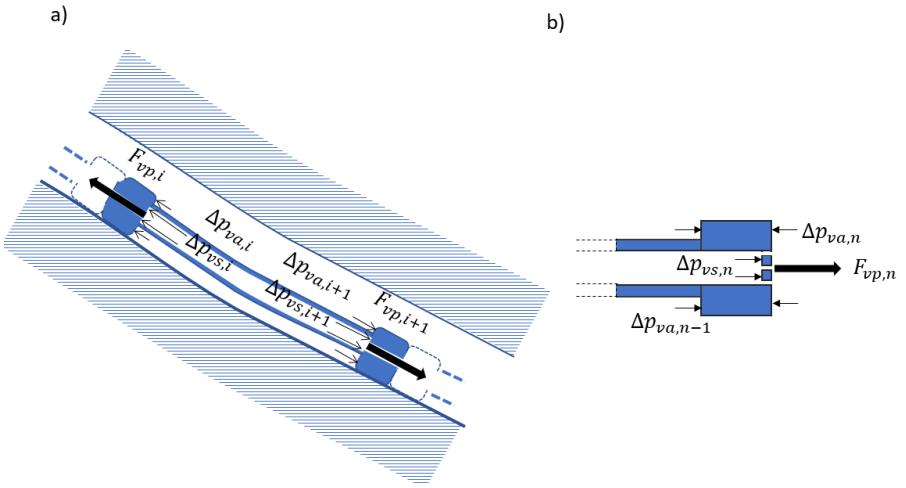

Fig. 121: The axially oriented pressure gradient resulting from viscous pressure losses engender a force on the flanks of tool-joint (a) and at the bit (b).

The resulting viscous pressure loss force, $F_{vp,i}$, exerted at one side of a tool-joint is:

$$F_{vp,i} = \Delta p_{vs,i}\left(A_{pi,i} - A_{tji,i}\right) + \Delta p_{va,i}\left(A_{tjo,i} - A_{po,i}\right) \qquad (167)$$

where $\Delta p_{vs,i}$ and $\Delta p_{va,i}$ are respectively the pressure difference between the inside and outside of the string at position i and the hydrostatic pressure at that location, $A_{pi,i}$ and $A_{po,i}$ are respectively the area of the inside and outside of the pipe body and $A_{tji,i}$ and $A_{tjo,i}$ are respectively the area of the inside and outside of a tool-joint. Similar calculations can be made for any change of pipe diameters.

Eq. (162) can now be updated with the additional effect of viscous pressure gradient:

$$\begin{aligned} m_i\ddot{x}_i = &-k_{a,i}(x_i - x_{i-1} - l_i) + k_{a,i+1}(x_{i+1} - x_i - l_{i+1}) \\ &+ F_{E",i} + \vec{F}_{g,i}.\hat{t} + \vec{F}_{b,i}.\hat{t} + \vec{F}_{\mu,i}.\hat{t} + \vec{F}_{v,i}.\hat{t} \\ &+ F_{vp,i} + \sum_j \vec{F}_{i,j} \end{aligned} \tag{168}$$

Note that the length at rest, l_i, is also impacted by the current conditions of pressure inside the string and the annulus through the ballooning effect as described by eq. (75).

During circulation and when steady state conditions are reached, the viscous pressure loss gradients inside the string and in the annulus are constant. The overall effect is a change of drag forces along the drill-string that is reflected on the hook-load. Fig. 122 shows how the free-rotating weight (FRW) is impacted by a change of flow rate and how it reasonably matches the measured FRW while performing two consecutive friction tests under different circulation rates (see Cayeux et al. 2017 for more details about that example).

Swab and surge pressure variations influence the viscous pressure loss force and the elastic-related force through at least pipe ballooning effect. To keep the force balance equations of the system of equations (168) in balance, the other terms of the equation shall change. The gravity force is not influenced by the hydraulic pressure variation. The buoyancy force is marginally influenced through pipe volume variations due to ballooning and drilling fluid mass density modifications caused by variations of the in-situ pressure conditions. Of course, the acceleration term, $m_i\ddot{x}_i$, can change, and less obviously, the axial component of the mechanical friction term, $\vec{F}_{\mu,i}.\hat{t}$. Indeed, as normal forces on the drill-string are not much impacted by swab and surge pressures, the kinetic friction force magnitude remains unaltered.

This being said, the axial component of the friction force can still change by changing the direction of the friction force, i.e. by changing the rotational speed at the level of the contact point (see Fig. 123). The resulting change of kinetic friction torque impacts eq. (163) and therefore generates a change of rotational speed.

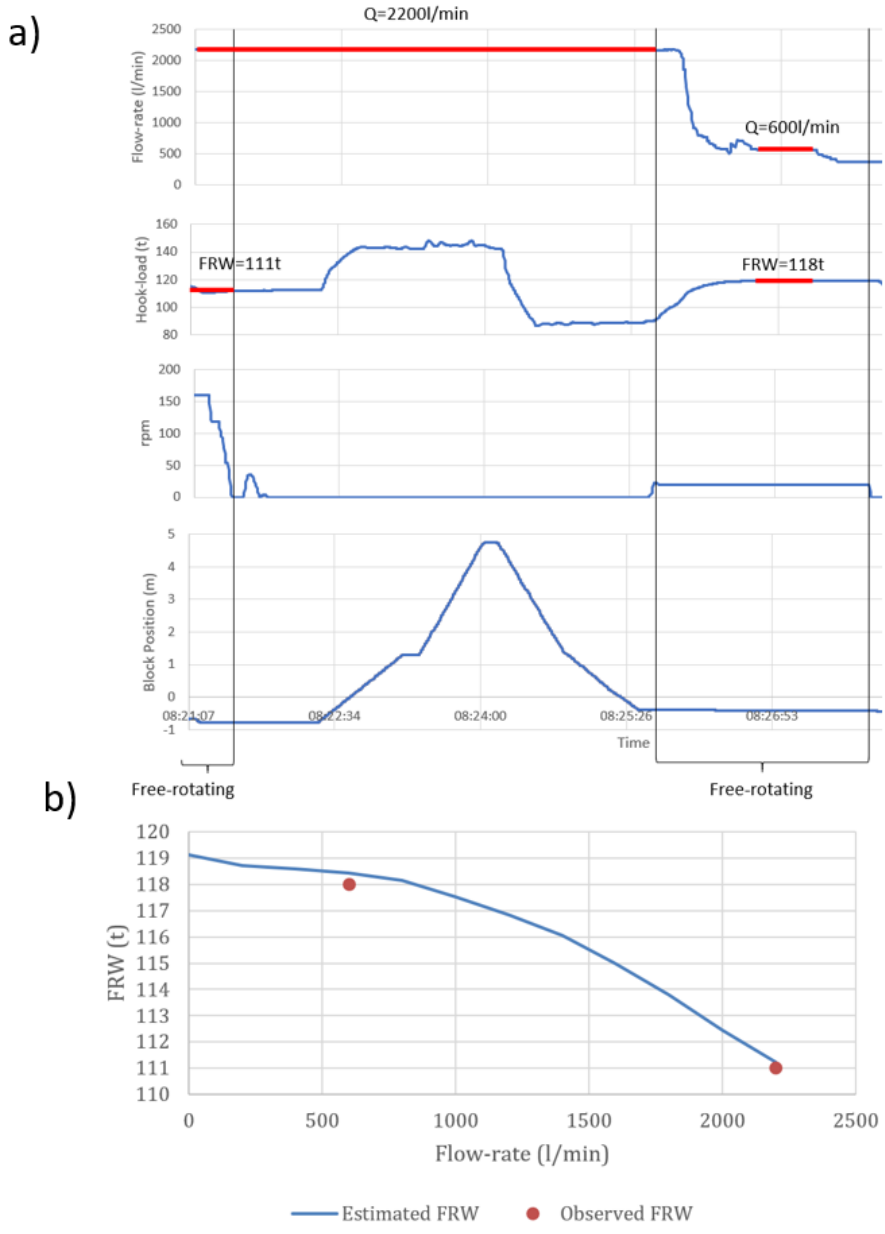

Fig. 122: Effect of circulation on the free rotating weight (FRW)(ref. fig. 21 in Cayeux et al. 2017).

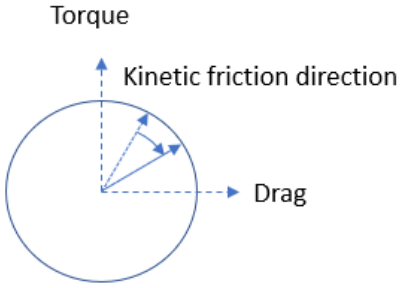

Fig. 123: If the magnitude of the kinetic friction force is constant, a change of axial kinetic friction results in a change of torsional friction.

Thus, axial movement of the drill-string may trigger a change of rotational speed by the effect of viscous pressure gradient induced forces. However, reaming up generates swabbing pressures. As swabbing decreases the annular viscous pressure forces, the sum of the other terms in the partial differential equation shall increase, that also includes the axial mechanical friction. An increase of the axial mechanical friction corresponds to a decrease of the tangential mechanical friction force, which in turn must reduce the mechanical friction torque. This has a positive damping effect on torsional oscillations. On the other hand, reaming down generates surging pressures, which increase the annular viscous pressure forces. Consequently, the sum of the other terms of the equation shall decrease, including the axial mechanical friction. A decrease of the axial mechanical friction results in an increase of the tangential mechanical friction and therefore of the mechanical frictional torque. This has a negative impact on torsional oscillation damping as increasing axial velocity tends to increase frictional torque.

This is illustrated by Fig. 124. The top-drive rotation is kept constant at 180rpm while the WOB drops to zero: there are no significant torsional oscillations. Then a ream-up sequence is initiated at 0.15m/s while keeping the rotational speed constant. Torsional oscillations are triggered, but they are damped out while raising the top of string by 9m. When the axial velocity returns to zero, new torsional oscillations are initiated, and they damp out slowly during the free rotating period of 60s. For the reaming-down sequence at -0.15m/s, torsional oscillations are again triggered. This time, the torsional

oscillations amplify throughout the 9m displacement. Note that during the whole simulation, the flow rate is kept constant.

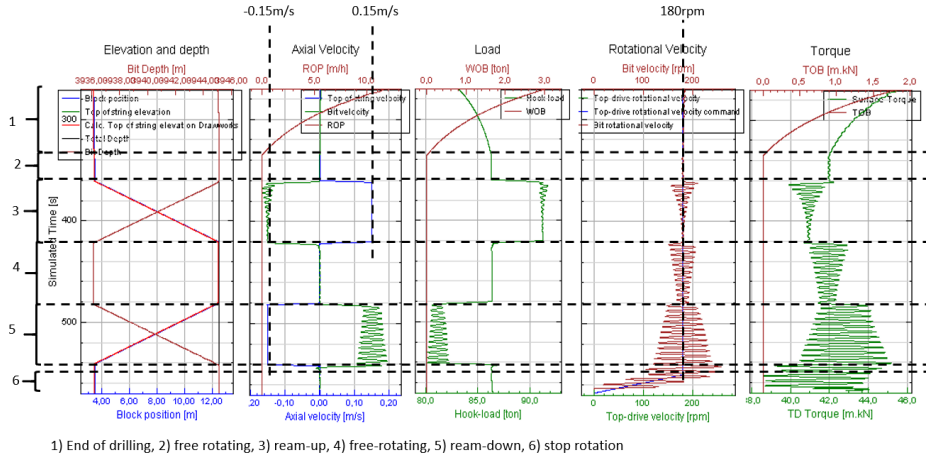

Fig. 124: In this simulation, after a free rotating period a ream-up followed by a free-rotating and finally a ream-down sequence is initiated. Each change of axial velocity (first from 0 to 0.15m/s, from 0.15 to 0ms/s and from 0 to -0.15m/s) trigger torsional oscillations. While reaming up, the torsional oscillations are damped, but for the reaming down sequence, the torsional oscillations are amplified. During the whole sequence the flowrate is constant.

The transient hydro-mechanical model predicts that changes in axial directions may cause torsional oscillations and that reaming up may be associated with positive damping of torsional oscillations while reaming down may cause negative damping and possibly stick-slip situations. This is counterintuitive and needs to be confirmed by actual measurements.

Fig. 125 shows the first reciprocation procedure that is performed after drilling about 300m of the reservoir section of a deviated well in the North Sea. First, we can see that the downhole high frequency rotational speed measurements confirm that torsional oscillations are triggered by both changing axial direction and top-drive speed. Second, the torsional oscillations during the ream-up sequence are damped out after 2.5m of top of string displacement. Third, during the ream-down leg of the reciprocation sequence, the torsional oscillations seem to amplify. We can also notice that the ream-up hook-load is larger than the free rotating weight and that the ream-down hook-load is lower

than the free rotating weight, therefore indicating that surging and swabbing pressures influence axial loads along the drill-string.

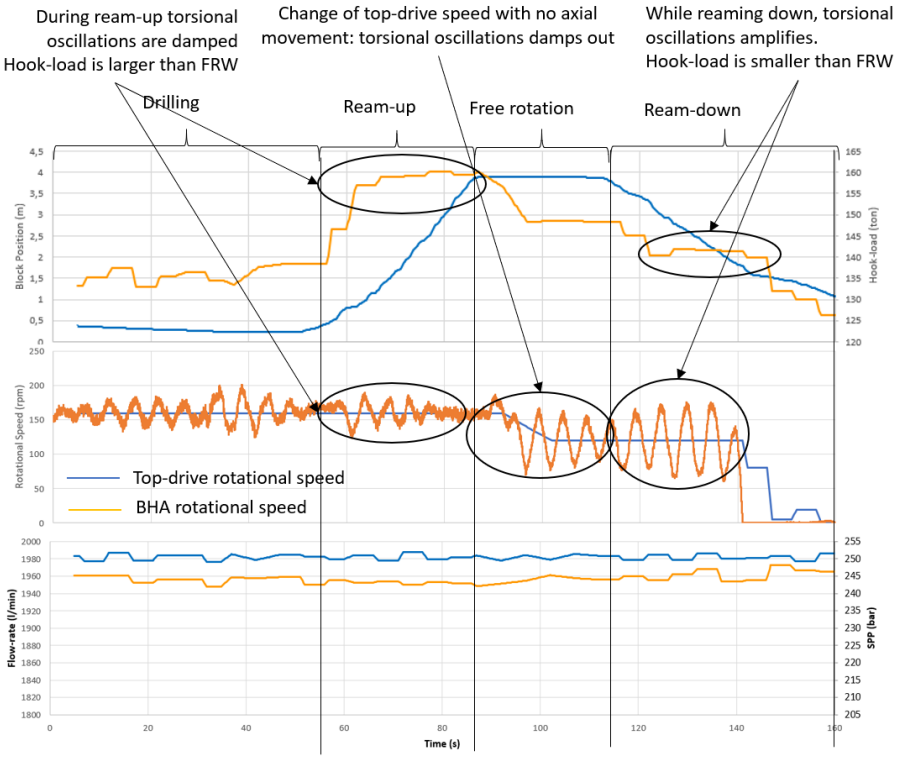

Fig. 125: Reciprocation procedure at bit depth 3574mMD after 300m of drilling (measurements made with a high frequency magnetometer).

Another reciprocation procedure executed after drilling 700m is shown on Fig. 126. Similar observations can be made as for Fig. 125 except that this time, the drill-string experiences stick-slip oscillations while reaming down.

This being said, swab and surge pressures do not generate systematically changes in torsional oscillations. In some case, their effects may be too small like when moving a drill-string in a 17 ½-in hole size, and in other conditions, the path of least resistance to balance eq. (168) may simply be a change of axial acceleration and/or elastic axial displacements.

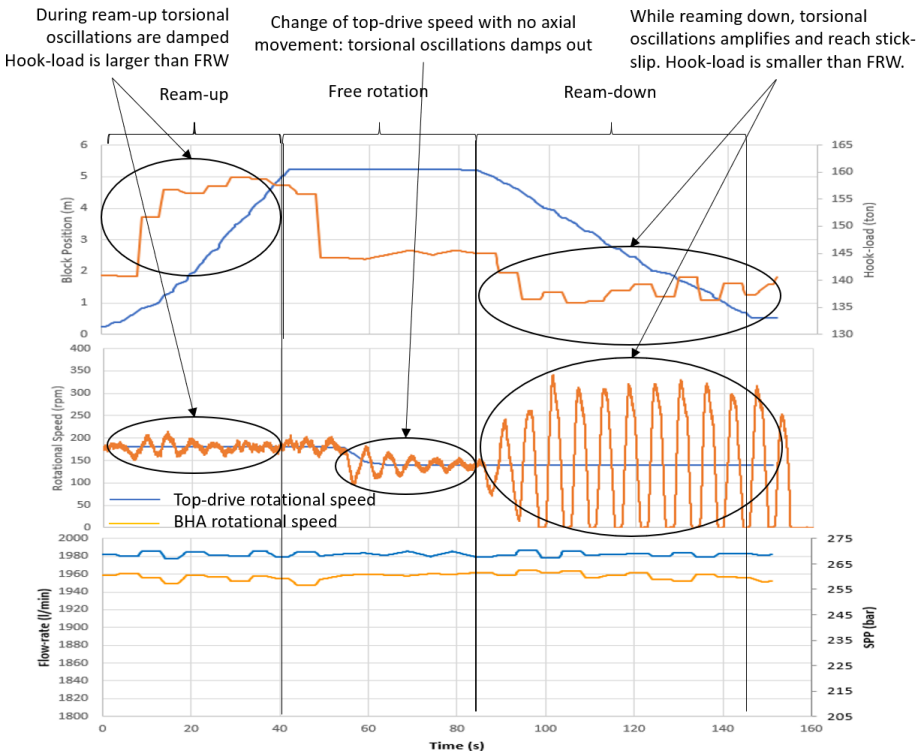

Fig. 126: Reciprocation procedure at bit depth 3956mMD after drilling 700m (measurements made with a high frequency magnetometer)."[39]

3.2.5 Boundary Condition at the Bit

When off bottom, the bit movement is governed by similar equations as eq. (166) and (168), except that there is no element below the bit:

$$m_n\ddot{x}_n = -k_{a,n}(x_n - x_{n-1} - l_i) + F_{E",i} + \vec{F}_{g,n}.\hat{t} + \vec{F}_{b,n}.\hat{t} + \vec{F}_{\mu,n}.\hat{t} + \vec{F}_{v,i}.\hat{t} + F_{vp,n} + \sum_j \vec{F}_{n,j} \quad (169)$$

and

39 Excerpt from my contribution to the text of the paper by Cayeux et al. 2020 [173]

$$I_n\ddot{\theta}_n = -k_{t,n}(\theta_n - \theta_{n-1}) + C_{G",n} + \tau_{\mu,n} + C_{v,n} + \sum_j C_{n,j} \tag{170}$$

where n is the index of the bit.

When the bit is on bottom, its axial position is constrained by the bottom hole depth. Yet, the bottom hole depth is not constant since we drill at a velocity $\bar{v}_{bit}$. Eq. (169) can now be written:

$$\begin{aligned} m_n\dot{\bar{v}}_{bit} = -k_{a,n}\left(\int_{t_0}^{t}\bar{v}_{bit}dt - x_{n-1} - l_i\right) + F_{E",n} + \vec{F}_{g,n}.\hat{t} \\ + \vec{F}_{b,n}.\hat{t} + \vec{F}_{\mu,n}.\hat{t} + \vec{F}_{v,n}.\hat{t} + F_{vp,n} + \bar{F}_{bit} \\ + \sum_j \vec{F}_{n,j} \end{aligned} \tag{171}$$

where $\bar{F}_{bit}$ is the axial force on the bit exerted by the formation and t_0 is the time at which the bit gets in contact with the formation . Furthermore, eq. (170) should be adjusted for the torque on bit ($\bar{\tau}_{bit}$):

$$\begin{aligned} I_n\ddot{\theta}_n = -k_{t,n}(\theta_n - \theta_{n-1}) + C_{G",n} + \tau_{\mu,n} + C_{v,n} + \bar{\tau}_{bit} \\ + \sum_j C_{n,j} \end{aligned} \tag{172}$$

To estimate the axial movement of the bit, we need to evaluate the rate of penetration and therefore we need to choose a bit/rock interaction model. We have opted for the ROP model based on the MSE as suggested by Dupriest and Koederitz (2005) [116] combined with the bit torque model of Pessier and Fear (1992) [107], both being succinctly described in section 2.1.2.7:

$$\begin{cases} \bar{v}_{bit} = \dfrac{|\bar{\tau}_{bit}|\dot{\bar{\theta}}_n}{\dfrac{CCS.A_{bit}}{\eta_{bit}} - |\bar{F}_{bit}|} \\ \bar{\tau}_{bit} = \mu_{k\,bit}d_{bit}|\bar{F}_{bit}|sign(\dot{\bar{\theta}}_n) \end{cases} \tag{173}$$

where $\dot{\bar{\theta}}_n$ is the average bit rotational velocity over a short time window (typically in the range of 100ms). We combine these equations with the bit friction model from Caicedo and Calhoun (2005) [108] which is described by eq. (78). We finally obtain:

$$\bar{v}_{bit} = \frac{\mu_{ref} e^{-\alpha_{ref}\, CCS} d_{bit} |\bar{F}_{bit}| \bar{\dot{\theta}}_n}{\left(\frac{CCSA_{bit}}{\eta_{bit}} - |\bar{F}_{bit}|\right)} = \frac{H_1 |\bar{F}_{bit}| \bar{\dot{\theta}}_n}{H_2 - |\bar{F}_{bit}|} \tag{174}$$

where we pose that $H_1 = \mu_{ref} e^{-\alpha_{ref}\, CCS} d_{bit}$ and $H_2 = \frac{CCSA_{bit}}{\eta_{bit}}$ as these two numerical groups are functions of the current bit condition ($\eta_{bit}, \mu_{ref}, \alpha_{ref}$) and the formation through the CCS, and therefore do not contribute to short time scale acceleration effects. In theory, the denominator of eq. (174) can turn to be zero or negative, if $\frac{CCS}{\eta_{bit}} A_{bit} \leq |\bar{F}_{bit}|$, which would mean that the ROP would be infinite or negative. In practice, CCS is usually a very large number and the denominator is therefore strictly positive. In unconsolidated or very weak formations, the CCS may be small, but then the WOB tends to be small as well. We have therefore a ROP model that depends on four parameters that need to be calibrated. Note that the calibration of the bit/rock model will be discussed in sections 3.4.6.3.

After injecting the expression of the bit velocity of eq. (174) and the expression of the torque on bit of the second eq. of (173) in eq. (171) and (172), those two equations only depend on $\bar{F}_{bit}$ and θ_n, which are then considered the two variables of the system of differential equations at the bit.

Note that if the bit rotational speed reaches zero while there is a WOB, static friction condition applies, i.e. it is only when the torque at the bit is larger than the static friction torque limit that the bit starts to rotate again. We utilize a Stribeck model for the transition to static friction conditions. The force and torque balance equations are:

$$\begin{aligned} 0 = -k_{a,n}(x_n - x_{n-1} - l_i) + F_{E",n} + \vec{F}_{g,n}.\hat{t} + \vec{F}_{b,n}.\hat{t} + \vec{F}_{\mu,n}.\hat{t} \\ + \vec{F}_{v,n}.\hat{t} + F_{vp,n} + \bar{F}_{bit} + \sum_j \vec{F}_{n,j} \end{aligned} \tag{175}$$

and

$$0 = -k_{t,n}(\theta_n - \theta_{n-1}) + C_{G",n} + \tau_{\mu,n} + C_{v,n} + \bar{\tau}_{bit} + \sum_j C_{n,j} \tag{176}$$

Consequently, the unknown of the problem at the bit are not anymore x_n and θ_n as they are known from the previous time step calculation, but $\bar{F}_{bit}$ and $\bar{\tau}_{bit}$. As soon as the torque on bit exceeds the static friction limit, eq. (171) and (172)

should be used. This corresponds to a stick-slip scenario caused by the bit/rock interaction.

At this point, it is possible to utilize the transient mechanical model to estimate the movement, forces and torques along the whole drilling system, when the bit is on bottom and drilling. Fig. 127 illustrates that with such a model, it is possible to estimate the smooth evolution of the bit depth while drilling a horizontal section from a floater utilizing passive heave compensation.

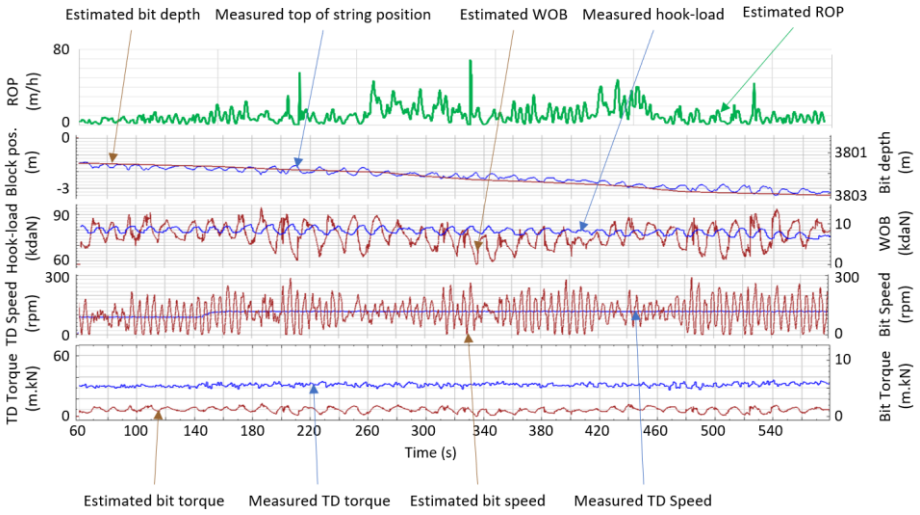

Fig. 127: Illustration of the estimation of the bit depth and ROP while drilling a horizontal section from a floater with passive heave compensation.

The estimated WOB and bit rotational velocity varies continuously as the consequence of the top of string residual movement caused by imperfect heave damping. The estimated instantaneous ROP varies according to those variations of WOB and bit rotational velocity, but it stays within physically sound limits (here less than 60m/h). This contrasts with the instantaneous ROP calculated only with the block position, which is zero most of the time with sporadic spikes reaching several hundred meters per hour. Therefore, we have a solution to the challenge described in section 2.1.2.2 and illustrated by Fig. 36: with such a model, the production of cuttings is continuous and more realistic than utilizing only surface measurements for the estimation of the bit depth and ROP.

3.2.6 Effect of Solid Particle Grinding on Torque

As discussed in section 3.1.4.3, solid particles may get trapped under the tool-joints and therefore be grinded. Eq. (146) relates the grinding power at the tool-joint to an additional torque and the rotational velocity.

"In the current context, we want to estimate the grinding torque arising from the change of particle size. Therefore, we need to estimate the particle dimension after it has passed between the tool-joint and the borehole wall. First, we assume that when a particle is ground, it breaks, in most cases, into two pieces of similar dimensions, i.e. the volume of a ground particle is about half of the original one:

$$V_2 = \frac{1}{2}V_1 \Leftrightarrow \frac{\pi}{6}d_2^3 = \frac{\pi}{12}d_1^3 \Leftrightarrow d_2 = \sqrt[3]{\frac{1}{2}}d_1 \tag{177}$$

where V_1 and V_2 are respectively the particle volume of generations 1 and 2, d_1 and d_2 are respectively the equivalent particle diameter of the particles for the generations 1 and 2. Recursively, the equivalent diameter at generation j is $d_j = \left(\sqrt[3]{\frac{1}{2}}\right)^j d_1 = 2^{-\frac{j}{3}}d_1$. We can therefore conclude that the particle diameter follows a logarithmic scale. Second, if the side force between the tool-joint and the borehole is zero, there is no grinding and therefore at $F_n = 0$, $d_{s_i} = d_{s_o}$. However, the larger the side force is, the more chances there are that a particle gets broken apart several times when passing under the tool-joint. So, the output particle size can be considered as a monotonic function of the side force at the tool-joint. Finally, if there is no rotation, there is no grinding, i.e. $\dot{\theta}_{TJ} = 0 \Longrightarrow d_{s_i} = d_{s_o}$, and the faster the rotation, the more grinding effect is produced (Jayasundar et al. 2010) [172]. So, as a simple approximation, we assume that the output particle size is related to the side force and the rotational speed of the tool-joint by:

$$\log\frac{d_{s_i}}{d_{s_o}} = K_s|F_n|\left|\dot{\theta}_{TJ}\right| \Leftrightarrow d_{s_o} = \frac{d_{s_i}}{10^{K_s|F_n|\left|\dot{\theta}_{TJ}\right|}} \tag{178}$$

where K_s is a scaling factor.

We can now integrate the grinding torque at the tool-joint in the torque equation:

$$I_i\ddot{\theta}_i = -k_{t,i}(\theta_i - \theta_{i-1}) + k_{t,i+1}(\theta_{i+1} - \theta_i) + C_{G",i} + \tau_{\mu,i} + C_{v,i} + \tau_{TJ_g} + \sum_j C_{i,j} \quad (179)$$

If the number of cuttings particles that pass between the tool-joint and the borehole increases, so does the grinding torque. To balance the torque equation, the rotational speed must decrease. But if the local rotational speed decreases then there are even fewer cuttings particles that can be transported in suspension. In a deviated well, that translates to even more particles that drop to the low side of the borehole therefore contributing further to the feed of particles to be ground. The effect is a negative damping of torsional oscillations that can end up to a full stop and therefore in a stick-slip situation (see Fig. 128). The ability to transport cuttings as a function of the current fluid velocity and drill-string rotational speed is estimated as described in section 3.1.4.2.

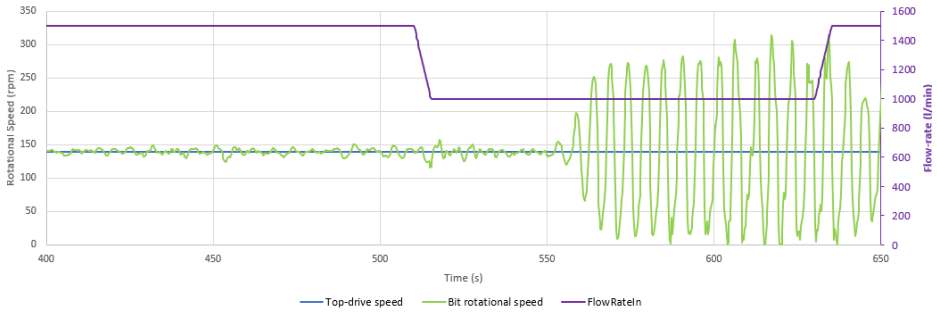

Fig. 128: Simulation of the change of flow-rate from 1500 to 1000l/min while transporting cuttings provoking stick-slip as cuttings that were transported in suspension at the high flow-rate sediment with the lower circulation rate.

Fig. 129 and Fig. 130 show the measured downhole rotational speed around the moment when downlinking to the RSS has been made for the 3rd, 4th and 6th stands after starting drilling the 8 ½-in section of a well in the North Sea. Note that there were two downlinks during the 3rd stand and no downlinking during the 5th stand.

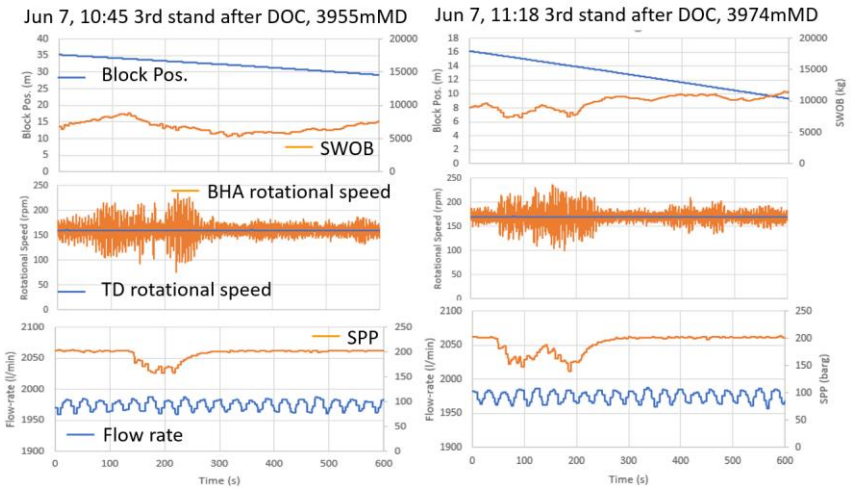

Fig. 129: Measured rotational speed in the BHA around the downlinking procedures to the RSS while drilling the 3rd stand (measurements made with a high frequency magnetometer).

We can notice that for stands #3 and #4 there are no exceptional torsional oscillations other than those that could be expected while drilling. However, for the 6th stand, the drill-string enters full stick-slip torsional oscillations, toward the end of the downlinking procedure. Thereafter, almost every downlinking procedure to the RSS is accompanied by full stick-slip conditions, except for a few ones where the top-drive speed has been kept around 180rpm.

A possible explanation for these observations could be the above-described interaction between cuttings transport and torque when the position of cuttings in a cross-section is disturbed by the flow rate variations utilized to downlink to the RSS. For this example, there is a tapered wellbore architecture with a 10 ¾-in liner hanging at 1615mMD in a 13 5/8-in casing (for more details see Cayeux et al. 2020 [173]). Indeed, for the first four drilled stands, cuttings are still inside the 10 ¾-in liner, while after the 5th stand, it is estimated that the cuttings shall be transported inside the 13 5/8-in casing at an inclination of about 43°. The reduction of fluid velocity in the larger borehole size makes it more difficult to keep the cuttings in suspension.

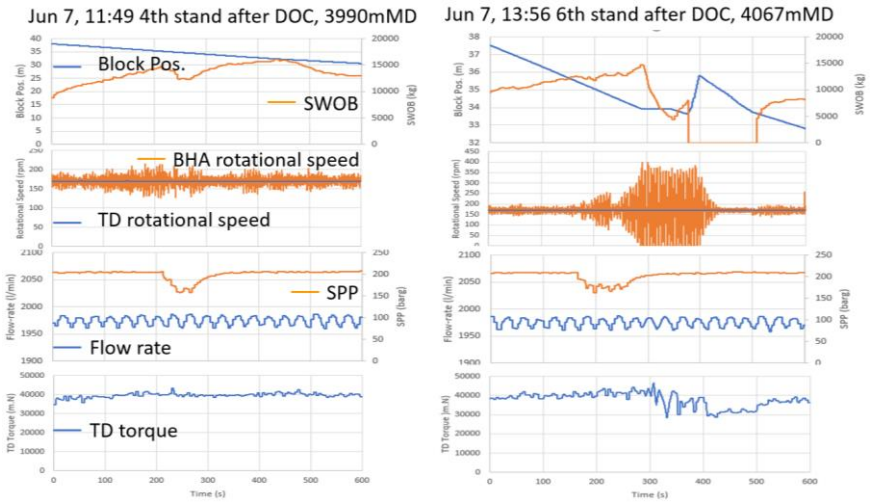

Fig. 130: Measured rotational speed in the BHA around the downlinking procedures to the RSS while drilling the 4th and 6th stand (measurements made with a high frequency magnetometer).

A hole cleaning characteristic is shown on Fig. 131 as a function of the flow rate and top-drive speed. This hole cleaning characteristic represents the integral along the annulus of the hole cleaning index (HCI) defined by Froitland et al. (2011) [43]. As the typical flow rate used to drill this section is just below 1900l/min, top-drive speeds that are lower than 160rpm may raise the risk for deteriorated cuttings transport. During down-linking, the flow rate reduces intermittently to 1500l/min, and for such a flow rate, the top-drive speed shall exceed 170rpm to provide enough cuttings transport capabilities.

The transient hydro-mechanical model is used to reproduce the first 15min of drilling with stand #7 at bit depth 4100mMD (see Fig. 132). Both the stick-slip situations occurring at the top-drive startup and toward the end of the downlinking procedure are reproduced with similar effects as those measured by the high frequency magnetometer. Per se, this is not a proof that cuttings transport interaction with dynamic drill-string mechanics is the cause for the observed stick-slip situations, but it is interesting to see the similarities between actual observations and modelling results.

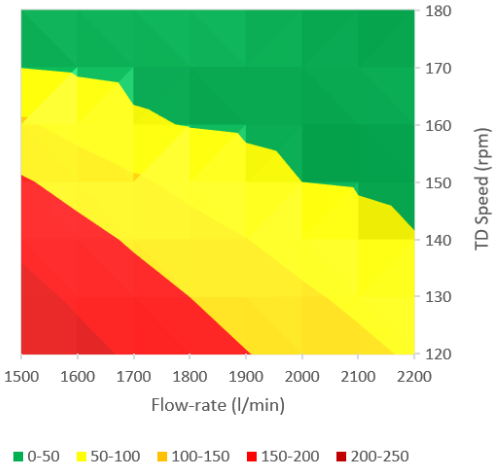

Fig. 131: Map of the hole cleaning characteristic estimated for bit depth 4100mMD as a function of flow rate and top-drive speed. Green regions indicate good hole cleaning while red areas indicate poor hole cleaning.

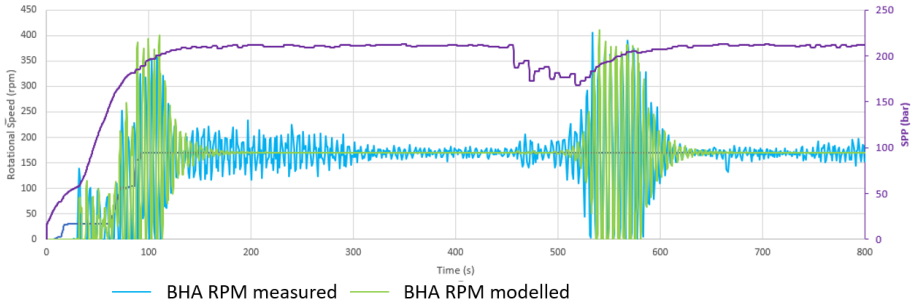

Fig. 132: Comparison of the measured (measurements made with a high frequency magnetometer) and simulated BHA rotational speed during the first 15 min of stand # at bit depth 4100mMD."[40]

40 Excerpt from my contribution to the text of the paper by Cayeux et al. 2020 [173]

3.2.7 Summary

A transient torque and drag model that is tightly coupled with transient hydraulic calculation has been described.
The model manages to reproduce effects where static friction is important like when the drill-string remains twisted after the top-drive has been turned off. But also, it replicates off bottom stick-slip situations when starting up the top-drive at low rotational velocities.
It also reproduces effects where the combined axial and torsional motion is important as when picking-up or slacking-off when the drill-string is still twisted, also when the top boundary condition is complex like when subject to heave motion.
Hydraulic pressure losses induce axial forces on the drill-string that impact the hook-load. But, swab and surge pressures along the drill-string can also induce torsional oscillations. This can be the source of either positive or negative damping of torsional oscillations, possibly leading to full stick-slip situations while reaming down.
Bit/rock interaction is also a source of non-linearity for transient torque and drag, In the presence of residual heave motion, it is nevertheless possible to estimate realistically the bit and bottom hole movements.
The grinding of cuttings particles is the source of an additional torque at the contacts points between the drill-string and the borehole. This can also be the source of negative damping of torsional oscillations.

3.3 Drilling Simulation

In the previous sections, we have seen how to model the drilling system. Yet, the actual drilling process is observed through sensors that provide a certain number of measurements. Many of the sensors utilized in the drilling context measure physical quantities in an indirect way and therefore they introduce their own biases of the desired quantities that are monitored.

With the objective to create an accurate digital twin of the drilling process, it is desirable to model how actual drilling sensors perform their measurements to reproduce as accurately as possible the response that we would have seen if we were using a real drilling setup (see Fig. 133).

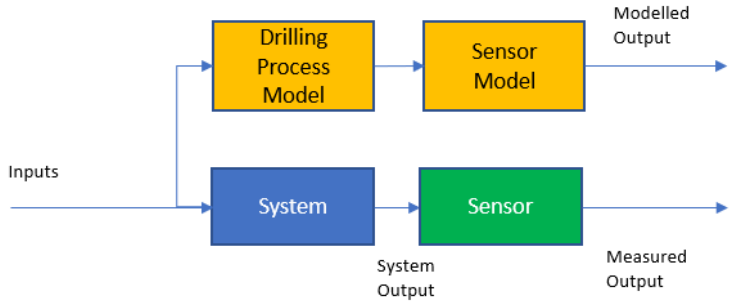

Fig. 133: The drilling digital twin concept needs to model both the drilling process but also the physical side effects of the measurement principles.

As an example, we will describe how the pit volume is impacted by the flow in flowlines and mud treatment equipment.

In conventional drilling, the drilling fluid is at atmospheric pressure when it exits the annulus through either the bell-nipple or a diverter. The drilling mud flows, by gravity, into an inclined flowline before reaching the mud treatment equipment. The drilling fluid treatment equipment consists of shale shakers, de-sanders and degassers. Finally, after formation solids and gas have been separated from the drilling fluid, it flows back into the mud tank. The passage of the drilling fluid in the flowline and inside the different mud treatment equipment, delays substantially the time by which the mud flows back into the pit, which is an important issue for the detection of gains and losses as described in section 2.3.1.1. We will now describe a transient model of the flow of drilling fluid through the flowline and the mud treatment equipment.

3.3.1 Retention Inside Return Flowline

"The drilling fluid can return to the pit through a pipe or an open channel. The typical channels used at the rig site are semi-cylindrical or rectangular (see Fig. 134). Assuming that the level of fluid in an open channel never exceeds the total height of the conduit, a semi-cylindrical channel or a flowline is described by its radius (R_{fl}) and a rectangular channel by its width (W_{fl}). The height of drilling fluid in a pipe or in an open channel, when not completely filled, depends on the volumetric flowrate (Q_{fl}) at its entrance, the geometrical dimensions of the channel or pipe (W_{fl} or R_{fl}), the surface roughness of the

wall sides (ϵ), the slope of the channel (s_{fl}) and the effective viscosity of the fluid (μ_{eff}).

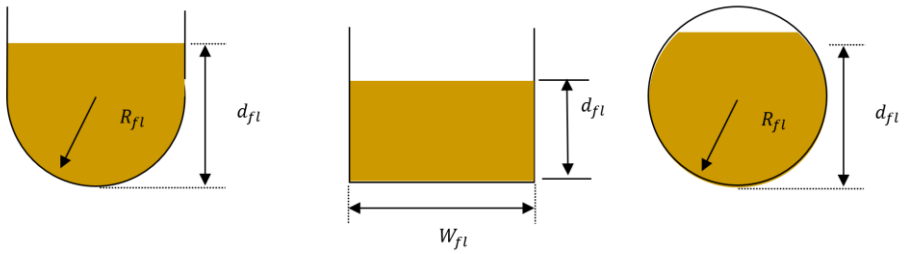

Fig. 134: Typical cross section of mud return channels or flowline.

The conduit is discretized in equally spaced sections by a distance δl_{fl} (see Fig. 135).

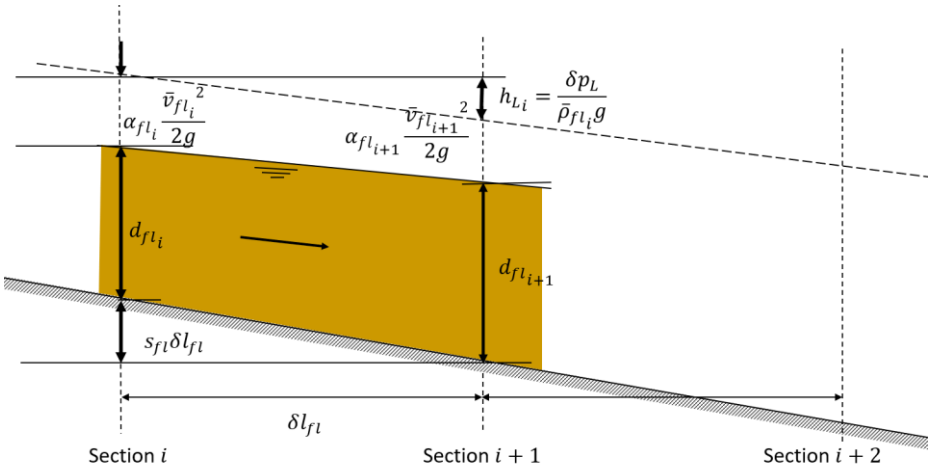

Fig. 135: Energy balance on a control volume of the conduit

The flow in the conduit is subject to very little pressure and it is therefore reasonable to consider that the fluid is incompressible. The generalized Bernoulli equation for an unsteady, but incompressible flow, in an open channel, i.e. with a constant boundary pressure, in between two sections indexed i and $i+1$ respectively is:

$$s_{fl}\delta l_{fl} + d_{fl_i} + \alpha_{fl_i}\frac{\bar{v}_{fl_i}{}^2}{2g} + \int_{A_{fl_i}} \frac{1}{g}\frac{\partial v}{\partial t} dA_{fl_i} = d_{fl_{i+1}} + \alpha_{fl_{i+1}}\frac{\bar{v}_{fl_{i+1}}{}^2}{2g} + h_{L_i} + \int_{A_{fl_i}+1} \frac{1}{g}\frac{\partial v}{\partial t} dA_{fl_{i+1}} \quad (180)$$

where s_{fl} is the slope of the conduit, d_{fl_i} and $d_{fl_{i+1}}$ are the depths of liquid at sections i and $i+1$, $\bar{v}_{fl_i}$ and $\bar{v}_{fl_{i+1}}$ are the bulk fluid velocities across the sections i and $i+1$, α_{fl_i} and $\alpha_{fl_{i+1}}$ are the kinetic energy correction factors at the respective sections, h_L is the head loss, and A_{fl_i} and $A_{fl_{i+1}}$ are the cross sectional area of the fluid at sections i and $i+1$ (they are therefore functions of d_i and d_{i+1} and the shape of the channel).

The term $\frac{\bar{v}_{fl_i}{}^2}{2g}$ in eq. (180) originates from the fact that the Bernoulli energy equation is derived using the assumption of a plug flow across the conduit, *i.e.* the velocity is identical anywhere in a cross-section of the channel. That is true for non-viscous fluid or in fully turbulent flow. But in case of a laminar or transitional flow regimes of a viscous fluid, there is a gradient of velocity from the wall of the conduit to the central part of the flow. To compensate for that approximation, the kinetic energy correction factor has been introduced by Coriolis in the Bernoulli equation. The definition of this coefficient is:

$$\alpha_{fl} = \frac{\int_A v^3 dA}{\bar{v}^3 A} \quad (181)$$

For a Newtonian fluid in laminar flow into a fully filled circular pipe, $\alpha_{fl} = 2$. But for non-filled conduits, as soon as the fluid velocity is not too small, the coefficient tends back to unity. Since the term $\frac{\bar{v}_{fl_i}{}^2}{2g}$ tends to be very small when $\bar{v}_{fl_i}{}^2$ is small and since the difference of bulk velocities $\bar{v}_{fl_i}$ and $\bar{v}_{fl_{i+1}}$, on the two sides of the considered cross sections, is also not much different, it does not influence greatly the accuracy of the calculations to consider $\alpha_{fl} \approx 1$ in all cases.

If we neglect the acceleration effects, eq. (180) simplifies into:

$$s_{fl}\delta l_{fl} + d_{fl_i} + \frac{\bar{v}_{fl_i}{}^2}{2g} = d_{fl_{i+1}} + \frac{\bar{v}_{fl_{i+1}}{}^2}{2g} + h_{L_i} \tag{182}$$

To determine the head loss (h_{L_i}) between sections i and $i+1$, the Darcy-Weisbach equation can be used, considering that for an open flow in a channel or a pipe, the equivalent pipe diameter is the hydraulic diameter:

$$h_{L_i} = \frac{\delta p_{fl_i}}{\bar{D}_{h_i} g} = \frac{f_{d_i}\delta l_{fl}\left(\frac{\bar{v}_{fl_i} + \bar{v}_{fl_{i+1}}}{2}\right)^2}{2\bar{D}_{h_i} g} \tag{183}$$

where δp_{fl_i} is the pressure loss over the distance δl_{fl}, $\bar{D}_{h_i}$ is the average hydraulic diameter between sections i and $i+1$, f_{d_i} is the Darcy friction factor to be used between sections i and $i+1$. Note that the bulk velocities are defined at the entries of each section and therefore we utilize the average bulk velocity between sections i and $i+1$, to approximate the bulk fluid velocity to be used in the pressure loss calculation. The hydraulic diameter at section i is defined by the ratio of the cross-sectional area (A_{fl_i}) of the fluid in the channel or pipe to the wetted perimeter (P_{w_i}):

$$D_{h_i} = \frac{A_{fl_i}}{P_{w_i}} \tag{184}$$

The Darcy friction factor is found by solving the Colebrook-White equation for open surface flow:

$$\frac{1}{\sqrt{f_{d_i}}} = -2\log_{10}\left(\frac{\epsilon}{3\bar{D}_{h_i}} + \frac{2.51}{\bar{R}_{e_i}\sqrt{f_{d_i}}}\right) \tag{185}$$

where $\bar{R}_{e_i}$ is the average Reynolds number between sections i and $i+1$. The average Reynolds number is defined by:

$$\bar{R}_{e_i} = \frac{\bar{\rho}_{fl_i}\left(\frac{\bar{v}_{fl_i} + \bar{v}_{fl_{i+1}}}{2}\right)\bar{D}_{h_i}}{\mu_{eff_i}} \tag{186}$$

where μ_{eff_i} is the effective viscosity of the fluid contained between sections i and $i+1$. "[41] The effective viscosity is defined as:

$$\mu_{eff_i} = \frac{\tau_{w_i}}{\dot{\gamma}_{w_i}} \tag{187}$$

with τ_{w_i} and $\dot{\gamma}_{w_i}$ being respectively the shear stress and shear rate at the wall in between sections i and $i+1$. For the sake of simplicity, the shear rate at the wall is estimated using the method of Kelessidis et al. (2006) [22] for laminar flow and Founargiotakis et al. (2008) [23] for turbulent flow, by considering a pipe with an equivalent diameter such that it would be just filled with the current flow conditions in between sections i and $i+1$.

Eq. (182) depends on both the bulk fluid velocity ($\bar{v}_{fl_i}$) and the liquid depth (d_{fl_i}) in each sections, therefore we need an additional equation in order to determine the two unknowns at the level of each sections. As a second equation, we utilize the mass conservation:

$$V_{fl_i}\frac{\partial \bar{\rho}_{fl_i}}{\partial t} = \bar{\rho}_{fl_{i-1}}\bar{v}_{fl_{i-1}}A_{fl_{i-1}} - \bar{\rho}_{fl_i}\bar{v}_{fl_i}A_{fl_i} \tag{188}$$

where V_{fl_i} is the fluid volume contained in between sections i and $i+1$.

After choosing a time step Δt, $\frac{\partial \bar{\rho}_{fl_i}}{\partial t}$ is approximated to $\frac{\bar{\rho}_{fl_{i,j}} - \bar{\rho}_{fl_{i,j-1}}}{\Delta t}$, where j is the time step index. The fluid density at time step j is calculated by utilizing eq. (103). This requires to calculate the mass of new fluid that enters the volume contained between sections i and $i+1$, i.e. $\bar{\rho}_{fl_{i-1}}\bar{v}_{fl_{i-1}}A_{fl_{i-1}}\Delta t$ and the mass of fluid that leaves the section $i+1$, i.e. $\bar{\rho}_{fl_i}\bar{v}_{fl_i}A_{fl_i}\Delta t$.

Similarly, the fluid rheological behavior is recalculated, at each time step, utilizing eq. (114) on the new composition of the fluid after considering the mass transfer from the upstream section and through the downstream section. Note that in a first approximation, these calculations assume that the process is isothermal and therefore it utilizes a single temperature for all the sections, namely the temperature of the fluid at the outlet of the well.

41 Excerpt from my contribution to the text of the paper by Cayeux et al. (2013) [197]

The boundary conditions at the first section are directly extracted from the transient borehole hydraulic calculations and provide a volumetric flowrate, the mud composition, temperature, density and rheological behavior. As there are no acceleration terms in this formulation, there is no need for an implicit scheme, and the system of equations is solved explicitly, i.e. by referring to the results of the previous time-step.

Fig. 16 of Paper I shows how drilling fluid flows into an inclined open channel when the flowrate out of the well increases. Similarly, fig. 17 of Paper I shows the drainage process of the inclined channel when the flowrate out of the well stops.

3.3.2 Flow in the Solid Control Equipment

"After flowing through the flowline, the mud goes into the shale shakers so that cuttings can be separated from the drilling fluid. The drilling fluid must pass through screens with a given mesh size and thickness (d_{screen}). This is equivalent to a flow through a porous medium (ASME Shale Shaker Committee 2005) [174] and the Darcy's law can be used:

$$v_{screen} = \frac{k_{screen} \Delta p_{screen}}{\mu_{eff} d_{screen}} \tag{189}$$

where v_{screen} is the velocity of the flow through the screen, k_{screen} is the permeability of the screen, Δp_{screen} is the pressure loss through the screen and μ_{eff} is the effective viscosity of the fluid. The factor $C_{screen} = \frac{k_{screen}}{d_{screen}}$, also called conductance, is a characteristic of the screen."[42]

Unless suction is used in the cuttings separation unit, as with the system described in Kroken et al. (2013) [175], the pressure loss across the shale shaker is simply due to gravity and can be expressed as:

$$\Delta p_{screen} = \rho_{screen} g \frac{V_{screen}}{A_{screen}} \tag{190}$$

42 Excerpt from my contribution to the text of the paper by Cayeux and Daireaux (2013) [197]

where ρ_{screen} is the mass density of the mud retained on the screen, V_{screen} is the volume of mud on the screen and A_{screen} is the area of the shale shaker mesh.

Evaluating the effective viscosity of the drilling fluid passing through the screen is a problem as drilling fluids are non-Newtonian. It is nevertheless possible to consider the shear rate at the wall as if the fluid passes through a tube with an equivalent diameter as the mesh size, and with a bulk velocity being v_{screen}. Yet, that would be an estimation made without accounting for the effect of the screen vibration. Indeed, the reason for vibrating the screen is to reduce the effective viscosity of the fluid as it passes the meshes by applying large accelerations. Saasen and Hodne (2016) [176] found that viscosity reduction, by vibrations, is larger on OBM (approx. 50%) and bentonite-based (approx. 65%) than with polymer-based WBM (approx. 25%).

By integrating the continuity equation over the volume of mud retained by the screen, we obtain:

$$\frac{d\rho_{screen}V_{screen}}{dt} = \rho_{fl_o}Q_{fl_0} - \rho_{clean}Q_{clean} - \rho_{cutt}Q_{cut} \quad (191)$$

where, ρ_{fl_o} and Q_{fl_0} are respectively the mass density and the volumetric flowrate of the mud arriving on the shale shaker from the flowline outlet, ρ_{clean} and Q_{clean} are respectively the mass density and volumetric flowrate of the cleaned mud, *i.e.* without the cuttings, ρ_{cutt} and Q_{cut} are respectively the mass density and volumetric flowrate of the cuttings separated from the mud.

It should be noted that the volume fraction of cuttings removed from the mud is not the same as the volume fraction of cuttings inside the mud, simply because a film of mud coats each cutting particles and therefore a volume of drilling fluid is also removed in the separation process. Let us call Λ the volume ratio of mud to cuttings and f_{fs} the real volume fraction of formation solid contained in the drilling fluid, then f_{cutt}, the volume fraction of coated cuttings that is removed from the drilling fluid is:

$$f_{cutt} = (1 + \Lambda)f_{fs} \quad (192)$$

The volume ratio of the mud coating the cuttings particles depends on the size of the particles and the properties of the mud. Typically, it is around one,

i.e. around each cuttings particle removed from the mud there is about an equivalent volume of mud coating the particle.

The mass density of the removed cuttings is also altered since it is a combination of the mass density of the formation solid particles and the mud coating the particles:

$$\rho_{cutt} = \frac{\Lambda}{1+\Lambda}\rho_{clean} + \frac{1}{1+\Lambda}\rho_{fs} \tag{193}$$

Furthermore, if the separated cuttings are evacuated from the shaker at the same tempo as the mud that filtrates through the mesh, we can state that:

$$Q_{cut} = f_{cutt}(Q_{cut} + Q_{clean}) \Longrightarrow Q_{cut} = \frac{f_{cutt}}{1-f_{cutt}} Q_{clean}, \forall f_{cutt} \neq 1 \tag{194}$$

We can now rewrite eq. (191):

$$\frac{d\rho_{screen}V_{screen}}{dt} = \rho_{fl_o}Q_{fl_0} - \rho_{clean}Q_{clean} - \rho_{cutt}\frac{f_{cutt}}{1-f_{cutt}}Q_{clean} \tag{195}$$

Considering that $Q_{clean} = v_{screen}A_{screen}$, we have:

$$\frac{d\rho_{screen}V_{screen}}{dt} = \rho_{fl_o}Q_{fl_0} - \left(\rho_{clean} + \frac{f_{cutt}}{1-f_{cutt}}\rho_{cutt}\right)\frac{C_{screen}\Delta p_{screen}}{\mu_{eff}}A_{screen} \tag{196}$$

which can finally be written as:

$$V_{screen}\frac{d\rho_{screen}}{dt}+\rho_{screen}\frac{dV_{screen}}{dt} = \rho_{fl_o}Q_{fl_0} - \left(\rho_{clean} + \frac{f_{cutt}}{1-f_{cutt}}\rho_{cutt}\right)\frac{C_{screen}\rho_{screen}gV_{screen}}{\mu_{eff}} \quad (197)$$

After denoting j the time step index, a time discretization of the above equation is:

$$V_{screen,j}\frac{\rho_{screen,j}-\rho_{screen,j-1}}{\Delta t}+\rho_{screen,j}\frac{V_{screen,j}-V_{screen,j-1}}{\Delta t} = \rho_{fl_{o,j}}Q_{fl_{0,j}} - \left(\rho_{clean,j} + \frac{f_{cutt,j}}{1-f_{cutt,j}}\rho_{cutt,j}\right)\frac{C_{screen}\rho_{screen,j}gV_{screen,j}}{\mu_{eff,j}} \quad (198)$$

In addition, the mass density of the fluid on top of the screen ($\rho_{screen,j}$) can be expressed as a function of its mass density at the previous time step and the mass density of the new fluid that pours on top of the screen by taking the weighted average of the mass densities based on volumetric fractions (ref. eq. (5)):

$$\rho_{screen,j} = \frac{Q_{fl_{0,j}}\Delta t}{V_{screen,j}}\rho_{fl_{o,j}} + \frac{V_{screen,j-1}-Q_{clean}\Delta t-\frac{f_{cutt}}{1-f_{cutt}}Q_{clean}\Delta t}{V_{screen,j}}\rho_{screen,j-1} \quad (199)$$

After replacing $\rho_{screen,j}$ in eq. (198) by its expression from eq. (199), we obtain an equation that depends solely on $V_{screen,j}$, values from the previous time steps and the new boundary condition given by $\rho_{fl_{o,j}}$ and $Q_{fl_{0,j}}$. This equation is solved numerically in order to obtain $V_{screen,j}$ for the current time step.

Fig. 16 of Paper III shows how pit volume variations calculated, using this principle, match the estimated quantity of cuttings arriving on the shale shakers. The estimation made with no loss of drilling fluid around the cuttings particle is colored blue, the one with an equal mud loss volume as the volume of cuttings is shown in green, while the red color is associated with twice as much volume of mud lost through the separation as the volume of drill cuttings.

3.3.3 Calculation of the Volume in the Pit

Using the continuity equation over the volume of mud contained in the active tank system, we can derive the evolution of the volume inside the active pit system. We will assume that the cross-sectional area is the same for any depth of the tank. If the fluid contained into the tank is homogenous and if we consider that the fluid contained in the tank is incompressible in view of the small range of pressure encountered inside the pit, then we can expect that the mass density of the fluid is the same at any depths of the tank (ρ_{tank}). By integrating over the height of liquid contained into the tank and by using the boundary conditions, we obtain:

$$\frac{d\rho_{tank}V_{tank}}{dt} = \rho_{clean}Q_{clean} - \rho_{tank}Q_{MP} \tag{200}$$

where V_{tank} is the volume of mud inside the tank, Q_{clean} is the volumetric flowrate of fluid entering the pit, and Q_{MP} is the volumetric flowrate of fluid being pumped out of the tank. "[43]

Here again, we need to calculate ρ_{tank} by using eq. (5) and by estimating the respective masses of new fluid entering the pit and of remaining fluid after removal of the quantity that is being pumped out of the pit.

But before doing that, we need to estimate the pit temperature as we need to transform the mass density of the arriving fluid to the one that it will have when it will be warmed up, or cooled down, to the temperature of the fluid contained in the pit.

If the temperature of the mud arriving at the pit at time step j is $T_{clean,j}$ with a specific heat capacity of $C_{p_{clean,j}}$ and the drilling fluid contained in the pit has

43 Excerpt from my contribution to the text of the paper by Cayeux and Daireaux (2013) [197]

a temperature $T_{tank,j-1}$ with a specific heat capacity $C_{p_{tank,j-1}}$ at the previous time step, then the new temperature, at time step j, of the drilling fluid contained in the tank is (see eq. (90)):

$$T_{tank,j} = \frac{m_{clean,j} C_{p_{clean,j}} T_{clean,j} + \left(m_{tank,j-1} - m_{MP,j}\right) C_{p_{tank,j-1}} T_{tank,j-1}}{m_{clean,j} + m_{tank,j-1} - m_{MP,j}} \tag{201}$$

where $m_{clean,j}$ is the mass of cleaned fluid entering the pit, $m_{tank,j-1}$ is the mass of fluid inside the tank at the previous time step, $m_{MP,j}$ is the mass of fluid exiting the tank to the mud pumps.

The specific heat capacity of the fluid contained in the tank is also modified. Using eq. (89), the specific heat capacity of a mix of fluids is:

$$C_{p_{tank,j}} = \frac{m_{clean,j} C_{p_{clean,j}} + \left(m_{tank,j-1} - m_{MP,j}\right) C_{p_{tank,j-1}}}{m_{clean,j} + m_{tank,j-1} - m_{MP,j}} \tag{202}$$

If we denote $\rho_{clean,j_{T_{tank,j}}}$ the mass density of the arriving fluid after conversion to the temperature of the tank at time step j, then the mass density of the fluid contained in the tank at time step j is:

$$\rho_{tank,j} = \frac{V_{clean,j}}{V_{tank,j-1} + V_{clean,j} - V_{MP,j}} \rho_{clean,j_{T_{tank,j}}} + \frac{V_{tank,j-1} - V_{MP,j}}{V_{tank,j-1} + V_{clean,j} - V_{MP,j}} \rho_{tank,j-1} \tag{203}$$

where $V_{clean,j}$ is the volume of the fluid arriving in the pit, $V_{tank,j-1}$ is the volume of fluid contained in the tank at the previous time step and $V_{MP,j}$ is the volume of fluid that leaves the tank in direction to the mud pumps. Note that all the volumes must be converted to the new temperature $T_{tank,j}$ by applying the conversion:

$$V_j = \frac{\rho_j}{\rho_{j-1}} V_{j-1} \tag{204}$$

where V_j and V_{j-1} are respectively the volumes at time step j and $j-1$, and ρ_j and ρ_{j-1} are respectively the mass densities at the time step j and $j-1$.

Finally, we can discretize eq. (200):

$$V_{tank,j}\frac{\rho_{tank,j}-\rho_{tank,j-1}}{\Delta t}+\rho_{tank,j}\frac{V_{tank,j}-V_{tank,j-1}}{\Delta t}=\rho_{clean,j}Q_{clean,j}-\rho_{tank,j}Q_{MP,j} \quad (205)$$

and after replacing $\rho_{tank,j}$ by its expression from eq. (203), we have an expression of $V_{tank,j}$ together with values from the previous time step and the current time step boundary conditions, i.e. $\rho_{clean,j}$, $Q_{clean,j}$ and $Q_{MP,j}$. This equation can be solved numerically in order to obtain $V_{tank,j}$.

At this point, the above-described model, together with the transient hydraulic model focusing on the circulation of fluid in the wellbore, allows to estimate the variation of the active pit volume for any change of flowrate and axial movement of the drill-string. Fig. 21 of Paper III illustrates the results of a simulation when the flowrate is first decreased for thereafter to be increased, yet at a different value than initially.

Consequently, the pit volume increases when the flowrate decreases and vice versa, it decreases when the flowrate is increased. The transient periods for the pit volume variations last for several minutes and in this example, it is unlikely that the maximum estimated pit volume is the true pit volume that would have been observed if the minimum flowrate had been kept constant for a longer duration. The results obtained with the simulation can be compared with the actual measurements that were recorded during this exact pump-rate modification sequence (see fig. 21 Paper III). This shows the benefit of utilizing a transient model that manages the time evolution of the drilling fluid retention in the flowline and mud treatment equipment.

3.3.4 Summary

A transient model of the flow of drilling in flowlines and shale shakers has been described.
It allows to estimate pit volume variations resulting from drilling fluid retention in the mud treatment equipment.
It also permits to estimate the amount of cuttings that are separated at the level of the shale shakers.

3.4 Drilling Interpretation

Thorogood et al. (2014) [177] explained that the correct interpretation of weak signals, while avoiding being blinded by confirmation bias thinking, can help avoiding serious drilling incidents. Indeed, it sounds reasonable that the earlier the deterioration of the drilling conditions is detected, the better are the chances to take actions and avoid an escalation of the situation into a serious drilling event.

We will now present a method to automatically quantify weak signals of the deterioration of the drilling conditions from real-time drilling signals available during drilling operations.

In this method, a high-fidelity drilling simulator is continuously calibrated to reproduce as closely as possible real-time measurements while monitoring a drilling operation. The deviation of the calibration parameters from optimum values is considered as a signal that the drilling conditions are deteriorating and this even though no drilling incidents have yet been observed.

This method can only work if the drilling simulator can reproduce all the intricate transient effects that exist during a drilling operation. Yet, even with an acceptable level of details for the simulations, it is essential that the accuracy of the estimations is constantly evaluated, as too much uncertainty in the inputs of the simulator can just lead to uninterpretable results.

We will therefore first describe how the uncertainty of a few inputs, but important ones, is undertaken. Then we will describe how ill-defined configuration information is calibrated before describing the calibration method for critical parameters of the drilling simulator. Thereafter, we will discuss how to deal with the non-holonomic nature of the drilling process. In the next step, the accuracy of the estimated signals is performed. An example is then given on how accuracy of estimated values is improved by utilizing the redundancy of measurements. Finally, it is possible to analyze whether there is a deterioration of the drilling conditions.

3.4.1 Estimation of Uncertainty of Drilling Fluid PVT Behavior

In section 3.1.1, we have seen how to estimate the mass density of drilling fluids and its dependence on pressure and temperature as a function of its

composition. Yet, it is common that the exact composition of the drilling fluid is not well-documented. As it can be seen on Fig. 16, the mass density of eight typical base oils used in drilling operations is quite variable, here when subjected to a large span of pressure while keeping the temperature constant.

It is the same for brine. Depending on whether the salt is natrium chloride, calcium chloride or potassium chloride, the PVT behavior can be quite different, even for the same weight fraction as it can be seen on fig. 5 of Paper II.

So, if we do not know anything about the drilling fluid except its mass density at a reference temperature, then it can be a WBM or an OBM and all the constituents can be of different proportions. Fig. 136a shows the 5, 50 and 95 percentiles of the estimation of the mass density at three different temperatures, i.e. 20, 50 and 80°C, and as a function of pressure in the range 0 to 1000bar, for such a case where the reference mass density is known with a standard deviation of 5kg/m^3. The bottom graph shows the hydrostatic pressure precision for a geothermal gradient of 3°C/100m.

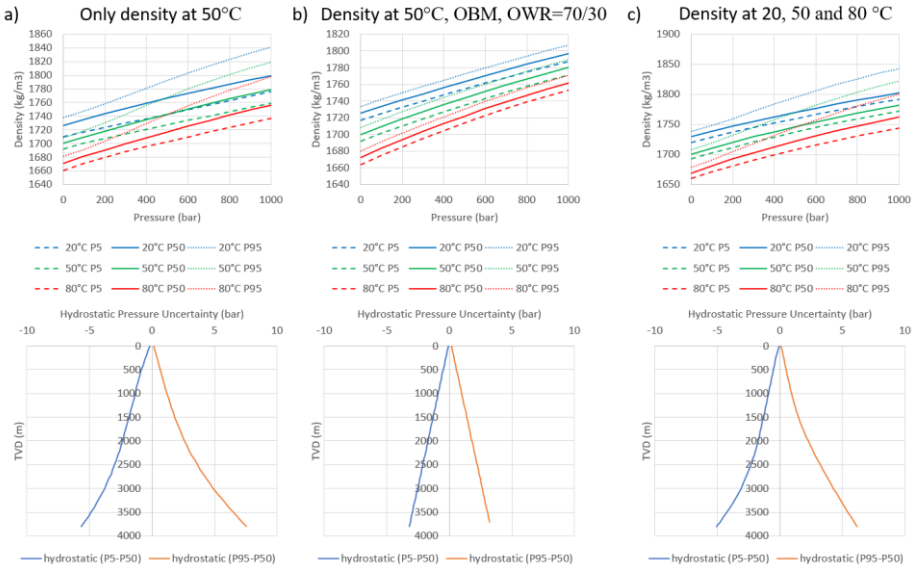

Fig. 136: On the left side (a) top, estimation of the probability variations of the PVT behavior a drilling fluid just knowing its mass density 1700kg/m3 at 50°C and on the bottom, associated uncertainty margins for the hydrostatic pressure as a function TVD and a temperature gradient of 3°C/100m. The middle graphs

(b) show the same but here we know in addition that it is an oil-based mud with an oil-water ratio of 70/30 and utilizing an EDC99 base oil. The right-side graphs (c) show the results when there are six mass density measurements at three different temperatures: 20, 50 and 80°C and two different pressures: atmospheric and 40bar.

Fig. 136b illustrates that if there is more information about the composition of the drilling fluid, then the uncertainty is reduced. Here, the additional information is that it is an oil-based mud with an oil-water ratio of 70/30 and that the base oil is an EDC99. If instead of providing more information about the composition, there are several mass density measurements at different temperatures and pressures, yet without knowing the composition, it is possible to reduce the uncertainty on the PVT behavior of the fluid and consequently on the estimation of the hydrostatic pressure at different TVDs. Fig. 136c shows the results for six measurements made at 20, 50 and 80 °C and at atmospheric pressure and 40barg. Nevertheless, with a standard deviation on the measurement of 5kg/m^3, the reduction of the uncertainty on the estimated hydrostatic pressure is not very large.

3.4.1.1 Summary

The extrapolation of the mass density of a fluid mix to different pressures and temperatures depends on its composition and the PVT behavior of its constituents.
Uncertainty on the proportion of the different constituents and their actual PVT behavior results in uncertainties in the estimation of hydrostatic pressures along the borehole.
Multiple mass density measurements made at different conditions of pressure and temperature help reduce this uncertainty without requiring an exact composition of the fluid mix, but to be effective the precision of the measurement shall be high.

3.4.2 Estimation of Uncertainty of Drilling Fluid Rheological Behavior

In section 3.1.3, we have seen that the Herschel-Bulkley rheological behavior fits with a great accuracy (within ±2%) to the shear stresses measured with a scientific rheometer. This accuracy has been obtained for hundreds of rheometer sweeps made with various formulations of a KCl/polymer drilling fluid.

"But in practice, a scientific rheometer is not available at the rig site. Instead, a mechanical one, with fixed rotational speeds, is used to measure the rheological behavior of the drilling fluid. The typical rheometer speeds are 3rpm ($5.109s^{-1}$), 6rpm ($10.218s^{-1}$), 100rpm ($170.3s^{-1}$), 200rpm ($340.6s^{-1}$), 300 rpm ($510.9s^{-1}$) and 600rpm ($1021.8s^{-1}$). Sometime, two additional speeds are also available 30rpm ($51.09s^{-1}$) and 60rpm ($102.18s^{-1}$).

Furthermore, the shear stress reading resolution is at most half of a rheometer graduation. One rheometer graduation is $1lb/100ft^2$ (0.4788Pa) and therefore the precision of the shear stress reading, with a mechanical rheometer, is at best in the range of ±0.24Pa.

As drilling fluids are thixotropic, each time the rheometer speed is changed, it takes some time before the shear stress stabilizes to a steady value. Fig. 22 shows the time evolution of the shear stress for sweeps from high to low and then from low to high of the standard rheometer speeds measured with a scientific rheometer. With a mechanical rheometer, it is not so easy to observe that time evolution, as static friction may apply, stopping the needle movement for a long duration before it jumps by a few fractions of degrees. Therefore, the readings made with a mechanical rheometer are quite often taken too early and therefore introduces a systematic error in the reported rheometer measurements.

Typically, a shear stress measurement is noted a few seconds after the speed has been changed and a new step change is performed a few seconds later, still respecting the recommended procedure from API [44] [45]. Let us consider that the time distributions for reading the shear stress and for changing the rheometer speed are trapezoidal functions with a uniform probability distribution between 5 and 30s and a maximum waiting time of 150s. Let us also consider that the duration of the initial shearing, at 600rpm, is also a trapezoidal probability distribution with a uniform probability between 30 and 300s and a maximum waiting duration of 600s. Then, we can make Monte Carlo

simulations in order to estimate the probability distribution of the shear stress biases for each shear rate step-changes. The shear stress bias is relative to the shear stress that would have been measured in steady state conditions.

Fig. 137 shows the estimated probability distributions for two KCl/polymer fluids, one with a mass density of 1250kg/m^3 and another one with a mass density of 1750kg/m^3. First, it can be noted that the systematic bias is larger for the step-changes corresponding to high shear rates. Second, such systematic biases have a direct consequence on the rheological behavior that can be extracted from the rheometer measurements and consequently on the ability to predict correct pressure losses.

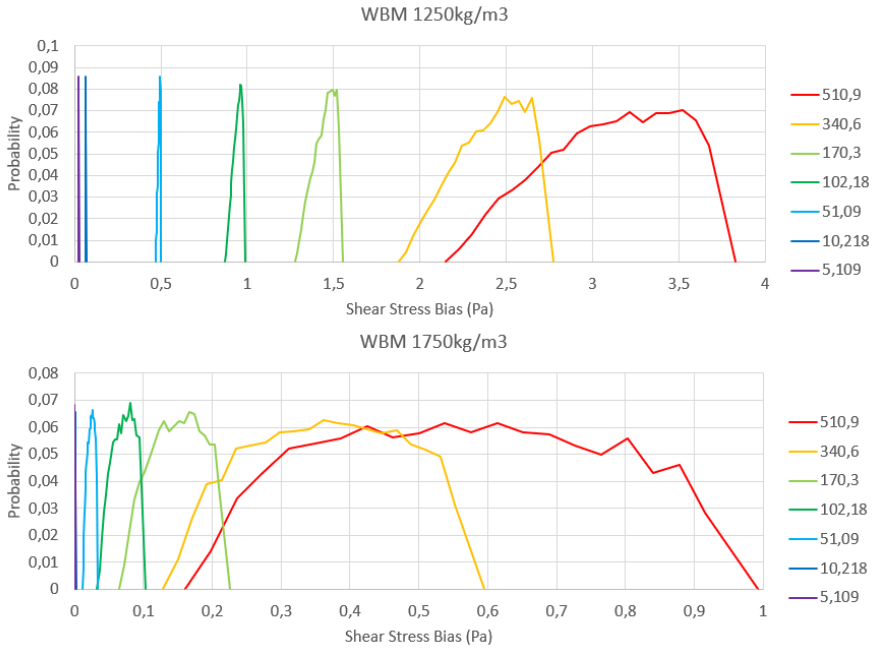

Fig. 137: Probability distribution of the shear stress bias when performing step-changes of shear rates (red being from 1020s^{-1} to 510s^{-1}, purple being from 10.218s^{-1} to 5.109s^{-1}) for a KCl/polymer of mass density 1250kg/m^3 (top) and a similar WBM of mass density 1750kg/m^3.

We can apply Monte-Carlo simulations based on the random error arising from measurement reading accuracy and the systematic error associated with the

thixotropic behavior of the fluid while determining the best fit Herschel-Bulkley parameters utilizing the method described by Mullineux (2008) [19]. We then obtain plausible triplets of Herschel-Bulkley parameters that can corresponds to the mechanical rheometer readings

Fig. 138 shows the probability distribution of the Herschel-Bulkley parameters corresponding to the true values $\tau_y = 3.88Pa, K = 1.47Pa.s^n$ and $n = 0.43$ when applying a random error of ±0.24Pa and a systematic error induced by thixotropic effects, to model 35 rheometer measurements. However, one shall keep in mind that the yield stress, consistency index and flow index shall be handled as triplets and it would be erroneous to apply individual probability distributions for each of the Herschel-Bulkley parameters based on the distributions shown on Fig. 138. The 10, 50 and 90 percentiles of the statistical variations resulting from random and systematic errors remain close to each other, as it can be seen on the flow-curves shown on the bottom graph of Fig. 138.

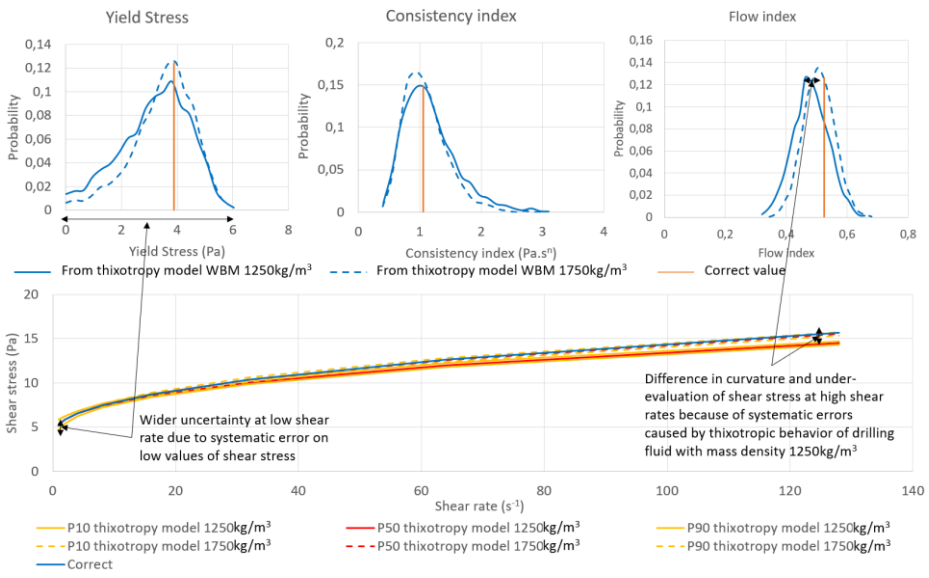

Fig. 138: Probability distributions of the yield stress, consistency index and flow index obtained when fittings a Herschel-Bulkley rheological behavior on model 35 rheometer readings when they are affected by a resolution error of ±0.24Pa and a systematic bias caused by thixotropy. The bottom graph shows the difference between the flow-curve obtained with the correct rheological behavior and the statistical spread resulting from random and systematic errors

with the model 35 rheometer measurements in terms of the 10%, 50% and 90% percentiles.

It is also noticeable that the shear stresses at low shear rates are more spread than for the rest of the flow-curve, therefore explaining the large variations of yield stress that is visible on the top-left graph. On the other hand, the systematic errors induced by thixotropy translate into a bias for the estimated flow index that is visible on the top-right graph and on the shear-stresses being underestimated for larger shear rates. Yet, this result is less significant with the thixotropy model extracted from the second sample of WBM, i.e. the one with a mass density of 1750kg/m^3. We can therefore conclude that the thixotropic behavior of the drilling fluid can influence the measurements made with a model 35 rheometer but not always and that without a specific procedure to assert the thixotropic behavior of the fluid, it is not possible to attempt compensating for these potential systematic biases. "[44]

Then, we can apply eq. (37) on each of the stochastic realizations to estimate the dependence of the rheological behavior on pressure and temperature. It should be noted that the parameters of eq. (37), i.e. $A_{\dot{\gamma}}$, $B_{\dot{\gamma}}$, $C_{\dot{\gamma}}$, $D_{\dot{\gamma}}$, $E_{\dot{\gamma}}$, depends on the type of drilling fluid, e.g. KCl/polymer, OBM, micronized-OBM, and have their own probability distribution to reflect with which accuracy one can expect to estimate the rheological curve at a different pressure and temperature than the original one.

Fig. 139 shows the results of the extrapolation at 50 and 80°C of a flow curve originally measured at 20°C. For each rheological behavior, there are three curves corresponding to the 5, 50 and 95 percentiles. Note that the original rheological behavior, i.e. the one at 20°C, has its own uncertainty as we have just explained above.

Now, if we want to estimate the impact of cuttings in suspension on the apparent rheological behavior of the drilling fluid, we can recourse to the results of section 3.1.3. Yet, these depend on the formulation of the drilling fluid, which is, as we have discussed earlier, seldom well specified in the drilling fluid

44 Excerpt from my contribution to the text of the paper by Cayeux and Leulseged (2019) [190]

reports. For instance, the quantity of polymer is rarely provided and, in many cases, even the salt concentration is not reported.

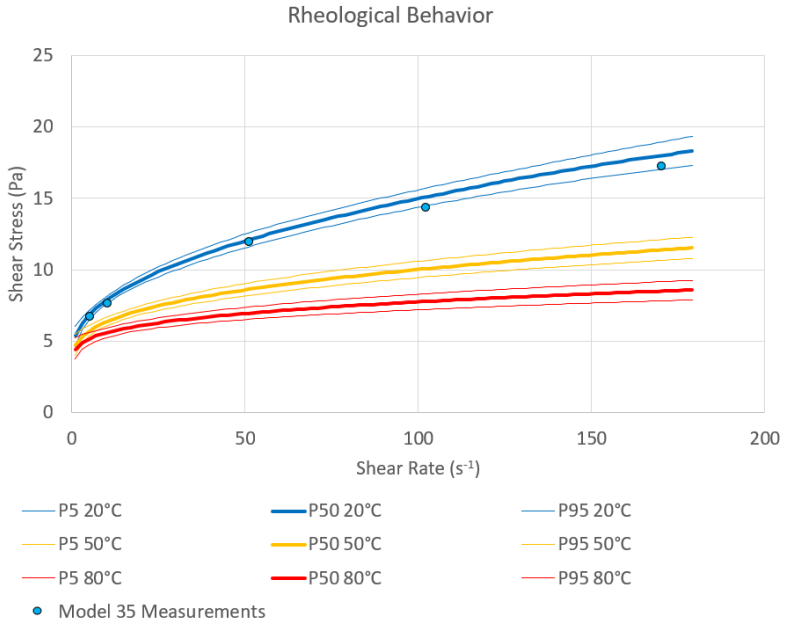

Fig. 139: Extrapolation of the rheological behavior at 50 and 80°C from an original rheological behavior measured at 20°C.

"If one or more of these parameters are missing, we can utilize eq. (108) to estimate the $\Phi_b^*, S_{KCl}^*, S_{XG}^*$ that minimizes the sum of the quadratic differences with the Herschel-Bulkley parameters:

$$\underset{\Phi_b^*>0, S_{KCl}^*>0, S_{XG}^*>0}{\arg\min} \left(\sqrt{\left(\frac{\tilde{\tau}_{\gamma_b} - \tau_{\gamma_b}}{\tau_{\gamma_b}}\right)^2 + \left(\frac{\tilde{K}_b - K_b}{K_b}\right)^2 + \left(\frac{\tilde{n}_b - n_b}{n_b}\right)^2} \right) \tag{206}$$

where τ_{γ_b}, K_b and n_b are the components of a sample triplet from the results of the Monte Carlo simulations described above. In our case, we use a particle swarm algorithm (Kennedy and Eberhart 1995) [178] to calculate arg min. This gives plausible values of the KCl concentration, polymer concentration and barite volumetric fraction. By plausible, we mean a probability distribution of these parameters, denoted here $f_{\phi_b^*}$ for the probability density function of the normalized barite volume fraction, $f_{S_{KCl}^*}$ for the probability density function of

the normalized KCl salinity and $f_{S^*_{XG}}$ for the probability density function of the normalized polymer volumetric concentration (see Fig. 140).

It is then possible to use $f_{\phi^*_b}, f_{S^*_{KCl}}$ and $f_{S^*_{XG}}$ to estimate the probability distribution of the Herschel-Bulkley parameters of the base fluid without barite by utilizing eq. (109). Then we can apply eq. (114) to obtain a probabilistic estimation of the impact of the formation material concentration on the rheological behavior of the drilling fluid."[45]

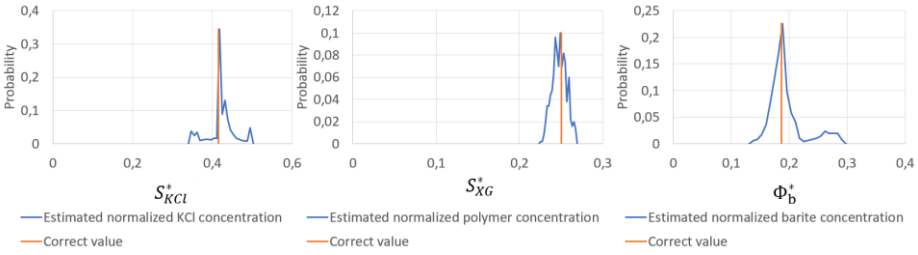

Fig. 140: Estimation of the probability distribution of the normalized KCl, polymer and barite concentrations by solving eq. (206) for the ensemble of Herschel-Bulkley parameters collected from the sensitivity analysis to measurement errors from the model 35 rheometer.

3.4.2.1 Summary

The yield stress of drilling fluids estimated from Model 35 rheometers is not very precise because of the low precision of the apparatus at low shear stresses.
The impact of drilling fluid thixotropy biases the measurements because readings are taken too early.

45 Excerpt from my contribution to the text of the paper by Cayeux and Leulseged (2019) [190]

The rheological behavior of drilling fluid is influenced by the various solid concentrations. We have described a method to estimate the in situ rheological behavior by combining the effect of pressure, temperature and additional solids being transported.

3.4.3 Impact of Wellbore Position Uncertainty on Geo-pressure Margins

3.4.3.1 Estimation of Vertical Depth Uncertainty Caused by Wellbore Position Uncertainty

"Any downhole pressure estimation in the open hole section of a well has to be related to a corresponding formation layer in order to retrieve the correct geo-pressure boundaries. In practical terms, that means a true vertical depth.

We would like to investigate the highest and lowest vertical position at a given confidence factor. We have seen in section 2.1.4 that it is possible to calculate the region of space that is likely to contain the trajectory at a given curvilinear abscissa by utilizing eq. (93). For simplicity, the elements of the inverse covariance matrix will be denoted as $H_{ij}, \forall i,j \in \{1,2,3\}$. The covariance matrix is a symmetric matrix and therefore $\Sigma = \Sigma^T$. This property implies that the inverse matrix will also be symmetric. In practice this gives, $H_{12} = H_{21}$, $H_{13} = H_{31}$ and $H_{23} = H_{32}$. This property is utilized to derive the Cartesian equation of the ellipsoid:

$$f_u(x,y,z) = H_{11}x^2 + H_{22}y^2 + H_{33}z^2 + 2H_{12}xy + 2H_{13}xz + 2H_{23}yz = \chi_3^2(p), \tag{207}$$

The maximum and minimum points in the z direction are characterized by a normal to the surface of the ellipsoid that is oriented in the z-direction and is described by:

$$\begin{cases} \dfrac{\partial f_u}{\partial x} = 0 \\ \dfrac{\partial f_u}{\partial y} = 0 \\ \dfrac{\partial f_u}{\partial z} = \alpha_z \end{cases} \tag{208}$$

where α_z is a scalar value. This can be re-written as:

$$\begin{cases} H_{11}x + H_{12}y + H_{13}z = 0 \\ H_{22}y + H_{12}x + H_{23}z = 0 \\ H_{13}x + H_{23}y + H_{33}z = \alpha_z \end{cases} \quad (209)$$

By solving this system of three linear equations, expressions for the *x*, *y* and *z* coordinates are given as follows:

$$\begin{cases} x = \dfrac{\alpha_z(H_{12}H_{23} - H_{13}H_{22})}{\Delta} \\ y = -\dfrac{\alpha_z(H_{11}H_{23} - H_{12}H_{13})}{\Delta} \\ z = \dfrac{\alpha_z(H_{11}H_{22} - H_{12}^2)}{\Delta} \end{cases} \quad (210)$$

where:

$$\Delta = H_{33}(H_{11}H_{22} - H_{12}^2) - H_{11}H_{23}^2 + 2H_{12}H_{13}H_{23} - H_{13}^2H_{22} \quad (211)$$

By inserting the three expressions for *x*, *y* and *z* in the Cartesian equation of the ellipsoid, an expression for α_z can be derived:

$$\alpha_z = \pm\sqrt{\frac{\chi_3^2(p)(H_{11}H_{22}H_{33} - H_{12}^2H_{33} - H_{11}H_{23}^2 + 2H_{12}H_{13}H_{23} - H_{13}^2H_{22}}{H_{11}H_{22} - H_{12}^2}} \quad (212)$$

Due to α_z having a positive and a negative value, two solutions $\vec{r}_h = (x_h, y_h, z_h)$ and $\vec{r}_l = (x_l, y_l, z_l)$ are obtained from this set of equations. These are the points of interest, denoted $\vec{r}_h$ for the highest point and $\vec{r}_l$ for the lowest point.

The size and direction of an ellipsoid at a given depth of the trajectory are the results of the accumulation of the systematic errors all along the trajectory prior to that depth. When using a single survey instrument, those systematic errors are unknown but do not change through the integration.

We can therefore consider that the location at the surface of the ellipsoid is a characteristic of the effect of the systematic errors on the inclination, azimuth and measured depth. By using the same relative position at each ellipsoid in the measurement series, we can reconstruct a trajectory that bears the effect of those systematic errors. To find that characteristic location, we will use the parametric coordinates of a point at the surface of the ellipsoid.

Let us consider the parametric equations of an ellipsoid in a coordinate system (X, Y, Z) that is oriented by the three axes (a_u, b_u, c_u) of the ellipsoid:

$$\forall \phi_u \in [0, \pi[, \forall \theta_u \in [0, 2\pi[, \begin{cases} X = \mathrm{a}_u \sin\phi_u \cos\theta_u \\ Y = b_u \sin\phi_u \sin\theta_u \\ Z = c_u \cos\phi_u \end{cases} \quad (213)$$

The angles ϕ_u and θ_u characterize the position of a point on the surface of that ellipsoid and are specific to the systematic errors that cause the trajectory to be at that position of the ellipsoid. Using the same parameters ϕ_u and θ_u at each ellipsoid along the wellbore, we can re-construct the trajectory that embeds the same systematic errors all along the measurements made in that wellbore.

To obtain the coordinate system oriented by the axes of the ellipsoid, we need to diagonalize the covariance matrix and find the transfer matrix that transforms the covariance matrix into its diagonalized version:

$$\Sigma = P_u D_u {P_u}^{-1}, \quad (214)$$

where P_u is the transfer matrix and D_u is the diagonal matrix. Note that the transfer matrix is in fact the multiplication of three rotations necessary to transform the global Cartesian system into a local Cartesian system defined by the axes of the ellipsoid. The following equation shows how to transform a point from the global coordinate system into the local coordinate system attached to the axes of the ellipsoid:

$$P_u \times \begin{bmatrix} x \\ y \\ z \end{bmatrix} = \begin{bmatrix} X \\ Y \\ Z \end{bmatrix}, \quad (215)$$

The diagonal values of the matrix D_u are the eigenvalues of the covariance matrix. The eigenvalues can be found by solving the equation in λ:

$$\det(\Sigma - \lambda I) = 0, \quad (216)$$

where I is the identity matrix.

So, to reconstruct a trajectory that corresponds to one of the extreme vertical depths associated with a given downhole pressure measurement, one shall apply the following procedure:

- Calculate the global coordinates of the extreme vertical point at the depth of interest using eq. (212) and (210)

- Transform that point into the local coordinate system of the ellipsoid using the eq. (215)
- Calculate the corresponding ellipsoid parameters (ϕ_u and θ_u) using eq. (213)
- Apply the same ellipsoid parameters (ϕ_u and θ_u) at all other survey stations of the wellbore and convert the local coordinates into the global coordinates. "[46]

Fig. 141 shows an example of reconstructed trajectories for the highest (in green) and lowest (in red) TVD based on the wellbore position uncertainty when the drill-string has reached the TD of the well, where the blue ellipses are the projected uncertainty ellipsoids.

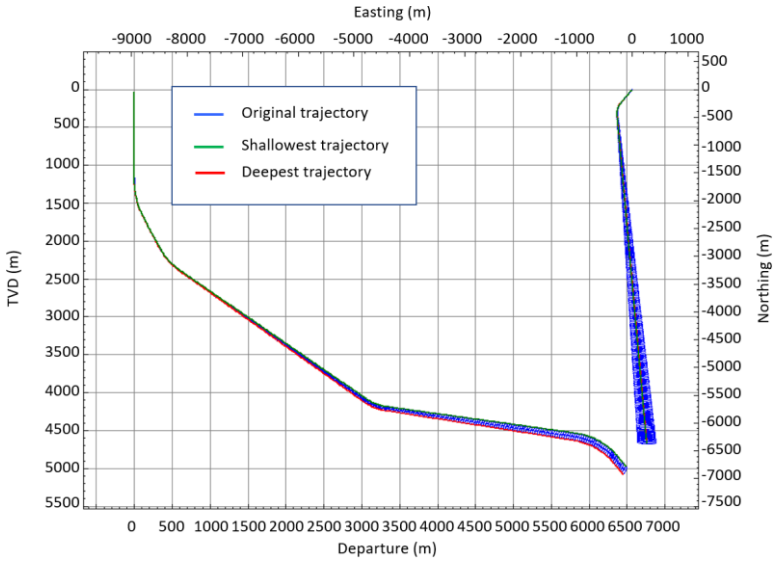

Fig. 141: Reconstruction of shallowest and deepest trajectories.

3.4.3.2 Geo-Pressure Margin Uncertainties

"At the planning stage, the thickness of the expected formation layers is not completely certain. If a layer is thicker than expected, then the absolute depth of any deeper formation layer is subsequently increased. Conversely, if a layer

46 Excerpt from my contribution to the text of the paper by Cayeux et al. (2014) [187]

is thinner than expected, the following formation layers will be encountered at shallower depths. The possible thickness variations of the formation layers result in as many stretch and squeeze deformation of the original stratigraphic prognosis.

The thickness of each layer is only known with a certain precision. This uncertainty is described by the standard deviation of the expected variations of the layer thickness assuming a normal distribution. A set of variations of formation layer thicknesses defines a transfer function that stretches and squeezes each of the original layers of the stratigraphic column (see Fig. 142).

The conversion from the true vertical thickness (TVT) perspective of the stratigraphic column into possible observations of formation tops along the trajectory depends on the inclination of the trajectory. The lower is the incidence angle, the larger is the range of measured depth by which the layer transition can be observed. As seen in section 3.4.3.1, there is an uncertainty on the trajectory position as well, which when combined with the stratigraphic layer thickness likelihood gives the probability of observing a formation top at a given MD along the trajectory (see Fig. 143).

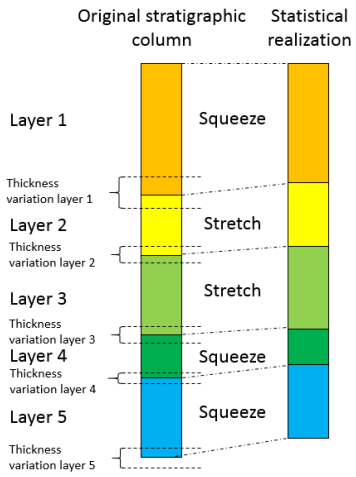

Fig. 142: Example of the statistical realization of stratigraphic column considering thickness uncertainties.

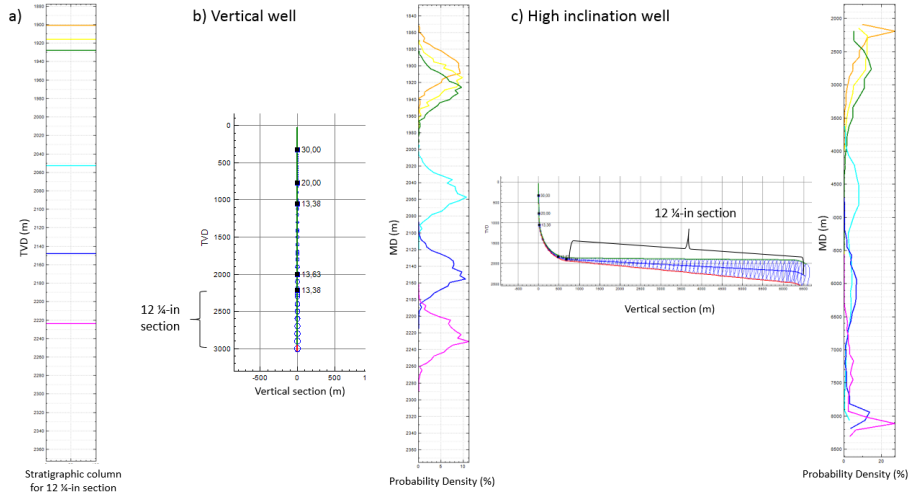

Fig. 143: Illustration of the effect of the inclination on the probability to observe a formation layer when combining the wellbore position uncertainty and the stratigraphic TVT uncertainty.

Furthermore, there is always some level of uncertainties in the absolute pressure gradients of a geo-pressure prognosis. It is also possible that some alternate conditions may occur or not, like penetrating a high-pressure zone or a depleted one. It is therefore necessary to estimate the domain of variability of the geo-pressure margins.

The uncertainty associated with the geo-pressure prognosis can be of two origins: a normal distribution of the possible gradients by TVD and the possible presence of an abnormally pressurized zone. For the former, different standard deviations at various depths are associated to the TVD-based pore, collapse and fracturing pressure gradients as well as the minimum horizontal stresses. Abnormally pressured zones are described as alternate geo-pressure prognosis with an associated probability of occurrence. Several such alternate layers can be defined, each with its own probability.

The TVD-based geo-pressure prognosis is then converted to the MD space, by applying the stratigraphic stretch and squeeze transformations described above. Fig. 144 shows an example of the transformation of a geo-pressure prognosis by accounting for the stratigraphic and wellbore position uncertainty (a).

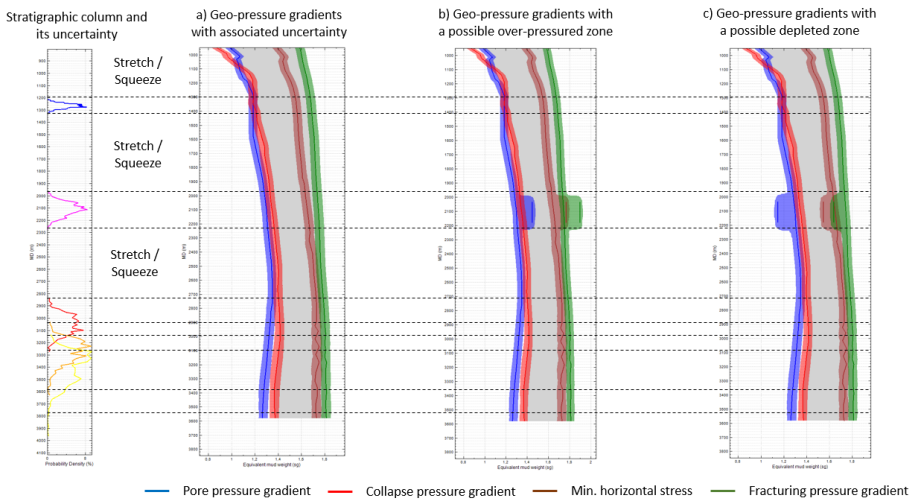

Fig. 144: The stratigraphic uncertainty is combined with the own uncertainty of the geo-pressure gradients (a). Also, alternate scenarios and their probability can be mixed with the main geo-pressure prognosis like a possible over-pressured zone (b) or a depleted zone (c).“[47]

It also shows two other configurations where a possible over-pressured zone (b) or a depleted zone could occur (c). It should be noted that when there are alternate abnormally pressurized zones, the probability distribution is not normal anymore as there are several maxima, one for the original prognosis and as many other maxima as there are alternate zones that may be encountered at a particular depth.

3.4.3.3 Summary

A method to estimate the highest and lowest possible TVD along a trajectory has been derived.

47 Excerpt from my contribution to the text of the paper by Cayeux et al. 2016 [199]

With the estimation of possible TVD variations, it is possible to associate the corresponding geo-pressure margins according to the original geo-pressure prognosis.

3.4.4 State Estimation of the non-Holonomic Drilling Process

The current state of the drilling process cannot be estimated without considering the history of actions that have been taken during the drilling operation. If the sequence of actions had been different, then the current state would not have been the same. This is illustrated by Fig. 145 where the same 8 ½-in horizontal section, with the same drilling fluid and drill-string, has been simulated drilled, with two different sequences of actions. One can see that the active pit temperature, corresponding to those two simulations, evolves differently.

As an example of the importance of the history of actions to reach the current state, Cayeux (2012) [179] describes a drilling operation where it is necessary to incorporate the temperature evolution of the drilling fluid in the pit while the drill-string is completely pulled out of hole, to explain the occurrence of a formation fracturing incident that occurred after running in hole with a new drill-string/BHA and while establishing circulation.

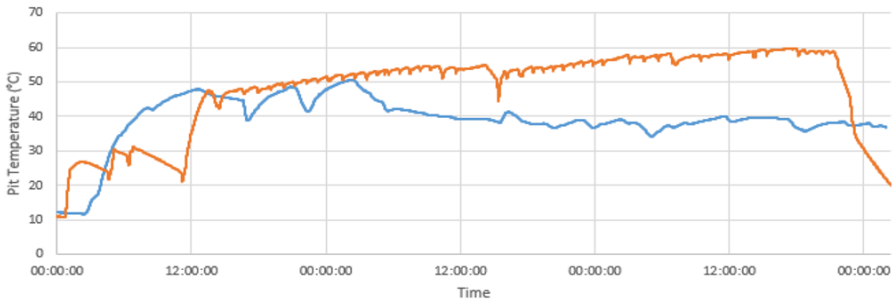

Fig. 145: Active pit temperature evolution while simulating the drilling of the 8 ½-in section of a horizontal with two different drilling sequences over a period of 3 days.

The drilling process is therefore a non-holonomic one and it is necessary to estimate the evolution of the internal state of the system, on a continuous basis, throughout the whole drilling operation, starting from before the drill-string is run in hole. At any instant, the state estimation consists in (see Fig. 146):

- The fluid composition at any depth along the drill-string and the borehole
- The pressure and temperature at any depth along the drill-string and the borehole
- The mass density of the drilling fluid at any depth along the drill-string and the borehole
- The rheological behavior of the drilling fluid at any depth along the drill-string and the borehole
- The volume fraction of cuttings in suspension at any depth along the borehole
- The cuttings bed height at any depth along the borehole
- The fluid bulk velocity at any depth along the drill-string and the borehole
- The side-force, tension, torque at any depth along the drill-string
- The local axial and rotational velocity of the drill-string at any depth
- The local elongation and twisting of the drill-string at any depth
- The bottom hole depths, including several top of rat holes when an under-reamer or hole-openers are used.

Concerning the last point in the list, i.e. bottom hole depths, it is important to continuously estimate the depths drilled by each drill-string element that is capable of drilling, e.g. a bit, an under-reamer or a hole-opener. Especially with an under-reamer, it is necessary to account for the moments by which the under-reamer arms are opened and closed. In some cases, the well is drilled only a few ten meters before the under-reamer is activated, i.e. just enough to ensure that the under-reamer has passed the casing shoe. In other cases, a section is drilled with the under-reamer arms retracted and at a later stage, the drill-string is pulled back to the casing shoe to enlarge the hole size (see Fig. 147). The time evolution of the bottom hole and top of rat hole depths has a direct impact on the quantity of cuttings being produced but also on the geometrical dimensions of the borehole, which in turn affects the wellbore volume, the drilling fluid velocity in the annulus, the drill-string buckling limits, etc.

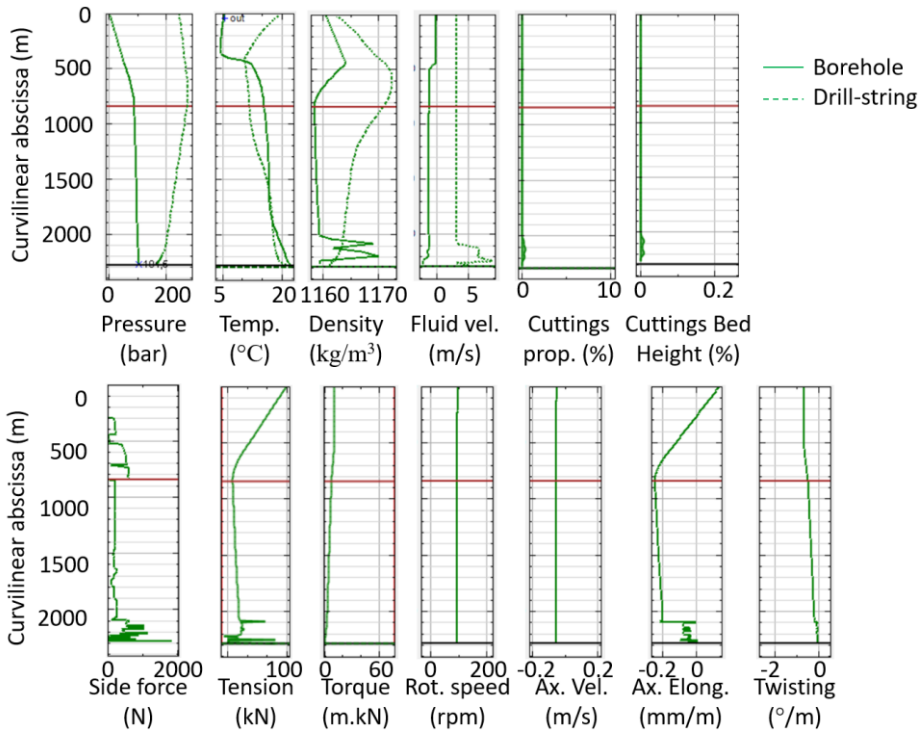

Fig. 146: Example of the typical results from the estimation of the internal state of the drilling system at any instant.

To perform this continuous evaluation, a transient hydraulic model as the one mentioned in section 2.1.1.22, coupled with a transient cuttings transport model as described in section 3.1.4, a transient torque and drag model as the one depicted in section 3.2 and a heat transfer model with the capabilities of the one mentioned in section 2.1.3 are utilized. The hydraulic, cuttings transport and heat transfer models run at 10Hz, while the transient torque and drag model runs at 100Hz. These models are also coupled to the return flow and pit volume model that has been described in section 3.3, such that measurements can be compared with modelled values (see Fig. 148).

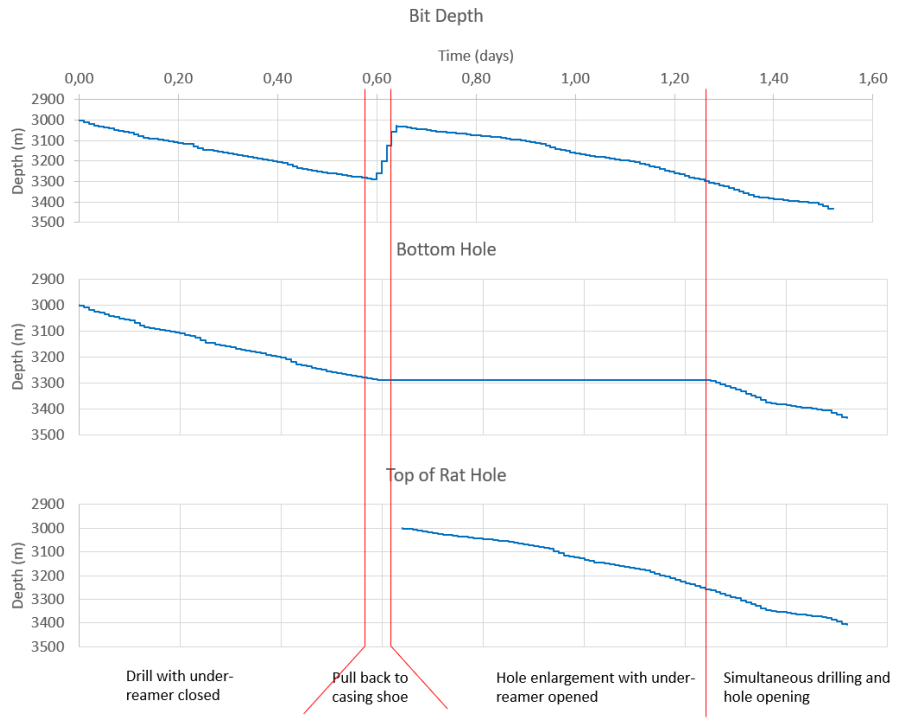

Fig. 147: Example of a sequence where the first 300m are drilled with the under-reamer closed, then the BHA is pulled back to the casing shoe and the under-reamer is opened to enlarge the first 300m of open hole. Thereafter drilling is resumed with simultaneous hole enlargement.

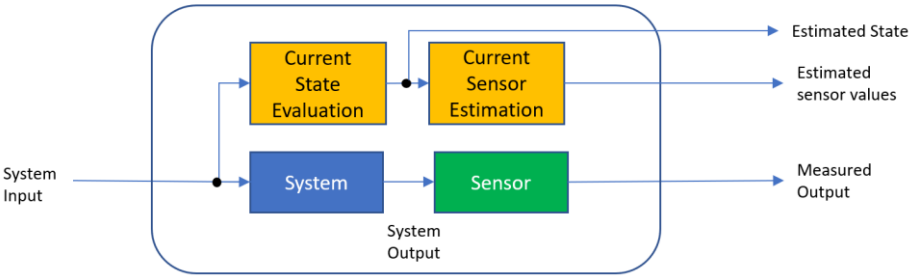

Fig. 148: Block diagram of the current state estimation

The estimated current state of the drilling process is then made available for further analysis with a refresh rate of 1Hz. The reason for reporting the internal state estimations at only 1Hz, is simply to reduce communication bandwidth.

Utilizing such principles, it has been possible to estimate the time at which cuttings should arrive at surface in a complex context where both the drill-string and the borehole were tapered. The time difference between the estimation and the observation of the arrival of the first cuttings to surface, was three minutes while the total delay for the first cuttings to arrive at surface was 16 hours (see Fig. 149 and Cayeux et al. 2016 [98] for a complete description).

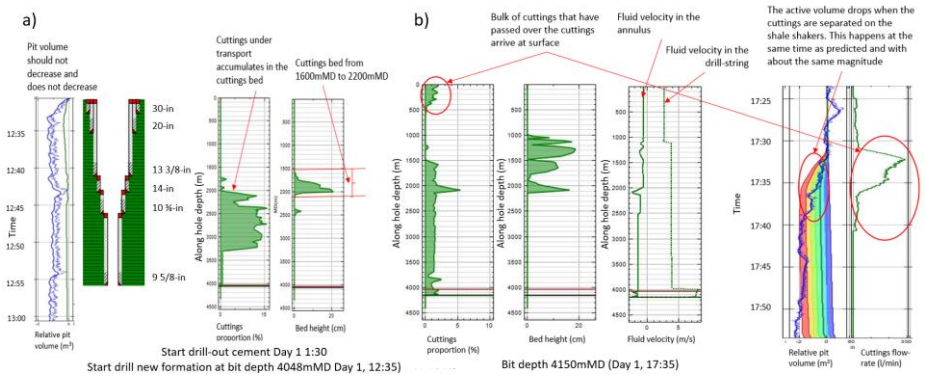

Fig. 149: Comparison between the prediction of the arrival time of the first cuttings to surface utilizing an early version of the described cuttings transport model and observations made during the drilling operation (ref. Cayeux et al 2016 [98]).

3.4.4.1 Summary

The drilling process in non-holonomic.
It is necessary to continuously estimate the internal state of the system from the start of the operation, as without tracking the history of all actions that have been performed it would not be possible to estimate the current state of the system.

The continuous tracking of the state of the system necessitates to utilize simultaneously hydraulic, mechanical, heat transfer and material transport calculations.

3.4.5 Global Calibration of Ill-defined Configuration Information

It is very likely that the modeled sensor values, obtained during the state evaluation described in section 3.4.4, will not match the measurements. A first cause for such a discrepancy is linked to ill-defined configuration information. For instance, the average linear weight of drill-pipe is not necessarily known with a great precision, or an error of a fraction of millimeter on the average internal diameter (ID) of the drill-pipes can lead to several ten bars difference for the estimation of the pump pressure. It is also difficult to obtain reliable information about the pressure losses generated by special elements in the BHA, like the MWD, PWD, LWD, RSS. Yet, the correct distribution of pressure losses between the drill-string and the BHA is essential for a proper estimation of the free rotating weight while circulating, because of the pressure-induced forces that influence the tension along the drill-string wherever there is a change of diameter (see section 3.2.4). Luckily, these information, e.g. linear weight of the pipes, pipe ID, equivalent nozzle ID for the pressure losses in special elements of the BHA, are unlikely to change throughout the drilling operation, and therefore they can be estimated utilizing a calibration method that accounts for all possible observations since the start of the run. We will refer to this calibration as a global one.

There are conditions for which measured values depend on time-variable parameters. For instance, a pick-up weight or a slack-off weight, in a deviated well, is a function of the mechanical friction, which in turn varies with time because of the presence of cuttings, either in suspension or in bed (see section 3.1.4.3 for considerations about the grinding of solid particles at the tool-joints). Fortunately, there are conditions where some measurements are independent of those time-variable parameters, like for example the free-rotating weight, as the mechanical friction translates solely in torque and not drag forces.

The criterion for considering that an observation is a candidate for global calibration purposes, is that the utilized measurements are marginally influenced by variations of time-dependent parameters. The time-dependent

parameters are the static and kinetic mechanical frictions, and the annulus hydraulic friction. If the measurements that are considered for global calibration are normalized and represented by a vector $\vec{q}$ and if we denote $\vec{\tilde{q}}$ the corresponding estimated sensor values, and if μ_k, μ_s and f_v, represent, respectively, the kinetic, static and annulus hydraulic frictions, then the criterion is expressed as:

$$\forall \mu_{k_1}, \mu_{k_2}, \mu_{s_1}, \mu_{s_2}, f_{v_1}, f_{v_2} | \mu_{k_1} \neq \mu_{k_2}, \mu_{s_1} \neq \mu_{s_2}, f_{v_1} \neq f_{v_2}, \forall t \in [t_s, t_f], \left\| \vec{\tilde{q}}(t, \mu_{k_1}, \mu_{s_1}, f_{v_1}) - \vec{\tilde{q}}(t, \mu_{k_2}, \mu_{s_2}, f_{v_2}) \right\| \leq \varepsilon_{gc} \quad (217)$$

where t_s and t_f are respectively the start and end of the considered time interval and ε_{gc} is an acceptable threshold. Note that f_v is a multiplicative factor used to increase or decrease the frictional pressure loss component in eq. (63) for the annulus branch of the hydraulic network, i.e. $f_v = 1$ means that the term is uncorrected.

Furthermore, for the purpose of global calibration, we only consider measurements that are made in steady state conditions because then we can use the steady state version of the mechanical and hydraulic models. This condition is respected when:

$$\underset{t_s \leq t \leq t_f}{\sigma} \|\vec{q}(t)\| \leq \varepsilon_{ss} \quad (218)$$

where $\underset{t_s \leq t \leq t_f}{\sigma}(.)$ is the standard deviation over a time window $[t_s, t_f]$ and ε_{ss} is a threshold for considering that the conditions are in steady state.

Note that the relevant time intervals are limited to at most one or two minutes, such that it is possible to consider that the temperature conditions are also steady state.

For each relevant time interval, $[t_{s_i}, t_{f_i}]$, i.e. those for which both logical expressions (217) and (218) are true, we collect the current estimated state as described in section 3.4.4, denoted here S_i, and the average values of all the inputs to the system, denoted as $\vec{\bar{c}}_i$. Let us call $\vec{p}_g$ a vector representing the parameters that shall be globally calibrated, then the current estimation of those parameters, $\vec{\hat{p}}_g$, is defined by:

$$\vec{\hat{p}}_g = \arg\min_{\vec{p}_g} \sqrt{\sum_{i=1}^{n} \left\| \vec{q}_i - \vec{\tilde{q}}(\vec{p}_g, \vec{\tilde{c}}_i, S_i) \right\|^2} \tag{219}$$

The typical parameters to be calibrated are a correction factor for the linear weight and an internal coating thickness per type of pipes, the equivalent pressure loss coefficients for special elements like PWD, LWD, RSS, and an adjustment factor of the bit nozzle total flow area.

The relevant measurements are the pump pressure, the downhole pressure in the BHA (including when available the inside pressure), along-string pressure measurements (including inside pressure when available), the hook-load, downhole WOB measured in the BHA and any additional tension measurements along the drill-string. If there are no downhole WOB, then only off bottom conditions shall be used for calibration as there is one missing parameter to calibrate weight effects.

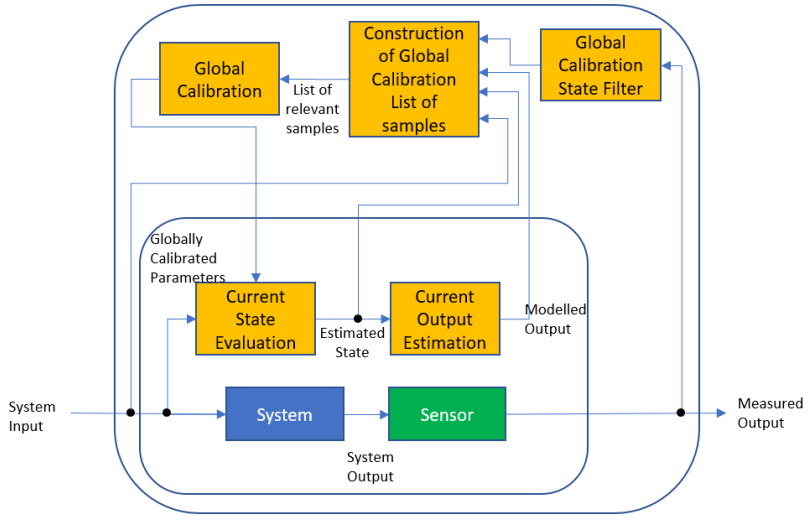

Fig. 150: Block diagram of the methodology used to calibrate ill-defined configuration information.

A block diagram of the global calibration method is shown on Fig. 150. The "Global Calibration State Filter" checks continuously when eq. (217) and (218) are satisfied. The "Construction of Global Calibration List of Samples"

accumulates the relevant conditions for global calibration together with their current estimated state and averaged measurements. Finally, "Global Calibration" solves eq. (219) over the whole list of samples, each time a new one is available. The globally calibrated parameters are then used by the current state evaluation. Of course, uncertainty on sensor measurements impacts the achievable calibration. This is why uncertainty propagation as described in sections 3.4.1, 0 and 0 is important.

3.4.5.1 Summary

There are special conditions by which measurements are independent of time variable parameters such as mechanical and hydraulic friction.
During these special conditions and when the system is in steady state, it is possible to collect measurements that can be used for the calibration of quasi invariant parameters, such as the pipe linear weight, pipe ID, etc.
The calibration of these so-called global parameters is achieved by solving a minimization problem.

3.4.6 Calibration of non-Constant Drilling Process Parameters

As it has been mentioned in the previous section, there are drilling process parameters that are not constant throughout a single run.

For instance, the mechanical friction is subject to the current drilling conditions. Indeed, the kinetic friction depends on the presence of cuttings either in suspension or in beds. The static friction may be larger when the BHA is in contact with porous and permeable formations because of an increased effect of differential sticking than when it is in contact with an impermeable material, either rock or casing.

The annulus friction correction factor compensates for ill-defined downhole conditions, like lateral drill-string vibrations, hole enlargement, cuttings beds, that can change during the total duration of the drilling operation. The rock-strength varies from formation layer to formation layer. Its current value impacts the ROP and consequently the production of cuttings, but also the potential for torsional drill-string vibrations. The bit aggressivity evolves with drilling time as the bit gets blunter and blunter.

Therefore, these drilling process parameters shall be calibrated on a continuous basis but only with data from the recent past. Fig. 151 shows a block diagram of the various calibration functions, including the calibration of kinetic and static friction, hydraulic annulus friction, formation strength, bit aggressivity and heave level.

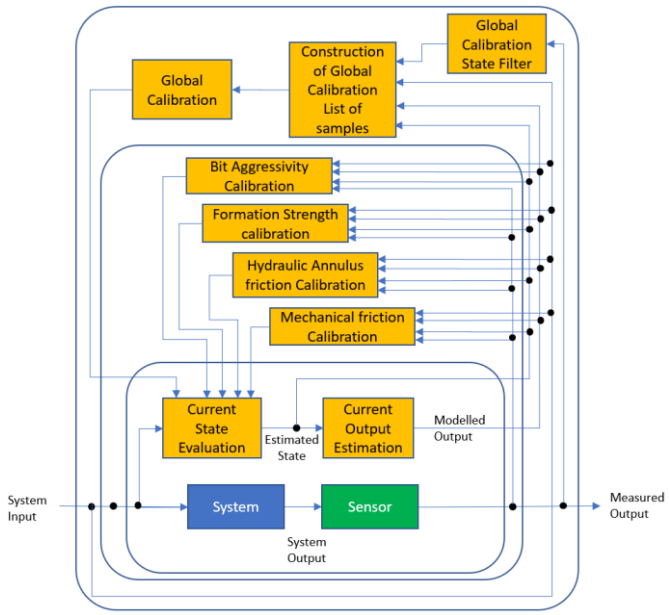

Fig. 151: Block Diagram of the methodology used to calibrate time-dependent parameters of the drilling process.

3.4.6.1 Estimation of Static and Kinetic Frictions

"When drilling from a floater, in weather conditions that cause substantial heave movement, it may be almost impossible to find periods of time where the observed values are not influenced by transient effects as can be seen on Fig. 35. Yet, any transient torque and drag simulations made under these conditions would be unlikely to reproduce the observed hook-loads and top-drive torques, simply because the model response depends on the static and kinetic friction between the drill-string and the borehole.

Let us consider the sum of the square of the differences between the observed and predicted hook-loads and top-drive torques as a factor that characterizes the match between the predicted response of the system and the observations. As

we want to simultaneously account for the hook-load and the top-drive torque, we need to ensure that cumulated values are normalized. For this purpose, we use the estimated free rotating top of string force ($\hat{F}_{FRW}$) and the estimated free-rotating torque ($\hat{\tau}_{FRT}$). Then, the evaluation factor (C_{μ_k,μ_s}) is defined as:

$$\forall \hat{\tau}_{FRT} > \varepsilon_{FRT}, C_{\mu_k,\mu_s} = \sum_{0 \le i \le n} \left(\frac{\left(\hat{F}_{tos,i} - F_{tos,i}\right)^2}{\hat{F}_{FRW}{}^2} + \frac{\left(\hat{\tau}_{TD,i} - \tau_{TD,i}\right)^2}{\hat{\tau}_{FRT}{}^2} \right) \quad (220)$$

where $\hat{F}_{tos,i}$ and $\hat{\tau}_{TD,i}$ are respectively the estimated top of string force and top-drive torque at time step i, and $F_{tos,i}$ and $\tau_{TD,i}$ are respectively the measured top of string force and top-drive torque at the time step i. "[48] Note that if the well is near vertical, then the estimated free rotating torque is closed to zero and the normalization of torque measurements does not make sense. Therefore, the estimation of the mechanical friction is only performed when the free rotating torque is greater than a given threshold limit ε_{FRT}.

A friction test executed in a deviated well drilled in the North sea is shown on Fig. 152. The graph on the right-hand side of the figure shows C_{μ_k,μ_s} as a function of μ_k and $\mu_s - \mu_k$. The minimum is obtained at $\mu_k = 0.14$ and $\mu_s - \mu_k = 0.04$, which also corresponds to the green curves on the left-hand side graphs.

As running the transient torque and drag model over a time window of several tens of seconds is costly in time and computer resources, the minimization algorithm shall make use of as few simulations as possible. A possible solution consists in constructing a proxy model which evaluation is light weight. Then the reduced model is utilized to search the minimum. Typical proxy models are polynomial and radial basis interpolators.

The apparent mechanical friction evolves with time because of varying downhole conditions. For instance, the drill-pipes may be moved axially in a cuttings bed resulting in the application of additional forces on the tool-joints. Through calibration of the mechanical friction, the effect of these additional forces is converted into an increase of the kinetic friction. There is also an

48 Excerpt from Cayeux (2018) [185]

uncertainty associated with the evaluation of the mechanical friction. Therefore, we utilize a moving window for which all gathered mechanical frictions are utilized to estimate a probability distribution. The P50 percentile of that probability distribution represents the average mechanical friction, while an indication of the variability of the estimated mechanical friction is given by the interval P15 and P85 of the probability distribution (see Fig. 153). The minimum of the P50 of the mechanical friction is considered as the currently best observed mechanical friction.

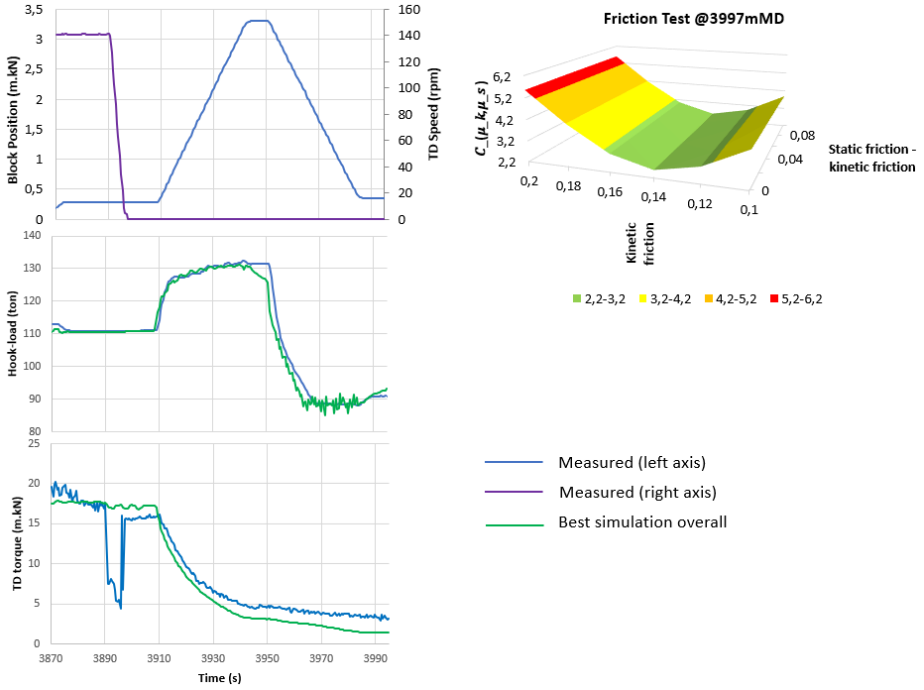

Fig. 152: Analysis of a friction test executed in a deviated well (North Sea). On the left-hand side, comparison between measured hook-loads and torques with estimated values with the transient torque and drag (green curves correspond to the overall best match). On the right-hand, the graph shows C_{μ_k,μ_s} values as a function of the kinetic and static friction increase.

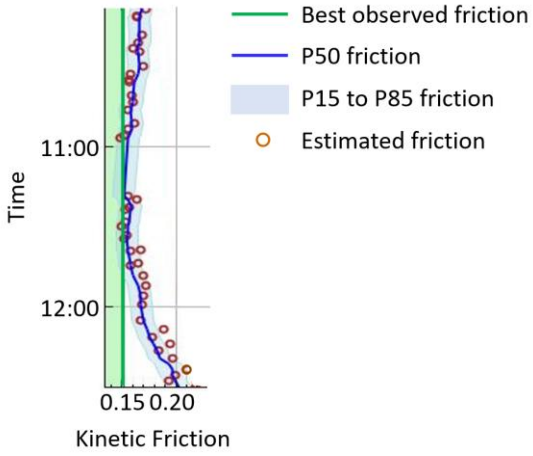

Fig. 153: Evolution of the kinetic friction while tripping out of a deviated well.

3.4.6.2 Estimation of Annulus Hydraulic Friction Correction Factor

Let us define a criterion for steady state flow conditions, based on observations made at the inlet and outlet of the hydraulic circuit:

$$\begin{aligned} \underset{0\le t\le \Delta t_{ss}}{\sigma}\left(Q_{MP}(t)\right) \le \varepsilon_{Q_{MP_{ss}}} \wedge \underset{0\le t\le \Delta t_{ss}}{\sigma}\left(p_{MP}(Q_{MP},t)\right) \\ \le \varepsilon_{p_{MP_{ss}}} \wedge \underset{0\le t\le \Delta t_{ss}}{\sigma}\left(Q_{out}(Q_{MP},t)\right) \le \varepsilon_{Q_{out_{ss}}} \end{aligned} \tag{221}$$

where Δt_{ss} is a minimum duration for which the flow can be considered in steady state conditions, Q_{MP} is the measured mud pump flowrate, $\varepsilon_{Q_{MP_{ss}}}$ is a threshold value for the standard deviation of the mud pump flowrate, p_{MP} is the measured mud pump pressure, $\varepsilon_{p_{MP_{ss}}}$ is a threshold value for the standard deviation of the mud pump pressure, Q_{out} is the measured flowrate out at the bell nipple or diverter and $\varepsilon_{Q_{out_{ss}}}$ is a threshold limit for the variance of the flowrate out of the well. As it is seldom to have a precise flowrate out sensor at the well outlet, Q_{out} can be replaced by $\hat{Q}_{out}$, an estimated flowrate out made with a transient hydraulic model.

When the mud pump flowrate is kept constant, and after a possibly long transient period after the flowrate is changed, as illustrated by Fig. 12, the flow condition reaches steady state. Yet the downhole pressure may fluctuate substantially because of rotational and lateral drill-string movements as well as the result of side effects of cuttings transport (see Fig. 33 for an illustration of

large downhole pressure variations associated with stick-slips). However, when downhole pressure measurements are sent by mud pulse telemetry, only average values, over several ten seconds are available, which rules out to attempt performing a transient calibration of the downhole pressure.

Therefore, the annulus hydraulic friction correction factor is calibrated using the steady state version of the hydraulic model. When all transient effects are disregarded, the estimated downhole pressure is a monotonic function of the annulus hydraulic friction factor. It is possible to take advantage of that facts, by calculating downhole pressure with the steady hydraulic model for just a few samples of annulus hydraulic friction factor and to construct an interpolator function calibrated with these reference values. Then the interpolator function is used to estimate the annulus hydraulic friction factor for which the modelled downhole pressure, in steady state conditions, matches the last measured average downhole pressure.

With this method it is possible to estimate the annulus hydraulic friction factor in constant time. In practice, only a dozen uniformly distributed samples are necessary.

The annulus hydraulic friction correction factor evolves with time as the downhole conditions varies. There may be more cuttings in suspension than expected or cuttings depositing in a bed in a different proportion than estimated. But, there also can be more drill-sting vibrations than anticipated, causing larger pressure losses. Furthermore, the estimation of the annulus hydraulic friction correction factor has its own uncertainty. Therefore, we gather estimated annulus hydraulic correction factors obtained in a moving time window and estimate its probability distribution. The P50 of this probability distribution is the average value, while the interval P15 to P85 gives an indication of the dispersion of the estimated values (see Fig. 154).

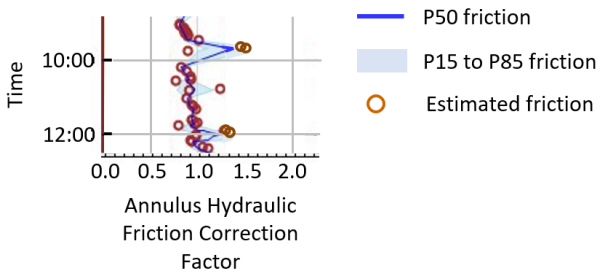

Fig. 154: Evolution of the annulus hydraulic friction correction factor while drilling a 12 ¼-in section of a deviated well.

3.4.6.3 Estimation of the Bit Aggressivity and Formation Strength

Fig. 36 illustrates that the estimation of the instantaneous ROP is not immediate when a rig is subject to heave movement. However, a transient torque and drag model as described in section 3.2 utilizes a ROP model to determine the forces and torques along the drill-string, as a function of the top of string axial and rotational movement, and the formation strength.

The formation strength can be estimated by using eq. (85). Let us consider the averaged measured force and torque on bit, respectively denoted $\tilde{F}_{bit}$ and $\tilde{\tau}_{bit}$, over a sampling time window of duration Δt_{ROP}. The time window is chosen to be longer than the current heave period, when drilling from a floater, and longer than the wavelength of the natural torsional resonance frequency of the drill-string. Then the CCS can be estimated:

$$CCS = \frac{\tilde{\tau}_{bit}\bar{\omega}_{bit}}{\bar{v}_{bit}\,A_{bit}} + \frac{\left|\tilde{F}_{bit}\right|}{A_{bit}} \tag{222}$$

where $\bar{\omega}_{bit}$ and $\bar{v}_{bit}$ are the average angular and axial rotational velocities during the time window Δt_{ROP}, estimated by the transient torque and drag mode.

Furthermore, in eq. (78), μ_{ref} defines a direct proportionality between WOB and bit torque when combined with eq. (77). Consequently, when the torque on bit fluctuates this is because of WOB variations. So, to calibrate μ_{ref}, we can utilize the average measured torque on bit ($\tilde{\tau}_{bit}$) and force on bit ($\tilde{F}_{bit}$) over a given time window, Δt_{ROP}:

$$\tilde{\tau}_{bit} = \mu_{ref} e^{-\alpha_{ref}\, CCS} d_{bit} \tilde{F}_{bit} \Leftrightarrow \mu_{ref} = \frac{\tilde{\tau}_{bit}}{e^{-\alpha_{ref}\, CCS} d_{bit} \tilde{F}_{bit}} \quad (223)$$

Eq. (222) is first solved, and then the updated value of CCS is injected in eq. (223), in order to retrieve μ_{ref}. The new estimated CCS and μ_{ref} are used during the next sequence of duration Δt_{ROP}.

Fig. 155 shows the estimated CCS and μ_{ref} during the drilling of the sequence shown on Fig. 127. This sequence corresponded to drilling from a floater with passive heave compensation. The time window, Δt_{ROP}, is 30s. $\tilde{F}_{bit}$ and $\tilde{\tau}_{bit}$ are here evaluated from surface measurements by subtracting the FRW and FRT, respectively. If downhole WOB and torque on bit had been available, they could have been used as well.

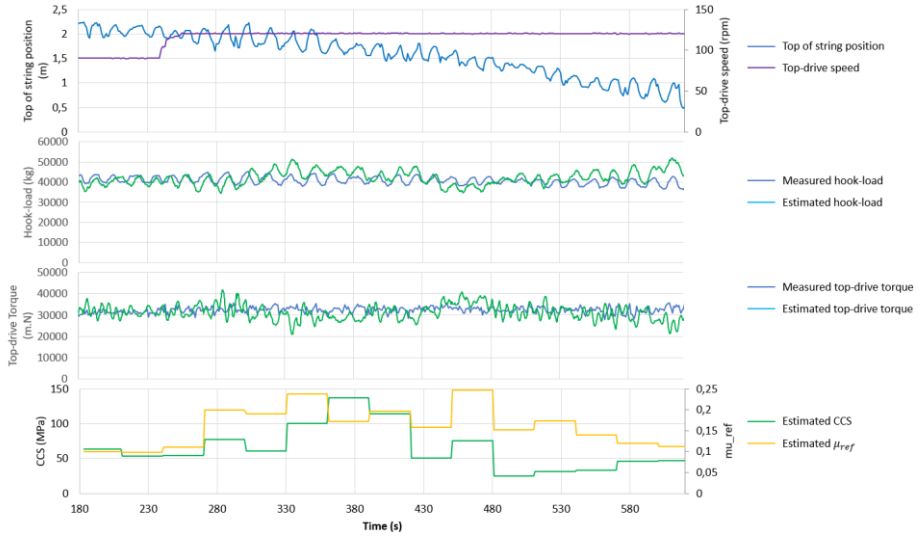

Fig. 155: Estimated CCS and μ_{ref} corresponding to the sequence drilled from a floater with passive heave compensation shown on Fig. 127.

3.4.6.4 Summary

Some model parameters need to be continuously evaluated as they depend on downhole conditions.
Different methods are used for the estimation of these time-varying parameters.
In the absence of clear steady state conditions, because of the side effects of heave on a floater or because of natural drill-string torsional oscillations, it may be necessary to calibrate the static and kinetic mechanical frictions during transient periods. In this case, the static and kinetic frictions need to be calibrated simultaneously by minimizing the difference between observations and estimations over a time window that is longer than the periods of the most important periodic phenomena such as the typical heave period or the natural drill-string torsional oscillation period.
In general, it is easier to find steady state conditions to calibrate the annulus hydraulic factor. Yet statistical analysis is applied on the calibrated factor to extract information about its trend and dispersion.
The bit rock interaction needs also to be calibrated. One of the parameters is the formation strength, which can be estimated by minimizing the difference between measured and estimated WOB. This estimation can be made recursively by modifying the previous CCS estimation. However, as the formation strength can change abruptly, the moving time window for this estimation shall be relatively short.
Another parameter of the bit rock interaction model is the bit aggressivity. It can also be estimated recursively, however using a long moving time window as the bit bluntness does not evolve fast.

3.4.7 Accuracy of Pressure, Tension and Torque Estimations

We have seen in sections 3.4.1, 0, 0 and 3.4.6 that the drilling fluid density, its rheological behavior, some configuration information of the drill-string like the linear-weight and the ID of drill-pipes, the mechanical friction factor and the annulus hydraulic friction correction factor have an associated uncertainty. There is also an uncertainty on TVD, as it has been described in section 3.4.3.1,

that influences the estimation of hydro-static pressures (ref eq. (1)). All these sources of uncertainty have an impact on estimated values such as those listed in section 3.4.4.

To propagate input uncertainties to estimated values, we utilize stochastic simulation. The propagation is made only in steady state conditions and with the steady state versions of the mechanical and hydraulic models. Fig. 156 shows the results of the propagation of drilling fluid mass density and rheological behavior uncertainties, linear weight and ID of drill-pipes and mechanical and hydraulic annulus friction correction factor uncertainties.

In this 12 ¼-in section, there are no downhole annulus pressure measurements and therefore the uncertainty on the annulus downhole pressure gradient is rather large.

The last asserted probability distribution made at the curvilinear abscissa of a measurement and in steady state conditions, is transposed for that measurement during transient conditions (see Fig. 157).

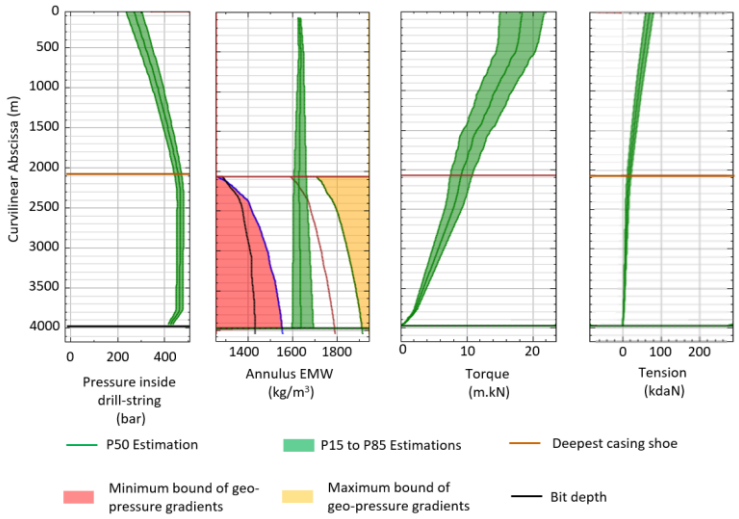

Fig. 156: Example of results obtained after propagation of input uncertainties on estimated pressures, torques and tensions along string and annulus pressure gradients. In this case there are no downhole annulus pressure measurements available.

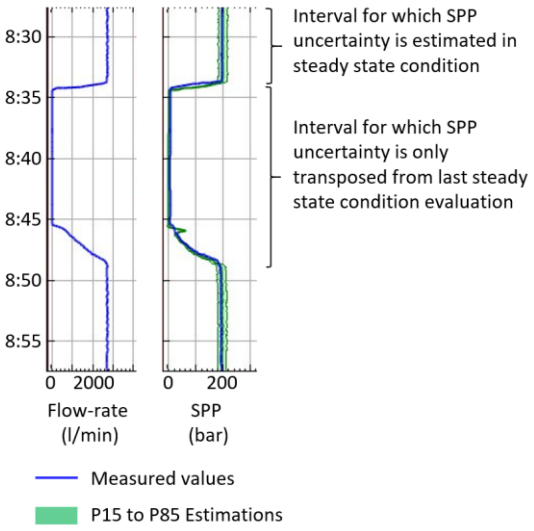

Fig. 157: Illustration of the transposition of SPP uncertainty during transient periods from last estimations in steady state conditions.

3.4.7.1 Summary

Uncertainty on model inputs can be propagated to estimate the uncertainty on modelled values by stochastic simulations.
To be compatible with real-time constraints, reduced models are used during the stochastic simulations.
Here the model reduction consists in utilizing steady state versions of the transient hydraulic and mechanical models.
The estimated probability distribution based on steady state conditions is then utilized to estimate the uncertainty on the modelled values during transient periods.

3.4.8 Integration of Distributed Measurements to Improve Estimation Accuracy

Additional measurements can help reduce the uncertainty of estimated values along the drill-sting and annulus.

Let us suppose that, while estimating the downhole pressure along the annulus, there are no downhole measurements at all. Then the uncertainty of the estimated hydrostatic and hydrodynamic pressures, as a function of the curvilinear abscissa along the annulus, must increase with depth (see Fig. 158), as the only known boundary condition is the one at the outlet of the well, i.e. atmospheric pressure in conventional drilling. However, if we have a downhole measurement with an uncertainty that is smaller than the estimated one, then it is possible to eliminate from the stochastic simulations, all the realizations that led outside the tolerances of that measurement. Note that there is still an increasing uncertainty the further away we are from known values, i.e. here in this schematic representation: the pressure at the outlet and the downhole pressure in the BHA.

So, in theory, the more distributed measurements, the better. Yet, the accuracy of the measurements shall be smaller than the uncertainty of the estimation propagated from the uncertainty on the input information. Fig. 159 shows real data from four distributed pressure sensors placed 400m apart from each other's while drilling a 16-in hole. The markers are the high-speed telemetry measurements, while the solid lines are calculated using a transient hydraulic model.

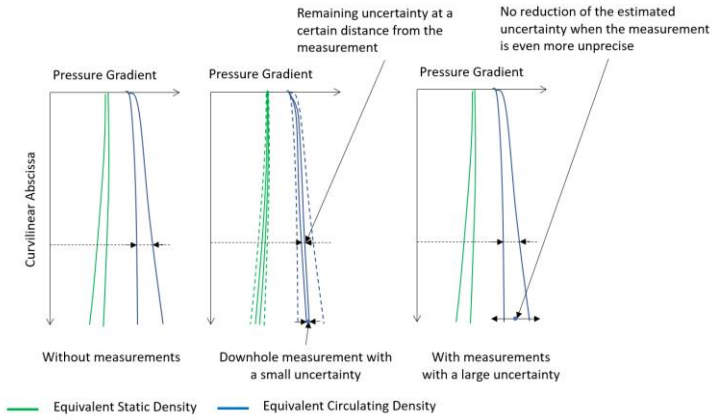

Fig. 158: Schematic representation of the influence of a low uncertainty downhole measurement on the reduction of the uncertainty along the whole annulus.

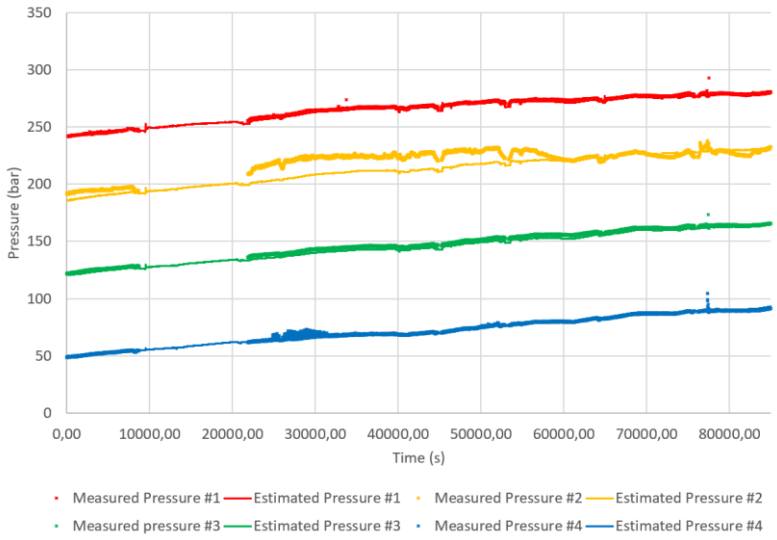

Fig. 159: Comparison of estimated values with pressure measurements taken from four along-string sensors placed 400m apart from each other's along a drill-string while drilling a 16-in hole with high-speed telemetry.

We can first notice that for the deepest sensor, i.e. the sensor labelled #1, and for the third sensor, there is a very good agreement between the estimated and measured pressures. However, it is puzzling to see that the measured and estimated pressures at the location of the second sensor differ for most of the time period (here 24 hours). Even a restriction between sensors #2 and #3 would not make sense, as it would have resulted in a larger downhole pressure that effectively could have been recorded on sensor #2, but should also have been visible on the deeper sensor as well, i.e. sensor #1. And this is not the case. Similarly, between 24000 and 32000s, the shallowest sensor, i.e. #4, measures some increase of pressure and yet, this pressure increase is unnoticeable on the deeper sensors.

It is also noticeable, that the pressure measurement errors of sensors #2 and #4 are not systematic, as the discrepancy with their associated estimated counter parts, varies throughout the displayed period. With such inconsistencies in the distributed measurements, it is not possible to reduce the uncertainty of estimated values at any positions along the annulus, at least if we consider all four sensors.

However, we can notice that at time approximatively 78000s, there is an over-pressure that is visible on all four sensors, indicating that its cause is above the shallowest sensor, i.e. sensor #4.

3.4.8.1 Summary

Additional measurements taken at different positions may help reduce uncertainty on model predictions.
Yet, to be effective, the measurement uncertainty shall be smaller than the modelled one.
Measurement uncertainty may be impacted by inconsistent results through time.

3.4.9 Closest Approach for Downhole Pressure Proximity to Geo-pressure Margins

To detect a risk of hole collapse, formation fluid influx or formation fracturing, we need to verify continuously that the annulus pressure stays within the geo-pressure margins for the whole open hole section. This can be expressed as:

$$\forall t, \forall s \in [s_{cs}, s_{bh}], \max\left(p_{pore}(s), p_{cp}(s)\right) \leq p_a(t,s) \leq p_{fp}(s) \qquad (224)$$

where s_{cs} is the curvilinear abscissa of the deepest casing shoe, s_{bh} is the bottom hole depth, p_{pore} is the pore pressure, p_{cp} is the collapse pressure, p_{fp} is the fracturing pressure and p_a is the borehole pressure.

But we can only estimate the borehole pressure and this estimation is uncertain as we have seen in section3.4.7. So, to integrate the borehole estimation pressure uncertainty, we modify eq. (224) into:

$$\forall t, \forall s \in [s_{cs}, s_{bh}], \begin{cases} \max\left(p_{pore}(s), p_{cp}(s)\right) \leq p_{a_{15}}(t,s) \\ p_{a_{85}}(t,s) \leq p_{fp}(s) \end{cases} \qquad (225)$$

where $p_{a_{15}}$ and $p_{a_{85}}$ are respectively the P15 and P85 percentiles of the borehole pressure estimation. Let us introduce, $p_{a_{50}}$, the P50 percentile of the borehole pressure estimation. Then eq. (225) can be rewritten:

$$\forall t, \forall s \in [s_{cs}, s_{bh}], \qquad (226)$$

$$\begin{cases} \max\left(p_{pore}(s), p_{cp}(s)\right) + p_{a_{50}}(t,s) - p_{a_{15}}(t,s) \leq p_{a_{50}}(t,s) \\ p_{a_{50}}(t,s) \leq p_{fp}(s) - p_{a_{85}}(t,s) + p_{a_{50}}(t,s) \end{cases}$$

We simplify the notation by defining $p_{a_{50-15}} = p_{a_{50}} - p_{a_{15}}$ and $p_{a_{85-50}} = p_{a_{85}} - p_{a_{50}}$, and we obtain:

$$\forall t, \forall s \in [s_{cs}, s_{bh}], \tag{227}$$
$$\begin{cases} \max\left(p_{pore}(s), p_{cp}(s)\right) + p_{a_{50-15}}(t,s) \leq p_{a_{50}}(t,s) \\ p_{a_{50}}(t,s) \leq p_{fp}(s) - p_{a_{85-50}}(t,s) \end{cases}$$

So, if we add to the minimum geo-pressure boundary the difference of the P50 and the P15 percentiles of the estimated borehole pressure and if we subtract to the maximum geo-pressure boundary the difference the P85 and P50 percentiles of the estimated borehole pressure, then we can simply refer to the averaged estimated borehole pressure.

The curvilinear abscissa, $s_{ca_{min}}$, of the closest approach to the minimum geo-pressure margin that accounts for the uncertainty on the estimated borehole pressure, is defined by:

$$\forall t, s_{ca_{min}}(t) = \arg \min_{s \in [s_{cs}, s_{bh}]} \Big(p_{a_{50}}(t,s) - \max\left(p_{pore}(s), p_{cp}(s)\right) - p_{a_{50-15}}(t,s) \Big) \tag{228}$$

And similarly, the curvilinear abscissa, $s_{ca_{max}}$, of the closest approach to the maximum geo-pressure margin that accounts for the uncertainty on the estimated borehole pressure, is:

$$\forall t, s_{ca_{max}}(t) = \arg \min_{s \in [s_{cs}, s_{bh}]} \Big(p_{fp}(s) - p_{a_{85-50}}(t,s) - p_{a_{50}}(t,s) \Big) \tag{229}$$

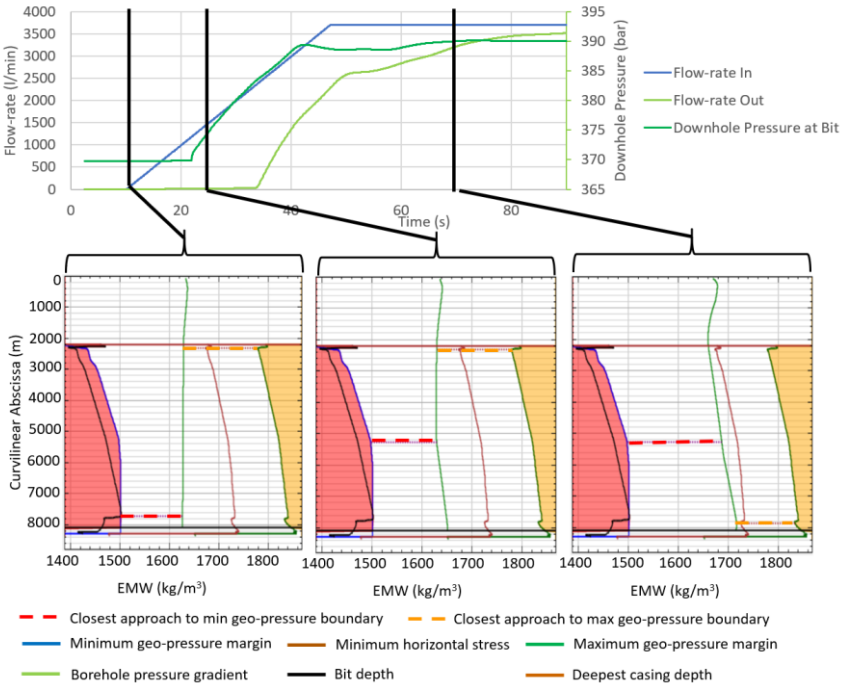

Fig. 160: Example showing the closest distance to the min geo-pressure margin and to the max geo-pressure margins are not necessarily at the bit and that they can change as a function of the annulus pressure gradient along the open hole section.

It should be noted that $s_{ca_{min}}$ and $s_{ca_{max}}$ are not necessarily equals and that they are function of time. This is illustrated by Fig. 160, where we can see that both the closest approach curvilinear abscissas never coincide and change position during a pump startup close to the end of a 12 ¼-in section of an ERD well inclined at 86°.

3.4.9.1 Summary

The geo-pressure margins can be modified to account for the uncertainty of the borehole pressure estimation.
Then, it is possible to determine the curvilinear abscissa by which the P50 borehole pressure and the modified minimum geo-pressure boundary are the closest.
Similarly, it is possible to calculate the curvilinear by which the P50 borehole pressure is the closest to the maximum geo-pressure boundary.
These two closest curvilinear abscissas are normally not identical and are time dependent.

3.4.10 Early Detection of the Deterioration of the Drilling Conditions

The transient mechanical and hydraulic models that have been referred so far, are capable of reproducing in details, the normal response of a drilling system to any time-dependent actions performed during a drilling operation. These models are continuously calibrated and the non-holonomy of drilling operations is managed by continuously estimating the state of the system in terms of temperature, cuttings load, etc. The uncertainty of the estimation is also asserted.

We can now envisage to use the continuously calibrated mechanical and hydraulic models to detect conditions for which the measurements deviate from the estimations. Discrepancies that are larger than the uncertainty of estimated values indicate that something that has not been modelled occurs, and as we have tried to model in great details the normal behavior, it is possible that the discrepancy is caused by an abnormal behavior.

Such abnormal behavior does not need to be at a level that would be considered as a drilling event. Here, we try to detect very early symptoms that the drilling conditions start to deteriorate, if possible, minutes or hours before a drilling event would take place, because we want to give the opportunity to the drilling team to be proactive and to take actions to improve the drilling conditions before any harm is made.

A first symptom is to look at the evolution of the mechanical friction. Fig. 3 of Paper III shows how the estimated mechanical friction starts to increase while pulling out of hole with a 12 ¼-in drill-string.

The benefit of the mechanical friction estimation method that has been described in section 3.4.6.1, is that it estimates kinetic and static frictions whenever it is possible and therefore also during tripping. This contrasts to traditional methods where measured pick-up and slack-off weights are reported on pre-calculated charts, usually made only for drilling conditions.

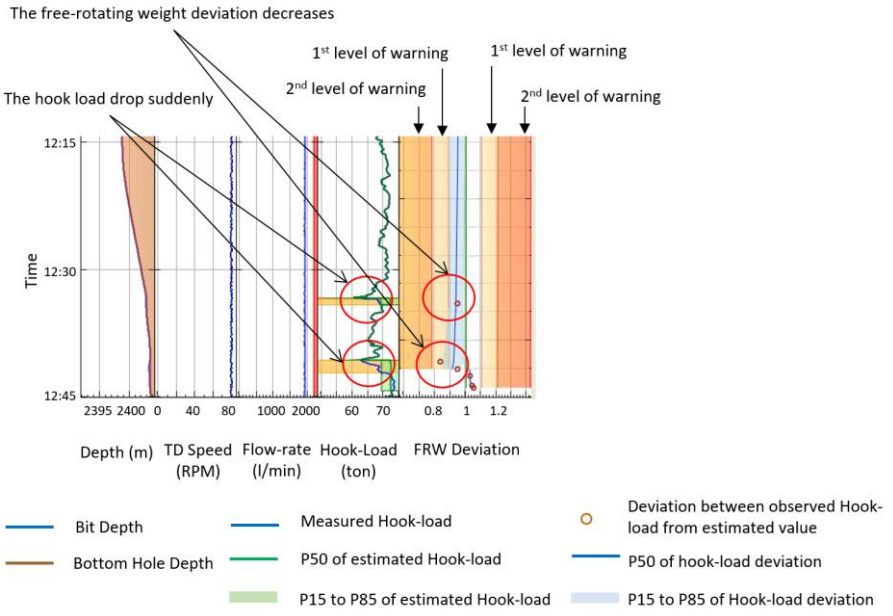

Fig. 161: Example from a real drilling operation where the free-rotating weight deviate abnormally from the estimated value.

A second symptom is to check how the free rotating weight evolves with time. For this, we calculate the ratio of the observed free rotating weight to the P50 estimated corresponding value. We call that ratio the free rotating weight deviation. If the model is well-calibrated and there are no abnormal drilling conditions, the FRW deviation should be one. But if there are unexpected lift forces, for example associated with the start of an obstruction in the annulus, then this ratio can be lower than one. Fig. 161 illustrates such a situation where

at two instances, the driller lifts the drill-string off bottom and the observed FRW is lower than expected.

Fig. 18 of Paper III shows that over a longer period, the monitoring of the FRW deviation gives indications that the downhole drilling conditions are deteriorating. Note that we calculate the statistical distribution of the FRW deviation over a moving time window to determine the dispersion of the observations.

The same method is applied to the pump pressure, i.e. we calculate the SPP deviation as the ratio of the measured SPP to the P50 estimated SPP in the current drilling conditions. Compared to the FRW deviation, the SPP deviation has the benefit of having access to many more observations and makes it easier to detect changes in the downhole drilling conditions based on this symptom. Fig. 162 illustrates that during a real drilling operation while drilling a cement plug with an 8 ½-in BHA utilizing an RSS, the SPP deviated from estimated values at several instances. The deviations are small but indicate that the downhole drilling conditions deteriorate and that it could be wise to apply counter measures in order to improve hole cleaning.

However, this drilling operation continued to drill with the same ROP for several hours. As it can be seen on fig. 19 of Paper III, the elevated SPP deviations could be observed for six hours before serious and multiple pack-offs have been experienced.

Yet another symptom is related to the expected pit volume variation due to cuttings being transported out of the hole and separated at the shale shakers. A transient cuttings transport model as the one described in section 3.1.4, can estimate when cuttings shall arrive at surface. After accounting for the retention of drilling fluid in the surface treatment installation as described in section 3.3 and the impact of compressibility on a mix of solids and liquids (see section 3.1.1), the time evolution of the pit volume can be estimated. Yet, we need to account for the uncertainty associated with how much mud is lost by the separation of drill-cuttings at the shale shakers.

Fig. 16 of Paper III shows that we consider from no losses up to 2.5 times the volume of cuttings. A general rule of thumb is that about the same amount of mud is lost as the volume of cuttings. In the example of fig. 16 of Paper III, corresponding to a real drilling operation, the observed decrease of the active

pit volume and the estimated one are both synchronized and of the same magnitude. So, the transport of cuttings appears to be normal.

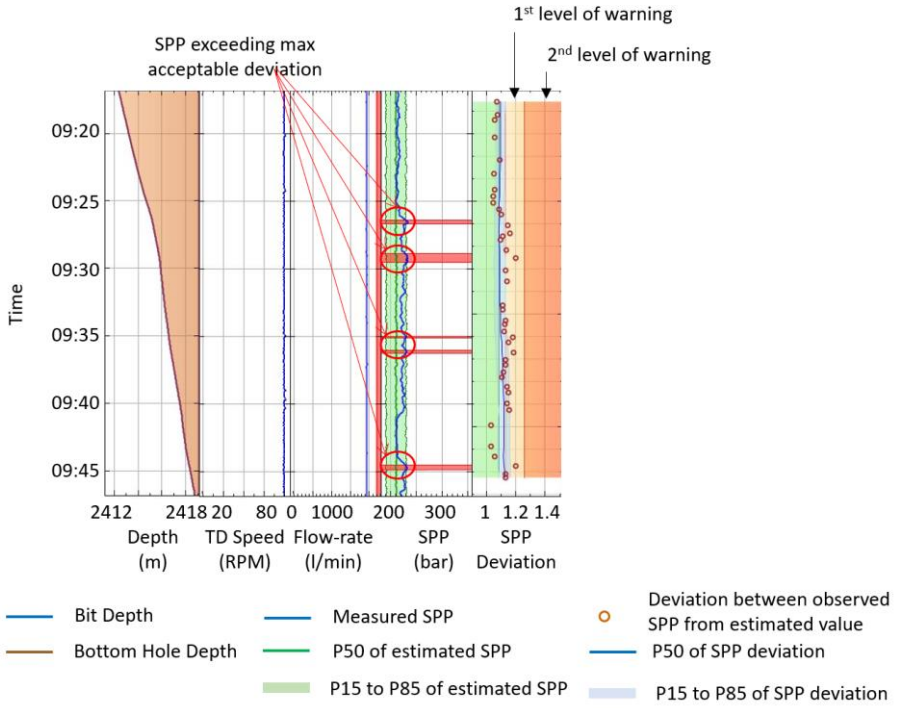

Fig. 162: Example from a real drilling operation of the intermittent SPP deviation compared to expected values while drilling with 8 ½-in BHA with an RSS.

This is not the case of the example of fig. 17 of Paper III, which also is based on a real drilling operation. Seven stands are drilled, and yet the measured active pit volume has slightly increased while the estimated value indicates that it should have decreased by at least $5m^3$ and most likely $10m^3$, if we consider that as much mud as the volume of cuttings is lost through the separation at the shale shakers. For this drilling operation the actual mass flowrate of cuttings after the shale shakers is measured and converted in an equivalent volumetric flowrate by assuming a default cuttings mass density. The last track of the time-based log of fig. 17 of Paper III shows that the measured volumetric cuttings flowrate is far lower than the estimated one.

Tracking the discrepancies between the measured active pit volume and the estimated one is yet another early symptom for detecting that the drilling operation is not performing as it should.

3.4.10.1 Summary

Precise transient models that are well calibrated provides modelled values that can be compared to measurements.
Discrepancies between modelled and the measured values may originate from changes in the downhole conditions.
These weak symptoms are observable prior to the occurrence of drilling incidents.
It is possible to use these early warnings to take proactive actions and cure the drilling problems before any serious damages have occurred.

3.5 Drilling Assistance

In conventional drilling, there are three machines that provide movement to the drill-sting and the drilling fluid: the hoisting system, the top-drive and the mud-pumps. The driller gives set-points for the speed of each machines and the drilling control system applies commands to the motor of each of these machines such that their actual speed respect the set-points. Feed-back control is usually applied by accounting for the difference between the desired speed value and the measured one (see Fig. 163). Of course, the drilling control system does much more than the closed loop control of the speed of the three main drilling machines, but in our context this simplification will be sufficient.

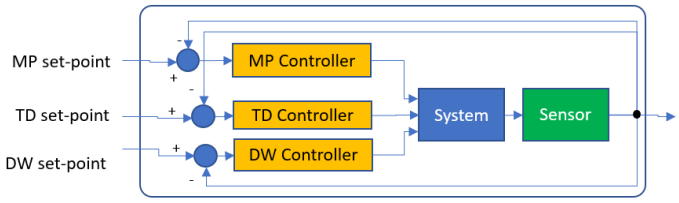

Fig. 163: Block diagram of the parts of the drilling control system associated with the drilling machines.

We would like to assist the driller by offering a set of functionalities that automate some of the repetitive functions that are executed during a drilling operation. When such an automated function is active, it provides directly the set-points to the drilling machines instead of those coming from the joysticks and keypads of the drilling workstation (see Fig. 164).

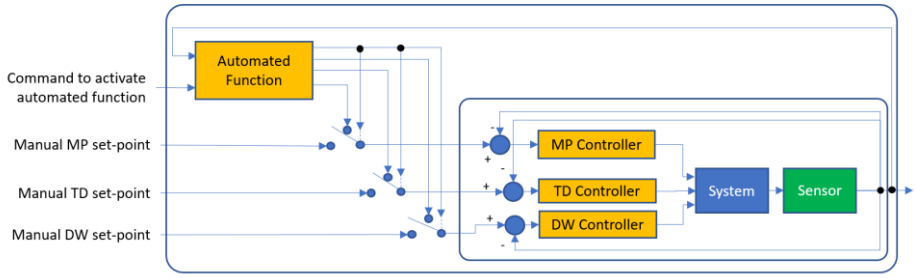

Fig. 164: Block diagram showing how an automated drilling function provides continuously set-points to the drilling machines during its execution.

In the eventuality of the occurrence of a drilling incident, while the automated function controls the drilling machines, it may take several seconds before the driller reacts and return to manual control. In the meantime, the drilling incident may have escalated to a level that can make it more difficult to mend. This is particularly true as the situation awareness of the driller is reduced while an automated function is running. Iversen et al. (2012) [180] utilized the drilling simulator environment described in Paper I, to test the reaction time of drillers to serious situations, while they were using drilling automation functions, and found that their situation awareness was qualitatively reduced. It is therefore important that automated functions are accompanied by a set of fault detection, isolation and recovery (FDIR) functionalities that can reduce the chance for an escalation of the drilling incident severity. An FDIR monitors the outputs of the drilling system for a potential misbehavior, and in case of detection, tries either to set the drilling system in a safe mode, where the human operator can regain manual control, or applies a first response procedure to attempt recovering from the detected problem, when possible (see Fig. 165). When the FDIR has triggered, the automated function that was running, is switched off and set-points, issued directly from the corrective action procedure, are sent to the drilling machines.

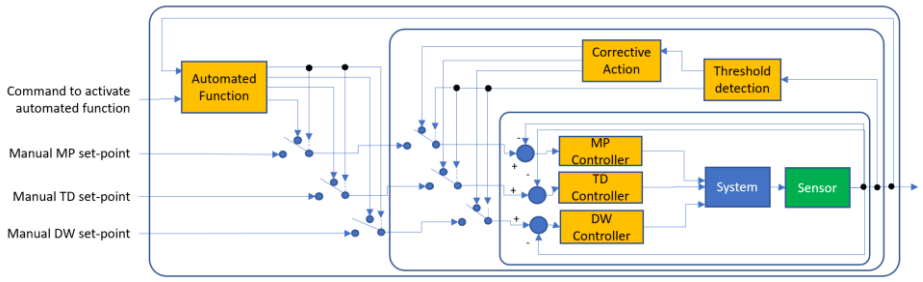

Fig. 165: Block diagram of the integration an FDIR function that can react to an unexpected situation while an automated drilling function is running.

Furthermore, the drilling system, constituted of the drill-string, the drilling fluid and the borehole, is elastic, has a large inertia, is subject to simultaneously Coulomb-like (i.e., a source of negative damping) and viscous-like frictions (i.e., a source of positive damping) and has fast-changing boundary conditions, especially when subject to heave. Therefore, a modification of the set-point of any of the three main drilling machines may have repercussions on the whole drilling system still a long time after the set-point has reached a constant value. Fig. 12 illustrates that kind of behavior, as during this ream-down sequence, the flowrate in set-point has been left constant for more than 6 minutes before the pump pressure stabilizes. Without accounting for that large delay, one could have thought that it was possible to continue increasing the flowrate far beyond the used value, with the consequence of experiencing a pump pressure far above the acceptable pressure tolerance of the pumping equipment.

This problem is also relevant for other industries like aircraft [181], submarine navigation [182] or nuclear plant control [183]. It has been treated by developing systems that calculate and impose safe operating envelopes (SOE). An SOE imposes that the set-points sent to a machine stay within operating envelopes that are compatible with the short to medium term integrity of the drilling system. If the set-point that is sent to a machine controller is too large, or too small, then a maximum or minimum value is sent instead (see Fig. 166).

An SOE protects the inputs to the drilling control system. An FDIR guards for unexpected situations that are detectable from the response of the drilling system, i.e. its outputs. With these two levels of protection, it is then possible to execute automated functions with a reasonable level of confidence that even

though the situation awareness of the driller is low, first action response is always ready to minimize the impact of a drilling event.

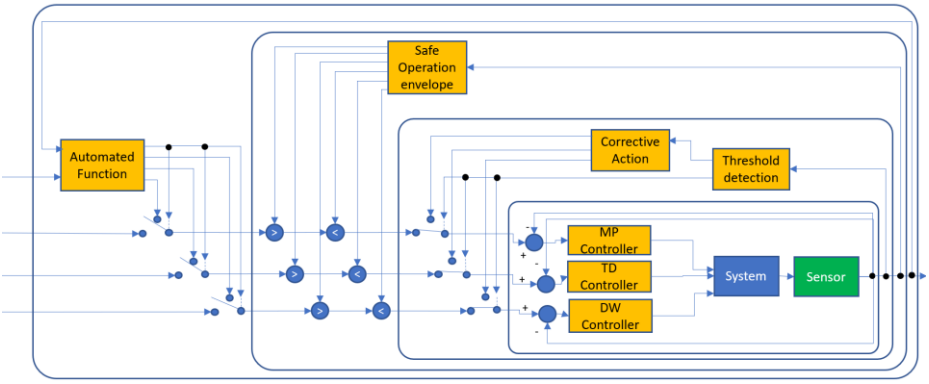

Fig. 166: Block diagram of the integration of a safe operation envelope function that can limit the set-points that are sent to the drilling machine controllers of the drilling control system to values that are compatible with the drilling operation.

3.5.1 Fault Detection Isolation and Recovery

There can be as many FDIR functions as there are measured outputs of the drilling system. We will present three:

- Detection and reaction to abnormal hook-load,
- Detection and reaction to abnormal top-drive torque,
- Detection and reaction to abnormal pump pressure.

This list could have been expanded with the monitoring of the flowrate out of the well, i.e. gain/loss detection. However, the measurement of the flowrate out of a well is most often indirect, e.g. pit volume, or imprecise, e.g. flow-paddle (see Cayeux and Daireaux 2016 [184]) and therefore leads to a relatively large number of false positives or negatives. FDIR based on downhole measurements, like those associated with mechanical subs, i.e. excessive vibrations, or annulus pressure, could also have been envisaged, but they would not be reliable with mud-pulse telemetry and even with wired pipe telemetry,

today's transmission delay of at least 2.5s, would be a limiting factor for obtaining a reliable FDIR based on such signals.

There are different ways to perform the detection stage of an FDIR function. In this work, we have chosen a model-based technique. More precisely, this is an observer-based approach where a model estimates continuously the expected output of the drilling system that is compared with the measured one. When the bias exceeds a chosen criterion then the FDIR function triggers.

3.5.1.1 Overpull and Set-down Weight Detection and Reaction

An abnormal hook-load is one that exceeds an expected value, i.e. an overpull, or one that is lower than expectation, i.e. a set-down weight. This should not be confused with the tensile and the buckling limits of the drill-string, as usually an overpull or a set-down weight happens at hook-load values that are far from these extreme limits (see Fig. 61 and Fig. 62 for example time-based logs of overpulls and set-down weights).

If there is an air gap inside the drill-string, for example while tripping with a float-valve, the top of string force is very different from the one obtained when circulation is established (see Fig. 167).

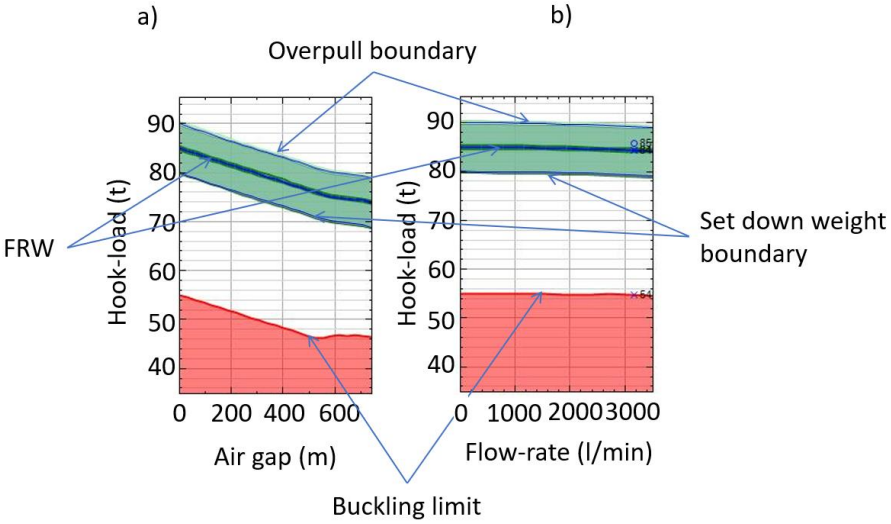

Fig. 167: Threshold limits for overpull and set-down weights a) when the drill-string is not filled and there is an air gap, b) when circulating in steady state conditions.

In addition, the overpull and set-down limits depend on the current conditions of mechanical friction, cuttings load and temperature.

The detection of set-down weights and overpulls is irrelevant when the bit is on bottom drilling. Therefore, the threshold detection is only allowed when the bit is off bottom. The contact condition at the bit is evaluated by a transient torque and drag model, as the one described in section 3.2, since it is not trivial to determine whether the bit is in contact with the formation without accounting for the elasticity of the drill-string.

If the bias between the measured hook-load and the estimated one exceeds one of the set-down and overpull limits, and the bit is off bottom, then the set-point to the hoisting system gets controlled by the first response algorithm in order to isolate and possibly recover from the problem (see Fig. 168).

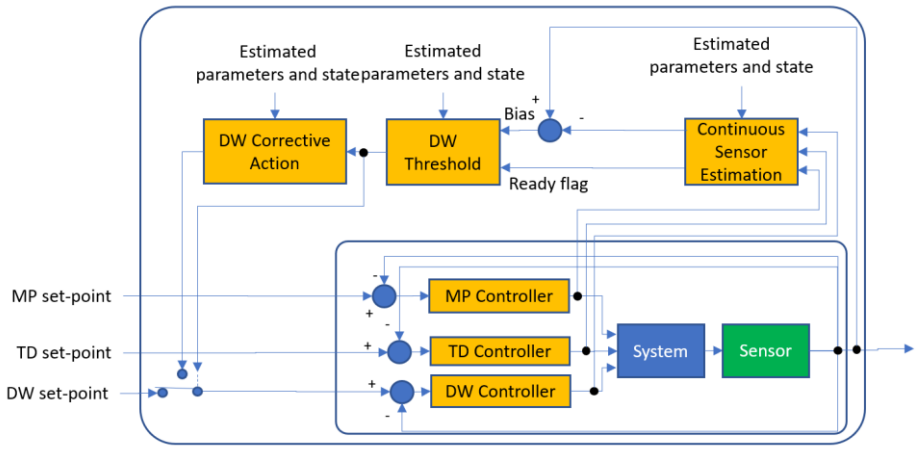

Fig. 168: Block diagram of the over-pull/set-down weight FDIR

The normal recovery action that a driller performs when a set-down or an overpull occurs, is to move in the opposite direction. It is unwise to do so when the driller has his hand on the joystick as it would be very perturbating for him that the drill-string starts to move in the opposite direction to his command on the joystick. Therefore, in this case, the only reaction of the FDIR function is to stop the axial movement (see Fig. 169a). Note that the diamond-symbol indicates the possibility of a conditional branching, here meaning that an

overpull or a set-down has been detected. In this condition, the function performs an isolation but no recovery procedure.

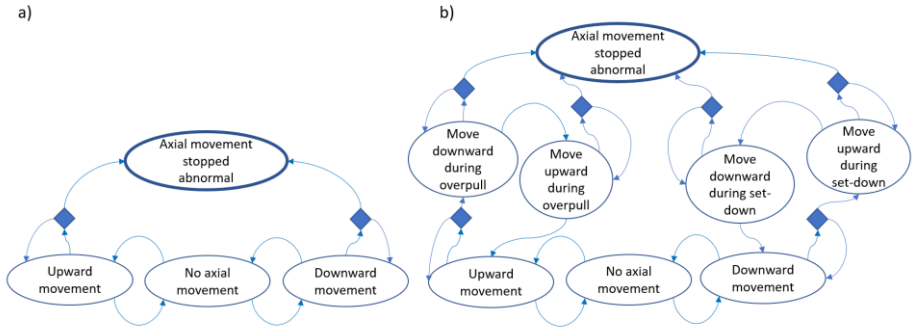

Fig. 169: State diagram of the reaction to an abnormal hook-load a) when the driller utilizes the joystick, b) when the hoisting system is controlled by an automated procedure.

However, if the drilling event occurs during the execution of an automated procedure, then it is possible to attempt to recover. Fig. 169b shows that, in this case, the procedure is to move in the opposite direction, i.e. upward if it was a set-down weight, downward if it was an overpull, and afterward tries to pass back the trouble-zone by moving passed the original position. If there is an overpull or set-down during the execution of the recovery procedure, the algorithm stops the axial movement. The opposite direction distance is calculated based on the proximity of the block position to the drill-floor and crown-block saver elevations, the distance of the bit to the bottom hole and the minimum distance for the bit to start moving in the opposite direction. The latter value depends on the drill-string elasticity and all other forces that influence the bit movement, e.g. mechanical friction, hydraulic forces. This value is calculated using a transient torque and drag model as the one described in section 3.2.

3.5.1.2 Top-drive Over-torque Detection and Reaction

The purpose of the top-drive over-torque FDIR is to detect situations where the drill-string gets stuck, therefore impeding its rotation at an unknown position. As for the overpull and set-down weight FDIR, the top-drive torque threshold,

for the over-torque limit is not the same as the maximum torsional limit of the drill-string. In general, it is much lower.

The free rotating torque can be evaluated utilizing steady state conditions, yet the torque can vary greatly, for example because of the negative damping effect arising from the transition between kinetic and static frictions along the drill-string, as illustrated by Fig. 170.

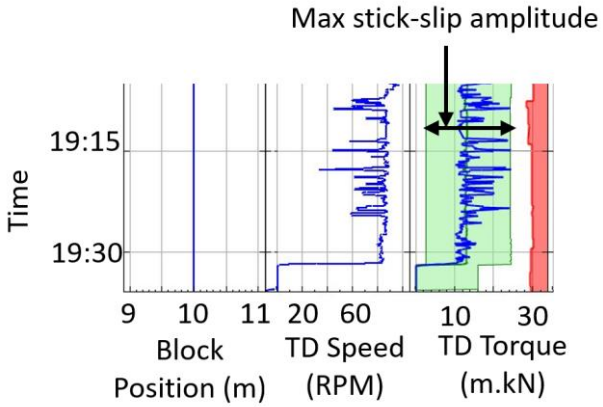

Fig. 170: Example of top-drive torque while experiencing off-bottom stick-slips.

Note that when on bottom and drilling, the top-drive over-torque limit depends on the torque on bit. The torque on bit is related to the ROP and the formation strength via eq. (173). Therefore, during the analysis, the UCS shall be varied from UCS_{min} to UCS_{max}. As usual, there is also a dependence on the mechanical friction, the cuttings load and the downhole temperature. The evaluation of the top-drive over-torque limit is made using a transient torque and drag model as the one described in section 3.2. Fig. 171 shows an example of top-drive over-torque limit in an off-bottom case.

Because of the dependence of the top-drive over-torque limit to many influencing factors, it is necessary to estimate continuously this value. However, the threshold detection is inhibited when the top-drive speed is changed, as very large top-drive torques can be experienced. This is caused by large torsional accelerations combined with the drill-string inertia and mechanical friction.

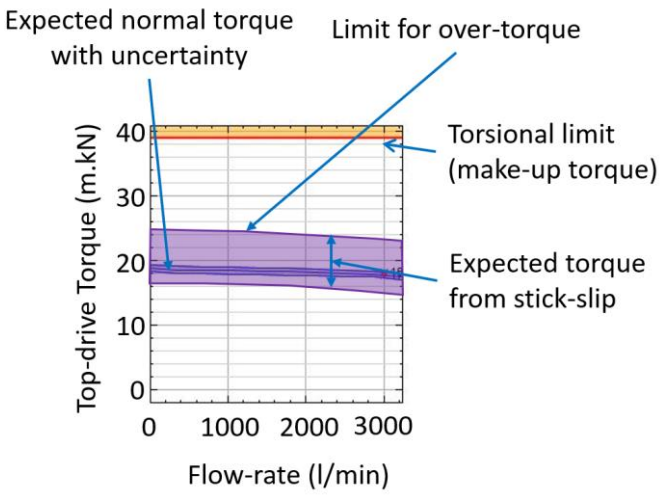

Fig. 171: Threshold limits for over-torque at the top-drive when the bit is off bottom.

If the measured top-drive torque exceeds the currently evaluated top-drive over-torque limit while the top-drive rotational speed is uniform, the isolation procedure is started and replaces the external top-drive speed and hoisting speed set-points. Fig. 172 shows a block diagram of the top-drive over-torque FDIR.

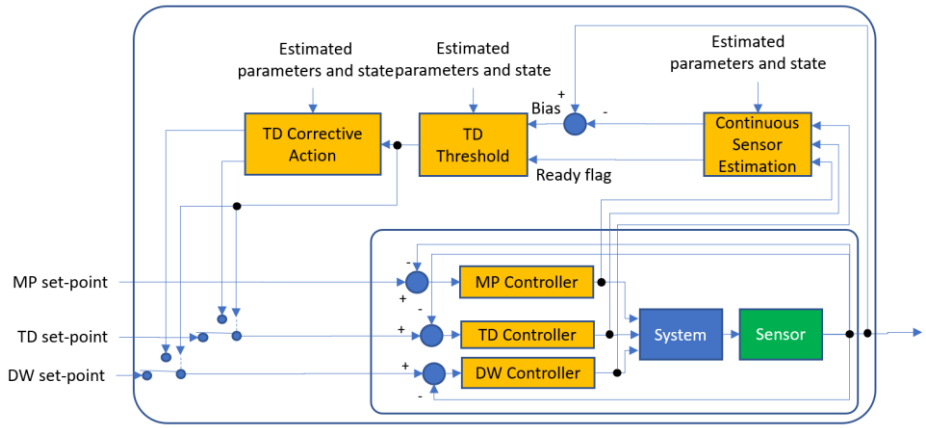

Fig. 172: Block diagram of the top-drive over-torque FDIR

In practice, the top-drive over-torque FDIR performs only an isolation of the problem and does not attempt to do a recovery (see Fig. 173): it stops both the top-drive and the hoisting system. The reason for stopping the hoisting system is simply because it would most likely be harmful to continue hoisting with a non-rotating drill-string, or conversely to continue lowering without rotation when the intention was to ream-down or drill.

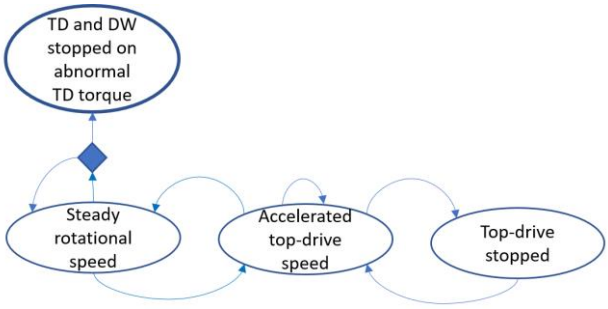

Fig. 173: State diagram of the reaction to an abnormal top-drive torque

3.5.1.3 Pump Overpressure Detection and Reaction

During a drilling operation, the mud pump pressure may start to increase abnormally, for instance because of an obstruction in the annulus, but also possibly because of a plugged bit nozzle. Here, we do not try to characterize the origin of the abnormal pressure development, we just want to detect and react in consequence, but assuming the worst-case scenario, i.e. an obstruction in the annulus.

We distinguish two cases: either steady state flow is reached or there is a pump acceleration and its effect still influences the pump pressure (see Fig. 12 for an example where the pump pressure continues to increase several minutes after the mud pump rate is constant).

In steady state conditions, i.e. when the expression (221) is true, then we compare the measured pump pressure with an estimated mud pump over-pressure limit. This value depends on the drill-string axial velocity, the top-drive rotational speed and the mud pump flowrate (see Fig. 174). In addition, it is influenced by the current heave amplitude and period, hydraulic friction conditions, cuttings load along the annulus and the temperature distribution.

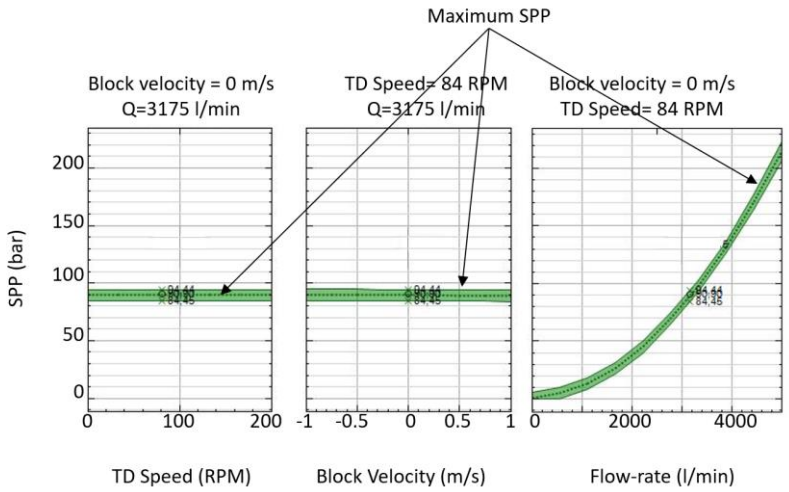

Fig. 174: Threshold limits for mud pump over-pressure in steady state conditions.

When a mud pump over-pressure is detected, the typical reaction of the driller is to reduce the flowrate by a few hundred liter per minute and to monitor the pump pressure. If the pump pressure continues to increase then he stops completely the mud pumps, otherwise he may keep the flowrate constant or he may reduce it even more if he suspects that the obstruction could risk to fracture the open hole formations (see Fig. 175).

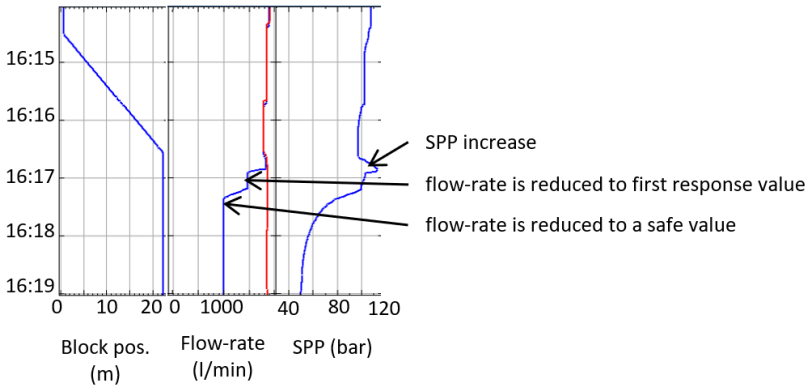

Fig. 175: Detection and reaction to a mud pump over-pressure situation.

In addition, the axial movement of the drill-string is stopped to avoid continuing drilling or reaming, as it would potentially worsen the situation.

The mud pump over-pressure FDIR reproduces this behavior. As it can be seen on the block diagram Fig. 175 , when the over-pressure is detected, the recovery part of the system takes control of the set-points passed to the mud pump and hoisting system controllers.

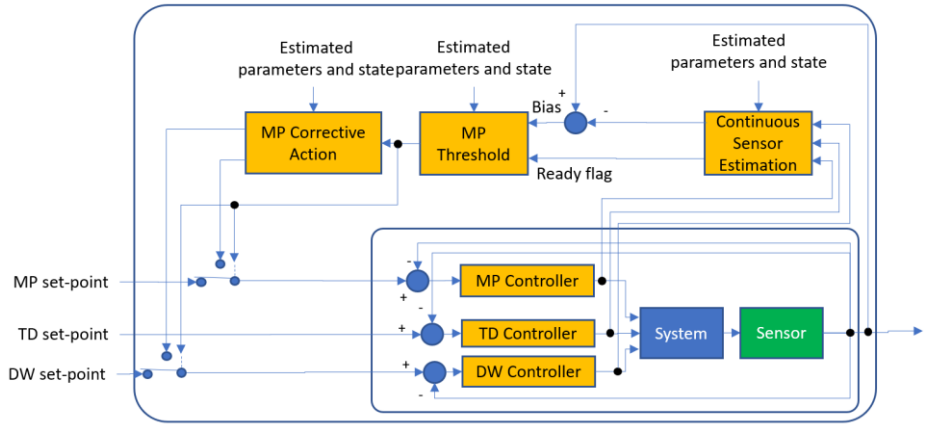

Fig. 176: Block diagram of the mud pump over-pressure FDIR.

The state diagram of Fig. 177 describes the response of the mud pump recovery function when an over-pressure is triggered while in steady state flow conditions.

The first response mud pump flowrate is defined as a user-specified reduction of the current flowrate (typically 80% of the flowrate that was used just before the function triggered). The time that is necessary to reach a sufficiently stable pump pressure is estimated using a transient hydraulic model.

If the pump pressure increases during this flowrate adjustment, then the mud pumps are stopped. Otherwise, the measured pump pressure, at the end of the waiting duration, is used to estimate whether a further mud pump flowrate reduction is necessary to ensure that the downhole pressure in the annulus is lower than the fracturing pressure.

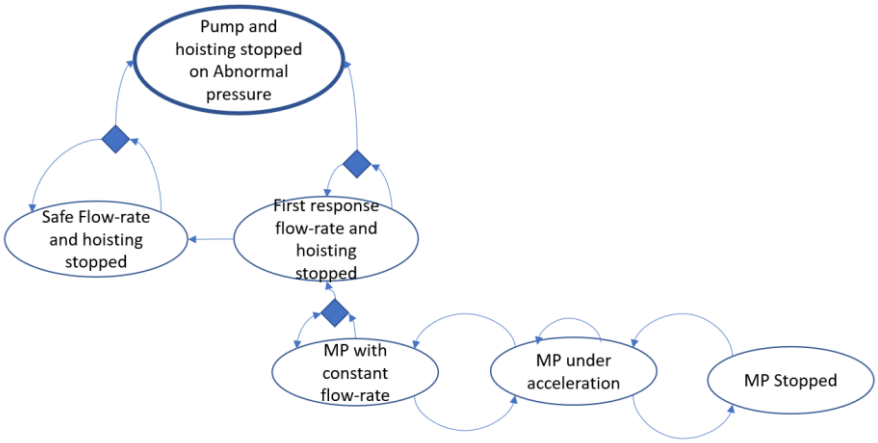

Fig. 177: State diagram for the recovery function of the mud pump over-pressure FDIR in steady state flow conditions.

First, we use a steady state hydraulic model to estimate the obstruction size that would result in the observed pump pressure at the end of the waiting duration while utilizing the first-response flowrate. We found that utilizing a 10m long obstruction just at the top of the open hole section is enough to obtain conservative results (see Paper V). Then we find, with a steady state hydraulic model configured with the equivalent obstruction, which mud pump flowrate, $Q_{MP_{safe}}$, that gives a downhole pressure along the annulus that does not exceed the fracturing pressure at any position along the open hole section (see Fig. 178).

If $Q_{MP_{safe}}$ is smaller than the first-response flowrate, then the mud pump flowrate is reduced to $Q_{MP_{safe}}$ and a minimum waiting duration is calculated. If during that waiting time, the pump pressure increases, then the mud pumps are immediately stopped. Otherwise, at the end of the waiting duration, the obtained pump pressure is compared with the estimated pump pressure that should have resulted from the estimated obstruction size (see red arrow on Fig. 178). If the pressure is greater than the expected value, then the obstruction is larger than what we expected, or the situation has worsened. In that case, we stop the mud pumps. Otherwise, we maintain that flowrate and leave to the driller to proceed with further actions to recover from the pack-off situation.

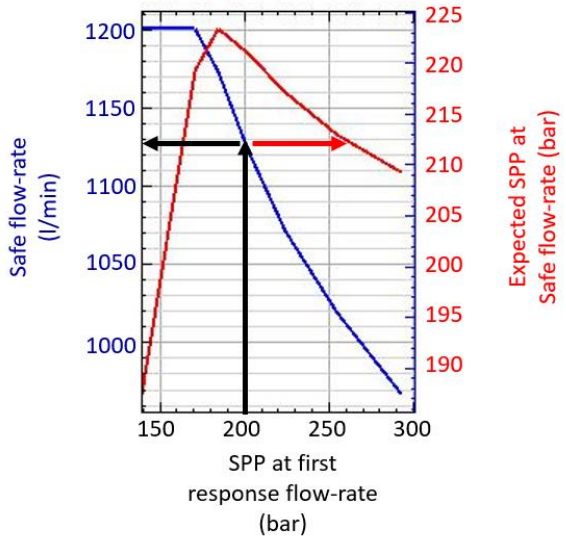

Fig. 178: Diagram showing how the safe flowrate is chosen from the measured pump pressure obtained after reaching the first-response flowrate.

An over-pressure can also happen while starting the mud pumps. A direct comparison of an estimated pump pressure with a measured one would probably require large threshold values because the pump pressure tends to increase rather rapidly during the pump acceleration. With the slightest delay between the signals, there could be several ten-bar differences, yet without experiencing a pack-off situation. For example, it is not unusual to observe that the pump pressure increases before the mud pump flowrate starts to rise. Fig. 179 illustrates that situation where the flowrate derived from a stroke counter is so much delayed that the pump pressure starts to increase 25s before the flowrate.

Instead, the threshold for abnormal pump pressure during pump acceleration, utilizes a combination of the maximum pump pressure, the maximum pump pressure rate of change (ROC) (see Fig. 180) and the maximum pump pressure standard deviation.

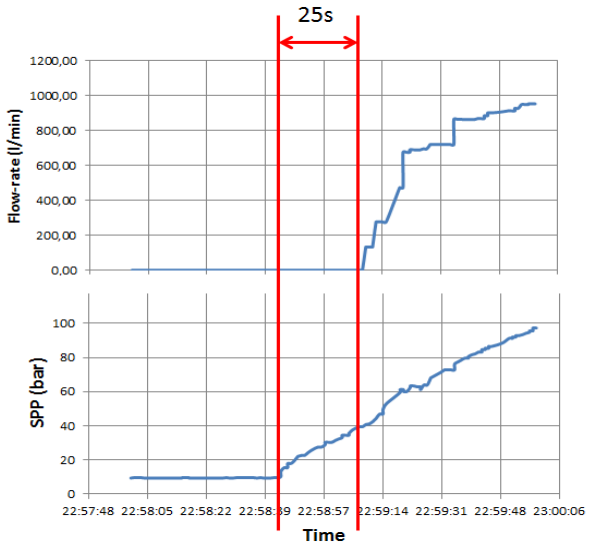

Fig. 179: In this example, the pump pressure starts to increase 25s before the reported flowrate starts to increase. This is typical for flowrates that are measured with a stroke counter as at low pump-rate, it may take several ten seconds before two strokes are counted.

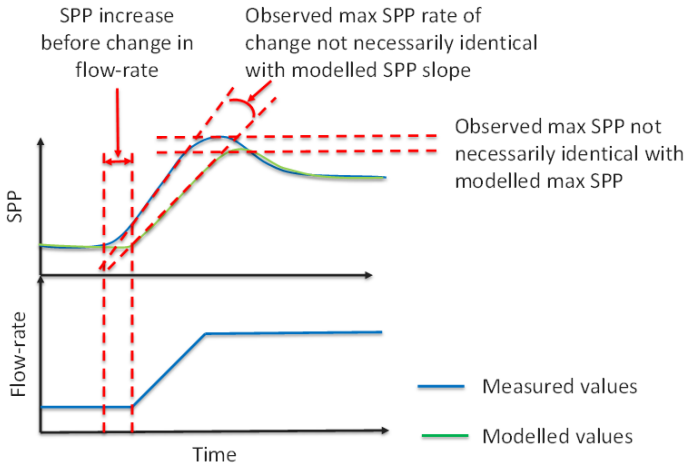

Fig. 180: During mud pump acceleration, the observed pump pressure rate of change may differ from the estimated one because of uncertainty in the modelling and asynchronous signals.

There is a delay before each of the three detection criteria are compared to their associated threshold values and the detection thresholds are changed to those corresponding to steady state conditions when the estimated duration of transient behavior has elapsed (see Fig. 181).

When it is possible to obtain a mud pump rate based on the actual motor rotational velocity, then the initial delay is usually a short duration, typically 5s, that permits to account for possible different latencies of the mud pump flowrate and pressure signals. However, if the mud pump rate is based on a stroke counter, this value must be large as it has been illustrated with Fig. 179.

Note that the criterion is only valid when we know, in advance, the target flowrate at the end of the mud pump acceleration. Therefore, the described mud pump over-pressure function described here is only available during automated pump startup procedure and not during manual changes of the pump rate.

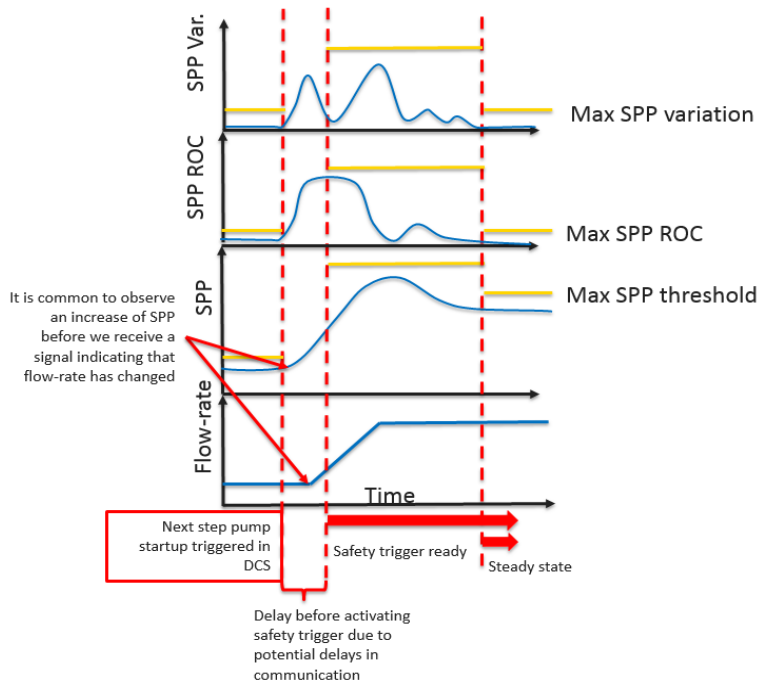

Fig. 181: During a mud pump acceleration, the mud pump over-pressure FDIR monitors the pump pressure, pump pressure rate of change and the pump pressure variance.

However, during an automated pump startup procedure, the mud pump overpressure detection is available most of the time, alternating between the acceleration-based detection criteria and the one for steady state conditions. The protection is unavailable only for a short duration after each new mud pump acceleration (see Fig. 182).

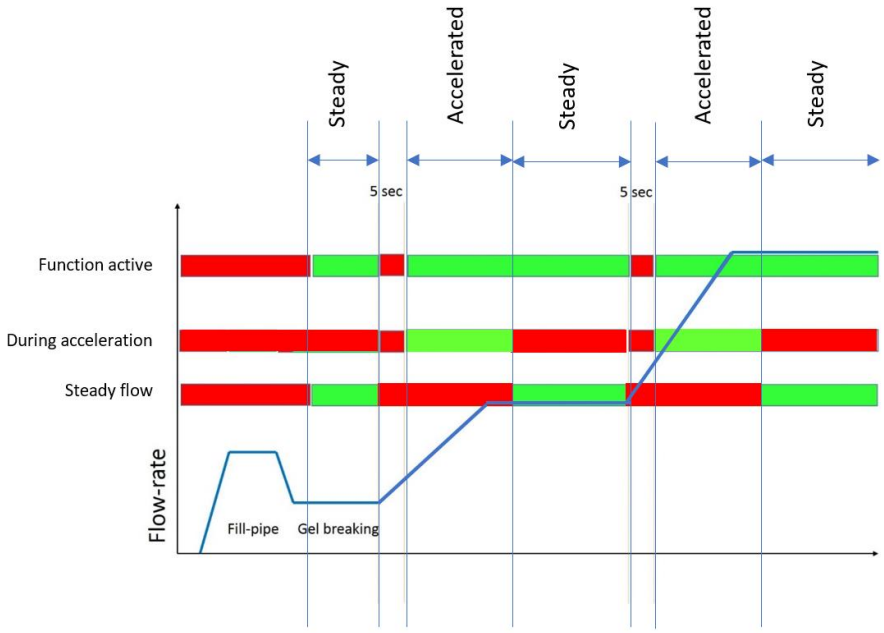

Fig. 182: Illustration of the function readiness during a mud pump startup with alternance between accelerated and steady flow periods.

In case an overpressure is detected during the mud pump acceleration, the only possible action is to stop the mud pumps and the hoisting system. This is obtained by extending the original state diagram of Fig. 177 with a possible path toward the final abnormal state from the loop associated with the pump acceleration state (see Fig. 183).

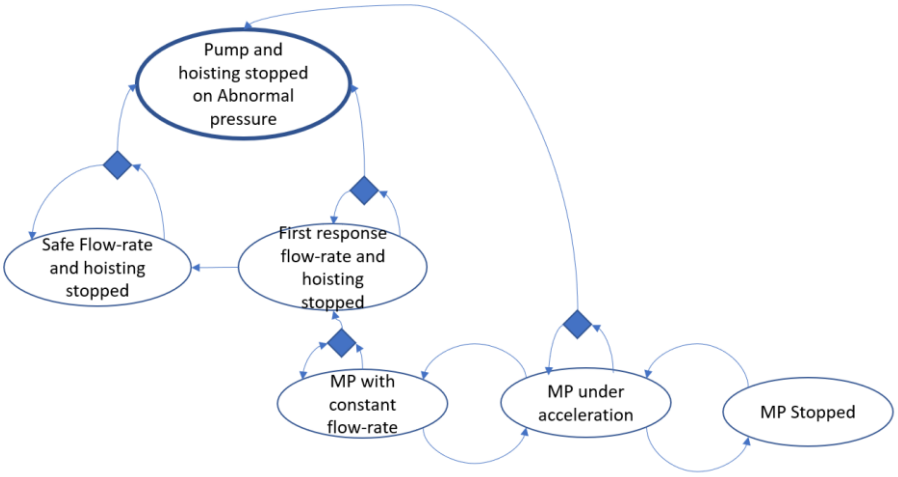

Fig. 183: State diagram of the reaction to an abnormal mud pump pressure for both steady state conditions and during pump acceleration.

3.5.1.4 Summary

Quickly developing drilling incidents such as over-pressures, over-pulls, set-down weights or over-torques are best managed by controlling actively the drilling machines.
This is done by utilizing safety triggers, i.e. fault detection and isolation schemes.
As the thresholds that should be used for detection are functions of the current context and the actions being executed, a model-based approach is used.
High fidelity models are used to generate a reduced model of the threshold levels.
The level of complexity of the isolation procedure depends on constraints imposed by human factors. It is the simplest when the hoisting system is involved and the most advanced when managing the mud.

3.5.2 Safe Operation Envelope

As it has been exemplified by Fig. 12, the consequence of a change of the set-point of one the drilling machine can only be seen several tens of seconds, even minutes, after the set-point is reached.

Fig. 184 shows a simulation where the mud pumps are accelerated to 2500l/min and afterward, the flowrate is maintained constant. When the downhole pressure gets as close as 10bar below the fracturing pressure at the bit, the mud pumps are turned off. Yet, because of inertia, drilling fluid compressibility and viscous friction, the downhole pressure continues to increase for about 25s, exceeding the fracturing pressure by 6bar.

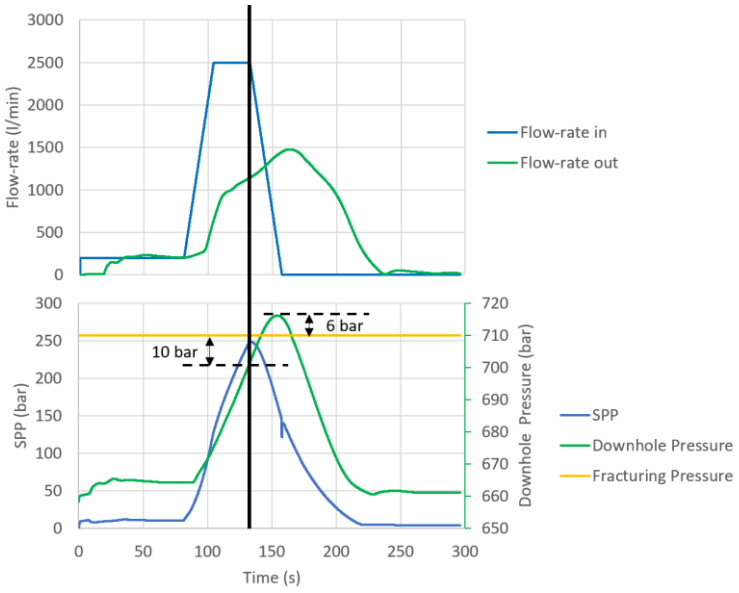

Fig. 184: The mud pumps are accelerated to 2500l/min and kept constant. When the downhole pressure gets as close as 10bar below the fracturing pressure margin, the mud pumps are turned off. Yet the downhole pressure continues to increase for about 25s and exceeds the fracturing pressure by approximatively 6bar.

This illustrates how the effects of inertia, elasticity and frictions, in the drilling process, cause large delays that, if not accounted for, can have negative impacts on the drilling operation. For this reason, it is useful to limit the set-points that

are passed to the drilling machines, to values that are compatible with the tolerance margins of the drilling operation.

We will review five such safe operation envelope functions:

- Maximum flowrate in steady state circulation to avoid fracturing the open hole formations,
- Minimum duration for breaking circulation to establish a steady state circulation,
- Maximum mud pump acceleration to avoid fracturing the open hole formations,
- Maximum axial acceleration, velocity and deceleration to avoid formation fluid influx, collapse and fracturing.

There are of course other safe operation envelopes that can be define such as WOB and top-drive speed margins while drilling to avoid damaging the bit, or minimum flowrate and top-drive speed to clean the borehole, just to name a few that are now being developed.

3.5.2.1 Maximum flowrate in steady state circulation

When utilizing a constant flowrate and when steady state conditions for circulation are reached, the downhole pressure in the annulus must not be larger than the fracturing pressure anywhere along the open hole section. Eq. (221) defines the condition for steady state circulation. Note that this equation does not mention the axial velocity, nor the top-drive speed, nor other effects that may disturb the uniformity of the values used in the logical conditions such as a PDM while on bottom and drilling. This means in practice that if the standpipe pressure is not stable because of torque variations on a PDM, or the estimated flowrate out is unstable as a result of the initial axial acceleration while lifting or slacking the drill-string, then the circulation is not in steady state conditions. However, the circulation can be in steady state condition when acceleration effects of the axial drill-string movement have dissipated, and similarly for the other sources of disturbance of the steady state circulation condition.

The maximum mud pump flowrate, $Q_{MP_{max}}$, is the value that ensures that in steady state conditions, the annulus downhole pressure along the open hole section stays below the fracturing pressure limit.

As the estimation corresponds to steady state circulation conditions, it can be estimated with a steady state hydraulic model. The result depends on the current conditions for the axial velocity and top-drive speed (see Fig. 185). But it is

also a function of the current heave level, current hydraulic friction, cuttings load and current temperature distribution.

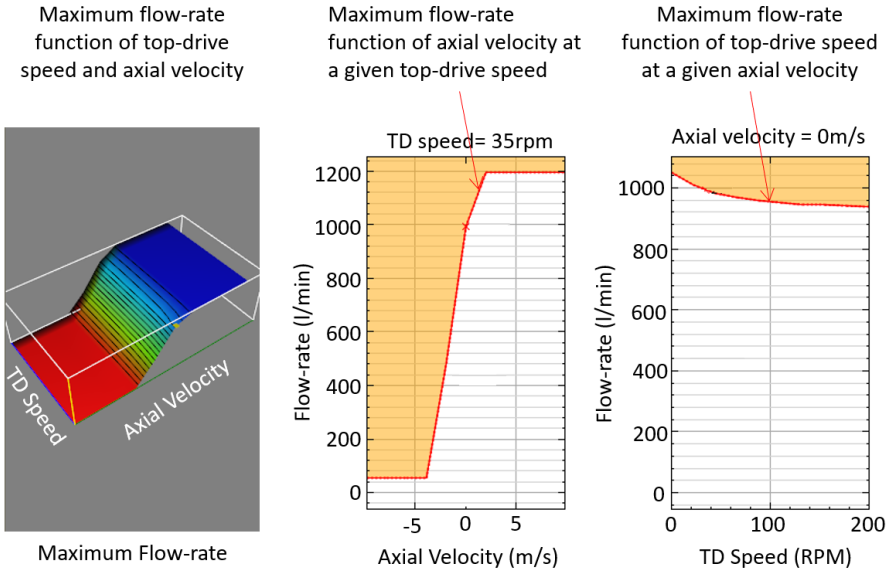

Fig. 185: Safe operational envelope for the mud pump flowrate as a function of the axial velocity and the top-drive speed.

The block diagram of the function is shown on Fig. 186. We can see that one of the functions is to determine if we are in steady circulation conditions. The maximum flowrate calculation depends directly on the axial velocity and top-drive speed, but of course on the steady state condition. The set-point value passed to the mud pumps is the minimum of the externally defined set-point and the estimated maximum flowrate.

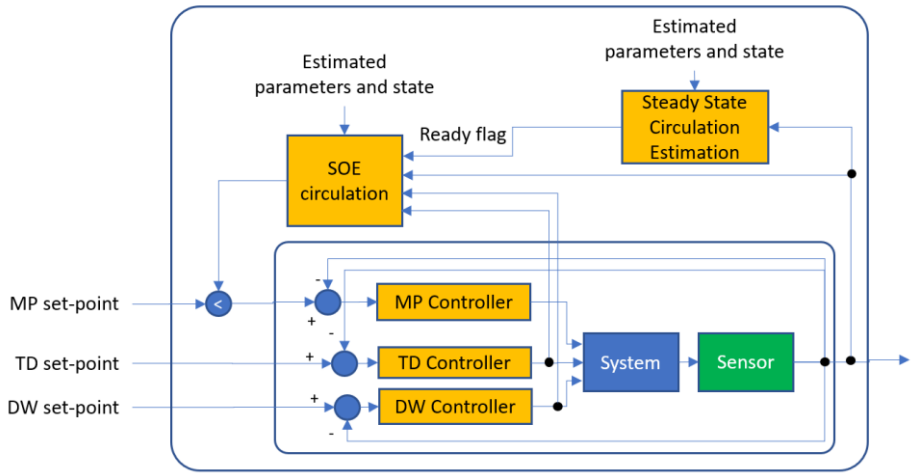

Fig. 186: Block diagram of the safe circulation operational envelope.

3.5.2.2 *Minimum Duration for Breaking Circulation*

As soon as the drilling fluid stops to move, it starts to build gel structures. We have seen in section 2.1.1.13 that the gel strength increases with duration and that it requires an additional pressure to break these gel structures when a shear rate is applied. We have also seen in section 2.1.1.15 that the effects of gelling continue to impact the rheological behavior of the drilling fluid for several minutes after the drilling fluid is being circulated.

In practice, the breaking circulation flowrate cannot be too large because of the build-up of pressure while changing the state of the viscoelastic fluid from an elastic solid to a viscous fluid. In the worst case, it could get larger than the fracturing pressure of the open hole formation rocks.

Fig. 187 illustrates the evolution of the downhole pressure in the annulus. For instance, it should be noticed that with this 3450m long drill-string, the annulus pressure starts to increase 28s after pumping has started. There is a transition delay where part of the annulus flows while the top is still in a gelled state (Fig. 187a). A peak of downhole pressure in the annulus is reached 88s seconds after the start of the mud pumps (Fig. 187b) and pressure fluctuations are damped approximatively 128s after the pump start (Fig. 187c).

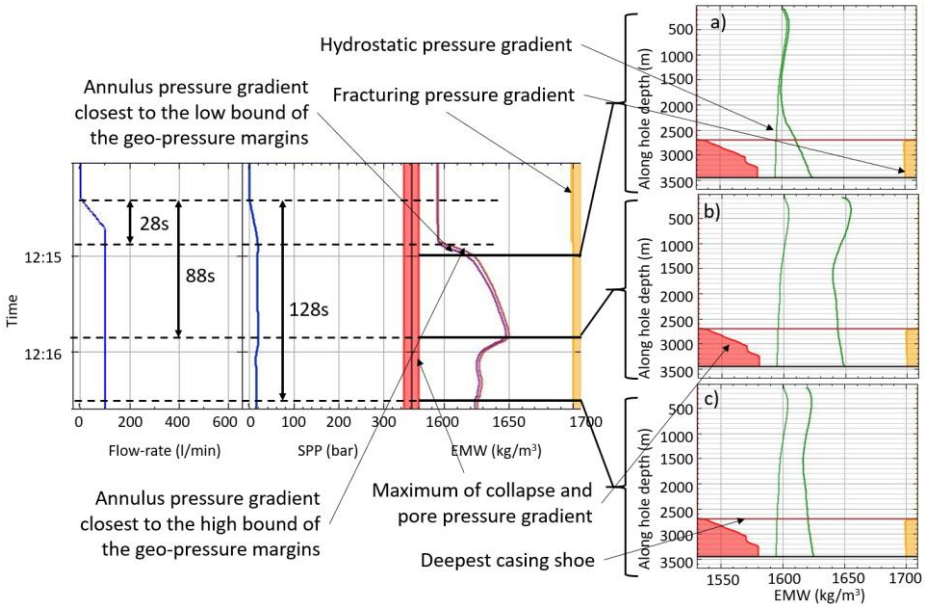

Fig. 187: Estimation of the annulus pressure gradient while breaking circulation at 100l/min: a) the pressure builds up while part of the mud contained in the annulus is still in a gel state, b) the maximum peak of downhole pressure is reached, c) after some oscillations in the flowrate out, the downhole pressures along the annulus stabilize to their new values.

Accelerating the mud pumps before the pressure fluctuations have been sufficiently damped, could result in generating a large pressure wave that could cause a formation fracturing. Therefore, it is desirable to maintain the gel breaking circulation flowrate constant for a minimum duration before continuing the mud pump acceleration.

The minimum gel breaking duration depends directly on the gel breaking circulation flowrate and the gel duration (see Fig. 188). It also depends indirectly on the current heave level, the current hydraulic friction, the cuttings load and the current temperature distribution. This evaluation must be made with a transient hydraulic model.

A block diagram of the gel breaking safety envelope function is shown on Fig. 189. One function is dedicated to monitor continuously the surface measurements in order to estimate when gelling starts and when circulation

starts to be established. Another function estimates the minimum gel breaking circulation duration that shall be applied.

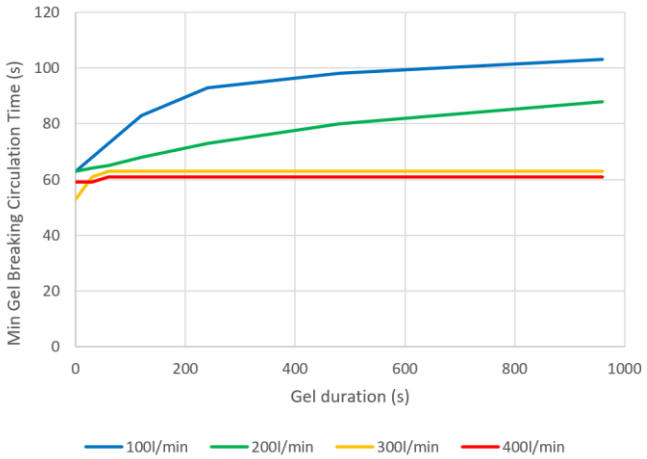

Fig. 188: Minimum gel breaking circulation duration as a function of gel duration and for four different gel breaking circulation flowrates.

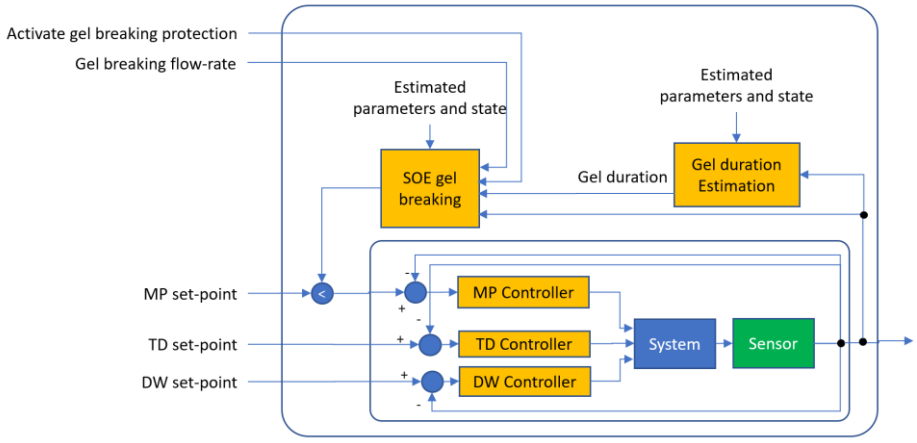

Fig. 189: Block diagram of the gel breaking minimum duration safe operating envelope function.

During that period, it is not possible to increase the flowrate. However, it is possible to decrease it. The gel breaking flowrate must be passed to the

function. In practice, this value is chosen by the mud pump startup procedure that is described in section 3.5.3.1, and the gel breaking duration protection is only available when the automatic pump startup activates the function.

3.5.2.3 Maximum Mud Pump Acceleration

After breaking circulation, the mud pumps shall be accelerated to a different flowrate. This can be done in one step or in multiple steps. Depending on the acceleration of the mud pumps, the pump and downhole pressure may respond as an underdamped or an overdamped system, i.e. that the time evolution of the pressure has an overshoot or is monotonic. An overshoot of pressure is not necessarily a problem if the pressure spike does not exceed any limits, e.g. pressure-relief valve on the mud pumps or fracturing pressure along the open hole annulus. But the drillers tend to prefer that at least the pump pressure evolution is monotonic as it is easier to detect if there is a pack-off situation during the change of flowrate.

So, we would like to find the maximum pump acceleration, when changing from one flowrate to another one that respects the monotony of the pump and downhole pressure until steady state conditions are reached.

Fig. 190 illustrates the acceleration of the mud pumps from 200 to 500l/min after breaking circulation at 200l/min with an 8 ½-in drill-string at 3000mMD and a micronized OBM of mass density 1680kg/m^3 at 50°C and atmospheric pressure.

The blue lines correspond to a mud pump acceleration of 10l/min/s. With such a low mud pump acceleration, the pump and bit annulus pressures are close to monotonic. However, when the mud pump acceleration is raised to 50l/min/s, corresponding to the green curves, then both the pump and bit annulus pressure responses are non-monotonic. At 500l/min/s, represented by the red curves, the pressure response is of course non-monotonic but does not differ substantially from the one at 50l/min/s.

It should be noted, all things equal otherwise, that if the target flowrate is 1500l/min, then monotony is achieved even with very high mud pump accelerations. Fig. 191 shows that even with 15000l/min/s, the pressure response at the pump and in the annulus at the bit, is overdamped.

So, acceleration limitations are quite often related to changing from a small flowrate to another relatively small flowrate. Fig. 192 shows that the mud pump acceleration limitations are only for the lower part of the acceleration envelope. However, those results depend on the compressibility of the drilling fluid, the amount of fluid in the borehole and the wellbore diameter. Subject to a mud pump acceleration envelope that is like the one of Fig. 192, it is more effective to have a single mud pump acceleration to a high flowrate than several steps to reach that same flowrate. These calculations are made with a transient hydraulic model and shall account for the current hydraulic friction, the current cuttings load and the current temperature distribution. Here, we suppose that the axial and rotational velocities are zero as normally, a pump startup is made without drill-string movements.

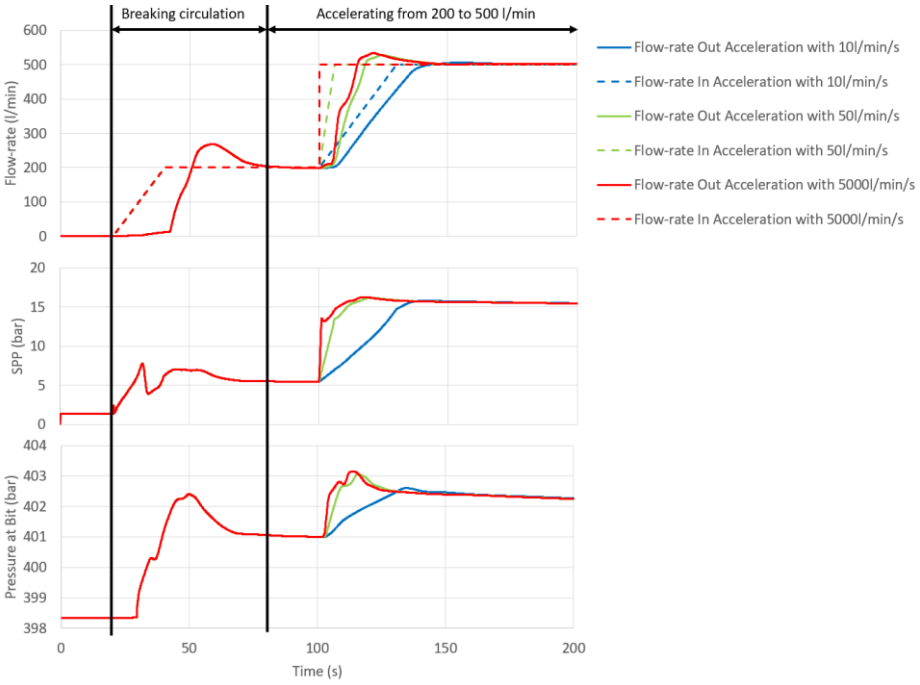

Fig. 190: Acceleration of the mud pumps from 200l/min to 500l/min, after breaking circulation at 200l/min, with three mud pump accelerations: 10l/min/s, 50l/min/s and 500l/min/s.

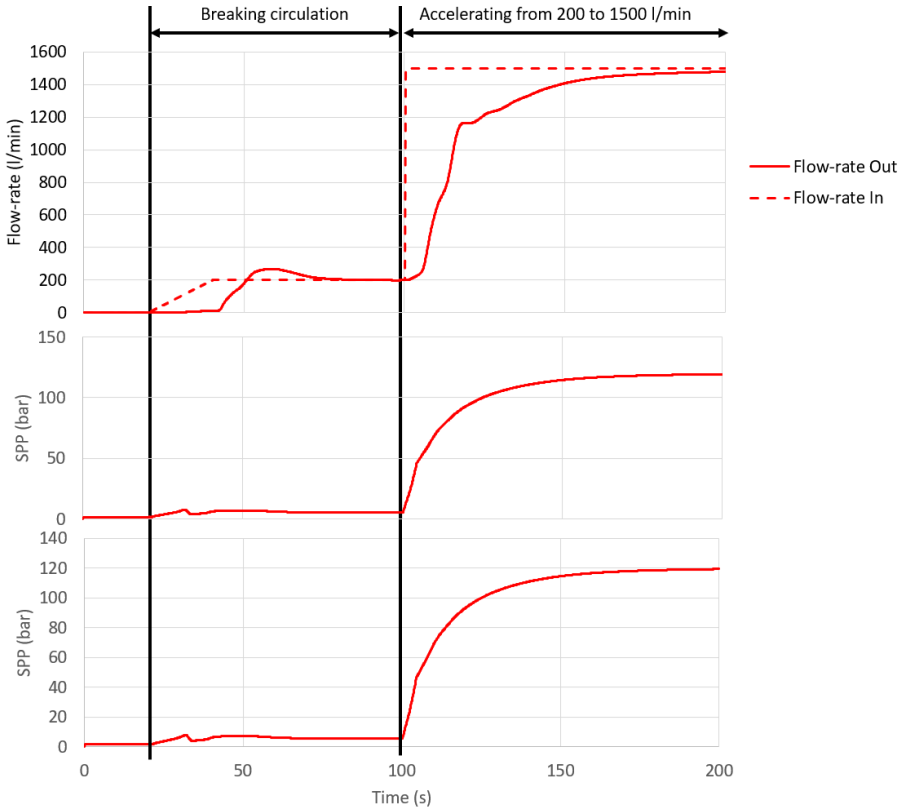

Fig. 191: When accelerating from 200 to 1500l/min, after breaking circulation at 200l/min, the annulus pressure at the bit and the pump pressure increases monotonically even with a very high mud pump acceleration (here 15000l/min/s).

The block diagram of the mud pump acceleration safe operation envelope is shown on Fig. 193. One can notice that this function is only available when running an automated mud pump acceleration procedure as it needs the target flowrate.

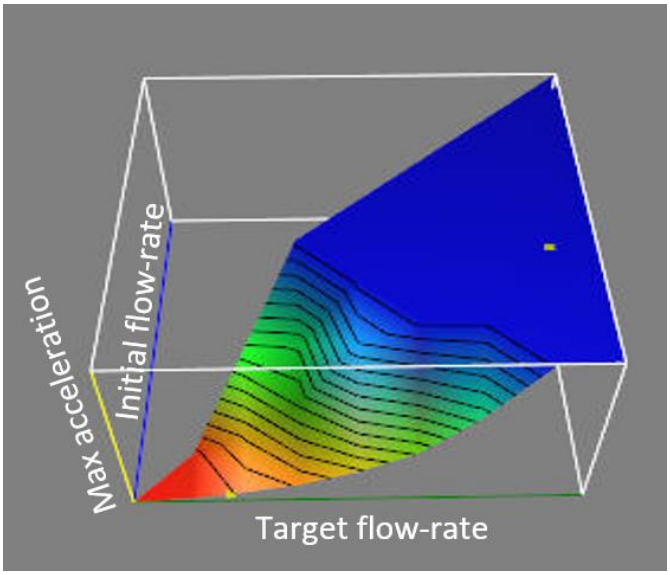

Fig. 192: Envelope of safe mud pump acceleration as a function of an initial and a target flowrate.

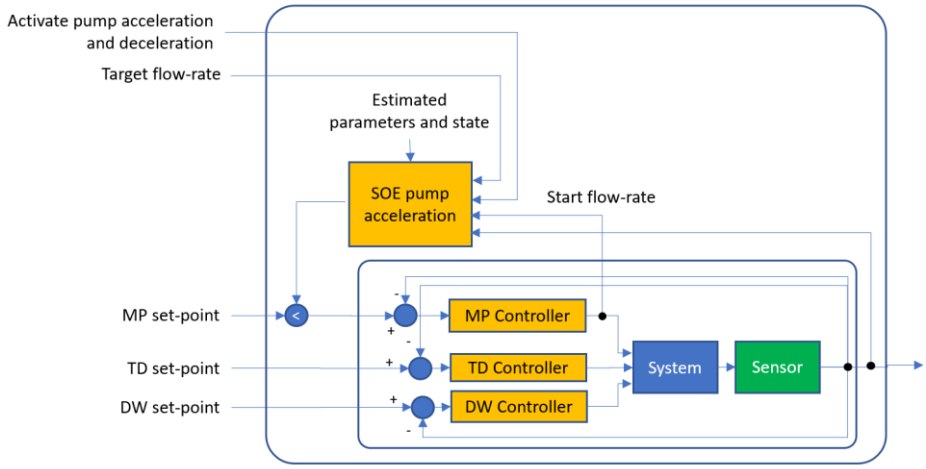

Fig. 193: Block diagram of the pump acceleration safe operation envelope protection.

3.5.2.4 Swab & Surge Safe Operation Envelope

The axial movement of the drill-string changes the drilling fluid velocity profile in the annulus as we have seen in section 2.1.1.8. Furthermore, the displacement of the bit itself, because of the axial displacement of the drill-string, forces the drilling fluid to be displaced. The resulting effect is an additional pressure loss which is positive when the drill-string moves downward, i.e. surging, and negative when it moves upward, swabbing.

When there is no circulation, the drilling fluid develops a gel structure that needs to be broken down before the drilling fluid can flow. The effect of gel has a direct consequence on the development of the downhole pressure. Fig. 194 shows how the evolution of the bottom hole pressure gradient differs while running out of hole at 0.1m/s for a complete stand in a lightly gelled drilling fluid (orange curve) and in a fully gelled mud (red curve). The gel duration has therefore a direct influence on how quickly the drill-string can be moved axially. It should also be noted that even though the drill-string is moved with a constant velocity, the pressure fluctuations span most of the stand length: the consequences of the initial movement last for many tens of seconds. In the case of Fig. 194, the bottom hole pressure gradient still decreases at the end of the movement, i.e. 280s after the start of the movement, and when the movement has stopped, it takes more than 300s before the bottom hole pressure gradient has stabilized.

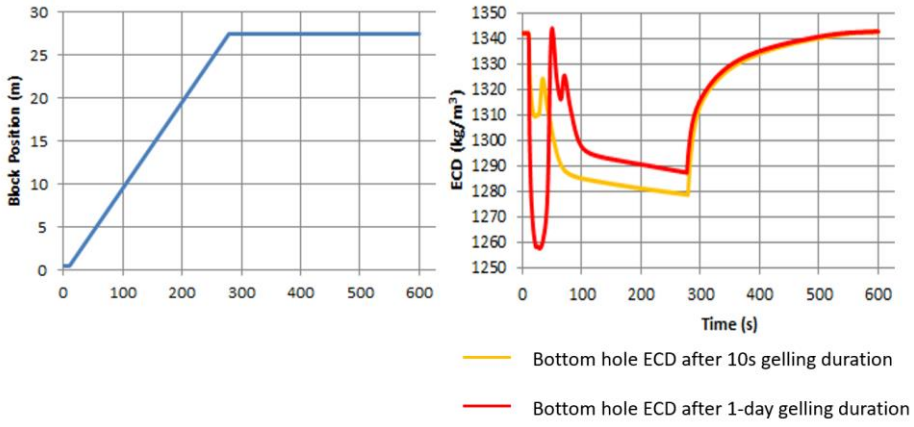

Fig. 194: Example of picking up a 28m long stand at 0.1m/s when the drilling fluid has just gelled for 10s and when it has gelled for 24hours.

Some time, to limit the effect of gelling and to reduce the impact of swabbing, a drill-string can be pulled out of hole with circulation, also called pulling out of hole with lubrication. Fig. 195 shows the effect of lubrication on the bottom hole pressure gradient. Not only the downhole pressure has much less transients, but it allows for larger axial velocities. Note also that the bottom hole pressure gradient stabilizes faster, after the start of the movement, with larger flowrates than with smaller ones.

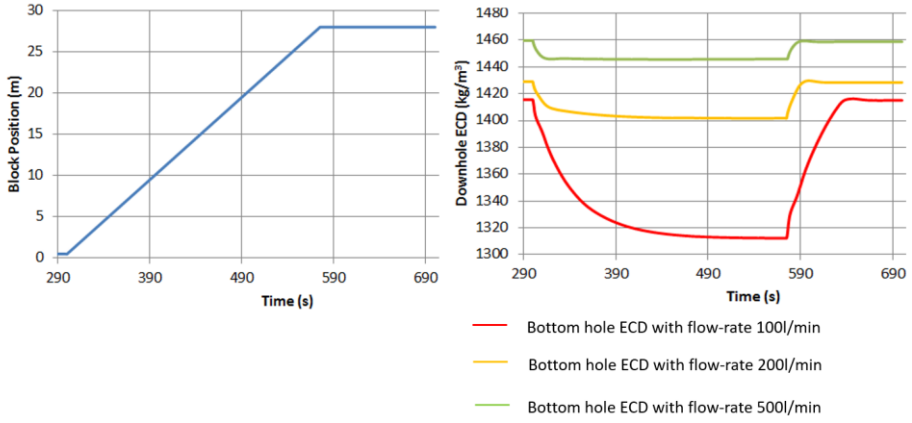

Fig. 195: Effect of flowrate while running out of hole with lubrication at 0.1m/s a complete stand of 28m.

However, if one applies a rotation on the drill-string, then the downhole pressure increases as it has been discussed in section 2.1.1.7. Fig. 196 shows that larger drill-string rotational speeds have an impact on the surge pressure while running in hole at 0.2m/s.

The initial acceleration has also an impact on the pressure pulses that are generated during an axial displacement of the drill-string. A lower acceleration may allow for a larger constant velocity. But a too low initial acceleration may look strange for the driller. After dialogue with several drillers, we arrived at the conclusion that the initial acceleration phase cannot be longer than one third of the current stand length.

As discussed earlier, a_{max} is such that we shall reach the desired uniform velocity within the first third of the stand length:

$$\frac{1}{2}a_{max}\left(\frac{v}{a_{max}}\right)^2 = \frac{1}{3}l_s \Leftrightarrow \frac{1}{2}\frac{v^2}{a_{max}} = \frac{1}{3}l_s \Leftrightarrow a_{max} = \frac{3}{2}\frac{v^2}{l_s} \qquad (230)$$

where l_s is the stand length.

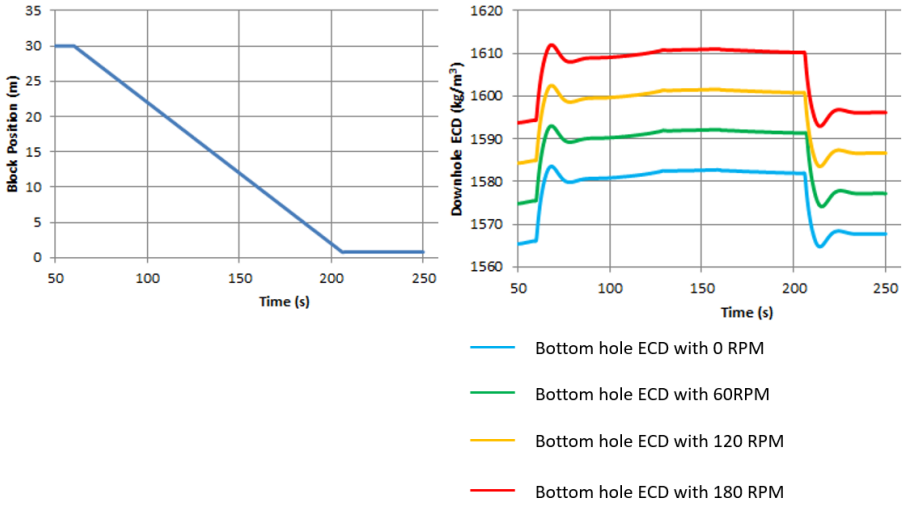

Fig. 196: Example of the influence of the drill-string rotation velocity while reaming down at 0.2m/s and pumping at 2200l/min.

Regarding the deceleration, it shall always be possible to stop the drill-string movement with maximum effect.

We can also calculate the duration of the uniform movement, by summing the travelled distances during the acceleration, uniform movement and deceleration phases:

$$\frac{1}{2}\frac{v^2}{a} + v\Delta t_u - \frac{1}{2}\frac{v^2}{a_b} = l_s \Leftrightarrow \Delta t_u = \frac{l_s}{v} - \frac{1}{2}v\left(\frac{1}{a} - \frac{1}{a_b}\right) \qquad (231)$$

where a_b is the braking acceleration and Δt_u is the duration of the uniform movement.

Swab & surge axial velocity limits shall be considered when there is no circulation as a function of the gel duration, and with circulation as a function of the flowrate and the drill-string rotational speed. The evaluation shall make use of a transient hydraulic model. The evaluation also depends on the current

heave level, the current hydraulic friction, the current cuttings load and the current temperature distribution.

Fig. 197 shows the safe operational envelopes for upward and downward movements, in a gelled-state and with circulation. Note that with circulation, the safe operation envelope is two dimensional and that for the sake of clarity, the graphs of Fig. 197 show only a cut through that surface at constant top-drive speed, here 0rpm. Note also that there are two limits on the graphs: one when the heave compensator is on and one when it is off. Both limits account for the remaining effects of top of string movement due to the current heave level.

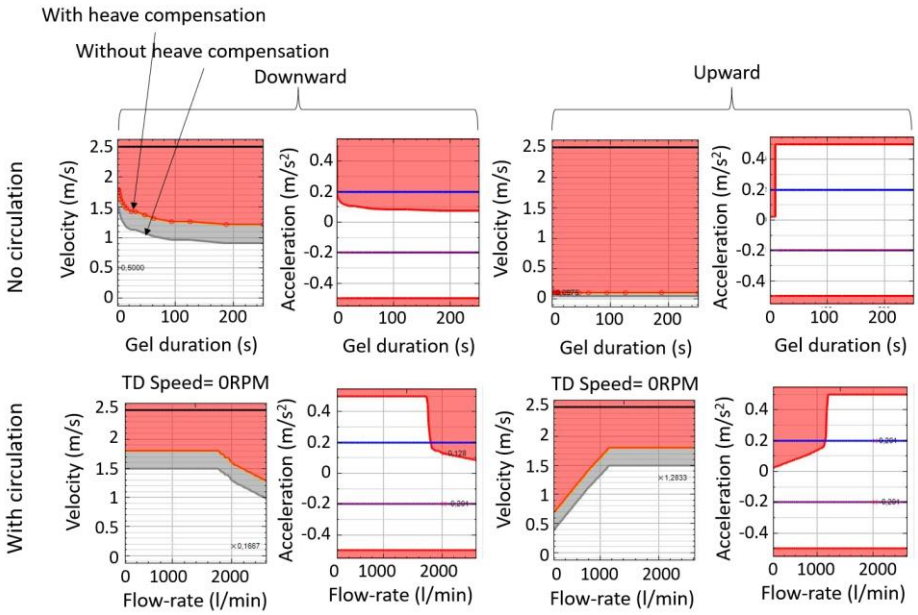

Fig. 197: Axial velocity and acceleration/deceleration limits for the case with gelled mud (top graphs) and with circulation (bottom graphs), for upward movement (left graphs) and bottom movement (right graphs).

The block diagram of the swab and surge safe operation functionality is shown on Fig. 198. There is a gel duration estimation function that is used for determining the axial velocity safe envelopes when there is no circulation. The function provides limits for both positive and negative axial velocities,

therefore the external axial velocity set-point is compared with both a minimum and a maximum value. The function requires access to current value of the mud pump flowrate and the top-drive speed. It also needs the current value of the block-position and velocity to determine whether the velocity limit that shall be applied, corresponds to an acceleration or deceleration phase or if it is a uniform movement. To determine when braking limits shall be applied, it is necessary to know the desired stick-up height. When running in hole, this is enough, but while pulling out of hole, we also need the current stand length to determine when to start decelerating.

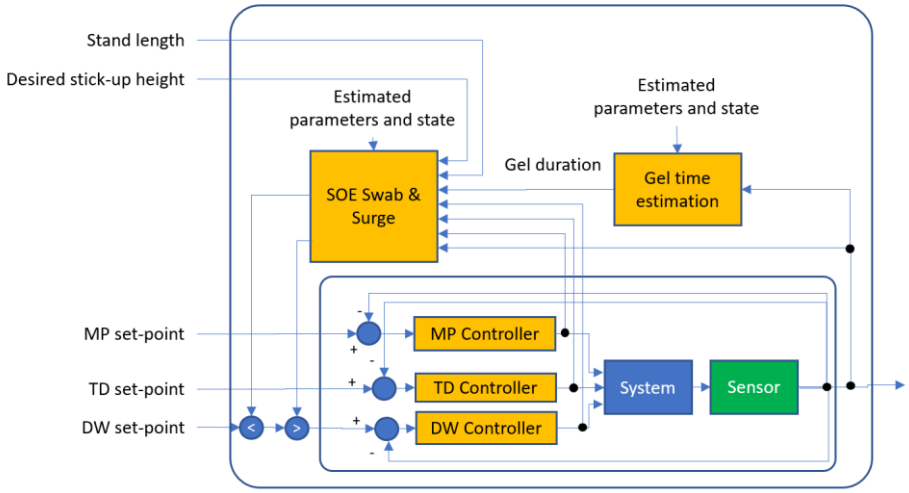

Fig. 198: Block diagram of the swab and surge safe operation envelope function.

3.5.2.5 Summary

The drilling system is both very elastic and has a large inertia. This concerns both the drill-string and the drilling fluid.
Consequently, the effects of actions performed with the drilling machines can be felt for several minutes after the command to the controller of the machine has reached its target set-point.

To avoid causing a drilling incident inadvertently, extremum values for these set-points are calculated.
These maximum values depend not only on the current context but also on the combination of actions that is performed, i.e. they are safe operating envelopes.

3.5.3 Automation of Drilling Procedures

Under the protection of the FDIR and SOE functions, it is now possible to define automated procedures. We will now detail the principles of three such functions:

- Pump startup procedure
- Friction test procedure
- Reciprocation procedure

3.5.3.1 Pump Startup

While starting the mud pumps, there are three different phases to consider:

- To fill the air gap at the top of the drill-string as quickly as possible,
- To break circulation,
- To accelerate the mud pumps to the desired flowrate.

If a new stand has been added to the drill-string, if the drill-string has been run in hole on the elevator and it has a float-sub in the BHA that prevents fluid to flow in the pipes, or if a slug has been pumped into the drill-string to have a dry trip when pulling out of hole, then there is an air gap at the top of the drill-string. When starting the mud pumps, it is necessary to fill this air gap. If we were filling the air gap at the gel breaking circulation rate, it would take a long time as the breaking circulation flowrate must be low to avoid potentially damaging surge pressures as seen in section 3.5.2.2. Therefore, it is desirable to utilize a larger flowrate than the breaking circulation one. It is possible to detect that filling the pipe is finished when the pump pressure starts to increase, but then gel breaking is performed for a few seconds at a relatively large flowrate and a surge pressure pulse is generated (see Fig. 199). Note that in this example, breaking circulation starts already before the pipes are full. This is because, a cold drilling fluid is pumped into the drill-string while the fluid in the annulus is at geothermal conditions. This corresponds to the first case of Fig. 200.

For a gentler pump startup, it is better to estimate the height of the air gap, or in other words, the liquid level in the drill-string, and to switch to gel breaking circulation rate just a few seconds, typically 5 to 10s, before the pipes should be filled. To evaluate the liquid level in the drill-string, it is necessary to account for the current context. Fig. 200 illustrates that, all things equal otherwise, the liquid level in the drill-string is 41m below the top of drill-string after having pumped a freshly mixed (20°C) drilling fluid for 2500s in a well in geothermal conditions while it is 25m below the top of drill-string after circulating of a drilling fluid for which temperature (60°C) is the results of several days of drilling operation. In the first case, the drill-string is filled with a heavier fluid than the one in the annulus. The difference of drilling fluid mass densities in the drill-string and in the annulus translates into a U-tube effect that explains the larger air gap with the cold fluid than with the warmer one.

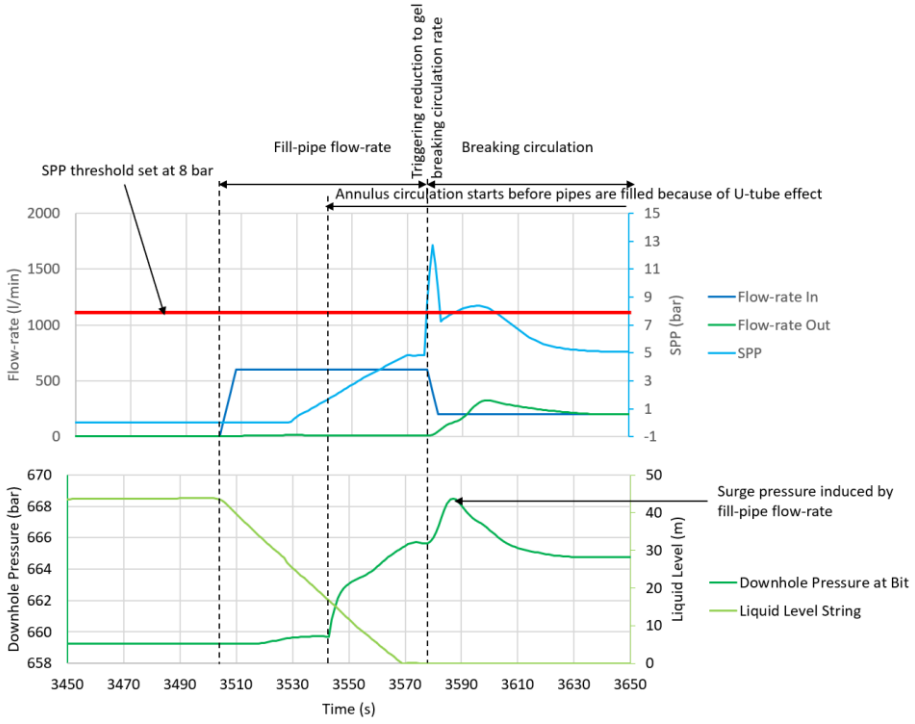

Fig. 199: The fill-pipe flowrate is reduced to the gel breaking flowrate, when the pump pressure exceeds a set threshold, here 8bar. Consequently, a pressure surge is generated in the annulus.

In practice, both the maximum pump pressure threshold and the estimated fill-pipe duration are used while filling the air gap. This is because there is always a risk that the estimation of the liquid level is overestimating the air gap length. Cayeux (2012) [6] gives an example of a situation where the estimation of the liquid level after tripping in hole with a float-valve in the BHA was difficult to evaluate because of badly documented drilling fluid temperature in the active pit and probable barite sag having taken place while there was no drill-string in the borehole.

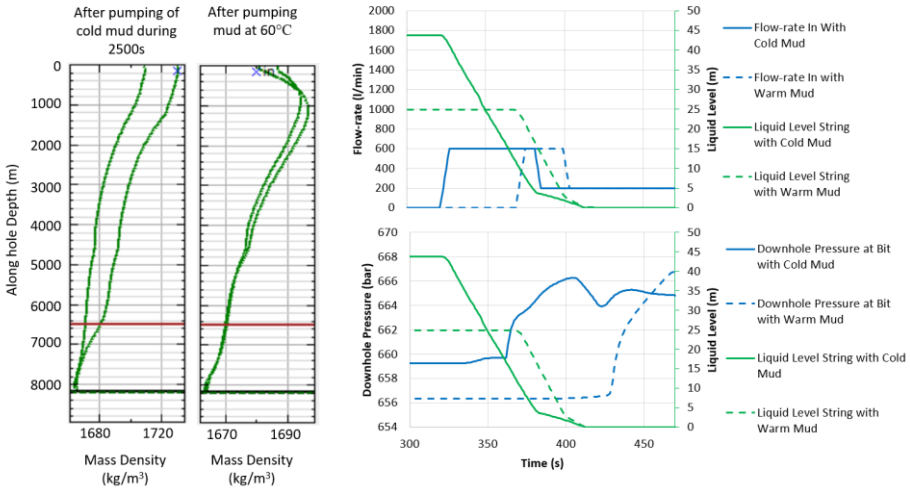

Fig. 200: Comparison of a fill-pipe procedure in two different contexts: a drilling fluid at 20°C has been pumped for 2500s in a well that was in geothermal conditions, or a drilling fluid with the same composition but with a temperature of 60°C has been pumped for a long duration inside the well.

When the pipes are filled, then the circulation is established. A minimum waiting time is enforced as described in section 3.5.2.2. Then the mud pumps are usually accelerated to a minimum flowrate that is necessary to ensure that enough electrical power is generated by the MWD turbine. We will refer to that flowrate as the MWD activation one. At that stage of the pump startup, there may be some variable waiting time depending on the MWD communication verification procedure. Finally, the mud pump rate is increased to the target flowrate (see Fig. 201). After breaking circulation, all mud pump accelerations

are limited by the maximum mud pump acceleration safe operational envelope (see section 3.5.2.3). Also, none of the used flowrates can exceed the maximum steady state flowrate that is estimated as a function of the current context as described in section 3.5.2.1.

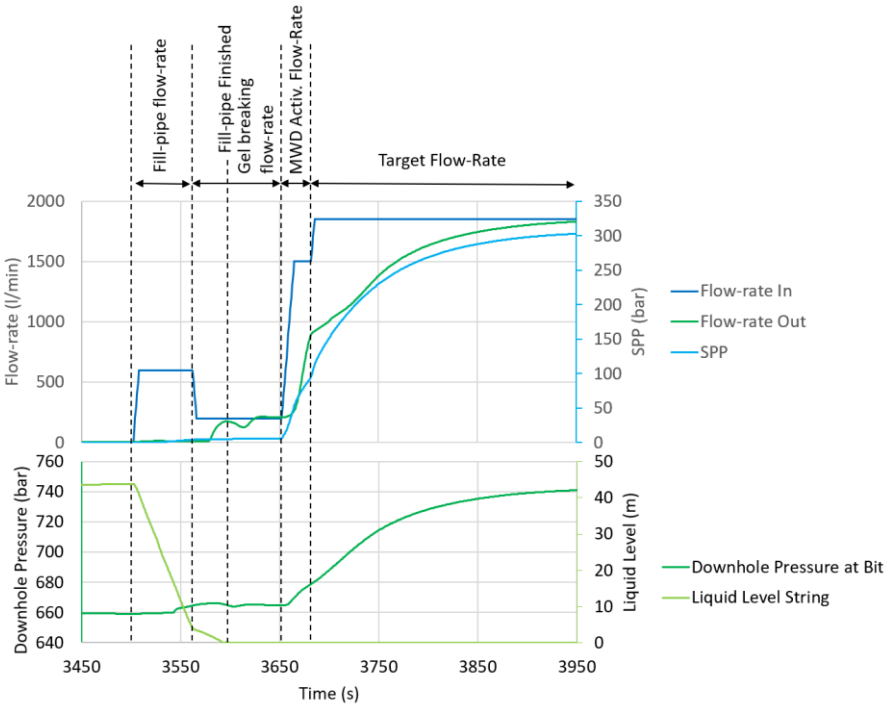

Fig. 201: Complete pump startup procedure with fill-pipe, breaking circulation, acceleration to MWD activation flowrate and a final stage to reach the target flowrate.

Sometime the detailed operation procedure specifies a more complex pump startup procedure with multiple intermediate staging of the pump rates before reaching the MWD activation flowrate. The state diagram of Fig. 202 allows for such a possibility. From this diagram, one can also notice that the acceleration to the fill-pipe flowrate and the waiting period during fill-pipe can be interrupted by the SPP exceeding the set threshold indicating that the pipes are filled.

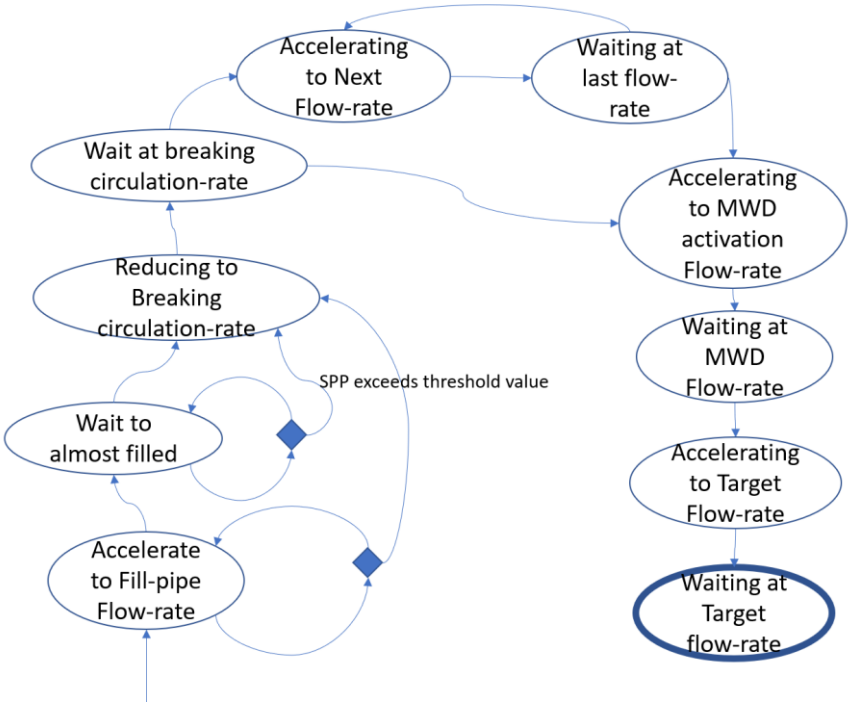

Fig. 202: State diagram of the automated pump startup procedure.

The automated pump startup function utilizes the maximum flowrate (see section 3.5.2.1), minimum waiting time for gel breaking (section 3.5.2.2), the maximum pump acceleration (section 3.5.2.3) safe operational envelopes. It also needs the pump over-pressure fault detection and recovery function described in section 3.5.1.3. The block diagram of Fig. 203 summarizes all the functions that are active during an automated pump startup.

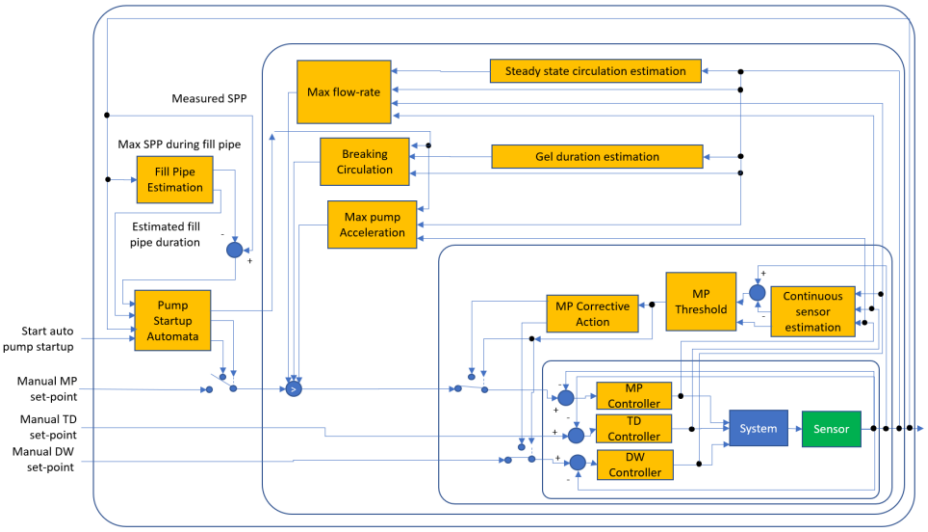

Fig. 203: Block diagram describing the automated pump startup procedure.

3.5.3.2 Friction Test

To evaluate the current mechanical friction in the well, it is common to perform a friction-test. This procedure has the objective to provide information about the free-rotating weight, the free-rotating torque, the pick-up weight and the slack-off weight. As the procedure is usually executed after drilling a stand, the drill-string is already rotating and if the bit is off bottom, the free-rotating torque and weight can be obtained by leaving the rotation as it is, without moving axially the drill-string for a few ten seconds. Then the top-drive speed is reduced to zero. As explained in section 3.2.3, in deviated wells, there is a remaining torque on the top-drive after its rotation has stopped. A zero-torque procedure shall therefore be applied to remove the torque on the top-drive. However, despite no torque on the top-drive, it is still possible that the drill-string is twisted and there is some torque along the drill-string as illustrated by Fig. 114.

When lifting the drill-string, there is a distance for which the drill-string both move axially and rotationally and therefore the hook-load does not reach immediately a stable pick-up weight. Furthermore, when the drill-string is slacked-off, it needs to be moved sufficiently to allow changing from a stretched condition to slacked-off state. If the pick-up and slack-off axial

velocities are too small, it is possible that static friction applies for parts of the drill-string while other parts are in kinetic friction conditions. It may then be impossible to have the whole drill-string moving axially altogether. In the example of Fig. 204, the drill-string is picked-up and slacked-off at 0.2m/s. It takes 3.2m of lift-up before the whole string moves without having any parts being subject to static friction and to remove the remaining torque along the drill-string. However, it takes 7m when slacking-off, before the whole drill-string moves without having any parts returning to static friction conditions.

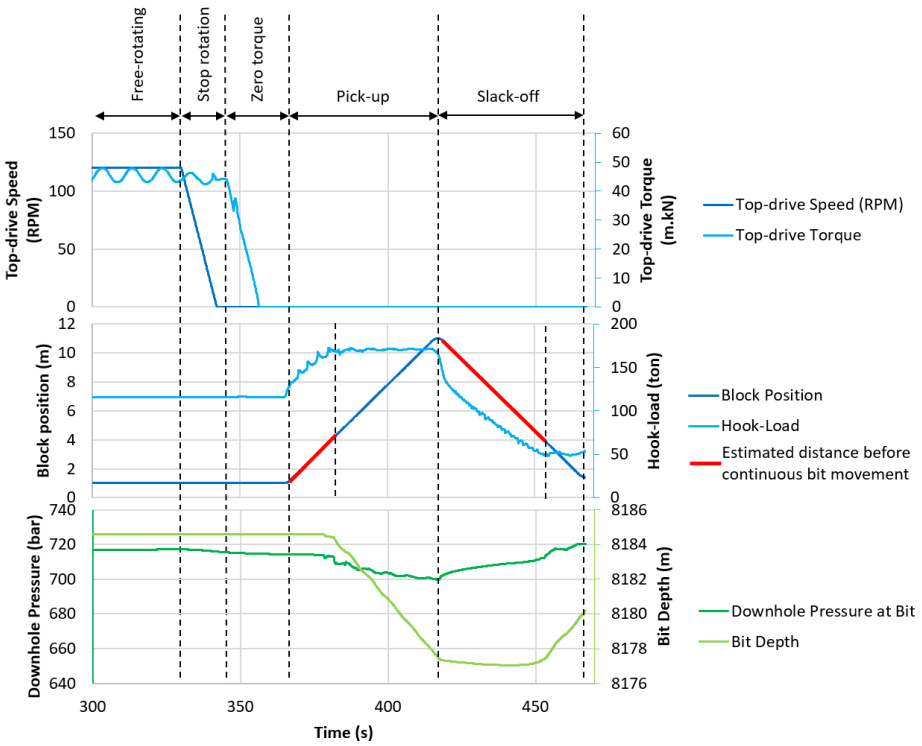

Fig. 204: A complete friction test procedure with a rotation off bottom, stopping of the top-drive, zero-torqueing the top-drive, pick-up and slack-off.

This shows that without having considered the minimum distance necessary to obtain an overall movement of the drill-string while slacking-off, a friction test that would have stopped when stable pick-up weight is observed, would have not been able to measure properly the slack-off weight.

The minimum distance for a friction test shall be evaluated with a transient torque and drag model as the one described in section 3.2.

Fig. 205 shows a state diagram of the automated friction test procedure.

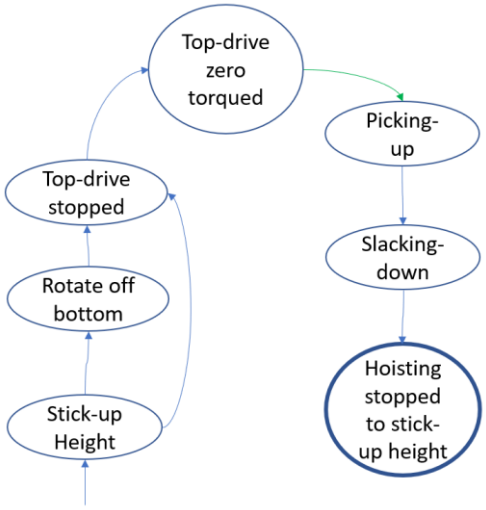

Fig. 205: State diagram of the automated friction test procedure.

Note that the free-rotating sequence is optional as if the friction test is started after drilling a stand, a period with rotation off bottom is already available when reaming up to the desired stick-up height.

The pick-up and slack-off velocities shall be limited to acceptable values with regards to the current downhole conditions in terms of risk of swab and surge, therefore the safe operating envelope for axial velocities described in section 3.5.2.4 must be available. There is also a risk of abnormal over-torque while rotating off bottom that shall be managed by the fault detection and isolation function described in section 3.5.1.2. Finally, the overpull/set-down weight fault detection and isolation function described in section 3.5.1.1 protects for abnormal hook-load evolution during the pick-up/slack-off section. Fig. 206 describes the block diagram of the complete automated friction test procedure.

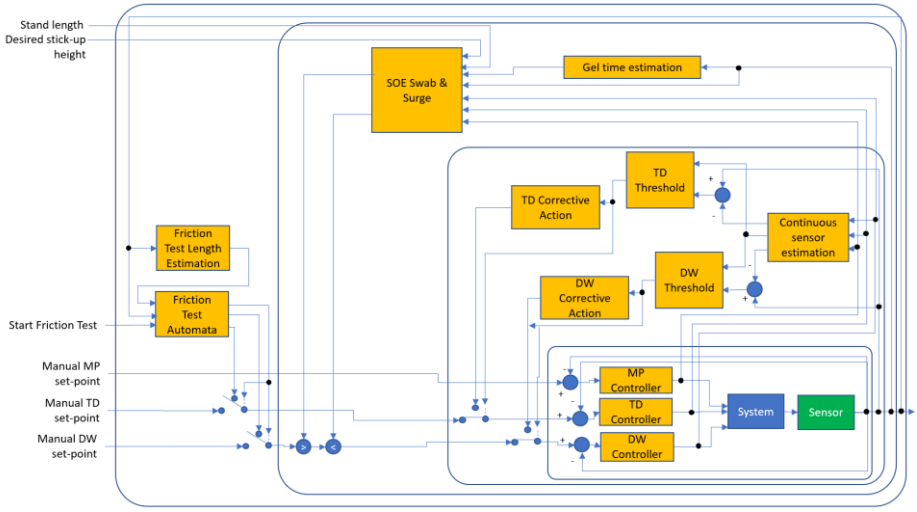

Fig. 206: Block diagram of the automated friction test procedure with its associated swab and surge safe operating envelope protection, abnormal top-drive torque fault detection and isolation and overpull/set-down weight fault detection and isolation.

3.5.3.3 Reciprocation

If additional cleaning is needed, for example after drilling a stand or after reaching the TD of the section, it may be necessary to maintain circulation for some time. As we have seen in section 3.1.4, rotation is also important for cleaning the borehole in deviated wells and therefore the top-drive speed shall also be maintained to a high level. However, if the bit stays at the same depth for a long duration, there is a risk to wash out the formation and therefore it is desirable to move the drill-string. Usually such cleaning operations start when the bit is closed to bottom hole and therefore the only possible direction of movement is upward, i.e. reaming up. After enough cleaning, if we need to continue drilling, the drill-string shall be moved downward to its original position. While reaming down, there is a risk to naturally sidetrack the well. To minimize that risk, the rotational speed is reduced, and the downward axial speed is chosen to be high such that the bit has less chances to sidetrack the original borehole. But because of the high ream-down velocity, there is a risk to generate large surge pressure waves that could fracture the open hole formation. Therefore, the flowrate shall be reduced. If one starts reaming down

at once while changing the flowrate and the rotational speed, there is still a risk for fracturing the formation (see Fig. 207).

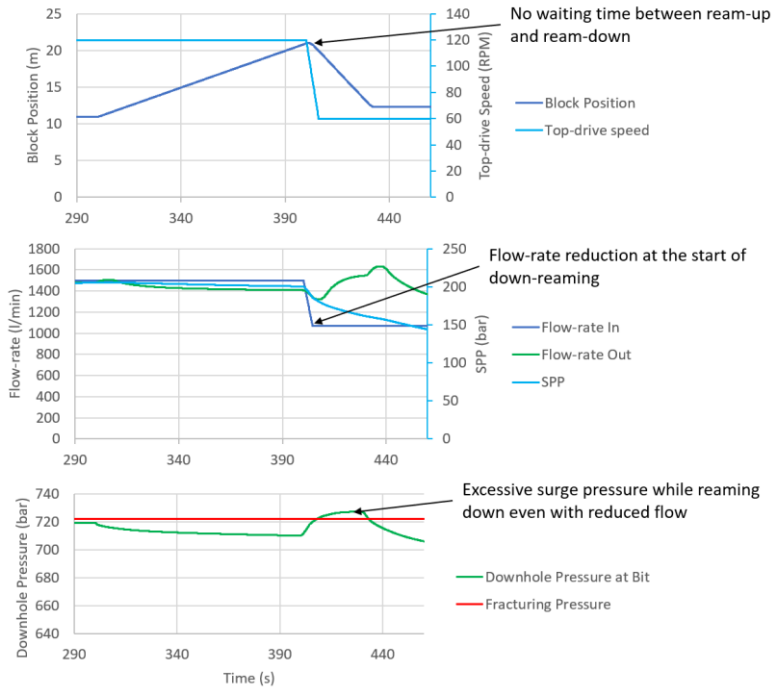

Fig. 207: In this example, the adjustment of the flowrate and top-drive speed for the ream-down sequence is performed at the same time as the change of direction. The generated surge pressure is high and could risk fracturing the open hole formations.

Instead, when the ream-up sequence is finished, the drill-string is maintained at the same axial position while the top-drive speed and the mud pump rate are adjusted. A minimum waiting duration is then necessary before the ream-down sequence starts to ensure that the downhole surge pressure will stay below the fracturing pressure limit of the open hole formations (see Fig. 208). This minimum duration shall be evaluated with a transient hydraulic model.

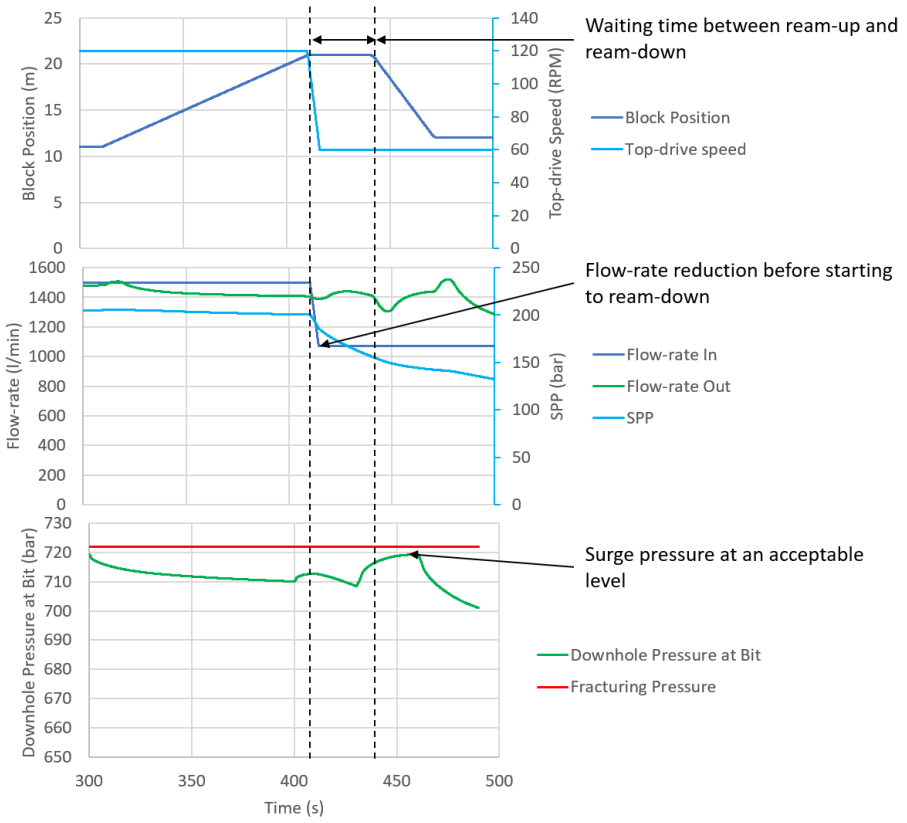

Fig. 208: In this example the ream-down top-drive velocity and flowrate are adjusted while the drill-string is axially steady and after a minimum necessary waiting duration the ream-down sequence is started.

If the driller wants to repeat the reciprocation procedure, he can at any time request to change the direction of movement with the hoisting joystick. If this happens while reaming down, then the axial movement is stopped, the flowrate and top-drive speed are adjusted to their original values and the ream-up sequence starts. Fig. 209 shows the state diagram of the automated reciprocation function.

Fig. 210 represents the block diagram of the automated reciprocation function. As it can be seen, the swab and surge safe operating envelope is necessary while running this automated procedure. It is also necessary to have active the over-

torque, overpull/set-down weight and over-pressure fault detection isolation and recovery functions.

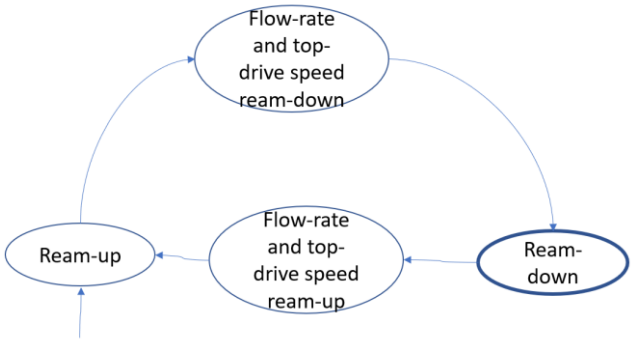

Fig. 209: State diagram of the automated reciprocation function.

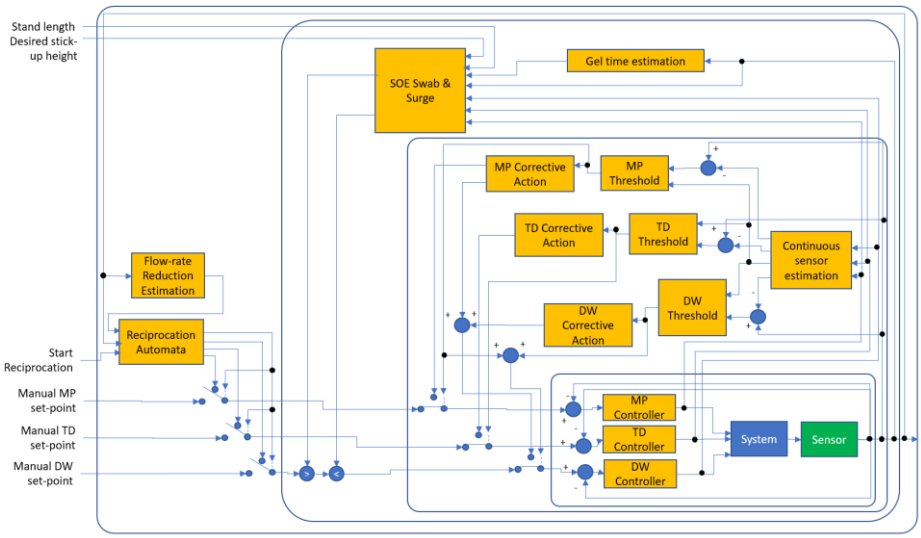

Fig. 210: Block diagram of the automated reciprocation function.

3.5.3.4 Summary

Under the protection of safety triggers and safeguards, it is then possible to automate standard drilling procedures, such as mud pump startup and shutdown, friction tests and reciprocation procedures.
The execution of these automated sequences depends also on the current context and their parameters are evaluated with high fidelity models.
Yet again a model reduction is performed on the results of these estimations before being passed to the machine controllers.

4 Overview of Published Work

The work described in this thesis is documented through many publications. Only six journal papers have been selected to accompany this document. However, along the text, it has been referred to, the following other papers:

- E. Cayeux and H. P. Lande, "Factors Influencing the Estimation of Downhole Pressure far Away From Measurement Points During Drilling Operation," in *54rd SIMS conference on Simulation and Modelling*, Bergen, Norway, 2013. [1]
- E. Cayeux, "Safe Mud Pump Management while Conditioning Mud: On the Adverse Effects of Complex Heat Transfer and Barite Sag when Establishing Circulation," in *IFAC Workshop on Automatic Control in Offshore Oil and Gas Production*, May 31 - June 1, Trondheim, Norway, 2012. [6]
- E. Cayeux, B. Daireaux, E. W. Dvergsnes and F. Florence, "Torward Drilling Automation: On the Necessity of Using Sensors that Relate to Physical Models," *SPE Drilling & Completion*, vol. 29, no. 2, pp. 236-255, 2014. [7]
- Cayeux, A. Leulseged, R. Kluge and J. Haga, "Use of a Transient Cuttings Transport Model in the Planning, Monitoringand Post Analysis of Complex Drilling Operations in the North Sea," in *SPE/IADC Drilling Conference*, Fort Worth, TX, USA, 2016. [98]
- E. Cayeux, "On the Importance of Boundary Conditions for Real-time Transient Drill-String Mechanical Estimations," in *SPE/IADC Drilling Conference*, Fort Worth, TX, USA, 2018. [185]
- E. Cayeux and B. Daireaux, "Early Detection of Drilling Conditions Deterioration Using Real-Time Calibration of Computer Models: Field Example from North Sea Drilling Operations," in *SPE/IADC Drilling Conference*, Amsterdam, The Netherlands, 2009. [151]
- E. Cayeux and A. Leulseged, "Impact of Drilling Fluid Thixotropy on the Calculations of Pressure Losses in Pipes and Annuli," in *37th International Conference on Ocean, Offshore & Arctic Engineering*, Madrid, Spain, 2018. [186]
- E. Cayeux, B. Daireaux, E. W. Dvergsnes, H. Siahaan and J. E. Gravdal, "Principles and Sensitivity Analysis of Automatic Calibration of MPD Methods Based on Dual-Gradient Drilling Solutions," in *SPE Deepwater Drilling and Completions Conference*, Galveston, Texas, USA, 2014. [187]

- E. Cayeux, H. J. Skadsem, B. Daireaux and R. Holand, "Challenges and Solutions to the Correct Interpretation of Drilling Friction Tests," in *SPE Drililng Conference*, The Hagues, The Netherlands, 2017. [188]
- E. Cayeux, H. J. Skadsem and R. Kluge, "Accuracy and Correction of Hook Load Measurements During Drilling Operations," in *SPE/IADC Drilling Conference*, London, England, UK, 2015. [189]
- E. Cayeux, T. Mesagan, S. Tanripada, M. Zidan and K. K. Fjelde, "Real-Time Evaluation of Hole Cleaning Conditions Using a Transient Cuttings Transport Model," in *SPE/IADC Drilling Conference*, Amsterdam, The Netherlands, 2013. [164]
- E. Cayeux and A. Leulseged, "Effect of Solid Particle Concentration on Drilling Fluid Rehological Behavior and its Impact on Pressure Losses," in *SPE Drilling Conference*, The Hague, The Netherlands, 2019. [190]
- E. Cayeux, «Time, Pressure And Temperature Dependent Rheological Properties Of Drilling Fluids And Their Automatic Measurements,» in SPE Drilling Conference, Galveston, Texas, USA, 2020. [191]
- E. Cayeux, A. Ambrus, L. Øy, A. Helleland, S. T. Brundtland and H. Nevøy, "Analysis of Torsional Stick-Slip Situations Observed with Downhole High-Frequency," in SPE Drilling Conference, Galveston, Texas, USA, 2020. [173]

As associated published work to this thesis, two publications per real-time application domains have been selected:

- For drilling simulation (4.1):
  - Cayeux, E., Daireaux, B., Dvergsnes, E.W., Leulseged, A., Bruun, B. T., Herbert, M.: *Advanced Drilling Simulation Environment for Testing New Drilling Automation Techniques and Practices.* SPE-150941-PA, published in SPE Drilling & Completion Journal, Volume 27, Number 4, December 2012, pp. 559-573. (Paper I)
  - Cayeux, E., Mesagan, T., Tanripada, S., Zidan, M., Fjelde, K.K.: *Real-Time Evaluation of Hole Cleaning Conditions Using a Transient Cuttings Transport Model*. SPE-163492-PA. Published in SPE Drilling and Completion, Volume 29, Number 1, 2014, pp. 5-21. (Paper II)
- For drilling interpretation (4.2):
  - Cayeux, E., Daireaux, B., Dvergsnes, E. W., Sælevik, G.: *Early Symptom Detection Based on Real-Time Evaluation of Downhole Conditions: Principles and Results from several North Sea Drilling Operations*. SPE-150422-PA, published in SPE Drilling & Completion Journal, Volume 27, Number 4, December 2012, pp. 546-558. (Paper III)

    - Cayeux, E., Kucs, R., Gibson, N.: *Mathematical Modeling of Drilling Operations by Use of Nitrogen-Enriched Mud: A Case Study by Use of a Recorded Drilling Data-Set*. SPE 167884-PA. Published in SPE Drilling & Completion, Volume 29, Number 4, 2014, pp. 438-453. (Paper IV)
- For drilling assistance (4.3):
    - Cayeux, E., Daireaux, B. and Dvergsnes, E. W.: *Automation of Mud-Pump Management Application to Drilling Operations in the North-Sea*. SPE-128285-PA, published in SPE Drilling & Completion Journal, Volume 26, Number 1, March 2011, pp. 41-51. (Paper V)
    - Cayeux, E., Daireaux, B. and Dvergsnes, E. W.: *Automation of Draw-works and Top-drive Management to Minimize Swab/Surge and Poor-Downhole-Condition Effects*. SPE-128286-PA, published in SPE Drilling & Completion Journal, Volume 26, Number 4, December 2011, pp. 557-568. (Paper VI)

4.1 Publications Related to Drilling Simulation

4.1.1 Paper I: Advanced Drilling Simulation Environment for Testing New Drilling Automation Techniques and Practices

This paper describes a testing environment for drilling automation systems. On the one hand, there is a drilling simulator engine that connects to a drilling control system and which settings are controlled by an experimentalist workstation. On the other hand, there is a testing environment that is suited to conduct teamwork simulations with in-house or external mud logging applications or other monitoring applications used to support a drilling team.

The drilling simulator engine utilizes transient models of the drilling process, like transient hydraulic and cuttings transport calculations as described in section 3.1.4. It also makes use of the surface equipment modelling like the flowline and mud treatment equipment transient model described in section 3.3. In addition, there are simulations of incidents like pack-offs, overpulls, set-down weights, over-torques, over-pump pressures. It is therefore suited to test automatic safety triggers as those described in section 3.5.1. The paper also describes that the drilling simulator engine can also manage back-pressure MPD operations and dual-gradients drilling in addition to conventional drilling.

4.1.2 Paper II: Real-Time Evaluation of Hole Cleaning Conditions Using a Transient Cuttings Transport Model

This paper describes the principles of a transient cuttings transport model. It addresses several aspects of the dependence of the drilling fluid properties to its composition and in situ conditions like pressure and temperature. For instance, there is a description on how cuttings particles influence not only the apparent drilling fluid density but more generally its PVT-behavior, as we have seen in section 3.1.1. Then it continues with a description of the principles of the transient cuttings transport model with the three competing phenomena: direct transport and associated slip velocity (see section 3.1.4.1), deposition on the low-side and finally resuspension or erosion (see section 3.1.4.2). The paper also presents two example cases one in conventional drilling and the other one with back-pressure MPD.

4.2 Publication Related to Drilling Interpretation

4.2.1 Paper III: Early Symptom Detection Based on Real-Time Evaluation of Downhole Conditions: Principles and Results from several North Sea Drilling Operations

This paper summarizes the results from the use of a drilling interpretation system while actively advising several drilling operations. It shows that many drilling incidents have warning signs way ahead of time of the occurrence of the incident itself. Warning signs can be detected ½ to 1 hour before the occurrence of drilling problems, for fast changing drilling conditions like tripping. But it can be as long as ½ to 1 day for drilling conditions evolving at slower pace.

The system utilizes the pit volume estimation described in section 3.3 to determine when cuttings are properly transported to surface or not. It also utilizes an early version of the automatic calibration of friction factors as the one described in section 3.4.6.1. It implements an initial version of uncertainty propagation on estimated values of standard top-side and downhole measurements of the method described in section 3.4.7.

4.2.2 Paper IV: Mathematical Modeling of Drilling Operations by Use of Nitrogen-Enriched Mud: A Case Study by Use of a Recorded Drilling Data-Set

The symptom detection method described in section 3.4 has been applied to post-analyze a drilling operation that was utilizing foam as a drilling fluid. The estimation of the drilling fluid density at any place along the hydraulic circuit utilizes the modelling described in section 3.1.1. An estimation of the rheological behavior of the foam is also described. With such a drilling operation, there is a large uncertainty on most inputs. This uncertainty is propagated while estimating the downhole conditions as described in section 3.4.7. It is then interesting to see that even though the uncertainty associated with the input is large, the results are still usable and comparison with observations made during the drilling operation matches with the probabilistic model estimations.

4.3 Publication Related to Drilling Assistance

4.3.1 Paper V: Automation of Mud-Pump Management Application to Drilling Operations in the North-Sea

This paper describes the functionalities of a system used to assist with the control of the mud pumps in drilling operations. As an introduction, it is highlighted that safe pressure management is achieved when the annulus pressure stays within a lower bound defined by the maximum of the pore and collapse pressure and an upper bound corresponding to the fracturing pressure as described in section 3.4.9. The proximity of the annulus pressure to its bounds shall be investigated for the whole depth range of open hole section. The mud pump management functionalities comprise a safety trigger for over-pressures as described in section 3.5.1.3, safe-guarding of the maximum flowrate (see section 3.5.2.1) and of the pump acceleration during startup (ref. section 3.5.2.3). Under the protection of the over-pressure safety trigger and the two safe guards, the mud pump startup procedure is semi-automated as described in section 3.5.3.1 by accounting for an efficient filling of the pipes, breaking circulation and bringing the mud pump rate according to a more or less complex procedure decided by the drilling operation.

4.3.2 Paper VI: Automation of Draw-works and Top-drive Management to Minimize Swab/Surge and Poor-Downhole-Condition Effects

In this paper the functionalities of a system designed to assist with the management of the draw-works and top-drive is described. It reviews the three safety triggers associated with these machines: over-torque (section 3.5.1.2), overpull and set-down weight (section 3.5.1.1). Then it describes the swab and surge safeguarding functionality (section 3.5.2.4). Finally, automatic procedures like friction tests (section 3.5.3.2) and reciprocation (section 3.5.3.3) are explained. It is also explained how the deterioration of the drilling conditions influences the behavior of each of these functions. This is achieved by automatically monitoring the evolution of mechanical friction as explained in section 3.4.6.1.

5 Conclusion

The motivation of this thesis was to define a sufficiently detailed mathematical model of the drilling process that would make it possible to create realistic drilling simulation environments, detect automatically weak signals during drilling operations prior to the occurrence of actual drilling events and to provide drilling assistance functions with a minimum number of safety features to improve the safety of drilling operations. This has led to model effects that have been observed in various different drilling contexts and that was not necessarily accounted for in other contexts such as in drilling engineering. Many of these effects result from the intertwined interaction of hydraulic, mechanical, heat transfer and solid transport causes. The complex interaction of different domains, e.g. hydraulic, mechanics, heat transfer, is one of the greatest challenges when attempting to model drilling operations for real-time applications. The availability of a high-fidelity mathematical model of the drilling process, including surface and downhole equipment, is yet insufficient to solve problems such as the early detection of the deterioration of drilling conditions. This is because the drilling process is non-holonomic and very sparsely observed (both in time and space). It is therefore necessary to account for uncertainties in the measurement and modelling, and to propagate them through the evaluation process. Then, with such a probabilistic framework, it is possible to detect early symptoms that the drilling operation is not optimal and therefore give the opportunity to take proactive actions to improve the situation. Automated assistance for performing drilling operations necessitates automatic fault detection and isolation functions, safe-guarding functions and adaptative automatic procedures. Such automation functions necessitate to be able to evaluate the drilling conditions that will be encountered in a short-term future (typically 15 to 30 minutes). An automatically calibrated high-fidelity model of the drilling process is then an important element to make estimations for the coming half hour.

In addition to the above described general results, specific findings have been exposed:

- The properties of drilling fluids, like the mass density (see section 3.1.1) and rheological behavior (see section 3.1.3), depend on their composition and in the situ conditions, i.e. pressure and temperature, but also on their shear

history. It has been discovered that the thixotropic behavior of drilling fluid does not respond in a similar way to most other thixotropic fluids, as they need a very long time to reach steady state response after being subjected to an increase of the shear rate (see section 2.1.1.14). We have proposed a new thixotropic model that fits better with drilling fluids (section 3.1.1.4). The composition of drilling fluids is altered during circulation, for example because of the transport of drill-cuttings. The dimensions of solid particles present in the annulus are modified by the grinding process performed by the rotation of the tool-joints against the borehole wall (see section 3.1.4.3), therefore changing the particle size distribution of the cuttings being transported.

- The ability to transport cuttings depends on the local 3-dimensional fluid velocity field in the annulus, and not only on the bulk fluid velocity. Therefore, the pipe rotational and lateral movement is also important (see section 3.1.4.2). As the apparent drilling fluid properties are altered by the presence of cuttings, as well as the geometrical dimensions of the annulus when there is sedimentation, it follows that the mechanism to transport cuttings is state dependent. It is therefore necessary to track the transport of cuttings particles along the annulus to determine the local states. Consequently, the transport of cuttings is a non-holonomic process.
- The axial and rotational motion of a drill-sting is tightly connected to hydraulic forces (see sections 3.2.4 and 3.2.6), and bottom boundary conditions (bit/rock interaction see section 3.2.5). Furthermore, as mechanical friction always acts in the opposite direction of sliding, it influences simultaneously the axial and torsional response of the drill-string (see section 3.2.3). The transition from and to static friction conditions at different locations along the drill-string is the cause of negative damping and can cause stick-slip oscillations, also when the bit is off-bottom. When drilling from a floater, the top of string movement, originating from heave movement, creates conditions by which it is extremely seldom to have uniform movements and therefore a transient torque and drag model is a must for the analysis of the drilling process.
- The flowline and mud treatment equipment cause a retention of drilling fluid that impacts the monitoring of the active pit volume and the ability to detect gains and losses (see section 3.3). To accommodate with a wide variety of flowrate variations and timing, a transient model has been described that manages to reproduce with fidelity of pit volume variations also caused by cuttings separation at the level of the shale shakers.
- The accuracy of the results produced by simulations depends on the quality of the inputs. For instance, section 3.4.1 described how inaccurate the PVT behavior of a drilling fluid can be as a function of which information is available about its composition. In the same line of thought, section 3.4.7 described how to propagate the inherent inaccuracies of the Model 35

rheometer readings in the estimation of the in situ rheological behavior, also including the impact of cuttings in suspension.

- Because of wellbore position uncertainty, even the TVD of the trajectory is not known with certainty. A methodology to estimate the plausible TVD range at any depth along the borehole, is presented in section 3.4.3.1.
- Some of the dimensions of the drilling system configuration are ill-defined. Their calibration takes advantage of the fact that these values do not change much during a drill-string run, as it is exposed in section 3.4.5. The methodology consists in utilizing, in the calibration process, sequences extracted from the drilling operation where current drilling conditions have a limited impact on the observations.
- On the other hand, there are unknown properties of the drilling process that change with the drilling context. These more dynamic unknown properties need also to be calibrated. An example of such properties is the mechanical friction as it varies as a function of the presence of cuttings, in bed or in suspension. When steady state conditions can be utilized, the calibration is straight forward, however it can be a challenge when transient effects dominate the measurements as explained in section 3.4.6.1.
- Similarly, the strength of formations can change abruptly and therefore influence drastically the ability to drill. Beside the formation strength, the time evolution of the bit aggressivity also influences drilling performance. The calibration of these values is essential to estimate realistic instantaneous ROP, and therefore obtain trustworthy estimations of cuttings production, while drilling from a floating rig (see section 3.4.6.3).
- The temperature evolution and the cuttings distribution along the borehole depend on the sequence of operations that have been undertaken for a long period of time. Therefore, the drilling process in non-holonomic. Consequently, it is necessary to estimates continuously the time evolution of the drilling system by accounting for all the variations of the commands provided to the drilling machines (see section 3.4.4).
- As inputs are inherently imperfect, it is important to propagate uncertainties while estimating likely values of measurable quantities like hook-load, top-drive torque, SPP or downhole ECD (see section 3.4.7). However, the more measurement points, in space and time, the better, as it is then possible to reduce the uncertainty at a distance from measurements.
- With this probabilistic framework that allows to estimate continuously what should be the normal response of the drilling system as a function of drilling commands, it is then possible to detect whether the measurements start to deviate from normality. Section 3.4.10 explains how these deviations can be used as indicators of the deterioration of the drilling conditions and therefore allow the drilling team to take proactive actions before any drilling incident has yet occurred.
- Quickly developing drilling incidents such as over-pressures, over-pulls, set-down weights or over-torques are best managed by controlling actively

the drilling machines. This is done by utilizing safety triggers (see section 3.5.1), i.e. fault detection and isolation schemes. As the thresholds that should be used for detection are functions of the current context and the actions being executed, a model-based approach is used. High fidelity models are used to generate a reduced model of the threshold levels. The level of complexity of the isolation procedure depends on constraints imposed by human factors. It is the simplest when the hoisting system is involved (see section 3.5.1.1) and the most advanced when managing the mud pumps (see section 3.5.1.3).

- The drilling system is both very elastic and has a large inertia. This is important for both the drill-string and the drilling fluid. Consequently, the effects of actions performed with the drilling machines can be felt for several minutes after the command to the controller of the machine has reached its target set-point (see section 3.5.2). To avoid causing a drilling incident inadvertently, extremum values for these set-points are calculated. These maximum values depend not only on the current context but also on the combination of actions that is performed, i.e. they are safe operating envelopes.
- Under the protection of safety triggers and safe guards, it is then possible to automate standard drilling procedures, such as mud pump startup and shutdown, friction tests and reciprocation procedures (see section 3.5.3). The execution of these automated sequences depends also on the current context and their parameters are evaluated with high fidelity models.

5.1 Future Work

Every single monitoring and analysis of actual drilling operations bring new challenges that require acquiring even more understanding of the physical phenomena that govern the drilling process. The remaining of this section will list some of those research directions that need more investigation.

- In section 3.1.3, we have developed a composition-based rheological model of KCl/polymer drilling fluids. The next step will be to carry on with similar modelling of standard oil-based muds and micronized OBM.
- A few decades back in time, Larsen, Bassal and Jalukar have made thousands of experiments with a flow-loop in order to derive an empirical model of the critical transport fluid velocity. Similarly, it will be necessary to perform numerous CFD simulations in order to use the methodology described in section 3.1.4.2 to expand the work started by Larsen, Bassal and Jalukar to larger hole sizes and more complex pipe movement.

- In section 3.2, we have described a transient torque and drag model that accounts for torsional and axial displacements of the drill-string. However, there are evidence that the lateral movement of drill-pipes can cause serious damage to the drill-string ([192], [193]). Accounting for lateral movement of the drill-string is therefore a natural extension of the transient torque and drag model.
- The model of the return flow to the pit described in section 3.3 neither accounts for the sedimentation of cuttings in the flowline nor the erosion of such cuttings bed. However, as it is shown on fig. 7 of Cayeux and Daireaux (2016) [184], the deposition and erosion of cuttings inside the flowline plays an important role on the flow-back to the pit. So, it is a natural extension of the model to incorporate solid sedimentation and bed erosion inside the flowline.
- In section 3.5.1, we have seen that a drilling automation system can react automatically to fast occurring drilling events and proceed with a minimum sequence of actions to avoid an escalation of the drilling problem. Yet, it is only when knowing the probable cause of the incident that a proper remedial plan can be put in action. It is therefore a natural extension of the described work to proceed with an automatic characterization of the current situation. In that context, it is envisaged that machine learning techniques as described by Ambrus et al. (2018) [148], can be helpful to reach such a goal.
- Section 3.4.10 described a method to detect the deterioration of drilling conditions prior to the occurrence of any drilling event. This analysis results in a series of weak symptoms upon which remedial actions can be taken to decrease the risk of drilling incidents to occur. However, the interpretation of these weak symptoms requires a deep knowledge of the drilling process that is not easily found in standard drilling operations. This approach for avoiding drilling incidents by being proactive instead of being reactive would benefit of an automatic classification of the probable causes for the observed weak symptoms. Deep machine learning solutions could be good candidates to perform an automatic causal analysis of early symptoms of the deterioration of the drilling conditions.
- In section3.5.2, we have described safe-guarding mechanisms that essentially apply for conditions were the bit is off bottom. We have started to extend those concepts to situation where the bit is on bottom and drilling. In that context, additional safety triggers to those described in section 3.5.1, are being added like for instance automatic reactions to intense lateral vibrations. Also, the solution being developed makes use of automatic procedures, kind of drill-off tests that are executed continuously, to seek for the optimum ROP that is best adapted to the current conditions. This optimum ROP takes into

consideration both short and medium terms analysis, like the ability to transport cuttings to surface.

- The system described in section 3.5 is currently being extended to achieve drilling autonomy. Besides automated pipe handling with robotic drilling machines to eliminate the need for manual rig crew intervention on the drill-floor, a new orchestration control loop is added to the control hierarchy of the system. The orchestration control loop optimizes the sequences that are performed to minimize an objective function that estimates the remaining drilling duration to reach TD. The estimation of the remaining drilling time is a probabilistic estimation of the drilling performance and the potential time delays incurred in case of the occurrence of drilling incidents. For that reason, it maintains a balance between maximizing performance and minimizing risks. This balance is influenced by the quality and availability of measurements, both at the top-side and downhole.
- The presented applications in sections 3.4 and 3.5 depends heavily on real-time drilling signals. However, a drilling operation is often conducted by many different service companies, each of them managing their own real-time signals. Yet, to manage and assist properly the drilling process, it is often necessary to get real-time information from several of these service companies. In view of the great disparity of signals managed by these companies and the modification of the availability of these signals, almost on a daily basis, it is highly desirable that these real-time data providers can publish their available signals in such a way that other computer systems can seamlessly interpret the meaning of the signals. This can be achieved by utilizing a computer readable semantical description of drilling real-time signals as described in Cayeux et al. 2019 [194].
- The Achilles heel of the work presented in this document is the necessity to have a detailed and correct description of the wellbore architecture, drill-string and BHA, trajectory, drilling fluid, geo-pressure margins, etc. In practice, it is not so easy to get all this information in a timely fashion prior to the start of a drilling operation. Adequately chosen measurements that have been selected for serving the automation of the management and assistance of the drilling process, can help reduce the burden on the manual collection of configuration data (see Cayeux et al. 2014 [7]). However, there is a still a need to design new types of sensors for the sole purpose of acquiring enough information, at an acceptable level of accuracy, to avoid any manual configuration. Examples of such sensors that would help with the automatization of the drilling process are:
    - Continuous measurement of the rheological behaviour of drilling fluids that account for pressure, temperature and time dependence (see Cayeux 2020 [191]).

- Precise, robust and easy to retrofit measurement of the flowrate out of a well (see Cayeux 2020 [195]).
- Automatic measurement of the drill-string length (see Cayeux [196]).

6 Bibliography

[1] E. Cayeux and H. P. Lande, "Factors Influencing the Estimation of Downhole Pressure far Away From Measurement Points During Drilling Operation," in *54rd SIMS conference on Simulation and Modelling*, Bergen, Norway, 2013.

[2] P. Charlez, Rock Mechanics - volume 2 - Petroleum Applications, Paris: Editions Technip, 1997.

[3] R. F. Mitchell, "Dynamic Surge/Swab Pressure Predictions," *SPE Drilling Engineering*, vol. 3, no. 3, pp. 325-333, 1988.

[4] F. E. Crespo, R. M. Ahmed, A. Saasen, M. Enfis and M. Amani, "Surge-and-Swab Pressure Predictions for Yield-Power-Law Drilling Fluids," *SPE Drilling & Completion*, vol. 27, no. 4, pp. 574-585, 2012.

[5] K. S. Bjørkevoll, R. Rommetveit, H. Gjeraldstveit and A. Merlo, "Field Data Verification Of Transient Surge Swab Model For Critical Wells Applications," in *Offshore Mediterranean Conference*, Ravenna, Italy, 2003.

[6] E. Cayeux, "Safe Mud Pump Management while Conditioning Mud: On the Adverse Effects of Complex Heat Transfer and Barite Sag when Establishing Circulation," in *IFAC Workshop on Automatic Control in Offshore Oil and Gas Production*, May 31 - June 1, Trondheim, Norway, 2012.

[7] E. Cayeux, B. Daireaux, E. W. Dvergsnes and F. Florence, "Torward Drilling Automation: On the Necessity of Using Sensors that Relate to Physical Models," *SPE Drilling & Completion*, vol. 29, no. 2, pp. 236-255, 2014.

[8] P. Isambourg, D. Bertin and M. Brangetto, "Field Hydraulic Tests Improve HPHT Drilling Safety and Performance," in *SPE Annual Technical Conference*, 27-30 Sep, New Orleans, Louisiana, USA, 1998.

[9] API, "API RP 13D: Recommended Practice for Rheology and Hydraulics of Oil-well Drilling Fluids," American Petroleum Institute, 2017.

[10] N. P. Kemp, D. C. Thomas, G. Atkinson and B. Atkinson, "Density Modelling of Brines as a Function of Composition, Pressure and Temperature," *SPE Production Engineering*, vol. 4, no. 4, pp. 394-400, 1989.

[11] M. Zamora, S. Roy, K. Slater and J. Troncoso, "Study on the Volumetric Behavior of Base Oils, Brines, and Drilling Fluids Under Extreme Temperatures and Pressures," *SPE Drilling & Completion*, vol. 28, no. 3, pp. 278-288, 2013.

[12] L. L. Hoberock, D. C. Thomas and H. C. Nickens, "Here's How Compressibility and Temperature Affect Bottom-Hole Mud Pressure," *Oil & Gas J.*, vol. 80, no. 12, pp. 159-164, 1982.

[13] E. J. Peters, M. E. Chenevert and C. Zang, "A Model for Predicting the Density of Oil-Based Mud at High Pressures and Temperatures," *SPE Drilling Engineering*, vol. 5, no. 2, pp. 141-148, 1990.

[14] Y. V. Rao, Chemical Engineering Thermodynamics, Universities Press (India), 1997.

[15] E. van Oort, S. Roy, M. Zamora and B. Toups, "Real-time ECD Simulation and Management Using a Remote Operations Center," in *SPE/IADC Drilling Conference*, 23-25 February, Amsterdam, Netherlands, 2005.

[16] W. H. Herschel and R. Bulkley, "Konsistenzmessungen von Gummi-Benzollösungen," *Kolloid Zeitschrift*, vol. 39, pp. 291-300, 1928.

[17] R. E. Robertson and H. A. Stiff, "An Improved Mathematical Model for Relating Shear Stress to Shear Rate in Drilling Fluids and Cement Slurries," *SPE Journal*, vol. 16, no. 1, pp. 31-36, 1977.

[18] A. T. Bourgoyne , K. K. Millheim, M. E. Chenevert and F. S. Young, Applied Drilling Engineering, Society of Petroleum Engineers, 1986.

[19] G. Mullineux, "Non-linear Least Square Fitting of coefficients in Herschel-Bulkley Model," *Applied Mathematical Modelling*, vol. 32, pp. 2538-2551, 2008.

[20] H. J. Skadsem, "Measurement of Flow and Viscoelastic Properties of Some Oil- and Water-Based Drilling Fluids," IRIS 2013/197 SINTEF 7020384/02/13, Stavanger, 2013.

[21] R. M. Beirute and R. W. Flumerfelt, "An Evaluation of the Robertson-Stiff Model Describing Rheological Properties of Drilling Fluids and Cement Slurries," *SPE Journal*, vol. 17, no. 2, pp. 97-100, 1977.

[22] V. C. Kelessidis, R. Maglione, C. Tsamantaki and Y. Aspirtakis, "Optimal determination of rheological parameters for Herschel-Bulkley drilling fluids and impact on pressure drop, velocity profiles and penetration rates during drilling," *J. Pet. Sci. Eng.*, vol. 53, p. 203 – 224, 2006.

[23] K. Founargiotakis, V. C. Kelessidis and R. Maglione, "Laminar, transitional and turbulent flow of Herschel–Bulkley fluids in concentric annulus," *Can. J. Chem. Eng.*, vol. 86, no. 4, pp. 676-683, 2008.

[24] O. Erge, E. M. Ozbayoglu, S. Z. Miska, M. Yu, N. Takach, A. Saasen and R. May, "CFD Analysis and Model Comparison of Annular Frictional Pressure Losses While Circulating Yield Power Law Fluids," *Journal of Petroleum Science and Engineering*, vol. 140, pp. 16-27, 2016.

[25] O. Erge, E. M. Ozbayoglu, S. Z. Miska, M. Yu, N. Takash, A. Saasen and R. May, "Effect of Drillstring Deflection and Rotary Speed on Annular Frictional Pressure Losses," *J. Energ. Resourc.*, vol. 136, no. 4, 2013.

[26] A. Pilehvari and R. Serth, "Generalized Hydraulic Calculation Method for Axial Flow of non-Newtonian Fluids in Eccentric Annuli," *SPE Drilling & Completion*, vol. 24, no. 4, pp. 553-563, 2009.

[27] M. Haciislamoglu og J. Langlinais, «Non-Newtonian flow in eccentric annuli,» *J. Energy Resources Technology*, vol. 112, nr. 3, pp. 163-169, 1990.

[28] M. Haciislamoglu and U. Cartalos, "Practical pressure loss predictions in realistic annular geometries," in *SPE Annual Technical Conference*, New Orleans, Louisiana, USA, 1994.

[29] V. C. Kelessidis, P. Dalamarinis and R. Maglione, "Experimental Study and Predictions of Pressure Losses of Fluids Modeled as Herschel-Bulkley in Concentric and Eccentric Annuli in Laminar, Transitional and Turbulent Flows," *Journal of Petroleum Science and Engineering*, vol. 77, no. 3, pp. 305-312, 2011.

[30] R. Ahmed and S. Z. Miska, "Advanced Wellbore Hydraulics," in *Advanced Drilling and Well Technology*, USA, Society of Petroleum Engineer, 2009, pp. 191-219.

[31] C. D. Marken, X. He and A. Saasen, "The Influence of Drilling Conditions on Annular Pressure Losses," in *SPE Annual Technical Conference*, Washington D.C., USA, 1992.

[32] Exlog/Whittaker, "Swab and Surge," in *Theory and Applications of Drilling Fluid Hydraulics*, Boston, MA, USA, Springer Netherlands, 1985, pp. 111-118.

[33] J. Azar and R. Samuel, Drilling Engineering, Tulsa, Oklahoma, USA: Penwell, 2007.

[34] E. W. Flumerfelt, M. W. Pierick, S. L. Cooper and R. B. Bird, "Generalized Plane Couette Flow of a Non-Newtonian Fluid," *Ind. Eng. Chem. Fundamen.*, vol. 8, no. 2, pp. 354-357, 1969.

[35] Y. Q. Liu and K. Q. Zhu, "Axial Couette-Poiseuille Flow of Bingham Fluids through Concentric Annuli," *J. Non-Newton. Fluid*, vol. 165, pp. 1494-1504, 2010.

[36] K. Gjerstad, R. Time and K. S. Bjørkevoll, "Simplified Explicit Flow Equations for Bingham Plastics in Couette-Poiseuille Flow - For Dynamic Surge and Swab Modeling," *J. Non-Newtonian Fluid*, Vols. 175-176, pp. 55-63, 2012.

[37] E. Podryadinkin, R. Ahmed, V. Tarasevich and R. May, "Evaluation of Pressure Change While Steady-State Tripping," in *ASME 2014 33rd International Conference on Ocean, Offshore and Arctic Engineering*, June 8–13, San Francisco, California, USA, 2014.

[38] K. Gjerstad og R. W. Time, «Simplified Explicit Flow Equations for Herschel-Bulkley Fluids in Couette-Poiseuille Flow - For Real-Time Surge and Swab Modeling in Drilling,» *SPE Journal*, vol. 20, nr. 3, pp. 610-627, 2015.

[39] S. Q. Simoes, S. Z. Miska, N. E. Takach and M. Yu, "The Effect of Tool Joints on ECD While Drilling," in *Production and Operations Symposium*, Oklahoma City, Oklahoma, U.S.A., 2007.

[40] M. Enfis, M. Ahmed and A. Saasen, "The Hydraulic Effect of Tool-joint on Annular Pressure Loss," in *SPE Production and Operations Symposium*, Oklahoma City, Oklahoma, USA, 2011.

[41] M. R. Wells and R. C. Pessier, "The Effects of Bit Nozzle Geometry on the Performance of Drill Bits," in *AADE 2003 National Technology Conference "Practical Solutions for Drilling Challenges"*, Houston, Texas, USA, 2003.

[42] O. H. Houwen and T. Geehan, "Rheology of Oil-Based Muds," in *SPE Annual Technical Conference*, Oct 5-8, New Orleans, Lousiana, USA, 1986.

[43] T. S. Froitland, S. Brekke, R. Mihai, G. Nygaard, N. Saaddallah, L. I. Nesheim and F. Iversen, "AutoFluid Yard Trial Report," IRIS, Stavanger, Norway, 2011.

[44] American Petroleum Institute, API Recommended Practice: 13B-1: Field Testing Water-based Drilling Fluids, American Petroleum Institute, 2019.

[45] American Petroleum Institute, API Recommended Practice 13B-2: Recommended Practice for Field Testing Oil-Based, USA: American Petroleum Institute, 2014.

[46] K. S. Bjørkevoll, R. Rommetveit, B. Aas, H. Gjeraldstveit and A. Merlo, "Transient gel breaking model for critical wells applications with field data verification," in *SPE/IADC Drilling Conference*, Amsterdam, the Netherlands, 2003.

[47] H. A. Barnes, "Thixotropy – a review," *J. Non-Newtonian Fluid MeCh.*, vol. 70, p. 1 – 33, 1997.

[48] D. H. Cheng and F. Evans, "Phenomenological characterization of the rheological behaviour of inelastic reversible thixotropic and anti-thixotropic fluids," *Br. J. Appl. Phys*, vol. 16, no. 11, 1965.

[49] J. Mewis and N. J. Wagner, "Thixotropy," *Advances in Colloid and Interface Science*, Vols. 147-148, pp. 214-227, 2009.

[50] P. Coussot, Q. D. Nguyen, H. T. Huynh og D. Bonn, «Viscosity bifurcation in thixotropic, yielding fluids,» *J. Rheol.*, vol. 46, p. 573–589, 2002.

[51] B. Hertzhaft, A. Ragouillaux and P. Coussot, "How To Unify Low-Shear-Rate Rheology and Gel Properties of Drilling Muds: A Transient Rheological and Structural Model for Complex Wells Applications," in *SPE Drilling Conference*, Miami, Florida, USA, 2006.

[52] P. Møller, J. Mewis and D. Bonn, "Yield stress and thixotropy: on the difficulty of measuring yield stresses in practice," *Journal of Soft Matter*, vol. 2, pp. 274-283, 2006.

[53] H. J. Skadsem, A. Leulseged and E. Cayeux, "Measurement of Drilling Fluid Rheology and Modelling of Thixotropic Behavior," *Appl. Rheol.*, vol. 29, no. 1, pp. 1-11, 2019.

[54] K. Dullaert and J. Mewis, "A structural kinetics model for thixotropy," *J. Non-Newtonian Fluid Mech.,* vol. 139, pp. 21-30, 2006.

[55] K. S. Bjørkevoll and H. Gjeraldstveit, "Gel Breaking Model," IRIS, Stavanger, Norway, 2003.

[56] K. S. Bjørkevoll, J. E. Gravdal, H. Gjeraldstveit and R. Rommetveit, "Comparison of Field Data and Models," IRIS, Stavanger, Norway, 2003.

[57] S. T. Johansen, *Non-newtonian fluids flow and particles,* Trondheim: NTNU and SINTEF, 2015.

[58] E. Loth, "Drag of non-spherical solid particles of regular and irregular shape," *Powder Technology,* vol. 182, pp. 342-353, 2008.

[59] A. Richter and P. Nikrityuk, "Drag forces and heat transfer coefficients for spherical, cuboidal and ellipsoidal particles in cross flow at sub-critical Reynolds numbers," *International Journal of Heat and Mass Transfer,* vol. 55, pp. 1343-1354, 2012.

[60] S. F. Chien, "Settling Velocity of Irregularly Shaped Particles," *SPE Drilling & Completion,* vol. 9, no. 4, pp. 281-289, 1994.

[61] J. Gabitto and C. Tsouris, "Drag coefficient and settling velocity for particles of cylindrical shape," *Powder Technology,* vol. 183, no. 2, p. 314–322, 2008.

[62] G. H. Ganser, "A rational approach to drag prediction of spherical and nonspherical particles," *Powder Technol.,* vol. 77, no. 2, pp. 143-152, 1993.

[63] G. H. Haider and O. Levenspiel, "Drag coefficient and terminal velocity of spherical and nonspherical particles," *Powder Technol.,* vol. 58, no. 1, pp. 63-70, 1989.

[64] A. Höltzer and M. Sommerfeld, "New simple correlation formula for the drag coefficient of non-spherical particles," *Powder Technology,* vol. 184, no. 3, p. 361–365, 2008.

[65] P. K. Swamee and C. Ojha, "Drag Coefficient and Fall Velocity of nonspherical particles," *Journal of Hydraulic Engineering,* vol. 117, no. 5, pp. 660-667, 1991.

[66] S. Moi, E. W. Dvergsnes og E. Cayeux, «Study on the Ability of Transporting Mini-Cores while Drilling Exploration Wells – Phase II,» IRIS, Stavanger, 2014.

[67] F. A. Morrison, An Introduction to Fluid Mechanics, New York, USA: Cambridge University Press, 2013.

[68] A. Einstein, "Eine neue Bestimmung der Moleküldimensionen," *Ann. Phys.*, vol. 19, pp. 289-306, 1906.

[69] E. Hatschek, "Die Viskosität der Dispersoide," *Zeitschrift für Chemie und Industrie der Kolloide*, vol. 8, no. 1, pp. 34-39, 1911.

[70] B. J. Mitchell, "Test data fill theory gap on using foam as drilling fluid," *Oil and Gas J.*, pp. 96-100, 1971.

[71] S. H. Maron and P. H. Pierce, "Application of Ree-Eyring generalized flow theory to suspensions of spherical particles," *J. Colloid Sci.*, vol. 11, pp. 80-95, 1956.

[72] S. Mueller, E. W. Llewellin and H. M. Mader, "The rheology of suspensions of solid particles," *Proceedings of the Royal Society A.*, vol. 466, pp. 1201-1228, 2009.

[73] J. T. Ford, J. M. Peden, M. B. Oyeneyin, E. Gao and R. Xarrough, "Experimental Investigation of Drilled Cuttings Transport in Inclined Boreholes," in *SPE Annual Technical Conference*, New Orleans, Lousiana, USA, 1990.

[74] T. I. Larsen, "A Study of the Critical Fluid Velocity in Cuttings Transport for Inclined Wellbores," University of Tulsa, Tulsa, Oklahoma, USA, 1990.

[75] T. I. Larsen, A. A. Pilehvari and J. J. Azar, "Development of a New Cuttings-Transport Model for High-Angle Wellbores Including Horizontal Wells," *SPE Drilling & Completion*, vol. 12, no. 2, pp. 129 - 136, 1997.

[76] L. S. Jalukar, "A Study of Hole Size Effect on Critical and Subcritical Drilling Fluid Velocities in Cuttings Transport in Inclined Wellbores," University of Tulsa, Tulsa, Oklahoma, USA, 1993.

[77] A. A. Bassal, "The Effect of Drillpipe Rotation on Cuttings Transport in Inclined Wellbores," University of Tulsa, Tulsa, Oklahoma, USA, 1995.

[78] P. H. Tomren, A. W. Iyodo and J. J. Azar, "Experimental Study of Cuttings Transport in Directional Wells," *SPE Drilling Engineering Journal*, vol. 1, no. 1, pp. 43-56, 1986.

[79] G. Sælevik, R. Mihai, E. Cayeux and F. Iversen, "Hole Cleaning Guidelines Study Phase 1 Report," IRIS, Stavanger, Norway, 2016.

[80] A. Saasen, B. Dahl and K. Jødestøl, "Particle Size Distribution of Top-Hole Drill Cuttings from Norwegian Sea Area Offshore Wells," *Particulate Science and Technology,* vol. 31, no. 1, pp. 85-91, 2013.

[81] P. Rosin and E. Rammler, "The Laws Governing the Fineness of Powdered Coal," *Journal of the Institute of Fuel,* vol. 7, p. 29–36, 1933.

[82] W. Weibull, " A statistical distribution function of wide applicability," *J. Appl. Mech.-Trans. ASME,* vol. 18, no. 3, p. 293–297, 1951.

[83] M. Belarde and O. Vestavik, "Deployment of Reelwell Drilling Method in Shale Gas Field in Canada," in *SPE Offshore Europe Oil and Gas Conference*, Aberdeen, UK, 2011.

[84] R. T. Hukki, "Proposal for a Solomonic Settlement between the Theories of von Rittinger, Kick and Bond," *Trans. AIME,* vol. 220, pp. 403-408, 1961.

[85] J. C. van Shoor and R. F. Sandenbergh, "Evaluation of the batch press as a laboratory tool to simulate medium-pressure roller crushers," *J. S. Afr. Inst. Min. Metall.,* vol. 112, no. 3, 2012.

[86] J. Froyen and O. Savareid, "Model equations and solution techniques for multiphase flow in pipe networks," IRIS, Stavanger, Norway, 2000.

[87] R. Courant, K. Friedrichs and H. Lewy, "On the partial difference equations of mathematical physics," *IBM Journal of Research and Development,* vol. 11, no. 2, p. 215–234, 1967.

[88] D. R. Liles og W. H. Reed, «A Semi-Implicit Method for Two-Phase Fluid Dynamics,» *J. Computational Physics,* vol. 26, nr. 3, pp. 390-407, 1978.

[89] J. A. Trapp and R. A. Riemke, "A Nearly-Implicit Hydrodynamic Numerical Scheme for Two-Phase Flows," *J. Computational Physics,* vol. 66, no. 1, pp. 62-82, 1986.

[90] B. Walker, "Some Technical and Economic Aspects of Stabilizer Placement," *Journal of Petroleum Technology,* vol. 25, no. 6, p. 663 – 672, 1973.

[91] P. Toutain, "Analysing drill string behaviour. 1: An introduction to deviation control parameters," *World Oil*, vol. 192, no. 6, p. 181 – 190, 1981.

[92] P. Toutain, "Analysing drill string behaviour. 2: Results of two-dimensional study give recommendations for inclination control," *World Oil*, vol. 193, no. 1, p. 221 – 226, 1981.

[93] P. Toutain, "Analysing drill string behaviour. 3," *World Oil*, vol. 193, no. 4, p. 143 – 150, 1981.

[94] M. Birades and R. Fenoul, "A Microcomputer Program for Prediction of Bottomhole Assembly Trajectory," *SPE Drilling Engineering*, vol. 3, no. 2, pp. 167 - 172, 1988.

[95] M. Birades, "Static and Dynamic Three-Dimensional Bottomhole Assembly Computer Models," *SPE Drilling Engineering*, vol. 3, no. 2, pp. 160 - 166, 1988.

[96] M. Birades and D. Gazaniol, "ORPHEE 3D: Original Results on the Directional Behavior of BHAs with Bent Subs," in *Offshore Europe*, Aberdeen, United Kingdom, 1989.

[97] C. A. Johanscik, D. B. Friesen and R. Dawson, "Torque and Drag in Directional Wells-Prediction and Measurement," *Journal of Petroleum Technology*, vol. 36, no. 6, pp. 987 - 992, 1984.

[98] E. Cayeux, A. Leulseged, R. Kluge and J. Haga, "Use of a Transient Cuttings Transport Model in the Planning, Monitoringand Post Analysis of Complex Drilling Operations in the North Sea," in *SPE/IADC Drilling Conference*, Fort Worth, TX, USA, 2016.

[99] Å. Kyllingstad, "Torque and Drag Interpretation," Rogaland Research, Stavanger, Norway, 1993.

[100] B. Bhushan, Principles and applications of tribology, John Wiley & Sons, 1999.

[101] R. Stribeck, "Die wesentlichen Eigenschaften der Gleit- und Rollenlager," *Zeitschrift des Vereins Deutscher Ingenieure*, vol. 36, no. 46, pp. 1341 – 1348, 1432 – 1438, 1463 – 1470, 1902.

[102] A. Tustin, "The effects of backlash and speed-dependent friction on the stability of closed-cycle control systems," *J. Institution of Electrical Engineers*, vol. 94, p. 143 – 151, 1947.

[103] R. Samuel, Formulas and Calculations dor Drilling Operations, Wiley, 2010.

[104] A. Lubinski and W. S. Althouse, "Helical Buckling of Tubing Sealed in Packers," *Journal of Petroleum Technology,* vol. 14, no. 06, pp. 655 - 670, 1962.

[105] E. M. Navarro-López and D. Cortéz, " Avoiding harmful oscillations in a drillstring through dynamical analysis," *Journal of Sound and Vibration,* vol. 307, pp. 152-171, 2007.

[106] Z. Huang, D. Xie, B. Xie, W. Zhang, F. Zhang and L. He, "Investigation of PDC bit failure base on stick-slip vibration analysis of drilling string system plus drill bit," *Journal of Sound and Vibration,* vol. 417, pp. 97-109, 2018.

[107] R. C. Pessier and M. C. Fear, "Quantifying Common Drilling Problems with Mechanical Specific Energy and a Bit-Specific Coefficient of Sliding Friction," in *SPE annual technical conference*, Washington, D.C., USA, 1992.

[108] H. U. Caicedo and W. M. Calhoun, "Unique ROP Predictor using Bit-specific Coefficient of Sliding Friction and Mechanical Efficiency as a Function of Confined Compressive Strength Impacts Drilling," in *SPE Drilling Conference*, Amsterdam, The Netherlands, 2005.

[109] W. Calhoun and R. Ewy, "New Confined Compressive Strength Calculation Improves Bit Selection and Bit Performance," in *AADE 2005 National Technical Conference* , Houston, TX, USA, 2005.

[110] Å. Kyllingstad, "A Comparison of Stick-slip Mitigation Tools," in *SPE Drilling conference*, The Hague, The Netherlands, 2017.

[111] G. W. Halsey, Å. Kyllingstad and A. Kylling, "Torque Feedback Used to Cure Slip-Stick Motion," in *SPE Annual Technical Conference*, Houston, TX, USA, 1988.

[112] D. J. Runia, S. Dwars and I. O. Stulemeijer, "A brief history of the Shell "Soft Torque Rotary System" and some recent case studies," in *SPE/IADC Drilling Conference*, Amsterdam, The Netherlands, 2013.

[113] Å. Kyllingstad and P. J. Nessjøen, "A New Stick-Slip Prevention System," in *SPE/IADC Drilling Conference*, Amsterdam, The Netherlands, 2009.

[114] S. Dwars, "Recent Advances in Soft Torque Rotary Systems," in *SPE/IADC Drilling Conference*, London, England, UK, 2015.

[115] M. A. Céspedes, "Heave effects on Drill String during connections," University of Stavanger, Stavanger, Norway, 2012.

[116] F. E. Dupriest and W. L. Koederitz, "Maximizing Drill Rates with Real-Time Surveillance of Mechanical Specific Energy," in *SPE Drilling Conference*, Amsterdam, The Netherlands, 2005.

[117] R. Teale, "The Concept of Specific Energy in Rock Drilling," *International Journal of Rock Mechanics and Mining Sciences & Geomechanics Abstracts,* vol. 2, no. 1, p. 57–73, 1965.

[118] Å. Kyllingstad, «Dual Drawworks Provide Operational Redundancy and Reduce Cut and Slip Costs,» i *SPE/IADC Drilling Conference*, Amsterdam, Netherlands, 2003.

[119] O. Fivelstad, R. Verhoef, O. Jeremy and S. Davila, "Dual Active Heave Drilling Drawworks: From Concept to Operational Life," in *IADC/SPE Drilling Conference*, Fort Worth. TX, USA, 2014.

[120] F. Bakhtiari-Nejad and A. Hosseinzadeh, “Nonlinear dynamic stability analysis of the coupled axial-torsional motion of the rotary drilling considering the effect of axial rigid-body dynamics,” *International Journal of Non-Linear Mechanics,* vol. 88, pp. 85-96, 2017.

[121] S. K. Gupta and P. Wahi, "Global axial-torsional dynamics during rotary drilling," *Journal of Sound and Vibration,* vol. 375, pp. 332-352, 2016.

[122] U. J. Aarsnes and N. van de Wouw, "Dynamics of a distributed drill string system: Characteristic parameters and stability maps," *Journal of Sound and Vibration,* vol. 417, pp. 376-412, 2017.

[123] P. Pastusek, M. Owens, D. Barrette, V. Wilkins, A. Bolzan, J. Ryan, K. Akyabi, M. Reichle and D. Pais, "Drill Rig Control Systems: Debugging, Tuning, and Long Term Needs," in *SPE Annual Technical Conference*, Dubai, UAE, 2016.

[124] J. L. Bergerot, "Advanced Drilling in HP/HT: Total's Experience on Elgin/Franklin (UK North Sea)," *Journal of Petroleum Technology*, vol. 63, no. 10, pp. 116-120, 2011.

[125] A. Stefánsson, R. Duerholt, J. Schroder, J. Macpherson, C. Hohl, T. Kruspe and T. J. Eriksen, "A 300 Degree Celsius Directional Drilling System," in *IADC/SPE Drilling Conference*, Fort Worth, Texas, USA, 2018.

[126] D. Wagner, F. J. Cavalieri, C. Bathias and N. Ranc, "Ultrasonic fatigue tests at high temperature on an austenitic steel," *Propulsion and Power Research,* vol. 1, no. 1, pp. 29-35, 2012.

[127] M. Ferreira, T. E. Hafemann, J. R. Barbosa, A. K. da Silva and R. Hasan, "A Numerical Study on the Thermal Behavior of Wellbores," *SPE Production & Operations,* vol. 32, no. 04, pp. 564 - 574, 2017.

[128] D. W. Marshall and R. G. Bentsen, "A Computer Model to Determine the Temperature Distribution in a Wellbore," *Journal of Canadian Petroleum Technology,* vol. 21, no. 1, pp. 63-75, 1982.

[129] B. Corre, R. Eymard and A. Guenot, "Numerical Computation of Temperature Distribution in a Wellbore While Drilling," in *SPE Annual Technical Conference*, Houston, Texas, USA, 1984.

[130] A. Kumar and R. Samuel, "Analytical Model To Predict the Effect of Pipe Friction on Downhole Fluid Temperatures," *SPE Drilling & Completion,* vol. 28, no. 03, pp. 270 - 277, 2013.

[131] C. J. Wolff and J. P. de Wardt, "Borehole Position Uncertainty- Analysis of Measuring Methods and Derivation of Systematic Error Model," *Journal of Petroleum Technology,* vol. 33, no. 12, pp. 2338-2350, 1981.

[132] H. Williamson, "Accuracy Prediction for Directional Measurement While Drilling," *SPE Drilling & Completion,* vol. 15, no. 4, pp. 221-233, 2000.

[133] T. Torkildsen, S. Håvardstein, J. Weston and R. Ekseth, "Prediction of Wellbore Position Accuracy When Surveyed With Gyroscopic Tools," *SPE Drilling & Completion,* vol. 23, no. 1, pp. 5-12, 2008.

[134] T. M. Croucher, "Integrated Team Approach to the Design, Construction, Start Up, and Operation of the World's Most Modern Drilling Rig," *SPE Drilling & Completion,* vol. 14, no. 03, pp. 201 - 207, 1999.

[135] O. E. T. Staff, "Aker Solutions to Open Hi-Tech Drilling Equipment Simulator in Houston, USA," *Offshore Energy Today*, 28 12 2011.

[136] R. K. Hodgson and P. Hassard, “Reducing the Learning Curve Through Use of an Advanced Drilling Simulator,” in *IADC/SPE Drilling Conference*, Miami, Florida, USA, 2006.

[137] H. Blikra, G. Pia, J. S. Wessel, M. Svendsen, R. Rommetveit and S. I. Ødegård, "The Operational Benefit of Testing HPHT/MPD Procedures Using an Advanced Full Scale Drilling Simulator," in *IADC/SPE Drilling Conference*, Fort Worth, Texas, USA, 2014.

[138] J. Petersen, R. Rommetveit, K. Bjørkevoll and J. Frøyen, "A General Dynamic Model for Single and Multi-phase Flow Operations during Drilling, Completion, Well Control and Intervention," in *IADC/SPE Asia Pacific Drilling Technology Conference*, Jakarta, Indonesia, 2008.

[139] L. Scott, J. S. Wessel, J. Nabavi and R. Rommetveit, "Use of a Life Cycle Drilling Simulation System on a Challenging HPHT Drilling Operation in the Norwegian Sea," in *SPE/IADC Middle East Drilling Technology Conference*, Abu Dhabi, UAE, 2016.

[140] S. A. Mirhaj, V. A. Oteri and G. Sælevik, "Tight Hole Spotting in 3D Virtual Drilling Simulator," in *SPE Offshore Europe Oil and Gas Conference*, Aberdeen, UK, 2013.

[141] W. Aldred, R. Hutin, J. C. Luppens and G. Ritchie, "Development and Testing of a Rig-Based Quick Event Detection System to Mitigate Drilling Risks," in *IADC/SPE Drilling Conference*, Orlando, Florida, USA, 2008.

[142] J. Brakel, B. Tarr, W. Cox, F. Jorgensen and H. Straume, "SMART Kick Detection: First Step on the Well-Control Automation Journey," *SPE Drilling & Completion*, vol. 30, no. 03, pp. 233 - 242, 2015.

[143] B. Tarr, D. W. Ladendorf, D. Sanchez and G. M. Milner, "Next-Generation Kick Detection During Connections: Influx Detection at Pumps Stop (IDAPS) Software," *SPE Drilling & Completion*, vol. 31, no. 04, pp. 250 - 260, 2016.

[144] J. M. Godhavn and E. Hauge, *Data-driven methods in drilling automation*, Trondheim, Norway: SINTEF Petroleum Conference, 2018.

[145] D. P. Arakkal and M. N. Belavadi, " Early Detection of Drillstring Washouts Based on Downhole Turbine RPM Monitoring Prevents Twist-offs in Challenging Drilling

Environment in India," in *IADC/SPE Asia Pacific Drilling Technology Conference*, Jakarta, Indonesia, 2008.

[146] H. F. Spoeker and C. H. Litzlbauer, "High-Frequency Mud Pump Pressure Monitoring Enables Timely Wear Detection," in *IADC/SPE Asia Pacific Drilling Technology*, Jakarta, Indonesia, 2002.

[147] Å. Kyllingstad and P. J. Nessjøen, "Condition Based Maintenance: A New Early Leak Detection System for Mud Pumps," in *SPE/IADC Drilling Conference*, Amsterdam, The Netherlands, 2011.

[148] A. Ambrus, P. Ashok, D. Ramos, A. Chintapalli, A. Susich, T. Theford, B. Nelson, M. Shahri, J. McNab and M. Behounek, "Self-Learning Probabilistic Detection and Alerting of Drillstring Washout and Pump Failure Incidents During Drilling Operations," in *IADC/SPE Drilling Conference*, Fort Worth, Texas, USA, 2018.

[149] C. Mason, J. K. Igland, E. Streeter and P. A. Andresen, "New Real-Time Casing Running Advisory System Reduces NPT," in *SPE Offshore Europe Oil and Gas Conference*, Aberdeen, UK, 2013.

[150] J. F. Brett, A. D. Beckett, C. A. Holt and D. L. Smith, "Uses and Limitations of Drillstring Tension and Torque Models for Monitoring Hole Conditions," *SPE Drilling Engineering*, vol. 4, no. 03, pp. 223 - 229, 1989.

[151] E. Cayeux and B. Daireaux, "Early Detection of Drilling Conditions Deterioration Using Real-Time Calibration of Computer Models: Field Example from North Sea Drilling Operations," in *SPE/IADC Drilling Conference*, Amsterdam, The Netherlands, 2009.

[152] T. O. Gulsrud, R. Nybø and K. S. Bjørkevoll, "Statistical Method for Detection of Poor Hole Cleaning and Stuck Pipe," in *Offshore Europe*, Aberdeen, UK, 2009.

[153] R. Wong, Q. Liu, M. Ringer, J. Dunlop, C. Luppens, H. Yu and C. D. Chapman, "Advances in Real-Time Event Detection While Drilling," in *SPE/IADC Drilling Conference*, Amsterdam, The Netherlands, 2013.

[154] P. Skalle, A. Aamodt and O. E. Gundersen, "Detection of Symptoms for Revealing Causes Leading to Drilling Failures," *SPE Drilling & Completion*, vol. 28, no. 02, pp. 182 - 193, 2013.

[155] D. Le, "Case-Based Reasoning Technology Used To Provide Early Indications of Potential NPT-Related Problems While Drilling the Viking," in *SPE Canadian Unconventional Resources Conference*, Calgary, Alberta, Canada, 2012.

[156] J. Macpherson, J. de Wardt, M. Laing og N. Zenero, «Data Ownership for Drilling Automation – Managing the Impact,» i *IADC/SPE Drilling Conference*, Fort Worth, Texas, USA, 2016.

[157] R. Rommetveit, K. S. Bjørkevoll, P. Cerasi, S. T. Håvardstein, M. Fjeldheim, H. M. Helset, S. I. Ødegaard and C. Nordstrand, "Real Time Integration of ECD, Temperature, Well Stability and Geo/Pore Pressure Simulations during drilling a challenging HPHT well," in *SPE Intelligent Energy Conference*, Utrecht, The Netherlands, 2010.

[158] R. Rommetveit, S. I. Ødegaard, C. Nordstrand, K. S. Bjørkevoll, P. Cesari, H. M. Helset, M. Fjeldheim and S. T. Håvardstein, "Drilling a Challenging HP/HT Well Utilizing an Advanced ECD Management System With Decision Support and Real-Time Simulations," in *IADC/SPE Drilling Conference*, New Orleans, Louisiana, USA, 2010.

[159] R. Rommetveit, S. I. Ødegaard, C. Nordstrand, K. S. Bjørkevoll og M. Fjeldheim, «Documentation Of Risk And Cost-Reducing Potential By Utilizing An Automatic Supervision And Decision Support System During Drilling A Challenging HPHT Well,» i *SPE/IADC Drilling Conference*, Amsterdam, The Netherlands, 2011.

[160] R. Rommetveit, K. S. Bjørkevoll, G. W. Halsey, E. Fjær, S. I. Ødegaard, M. Herbert, O. Sandve and B. Larsen, "e-Drilling: A System for Real-Time Drilling Simulation, 3D Visualization and Control," in *Digital Energy Conference*, Houston, Texas, U.S.A., 2007.

[161] A. P. Pink, H. Kverneland, A. Bruce and J. B. Applewhite, "Building an Automated Drilling System Where the Surface Machines are Controlled by Downhole and Surface Data to Optimize the Well Construction Process," in *IADC/SPE Drilling Conference*, San Diego, California, USA, 2012.

[162] J. A. Anderson and T. J. Head, Automata theory with modern applications, New York, USA: Cambridge University Press, 2006.

[163] F. P. Iversen, J. L. Thorogood, J. D. Macpherson and R. A. Macmillan, "Business Models and KPIs as Drivers for Drilling Automation," in *SPE Intelligent Energy International Conference*, Aberdeen, Scotland, UK, 2016.

[164] E. Cayeux, T. Mesagan, S. Tanripada, M. Zidan and K. K. Fjelde, "Real-Time Evaluation of Hole Cleaning Conditions Using a Transient Cuttings Transport Model," in *SPE/IADC Drilling Conference*, Amsterdam, The Netherlands, 2013.

[165] Schlumberger, "M-I Wate Barite 4.1sg Technical Bulletin," [Online]. Available: https://www.slb.com/-/media/Files/miswaco/ps-drilling-fluids/m-i_wate_barite.PDF. [Accessed 19 08 2018].

[166] D. B. McDonald, W. J. Grantham, W. L. Tabor and M. J. Murphy, "Global and local optimization using radial basis function response surface models," *Applied Mathematical Modelling*, vol. 31, pp. 2095-2110, 2006.

[167] S. Rubinow and J. Keller, "The transverse force on a spinning sphere moving in a viscous fluid," *Journal of Fluid Mechanics*, vol. 11, p. 447–459, 1961.

[168] P. Cherukat, J. McLaughlin and D. Dandy, "A computational study of the inertial lift on a sphere in a linear shear flow field," *International Journal of Multiphase Flow*, vol. 25, p. 15–33, 1999.

[169] M. Zastawny, G. Mallouppas, F. Zhao and B. van Wachem, "Derivation of drag and lift force and torque coefficients for non-spherical particles in flows," *Int J Multiphase Flow*, vol. 101, p. 288–95, 2012.

[170] R. Ouchene, M. Khalij, A. Tanière and B. Arcen, "Drag, lift and torque coefficients for ellipsoidal particles: From low to moderate particle Reynolds numbers," *Computers & Fluids*, vol. 113, pp. 53-64, 2015.

[171] R. Ouchene, M. Khalij, B. Arcen and A. Tanière, "A new set of correlations of drag, lift and torque coefficients for non-spherical particles and large Reynolds numbers," *Powder Technology*, vol. 303, pp. 33-43, 2016.

[172] C. T. Jayasundara, R. Y. Yang, A. B. Yu and J. Rubenstein, "Effects of disc rotation speed and media loading on particle flow and grinding performance in a horizontal stirred mill," *International Journal of Mineral Processing*, vol. 96, pp. 27-35, 2010.

[173] E. Cayeux, A. Ambrus, L. Øy, A. Helleland, S. T. Brundtland and H. Nevøy, "Analysis of Torsional Stick-Slip Situations Observed with Downhole High-Frequency," in *SPE Drilling Conference*, Galveston, Texas, USA, 2020.

[174] ASME Shale Shaker Committee, Drilling Fluid Processing Handbook, Elsevier ISBN 978-0-7506-7775-2, 2005.

[175] A. Kroken, E. Souza, A. L. Martins, J. Vasshus, C. M. D. Panisset, and B. Lomba, "Evaluating an Alternate Cutting Separation Technology: Is the MudCube a Fit for Brazilian Offshore Drilling?," in *Offshore Technology Conference*, Rio de Janeiro, Brazil, 2013.

[176] A. Saasen and H. Hodne, "The influence of vibrations on drilling fluid rheological properties and the consequence for solids control," *Applied Rheology*, vol. 26, no. 2, p. 6, 2016.

[177] J. L. Thorogood, M. Critchon and A. Bahamondes, "Case Study of Weak Signals and Confirmation Bias in Drilling Operations," *SPE Drilling & Completion*, vol. 29, no. 3, pp. 304-310, 2014.

[178] J. Kennedy and R. Eberhart, "Particle Swarm Optimization," in *IEEE International Conference on Neural Networks*, Perth, Australia, 1995.

[179] E. Cayeux, "Safe Mud Pump Management while Conditioning Mud," in *IFAC Workshop on Automatic Control in Offshore Oil and Gas Production*, Trondheim, Norway, 2012.

[180] F. Iversen, L. J. Gressgaard, J. L. Thorogood, M. K. Balov and V. Hepsoe, "Drilling Automation: Potential for Human Error," in *IADC/SPE Drilling Conference*, San Diego, California, USA, 2012.

[181] R. van den Brandt and C. C. de Visser, "Safe Flight Envelope Uncertainty Quantification using Probabilistic Reachability Analysis," *IFAC*, vol. 51, no. 24, pp. 628-635, 2018.

[182] J. Y. Park and N. Kim, "Design of a safety operational envelope protection system for a submarine," *Ocean Engineering*, vol. 148, pp. 602-611, 2018.

[183] R. Prime, M. McIntyre and D. Reeves, "Implementation of an Improved Operating Safe Envelope," in *International Youth Nuclear Congress*, Interlaken, Switzerland, 2008.

[184] E. Cayeux and B. Daireaux, "Insights Into the Physical Phenomena That Influence Automatic Gain/Loss Detection During Drilling Operations," *SPE Drilling & Completion*, vol. 32, no. 1, pp. 13 - 24, 2016.

[185] E. Cayeux, "On the Importance of Boundary Conditions for Real-time Transient Drill-String Mechanical Estimations," in *SPE/IADC Drilling Conference*, Fort Worth, TX, USA, 2018.

[186] E. Cayeux and A. Leulseged, "Impact of Drilling Fluid Thixotropy on the Calculations of Pressure Losses in Pipes and Annuli," in *37th International Conference on Ocean, Offshore & Arctic Engineering*, Madrid, Spain, 2018.

[187] E. Cayeux, B. Daireaux, E. W. Dvergsnes, H. Siahaan and J. E. Gravdal, "Principles and Sensitivity Analysis of Automatic Calibration of MPD Methods Based on Dual-Gradient Drilling Solutions," in *SPE Deepwater Drilling and Completions Conference*, Galveston, Texas, USA, 2014.

[188] E. Cayeux, H. J. Skadsem, B. Daireaux and R. Holand, "Challenges and Solutions to the Correct Interpretation of Drilling Friction Tests," in *SPE Drililng Conference*, The Hagues, The Netherlands, 2017.

[189] E. Cayeux, H. J. Skadsem and R. Kluge, "Accuracy and Correction of Hook Load Measurements During Drilling Operations," in *SPE/IADC Drilling Conference*, London, England, UK, 2015.

[190] E. Cayeux and A. Leulseged, "Effect of Solid Particle Concentration on Drilling Fluid Rehological Behavior and its Impact on Pressure Losses," in *SPE Drilling Conference*, The Hague, The Netherlands, 2019.

[191] E. Cayeux, "Time, Pressure And Temperature Dependent Rheological Properties Of Drilling Fluids And Their Automatic Measurements," in *SPE Drilling Conference*, Galveston, Texas, USA, 2020.

[192] E. Cayeux, "Reconstruction of Pipe Displacement Based on High-Frequency Triaxial Accelerometer Measurements," in *SPE Drilling Conference*, Fort Worth, TX, USA, 2018.

[193] E. Cayeux, P. Seim, L. Solvi, H. Ulvik and E. Solbu, "Reconstruction of Pipe Movement from Downhole High Frequency Measurements," in *SPE Norway One Day Seminar*, Bergen, Norway, 2019.

[194] E. Cayeux, B. Daireaux, N. Saadallah and S. Alyaev, "Toward Seamless Interoperability Between Drilling Real-time Management and Control Applications," in *SPE Drilling Conference*, The Hague, The Netherlands, 2019.

[195] E. Cayeux, "Measurement Of The Flowrate Out Of A Well For Conventional Drilling Operations," in *SPE Drilling Conference*, Galveston, TX, USA, 2020.

[196] E. Cayeux, "Method and device for determining a drill bit's position in a borehole". US Patent US9605532B2, 28 March 2017.

[197] E. Cayeux and B. Daireaux, "Precise Gain and Loss Detection Using a Transient Hydraulic Model of the Return Flow to the Pit," in *SPE/IADC Middle East Drilling Technology Conference*, 7-9 October, Dubai, UAE, 2013.

[198] E. Cayeux, "Modelling of the Movement of a Prolate particle in the Steady State Flow of a non-Newtonian Fluid in an Inclined Annulus with Inner String Rotation," in *ASME Conference on Ocean, Offshore and Arctic Engineering*, Glasgow, Scotland, 2019.

[199] E. Cayeux, B. Daireaux, M. K. Balov, S. Haavardstein, L. M. Stokland and A. Saasen, "Automatic Performance Analysis and Estimation of Risk Level Embedded in Drilling Operational Plans," in *SPE Intelligent Energy International Conference*, Aberdeen, Scotland, UK, 2016.

[200] P. Pastusek, G. Payette, R. Shor, E. Cayeux, U. Aarsnes, J. Hedengren, J. Macpherson and R. Harmer, "Creating Open Source Models, Test Cases, and Data for Oilefiled Drilling Challenges," in *SPE Drilling Conference*, The Hague, The Netherlands, 2019.

A Absolute Volume Fraction of a Component in a Fluid Mix

The demonstration of eq. (98) is done by recurrence reasoning.

When the last component is added to the fluid mix, we have, according to eq. (97):

$$\rho_{f_N} = f'_{c_N}\rho_{c_N} + (1 - f'_{c_N})\rho_{f_{N-1}} \tag{232}$$

and since the N-component was not part of the formulation of the mix at the $N-1$ iteration, the term $\rho_{f_{N-1}}$ is independent of any information about the N-component, therefore we can conclude that the absolute volume fraction of the N-component is the same as its relative volume fraction: $f_{c_N} = f'_{c_N}$.

Let us suppose that the recurrence is true until iteration $n-1$, i.e. $\rho_{f_{n-1}} = \sum_{i=1}^{n-1} f_{c_i}\rho_{c_i} = f'_{c_{n-1}}\rho_{c_{n-1}} + \sum_{i=1}^{n-2} \rho_{c_i} f'_{c_i} \prod_{j=i+1}^{n-1} \left(1 - f'_{c_j}\right)$ then when mixing the n-component, we can write:

$$\rho_{f_n} = f'_{c_n}\rho_{c_n} + \left(1 - f'_{c_n}\right)\rho_{f_{n-1}} \tag{233}$$

$$= f'_{c_n}\rho_{c_n} + \left(1 - f'_{c_n}\right)\left(f'_{c_{n-1}}\rho_{c_{n-1}} + \sum_{i=1}^{n-2} \rho_{c_i} f'_{c_i} \prod_{j=i+1}^{n-1} \left(1 - f'_{c_j}\right)\right)$$

$$= f'_{c_n}\rho_{c_n} + f'_{c_{n-1}}\left(1 - f'_{c_n}\right)\rho_{c_{n-1}} + \sum_{i=1}^{n-2} \rho_{c_i} f'_{c_i} \prod_{j=i+1}^{n} \left(1 - f'_{c_j}\right)$$

$$= f'_{c_n}\rho_{c_n} + \rho_{c_{n-1}} f'_{c_{n-1}} \prod_{j=n}^{n} \left(1 - f'_{c_j}\right) + \sum_{i=1}^{n-2} \rho_{c_i} f'_{c_i} \prod_{j=i+1}^{n} \left(1 - f'_{c_j}\right)$$

$$= f'_{c\,n}\rho_{c_n} + \sum_{i=1}^{n-1} \rho_{c\,i} f'_{c\,i} \prod_{j=i+1}^{n} \left(1 - f'_{c\,j}\right)$$

$$\Rightarrow \forall i \in [1, n-1], f_{c_i} = f'_{c\,i} \prod_{j=i+1}^{n} \left(1 - f'_{c\,j}\right)$$

Therefore, we find that the recurrence is also true at iteration n.

B Effect of Sand Particles Concentration and Size on the Rheological Behavior of an Unweighted WBM

The following tables collect measurements made with a Physica MCR 301 scientific rheometer manufactured by Anton Paar™.

For each sample, two mass density measurements have been made ($\rho\#1$ and $\rho\#2$) and the reported density (ρ) is the average of those two values. All measurements are taken at 20°C. The particle concentration (Φ) is calculated using the average mass density (ρ) of these two measurements. Φ^* is the dimensionless particle concentration compared to the maximum particle concentration (Φ_m) that can be achieved with the average aspect ratio (r_p) of the particles.

The Herschel-Bulkley parameters (τ_γ, K, n) have been calculated utilizing the method described in Mullineux (2008) [19]. Dimensionless Herschel-Bulkley parameters denoted τ_γ^*, K^*, n^* are calculated by dividing the Herschel-Bulkley parameters by their counter-part values from the base fluid, i.e. without solids.

Table 2 and Table 3 provide the measurements obtained with an unweighted KCl/polymer-based fluid and sand particles between 0 and 45 µm for volumetric concentrations between 0 and 23%.

Table 4 and Table 5 provide the measurements obtained with an unweighted KCl/polymer-based fluid and sand particles between 45 and 63 µm for volumetric concentrations between 0 and 23%.

Table 6 and Table 7 provide the measurements obtained with an unweighted KCl/polymer-based fluid and sand particles between 63 and 90 µm for volumetric concentrations between 0 and 23%.

Table 8 and Table 9 provide the measurements obtained with an unweighted KCl/polymer-based fluid and sand particles between 90 and 125µm for volumetric concentrations between 0 and 23%.

Table 10 and Table 11 provide the measurements obtained with an unweighted KCl/polymer-based fluid and sand particles between 125 and 150µm for volumetric concentrations between 0 and 23%.

Table 2: Measurements obtained with an unweighted KCl/polymer-based fluid and sand particles between 0 and 45µm for volumetric concentrations between 0 and 11%.

	Base	Mix#1	Mix#2	Mix#3	Mix#4	Mix#5	Mix#6
ρ (kg/m^3)	1083	1098	1128	1158	1191	1220	1249
Φ	0.000	0.010	0.029	0.048	0.069	0.087	0.106
Φ*	0.000	0.014	0.043	0.070	0.101	0.128	0.155
$\dot{\gamma}$ (s^{-1})	τ (Pa)						
100.00	7.99	8.16	8.55	8.98	9.53	10.20	11.00
79.40	7.46	7.62	7.97	8.35	8.85	9.45	10.20
63.10	6.99	7.14	7.45	7.80	8.26	8.80	9.49
50.10	6.58	6.71	7.00	7.31	7.73	8.23	8.86
39.80	6.21	6.33	6.59	6.87	7.26	7.72	8.30
31.60	5.87	5.98	6.22	6.48	6.84	7.27	7.80
25.10	5.57	5.67	5.89	6.13	6.46	6.86	7.36
20.00	5.30	5.39	5.60	5.81	6.12	6.49	6.96
15.80	5.05	5.14	5.32	5.52	5.80	6.15	6.59
12.60	4.82	4.90	5.08	5.26	5.52	5.85	6.26
10.00	4.61	4.69	4.85	5.02	5.26	5.57	5.96
7.94	4.42	4.49	4.64	4.79	5.03	5.31	5.69
6.31	4.24	4.31	4.44	4.59	4.81	5.08	5.44
5.01	4.08	4.14	4.27	4.40	4.60	4.86	5.20
3.98	3.92	3.98	4.10	4.22	4.42	4.67	4.99
3.16	3.78	3.83	3.94	4.06	4.24	4.48	4.79
2.51	3.64	3.69	3.79	3.90	4.08	4.30	4.60
2.00	3.51	3.55	3.65	3.76	3.92	4.14	4.43
1.58	3.38	3.42	3.52	3.62	3.78	3.99	4.27
1.26	3.26	3.30	3.39	3.48	3.64	3.84	4.11
1.00	3.15	3.18	3.27	3.36	3.50	3.70	3.96
τ_γ (Pa)	2.213	2.220	2.286	2.362	2.466	2.637	2.859
K (Pa.s^n)	0.992	1.020	1.042	1.058	1.101	1.130	1.174
n	0.380	0.380	0.387	0.396	0.402	0.411	0.419
τ_γ^*	1.000	1.003	1.033	1.067	1.114	1.192	1.292
K*	1.000	1.029	1.050	1.066	1.110	1.139	1.183
n*	1.000	1.000	1.018	1.041	1.056	1.079	1.101

Table 3: Measurements obtained with an unweighted KCl/polymer-based fluid and sand particles between 0 and 45µm and for volumetric concentrations between 13 and 23%.

	Mix#7	Mix#8	Mix#9	Mix#10	Mix#11	Mix#12
ρ (kg/m^3)	1282	1312	1346	1377	1408	1442
Φ	0.127	0.146	0.168	0.188	0.208	0.229
Φ*	0.186	0.214	0.246	0.275	0.304	0.335
$\dot{\gamma}$ (s^{-1})	τ (Pa)					
100.00	11.90	13.20	14.70	16.50	18.80	21.50
79.40	11.00	12.20	13.50	15.20	17.30	19.80
63.10	10.30	11.30	12.60	14.10	16.00	18.30
50.10	9.58	10.60	11.70	13.10	14.80	16.90
39.80	8.97	9.88	10.90	12.20	13.80	15.80
31.60	8.43	9.27	10.20	11.40	12.90	14.70
25.10	7.95	8.73	9.62	10.80	12.10	13.90
20.00	7.51	8.24	9.07	10.10	11.40	13.10
15.80	7.11	7.80	8.58	9.59	10.80	12.40
12.60	6.75	7.40	8.14	9.10	10.30	11.80
10.00	6.43	7.05	7.75	8.66	9.80	11.20
7.94	6.13	6.72	7.39	8.27	9.37	10.70
6.31	5.86	6.43	7.07	7.91	8.97	10.30
5.01	5.61	6.15	6.77	7.59	8.62	9.93
3.98	5.38	5.91	6.51	7.30	8.31	9.59
3.16	5.17	5.68	6.26	7.03	8.02	9.29
2.51	4.97	5.46	6.03	6.78	7.76	9.01
2.00	4.79	5.27	5.82	6.56	7.52	8.76
1.58	4.62	5.08	5.62	6.34	7.31	8.52
1.26	4.45	4.90	5.43	6.14	7.09	8.29
1.00	4.29	4.73	5.25	5.95	6.89	8.07
τ_γ (Pa)	3.127	3.557	4.089	4.759	5.783	6.924
K (Pa.s^n)	1.235	1.255	1.253	1.285	1.217	1.257
n	0.424	0.441	0.462	0.479	0.513	0.531
τ_γ^*	1.413	1.607	1.848	2.151	2.613	3.129
K*	1.245	1.266	1.263	1.296	1.227	1.268
n*	1.114	1.159	1.214	1.259	1.349	1.397

Table 4: Measurements obtained with an unweighted KCl/polymer-based fluid and sand particles between 45 and 63µm for volumetric concentrations between 0 and 11%.

	Base	Mix#1	Mix#2	Mix#3	Mix#4	Mix#5	Mix#6
ρ (kg/m^3)	1084	1097	1126	1156	1186	1218	1247
Φ	0.000	0.009	0.027	0.046	0.065	0.086	0.104
Φ*	0.000	0.014	0.044	0.075	0.106	0.138	0.168
$\dot{\gamma}$ (s^{-1})	τ (Pa)						
100.00	8.08	8.17	8.39	8.85	9.35	9.84	10.50
79.40	7.54	7.62	7.82	8.23	8.69	9.12	9.73
63.10	7.07	7.14	7.32	7.68	8.10	8.48	9.04
50.10	6.64	6.70	6.87	7.20	7.57	7.93	8.44
39.80	6.27	6.32	6.47	6.77	7.11	7.44	7.91
31.60	5.93	5.97	6.11	6.39	6.70	7.00	7.43
25.10	5.62	5.66	5.78	6.05	6.34	6.60	7.00
20.00	5.34	5.38	5.49	5.73	6.00	6.24	6.61
15.80	5.09	5.12	5.22	5.45	5.70	5.92	6.26
12.60	4.86	4.88	4.98	5.19	5.42	5.62	5.94
10.00	4.65	4.67	4.75	4.95	5.16	5.35	5.64
7.94	4.45	4.47	4.55	4.73	4.93	5.11	5.37
6.31	4.27	4.28	4.35	4.53	4.71	4.88	5.12
5.01	4.10	4.11	4.18	4.34	4.51	4.66	4.90
3.98	3.94	3.95	4.01	4.16	4.33	4.47	4.68
3.16	3.79	3.80	3.86	4.00	4.15	4.28	4.49
2.51	3.65	3.66	3.71	3.84	3.99	4.11	4.30
2.00	3.52	3.53	3.57	3.70	3.83	3.95	4.13
1.58	3.39	3.40	3.44	3.56	3.69	3.79	3.96
1.26	3.27	3.27	3.31	3.43	3.55	3.65	3.81
1.00	3.15	3.15	3.19	3.30	3.41	3.51	3.66
τ_γ (Pa)	2.188	2.194	2.205	2.295	2.373	2.442	2.509
K (Pa.s^n)	1.021	1.018	1.044	1.069	1.107	1.137	1.220
n	0.378	0.382	0.384	0.392	0.398	0.404	0.406
τ_γ^*	1.000	1.003	1.008	1.049	1.085	1.116	1.147
K*	1.000	0.997	1.023	1.047	1.084	1.113	1.195
n*	1.000	1.010	1.015	1.035	1.050	1.069	1.073

Table 5: Measurements obtained with an unweighted KCl/polymer-based fluid and sand particles between 45 and 63µm and for volumetric concentrations between 13 and 23%.

	Mix#7	Mix#8	Mix#9	Mix#10	Mix#11	Mix#12
ρ (kg/m^3)	1277	1308	1341	1375	1409	1443
Φ	0.123	0.143	0.164	0.186	0.208	0.230
Φ*	0.199	0.231	0.265	0.301	0.336	0.371
$\dot{\gamma}$ (s^{-1})	τ (Pa)					
100.00	11.20	12.10	13.10	14.30	15.90	17.90
79.40	10.30	11.20	12.10	13.10	14.60	16.30
63.10	9.58	10.40	11.20	12.10	13.40	15.00
50.10	8.93	9.64	10.40	11.20	12.40	13.80
39.80	8.35	9.00	9.68	10.40	11.50	12.70
31.60	7.83	8.42	9.04	9.70	10.60	11.80
25.10	7.36	7.90	8.47	9.07	9.92	11.00
20.00	6.94	7.43	7.95	8.50	9.27	10.20
15.80	6.55	7.01	7.48	7.98	8.68	9.54
12.60	6.20	6.62	7.06	7.51	8.16	8.95
10.00	5.89	6.27	6.68	7.09	7.68	8.40
7.94	5.60	5.96	6.33	6.71	7.25	7.91
6.31	5.33	5.66	6.01	6.35	6.85	7.46
5.01	5.08	5.39	5.72	6.03	6.49	7.05
3.98	4.86	5.15	5.45	5.74	6.16	6.68
3.16	4.64	4.91	5.19	5.46	5.85	6.33
2.51	4.44	4.70	4.96	5.20	5.57	6.01
2.00	4.26	4.50	4.74	4.97	5.30	5.71
1.58	4.08	4.30	4.53	4.74	5.06	5.43
1.26	3.91	4.12	4.34	4.53	4.82	5.17
1.00	3.75	3.95	4.15	4.33	4.60	4.92
τ_γ (Pa)	2.543	2.648	2.756	2.888	3.060	3.241
K (Pa.s^n)	1.287	1.381	1.479	1.520	1.647	1.803
n	0.411	0.416	0.421	0.433	0.445	0.453
τ_γ^*	1.162	1.210	1.260	1.320	1.399	1.481
K*	1.260	1.352	1.448	1.489	1.613	1.766
n*	1.087	1.100	1.112	1.144	1.175	1.197

Table 6: Measurements obtained with an unweighted KCl/polymer-based fluid and sand particles between 63 and 90µm for volumetric concentrations between 0 and 11%.

	Base	Mix#1	Mix#2	Mix#3	Mix#4	Mix#5	Mix#6
ρ (kg/m^3)	1081	1098	1127	1156	1186	1217	1247
Φ	0.000	0.011	0.029	0.048	0.067	0.087	0.106
Φ*	0.000	0.018	0.047	0.078	0.108	0.140	0.172
$\dot{\gamma}$ (s^{-1})	τ (Pa)						
100.00	8.07	8.27	8.45	9.04	9.58	9.74	10.30
79.40	7.54	7.71	7.87	8.39	8.89	9.02	9.56
63.10	7.07	7.22	7.36	7.83	8.27	8.39	8.88
50.10	6.65	6.79	6.91	7.33	7.74	7.84	8.30
39.80	6.27	6.40	6.51	6.88	7.26	7.35	7.78
31.60	5.94	6.05	6.15	6.48	6.84	6.92	7.32
25.10	5.63	5.74	5.82	6.12	6.45	6.53	6.89
20.00	5.36	5.46	5.53	5.79	6.11	6.18	6.51
15.80	5.11	5.20	5.26	5.50	5.80	5.86	6.17
12.60	4.88	4.96	5.01	5.23	5.51	5.57	5.85
10.00	4.67	4.74	4.79	4.99	5.26	5.30	5.57
7.94	4.47	4.54	4.58	4.76	5.02	5.06	5.30
6.31	4.29	4.36	4.39	4.55	4.79	4.83	5.06
5.01	4.12	4.18	4.22	4.36	4.59	4.62	4.83
3.98	3.97	4.02	4.05	4.18	4.40	4.42	4.63
3.16	3.82	3.87	3.90	4.01	4.22	4.24	4.43
2.51	3.68	3.73	3.75	3.85	4.05	4.07	4.24
2.00	3.55	3.59	3.61	3.70	3.89	3.90	4.07
1.58	3.42	3.47	3.48	3.56	3.74	3.75	3.91
1.26	3.30	3.34	3.35	3.42	3.59	3.60	3.75
1.00	3.19	3.22	3.23	3.29	3.45	3.46	3.60
τ_γ (Pa)	2.233	2.274	2.268	2.283	2.407	2.395	2.437
K (Pa.s^n)	1.009	1.010	1.023	1.074	1.122	1.141	1.237
n	0.379	0.384	0.388	0.397	0.401	0.402	0.400
τ_γ^*	1.000	1.018	1.016	1.022	1.078	1.073	1.091
K*	1.000	1.000	1.014	1.065	1.111	1.130	1.225
n*	1.000	1.013	1.025	1.048	1.057	1.060	1.054

Table 7: Measurements obtained with an unweighted KCl/polymer-based fluid and sand particles between 63 and 90µm and for volumetric concentrations between 13 and 23%.

	Mix#7	Mix#8	Mix#9	Mix#10	Mix#11	Mix#12
ρ (kg/m^3)	1280	1309	1346	1375	1409	1440
Φ	0.127	0.145	0.169	0.187	0.209	0.229
Φ*	0.205	0.235	0.273	0.303	0.338	0.370
$\dot{\gamma}$ (s^{-1})	τ (Pa)					
100.00	11.10	11.90	13.00	14.20	15.60	17.70
79.40	10.30	11.00	12.00	13.00	14.30	16.20
63.10	9.53	10.20	11.10	12.00	13.20	14.90
50.10	8.89	9.51	10.30	11.20	12.20	13.70
39.80	8.31	8.88	9.61	10.40	11.30	12.70
31.60	7.80	8.32	8.98	9.67	10.50	11.80
25.10	7.34	7.81	8.42	9.04	9.81	10.90
20.00	6.92	7.36	7.91	8.48	9.18	10.20
15.80	6.54	6.95	7.45	7.98	8.62	9.57
12.60	6.20	6.57	7.04	7.52	8.10	8.98
10.00	5.88	6.23	6.66	7.11	7.64	8.45
7.94	5.60	5.92	6.32	6.73	7.22	7.97
6.31	5.33	5.64	6.00	6.38	6.83	7.53
5.01	5.09	5.38	5.71	6.07	6.48	7.12
3.98	4.87	5.13	5.45	5.77	6.16	6.76
3.16	4.65	4.90	5.20	5.50	5.85	6.41
2.51	4.46	4.69	4.96	5.25	5.58	6.09
2.00	4.27	4.49	4.75	5.01	5.32	5.80
1.58	4.10	4.31	4.54	4.79	5.07	5.52
1.26	3.93	4.13	4.35	4.58	4.84	5.26
1.00	3.77	3.96	4.16	4.38	4.62	5.01
τ_γ (Pa)	2.577	2.671	2.799	2.943	3.085	3.342
K (Pa.s^n)	1.273	1.367	1.452	1.533	1.644	1.797
n	0.411	0.413	0.422	0.431	0.439	0.450
τ_γ^*	1.154	1.196	1.253	1.318	1.382	1.496
K*	1.261	1.354	1.439	1.519	1.629	1.780
n*	1.085	1.089	1.112	1.136	1.158	1.186

Table 8: Measurements obtained with an unweighted KCl/polymer-based fluid and sand particles between 90 and 125µm for volumetric concentrations between 0 and 11%.

	Base	Mix#1	Mix#2	Mix#3	Mix#4	Mix#5	Mix#6
ρ (kg/m^3)	1082	1097	1123	1153	1185	1216	1250
Φ	0.000	0.010	0.027	0.046	0.066	0.086	0.107
Φ*	0.000	0.016	0.043	0.074	0.107	0.139	0.173
$\dot{\gamma}$ (s^{-1})	τ (Pa)						
100.00	8.04	8.21	8.47	8.75	9.09	9.49	9.97
79.40	7.51	7.65	7.89	8.14	8.43	8.79	9.23
63.10	7.04	7.16	7.38	7.60	7.85	8.18	8.60
50.10	6.63	6.73	6.93	7.12	7.34	7.65	8.04
39.80	6.25	6.34	6.53	6.70	6.90	7.19	7.54
31.60	5.92	6.00	6.17	6.33	6.51	6.78	7.10
25.10	5.62	5.69	5.84	5.99	6.15	6.40	6.70
20.00	5.34	5.40	5.55	5.69	5.84	6.06	6.34
15.80	5.10	5.15	5.28	5.41	5.55	5.75	6.01
12.60	4.87	4.91	5.04	5.16	5.28	5.47	5.71
10.00	4.66	4.70	4.81	4.93	5.04	5.21	5.44
7.94	4.46	4.50	4.61	4.72	4.82	4.97	5.19
6.31	4.29	4.31	4.42	4.52	4.62	4.75	4.95
5.01	4.12	4.14	4.24	4.34	4.43	4.55	4.74
3.98	3.96	3.98	4.08	4.17	4.25	4.36	4.54
3.16	3.82	3.83	3.92	4.01	4.08	4.18	4.35
2.51	3.68	3.69	3.77	3.86	3.92	4.01	4.17
2.00	3.55	3.56	3.63	3.71	3.78	3.85	4.01
1.58	3.42	3.43	3.50	3.58	3.64	3.70	3.85
1.26	3.30	3.30	3.37	3.45	3.50	3.56	3.69
1.00	3.19	3.19	3.25	3.32	3.37	3.42	3.55
τ_γ (Pa)	2.242	2.246	2.281	2.378	2.435	2.366	2.439
K (Pa.s^n)	1.002	1.001	1.031	1.014	1.012	1.128	1.186
n	0.379	0.385	0.387	0.397	0.406	0.398	0.399
τ_γ^*	1.000	1.002	1.018	1.061	1.086	1.055	1.088
K*	1.000	0.999	1.029	1.012	1.010	1.125	1.184
n*	1.000	1.016	1.021	1.047	1.072	1.049	1.052

Table 9: Measurements obtained with an unweighted KCl/polymer-based fluid and sand particles between 90 and 125µm and for volumetric concentrations between 13 and 23%.

	Mix#7	Mix#8	Mix#9	Mix#10	Mix#11	Mix#12
ρ (kg/m^3)	1281	1316	1344	1382	1416	1443
Φ	0.127	0.150	0.167	0.192	0.213	0.230
Φ*	0.205	0.242	0.270	0.310	0.344	0.372
$\dot{\gamma}$ (s^{-1})	τ (Pa)					
100.00	10.60	11.50	12.40	13.80	15.40	17.00
79.40	9.81	10.70	11.50	12.70	14.10	15.60
63.10	9.13	9.90	10.60	11.70	13.00	14.30
50.10	8.53	9.22	9.89	10.90	12.00	13.20
39.80	7.99	8.62	9.23	10.10	11.10	12.20
31.60	7.51	8.08	8.64	9.44	10.40	11.40
25.10	7.08	7.61	8.11	8.84	9.69	10.60
20.00	6.69	7.17	7.64	8.30	9.07	9.89
15.80	6.34	6.78	7.21	7.82	8.52	9.26
12.60	6.02	6.43	6.82	7.38	8.02	8.70
10.00	5.72	6.10	6.47	6.98	7.57	8.20
7.94	5.45	5.81	6.14	6.62	7.16	7.74
6.31	5.20	5.53	5.84	6.28	6.78	7.31
5.01	4.97	5.28	5.57	5.97	6.44	6.92
3.98	4.76	5.04	5.31	5.69	6.12	6.57
3.16	4.55	4.82	5.07	5.42	5.82	6.24
2.51	4.36	4.61	4.85	5.18	5.55	5.93
2.00	4.19	4.42	4.64	4.95	5.29	5.65
1.58	4.02	4.23	4.44	4.73	5.05	5.37
1.26	3.86	4.06	4.25	4.52	4.82	5.12
1.00	3.70	3.89	4.07	4.32	4.60	4.88
τ_γ (Pa)	2.523	2.632	2.733	2.938	3.128	3.282
K (Pa.s^n)	1.258	1.344	1.429	1.490	1.592	1.730
n	0.401	0.408	0.414	0.429	0.441	0.449
τ_γ^*	1.125	1.174	1.219	1.311	1.396	1.464
K*	1.256	1.341	1.425	1.487	1.589	1.726
n*	1.059	1.077	1.091	1.133	1.164	1.185

Table 10: Measurements obtained with an unweighted KCl/polymer-based fluid and sand particles between 125 and 150µm for volumetric concentrations between 0 and 11%.

	Base	Mix#1	Mix#2	Mix#3	Mix#4	Mix#5	Mix#6
ρ (kg/m^3)	1083	1098	1125	1155	1184	1219	1243
Φ	0.000	0.010	0.027	0.046	0.064	0.087	0.102
Φ*	0.000	0.016	0.044	0.074	0.103	0.139	0.165
$\dot{\gamma}$ (s^{-1})	τ (Pa)						
100.00	7.85	8.27	8.27	8.53	8.77	9.10	9.60
79.40	7.32	7.70	7.70	7.91	8.13	8.46	8.89
63.10	6.86	7.19	7.19	7.38	7.58	7.89	8.28
50.10	6.45	6.74	6.74	6.91	7.09	7.38	7.75
39.80	6.08	6.35	6.35	6.49	6.66	6.94	7.29
31.60	5.75	5.99	5.99	6.12	6.28	6.53	6.88
25.10	5.45	5.67	5.67	5.79	5.94	6.18	6.50
20.00	5.18	5.38	5.38	5.49	5.64	5.85	6.16
15.80	4.93	5.11	5.11	5.22	5.36	5.56	5.85
12.60	4.70	4.87	4.87	4.98	5.10	5.29	5.57
10.00	4.49	4.65	4.65	4.75	4.87	5.05	5.31
7.94	4.30	4.45	4.45	4.55	4.65	4.82	5.07
6.31	4.12	4.26	4.26	4.35	4.45	4.61	4.84
5.01	3.96	4.09	4.09	4.17	4.27	4.42	4.64
3.98	3.81	3.93	3.93	4.01	4.10	4.24	4.44
3.16	3.66	3.77	3.77	3.85	3.93	4.07	4.26
2.51	3.52	3.63	3.63	3.70	3.78	3.91	4.09
2.00	3.39	3.49	3.49	3.56	3.64	3.76	3.93
1.58	3.27	3.36	3.36	3.43	3.50	3.61	3.78
1.26	3.15	3.24	3.24	3.30	3.37	3.47	3.63
1.00	3.03	3.12	3.12	3.18	3.24	3.34	3.49
τ_γ (Pa)	2.089	2.189	2.189	2.285	2.312	2.331	2.399
K (Pa.s^n)	1.000	0.991	0.991	0.965	1.002	1.081	1.166
n	0.378	0.392	0.392	0.403	0.402	0.396	0.392
τ_γ^*	1.000	1.048	1.048	1.094	1.107	1.116	1.149
K*	1.000	0.991	0.991	0.965	1.002	1.081	1.166
n*	1.000	1.036	1.036	1.065	1.063	1.048	1.037

Table 11: Measurements obtained with an unweighted KCl/polymer-based fluid and sand particles between 125 and 150µm and for volumetric concentrations between 13 and 23%.

	Mix#7	Mix#8	Mix#9	Mix#10	Mix#11	Mix#12
ρ (kg/m^3)	1278	1314				
Φ	0.124	0.147	0.170	0.190	0.210	0.230
Φ*	0.200	0.238	0.274	0.306	0.338	0.371
$\dot{\gamma}$ (s^{-1})	τ (Pa)					
100.00	10.30	11.10	12.00	13.90	16.00	17.70
79.40	9.53	10.30	11.10	12.80	14.70	16.20
63.10	8.88	9.60	10.30	11.80	13.50	14.90
50.10	8.30	8.96	9.62	10.90	12.50	13.80
39.80	7.79	8.38	8.98	10.20	11.60	12.70
31.60	7.33	7.87	8.41	9.50	10.80	11.80
25.10	6.92	7.41	7.91	8.90	10.00	11.00
20.00	6.54	7.00	7.45	8.36	9.41	10.30
15.80	6.20	6.62	7.03	7.87	8.84	9.66
12.60	5.89	6.28	6.66	7.42	8.32	9.08
10.00	5.61	5.96	6.32	7.02	7.85	8.56
7.94	5.34	5.67	6.00	6.66	7.42	8.08
6.31	5.10	5.41	5.71	6.32	7.03	7.64
5.01	4.87	5.16	5.44	6.01	6.67	7.24
3.98	4.66	4.93	5.19	5.72	6.34	6.87
3.16	4.46	4.72	4.96	5.45	6.04	6.53
2.51	4.28	4.51	4.74	5.20	5.75	6.21
2.00	4.10	4.33	4.53	4.97	5.48	5.92
1.58	3.94	4.14	4.34	4.75	5.23	5.64
1.26	3.78	3.97	4.15	4.54	4.99	5.38
1.00	3.62	3.81	3.98	4.34	4.77	5.13
τ_γ (Pa)	2.427	2.496	2.602	2.945	3.248	3.467
K (Pa.s^n)	1.274	1.388	1.459	1.503	1.641	1.796
n	0.393	0.394	0.403	0.429	0.444	0.448
τ_γ^*	1.162	1.195	1.246	1.410	1.555	1.660
K*	1.274	1.388	1.459	1.503	1.641	1.797
n*	1.039	1.043	1.065	1.135	1.173	1.184

C Effect of Barite Concentration on the Rheological Behavior of a WBM

Table 12 and Table 13 provide the measurements obtained with a KCl/polymer-based fluid and barite for volumetric concentrations between 0 and 23%.

Table 12: Measurements obtained with KCl/polymer-based fluid and barite for volumetric concentrations between 0 and 11%.

	Base	Mix#1	Mix#2	Mix#3	Mix#4	Mix#5	Mix#6
ρ (kg/m³)	1083	1114	1177	1239	1301	1364	1426
Φ	0.000	0.010	0.030	0.050	0.070	0.090	0.110
Φ*	0.000	0.016	0.048	0.079	0.111	0.143	0.175
$\dot{\gamma}$ (s^{-1})	τ (Pa)						
100.00	8.06	8.24	8.64	9.12	9.50	10.20	10.80
79.40	7.53	7.69	8.04	8.46	8.79	9.38	9.93
63.10	7.05	7.19	7.51	7.89	8.17	8.69	9.17
50.10	6.63	6.76	7.04	7.38	7.62	8.08	8.51
39.80	6.26	6.37	6.63	6.93	7.14	7.55	7.92
31.60	5.92	6.02	6.25	6.52	6.71	7.08	7.41
25.10	5.62	5.70	5.92	6.16	6.32	6.65	6.94
20.00	5.34	5.42	5.61	5.83	5.97	6.27	6.52
15.80	5.09	5.16	5.33	5.53	5.65	5.93	6.14
12.60	4.86	4.92	5.08	5.26	5.37	5.61	5.80
10.00	4.65	4.70	4.85	5.01	5.10	5.33	5.49
7.94	4.45	4.50	4.64	4.79	4.87	5.07	5.21
6.31	4.27	4.32	4.44	4.58	4.65	4.83	4.95
5.01	4.10	4.14	4.26	4.38	4.44	4.61	4.72
3.98	3.94	3.98	4.09	4.20	4.26	4.41	4.50
3.16	3.80	3.83	3.93	4.04	4.08	4.23	4.30
2.51	3.65	3.69	3.78	3.88	3.92	4.05	4.11
2.00	3.52	3.55	3.64	3.73	3.77	3.89	3.94
1.58	3.40	3.42	3.50	3.59	3.62	3.74	3.78
1.26	3.27	3.30	3.37	3.46	3.49	3.60	3.63
1.00	3.16	3.18	3.25	3.33	3.36	3.46	3.48
τ_y (Pa)	2.192	2.221	2.327	2.356	2.398	2.502	2.458
K (Pa.s^n)	1.021	1.017	0.990	1.037	1.024	1.028	1.094
n	0.378	0.384	0.402	0.405	0.418	0.435	0.439
τ_y^*	1.000	1.013	1.061	1.075	1.094	1.141	1.121
K*	1.000	0.995	0.969	1.015	1.003	1.007	1.071
n*	1.000	1.017	1.065	1.073	1.108	1.151	1.163

Table 13: Measurements obtained with KCl/polymer-based fluid and barite for volumetric concentrations between 13 and 23%.

	Mix#7	Mix#8	Mix#9	Mix#10	Mix#11	Mix#12
ρ (kg/m^3)	1488	1551	1613	1675	1738	1800
Φ	0.130	0.150	0.170	0.190	0.210	0.230
Φ*	0.206	0.238	0.270	0.302	0.333	0.365
$\dot{\gamma}$ (s^{-1})	τ (Pa)					
100.00	11.50	12.30	12.70	13.80	14.90	16.00
79.40	10.60	11.20	11.60	12.50	13.50	14.40
63.10	9.73	10.30	10.60	11.40	12.20	13.00
50.10	9.01	9.51	9.73	10.40	11.10	11.80
39.80	8.37	8.80	8.97	9.60	10.20	10.80
31.60	7.80	8.18	8.31	8.85	9.37	9.84
25.10	7.29	7.62	7.72	8.19	8.64	9.04
20.00	6.83	7.12	7.19	7.61	8.00	8.34
15.80	6.42	6.67	6.72	7.09	7.43	7.72
12.60	6.05	6.27	6.30	6.63	6.93	7.18
10.00	5.71	5.91	5.93	6.22	6.48	6.70
7.94	5.41	5.59	5.60	5.86	6.09	6.28
6.31	5.13	5.29	5.30	5.53	5.73	5.90
5.01	4.88	5.03	5.02	5.23	5.42	5.57
3.98	4.65	4.78	4.78	4.97	5.14	5.27
3.16	4.44	4.56	4.55	4.73	4.88	5.00
2.51	4.24	4.35	4.35	4.51	4.65	4.76
2.00	4.06	4.17	4.16	4.31	4.44	4.54
1.58	3.89	3.99	3.99	4.12	4.25	4.35
1.26	3.73	3.83	3.83	3.95	4.07	4.17
1.00	3.58	3.67	3.67	3.80	3.91	4.00
τ_γ (Pa)	2.530	2.647	2.724	2.832	2.956	3.059
K (Pa.s^n)	1.119	1.096	1.020	1.038	1.029	1.015
n	0.451	0.470	0.494	0.510	0.531	0.552
τ_γ^*	1.154	1.208	1.242	1.292	1.348	1.395
K*	1.096	1.074	0.999	1.017	1.008	0.994
n*	1.194	1.245	1.308	1.352	1.407	1.461

D Effect of Sand Particle Concentration on the Rheological Behavior of a Weighted WBM

Table 14 and Table 15 provide the measurements obtained with a 1250kg/m^3 KCl/polymer-based fluid and fine sand particles (< 45µm) for volumetric concentrations between 0 and 23%.

Table 16 and Table 17 provide the measurements obtained with a 1500kg/m^3 KCl/polymer-based fluid and fine sand particles (< 45µm) for volumetric concentrations between 0 and 23%.

Table 18 and Table 19 provide the measurements obtained with a 1750kg/m^3 KCl/polymer-based fluid and fine sand particles (< 45µm) for volumetric concentrations between 0 and 23%.

Table 14: Measurements obtained with a 1250kg/m^3 KCl/polymer-based fluid and fine sand particles (< 45µm) for volumetric concentrations between 0 and 11%.

	Base	Mix#0	Mix#1	Mix#2	Mix#3	Mix#4	Mix#5
ρ (kg/m^3)	1085	1246	1260	1291	1319	1346	1377
Φ	0.000	0.052	0.061	0.082	0.101	0.119	0.140
Φ*	0.000	0.082	0.096	0.128	0.157	0.185	0.215
$\dot{\gamma}$ (s^{-1})	τ (Pa)						
100.00	8.04	9.19	9.41	9.80	10.50	11.40	12.40
79.40	7.51	8.53	8.72	9.07	9.65	10.50	11.40
63.10	7.03	7.94	8.12	8.42	8.94	9.72	10.50
50.10	6.61	7.43	7.58	7.85	8.32	9.03	9.76
39.80	6.23	6.97	7.11	7.34	7.77	8.42	9.09
31.60	5.90	6.56	6.68	6.89	7.28	7.88	8.49
25.10	5.59	6.19	6.30	6.49	6.84	7.39	7.95
20.00	5.31	5.86	5.96	6.12	6.45	6.95	7.46
15.80	5.06	5.56	5.65	5.79	6.09	6.56	7.03
12.60	4.83	5.29	5.37	5.50	5.77	6.20	6.63
10.00	4.62	5.04	5.11	5.22	5.48	5.87	6.28
7.94	4.42	4.81	4.88	4.98	5.21	5.58	5.95
6.31	4.24	4.60	4.66	4.75	4.96	5.31	5.66
5.01	4.07	4.40	4.46	4.54	4.74	5.06	5.39
3.98	3.91	4.22	4.27	4.35	4.53	4.83	5.14
3.16	3.77	4.05	4.10	4.17	4.34	4.62	4.91
2.51	3.62	3.89	3.94	4.00	4.16	4.42	4.70
2.00	3.49	3.74	3.78	3.84	4.00	4.24	4.51
1.58	3.37	3.60	3.64	3.69	3.84	4.07	4.32
1.26	3.24	3.46	3.50	3.55	3.69	3.90	4.15
1.00	3.12	3.34	3.37	3.42	3.55	3.75	3.99
τ_γ (Pa)	2.160	2.355	2.388	2.439	2.561	2.634	2.829
K (Pa.s^n)	1.021	1.045	1.048	1.046	1.062	1.189	1.233
n	0.378	0.406	0.411	0.422	0.434	0.432	0.443
τ_γ^*	1.000	1.090	1.106	1.129	1.186	1.219	1.310
K*	1.000	1.023	1.026	1.024	1.040	1.165	1.208
n*	1.000	1.073	1.087	1.116	1.149	1.142	1.172

Table 15: Measurements obtained with a 1250kg/m^3 KCl/polymer-based fluid and fine sand particles (< 45µm) for volumetric concentrations between 13 and 23%.

	Mix#6	Mix#7	Mix#8	Mix#9	Mix#10	Mix#11	Mix#12
ρ (kg/m^3)	1406	1434	1462	1494	1523	1552	1579
Φ	0.159	0.178	0.197	0.219	0.239	0.259	0.2762
Φ*	0.244	0.272	0.300	0.332	0.361	0.390	0.4153
$\dot{\gamma}$ (s^{-1})	τ (Pa)						
100.00	13.50	14.90	16.50	18.00	20.50	23.40	27
79.40	12.40	13.60	15.10	16.40	18.70	21.30	24.6
63.10	11.40	12.50	13.90	15.10	17.10	19.50	22.5
50.10	10.60	11.60	12.80	13.90	15.80	17.90	20.6
39.80	9.82	10.70	11.90	12.80	14.60	16.50	19
31.60	9.15	10.00	11.00	11.90	13.50	15.30	17.6
25.10	8.56	9.33	10.30	11.10	12.50	14.20	16.4
20.00	8.02	8.74	9.60	10.40	11.70	13.30	15.3
15.80	7.54	8.20	9.00	9.74	11.00	12.40	14.3
12.60	7.11	7.72	8.47	9.17	10.30	11.70	13.4
10.00	6.72	7.29	7.99	8.65	9.73	11.00	12.7
7.94	6.37	6.90	7.55	8.19	9.20	10.40	12
6.31	6.05	6.55	7.16	7.77	8.73	9.89	11.4
5.01	5.76	6.23	6.81	7.40	8.31	9.42	10.9
3.98	5.49	5.94	6.49	7.06	7.93	9.00	10.5
3.16	5.24	5.67	6.19	6.76	7.59	8.62	10
2.51	5.02	5.42	5.93	6.48	7.28	8.27	9.66
2.00	4.81	5.20	5.68	6.22	6.99	7.96	9.32
1.58	4.61	4.99	5.45	5.98	6.73	7.68	9.01
1.26	4.42	4.79	5.24	5.76	6.48	7.41	8.72
1.00	4.25	4.60	5.03	5.55	6.25	7.15	8.44
τ_γ (Pa)	3.053	3.362	3.677	4.260	4.833	5.666	6.8916
K (Pa.s^n)	1.278	1.328	1.440	1.390	1.517	1.597	1.6607
n	0.455	0.467	0.473	0.496	0.506	0.522	0.5408
τ_γ^*	1.414	1.556	1.702	1.972	2.237	2.623	3.1902
K*	1.252	1.301	1.410	1.361	1.486	1.564	1.6265
n*	1.202	1.236	1.252	1.312	1.338	1.380	1.4305

Table 16: Measurements obtained with a 15000kg/m^3 KCl/polymer-based fluid and fine sand particles (< 45µm) for volumetric concentrations between 0 and 11%.

	Base	Mix#0	Mix#1	Mix#2	Mix#3	Mix#4	Mix#5
ρ (kg/m^3)	1084	1492	1506	1527	1551	1575	1600
Φ	0.000	0.132	0.142	0.158	0.176	0.194	0.213
Φ*	0.000	0.209	0.226	0.250	0.277	0.305	0.332
$\dot{\gamma}$ (s^{-1})	τ (Pa)						
100.00	7.97	11.00	11.30	12.20	13.20	14.40	15.70
79.40	7.44	10.10	10.30	11.10	12.00	13.10	14.30
63.10	6.96	9.31	9.51	10.20	11.00	12.00	13.10
50.10	6.54	8.63	8.79	9.43	10.20	11.00	12.00
39.80	6.17	8.02	8.16	8.73	9.38	10.10	11.00
31.60	5.83	7.48	7.60	8.11	8.70	9.36	10.20
25.10	5.53	7.00	7.10	7.56	8.09	8.69	9.42
20.00	5.25	6.57	6.65	7.07	7.55	8.10	8.77
15.80	5.00	6.18	6.25	6.63	7.07	7.57	8.18
12.60	4.77	5.84	5.89	6.24	6.64	7.10	7.66
10.00	4.56	5.52	5.57	5.89	6.25	6.67	7.20
7.94	4.37	5.24	5.28	5.57	5.91	6.30	6.78
6.31	4.19	4.98	5.01	5.28	5.60	5.96	6.41
5.01	4.02	4.75	4.77	5.02	5.31	5.65	6.07
3.98	3.87	4.53	4.55	4.79	5.06	5.37	5.77
3.16	3.72	4.33	4.35	4.57	4.82	5.12	5.50
2.51	3.58	4.15	4.17	4.37	4.61	4.88	5.25
2.00	3.45	3.98	4.00	4.19	4.41	4.67	5.02
1.58	3.32	3.83	3.84	4.02	4.23	4.48	4.81
1.26	3.20	3.68	3.69	3.86	4.06	4.30	4.61
1.00	3.09	3.54	3.54	3.71	3.90	4.13	4.43
τ_γ (Pa)	2.154	2.593	2.619	2.747	2.870	3.085	3.286
K (Pa.s^n)	0.991	1.012	0.995	1.036	1.102	1.125	1.222
n	0.382	0.458	0.468	0.478	0.484	0.500	0.503
τ_γ^*	1.000	1.204	1.216	1.275	1.333	1.433	1.526
K*	1.000	1.021	1.004	1.045	1.112	1.135	1.232
n*	1.000	1.198	1.225	1.251	1.267	1.308	1.316

Table 17: Measurements obtained with a 1500kg/m^3 KCl/polymer-based fluid and fine sand particles (< 45µm) for volumetric concentrations between 13 and 23%.

	Mix#6	Mix#7	Mix#8	Mix#9	Mix#10	Mix#11	Mix#12
ρ (kg/m^3)	1625	1649	1670	1699	1721	1743	1765
Φ	0.232	0.249	0.266	0.287	0.303	0.320	0.337
Φ*	0.361	0.388	0.412	0.443	0.468	0.492	0.516
$\dot{\gamma}$ (s^{-1}))	τ (Pa)						
100.00	17.10	18.90	21.40	24.00	26.90	30.20	33.9
79.40	15.50	17.10	19.30	21.70	24.30	27.20	30.6
63.10	14.10	15.60	17.60	19.70	22.10	24.70	27.8
50.10	12.90	14.30	16.00	18.00	20.10	22.50	25.3
39.80	11.90	13.10	14.70	16.40	18.40	20.60	23.2
31.60	11.00	12.00	13.50	15.10	17.00	19.00	21.3
25.10	10.20	11.10	12.50	14.00	15.60	17.50	19.7
20.00	9.43	10.30	11.60	12.90	14.50	16.30	18.3
15.80	8.80	9.64	10.80	12.00	13.50	15.20	17.1
12.60	8.23	9.01	10.10	11.20	12.60	14.20	16
10.00	7.73	8.46	9.43	10.50	11.80	13.30	15
7.94	7.29	7.96	8.88	9.93	11.20	12.60	14.2
6.31	6.88	7.52	8.38	9.39	10.60	11.90	13.4
5.01	6.52	7.13	7.94	8.90	10.00	11.30	12.8
3.98	6.20	6.78	7.55	8.47	9.54	10.80	12.2
3.16	5.91	6.46	7.19	8.08	9.12	10.30	11.7
2.51	5.64	6.17	6.87	7.73	8.73	9.89	11.2
2.00	5.40	5.91	6.58	7.41	8.39	9.51	10.8
1.58	5.18	5.66	6.31	7.12	8.08	9.16	10.4
1.26	4.97	5.44	6.07	6.86	7.78	8.84	10
1.00	4.78	5.23	5.84	6.61	7.51	8.54	9.71
τ_γ (Pa)	3.616	4.031	4.512	5.246	6.022	6.951	7.9729
K (Pa.s^n)	1.248	1.300	1.428	1.477	1.609	1.734	1.8966
n	0.515	0.528	0.535	0.551	0.556	0.562	0.5668
τ_γ^*	1.679	1.872	2.095	2.436	2.796	3.228	3.702
K*	1.259	1.312	1.440	1.490	1.623	1.749	1.9132
n*	1.348	1.382	1.400	1.442	1.454	1.471	1.4833

Table 18: Measurements obtained with a 1750kg/m^3 KCl/polymer-based fluid and fine sand particles (< 45µm) for volumetric concentrations between 0 and 11%.

	Base	Mix#0	Mix#1	Mix#2	Mix#3	Mix#4	Mix#5
ρ (kg/m^3)	1082	1755	1765	1781	1802	1823	1841
Φ	0.000	0.217	0.226	0.241	0.258	0.277	0.293
Φ*	0.000	0.345	0.358	0.381	0.408	0.436	0.460
$\dot{\gamma}$ (s^{-1})	τ (Pa)						
100.00	7.98	15.80	16.20	17.60	19.10	21.00	23.40
79.40	7.44	14.30	14.70	15.80	17.10	18.90	21.00
63.10	6.97	13.00	13.30	14.30	15.50	17.00	18.90
50.10	6.55	11.80	12.10	13.00	14.00	15.40	17.00
39.80	6.17	10.80	11.00	11.80	12.80	14.00	15.40
31.60	5.83	9.94	10.10	10.80	11.70	12.70	14.10
25.10	5.53	9.17	9.33	9.96	10.70	11.70	12.90
20.00	5.25	8.48	8.62	9.19	9.84	10.70	11.80
15.80	5.00	7.87	7.99	8.51	9.10	9.89	10.90
12.60	4.77	7.34	7.44	7.91	8.44	9.16	10.10
10.00	4.55	6.86	6.95	7.38	7.87	8.53	9.36
7.94	4.36	6.44	6.52	6.91	7.36	7.97	8.74
6.31	4.18	6.06	6.13	6.49	6.91	7.47	8.19
5.01	4.01	5.72	5.78	6.12	6.51	7.03	7.71
3.98	3.85	5.42	5.48	5.79	6.15	6.65	7.29
3.16	3.70	5.15	5.20	5.49	5.84	6.30	6.91
2.51	3.56	4.90	4.95	5.23	5.55	5.99	6.57
2.00	3.43	4.68	4.72	4.99	5.30	5.72	6.27
1.58	3.30	4.48	4.52	4.77	5.07	5.47	6.01
1.26	3.17	4.29	4.33	4.57	4.86	5.25	5.76
1.00	3.06	4.12	4.15	4.39	4.67	5.04	5.54
τ_γ (Pa)	2.089	3.078	3.122	3.342	3.542	3.842	4.263
K (Pa.s^n)	1.028	1.113	1.106	1.129	1.197	1.269	1.351
n	0.377	0.528	0.536	0.549	0.556	0.565	0.575
τ_γ^*	1.000	1.474	1.495	1.600	1.696	1.839	2.041
K*	1.000	1.083	1.076	1.098	1.165	1.235	1.315
n*	1.000	1.401	1.422	1.457	1.474	1.499	1.525

Table 19: Measurements obtained with a 1750kg/m^3 KCl/polymer-based fluid and fine sand particles (< 45µm) for volumetric concentrations between 13 and 23%.

	Mix#6	Mix#7	Mix#8	Mix#9	Mix#10	Mix#11	Mix#12
ρ (kg/m^3)	1857	1874	1889	1905	1924	1940	1958
Φ	0.307	0.322	0.335	0.348	0.366	0.380	0.395
Φ*	0.482	0.503	0.523	0.544	0.569	0.590	0.612
$\dot{\gamma}$ (s^{-1})	τ (Pa)						
100.00	25.30	28.00	31.00	35.00	40.70	46.60	53.5
79.40	22.60	25.00	27.70	31.20	36.30	41.60	47.7
63.10	20.30	22.50	24.80	28.00	32.50	37.30	42.8
50.10	18.30	20.20	22.40	25.20	29.40	33.60	38.6
39.80	16.60	18.30	20.20	22.80	26.60	30.50	35
31.60	15.10	16.70	18.40	20.80	24.20	27.70	31.9
25.10	13.80	15.20	16.80	19.00	22.10	25.40	29.2
20.00	12.70	14.00	15.40	17.40	20.30	23.30	26.8
15.80	11.70	12.90	14.20	16.00	18.70	21.50	24.8
12.60	10.80	11.90	13.10	14.90	17.30	20.00	23
10.00	10.10	11.10	12.20	13.80	16.20	18.60	21.5
7.94	9.39	10.30	11.40	12.90	15.10	17.40	20.1
6.31	8.81	9.70	10.70	12.20	14.20	16.40	18.9
5.01	8.30	9.14	10.10	11.50	13.40	15.50	17.9
3.98	7.85	8.65	9.58	10.90	12.70	14.80	17
3.16	7.45	8.21	9.10	10.40	12.10	14.10	16.3
2.51	7.09	7.83	8.69	9.89	11.60	13.50	15.6
2.00	6.78	7.49	8.32	9.49	11.20	13.00	15
1.58	6.50	7.18	8.00	9.13	10.70	12.50	14.5
1.26	6.25	6.91	7.70	8.81	10.40	12.10	14
1.00	6.02	6.66	7.44	8.52	10.10	11.70	13.6
τ_y (Pa)	4.729	5.269	5.980	6.924	8.204	9.686	11.256
K (Pa.s^n)	1.371	1.472	1.541	1.692	1.931	2.145	2.4474
n	0.587	0.594	0.605	0.609	0.612	0.617	0.6177
τ_y^*	2.264	2.523	2.863	3.315	3.928	4.637	5.389
K*	1.335	1.433	1.500	1.646	1.880	2.087	2.382
n*	1.557	1.575	1.604	1.616	1.624	1.637	1.638

Part II

Published papers

Unfortunately, the papers cannot be included in the online version due to copyright.

Paper I

Cayeux, E., Daireaux, B., Dvergsnes, E.W., Leulseged, A., Bruun, B. T., Herbert, M. : *Advanced Drilling Simulation Environment for Testing New Drilling Automation Techniques and Practices.* Paper SPE-150941-PA. In the proceedings of the SPE/IADC Drilling Conference and Exhibition held in San Antonio, California, USA, 6-8 March, 2012, and revised for publication. Original manuscript received for review 10 March, 2012. Revised manuscript received for review 22 June 2012. Paper peer approved 4 July, 2012 and printed in SPE Drilling & Completion Journal, Volume 27, Number 4, December 2012, pp. 559-573.

Paper II

Cayeux, E., Mesagan, T., Tanripada, S., Zidan, M., Fjelde, K.K.: *Real-Time Evaluation of Hole Cleaning Conditions Using a Transient Cuttings Transport Model*. SPE-163492-PA. In the proceedings of the SPE/IADC Drilling Conference and Exhibition held in Amsterdam, Netherlands, 5-7 March, 2013, and revised for publication. Original manuscript received for review 25 March, 2013. Revised manuscript received for review 17 December 2013. Paper peer approved 10 January, 2014 and printed in SPE Drilling and Completion, Volume 29, Number 1, 2014, pp. 5-21.

Paper III

Cayeux, E., Daireaux, B., Dvergsnes, E. W., Sælevik, G.: *Early Symptom Detection Based on Real-Time Evaluation of Downhole Conditions: Principles and Results from several North Sea Drilling Operations*. Paper SPE-150422-PA. In the proceedings of the SPE Intelligent Energy International held in Utrecht, The Netherlands, 27-29 March, 2012, and revised for publication. Original manuscript received for review 2 April, 2012. Revised manuscript received for review 22 June 2012. Paper peer approved 3 July, 2012 and printed in SPE Drilling & Completion Journal, Volume 27, Number 4, December, 2012, pp. 546-558

Paper IV

Cayeux, E., Kucs, R., Gibson, N.: *Mathematical Modelling of Drilling Operations Using Nitrogen Enriched Mud - a Case Study Using a Recorded Drilling Dataset*. SPE-167884-PA. In the proceedings of the Intelligent Energy Conference and Exhibition held in Utrecht, The Netherlands, 1–3 April 2014, and revised for publication. Original manuscript received for review 22 April, 2014. Revised manuscript received for review 31 July 2014. Paper peer approved 22 September, 2014 and printed in SPE Drilling and Completion, Volume 29, Number 4, 2014, pp. 438-453.

Paper V

Cayeux, E., Daireaux, B. and Dvergsnes, E. W: *Automation of Mud-Pump Management Application to Drilling Operations in the North-Sea*. Paper SPE-128285-PA. In the proceedings of the SPE/IADC Drilling Conference and Exhibition held in New Orleans, Louisiana, USA, 2-4 February, 2010, and revised for publication. Original manuscript received for review 11 February, 2010. Revised manuscripts received for review 15 July and 2 September, 2010. Paper peer approved 3 September, 2010 and printed in SPE Drilling & Completion Journal, Volume 26, Number 1, March 2011, pp. 41-51.

Paper VI

Cayeux, E., Daireaux, B. and Dvergsnes, E. W.: *Automation of Draw-works and Top-drive Management to Minimize Swab/Surge and Poor-Downhole-Condition Effects*. Paper SPE-128286-PA. In the proceedings of the SPE/IADC Drilling Conference and Exhibition held in New Orleans, Louisiana, USA, 2-4 February, 2010, and revised for publication. Original manuscript received for review 11 February, 2010. Revised manuscripts received for review 1 November, 2010 and 5 March, 2011. Paper peer approved 7 March, 2011 and printed in SPE Drilling & Completion Journal, Volume 26, Number 4, December 2011, pp. 557-568.